

S

SBML

- ▶ [Systems Biology Markup Language \(SBML\)](#)

Segmental Control

- ▶ [Spinal Cord, Integrated \(Non CPG\) Models of](#)

Self-Organizing Maps

- ▶ [Cortical Maps, Activity-Dependent Development](#)

SenseLab: Integration of Multidisciplinary Neuroscience Data

Gordon M. Shepherd¹, Thomas M. Morse¹, Luis Marenco^{2,3}, Kei Cheung^{2,3}, Ted Carnevale¹, Michele Migliore^{1,4}, Robert A. McDougal¹, Michael Hines¹ and Perry Miller^{2,3}

¹Department of Neurobiology, Yale University School of Medicine, New Haven, CT, USA

²Center for Medical Informatics, Yale University School of Medicine, New Haven, CT, USA

³VA Connecticut Healthcare System, West Haven, CT, USA

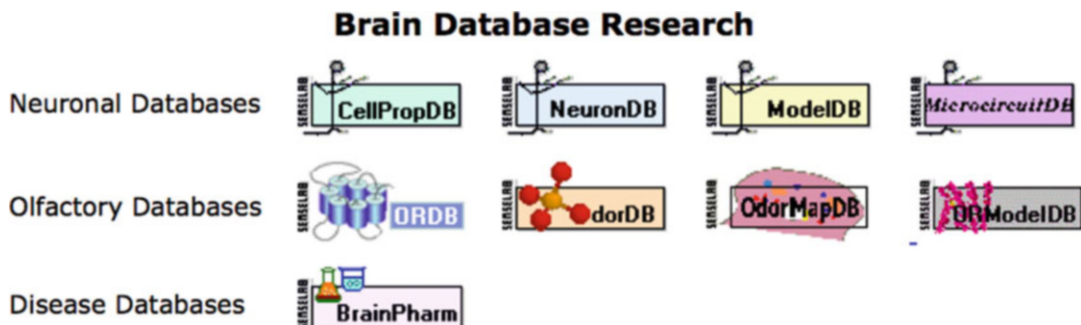
⁴Institute of Biophysics, National Research Council, Palermo, Italy

Definition

The SenseLab project involves novel informatics approaches to constructing databases and Web-enabled applications for collecting, modeling, analyzing, and sharing neuroscience information. The emphasis of SenseLab (<http://senselab.org>) is on building experimental data into integrated, multidisciplinary models of neurons and neural systems in order to gain insight into the neural basis of behavior. SenseLab is also part of the ▶ [Neuroscience Information Framework \(NIF\)](#) project and the International Neuroinformatics Coordinating Facility (INCF).

Detailed Description

SenseLab was founded in 1993 as part of the original Human Brain Project sponsored by the National Institutes of Health, National Science Foundation, and several other government funding agencies in the United States, which began the development of neuroinformatics tools in support of neuroscience research. Using the olfactory system as a model, SenseLab has built a suite of nine databases (see Fig. 1) to support research across multiple disciplines and at multiple scales of time and space. We test the validity and value of each database for its usefulness for our own research on synaptic organization and sensory processing and seek to develop



SenseLab: Integration of Multidisciplinary Neuroscience Data, Fig. 1 Suite of databases in SenseLab

principles for general application to other neural systems, as summarized in *The Synaptic Organization of the Brain* (Shepherd 2004) and *Handbook of Brain Microcircuits* (Shepherd and Grillner 2010).

SenseLab is built on three foundations. First is the informatics expertise provided by the Yale Center for Medical Informatics (<http://ycmi.med.yale.edu>). This was one of the first such centers in the United States, formed by Dr. Perry Miller in the 1980s, and has enabled SenseLab to have state-of-the-art informatics as an integral part of our approach by providing the digital infrastructure for the experimental data and for the online databases. This has enabled the different SenseLab databases to be developed in a tightly interoperational framework.

Second are databases for neuroscience data and computational models. The aim is to provide curated published models to enable computational neuroscientists efficiently to run published models to check them and use them to apply to their own research. The importance of computational models for integrating neuroscience data was envisaged in the original Human Brain Project (see Pechura and Martin 1991). This approach is being supported by four interoperational databases, starting with a simple neuron inventory and working up through canonical neurons to neuron models and finally microcircuit models. This sequence starts with **CellPropDB**, a database of currents, neurotransmitter receptors, and neurotransmitters

expressed in 30 types of neurons that can be searched across neurons (in parallel to Neurolex Neuron in the NIF). **NeuronDB** expands this to expression in different parts of the dendrites and axons of canonical neuron representations, enabling properties to be searched across neuronal compartments.

The quantitative integration of these properties occurs in the models contained in **ModelDB**. The modeling methods were introduced in neuroscience by Wilfrid Rall, with the first applications to brain neurons in the olfactory bulb (Rall and Shepherd 1968). Current studies rely widely on the modeling environment NEURON (Hines and Carnevale 2014). Dr. Michael Hines brought the NEURON simulation environment to SenseLab in 1995. ModelDB contains fully curated published models running in NEURON and over 50 other modeling programs, with functionality for searching for specific properties. The total number of entries is currently 801 models. Recently, **MicrocircuitDB** has been introduced to cover multineuronal circuits within specific brain regions. It currently contains 180 models for microcircuits in 24 brain regions.

In addition to these general neuron databases, SenseLab also supports research in the olfactory system with an extensive archive of properties related to the olfactory receptors. This is a particularly challenging task given that these receptors are the largest family in the genome (Buck and Axel 1991). The olfactory receptor

database (**ORDB**) serves this function with information related to over 14,000 chemosensory genes and proteins. A recent addition is **ModelORDB** for molecular models of olfactory ligand–olfactory receptor interactions, closely related to **OdorDB**, which contains data on the odor molecules that have been shown to interact with the olfactory receptors. These interactions generate activity in the receptor cells which set up different activity patterns representing different odors in the olfactory glomeruli of the olfactory bulb. **OdorMapDB** contains experimental data from functional imaging of these activity patterns, which are believed to be critical for the neural basis of olfactory perception.

A final database still under construction covers the domain of brain pharmacology (**BrainPharmDB**), which expands the information for normal function contained in the other databases to neurological disorders.

The third foundation of SenseLab is integration of our own research data, by developing computational models based on state-of-the-art computational techniques. Currently, we are applying the Rall approach to analyzing the lateral inhibitory network formed by mitral and granule cells in the olfactory bulb. Studies led by Michael Hines and Michele Migliore are constructing models which accurately represent experimental data on the differential distribution of olfactory inputs in the olfactory glomerular layer (Yu et al. 2013). We are introducing a new generation of three-dimensional models of the overlapping dendritic trees of mitral and granule cells (Migliore et al. 2013). This approach is being applied to experimental data from our own lab as well as in collaboration with other experimental labs.

SenseLab's current activities also include major contributions to neuroinformatics through participation in the Neuroscience Information Framework (NIF), the International Neuroinformatics Coordinating Facility (INCF), the Blue Brain Project (<http://bluebrain.epfl.ch/>), and the Human Brain Project (<http://humanbrainproject.eu/>). This work has included

developing **DISCO**, an automated resource discovery, registration, and interoperation framework designed to facilitate data integration among Internet resources for the NIF, and **Neurolex Neuron** as an inventory of basic properties characterizing different types of neurons (see <http://neuinfo.org>).

Acknowledgments We gratefully acknowledge funding from NIH grant DC009977.

References

- Buck L, Axel R (1991) A novel multigene family may encode odorant receptors – a molecular-basis for odor recognition. *Cell* 65:175–187
- Hines ML, Carnevale NT (2014) NEURON Simulation Environment. In: Kötaleksi JH, Crook S, (eds) Encyclopedia of computational neuroscience, Springer
- Migliore M, Cavarretta F, Hines ML, Shepherd GM (2013) Functional neurology of a brain system: a 3D olfactory bulb model to process natural odorants. *Funct Neurol* 2013 28(3):241–243
- Pechura CM, Martin JB (1991) Mapping the brain and its functions: integrating enabling technologies into neuroscience research. National Academy Press, Washington, DC
- Rall W, Shepherd GM (1968) Theoretical reconstruction of field potentials and dendrodendritic synaptic interactions in olfactory bulb. *J neurophysiol* 31:884–915
- Shepherd GM (2004) The synaptic organization of the brain, 5th edn. Oxford University Press, Oxford
- Shepherd GM, Grillner S (2010) Handbook of brain microcircuits. Oxford University Press, New York
- Yu Y, McTavish TS, Hines ML, Shepherd GM, Valenti C, Migliore M (2013) Sparse distributed representation of odors in a large-scale olfactory bulb circuit. *PLoS Comput Biol* 9:e1003014

Sensitivity Analysis

► Neuronal Parameter Sensitivity

Sensorimotor Control of Balance

► Neuromechanics of Postural Control

Sensorimotor Control of Posture

► Neuromechanics of Postural Control

Sensory Coding, Efficiency

Franz Weber and Christian K. Machens
Molecular and Cell Biology, University of California, Berkeley, USA

Definition

If a neuron's spikes are highly informative about an ensemble of stimuli, then the generated code is called efficient. The efficient coding hypothesis states that the highest levels of efficiency are reached when the ensemble of stimuli encoded by sensory neurons captures important aspects of an animal's natural environment. This notion of efficiency has been employed to explain various properties of sensory neurons including their stimulus-response functions, gain, and connectivity. Specifically, research on insect systems has shown that the stimulus-response function of many insect sensory neurons matches behaviorally relevant stimuli, while the neural gain is adjusted to the current stimulus statistics and behavioral state.

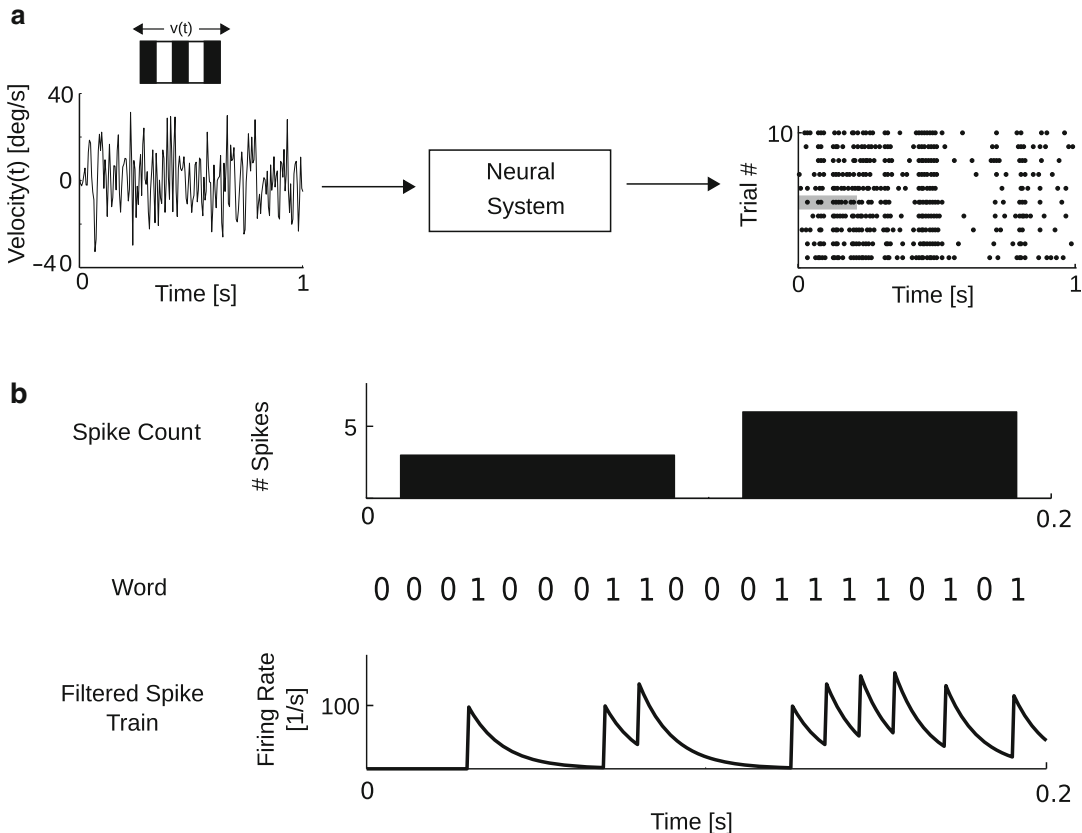
Detailed Description

To probe the properties of sensory neurons, neurophysiologists present various stimuli (e.g., gratings with different orientations for visual neurons or tones with different frequencies for auditory neurons), while recording the neural responses. Information theory provides a theoretical framework to study how much and what information a recorded neural response carries about the presented stimulus. Early influential studies focused on how single neurons in insects efficiently encode stimuli (Laughlin 1981; Bialek et al. 1991; Van Hateren 1992). In this context, a sensory neuron is defined as efficient, if its

response is highly informative about behaviorally important stimuli. The efficiency of the neural code served as a first principle explaining various properties of sensory neurons including their tuning, gain, and adaptive features. More recent studies in insects have furthermore explored how changes in the behavioral state of the animal affect the efficiency of sensory processing (Maimon et al. 2010; Chiappe et al. 2010; Jung et al. 2011). Here, we will discuss concepts that have been proven important for the understanding of experimental results from invertebrate systems. Especially insect studies provided many insights on how single neurons efficiently encode stimuli. For completeness, we briefly discuss efficient coding in neural populations, even though most work on population coding has been done for mammalian systems.

Neural Codes

Most sensory neurons respond to sensory stimuli with series of action potentials, also called spike trains. These responses are usually quantified with respect to different "neural codes," as shown in Fig. 1. The most common codes are (1) spike count or firing rate codes, in which the number of spikes within a given time window is counted; (2) spike timing codes or words, in which a spike train is binned in very short time windows, and thereby converted into a sequence of zeros (no spike) and ones (spike); and (3) time-varying rate codes, in which a spike train is filtered, e.g., with an exponential filter with a given decay time constant (similar to a postsynaptic potential). This type of filtered spike train interpolates between the spike count and spike timing codes. For very short time constants (1–2 ms), the code resembles a spike timing code; for very long time constants (100 s of milliseconds), the code resembles a spike count code. Especially in insects, one also finds quite often neurons with a graded voltage response, or neurons that mix such graded responses with small spikes (or spikelets) (Borst and Haag 2002). In these cases, the definition of the neural code has to be tailored towards the properties of the specific neuron.



Sensory Coding, Efficiency, Fig. 1 Neural codes. (a) Sensory neurons transform external stimuli into neural responses. In the example, a white-noise velocity stimulus (*left*) is presented to the identified motion-sensitive neuron H1 in the visual system of the blowfly. The velocity stimulus determines the speed $v(t)$ at which a vertical grating within the receptive field of H1 moves along the horizontal axis (see inset). Positive values represent rightward motion; negative values correspond to leftward motion. The stimulus is processed by the visual system including H1, yielding a sequence of action potentials

For all practical purposes, both the presented stimuli s and the measured responses r are often discretized and enumerated. Importantly, the mapping of a stimulus onto a neural response is usually corrupted by noise. As shown in Fig. 1a for the motion-sensitive neuron H1 in the blowfly, each presentation of the same stimulus yields a slightly different spike pattern. This variability in the neural response can be quantified by the distribution $p(r|s)$, i.e., the probability of observing response r , given that the stimulus was s . This distribution quantifies the noise in the

fired by H1. The responses of H1 elicited by the stimulus are represented on the *right*. Each row corresponds to one repetition of the stimulus, and each dot represents the time point of a single spike. (b) Three common schemes to quantify the neural response. The 200 ms long response by H1 indicated by the gray box in (a) is represented in three different ways: as the number of spikes within two 100 ms windows (“spike count”), as a series of zeros and ones, obtained by discretizing the spike train into 10 ms bins (“word”), and as a spike train filtered with an exponential kernel

transmission of the stimulus s to the responses r . If the distribution is peaked around a single stimulus value, the neuron’s response is reliable; if the distribution is broad, the neuron’s response is unreliable.

The noise in the neural response, here defined as trial-to-trial fluctuations elicited by the repeated representation of the same stimulus, can arise from multiple sources (Faisal et al. 2008), including the stimulus itself: External stimuli are noisy in nature. For example, the binding of olfactory molecules to taste receptors

is affected by thermal noise. Vision is based on the absorption of photons which is a highly stochastic process. A further prominent source of noise stems from stochastic events in the molecular transduction machinery of sensory neurons, as, e.g., the synthesis and degradation of proteins. So-called electrical noise is generated by random openings and closings of voltage- and ligand-gated ion channels. Moreover, the biochemical communication between neurons is afflicted by noise arising from stochastic events in synaptic mechanisms (as the docking of vesicles to the membrane, the number of available vesicles, their exact locations, etc.).

The Efficiency of Neural Codes

Once the mapping between a set of sensory stimuli and the responses of a neuron has been determined, the neural efficiency can be quantified. Common measures of efficiency are the quality and precision of representation or the amount of transmitted information.

Reconstruction Quality and Precision

One particularly straightforward way of measuring the efficiency of a neural code is to try to reconstruct the original stimulus from the neural response and then simply measure the mean squared error between the original and the reconstructed stimulus. This method requires a specification of how such a reconstruction should be done. One simple method is to assume that the original stimulus information can be read out by a linear filtering operation of the spike train. If we denote the original, time-varying stimulus by s_t , where t is a time index, and the reconstructed stimulus by \hat{s}_t , then a normalized measure for the efficiency of the neural code is given by the coding fraction (Gabbiani and Metzner 1999)

$$\varepsilon = 1 - \frac{\sum_{t=1}^N (s_t - \hat{s}_t)^2}{\sum_{t=1}^N s_t^2}, \quad (1)$$

where we assumed that the stimulus s_t has mean zero. This measure takes a value of zero if the

reconstruction fails completely and a value of one if the reconstruction perfectly recovers the original stimulus. An important caveat is that one can only attempt to reconstruct the part of a stimulus that is represented by the neuron. Stimuli that a neuron does not respond to, e.g., because they are outside of the neuron's receptive field, or below a neuron's threshold, cannot be reconstructed (Bialek et al. 1991; Machens et al. 2001).

In a realistic experimental setting, the coding fraction ε is always smaller than one, i.e., the stimulus cannot be exactly reconstructed from the observed neural response. First, the reconstruction algorithm or estimator may be incorrect, e.g., it could be biased. Second, the transmission from the stimulus to the response is affected by noise. Given an unbiased estimator, how precisely can the stimulus be reconstructed from the response? Intuitively, the reconstruction is directly related to the shape of the likelihood function $p(r|s)$ describing the probability to observe the response r given the stimulus s . The reconstruction will be the better, the more the response distribution $p(r|s)$ varies with s , and the less $p(r|s)$ is spread out for a given value of s . For an unbiased estimator \hat{s} of s , the variance of \hat{s} , σ_s^2 , is bounded from below by the Cramer-Rao bound

$$\sigma_s^2 \geq \frac{1}{I(s)} \quad (2)$$

where $I(s)$ denotes the Fisher information

$$I(s) = \left\langle -\frac{\partial^2 \ln P(r|s)}{\partial r^2} \right\rangle, \quad (3)$$

with $\langle \cdot \rangle$ denoting the expectation value over r for a given s . The Fisher information has become a theoretically important quantity in the study of population coding (Brunel and Nadal 1998), but has not been widely applied in the analysis of insect model systems.

Mutual Information

The reconstruction error is based on an explicit reconstruction of the original stimulus and thereby makes implicit assumptions about how

the stimulus information is embedded in the neural response. A different measure that is free of these assumptions is the mutual information, which is conventionally measured in bits.

If the mapping between the stimuli s and the responses r is deterministic, then the information conveyed by the neural response is given by the entropy of the response distribution. In general, the entropy of a distribution measures how spread or peaked a distribution is. The response entropy is given by

$$H(R) = -\sum_{i=1}^N p(r_i) \log_2 p(r_i), \quad (4)$$

where each r_i , with $i = 1 \dots N$, denotes one of the possible responses. To ensure that a response r_i that is not observed, i.e., $p(r_i) = 0$, does not contribute to the entropy, it is assumed that $0 \log_2 0 = 0$. Intuitively, the response entropy increases with the number of responses encoded by the neuron. The entropy is zero, $H(R) = 0$ bits, if the neuron generates only a single response, say $r = r_0$, irrespective of the stimulus. In this case, the response is completely predictable, and the neuron thus conveys no information about the stimuli. On the other hand, the response entropy is maximal if each response symbol is observed equally often. In this case, the response is completely unpredictable, $H(R) = \log_2 N$ bits, and the neuron transmits the maximum information possible.

In real neurons, the mapping between stimuli s and responses r is usually stochastic, in which case the neural response becomes less predictable from the stimulus. To compute the actual information conveyed, this undesirable effect needs to be measured and subtracted from the response entropy. The so-called noise entropy measures how much the response fluctuates for a given stimulus s and is evaluated as

$$H(R|s) = -\sum_{i=1}^N p(r_i|s) \log_2 p(r_i|s) \quad (5)$$

The mutual information is defined as the difference between the response entropy and the average noise entropy so that

$$I(R; S) = H(R) - \langle H(R|s) \rangle \quad (6)$$

where the angular brackets denote averaging over all stimuli s . Note that if $H(R|s) = 0$ bits, i.e., the mapping between stimulus and response is noise-free, the mutual information equals the response entropy.

The efficiency of a neural code is often quantified either directly as the mutual information, $I(R; S)$ (Borst and Theunissen 1999), or as the ratio

$$\varepsilon = \frac{I(R; S)}{H(R)} \quad (7)$$

(Rieke et al. 1997). The closer ε to one, the smaller the noise, and the more the neuron makes use of its full capacity to encode information about the stimulus.

The Efficient Coding Hypothesis

The efficient coding hypothesis states that neural systems strive to employ their full information capacity in response to natural stimuli. The natural stimuli encountered by animals are often characterized by high redundancy, meaning that parts of an image or a sound can often be predicted by knowing the rest of the image (or the sound). The task of a sensory representation is then to eliminate this redundancy. If the response entropy is maximized, the neural responses by themselves are unpredictable, and all redundancy has been removed. If at the same time, the noise entropy is minimal, then the responses are also highly informative about the stimulus (see Eq. 6). The original formulation of the efficient coding hypothesis relied on mutual information as the key quantity to measure efficiency (Attneave 1954; Barlow 1961). However, in many instances, it has proven fruitful to assume a specific neural code, then reconstruct the original stimulus, and use the quality of this stimulus reconstruction to evaluate efficiency (Bialek et al. 1991; Rieke et al. 1997). The efficient coding hypothesis has been successfully applied both to invertebrate systems (Rieke et al. 1997; Borst and Theunissen 1999; Fairhall et al. 2001; Machens et al. 2001, 2005), mostly focusing on

single neurons, and to vertebrate systems (Olshausen and Field 1996; Simoncelli and Olshausen 2001; Smith and Lewicki 2006), mostly focusing on populations of neurons. Here we focus on invertebrate systems.

Consequences and Experimental Evidence

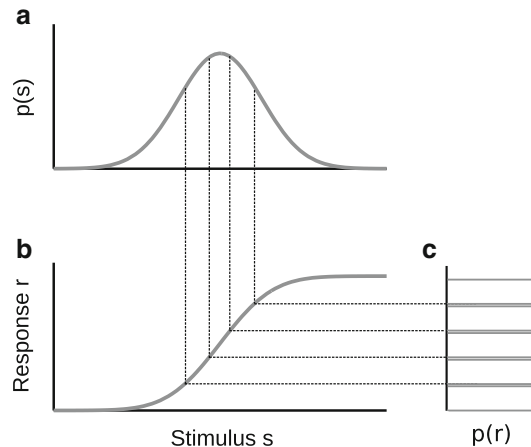
Stimulus–Response Function of Single Neurons

In the simplest case, the stimulus s and response r are one dimensional (e.g., sound intensity or luminance of a stimulus, and firing rate or voltage response of a single neuron). The so-called input–output or stimulus–response function f maps the stimulus s onto the response r , i.e., $r = f(s)$. How should the stimulus–response function be shaped to maximize the efficiency of a sensory system?

In the limit of relatively small noise or response variability, the question can be answered precisely by resorting to probability densities and differential entropies (Laughlin 1981). The stimulus–response function should then be the cumulative probability function of the stimulus distribution $p(s)$, or

$$r = f(s) \propto \int_{-\infty}^s p(s')ds', \quad (8)$$

because in this case, all responses are equally likely. This so-called histogram equalization maximizes the response entropy and thereby the mutual information in the noise-free case (see explanations above and Fig. 2). Evidence that the input–output function of sensory neurons is indeed matched to the stimulus statistics has been provided for the large monopolar cells in the visual system of the blowfly (Laughlin 1981). The voltage of these neurons is sensitive to luminance contrasts. Measuring the contrast distribution within typical habitats of the fly revealed that the input–output function of the monopolar cells is indeed very close to the integrated stimulus distribution.

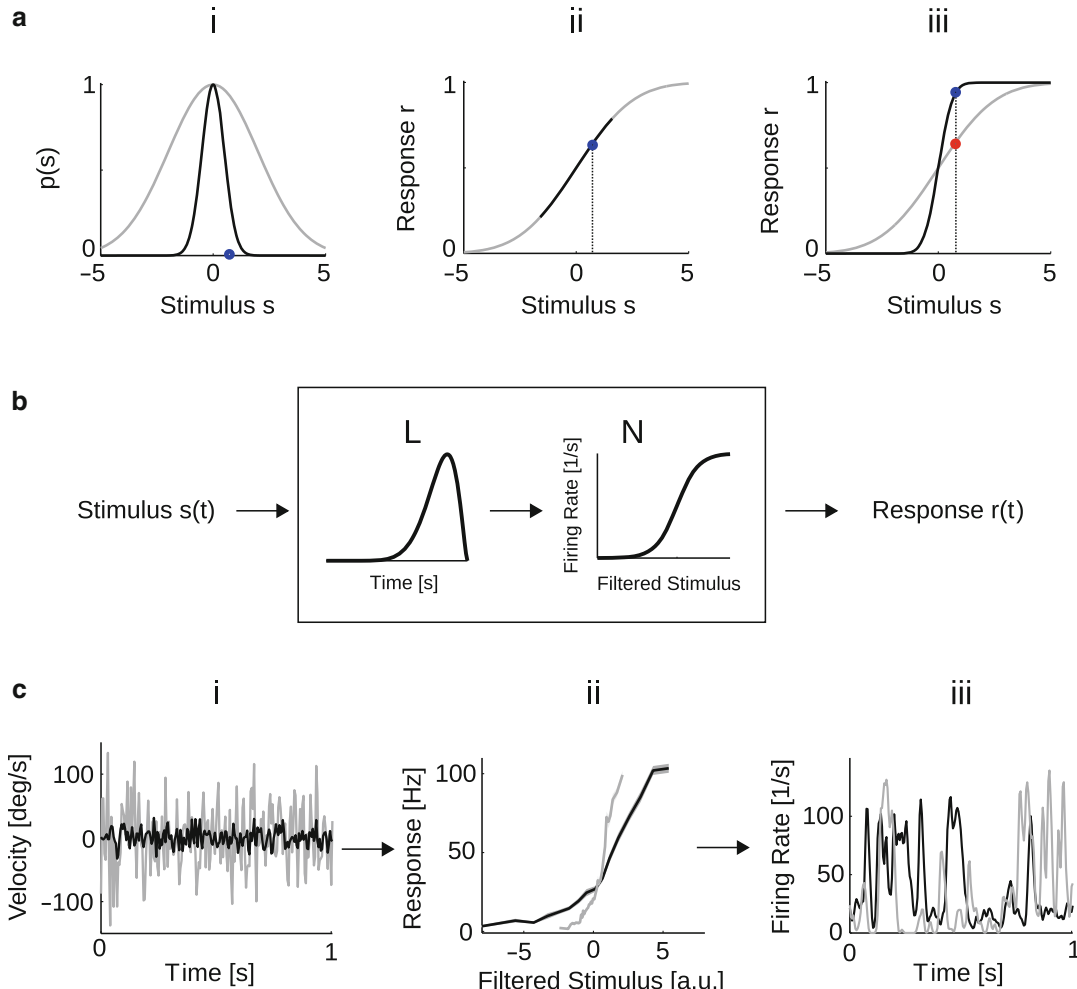


Sensory Coding, Efficiency, Fig. 2 Optimal stimulus–response function for a single neuron. (a) The stimuli represented by the sensory neuron follow the distribution $p(s)$. (b) The sensory system transforms the stimulus s to the neural response r carrying information about s . (c) According to the efficient coding hypothesis, the neural code is most efficient, if each response r occurs with equal probability $p(r)$. This is the case, if the stimulus–response function is proportional to the integral of the stimulus distribution $p(s)$

Adaptation of Stimulus–Response Functions in Single Neurons

The distribution of stimuli experienced by an animal will vary over time. Typically, the “local” distribution of stimuli encountered over a shorter time interval will differ from the “global” distribution of stimuli encountered over long stretches of time (Wark et al. 2007). A simple example is the distribution of light intensities or contrasts, which change strongly throughout the day or with the weather. For illustration, Fig. 3ai shows two different local stimulus distributions which differ in their standard deviation.

An “efficient” sensory neuron can deal with this problem in two possible ways, as illustrated in Fig. 3a. In the first solution (Fig. 3aii), the input–output function of the neuron is fixed and proportional to the global stimulus distribution. The neuron will be efficient for the global distribution, but inefficient for any local distribution. In the second solution (Fig. 3aiii), the input–output function of the neuron changes with the local stimulus distribution such that it is proportional to



Sensory Coding, Efficiency, Fig. 3 Gain control and efficient coding. (a) Two local stimulus distributions differing in their standard deviation (a i). a ii and a iii illustrate two different coding schemes: For each local distribution, the stimulus s is represented by the same, fixed input–output function (a ii). Contrarily in a iii, the input–output function adjusts its gain to the current stimulus statistics such that each local distribution is efficiently encoded by the neural response. (b) Linear–nonlinear models are frequently applied to characterize sensory neurons. In this model, the stimulus is first convolved with a linear filter (L). The filter output is

then fed through a static nonlinearity (N) yielding a prediction of the instantaneous firing rate. The static nonlinearity can be viewed as the time-averaged stimulus–response function of the neuron. (c) The H1 neuron adjusts its gain to the statistics of the presented white-noise stimulus. In this example, two white-noise stimuli differing in their standard deviation have been presented to H1 (c i). Increasing the standard deviation of the stimulus leads to a decrease of the slope (gain) of H1’s input–output function (c ii). Consequently, H1 represents both stimuli with its full response range (c iii)

the integral of the current distribution. It will now be efficient for the local distribution, but inefficient for the global distribution. Given that neural responses are usually corrupted by noise, the two solutions represent trade-offs. In the first coding scheme, the local stimulus distributions are

mapped onto a rather small response range (Fig. 3aii), and many of the smaller stimulus changes may be lost in the response noise. In the second coding scheme, the responses become ambiguous across different local stimulus ensembles, and the respective global information is lost

(Fig. 3aiii). In practice, some of the ambiguities can often be avoided if the neuron's responses can vary on different time scales. In the fly, for instance, the motion-sensitive neuron H1 changes its gain instantaneously when the variance of the presented stimulus ensemble is changed, yet the mean firing rate changes only slowly. Hence, the slow changes of the mean firing rate allow the sensory system to track slow changes in the encountered stimulus distribution (Fairhall et al. 2001).

Various studies demonstrated that sensory neurons adjust their input–output function to the local stimulus distribution (Fairhall et al. 2001; Brenner et al. 2000; Borst 2003; Borst et al. 2005; Weber et al. 2010; Rinberg and Davidowitz 2000; Geffen et al. 2009; Laughlin 1981). As an example from the fly, responses of the motion-sensitive neuron H1 to varying stimuli are shown in Fig. 3c. Here, two sets of motion stimuli that differ in the standard deviation of their velocities have been presented to the fly (Fig. 3ci). To analyze the neuron's input–output function, a so-called linear–nonlinear (LN) model was fitted to the neural responses (see Fig. 3b). In this model, the time-varying stimulus is first convolved with a linear filter, and the filtered stimulus is then fed through a static nonlinearity, which models the neuron's input–output function. As shown in Fig. 3cii, the gain of the input–output function, as given by its slope at half maximum, is larger for the velocity profile with smaller standard deviation. Hence, the neuron is sensitive to small changes in the stimulus. Contrarily, if the gain is small, similar stimulus values elicit similar responses. Since the gain of H1 is adjusted to the statistics of the applied velocity distribution, both stimuli are represented with H1's full response range: While the variance of both stimuli strongly differs, both response profiles in Fig. 3ciii exhibit a similar variance. Thus, both stimulus distributions are efficiently represented with H1's full dynamic response range.

Maximization of Information Rates in Single Neurons

The stimulus–response functions considered above operate with spike counts or firing rates

and therefore do not fully capture the inherent capacity of spike trains. The information present in a neural spike train can be measured by using the mutual information, either indirectly (e.g., by assessing the quality of a reconstruction Bialek et al. 1991; Theunissen and Miller 1991) or by binning spike trains into words and computing the mutual information between the spike timing code and the stimulus (Strong et al. 1998). In practice, these computations usually require large amounts of data since the number of stimulus and response symbols increases exponentially with the number of neurons or the length of time windows. Additionally, estimating mutual information is prone to systematic errors (or biases) if the amount of data is insufficient (Strong et al. 1998; Paninski 2003).

For single neurons, such estimates of the mutual information have usually been possible and have been computed in many systems (Rieke et al. 1997; Borst and Theunissen 1999). In turn, the information rates of different stimulus ensembles can be compared. In cockroaches, for instance, the information rates of wind-sensitive neurons change with the overall shape of the wind spectrum. If the wind spectrum shape is similar to that of an approaching predator, such as a spider, information rates are maximized (Rinberg and Davidowitz 2000). Consequently, the sensory neurons are tuned to a subspace of behaviorally relevant stimuli that convey information about predators.

In the grasshopper auditory system, information rates are maximized when the spectrum of the sounds approaches the frequencies common in grasshopper communication calls (Machens et al. 2001). Using these measures of information rates, the efficient coding hypothesis can also be inverted: Knowing the input–output function of a neuron allows one to deduce the distribution of the optimally represented stimuli. This approach has been applied to grasshopper auditory receptor neurons (Machens et al. 2005). Instead of being tuned for the average distribution of natural stimuli, the investigated neurons have been found to be optimized for behaviorally important sub-ensembles of natural sounds, which are related to grasshopper sounds. These studies

demonstrate that sensory neurons rather encode a behaviorally relevant subspace of stimuli than the distribution of all naturally occurring stimuli.

Information rates can also be used to test a system's efficiency with respect to its biophysical parameters such as the connection weights between two neurons. Using a combination of data analysis and modeling, it was shown that the coupling strength between two global motion-sensitive neurons in the blowfly, Vi and H1, is information-theoretically optimal: Changing its value, either experimentally or in simulations, led to a decrease of the information carried by the spikes (Weber et al. 2012).

Efficiency of Neural Populations

Many studies of sensory coding in insect systems have focused on single neurons. While the insect nervous system knows many instances where single neurons represent actual information bottlenecks, most information is still processed in (small) neural populations. What does the efficient coding hypothesis predict about neural populations?

In general, the efficiency of a population code can be evaluated with the same criteria as the efficiency of a single neuron. If the efficiency is measured through the mutual information, then one important aspect of an efficient code is that the response distributions of all neurons need to be statistically independent of each other. For a population with M neurons, an efficient code therefore requires that $p(r_1, \dots, r_M) = \prod_{k=1}^M p(r_k)$. A neural population code that fulfills this condition is called a factorial code. This requirement is often difficult to fulfill. A weaker condition is that the response distributions of each neuron pair are decorrelated.

These considerations illustrate the importance of redundancy reduction as an integral part of the efficient coding hypothesis. Statistically independent or decorrelated representations will generally have a much lower degree of redundancy than the original stimulus input. The efficient coding of neural populations has been extensively investigated in various vertebrate systems (Simoncelli and Olshausen 2001; Simoncelli

2003), with only some studies on insect sensory systems (Broome et al. 2006; Geffen et al. 2009; Olsen et al. 2010). Similar to neural populations in vertebrate systems, neural populations in insects decorrelate their responses. This has been demonstrated in the olfactory system of the fly (Olsen and Wilson 2008; Olsen et al. 2010). In the antennal lobe, the second stage of olfactory processing, the so-called projection neurons receive input from the presynaptic olfactory receptor neurons (ORNs). ORNs expressing the same odorant receptor project to the same glomerulus. Different glomeruli within the antennal lobe are interconnected by inhibitory interneurons. The size of the inhibition mediated by the interneurons scales with the strength of the feedforward input from the ORNs to a glomerulus. Interestingly, the interglomerular inhibition acts at the presynaptic locus of synapses connecting the ORNs to PNs. Hence, lateral presynaptic inhibition between glomeruli mediates a gain control mechanism which accounts for variations in the strength of odorant signals (Olsen and Wilson 2008). Second, modeling of the projection neuron responses revealed that the lateral inhibition decorrelates the population response (Olsen et al. 2010).

State-Dependent Efficient Coding

Sensory neurons adjust various properties such as their gain or connectivity to match the current behaviorally important stimulus ensemble. However, the relevance of a particular stimulus set might depend on the behavioral state of the animal. For instance, animals that are hungry show a stronger attraction to food stimuli, than animals that are full (Sengupta 2013). This type of behavioral modulation and its implications on sensory processing have been studied in fruit flies. When flies are starved, olfactory receptor neurons express higher levels of a receptor for neuropeptide F. An increased level of neuropeptide F receptors leads to a facilitation of the synapse between the olfactory receptor neurons and secondary olfactory neurons. Hence, starvation enhances the strength of synapses in the olfactory system and, thus, causes an increased sensitivity to food odors (Root et al. 2011).

Apart from hunger, an animal's locomotion state also influences the response properties of its sensory neurons, as has recently been demonstrated for flying and walking flies (Maimon et al. 2010; Chiappe et al. 2010; Jung et al. 2011). Generally, the gain of motion-sensitive lobula plate neurons in walking or flying flies is strongly increased compared to stationary animals. This gain modulation is caused by increased inputs from presynaptic elements (Maimon et al. 2010). Assuming that increased synaptic inputs correlate with an increased energy consumption, the fly's visual system seems to tightly control its resources depending on the organism's needs. During flight, visual motion stimuli might be more relevant than during a quiescent state such that the overall activity can be lowered when the fly is not flying. Moreover, since the statistics of velocities is predictably different during flight, the gain increase might be interpreted as an adjustment of the neurons' coding properties to the velocity distribution encountered during flight.

In line with this hypothesis, flying and walking induce a pronounced shift in the velocity tuning curve of lobula plate neurons. When moving, the velocity tuning is shifted towards higher speeds. This effect is likely mediated by the neuromodulator octopamine. Direct application of the octopamine agonist CDM induces a similar shift in the tuning (Jung et al. 2011). Moreover, CDM causes an increase in the baseline firing rate similar to that observed for flying or walking flies. Additionally, CDM application enhanced the information rate (Longden and Krapp 2009, 2010). Hence, the release of a neuromodulator can adjust the coding properties of sensory neurons to the current locomotor state.

Assuming that the relevance of particular stimuli changes with the behavioral state, these results can be reconciled with the efficient coding hypothesis: Sensory neurons regulate their properties to efficiently encode what is currently behaviorally important.

Outlook

Many insect sensory neurons seem to be adjusted to the currently prevailing stimulus statistics and to the behavioral state of the animal. A large set of studies has furthermore elucidated the adaptation of sensory neurons to the ever-changing stimulus statistics of their environment. Most of these studies have been performed in "passive" animals that were not interacting with their environment. In contrast, the dependency of sensory processing on an animal's internal state or its current behavior has been less well studied. In the future, experimental work may give more insight into the biophysical mechanisms and circuits that underlie these state-driven changes in the tuning of sensory neurons. Furthermore, theoretical concepts may help to explain these changes from a normative point of view. For instance, is the state dependency of sensory neurons, such as the gain decreases in fly visual neurons during immobility, due to a necessity to save metabolic energy? Or is the state dependency fully explained by sensory adaptation to the animal's internal expectations, such as the expected distribution of motion stimuli during immobility or flight? We believe that addressing these types of questions will help us to more thoroughly understand sensory processing in animals that interact actively with their environment.

References

- Attneave F (1954) Some informational aspects of visual perception. *Psychol Rev* 61(3):183
- Barlow HB (1961) Possible principles underlying the transformations of sensory messages. In Rosenblith WA (Ed.), *Sensory communication*, MIT Press, Cambridge, MA, pp 217-234
- Bialek W, Rieke F, de Ruyter van Steveninck R, Warland D (1991) Reading a neural code. *Science* 252:1854-1857
- Borst A (2003) Noise, not stimulus entropy, determines neural information rate. *J Comput Neurosci* 14:23-31

- Borst A, Haag J (2002) Neural networks in the cockpit of the fly. *J Comp Physiol A Neuroethol Sens Neural Behav Physiol* 188:419–437
- Borst A, Theunissen FE (1999) Information theory and neural coding. *Nat Neurosci* 2:947–957
- Borst A, Flanagan VL, Sompolinsky H (2005) Adaptation without parameter change: dynamic gain control in motion detection. *Proc Natl Acad Sci USA* 102:6172–6176
- Brenner N, Bialek W, de Ruyter van Steveninck R (2000) Adaptive rescaling maximizes information transmission. *Neuron* 26:695–702
- Broome BM, Jayaraman V, Laurent G (2006) Encoding and decoding of overlapping odor sequences. *Neuron* 51:467–482
- Brunel N, Nadal J-P (1998) Mutual information, Fisher information, and population coding. *Neural Comput* 10:1731–1757
- Chiappe ME, Seelig JD, Reiser MB, Jayaraman V (2010) Walking modulates speed sensitivity in *Drosophila* motion vision. *Curr Biol* 20:1470–1475
- Fairhall AL, Lewen GD, Bialek W, De Ruyter Van Steveninck RR (2001) Efficiency and ambiguity in an adaptive neural code. *Nature* 412:787–792
- Faisal AA, Selen LPJ, Wolpert DM (2008) Noise in the nervous system. *Nat Rev Neurosci* 9:292–303
- Gabbiani F, Metzner W (1999) Encoding and processing of sensory information in neuronal spike trains. *J Exp Biol* 202(10):1267–1279
- Geffen MN, Broome BM, Laurent G, Meister M (2009) Neural encoding of rapidly fluctuating odors. *Neuron* 61:570–586
- Jung SN, Borst A, Haag J (2011) Flight activity alters velocity tuning of fly motion-sensitive neurons. *J Neurosci* 31:9231–9237
- Laughlin S (1981) A simple coding procedure enhances a neuron's information capacity. *Z Naturforsch C* 36:910–912
- Longden KD, Krapp HG (2009) State-dependent performance of optic-flow processing interneurons. *J Neurophysiol* 102:3606–3618
- Longden KD, Krapp HG (2010) Octopaminergic modulation of temporal frequency coding in an identified optic flow-processing interneuron. *Front Syst Neurosci* 4:153
- Machens CK, Stemmler MB, Prinz P, Krahe R, Ronacher B, Herz AV (2001) Representation of acoustic communication signals by insect auditory receptor neurons. *J Neurosci* 21:3215–3227
- Machens CK, Gollisch T, Kolesnikova O, Herz AVM (2005) Testing the efficiency of sensory coding with optimal stimulus ensembles. *Neuron* 47:447–456
- Maimon G, Straw AD, Dickinson MH (2010) Active flight increases the gain of visual motion processing in *Drosophila*. *Nat Neurosci* 13:393–399
- Olsen SR, Wilson RI (2008) Lateral presynaptic inhibition mediates gain control in an olfactory circuit. *Nature* 452:956–960
- Olsen SR, Bhandawat V, Wilson RI (2010) Divisive normalization in olfactory population codes. *Neuron* 66:287–299
- Olshausen BA, Field DJ (1996) Emergence of simple-cell receptive field properties by learning a sparse code for natural images. *Nature* 381:607–609
- Paninski L (2003) Estimation of entropy and mutual information. *Neural Comput* 15:1191–1253
- Rieke F, Bialek W, Warland D (1997) Spikes: Exploring the Neural Code. MIT Press, Cambridge
- Rinberg D, Davidowitz H (2000) Do cockroaches 'know' about fluid dynamics? *Nature* 405:756
- Root CM, Ko KI, Jafari A, Wang JW (2011) Presynaptic facilitation by neuropeptide signaling mediates odor-driven food search. *Cell* 145:133–144
- Sengupta P (2013) The belly rules the nose: feeding state-dependent modulation of peripheral chemosensory responses. *Curr Opin Neurobiol* 23:68–75
- Simoncelli EP (2003) Vision and the statistics of the visual environment. *Curr Opin Neurobiol* 13(2):144–149
- Simoncelli EP, Olshausen BA (2001) Natural image statistics and neural representation. *Ann Rev Neurosci* 24:1193–1216
- Smith EC, Lewicki MS (2006) Efficient auditory coding. *Nature* 439:978–982
- Strong SP, Koberle R, de Ruyter van Steveninck R, Bialek W (1998) Entropy and information in neural spike trains. *Phys Rev Lett* 80:197
- Theunissen FE, Miller JP (1991) Representation of sensory information in the cricket cercal sensory system. II. Information theoretic calculation of system accuracy and optimal tuning-curve widths of four primary interneurons. *J Neurophysiol* 66: 1690–1703
- Van Hateren JH (1992) Theoretical predictions of spatio-temporal receptive fields of fly LMCs, and experimental validation. *J Comp Physiol A* 171:157–170
- Wark B, Lundstrom BN, Fairhall A (2007) Sens Adapt Curr Opin Neurobiol 17:423–429
- Weber F, Machens CK, Borst A (2010) Spatiotemporal response properties of optic-flow processing neurons. *Neuron* 67:629–642
- Weber F, Machens CK, Borst A (2012) Disentangling the functional consequences of the connectivity between optic-flow processing neurons. *Nat Neurosci* 15: 441–448, S1–S2

Sensory Drive to Rhythmic Neuronal Networks

► [Sensory Input to Central Pattern Generators](#)

Sensory Input to Central Pattern Generators

Wolfgang Stein

School of Biological Sciences, Illinois State University, Normal, IL, USA

Synonyms

Afferent feedback to neural oscillators; Afferent input to rhythm generating networks; Proprioceptive feedback to central pattern generators; Sensory drive to rhythmic neuronal networks; Sensory modulation of central pattern generators

Definition

A central pattern generator (CPG) is an assembly of neurons (neuronal network) that produces rhythmic activity without requiring phasic input signals and often drives the motor system and rhythmic muscle movements. Sensory feedback to a CPG circuit is the return signal from the sensory system in response to this rhythmic muscle movement, which conveys a continuous measurement of the output behavior to the CPG.

Detailed Description

Individual neural networks, such as CPGs, can generate rhythmic output patterns even in the absence of any phasic input. They drive vital behaviors such as breathing, swallowing, and chewing, as well as locomotion and saccadic eye movements, and often continue to function even in isolated nervous system (i.e., *in vitro*) preparations (Marder and Calabrese 1996; Grillner et al. 2005; Dickinson 2006; Gordon and Whelan 2006; Isa and Sparks 2006; Kiehn 2006; Katz and Hooper 2007; Chevallier et al. 2008; Doi and Ramirez 2008; Berkowitz et al. 2010; El Manira et al. 2010; Büschges et al. 2011; Harris-Warrick 2011; Marder 2012). Given the

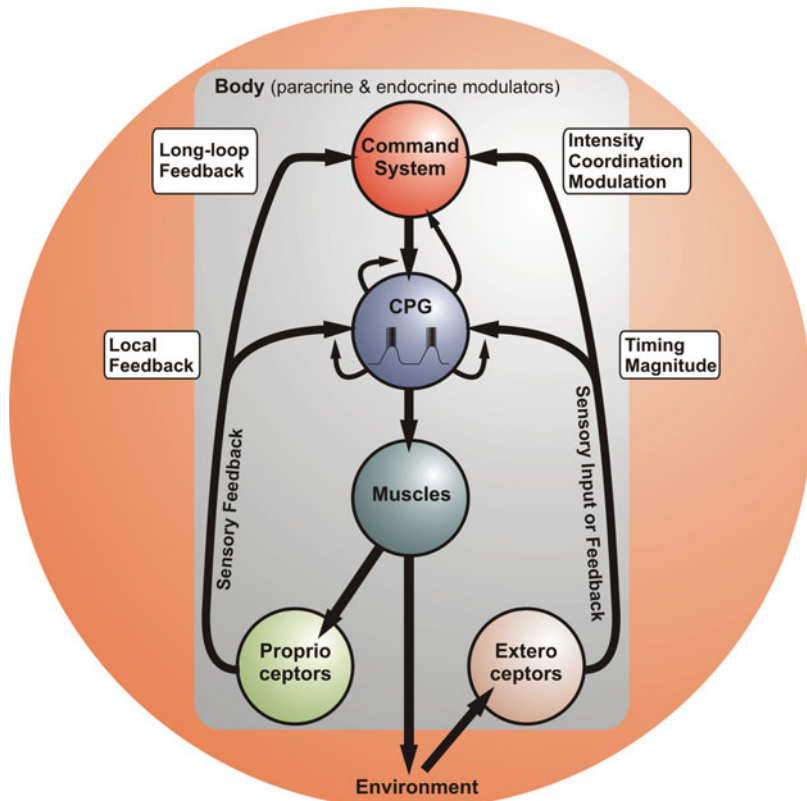
improved accessibility for neuronal manipulations *in vitro*, it is not surprising that most insights into the rhythm generating mechanisms of CPGs have been derived from this condition, hence using preparations deprived of sensory information. *In vivo*, however, numerous additional influences have access to the CPG circuit from other CNS regions, circulating hormones, and sensory systems (Fig. 1). In particular for driving motor behaviors, CPGs receive constant feedback from peripheral sense organs, including proprioceptors. While CPGs may also contribute to cognitive functions (e.g., theta and gamma rhythms in the hippocampus; Grillner et al. 2005), this entry focuses on CPGs underlying motor pattern generation because the influence of sensory feedback is particularly obvious in these CPGs.

Sensory Feedback Versus Sensory Input

Sensory *feedback* differs from sensory *input* in that it provides the CPG with a continuous read-out of the consequences of CPG activity on the resulting behavior. Typically, the sense organs providing sensory *feedback* to CPGs are proprioceptive, i.e., they continuously measure the response of the muscles to the rhythmic motor output and thus show phasic activity patterns. Exteroceptive sense organs, in contrast, typically provide sensory *input*, rather than *feedback*, about changes in external conditions. They are not necessarily related to CPG activity, although in some cases they can be. To demonstrate this difference, imagine eating an almond chocolate truffle. You take a first bite from the soft chocolate layer of the truffle, and your periodontal mechanoreceptors (peripheral receptors that signal information about tooth load, Bonte et al. 1993) will initially encounter little resistance and will thus either be inactive or continuously active at a low level and hence provide sensory *input*. As you encounter the almond with your second bite, this changes dramatically and the periodontal mechanoreceptors now register a strong mechanical load, and they do so whenever your teeth meet the almond, in phase with the chewing pattern, providing a signal that chewing strength needs to be increased. In other

Sensory Input to Central Pattern Generators,

Fig. 1 Schematic overview of sensory input to CPG circuits. For simplicity, the motor neurons are not shown separately. The CPG receives input from proprioceptive and exteroceptive pathways. This input either directly affects the CPG (local feedback) and / or is mediated via upstream control neurons (long-loop feedback). Local feedback mainly determines the magnitude and timing of CPG activity, while long-loop feedback has modulatory effects, regulates intensity and coordinates CPG activity with other motor acts. CPG activity itself can modulate incoming sensory feedback, for example via presynaptic inhibition of the afferent pathways



words, they now provide sensory *feedback* that is directly related to the motor output. In contrast, typical proprioceptors, such as muscle spindles that mainly measure the stretch of muscles, provide phasic *feedback* at all times, even in the unlikely event that the manufacturer of the chocolate truffle forgot to put in the almond.

Sensory *input*, due to its (partial) independence of CPG activity, often initiates or modulates the intensity of the motor pattern on a longer time scale, adapts CPG activity to external conditions, and coordinates it with other motor acts to maintain equilibrium during behavior (Grillner 2003; Dickinson 2006; Stein 2009; Blitz and Nusbaum 2011; Harris-Warrick 2011; Marder 2012). Many actions of sensory input pathways are mediated via intercalated interneurons that process many different sensory modalities and often exert modulatory influences on the CPG circuits.

Local Sensory Feedback

The role of local sensory feedback on CPG activity has been particularly well studied. CPGs are often located close to the musculoskeletal system they control, and they receive local feedback from that system (via proprioceptive pathways, or, in some cases, directly from dendrites of CPG motor neurons, Garcia-Crescioni et al. 2010). Local sensory feedback typically modifies and adapts CPG activity on a short time scale (Pearson 2004) by altering magnitude and relative timing of muscle activity. Conceptually, local sensory feedback to a CPG serves at least three main functions:

1. *Corrective input*: It can provide a corrective signal to adapt CPG patterns to deal with environmental perturbations. Corrective feedback is necessary in an unpredictable environment, for instance, to reinforce CPG activities that drive fin or body movements during

swimming in rough water or to adjust wing beat in a turbulent air stream.

2. *Timing*: It can contribute to CPG activity in an *ongoing* fashion, during unperturbed motor pattern production, by providing timing cues about the biomechanical state of the moving body part(s). During walking in cats and insects, for example, phase transitions are facilitated by sensory feedback that depends on the biomechanical state of the leg (Büsches [2005](#)). This sensory feedback ensures that a certain phase of the movement (e.g., the swing phase) is not initiated until the appropriate biomechanical state of the leg (the posterior extreme position) has been achieved. It provides information about limb and appendage position in space and thus allows for adapting and planning of movements.
3. *Stability*: By ensuring that the timing and force output of a motor pattern is appropriate for the task at hand, local sensory feedback can also lead to a stabilization of the motor pattern. The tegula, a wing proprioceptor in locusts, for example, is excited during wing depression and hence provides feedback about the position of the wing and facilitates phase transitions (Wolf [1993](#)). In addition, however, the tegula acts to stabilize the flight rhythm: If its nerve is stimulated with a relatively weak shock, activating only a few of the tegula's sensory neurons, the flight rhythm speeds up (Ausborn et al. [2007](#)). If it is stimulated strongly, the pattern slows. This example nicely demonstrates that proprioceptors can have a pivotal influence on the pattern-generating machinery *in vivo*: They work together with the CPG to ensure that the behavioral output is continuously adjusted to maintain functioning and stability of the desired pattern.

Due to these essential functions of local sensory feedback, in most systems behaviorally appropriate motor pattern generation requires both CPG activity and sensory feedback, with sensory and central mechanisms being integrated to produce a robust rhythmic activity pattern that can be rapidly adjusted to cope with unpredictable environmental disturbances.

Sensory Gating and Phase-Dependent Modulation of Sensory Feedback

As is likely true for all aspects of neural signaling, the effect of sensory feedback on CPG activity is modified by many influences. For example, it can vary with the phase of the motor pattern at which it is given.

For example, during stick insect walking, the influence of the campaniform sensilla, which measure load of the leg, always supports phase transitions from swing to stance phase (Akay et al. [2007](#)). Functionally, this makes sense: When load is high, this means that the leg must be on the ground and stance phase should commence. Interestingly, the effect of the load receptors on the protractor and retractor muscles that move the leg forward and backward changes in sign with a switch from forward to backward walking. During forward walking, a transition from protractors to retractors is facilitated, while during backward walking, transitions from retractor to protractor activity are elicited.

Another example, also from the walking system, is the phase dependence of local sensory feedback. A perturbation that occurs during the swing phase of the leg (e.g., when the foot hits a step when climbing up a stairway) usually results in the leg being lifted to enable it to reach the next step. During the stance phase, the same stimulus causes a further descending of the leg to increase force between foot and ground, which enhances stability. Such reflex reversals have been observed in many motor systems (Skorupski and Sillar [1986](#); Bässler [1993](#); Burrows [1996](#)), but the neuronal basis for this switch in sign is not well understood.

There are two principle possibilities for how such a reflex reversal can be achieved (Hooper [2000](#)): (1) a differential (phase-dependent) routing of sensory feedback to different CPG neurons and (2) a varying response by the CPG network to sensory feedback due to how the network integrates the input during different phases of the pattern. In locusts, for example, the sensory feedback from the femoral chordotonal organ, which measures the position of the femur-tibia joint during walking, is gated with the phase of the walking motor pattern, disabling feedback

during certain phases of this pattern (Wolf and Burrows 1995). The underlying mechanism is a phase-dependent presynaptic inhibition of the sensory terminals and a concomitant decrease in transmitter output. While sensory activity remains unchanged, sensory transmission to the CNS is impaired. Since presynaptic inhibition is typically strongest whenever sensory activity is high, it reduces the overall amount of sensory feedback, and, quite peculiarly, it also diminishes *expected* sensory feedback at certain phases of the CPG pattern. Presynaptic inhibition could thus be one mechanism that underlies the reaference principle, which tries to explain the fact that self-initiated motions do not interfere with the perception of constancy [proposed by von Holst and Mittelstaedt (1950)]. One way to achieve this goal is via an efference copy of the motor signal (in this case the CPG output) which provides the input to a forward internal model. This model is then used to generate the predicted sensory feedback that estimates the sensory consequences of the motor command. This signal is sent to the periphery, where it (presynaptically) inhibits any proprioceptor response to the CPG-generated movement which could interfere with the execution of the motor task. Differences in the actual from the predicted sensory activity are then sent back to the CPG as an error signal to adapt the motor output. While the pathways that elicit the presynaptic inhibition are still somewhat nebulous, it has been demonstrated that proprioceptors can presynaptically inhibit the terminals of neurons from other proprioceptive sense organs (Stein and Schmitz 1999). Since proprioceptors typically show phasic activity, this could contribute to the gating of sensory feedback at specific phases of the motor pattern.

While CPG activity can affect transmitter release from sensory neurons (Wolf and Burrows 1995), so far there are no indications that CPGs can directly modulate sensory spike activity. However, CPGs may indirectly affect sensory spike activity via feedback onto modulatory neurons that not only control CPG activity but also release neuromodulatory substances in a paracrine fashion. Neuromodulators, in turn, affect both muscle contraction and sensory

activity, which makes it possible for CPGs to interfere with sensory spike activity, at least in principle. The activity of the anterior gastric receptor (AGR) in the stomatogastric nervous system of crustaceans, for example, can switch from spiking to bursting, depending on the modulatory conditions present (Birmingham et al. 1999). While in spiking mode, AGR encodes both rapid and slow stimuli and thus reports cycle-by-cycle muscle movements that are driven by the CPG. In bursting mode, however, only persistent stimuli are detected, and thus, average levels of muscle tension are reported. This example demonstrates that the same proprioceptor can provide feedback about different qualities of the CPG output.

Context or Task-Dependent Modulation of Sensory Feedback

While phase-dependent modulation affects sensory feedback on a cycle-by-cycle basis, sensory feedback can also be subject to long-term modulation, either via the actions of neuromodulators released from neurons (paracrine, as stated in the previous paragraph) or the endocrine system (hormones) that modify the sensory response itself (Birmingham 2001) or via a modulation of the response of the CPG network to sensory input. In the stomatogastric nervous system of crustaceans, for example, changes of a few Hertz in the tonic activity of the AGR muscle proprioceptor modify the response of the gastric mill (chewing) CPG network to sensory input from mechanoreceptors in the stomach (Daur et al. 2009). Magnitude and timing of the gastric mill motor pattern elicited by the mechanoreceptive input correlate with the tonic spike activity of the muscle receptor, which means that the state of the system and its response to incoming sensory input is modified.

What Drives Rhythmic Behavior *In Vivo*: Sensory Feedback or CPG Activity?

Discussion regarding whether the CPG or the sensory feedback drives the actual behavior of an animal *in vivo* is as old as the discovery of CPG circuits. There is no universal answer, because their relative impact appears to differ from system to system. Büschges and

El Manira (2011) draw the conclusion that, although clearly affected by sensory feedback, CPGs that drive locomotor movements in homogeneous media such as air (flying) or water (swimming) often continue to be rhythmically active even when isolated from sensory feedback. In contrast, CPGs that drive locomotion in heterogeneous environments, such as terrestrial locomotion, typically lack rhythmic activity in isolation from local sensory feedback. This distinction, however, does not necessarily mean that sensory feedback does not shape the rhythmic movement. In locust flight, for example, the CPG can be activated in isolation and will show a stable flight pattern, but *in vivo* several sense organs, including the tegula, provide feedback to the CPG and dominate the motor pattern. The frequency of the rhythm, however, increases by a factor of two, which is why in this system sensory feedback is seen as a major contributor to the functional motor pattern (Ausborn et al. 2007).

While in this example there would be no flight pattern without CPG activity, theoretical approaches have proposed that sensory feedback itself could act as an oscillator if provided with the adequate properties, such as delay lines and gain (Cruse 2002). For example, a network with negative sensory feedback will produce stable oscillations if the open-loop gain is equal or larger than 1 at a frequency where the phase shift is 180° (Nyquist criterion). It should be noted though that for nonlinear systems such as neural networks, more complex stability criteria such as Lyapunov or the circle criterion might be necessary. Networks with positive feedback, on the other hand, need a high-pass filter or related mechanism that reduces the positive feedback to create stable oscillations (Bässler 1986). In both cases, the oscillations would be driven entirely by sensory feedback and might not even require a central oscillatory network. In such a case the system would be called a chain reflex (because a system that *must* be driven by sensory input is defined as a reflex). In fact, a chain reflex may not be distinguishable from a CPG *in vivo* (Bässler 1986). If we consider a relaxation oscillator as a pattern-generating circuit (e.g., a half-center circuit with reciprocal inhibition, as is found in

many systems), the frequency of the oscillations would depend on the endogenous excitation of the loop and its internal characteristics (gain and time constant of the fatigue of the positive feedback). Sensory feedback could affect oscillation frequency either by affecting the intrinsic characteristics or by modifying the excitation state of the network. Even in the easiest situation of a simple addition of excitation to the oscillator neurons by the sensory feedback, the timing cues for switching between oscillation states would depend on the sensory feedback, and the CPG would only be responsible for managing the actual switch between phases. If the endogenous excitation in such a relaxation oscillator network would fall below the threshold for oscillations, the sensory feedback could substitute for the lack of endogenous excitation and elicit oscillations. Per definition, this would then be a chain reflex.

Even if the CPG consists of a negative feedback loop (such as serial inhibition in a network with an odd number of neurons), sensory feedback would drive the frequency of the oscillation. In such a system, the CPG oscillation frequency depends on the amplitude and phase-frequency oscillations of the open-loop system. If sensory feedback is added to the system, the eigenfrequency stays the same, and the sensory input will be damped and superimposed on the inherent (CPG) oscillations (Cruse 2009). The resulting frequency will thus be a superposition of central and sensory oscillations. Sensory feedback, however, will entrain the central oscillations within a given range. Thus, the CPG represents a band-pass filter for the sensory oscillation. In the passband, the timing cues of the oscillations are determined by the sensory feedback. In summary, determining whether the CPG or sensory feedback dominates the behavior of the oscillatory system *in vivo*, although of pivotal importance for understanding the dynamics of motor systems, continues to challenge studies of CPG function.

Long-Loop Sensory Feedback and Long-Lasting Effects of Sensory Feedback

While one role of sensory feedback is to allow the CPG to deal with environmental perturbations

(corrective input), certain motor pattern characteristics such as phase relationships must be maintained to guarantee functional and behavioral homeostasis. Sensory changes from one part of the pattern, for example, might require compensatory changes in other parts. Thus, the effects of local sensory feedback might have widespread and possibly long-lasting effects.

Sensory pathways also affect CPGs indirectly, by influencing the neurons that control the CPGs. In the locomotor systems of cats and lampreys, for example, supraspinal networks in the brainstem receive sensory input from many modalities, including proprioceptive feedback (Rossignol et al. 2006). While in general these upstream neurons are involved in pattern initiation, modulation, and selection, the uniquely identifiable reticulospinal Mauthner and Müller cells in lampreys display movement-related activities that appear to be elicited by ascending feedback from the CPGs (Antri et al. 2009; Buchanan 2011). This is similar to modulatory projection neurons that control the CPGs in the stomatogastric nervous system (Blitz and Nusbaum 2012). Here, ascending feedback from CPG neurons imposes a rhythmic activity pattern onto these modulatory neurons. In both cases, neurons outside of the CPG have access to the timing of the CPG, and they are affected by sensory input. In the stomatogastric nervous system, phasic sensory feedback affects the very set of projection neurons that shows CPG timing (Hedrich et al. 2009), which allows for a long-loop sensory control of CPG activity. In lobsters, for example, the phasing of CPG activity can reverse activity if the proprioceptive AGR neuron exceeds a certain threshold (Combes et al. 1999), due to the bistable intrinsic properties of modulatory projection neurons that process sensory feedback from AGR.

Open-Loop Versus Closed-Loop Sensorimotor Interactions

Even if sensory feedback only exerts short-acting effects, compensatory changes in the motor pattern may occur and induce global, long-lasting changes in the CPG pattern, because the activity changes of the neurons targeted by sensory

feedback may induce changes in a chain of followers. Yet, relatively little is known about such holistic sensorimotor interactions. This is mostly due to the fact that while sensory feedback has been studied in many motor circuits, this was typically done in open-loop conditions, i.e., with emphasis on how sensory signals alter motor output (rather than interact with it), or on information flow toward that output. The dynamical components determined by the interaction of motor and sensory activities, however, can create emergent properties that govern the functional characteristics of the system. While already a standard for investigating movement or behavior in general (e.g., fly and bee flight: Dickinson 2005; Fry et al. 2008; Mronz and Lehmann 2008; Sareen et al. 2011; Srinivasan 2011; monkey motor control & vision: Nicolelis 2003), the idiosyncratic dynamics created by the sensorimotor interaction have only rarely been elucidated at the level of the nervous system.

One reason for the discrepancy between closed-loop behavioral and open-loop nervous system studies is the unfortunate fact that sensory structures, and thus also sensory feedback, are typically not available in experiments performed in isolation from the body. The functional and circuit properties as well as the cellular characteristics of CPG networks, however, are only known in great detail because of their accessibility in isolated preparations. In contrast, in systems with well-characterized behavior and sensory structures, the underlying neural network is usually not well described. One way to circumvent this problem is to provide artificial sensory feedback that depends on the motor output, in real time, to the isolated CPG circuit. Thus far, in the few instances in which such closed-loop experiments have been performed (Bässler and Nothof 1994; Ausborn et al. 2007; Smarandache et al. 2008; Ausborn et al. 2009), it is clear that sensorimotor interactions pivotally shape the motor output. Given the fact that sensory feedback also affects the upstream neural structures that control the motor circuits, it seems reasonable to assume that sensory feedback in closed-loop conditions will have an impact on the motor pattern that goes beyond simple influences on timing and

magnitude. Rather, emergent properties of sensorimotor interactions are to be expected.

Indirect and Long-Term Influences of Sensory Feedback

While the immediate influences on timing and magnitude of sensory feedback are well studied, sensory feedback also has long-term influences on CPG activity:

1. Development of vital rhythmic activities. It is still unclear whether sensory feedback is needed during early nervous system development (Suster and Bate 2002). A lack of feedback, however, leads to dysplasia or coordination problems later in life.
2. Stability and robustness of the motor pattern during the life span of the animal. While motor circuits must be flexible in order to respond to changes in the environment or the body conditions, they must also generate stable patterns and be robust against perturbations. Emergent properties of sensorimotor interactions may well supply the basis for stability and robustness and may even help to select the adequate motor pattern, biasing the system toward specific patterns. In particular when environmental or neuromodulatory conditions change, robustness must be present. Failures of this control may be fatal (e.g., sudden infant death syndrome).
3. Recovery from injury. Continuous CPG activity requires CNS input, and removal of this input causes a failure of the motor pattern. While there is some evidence that continuous entrainment of the motor patterns via sensory feedback supports recovery (e.g., after spinal cord injury, Rossignol and Frigon 2011; Mehrholz et al. 2012), it is far from clear what mechanisms drive recovery. Emergent properties during sensorimotor interactions might support recovery, in particular if neuromodulatory neurons (long-loop sensory influences) are involved. Sensory feedback could in this case replace the missing endogenous excitation of the CPG network.

In summary, while CPGs generate rhythmic activity patterns that have similarities to the behavioral patterns, sensory feedback pivotally

shapes the CPG output. While the short-term and direct actions of sensory feedback on CPG activity are well described, their long-term actions and sensorimotor interactions in closed-loop conditions are a focus of current studies.

References

- Akay T, Ludwar B, Goritz ML, Schmitz J, Buschges A (2007) Segment specificity of load signal processing depends on walking direction in the stick insect leg muscle control system. *J Neurosci* 27:3285–3294
- Antri M, Fenelon K, Dubuc R (2009) The contribution of synaptic inputs to sustained depolarizations in reticulospinal neurons. *J Neurosci* 29:1140–1151
- Ausborn J, Stein W, Wolf H (2007) Frequency control of motor patterning by negative sensory feedback. *J Neurosci* 27:9319–9328
- Ausborn J, Wolf H, Stein W (2009) The interaction of positive and negative sensory feedback loops in dynamic regulation of a motor pattern. *J Comput Neurosci* 27:245–257
- Bässler U (1986) On the definition of central pattern generator and its sensory control. *Biol Cybern* 54:65–69
- Bässler U (1993) The femur-tibia control system of stick insects—a model system for the study of the neural basis of joint control. *Brain Res Brain Res Rev* 18:207–226
- Bässler U, Nothof U (1994) Gain control in a proprioceptive feedback loop as a prerequisite for working close to instability. *J Comput Biol* 175:23–33
- Berkowitz A, Roberts A, Soffe SR (2010) Roles for multifunctional and specialized spinal interneurons during motor pattern generation in tadpoles, zebrafish larvae, and turtles. *Front Behav Neurosci* 4:36
- Birmingham JT (2001) Increasing sensor flexibility through neuromodulation. *Biol Bull* 200:206–210
- Birmingham JT, Szuts ZB, Abbott LF, Marder E (1999) Encoding of muscle movement on two time scales by a sensory neuron that switches between spiking and bursting modes. *J Neurophysiol* 82:2786–2797
- Blitz DM, Nusbaum MP (2011) Neural circuit flexibility in a small sensorimotor system. *Curr Opin Neurobiol* 21:544–552
- Blitz DM, Nusbaum MP (2012) Modulation of circuit feedback specifies motor circuit output. *J Neurosci* 32:9182–9193
- Bonte B, Linden RW, Scott BJ, van Steenberghe D (1993) Role of periodontal mechanoreceptors in evoking reflexes in the jaw-closing muscles of the cat. *J Physiol* 465:581–594
- Buchanan JT (2011) Spinal locomotor inputs to individually identified reticulospinal neurons in the lamprey. *J Neurophysiol* 106:2346–2357
- Burrows M (1996) The neurobiology of an insect brain. Oxford University Press, New York
- Büsches A (2005) Sensory control and organization of neural networks mediating coordination of

- multisegmental organs for locomotion. *J Neurophysiol* 93:1127–1135
- Büsches A, Scholz H, El Manira A (2011) New moves in motor control. *Curr Biol* 21:513–524
- Chevallier S, Jan Ijspeert A, Ryczko D, Nagy F, Cabelguen JM (2008) Organisation of the spinal central pattern generators for locomotion in the salamander: biology and modelling. *Brain Res Rev* 57:147–161
- Combes D, Meyrand P, Simmers J (1999) Dynamic restructuring of a rhythmic motor program by a single mechanoreceptor neuron in lobster. *J Neurosci* 19:3620–3628
- Cruse H (2002) The functional sense of central oscillations in walking. *Biol Cybern* 86:271–280
- Cruse H (2009) Neural networks as cybernetic systems, 3rd and revised edn. Brains, Minds & Media. <http://www.brains-minds-media.org/archive/1990/bmm1841.pdf>
- Daur N, Nadim F, Stein W (2009) Regulation of motor patterns by the central spike-initiation zone of a sensory neuron. *Eur J Neurosci* 30:808–822
- Dickinson MH (2005) The initiation and control of rapid flight maneuvers in fruit flies. *Integr Comp Biol* 45:274
- Dickinson PS (2006) Neuromodulation of central pattern generators in invertebrates and vertebrates. *Curr Opin Neurobiol* 16:604–614
- Doi A, Ramirez JM (2008) Neuromodulation and the orchestration of the respiratory rhythm. *Respir Physiol Neurobiol* 164:96–104
- El Manira A, Kyriakatos A, Nanou E (2010) Beyond connectivity of locomotor circuitry-ionic and modulatory mechanisms. *Prog Brain Res* 187:99–110
- Fry SN, Rohrseitz N, Straw AD, Dickinson MH (2008) TrackFly: virtual reality for a behavioral system analysis in free-flying fruit flies. *J Neurosci Methods* 171:110–117
- Garcia-Crescioni K, Fort TJ, Stern E, Brezina V, Miller MW (2010) Feedback from peripheral musculature to central pattern generator in the neurogenic heart of the crab *Callinectes sapidus*: role of mechanosensitive dendrites. *J Neurophysiol* 103:83–96
- Gordon IT, Whelan PJ (2006) Deciphering the organization and modulation of spinal locomotor central pattern generators. *J Exp Biol* 209:2007–2014
- Grillner S (2003) The motor infrastructure: from ion channels to neuronal networks. *Nat Rev Neurosci* 4:573–586
- Grillner S, Markram H, De Schutter E, Silberberg G, LeBeau FE (2005) Microcircuits in action—from CPGs to neocortex. *Trends Neurosci* 28:525–533
- Harris-Warrick RM (2011) Neuromodulation and flexibility in central pattern generator networks. *Curr Opin Neurobiol* 21:685–692
- Hedrich UB, Smarandache CR, Stein W (2009) Differential activation of projection neurons by two sensory pathways contributes to motor pattern selection. *J Neurophysiol* 102:2866–2879
- Hooper SL (2000) Central pattern generators. *Curr Biol* 10:R176
- Isa T, Sparks DL (2006) Microcircuit of the superior colliculus. A neuronal machine that determines timing and endpoint of saccadic eye movements. In: Grillner S, Graybiel AM (eds) *Microcircuits: the interface between neurons and global brain function*. MIT Press, Cambridge, MA, pp 5–34
- Katz PS, Hooper SL (2007) Invertebrate central pattern generators. *Cold Spring Harb Monogr Ser* 49:251
- Kiehn O (2006) Locomotor circuits in the mammalian spinal cord. *Annu Rev Neurosci* 29:279–306
- Marder E (2012) Neuromodulation of neuronal circuits: back to the future. *Neuron* 76:1–11
- Marder E, Calabrese RL (1996) Principles of rhythmic motor pattern generation. *Physiol Rev* 76:687–717
- Mehrholz J, Kugler J, Pohl M (2012) Locomotor training for walking after spinal cord injury. *Cochrane Database Syst Rev* 11, CD006676
- Mronz M, Lehmann FO (2008) The free-flight response of *Drosophila* to motion of the visual environment. *J Exp Biol* 211:2026–2045
- Nicolelis MA (2003) Brain-machine interfaces to restore motor function and probe neural circuits. *Nat Rev Neurosci* 4:417–422
- Pearson KG (2004) Generating the walking gait: role of sensory feedback. *Prog Brain Res* 143:123–129
- Rossignol S, Frigon A (2011) Recovery of locomotion after spinal cord injury: some facts and mechanisms. *Annu Rev Neurosci* 34:413–440
- Rossignol S, Dubuc R, Gossard JP (2006) Dynamic sensorimotor interactions in locomotion. *Physiol Rev* 86:89–154
- Sareen P, Wolf R, Heisenberg M (2011) Attracting the attention of a fly. *Proc Natl Acad Sci USA* 108:7230–7235
- Skorupski P, Sillar KS (1986) Phase-dependent reversal of reflexes mediated by the thoracocoxal muscle receptor organ in the crayfish, *Procambarus leniusculus*. *J Neurophysiol* 55:689–695
- Smarandache CR, Daur N, Hedrich UB, Stein W (2008) Regulation of motor pattern frequency by reversals in proprioceptive feedback. *Eur J Neurosci* 28:460–474
- Srinivasan MV (2011) Honeybees as a model for the study of visually guided flight, navigation, and biologically inspired robotics. *Physiol Rev* 91:413–460
- Stein W (2009) Modulation of stomatogastric rhythms. *J Comp Physiol A Neuroethol Sens Neural Behav Physiol* 195:989–1009
- Stein W, Schmitz J (1999) Multimodal convergence of presynaptic afferent inhibition in insect proprioceptors. *J Neurophysiol* 82:512–514
- Suster ML, Bate M (2002) Embryonic assembly of a central pattern generator without sensory input. *Nature* 416:174–178
- von Holst E, Mittelstädt H (1950) The reaference principle. Interaction between the central nervous system and the periphery. In: Selected papers of Erich von Holst: the behavioural physiology of animals and man. Methuen, London, pp 39–73

- Wolf H (1993) The locust tegula: significance for flight rhythm generation, wing movement control and aerodynamic force production. *J Exp Biol* 182:229–253
- Wolf H, Burrows M (1995) Proprioceptive sensory neurons of a locust leg receive rhythmic presynaptic inhibition during walking. *J Neurosci* 15:5623–5636

Further Reading

- Central Pattern Generation. http://en.wikipedia.org/wiki/Central_pattern_generator
- Facebook pages on Central pattern generators
Feedback. <http://en.wikipedia.org/wiki/Feedback>
<https://www.facebook.com/pages/Central-pattern-generator/138633789494277?nr>
- Locomotion and the Spinal Cord. http://en.wikipedia.org/wiki/Spinal_Locomotion
- Motor coordination. http://www.scholarpedia.org/article/Motor_coordination
- Neural Oscillations. http://en.wikipedia.org/wiki/Neural_oscillation
- Periodic Orbits and Dynamical Systems. http://www.scholarpedia.org/article/Periodic_orbit
- Scholarpedia articles on Central Pattern Generators and Sensory Feedback
- The Efference Copy. http://en.wikipedia.org/wiki/Efference_copy
- The Scratch Reflex. http://en.wikipedia.org/wiki/Scratch_reflex
- The Spinal Cord. http://www.scholarpedia.org/article/Spinal_cord
- The Stomatogastric Ganglion. http://www.scholarpedia.org/article/Stomatogastric_ganglion
- The *Tritonia* Swim Network. http://www.scholarpedia.org/article/Tritonia_swim_network
- Wikipedia articles on Central Pattern Generators and Feedback

Sensory Modulation of Central Pattern Generators

- ▶ Sensory Input to Central Pattern Generators

Sensory Stimulation

- ▶ Peripheral Nerve Interface Applications, Sensory Restoration

Serial Sectioning Microscopy

- ▶ Physical Sectioning Microscopy

Serpentine Receptors

- ▶ Metabotropic Receptors (G Protein Coupled Receptors)

Servo Control

- ▶ Spinal Cord, Integrated (Non CPG) Models of

Seven-Transmembrane Domain Receptors

- ▶ Metabotropic Receptors (G Protein Coupled Receptors)

SFC

- ▶ Spike Triggered Average

Shaking Palsy

- ▶ Parkinson's Disease: Deep Brain Stimulation

Short-Term Plasticity, Biophysical Models

Robert Rosenbaum
Department of Applied and Computational Mathematics and Statistics, University of Notre Dame, Notre Dame, IN, USA

Definition

Short-term plasticity refers to changes in synaptic efficacy in response to presynaptic spiking that persist for a few seconds at most but more

often decay over a timescale of a few hundred milliseconds. There are two primary types of short-term plasticity: short-term depression and short-term facilitation. Short-term depression is a reduction in synaptic efficacy that is often, but not always, caused by a transient depletion of neurotransmitter vesicles. Short-term facilitation is an increase in synaptic efficacy often caused by a transient increase in the number of vesicles released by presynaptic action potentials. The detailed biophysical mechanisms underlying synaptic facilitation are discussed in Facilitation, Biophysical Models, and we therefore focus on more phenomenological models of facilitation here.

Detailed Description

Stochastic Models of Short-Term Depression Arising from Neurotransmitter Depletion

Short-term depression is often believed to arise primarily from the depletion of neurotransmitter vesicles, and therefore a large proportion of short-term depression models rely solely on the mechanism of vesicle depletion. It should be noted, though, that some synapses exhibit short-term depression that is inconsistent with vesicle depletion alone (Branco and Staras 2009; Zucker and Regehr 2002; Wong et al. 2003; Xu and Wu 2005).

We begin by describing a model of short-term depression that takes into account the stochastic nature of vesicle release and recovery. The model was introduced in Vere-Jones (1966), and various formulations of it have since been used extensively (Senn et al. 2001; Zador 1998; Wang 1999; Matveev and Wang 2000; Fuhrmann et al. 2002; Goldman et al. 2002; Goldman 2004; de la Rocha and Parga 2005; Pfister et al. 2010; Rosenbaum et al. 2012, 2013, 2014; Reich and Rosenbaum 2013). A presynaptic neuron makes M functional contacts onto a postsynaptic neuron, and each functional contact contains N_0 release sites that can each dock at most one vesicle, so that the maximum number of docked vesicles is $M \times N_0$. Of course, the model can easily be extended to allow heterogeneity in the number of release sites at each contact. Here,

the term “functional contact” (hereafter, simply “contact”) refers to a group of vesicle release sites where the grouping is chosen so that release sites at different contacts release vesicles independently from one another, but release sites on the same contact are not necessarily independent. Functional contacts need not necessarily correspond to anatomical contacts in a one-to-one fashion. The most widely assumed dependence between release sites arises from the “univesicular hypothesis” which states that each contact can release at most one vesicle in response to a single presynaptic spike. If this constraint is to be met, then release sites at the same contact cannot be independent.

Since release sites at different contacts are independent, we need only specify the probability distribution of the number of vesicles released by a presynaptic spike at each contact. A widely used rule (Vere-Jones 1966; Wang 1999; Matveev and Wang 2000; Goldman et al. 2002; de la Rocha and Parga 2005; Rosenbaum et al. 2014) that is consistent with the univesicular hypothesis states one vesicle is released at a particular contact with probability $1 - (1 - p)^n$; otherwise, no vesicles are released. Here p is a number between 0 and 1, and $n \in [0, N_0]$ is a dynamical variable representing the number of docked vesicles at the contact in question at the moment when the presynaptic spike occurs. When $n = 0$, the release probability is zero, as expected. When $n = 1$, the release probability is p . In general, the probability of release increases with the number of docked vesicles.

While the rule above is straightforward to simulate numerically, it is difficult to treat analytically due to the non-independence of release sites. Some analytical tractability can be gained by assuming that the release of a vesicle at each release site is independent. This is equivalent to assuming that each functional contact has exactly one release site (i.e., making the substitutions, $M = M \times N_0$ and $N_0 = 1$). In this widely used version of the model (Zador 1998; Matveev and Wang 2000; Fuhrmann et al. 2002; Goldman 2004; Pfister et al. 2010; Rosenbaum et al. 2012, 2013; McDonnell et al. 2013; Reich and Rosenbaum 2013), each presynaptic spike

releases each docked vesicle independently with probability p . Thus, the number of vesicles released by a presynaptic spike is a binomial random variable with parameters n and p , where n is the number of docked vesicles when the spike arrives.

When a vesicle is released at a contact, the number of docked vesicles at that contact is decremented. The waiting time until a released vesicle is recovered is an exponentially distributed random variable with mean τ_u . Equivalently, it is the waiting time for the first event in a Poisson process with rate $1/\tau_u$. Due to the memoryless property of Poisson processes, this rule allows the modeler to keep track of only the *number* of docked vesicles at each contact and ignore the time at which empty release sites became empty. In particular, the probability that one empty release site is filled during the time interval $(t, t + dt)$, i.e., that the number of releasable vesicles is incremented during that time interval, is given by $(N_0 - n)dt + o(dt)$, where n is the number of docked vesicles at that release site and $o(dt)/dt \rightarrow 0$ as $dt \rightarrow 0$.

Each released vesicle induces a change in conductance of the postsynaptic neuron's membrane. This is often modeled by setting the postsynaptic conductance to $g(t) = \sum w_j \alpha(t-t_j)$, where t_j is the time of the j th presynaptic spike, w_j is the number of vesicles released by the j th spike, and $\alpha(t)$ is a stereotyped synaptic conductance waveform representing the change in postsynaptic conductance elicited by the release of a single vesicle. In general, $w_j \in [0, M \times N_0]$ but $w_j \in [0, M]$ whenever the univesicular hypothesis is satisfied.

Pseudo-code for implementing this and similar models of stochastic vesicle dynamics is provided in McDonnell et al. (2013) along with a review and discussion of some effects of stochastic vesicle dynamics on neural coding and the statistics of the synaptic response.

Deterministic Models of Short-Term Facilitation and Depression

The stochastic model of short-term depression discussed above can be difficult to analyze

mathematically, and it can also be difficult to fit the model's parameters to data. Moreover, the model assumes that short-term depression is due solely to the depletion of neurotransmitter vesicles even though other factors sometimes play a role. Finally, the model does not account for the effects of short-term facilitation on synaptic efficacy.

These difficulties are partly overcome by a deterministic model in which synaptic efficacy is treated as an abstract, continuous variable that is modified by each presynaptic spike. This model is mostly agnostic to the precise mechanisms responsible for changes in synaptic efficacy, but it can accurately reproduce experimental data after the model parameters are fit to the data using statistical fitting algorithms. Due to its amenability to mathematical analysis and its ability to reproduce experimental data, this deterministic model and its variations are widely used in both theoretical and experimental studies (Tsodyks and Markram 1997; Varela et al. 1997; Tsodyks et al. 1998; Markram et al. 1998; Chance et al. 1998; Maas and Zador 1999; Fuhrmann et al. 2002; Hanson and Jaeger 2002; Cook et al. 2003; Grande and Spain 2005; Rothman et al. 2009; Lindner et al. 2009; Merkel and Lindner 2010; Pfister et al. 2010; Rosenbaum et al. 2012; Scott et al. 2012; Mohan et al. 2013).

We describe the model as presented in Varela et al. (1997) and then discuss some common variations of the model. The efficacy of a synapse is defined by $A(t) = A_0 F(t) D_1(t) D_2(t) D_3(t)$, where A_0 is a constant representing a baseline efficacy, $F(t)$ is a dynamic variable representing facilitation, and each $D_k(t)$ is a dynamic variable representing depression.

Immediately after each presynaptic spike, each depression variable is updated according to the rule $D_k \leftarrow D_k d_k$ for $k = 1, 2, 3$, where each d_k is a number between 0 and 1 representing the amount of depression evoked by each spike. Between presynaptic spikes, the depression variables decay exponentially back to their maximal values, which can be normalized to one without loss of generality, so that $\tau_{Dk} \frac{dD_k}{dt} = 1 - D_k$, where τ_{Dk} is the timescale of recovery for the k th depression variable.

Similarly, the facilitation variable is updated after each presynaptic spike according to $F \leftarrow F + f$, and the evolution between spikes is defined by $\tau_F \frac{dF}{dt} = 1 - F$.

The postsynaptic conductance (or current for current-based modeling) can then be written in terms of the synaptic efficacy as $g(t) = \sum_j A(t_j) \alpha(t - t_j)$, where $\alpha(t)$ is a ste-

reotyped waveform and t_j is the time of the j th presynaptic spike.

This model is commonly modified by changing the number of facilitation or depression variables. A common variation uses only one facilitation and one depression variable so that $A(t) = A_0 F(t) D(t)$. Some synapses exhibit short-term depression but not facilitation, in which case the facilitation variable can be removed completely and we can simply write $A(t) = A_0 D(t)$. These two variations of the model are amenable to mathematical analysis (Lindner et al. 2009; Merkel and Lindner 2010; Rosenbaum et al. 2012).

In the form of the model described above, the depression variables are updated multiplicatively, while the facilitation variable is updated additively. Updating facilitation multiplicatively can cause synaptic efficacy to grow unrealistically large at high presynaptic rates (Varela et al. 1997), but a saturating multiplicative update rule was applied in Hanson and Jaeger (2002) and accurately captured recorded data. In other variations of the model, updates to the depression variables depend on the value of the facilitation variables, for example, in Lindner et al. (2009) and Merkel and Lindner (2010), the update rule for the depression is given by, $D_k \leftarrow (1 - F)D_k$.

It should be noted that the deterministic model with one depression variable and no facilitation variables is equivalent to the mean field of the stochastic model of short-term depression with $N_0 = 1$. Specifically, if the stochastic model is simulated over several trials with the same presynaptic spike train, then the trial average of the postsynaptic conductance it produces is proportional to the postsynaptic conductance produced by one trial of the deterministic model driven by the same presynaptic spike train whenever $\tau_u = \tau_D$ and $p_r = d$.

References

- Chance F, Nelson S, Abbott L (1998) Synaptic depression and the temporal response characteristics of v1 cells. *J Neurosci* 18:4785
- Cook DL, Schwindt PC, Grande LA, Spain WJ (2003) Synaptic depression in the localization of sound. *Nature* 421:66–70
- de la Rocha J, Parga N (2005) Short-term synaptic depression causes a non-monotonic response to correlated stimuli. *J Neurosci* 25:8416–8431
- Fuhrmann G, Segev I, Markram H, Tsodyks M (2002) Coding of temporal information by activity dependent synapses. *J Neurophysiol* 87:140
- Goldman M (2004) Enhancement of information transmission efficiency by synaptic failures. *Neural Comput* 16:1137–1162
- Goldman MS, Maldonado P, Abbott L (2002) Redundancy reduction and sustained ring with stochastic depressing synapses. *J Neurosci* 22:584–591
- Grande LA, Spain WJ (2005) Synaptic depression as a timing device. *J Physiol* 20:201–210
- Hanson JE, Jaeger D (2002) Short-term plasticity shapes the response to simulated normal and parkinsonian input patterns in the globus pallidus. *J Neurosci* 22:5164–5172
- Lindner B, Ganglo D, Longtin A, Lewis JE (2009) Broadband coding with dynamic synapses. *J Neurosci* 29:2076–2087
- Maass W, Zador AM (1999) Dynamic stochastic synapses as computational units. *Neural Comput* 11:903–917
- Markram H, Wang Y, Tsodyks M (1998) Differential signaling via the same axon of neocortical pyramidal neurons. *Proc Natl Acad Sci U S A* 95:5323
- Matveev V, Wang XJ (2000) Implications of all-or-none synaptic transmission and short term depression beyond vesicle depletion: a computational study. *J Neurosci* 20:1575–1588
- McDonnell MD, Mohan A, Stricker C (2013) Mathematical analysis and algorithms for efficiently and accurately implementing stochastic simulations of short-term synaptic depression and facilitation. *Front Comput Neurosci* 7:58
- Merkel M, Lindner B (2010) Synaptic filtering of rate-coded information. *Phys Rev E* 81:041921
- Mohan A, McDonnell MD, Stricker C (2013) Interaction of short-term depression and ring dynamics in shaping single neuron encoding. *Front Comput Neurosci* 7:41
- Pfister JP, Dayan P, Lengyel M (2010) Synapses with short-term plasticity are optimal estimators of presynaptic membrane potentials. *Nat Neurosci* 13:1271–1275
- Reich S, Rosenbaum R (2013) The impact of short term synaptic depression and stochastic vesicle dynamics on neuronal variability. *J Comput Neurosci* 35:1–15
- Rosenbaum R, Rubin J, Doiron B (2012) Short term synaptic depression imposes a frequency dependent filter on synaptic information transfer. *PLoS Comput Biol* 8: e1002557

- Rosenbaum R, Rubin JE, Doiron B (2013) Short-term synaptic depression and stochastic vesicle dynamics reduce and shape neuronal correlations. *J Neurophysiol* 109:475–484
- Rosenbaum R, Zimnik A, Zheng F, Turner RS, Alzheimer C, Doiron B, Rubin JE (2014) Axonal and synaptic failure suppress the transfer of ring rate oscillations, synchrony and information during high frequency deep brain stimulation. *Neurobiol Dis* 62:86–99
- Rothman JS, Cathala L, Steuber V, Silver RA (2009) Synaptic depression enables neuronal gain control. *Nature* 457:1015–1018
- Scott P, Cowan AI, Stricker C (2012) Quantifying impacts of short-term plasticity on neuronal information transfer. *Phys Rev E* 85:041921
- Tsodyks MV, Markram H (1997) The neural code between neocortical pyramidal neurons depends on neurotransmitter release probability. *Proc Natl Acad Sci U S A* 94:719–723
- Tsodyks M, Pawelzik K, Markram H (1998) Neural networks with dynamic synapses. *Neural Comput* 10:821–835
- Varela JA, Sen K, Gibson J, Fost J, Abbott LF et al (1997) A quantitative description of short-term plasticity at excitatory synapses in layer 2/3 of rat primary visual cortex. *J Neurosci* 17:7926–7940
- Vere-Jones D (1966) Simple stochastic models for the release of quanta of transmitter from a nerve terminal. *Aust NZ J Stat* 8:53–63
- Wang XJ (1999) Fast burst ring and short-term synaptic plasticity: a model of neocortical chattering neurons. *J Neurosci* 89:347–362
- Wong AY, Graham BP, Billups B, Forsythe ID (2003) Distinguishing between presynaptic and postsynaptic mechanisms of short-term depression during action potential trains. *J Neurosci* 23:4868–4877
- Xu J, Wu LG (2005) The decrease in the presynaptic calcium current is a major cause of short-term depression at a calyx-type synapse. *Neuron* 46:633–645
- Zador A (1998) Impact of synaptic unreliability on the information transmitted by spiking neurons. *J Neurophysiol* 79:1219
- Zucker R, Regehr W (2002) Short-term synaptic plasticity. *Annu Rev Physiol* 64:355–405

Further Reading

- Branco T, Staras K (2009) The probability of neurotransmitter release: variability and feedback control at single synapses. *Nat Rev Neurosci* 10:373–383
- Senn W, Markram H, Tsodyks M (2001) An algorithm for modifying neurotransmitter release probability based on pre- and postsynaptic spike timing. *Neural Comput* 13:35–67

Short-Term Synaptic Facilitation

- [Facilitation, Biophysical Models](#)

Short-Term Synaptic Plasticity in Central Pattern Generators

Diana Martinez¹, Victor Matveev² and Farzan Nadim^{1,2}

¹Federated Department of Biological Sciences, New Jersey Institute of Technology/Rutgers University, Newark, NJ, USA

²Department of Mathematical Sciences, New Jersey Institute of Technology, Newark, NJ, USA

Synonyms

[Augmentation](#); [Depression](#); [Enhancement](#); [Facilitation](#); [Post-tetanic Potentiation](#)

Definition

Short-term synaptic plasticity (STP) is a transient (milliseconds to minutes) activity-dependent change in the amplitude of the postsynaptic current in response to presynaptic activity. Central pattern generators (CPGs) are neural networks in the central nervous system capable of producing coordinated rhythmic output without rhythmic input from sensory organs or from higher control centers.

Detailed Description

Short-term synaptic plasticity (STP) is a transient (milliseconds to minutes) activity-dependent change in the amplitude (strength) of the postsynaptic current in response to presynaptic activity. It has clear implications for neural signaling and has been studied for several decades. Much of the modeling work has focused on the events in the presynaptic terminal and primarily on the role of Ca^{2+} in synaptic release of neurotransmitters (Zucker and Regehr 2002; Fioravante and Regehr 2011). However, postsynaptic effects such as saturation of postsynaptic receptors can also contribute to STP (Hennig 2013; Xu-Friedman and Regehr 2004). A complete understanding of

short-term synaptic plasticity requires knowing how the pre- and postsynaptic neurons interact to alter synaptic strength.

The contribution of short-term synaptic plasticity to network-level output has probably been best examined in studies of central pattern generator (CPG) networks. CPG networks produce rhythmic patterned outputs without patterned input and are best understood in the analysis of rhythmic motor activities such as locomotion and respiration. For instance, the CPG underlying the inspiratory phase of respiration is located in the pre-Bötzinger complex found within the ventrolateral medulla of the mammalian brain (Grillner 2003). Identified CPG circuits are known to govern locomotion in invertebrates, including leeches, mollusks, and crustaceans (Arshavsky Yu et al. 1993; Ayers 2004; Friesen and Kristan 2007). Additionally, locomotion in mammals is believed to be governed by CPG networks in the spinal cord (MacKay-Lyons 2002). The understanding of CPGs in producing motor behaviors has been greatly advanced through the use of computational models (Butera et al. 1999; Tabak et al. 2000; Oh et al. 2012; Vavoulis et al. 2007; Sherwood et al. 2011).

Almost all synapses are regulated by a variety of short- or long-term activity-dependent processes that alter the strength of the synapse. Depending on the behavioral needs, CPGs alter their rhythmic activity patterns by changing the cycle frequency and the relative activity phases of the participating neurons. Synapses in CPG networks are naturally subject to short-term activity-dependent modifications due to the rhythmic nature of the network output. This review examines the mechanisms and consequences of short-term changes in synaptic strength within CPGs. Although both pre- and postsynaptic mechanisms have been implicated in short-term plasticity, the majority of known STP effects are presynaptic (Wadiche and Jahr 2001).

Neurobiology of Central Pattern Generators

CPG networks often involve neurons that produce bursting oscillations. Bursting refers to an interval of rapid firing of spikes, bookended by intervals of quiescence. Bursting activity in

neurons is often the result of a slow-wave oscillation in the membrane potential which, on the depolarized portion, crosses spike threshold. The slow-wave oscillations that underlie bursting activity result from the interaction of low-threshold-activated inward currents and slow voltage- or Ca^{2+} -gated outward currents.

In cases where the mechanisms underlying rhythm generation have been described, CPG oscillations have been shown to arise in one of two ways: either through the activity of endogenously oscillatory (pacemaker) neurons or through the synaptic interactions of neurons within a network (Goldin-Meadow et al. 2001). Pacemaker neurons produce oscillations when they are synaptically isolated from the network. However, these oscillations may be conditional upon the presence of the appropriate neuromodulatory substances. Although pacemaker neurons can be the rhythm-generating kernel of a CPG network, the proper output of the CPG usually requires the synaptic interaction of the pacemaker neurons with non-oscillatory (follower) neurons whose activity is important in producing the proper output pattern.

In contrast to pacemaker-driven CPGs, network oscillators produce rhythmic output through synaptic interactions of pairs or groups of neurons, which may not be oscillatory when synaptically isolated. The most prominent example of such network oscillations is half-center oscillators that drive the activities of antagonistic muscles. First proposed by T. Graham-Brown in the early 1900s, half-center oscillators are responsible for producing rhythmic behavior in these types of networks (Brostoff et al. 2008). Half-center oscillators are driven by neurons (or neuron groups) that are antagonistic in their activity. The two groups of neurons are rhythmically active but activity in one group inhibits the activity of the other. In the first classification of half-center oscillators by Wang and Rinzel, they demonstrated that the transition between the two halves of the half-center oscillation can occur through one of two distinct mechanisms: escape and release. In escape mode, the inhibited neurons transition to active mode due to their own intrinsic properties. In contrast, in release mode,

the active neurons terminated their activity due to their intrinsic properties and thereby release the inhibited neuron which rebounds from inhibition to produce activity (Wang and Rinzel 1992). The frequency and relative phases of the two halves of the half-center are controlled by the intrinsic properties of the neurons as well as the strength and dynamics of the reciprocal synapses. The extent to which intrinsic versus synaptic properties control the half-center oscillations can be used to further divide these networks into intrinsic or synaptic (Skinner et al. 1994). In biological systems, the transitions between the two halves of the half-center oscillator are often through a combination of escape and release mechanisms (Nadim et al. 1995).

Invertebrate CPG studies provided crucial results for the understanding of the mechanisms of neural network connectivity and CPG functions. The ease of accessibility of many of the invertebrate networks has allowed for a mapping of the synaptic connectivity and therefore the identification of the CPG circuits. Additionally, in many invertebrate networks, the voltage-gated ionic currents of the component neurons and the short-term dynamics of the synapses have been characterized. Examples of well-studied invertebrate CPG networks include those underlying tritonia swimming, feeding in crustaceans, and leech heartbeat (Marder and Calabrese 1996).

CPGs have also been the subject of intensive research in vertebrate systems, in particular, lamprey swimming, salamander locomotion, and rodent models of respiration. Lampreys are primitive fish whose spinal cords are easily dissected and are capable of producing fictive locomotion *in vitro*. As such, this preparation has become the best studied example of rhythmic locomotor activity in vertebrates (Grillner 2003). Salamanders offer an insight into the switching of two different types of locomotor modalities: swimming or stepping. Of particular interest is the stepping gait, in which the body makes an S-shape wave with coordinate movement of the limbs (Ijspeert et al. 2007). This stepping gait can either be fast or slow, but salamanders prefer the faster trotting gait. When trotting, diagonal limbs are in phase while opposite limbs are out of

phase. Both the switching between swimming and stepping, as well as the simulation of stepping, have been modeled and studied (Ijspeert et al. 2007) but the full understanding of the behaviors has been elusive.

The medullar pre-Bötzinger complex contains the CPG responsible for the genesis of breathing in mammals (Smith et al. 1991). The pre-Bötzinger complex controls the inspiratory phase of breathing through the activity of a set of pacemaker neurons that are state dependent. In particular, there are two subsets of pacemaker neurons within the system which have been characterized based on their pharmacological properties. During normoxia, respiratory rhythm generation is driven through a heterogeneous population of pacemaker neurons, while during hypoxia the respiratory rhythm is driven by only one type of pacemaker (Pena et al. 2004). The pacemaker groups and the properties of the network have been the subject of many computational models (Butera et al. 1999; Del Negro et al. 2002a, b; Cordovez et al. 2010).

Molecular Mechanisms of Neurotransmitter Release

Presynaptic Machinery Responsible for Neurotransmitter Release

Neurotransmitter release is achieved through the interplay of a variety of proteins associated with the presynaptic terminal. Once transmitter-filled vesicles are transported to the synaptic terminal, they dock and are primed for release. This process involves the attachment of vesicles to the membrane through the SNARE complex, a set of interacting proteins found on the vesicle and cytoplasmic membranes (Jahn and Fasshauer 2012). Only primed vesicles can fuse with the membrane and release neurotransmitter into the presynaptic cleft through the process of exocytosis, triggered by the interaction of Ca^{2+} with the SNARE complex. Depolarization of the presynaptic terminal, usually due to the arrival of an action potential, activates voltage-gated Ca^{2+} channels (VGCCs) and results in a rapid increase of the local concentration of Ca^{2+} , which then binds to synaptotagmin, causing the vesicle membrane to fuse with the plasma membrane

(Mehta et al. 1996). The SNARE complex is a helical protein complex composed of the v-SNARE protein synaptobrevin (also known as vesicle-associated membrane protein [VAMP-2]) and the t-SNARE (“target” SNARE) proteins localized to the presynaptic plasma membrane, SNAP-25 (synaptosome-associated protein of 25 kDa), and syntaxin. Apart from its interaction with v-SNARE, t-SNARE proteins syntaxin also directly interact with the Ca^{2+} channels to promote vesicular fusion (Stanley 1997). Finally, synaptic function also requires the interaction of SNARE proteins with Munc-18, which has been found to allow for syntaxin and SNAP-25 to form a complex that serves as an intermediate in the exocytic pathway (Zilly et al. 2006). The three SNARE proteins, syntaxin, SNAP-25, and synaptobrevin, have been found to be the minimal set of proteins required for fusion (Sudhof 2012).

Pools of Neurotransmitters: Ready or Not

The presynaptic terminal may contain hundreds of neurotransmitter vesicles; however, only a fraction of these, the readily releasable pool (RRP), are docked at the active zones of the membrane awaiting release. The remaining vesicles are divided between the reserve pool, the vesicles that are ready to be moved to the docking position, and the non-recycling pool (Regehr 2012).

Short-term synaptic plasticity is affected by the size of the RRP. The number of vesicles in the RRP varies across species and measuring it could be difficult due to the replenishment from the reserve pool. Earlier studies estimated the range of the RRP to vary from 7 to 130 depending on the type and location of synapse (Rosenmund and Stevens 1996; Xu-Friedman et al. 2001; Zucker and Regehr 2002). However, that number can average as high as 1,700 as measured in the mouse neuromuscular junction (Ruiz et al. 2011) and is also high at special high-throughput synapses such as calyx of Held, which contains hundreds of active zones (Schneggenburger et al. 2002). More recent studies have found those numbers to be much smaller than originally estimated. For instance, at certain GABAergic

synapses within the cerebellum, the number of vesicles was found to be maximally 4 (Trigo et al. 2012). The size of the RRP may be regulated by a variety of factors, including the actions of the Na^+/K^+ ATPase pump (Taruno et al. 2012).

Postsynaptic Factors Influence Short-Term Plasticity

While many studies have concentrated on the presynaptic mechanism of short-term plasticity, postsynaptic factors also contribute to changes in the synaptic transmission strength. The postsynaptic response depends on the amount of transmitter release from the presynaptic neuron, kinetics of the receptor, and other factors. Postsynaptic Ca^{2+} contributes significantly to post-tetanic potentiation in sensory-motor neurons of Aplysia, by facilitating the induction of plasticity at neighboring neurons (Schaffhausen et al. 2001). Additionally, when postsynaptic receptors are saturated, this may limit responses by the cell, as shown at the climbing fiber synapse (Wadiche and Jahr 2001). Desensitization of postsynaptic receptors can cause a temporary decrease in synaptic responses (Xu-Friedman and Regehr 2004). Additionally, saturation of the postsynaptic receptors may have a significant impact on recovery from depression (Foster et al. 2002).

The Role of Ca^{2+} in Neurotransmitter Release

Ca^{2+} entry through VGCCs in the presynaptic terminal results in vesicle fusion and the release of neurotransmitters. Synaptic strength is dependent on Ca^{2+} levels in the presynaptic active zone. This is believed to be partially due to Ca^{2+} interaction with multiple low-affinity binding sites on synaptotagmin, several of which have to be bound to trigger vesicle fusion (Felmy et al. 2003). If Ca^{2+} binds one or more sites, it increases the probability of release upon subsequent depolarization of the presynaptic membrane. Elevated amounts of local Ca^{2+} , however, are transient and highly sensitive to the distance from the VGCCs and the site of release. Local Ca^{2+} concentrations are also affected by Ca^{2+} -binding proteins that exist in the presynaptic bouton (Regehr 2012). Not all

Ca^{2+} that enters the presynaptic cell, however, binds to the docked vesicles: it diffuses away from the active site, is rapidly buffered (Burroni et al. 2002; Burnashev and Rozov 2005), or is actively pumped out of the presynaptic terminal (Regehr 2012). The residual Ca^{2+} is then gradually removed from the presynaptic bouton (Scott and Rusakov 2006). Ca^{2+} diffusion in the presynaptic terminal has been extensively studied and modeled (Simon and Llinas 1985; Zucker and Fogelson 1986; Bertram et al. 1999; Matveev et al. 2004).

Multiple Forms of Synaptic Plasticity Coexist at a Synapse

The interactions of different types of synaptic plasticity found at most synapses allows for an alteration in synaptic strength. Short-term depression, facilitation, augmentation, and post-tetanic potentiation can coexist at the synapse; however, the dominance of each of the mechanisms at a given time point is controlled by the activity of the presynaptic neuron.

Short-term plasticity is often measured using a paired-pulse protocol. The presynaptic neuron is stimulated with a square pulse two to five times with an appropriately chosen interpulse interval. The postsynaptic response is then measured for each stimulus and the ratio of the postsynaptic response to the presynaptic response becomes the measure of short-term plasticity. If the ratio is greater than 1, the response is deemed facilitatory, and when it is less than 1 then it is deemed depressing. This method has been used in a variety of systems including different CPGs such as the pre-Bötziinger complex, the pyloric network of the stomatogastric system, and leech feeding behavior.

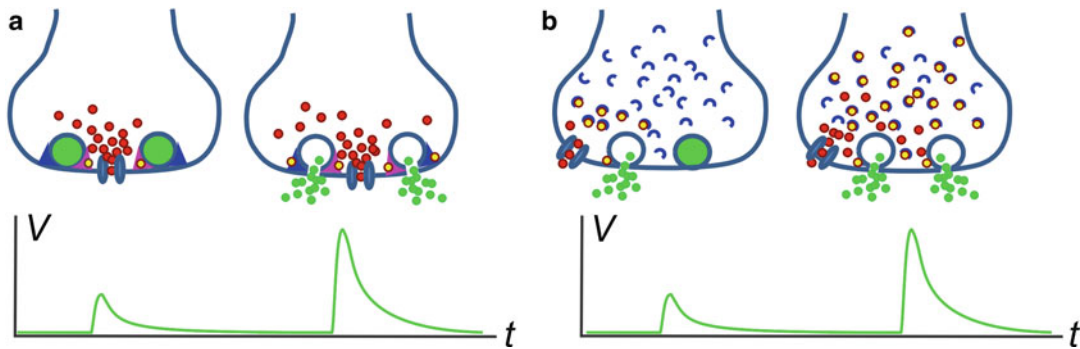
Facilitation

Synaptic facilitation is a type of short-term plasticity where the amount of neurotransmitter released is increased during a sequence of action potentials reaching the synaptic bouton. This increase leads to a prolonged effect of the neurotransmitter on the postsynaptic membrane. This type of short-term plasticity occurs at the fastest time scale and is measured using a paired-

pulse protocol. Facilitation is subdivided into two different stages: F1 facilitation which lasts tens of milliseconds and F2 facilitation which lasts hundreds of milliseconds (Zucker and Regehr 2002).

Many ideas were put forward to explain pre-synaptic facilitation (Regehr 2012). The simplest hypothesis states that the arrival of the action potential at the presynaptic bouton evokes a rise in local Ca^{2+} which triggers neurotransmitter release and which then persists at a lower concentration in the presynaptic bouton. Since such low residual Ca^{2+} concentration is insufficient by itself to trigger low-affinity vesicle release gates, this hypothesis requires the residual Ca^{2+} to act at a high-affinity presynaptic Ca^{2+} sensor other than synaptotagmin. Further, such a high-affinity second sensor should be located farther from the channel in order to prevent its rapid saturation; for this reason, this model is sometimes referred to as the two-site model of synaptic facilitation (Matveev et al. 2002) (Fig. 1a). A second possibility is that this second, high-affinity Ca^{2+} binding site possesses slower Ca^{2+} kinetics, allowing its Ca^{2+} -bound state to outlive the Ca^{2+} residual signal. This mechanism is often referred to as the bound residual Ca^{2+} mechanism of synaptic facilitation (Matveev et al. 2006) and was historically the first facilitation model proposed in the pioneering studies by Katz and Miledi (1968), who called such bound Ca^{2+} the “active” Ca^{2+} (Bornschein et al. 2013; Isope 2013). Finally, it is also possible that this additional slower Ca^{2+} binding process may represent Ca^{2+} -dependent vesicle priming or other Ca^{2+} -dependent process upstream of vesicle (Pan and Zucker 2009).

The action of endogenous Ca^{2+} buffers has been proposed as an alternative mechanism of synaptic facilitation. Both fast, high-affinity Ca^{2+} buffers and those that slowly bind Ca^{2+} can influence facilitation. Ca^{2+} binding proteins reduce the concentration of local Ca^{2+} at the release site (Regehr 2012). However, high-affinity Ca^{2+} buffers bind Ca^{2+} at the presynaptic bouton when concentrations are sufficiently high, which leaves them unable to bind additional Ca^{2+} . As a result, the additional Ca^{2+} that enters and is not bound by buffers will reach the release site. In this manner, local buffer saturation can



Short-Term Synaptic Plasticity in Central Pattern Generators, Fig. 1 Models of facilitation (a) **Residual-free Ca²⁺ accumulation: the two-site model of synaptic facilitation.** Exocytosis requires simultaneous binding of Ca²⁺ (red circles) to a low-affinity sensor located within the channel nanodomains (magenta at the vesicle base) and more remotely located low-affinity sensors (blue on the far side of the vesicle). The accumulation of free residual Ca²⁺ is small but more significant far from the channel, allowing for a significant increase in the binding of remote Ca²⁺ sensor from the first stimulus to the second

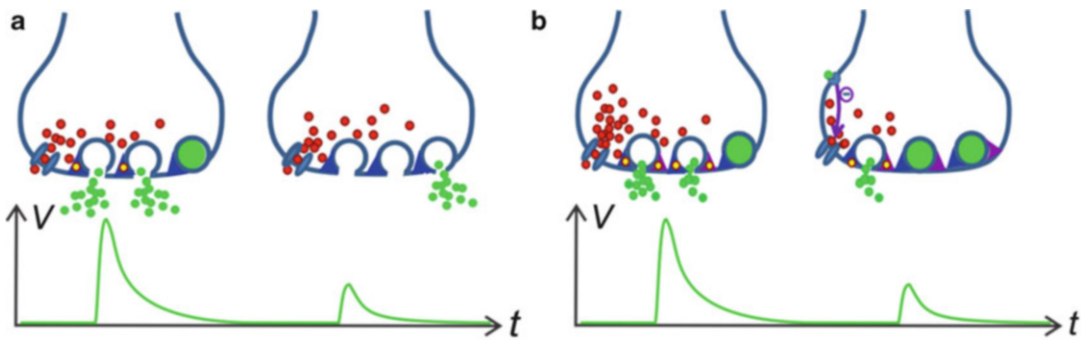
and, therefore, more transmitter release and a larger postsynaptic response (bottom traces). (b) **Facilitation by saturation of high-affinity buffer.** The postsynaptic response (bottom trace) to the first presynaptic stimulus is small, because most of the free Ca²⁺ ions entering the presynaptic site are bound (yellow circles) by the Ca²⁺ buffer molecules (blue crescents) before they reach the vesicles. However, the postsynaptic response to the second presynaptic stimulus will be large because there are fewer free buffer molecules around, thus increasing the probability of Ca²⁺ ions reaching the targets for exocytosis

contribute to paired-pulse facilitation (Burnashev and Rozov 2005; Matveev et al. 2006; Neher 1998) (Fig. 1b). Slow Ca²⁺ binding proteins can also influence facilitation. By controlling the concentration of residual Ca²⁺ and accelerating its decay in the presynaptic bouton, slow endogenous buffers act like the slow buffer EGTA (Atluri and Regehr 1996), which then provides a mechanism to control the rate of Ca²⁺ decay, thereby influencing facilitation rates (Regehr 2012). However, the contribution of both fast and slow buffers to facilitation is still a matter of debate (Bornschein et al. 2013).

An important example of a CPG where synaptic facilitation has been observed and studied both experimentally and using computational modeling is the lamprey swim CPG. In control conditions, activity-dependent plasticity does not contribute to the patterning of network activity. However, Kozlov et al. found that substance P can lead to an activity-dependent facilitation during repetitive activation of the inhibitory cross caudal interneurons (CCINs) in the lamprey swim CPG (Parker and Grillner 1999; Kozlov et al. 2001). This is accomplished through control of the release of the neuromodulators from the

presynaptic side as well as postsynaptic modulation of different ionic conductances (Kozlov et al. 2001). In order to examine the activity-dependent facilitation in this system, they used a compartmentalized Hodgkin-Huxley model neuron with the synaptic activation modeled as a leaky integrator and synapse activation summing input spike events of constant duration. Their study aimed to elucidate the two alternate modes of activity within the lamprey spinal locomotor network, showing that facilitation has a strong effect on frequency regulation in this CPG (Kozlov et al. 2001).

Facilitation has also been observed in the crustacean stomatogastric nervous system, specifically in the synapses of the pyloric CPG. The synapse from the lateral pyloric (LP) neuron to the pyloric dilator (PD) neurons is the sole chemical feedback to the pacemaker group and exhibits short-term depression. This synapse possesses both a graded and spike-mediated component (Zhao et al. 2011). However, the presence of the endogenously released neuromodulatory peptide proctolin switches the dynamics of this synapse from depression to facilitation. The mechanism of this switch was investigated in



Short-Term Synaptic Plasticity in Central Pattern Generators, Fig. 2 Models of depression **(a)** Synaptic depression by vesicle depletion. The postsynaptic response (bottom panel) to the second presynaptic stimulus is greater compared to the response to the first presynaptic stimulus because of the reduction in the number of available neurotransmitter-filled vesicles (green circles). **(b)** Ca²⁺ channel inactivation/presynaptic modulation.

the modeling study of Oh et al. (2012), who proposed that the low-voltage-activated Ca²⁺ current possesses both fast and slow kinetic components and that proctolin adjusts the activation rate of the slow component, leading to an accumulation of local Ca²⁺ in response to low-voltage presynaptic stimuli, resulting in synaptic facilitation (Oh et al. 2012).

Depression

At many synapses, elevated activity or repeated stimulation leads to a decrease in synaptic strength. As is the case for facilitation, multiple mechanisms can contribute to synaptic depression (Zucker and Regehr 2002; Regehr 2012). Depression is believed to be caused in large part by the reversible depletion of available synaptic resources, mainly the release-ready pool of vesicles (RRP; Fig. 2a). Such vesicle depletion is an example of use-dependent synaptic depression, with higher levels of use associated with larger degree of synaptic depression (Markram et al. 1998). Reducing the level of synaptic transmission relieves use-dependent synaptic depression, while at high sustained synaptic activity, the replenishment of the RRP from the reserve vesicle pool cannot keep up with the depletion of the RRP (Zucker and Regehr 2002; Regehr 2012). Therefore, the extent to which depletion occurs

Presynaptic Ca²⁺ channel opening probability may decrease during the presynaptic stimulus train, due to one of two mechanisms: (i) inactivation of presynaptic voltage-dependent Ca²⁺ channels or (ii) activation of presynaptic metabotropic receptors that modulate the gating of presynaptic Ca²⁺ channels (e.g., through G-protein-regulated pathways). Reduction in the presynaptic Ca²⁺ current leads to a reduction in the vesicle release rate

is dependent on the number of vesicles in the RRP at each active zone and the number of vesicles that are released by an action potential. This depletion model accounts for the properties of the paired-pulse depression that is seen in many different types of synapses. According to the depletion model, the more vesicles released with the initial stimulus, the fewer will be released by the second and subsequent pulses. Depression by vesicle depletion is particularly pronounced following high-frequency tetanic stimulation, which strongly depletes the RRP so that the subsequent recovery may take tens of seconds, rather than seconds.

Another mechanism of activity-dependent depression involves inhibition of the response caused by the vesicle fusion with the active zone. Vesicle fusion may transiently disrupt the morphology of the active zone and may inhibit the time it takes for membrane proteins to clear the active zone. This mechanism is supported by experimental evidence that blocking endocytosis can increase synaptic depression during pulse trains (Regehr 2012).

Other depression mechanisms may depend on the intensity of stimulation rather than amount of neurotransmitter released. This is true, for instance, in the case of inactivation of Ca²⁺ channels that has been found to account for depression at some synapses (Bertram et al. 2003).

Presynaptic recordings from the calyx of Held have shown that high-frequency stimulation reduces Ca^{2+} entry. Decreased Ca^{2+} entry was found at frequencies greater than 30 Hz and depletion was found when the stimulus was in excess of 100 Hz (Xu and Wu 2005).

Also on the presynaptic side, depression can arise through the activation of metabotropic presynaptic receptors activated by modulatory substances released from the activated presynaptic terminals, postsynaptic cells, or neighboring cells (Fig. 2b). Metabotropic receptors may be selective either for the neurotransmitter released by the terminal itself (autoreceptor-mediated depression), for retrograde messengers (e.g., endocannabinoid receptors), or for neuromodulatory substances projecting from elsewhere in the nervous system (neuromodulatory receptors). Depression may also arise from postsynaptic mechanisms such as postsynaptic receptor desensitization, which in fact represents another form of use-dependent synaptic depression. Another mechanism of synaptic depression was demonstrated in the developing spinal cord (Tabak et al. 2000, 2001). In this system, GABA is functionally excitatory because intracellular Cl^- is high. During an episode of activity, Cl^- ions leave the neurons so the GABA reversal potential becomes more negative. This mechanism seems quite important for the episodic activity in the developing spinal cord.

Regulation of and recovery from depression are also important factors in short-term synaptic plasticity. Bassoon, a large presynaptic protein present at the active zone, has been found to minimize depression by replenishing vesicles at release sites (Hallermann et al. 2010; Regehr 2012). When Bassoon is experimentally removed, synaptic depression is enhanced. Rab3-interacting molecules (RIM) are vital components of the active zone (Kaeser et al. 2011), serving two critical functions: priming of synaptic vesicles and tethering of Ca^{2+} channels to the active zone (Kaeser 2011; Kaeser et al. 2011). RIM proteins have been implicated in influencing depression: when they are removed, depression is dramatically alleviated (Calakos et al. 2004; Sudhof 2012).

The role of synaptic depression in CPG networks has been studied in great detail. For instance, synaptic depression has been determined to be pivotal in the maintenance of phase relationships within CPGs (Mamiya et al. 2003; Manor et al. 2003). Depression of synapses of the pyloric network leads to synaptic weakening during fast rhythmic behavior while allowing the synapses to remain strong during a slow rhythm (Marder et al. 2005). Manor et al. examined the effect of synaptic depression using a model of an oscillator neuron and a follower neuron coupled with an inhibitory synapse from the oscillator to the follower (Manor et al. 2003). An important result from their study was that depression in inhibitory synapses always promotes a constant relative phase between the pre- and postsynaptic neurons in an oscillatory network. The strength of a depressing synapse in an oscillatory network is dependent on the cycle frequency: the faster the oscillation, the more depression and therefore the weaker the synapse. This frequency dependence implies that synaptic inhibition gets weaker if the network operates at a faster pace, thus reducing the latency between the pre- and postsynaptic neuron activity. Because relative phase is defined as latency over period, this simple observation implies that a depressing synapse will always promote phase constancy (as opposed to a constant latency) compared to a synapse that is nondepressing.

In order to maintain stability, a network may reconfigure itself to produce different patterning behaviors. Li et al. explored the mechanisms by which sensory activity led to the selection and generation of swimming and struggling in *Xenopus* tadpoles (Li et al. 2007). In *Xenopus* tadpoles, two different behaviors can be triggered: struggling, which is elicited if the animal is held or pinned against a silicone-gel-lined Petri dish and involves strong head-to-tail bends, and swimming, which is elicited if the animal is touched lightly and involves low-amplitude bends (Kahn and Roberts 1982; Li et al. 2007). In immobilized tadpoles, stimulation of the skin causes a switch of the struggling CPG by reconfiguration of the locomotor network. This switch is thought to be caused by a

context-dependent short-term depression of the reciprocally inhibitory synapses between two CPG neurons, the commissural interneurons (cINs). When synaptic depression was included in these synapses in a model network, activation of the network at higher firing frequencies characteristic of struggling led to robust bursting activity. In contrast, when the network was activated at lower firing rates, depression was not active and the network output resembled more the swimming behavior which involves a single spike per cycle (Li et al. 2007). Thus, as shown in this system, synaptic depression of reciprocal inhibition may play a key role in one behavior (struggling) but be mostly absent in another (swimming).

Synaptic depression was also proposed as the principal mechanism of rhythmogenesis in the developing chick spinal cord (Tabak et al. 2000). These studies proposed that synaptic depression accumulates during the active burst phase of the rhythm, ultimately terminating the active phase, and that the recovery from depression during the inactive state allows the bursting activity to resume in the next cycle of activity. Within certain networks, rhythm generation may depend on specific types of synaptic depression which are more complex than simple vesicle depletion. For example, this is the case in the group pacemaker model of rhythmic activity in the pre-Bötzinger complex developed by Rubin et al. (2009) based on a Hodgkin-Huxley style conductance-based model of spiking activity. In this model, glutamatergic synapses and short-term depression of excitatory transmission have roles in the rhythmogenesis of a particular type of pacemaker group within the pre-Bötzinger complex. A network-wide burst is generated through recurrent synaptic excitation that initiates the postsynaptic Ca^{2+} -activated nonspecific cation current (I_{CAN}). The depolarization due to I_{CAN} causes a voltage-dependent spike inactivation, diminishing recurrent excitation and therefore attenuating the postsynaptic accumulation of Ca^{2+} . The burst is then terminated through activity-dependent outward currents, resulting in a quiescent state in the network. A new cycle is then initiated when sporadic spiking activity rekindles excitatory interactions (Rubin et al. 2009).

Augmentation and Post-tetanic Potentiation

While facilitation has been shown to last no more than hundreds of milliseconds, two other forms of potentiating short-term synaptic plasticity, last tens of seconds to minutes in duration. Augmentation and post-tetanic potentiation (PTP) are related forms of synaptic plasticity that are observed after sustained high-frequency stimulation (Zucker and Regehr 2002; Regehr 2012). Augmentation is an increase in the synaptic potential amplitude that is produced by repetitive stimulation which has been found to act by potentiating vesicle fusion (Zucker and Regehr 2002). Post-tetanic potentiation is a common form of short-term plasticity that leads to an increase in synaptic strength for several minutes after increased stimulation. PTP is closely related to augmentation and lasts tens of seconds to minutes in duration and increases with the presence of additional or sustained stimuli.

Augmentation was originally described in the frog neuromuscular junction and now has been observed in many synapses, including in mammalian cortex (Regehr 2012). Augmentation increases during a stimulus train, but decays slower than facilitation with a time constant of 5–8 s. The decay of augmentation has been shown to be insensitive to stimulation duration and frequency. Additionally, augmentation shares other properties with facilitation. Augmentation is dependent on the buildup of Ca^{2+} in the presynaptic terminals during spike trains, after the development of a significant level of facilitation. Several mechanisms are believed to contribute to augmentation and PTP, including action potential broadening, increase in quantal size, and changes in the RRP (Zucker and Regehr 2002).

Several functional roles of augmentation and PTP in synaptic plasticity have been suggested. Augmentation is believed to be a counteracting mechanism against depression during times of high levels of neural activity (Deng and Klyachko 2011). Furthermore, it has been shown that transmitter release is sustained during trains of stimuli by increasing the release probability of vesicles within the RRP. In addition to maintaining transmitter release during high-frequency

stimulation, augmentation has been found to directly counteract depression in hippocampal excitatory synapses (Deng and Klyachko 2011). The mechanisms for both augmentation and PTP have been studied and debated for many years. Early studies proposed the accumulation of residual Ca^{2+} as a primary mechanism, but more recent results have implicated both PKC activation and CaM kinase II activity (Hennig 2013). However, very few studies have concentrated on these phenomena in CPGs.

In the crustacean STG, the gastric mill network is responsible for movement of muscles that control chewing within the foregut. Stein et al. characterized the temporal dynamics of the gm6 gastric mill muscle and explored the response of this muscle to different patterns of input during the gastric mill CPG activity (Stein et al. 2006). Using train stimulations of various frequencies, they found that augmentation increased the amplitude of the EJPs at certain frequencies while not at others. During the ongoing gastric mill rhythm, augmentation contributed to the response of the muscle as well as muscle force.

Outlook

Theoretical models have contributed greatly to the advancement in understanding of synaptic transmission and short-term plasticity in CPGs. In concert with experimental data, studies of both vertebrates and invertebrate CPGs have provided insight and mechanisms by which neural circuits reconfigure in order to generate different patterns to alter behavior. Many of the models discussed capture the processes involved in short-term synaptic release in a relatively simple way. Additionally, many studies on the effects of short-term synaptic plasticity on CPG activity suggest that neuromodulators play an important role in the network behavior through their effects on synaptic properties. As CPG circuits continue to be mapped, it will be essential to gain insight about mechanisms which cause switches in behavior, changes in synaptic strength, and remodeling of the circuits in general. The mutual relationship between computational modeling and experimental studies will continue to be

important for the understanding of the role of STP in CPG function.

Acknowledgement This work was supported in part by NIH grant MH060605.

Cross-References

- ▶ [Calcium-Dependent Exocytosis, Biophysical Models of](#)
- ▶ [Rhythm Generation in Embryonic Chick Spinal Cord](#)

References

- Arshavsky YuI, Orlovsky GN, Panchin YuV, Roberts A, Soffe SR (1993) Neuronal control of swimming locomotion: analysis of the pteropod mollusc Clione and embryos of the amphibian Xenopus. *Trends Neurosci* 16:227–233
- Atluri PP, Regehr WG (1996) Determinants of the time course of facilitation at the granule cell to Purkinje cell synapse. *J Neurosci* 16:5661–5671
- Ayers J (2004) Underwater walking. *Arthropod Struct Dev* 33:347–360
- Bertram R, Smith GD, Sherman A (1999) Modeling study of the effects of overlapping Ca^{2+} microdomains on neurotransmitter release. *Biophys J* 76:735–750
- Bertram R, Swanson J, Yousef M, Feng ZP, Zamponi GW (2003) A minimal model for G protein-mediated synaptic facilitation and depression. *J Neurophysiol* 90:1643–1653
- Bornschein G, Arendt O, Hallermann S, Brachtendorf S, Eilers J, Schmidt H (2013) Paired-pulse facilitation at recurrent Purkinje neuron synapses is independent of calbindin and parvalbumin during high-frequency activation. *J Physiol* 591:3355–3370
- Brostoff JM, Birns J, McCrea D (2008) Phenytoin toxicity: an easily missed cause of cerebellar syndrome. *J Clin Pharm Ther* 33:211–214
- Burnashev N, Rozov A (2005) Presynaptic Ca^{2+} dynamics, Ca^{2+} buffers and synaptic efficacy. *Cell Calcium* 37:489–495
- Burrone J, Neves G, Gomis A, Cooke A, Lagnado L (2002) Endogenous calcium buffers regulate fast exocytosis in the synaptic terminal of retinal bipolar cells. *Neuron* 33:101–112
- Butera RJ Jr, Rinzel J, Smith JC (1999) Models of respiratory rhythm generation in the pre-Botzinger complex. II. Populations of coupled pacemaker neurons. *J Neurophysiol* 82:398–415
- Calakos N, Schoch S, Sudhof TC, Malenka RC (2004) Multiple roles for the active zone protein

- RIM1alpha in late stages of neurotransmitter release. *Neuron* 42:889–896
- Cordovez JM, Wilson CG, Solomon IC (2010) Geometrical analysis of bursting pacemaker neurons generated by computational models: comparison to *in vitro* pre-Botzinger complex bursting neurons. *Adv Exp Med Biol* 669:45–48
- Del Negro CA, Koshiya N, Butera RJ Jr, Smith JC (2002a) Persistent sodium current, membrane properties and bursting behavior of pre-botzinger complex inspiratory neurons *in vitro*. *J Neurophysiol* 88:2242–2250
- Del Negro CA, Morgado-Valle C, Feldman JL (2002b) Respiratory rhythm: an emergent network property? *Neuron* 34:821–830
- Deng PY, Klyachko VA (2011) The diverse functions of short-term plasticity components in synaptic computations. *Commun Integr Biol* 4:543–548
- Felmy F, Neher E, Schneggenburger R (2003) Probing the intracellular calcium sensitivity of transmitter release during synaptic facilitation. *Neuron* 37:801–811
- Fioravante D, Regehr WG (2011) Short-term forms of presynaptic plasticity. *Curr Opin Neurobiol* 21:269–274
- Foster KA, Kreitzer AC, Regehr WG (2002) Interaction of postsynaptic receptor saturation with presynaptic mechanisms produces a reliable synapse. *Neuron* 36:1115–1126
- Friesen WO, Kristan WB (2007) Leech locomotion: swimming, crawling, and decisions. *Curr Opin Neurobiol* 17:704–711
- Goldin-Meadow S, Nusbaum H, Kelly SD, Wagner S (2001) Explaining math: gesturing lightens the load. *Psychol Sci* 12:516–522
- Grillner S (2003) The motor infrastructure: from ion channels to neuronal networks. *Nat Rev Neurosci* 4:573–586
- Hallermann S, Fejtová A, Schmidt H, Weyhersmüller A, Silver RA, Gundelfinger ED, Eilers J (2010) Bassoon speeds vesicle reloading at a central excitatory synapse. *Neuron* 68:710–723
- Hennig MH (2013) Theoretical models of synaptic short term plasticity. *Front Comput Neurosci* 7:45
- Ijspeert AJ, Crespi A, Ryczko D, Cabelguen JM (2007) From swimming to walking with a salamander robot driven by a spinal cord model. *Science* 315:1416–1420
- Isopo P (2013) Short-term synaptic plasticity and the ‘active calcium’ hypothesis at a central synapse. *J Physiol* 591.19:4681–4682
- Jahn R, Fasshauer D (2012) Molecular machines governing exocytosis of synaptic vesicles. *Nature* 490:201–207
- Kaeser PS (2011) Pushing synaptic vesicles over the RIM. *Cell Logist* 1:106–110
- Kaeser PS, Deng L, Wang Y, Dulubova I, Liu X, Rizo J, Sudhof TC (2011) RIM proteins tether Ca^{2+} channels to presynaptic active zones via a direct PDZ-domain interaction. *Cell* 144:282–295
- Kahn JA, Roberts A (1982) The neuromuscular basis of rhythmic struggling movements in embryos of *Xenopus laevis*. *J Exp Biol* 99:197–205
- Katz B, Miledi R (1968) The role of calcium in neuromuscular facilitation. *J Physiol* 195:481–492
- Kozlov A, Kortaleski JH, Aurell E, Grillner S, Lansner A (2001) Modeling of substance P and 5-HT induced synaptic plasticity in the lamprey spinal CPG: consequences for network pattern generation. *J Comput Neurosci* 11:183–200
- Li WC, Sautois B, Roberts A, Soffe SR (2007) Reconfiguration of a vertebrate motor network: specific neuron recruitment and context-dependent synaptic plasticity. *J Neurosci* 27:12267–12276
- MacKay-Lyons M (2002) Central pattern generation of locomotion: a review of the evidence. *Phys Ther* 82:69–83
- Mamiya A, Manor Y, Nadim F (2003) Short-term dynamics of a mixed chemical and electrical synapse in a rhythmic network. *J Neurosci* 23:9557–9564
- Manor Y, Bose A, Booth V, Nadim F (2003) Contribution of synaptic depression to phase maintenance in a model rhythmic network. *J Neurophysiol* 90:3513–3528
- Marder E, Calabrese RL (1996) Principles of rhythmic motor pattern generation. *Physiol Rev* 76:687–717
- Marder E, Bucher D, Schulz DJ, Taylor AL (2005) Invertebrate central pattern generation moves along. *Curr Biol* 15:R685–R699
- Markram H, Gupta A, Uziel A, Wang Y, Tsodyks M (1998) Information processing with frequency-dependent synaptic connections. *Neurobiol Learn Memory* 70:101–112
- Matveev V, Sherman A, Zucker RS (2002) New and corrected simulations of synaptic facilitation. *Biophys J* 83:1368–1373
- Matveev V, Zucker RS, Sherman A (2004) Facilitation through buffer saturation: constraints on endogenous buffering properties. *Biophys J* 86:2691–2709
- Matveev V, Bertram R, Sherman A (2006) Residual bound Ca^{2+} can account for the effects of Ca^{2+} buffers on synaptic facilitation. *J Neurophysiol* 96:3389–3397
- Mehta PP, Battenberg E, Wilson MC (1996) SNAP-25 and synaptotagmin involvement in the final $\text{Ca}(2+)$ -dependent triggering of neurotransmitter exocytosis. *Proc Natl Acad Sci USA* 93:10471–10476
- Nadim F, Olsen OH, De Schutter E, Calabrese RL (1995) Modeling the leech heartbeat elemental oscillator. I. Interactions of intrinsic and synaptic currents. *J Comput Neurosci* 2:215–235
- Neher E (1998) Vesicle pools and Ca^{2+} microdomains: new tools for understanding their roles in neurotransmitter release. *Neuron* 20:389–399
- Oh M, Zhao S, Matveev V, Nadim F (2012) Neuromodulatory changes in short-term synaptic dynamics may be mediated by two distinct mechanisms of presynaptic calcium entry. *J Comput Neurosci* 33:573–585

- Pan B, Zucker RS (2009) A general model of synaptic transmission and short-term plasticity. *Neuron* 62:539–554
- Parker D, Grillner S (1999) Long-lasting substance-P-mediated modulation of NMDA-induced rhythmic activity in the lamprey locomotor network involves separate RNA- and protein-synthesis-dependent stages. *Eur J Neurosci* 11:1515–1522
- Pena F, Parkis MA, Tryba AK, Ramirez JM (2004) Differential contribution of pacemaker properties to the generation of respiratory rhythms during normoxia and hypoxia. *Neuron* 43:105–117
- Regehr WG (2012) Short-term presynaptic plasticity. *Cold Spring Harb Perspect Biol* 4:a005702
- Rosenmund C, Stevens CF (1996) Definition of the readily releasable pool of vesicles at hippocampal synapses. *Neuron* 16:1197–1207
- Rubin JE, Hayes JA, Mendenhall JL, Del Negro CA (2009) Calcium-activated nonspecific cation current and synaptic depression promote network-dependent burst oscillations. *Proc Natl Acad Sci USA* 106:2939–2944
- Ruiz R, Cano R, Casanas JJ, Gaffield MA, Betz WJ, Tabares L (2011) Active zones and the readily releasable pool of synaptic vesicles at the neuromuscular junction of the mouse. *J Neurosci* 31:2000–2008
- Schaffhausen JH, Fischer TM, Carew TJ (2001) Contribution of postsynaptic Ca^{2+} to the induction of post-tetanic potentiation in the neural circuit for siphon withdrawal in Aplysia. *J Neurosci* 21:1739–1749
- Schneggenburger R, Sakaba T, Neher E (2002) Vesicle pools and short-term synaptic depression: lessons from a large synapse. *Trends Neurosci* 25:206–212
- Scott R, Rusakov DA (2006) Main determinants of presynaptic Ca^{2+} dynamics at individual mossy fiber-CA3 pyramidal cell synapses. *J Neurosci* 26:7071–7081
- Sherwood WE, Harris-Warrick R, Guckenheimer J (2011) Synaptic patterning of left-right alternation in a computational model of the rodent hindlimb central pattern generator. *J Comput Neurosci* 30:323–360
- Simon SM, Llinás RR (1985) Compartmentalization of the submembrane calcium activity during calcium influx and its significance in transmitter release. *Biophys J* 48:485–498
- Skinner FK, Kopell N, Marder E (1994) Mechanisms for oscillation and frequency control in reciprocally inhibitory model neural networks. *J Comput Neurosci* 1:69–87
- Smith JC, Ellenberger HH, Ballanyi K, Richter DW, Feldman JL (1991) Pre-Botzinger complex: a brainstem region that may generate respiratory rhythm in mammals. *Science* 254:726–729
- Stanley (1997) The calcium channel and the organization of the presynaptic release face. *Trends Neurosci* 20:404–409
- Stein W, Smarandache CR, Nickmann M, Hedrich UB (2006) Functional consequences of activity-dependent synaptic enhancement at a crustacean neuromuscular junction. *J Exp Biol* 209:1285–1300
- Sudhof TC (2012) The presynaptic active zone. *Neuron* 75:11–25
- Tabak J, Murphrey CR, Moore LE (2000) Parameter estimation methods for single neuron models. *J Comput Neurosci* 9:215–236
- Tabak J, Rinzel J, O'Donovan MJ (2001) The role of activity-dependent network depression in the expression and self-regulation of spontaneous activity in the developing spinal cord. *J Neurosci Off J Soc Neurosci* 21:8966–8978
- Taruno A, Ohmori H, Kuba H (2012) Inhibition of presynaptic Na^+/K^+ -ATPase reduces readily releasable pool size at the avian end-bulb of Held synapse. *Neurosci Res* 72:117–128
- Trigo FF, Sakaba T, Ogden D, Marty A (2012) Readily releasable pool of synaptic vesicles measured at single synaptic contacts. *Proc Natl Acad Sci USA* 109:18138–18143
- Vavoulis DV, Straub VA, Kemenes I, Kemenes G, Feng J, Benjamin PR (2007) Dynamic control of a central pattern generator circuit: a computational model of the snail feeding network. *Eur J Neurosci* 25:2805–2818
- Wadiche JI, Jahr CE (2001) Multivesicular release at climbing fiber-Purkinje cell synapses. *Neuron* 32:301–313
- Wang XJ, Rinzel J (1992) Alternating and synchronous rhythms in reciprocally inhibitory model neurons. *Neural Comput* 4:84–97
- Xu J, Wu LG (2005) The decrease in the presynaptic calcium current is a major cause of short-term depression at a calyx-type synapse. *Neuron* 46:633–645
- Xu-Friedman MA, Regehr WG (2004) Structural contributions to short-term synaptic plasticity. *Physiol Rev* 84:69–85
- Xu-Friedman MA, Harris KM, Regehr WG (2001) Three-dimensional comparison of ultrastructural characteristics at depressing and facilitating synapses onto cerebellar Purkinje cells. *J Neurosci* 21:6666–6672
- Zhao S, Sheibanie AF, Oh M, Rabbah P, Nadim F (2011) Peptide neuromodulation of synaptic dynamics in an oscillatory network. *J Neurosci* 31:13991–14004
- Zilly FE, Sorensen JB, Jahn R, Lang T (2006) Munc18-bound syntaxin readily forms SNARE complexes with synaptobrevin in native plasma membranes. *PLoS Biol* 4:e330
- Zucker RS, Fogelson AL (1986) Relationship between transmitter release and presynaptic calcium influx when calcium enters through discrete channels. *Proc Natl Acad Sci USA* 83:3032–3036
- Zucker RS, Regehr WG (2002) Short-Term Synaptic Plasticity. *Annu Rev Physiol* 64:355–405

Signaling Pathways, Modeling of

Jeanette Hellgren Kotaleski

School of Computer Science and
Communication, KTH Royal Institute of
Technology, Stockholm, Sweden

Synonyms

Kinetic modeling

Definition

The use of models to study the dynamical behavior of a biological (sub)system described as a set of biochemical reactions and diffusion. Here, the evolution in time for quantities such as protein concentrations or amount of enzyme activation is typically described using ordinary differential equations. The evolution in time of second messengers is typically described using partial differential equations. Alternatively, stochastic methods can be used to determine evolution in time of all molecules in a simulation.

Detailed Description

The development of quantitative models at multiple spatial and temporal scales is necessary for integrating the knowledge obtained from diverse experimental approaches into a coherent picture. Such models represent current knowledge in a compact and standardized way and constitute a tool for guiding experiments and generating predictions.

Modeling of intracellular signaling within the field of computational neuroscience is typically done to better understand how events on the subcellular level affect, or even may explain, higher-level phenomena. For example, subcellular mechanisms underlying synaptic long-term potentiation (LTP) and long-term depression (LTD) could be investigated in models of receptor-induced cascades of signaling

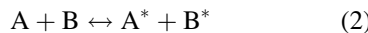
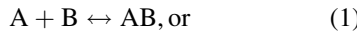
molecules activated during typical experimental protocols. Commonly modeled LTP or LTD systems begin with the activation of transmembrane receptors or the influx of calcium and include the activation of kinases and/or phosphatases and their phosphoprotein targets (see, e.g., Kotaleski and Blackwell 2010).

Dynamical modeling of signaling pathways is required because steady states are rarely achieved. Most of the time activation of signaling pathways is transient, and thus, the response of the system is transient. Intracellular signaling pathways may reach a steady state solution if the activation is kept constant, but sometimes such systems can show oscillations or behave as a bistable (or even multistable) biochemical switch.

How to Represent the Reactions in the Signaling Pathway?

Signaling pathways are represented as cascades of biochemical reactions, together with the diffusion of a subset of the molecular species. It is not plausible to include every reaction known to occur in neurons or cells; thus, the modeled pathway includes those components, such as enzymes, proteins, calcium ions, etc, judged to be relevant for the research question. The identification of critical components and how they interact or react typically are based on experimental data. Such data is often qualitative, but quantitative data are required for model development. Once the relevant molecules and reactions have been identified, the system can be specified and simulated. Two general approaches to the simulations are *stochastic* and *deterministic*. When using a deterministic approach, the system of biochemical reactions are described using a system of ordinary differential equations, which describe the rate of change in the concentrations/amounts of each component. The rate of change is based on the concentrations of all other reactants involved in a reaction. In addition, the *diffusion* of molecules is represented using discretized versions of partial differential equations. Various software packages that include numerical integrators can then be used to simulate the dynamics of the system if initial conditions and reaction rate parameters are provided.

To capture the individual steps in a signaling pathway, bimolecular and enzymatic reactions as well as protein modifications need to be included. Simple biochemical reactions, where one reacting substance (A) binds to another one (B) to form a product (AB) or to modify each other (A^* , B^*), can be represented as



Here, it is assumed that in both these cases, the reaction can be reversed. The speed of the forward and backward reactions is described by corresponding reaction rate parameters, k_f and k_b .

The “ $A + B \leftrightarrow AB$ ” system in Eq. 1, for example, is modeled deterministically using the following first-order differential equations:

$$\frac{d[A]}{dt} = \frac{d[B]}{dt} = -k_f \cdot [A] \cdot [B] + k_b \cdot [AB] \text{ and} \quad (3a)$$

$$\frac{d[AB]}{dt} = k_f \cdot [A] \cdot [B] - k_b \cdot [AB], \quad (3b)$$

where $[A]$, $[B]$, and $[AB]$ stand for the concentrations (e.g., measured in μM) of the corresponding reactants or products. The k_f and k_b rate parameters have here units of $\text{concentration}^{-1} \text{time}^{-1}$ and time^{-1} , respectively. The units for concentration of molecules must match the units of the rate constants. One additional set of values are required: given the initial concentrations for A, B, and AB, one can numerically integrate the behavior of the system over time.

When the system Eq. 1 above has reached steady state, ss , so that all time derivatives of the concentrations are zero, then

$$k_b/k_f = [A_{ss}] \cdot [B_{ss}] / [AB_{ss}], \quad (4)$$

where k_b/k_f defines the dissociation constant, K_D , which thus can be estimated from the steady state concentrations of the involved species. (Note that sometimes the affinity constant, $K_A = 1/K_D$, is given instead.) Measures of K_D are provided in

the biochemical literature more frequently than individual rate constants, because to estimate k_b and k_f individually requires data on the dynamics in the system, which are difficult experiments to perform.

The above approach assumes *mass action kinetics* which states that the rate of a reaction is the product of a rate constant (k) times the concentrations of the reacting species. This approach can be used to describe the behavior of both reversible and irreversible reactions, also when these reactions are part of reaction cascades, such as simple enzymatic reactions, as explained below. A similar framework, $A \leftrightarrow A^*$, can also represent the exchange of mass through diffusion between different compartments (dendritic spines, dendritic shaft, or different subvolumes within a spine or a dendrite). The rate by which the species move between compartments can be represented by the diffusion coefficient adjusted for the volume and contact areas of the adjacent compartments.

Mass action kinetics grew out of the work by Guldberg and Waage (reviewed by Lund 1965) who investigated, and tried to find laws for, how the velocity of chemical reactions could be described. This law describes how fast the molecules in a well-stirred solution collide and interact on average (and thus, stochastic interactions between individual species molecules are ignored).

Enzymatic reactions can be modeled as a cascade of biochemical reactions with the approach above. Enzymes speed up the rate by which the substrate of the enzyme is transformed into a product. The underlying reactions are assumed to be captured by the following scheme, which in the simplest case assumes a nonreversible catalytic step, a scheme developed successively in the early twentieth century by Michaelis and Menten (1913) and Briggs and Haldane (1925):



In the first step, described as above by a k_f and k_b rate parameter, the enzyme (E) binds to the substrate (S) in an enzyme-substrate

compound (ES). The second reaction step, where the enzyme is catalyzing the formation of the product, is controlled by the catalytic rate parameter, k_{cat} . Again, given some initial conditions and some values on the rate parameters, k_f , k_b , and k_{cat} , these two reaction steps can be modeled *deterministically* using first-order differential equations of the form

$$\frac{d[E]}{dt} = -k_f \cdot [E] \cdot [S] + k_b \cdot [ES] + k_{\text{cat}} \cdot [ES] \quad (6a)$$

$$\frac{d[S]}{dt} = -k_f \cdot [E] \cdot [S] + k_b \cdot [ES] \quad (6b)$$

$$\frac{d[ES]}{dt} = k_f \cdot [E] \cdot [S] - k_b \cdot [ES] - k_{\text{cat}} \cdot [ES] \quad (6c)$$

$$\frac{d[P]}{dt} = k_{\text{cat}} \cdot [ES] \quad (6d)$$

A common example is the reaction catalyzed by a kinase, which phosphorylates a substrate, $S + ATP \rightarrow P + ADP$, where the substrate, S , is a protein to be phosphorylated, P . This simple, one-step reaction assumes that ATP is constant (and sufficiently high that it is not rate limiting) and all substrate molecules have formed a complex with the enzyme. Then, the reaction rate is captured by the k_{cat} rate constant above. In theory, an enzymatic reaction must be reversible since an enzyme just speeds up the reaction, but does not change the steady state, which is decided by the thermodynamics constraints. Thus, if the product is accumulating in high enough amounts, a reversible reaction may need to be accounted for. Whether this needs to be represented in a model depends on the equilibrium constants for the enzymatic reactions considered.

Enzymatic reactions are sometimes modeled deterministically using the *Michaelis-Menten kinetics*. With this simplification, the variations in $[E]$ and $[ES]$ are discarded from Eq. 6a–d and instead assumed to be constant, i.e., $d[ES]/dt = 0$, as during steady state conditions. Since the amounts of the substrate and product change over time, this assumption requires that the substrate be present in sufficient amount, else the amount of $[ES]$ will change over time.

Whether the enzymatic reaction can be simplified to the Michaelis-Menten (MM) formalism or needs to be modeled explicitly using Eq. 6 depends therefore on the particular system modeled.

When modeling a set of signaling pathways as a cascade of biochemical reactions, the product of one reaction is usually the substrate of a subsequent reaction. Alternatively, active enzymes are often the product of a reaction. Frequently, enzyme and bimolecular reactions alternate. For example, first a ligand binds to a receptor; second, the ligand receptor complex is an enzyme; third, product of the enzyme reaction binds to and activates another enzyme, etc. When the product of the enzyme is a diffusible molecule, it is often called a second messenger. The diffusion and degradation of the second messenger must be modeled carefully to correctly represent its spatial and temporal dynamics.

When searching for parameter values in the literature for the various enzymatic reactions to be represented in the model, usually only k_{cat} (or more often V_{max} which is $k_{\text{cat}} \cdot$ total amount of enzyme) and the concentration of substrate when the production of product is half-maximal, K_M , is reported. Thus, the k_f , k_b , and k_{cat} in the equations above need to be mapped onto K_M , and it can be shown that $(k_b + k_{\text{cat}})/k_f = K_M$. This, however, means that we only have two measured values but three parameters to set. Thus, when k_b is not known explicitly, it needs to be set, e.g., as $4 \cdot k_{\text{cat}}$ as motivated in Bhalla and Iyengar (1999). Under the assumption that $d[ES]/dt = 0$, and setting $[E] = [E_{\text{total}}] - [ES]$, then

$$\frac{d[P]}{dt} = k_{\text{cat}} \cdot [E_{\text{total}}] \cdot [S] / (K_M + [S]) \quad (7)$$

Whether the Michaelis-Menten (MM) representation, Eq. 7, and the explicit formulation above, Eqs. 6a–6d, give similar results or not depends on to what extent the assumptions underlying the MM formalism are fulfilled. In, e.g., Ramakrishnan and Bhalla (2008), there is one example of a minimal biochemical system that can behave as a switch when the system is modeled using the MM formalism, but not when the explicit formulation above is used.

Limitations

Although the above deterministic approaches are commonly used within the computational neuroscience field (Manninen et al. 2010), several factors should be considered when representing a signaling pathway with a set of ordinary differential equations, assuming well-stirred solutions. For example, receptor-induced cascades involved in synaptic plasticity typically are localized in dendritic spines, and compartmentalization with regard to functions of different molecules might be common. Also proteins are heterogeneously distributed in different parts of the cytosol and membrane, and some molecules are anchored, while others might diffuse freely. Modeling these reactions across different compartments requires diffusion. If reacting or diffusing species are present in small quantities, then reactions and diffusion occur stochastically, in which case they cannot be modeled deterministically, and stochastic approaches must be used.

One overall challenge when building models of signaling pathways is the estimation of the reaction rate constants and amounts of the different molecular species. Biochemical estimates of model parameters can, for instance, be obtained through “test tube” experiments. However, the conditions in real cells might vary significantly from those in the experiments.

Although one often talks about a signaling pathway, it should be realized that such a reaction cascade is most likely embedded in a larger signaling network and that many interactions from other parts of the bigger system are left out. This also makes it difficult to validate pathways models, e.g., a pathway leading from a certain G-protein-coupled receptor to the activation of an enzyme, if those pathways are present in different cell types. Although the reaction rates between the pathway’s individual components are assumed to be similar, differences in the left-out interacting network might affect effective concentrations of enzymes and substrates through sequestration effects, for example, through the competition for available pools of enzymes and substrates.

References

- Bhalla US, Iyengar R (1999) Emergent properties of networks of biological signaling pathways. *Science* 283(5400):381–387
- Briggs GE, Haldane JB (1925) A note on the kinetics of enzyme action. *Biochem J* 19:338–339
- Kotaleski JH, Blackwell KT (2010) Modelling the molecular mechanisms of synaptic plasticity using systems biology approaches. *Nat Rev Neurosci* 11:239–251
- Lund EW (1965) Gulberg and Waage and the law of mass action. *J Chem Ed* 42:548–550
- Manninen T, Hituri K, Kotaleski JH, Blackwell KT, Linne ML (2010) Postsynaptic signal transduction models for long-term potentiation and depression. *Front Comput Neurosci* 4:152
- Michaelis L, Menten ML (1913) Die Kinetik der Invertinwirkung. *Biochem Z* 49:333–369
- Ramakrishnan N, Bhalla US (2008) Memory switches in chemical reaction space. *PLoS Comput Biol* 4(7): e1000122

Further Reading

- Cornish-Bowden A (2012) Fundamentals of enzyme kinetics, 4th edn. Wiley-Blackwell, Weinheim, ISBN 978-3-527-33074-4
- Johnson KA, Goody RS (2011) The original Michaelis constant: translation of the 1913 Michaelis-Menten paper. *Biochemistry* 50:8264–8269

Significance Evaluation

Matthew T. Harrison
Division of Applied Mathematics, Brown University, Providence, RI, USA

S

Synonyms

Hypothesis testing; p-value; Statistical significance

Definition

Broadly speaking: assigning a numerical score to the “unusualness” of data relative to a specific theory. In this entry: computing a p-value for a statistical hypothesis test with emphasis on spike-train resampling.

Detailed Description

Deciding whether the patterns observed in experimental data support or challenge existing theories is a recurring theme in data analysis. Assigning a numerical score, or *significance*, is a central part of the decision process. *Hypothesis testing* is the classical statistical approach with *p-values* being the most common (but not the exclusive) method of communicating statistical significance. This entry is about basic statistical hypothesis testing with a focus on the connection between hypothesis testing and the so-called resampling methods that are gaining widespread popularity in the statistical analysis of neural firing patterns.

A comprehensive statistical analysis rarely stops with hypothesis testing. Parameter estimation and confidence intervals are often more useful statistical tools. This entry, however, focuses exclusively on hypothesis testing and, in particular, on p-values. (Bayes factors and more generic model selection tools are not discussed.) Although hypothesis testing may not be the ending point of data analysis, it is often an insightful starting point and typically requires simpler statistical models and methods than a more complete analysis.

Statistical Versus Scientific Significance

Statistical significance should never be equated with scientific or experimental significance. Although establishing statistical significance may be an important prerequisite for establishing scientific significance, the latter requires additional analyses, interpretations, and, quite often, experiments. Statistical significance tries to quantify how unusual the data appear with respect to a given statistical model. If the statistical model is not appropriate for the experimental question or if the measured effect is too small to be of scientific importance, then statistical significance, no matter how striking, may have little or no scientific significance. This entry is about *statistical significance* only.

Hypothesis Testing and p-Values

Hypothesis testing begins with a null hypothesis H_0 which can be viewed as a collection of hypothesized probability distributions for the data. Often, H_0 is specified in two steps. The first step involves various underlying *modeling assumptions*, such as the data consist of n independent coin flips with a common probability θ of observing a head on each flip. The second step involves additional restrictions within this basic modeling paradigm, such as the probability, θ , is exactly one-half, which might be written as

$$H_0 : \theta = 0.5.$$

Or, for another example, the null hypothesis might be that the coin is biased towards heads, namely,

$$H_0 : \theta > 0.5.$$

When interpreting the conclusions of a hypothesis test, it is important to inspect both the obviously stated null hypothesis (such as $\theta = 0.5$) and the sometimes not-so-obvious modeling assumptions (such as independent coin flips or constant θ) for their fidelity to the scientific questions at hand.

In most cases, a hypothesis test also comes equipped with a *p-value*. A p-value is any function of the data, say $p(X)$, where X is the data, with the property that

$$\text{Prob}(p(X) \leq \alpha) \leq \alpha \text{ for all } 0 \leq \alpha \leq 1 \quad (1)$$

whenever X satisfies H_0 ,

where $\text{Prob}(A)$ denotes the probability of the event A – in this case, the event that the p-value is at least as small as the number α . Loosely speaking, if the null hypothesis is true, then it is unusual to see a small p-value. For instance, the probability of seeing a p-value less than 0.1 is at most 10 % when H_0 is true.

Sometimes, we redundantly say that a p-value is *valid* to emphasize that it has property (1) and

to distinguish it from other objects, such as approximations of p-values, that might be (mis-)interpreted as p-values or mistakenly called p-values, even though they are not valid p-values. For any given null hypothesis, there will be many potential ways to create a p-value. It is extremely important to decide which type of p-value will be used before observing the data; otherwise, the “p-value” will lose its validity and will not satisfy property (1) – it will no longer be a p-value! (See section “[Choice of \$T\$ and the Alternative Hypothesis](#)”.)

P-values are particularly useful for communicating statistical significance, because they have a common interpretation regarding type I error rates. A *type I error* occurs when we reject a null hypothesis even though it is true. P-values have the nice property that if we pick a threshold, say 0.05, and reject null hypotheses whenever the corresponding p-values are 0.05 or less, then our type I error rate is at most 5 %. Similarly, if we use a threshold of 0.01, then our type I error rate is at most 1 %. In light of these formal guarantees, it is commonplace for smaller p-values to be interpreted as stronger statistical evidence against the null hypothesis than larger p-values.

When the null hypothesis is true, p-values tend to not be small. For a p-value to be useful, however, it should also have good *power*, meaning that it does tend to be small when the null hypothesis is false and some competing alternative hypothesis is true instead. The *alternative hypothesis* is a different collection of hypothesized probability distributions for the data that is distinct from the collection defined by H_0 . A *type II error* occurs when the alternative hypothesis is true, but we do not reject the null hypothesis (because the p-value was too large). Type I and type II errors are in opposition to one another. For a given type of p-value, we can lower the type I error rate only by raising the type II error rate. Using a p-value threshold of 0.01 will lead to less type I errors, but more type II errors, than using a p-value threshold of 0.05.

A rejection of the null hypothesis should not lead to unscrutinized acceptance of the alternative hypothesis. The alternative hypothesis may also be a poor description of the data, perhaps

even more so. Similarly, a failure to reject the null hypothesis does not mean that the null hypothesis is a better description of the data than the alternative. It simply means that the statistical evidence is insufficient to rule out the null hypothesis (for the type I error rates that we are willing to tolerate).

A full discussion of p-values and their connections to other common concepts in hypothesis testing, such as power, critical region, size, and level, is beyond the scope of this entry. Any introductory statistics textbook is likely to have a thorough exposition of these and other hypothesis testing concepts. Casella and Berger (2002) is an intermediate-level reference. Lehmann and Romano (2005) is an advanced, comprehensive source. Kass et al. (2014) is an accessible reference aimed for the neuroscience community.

Construction of p-Values

Here, we will focus on a special type of p-value that is particularly relevant for resampling methods in neurostatistics. Let T be any function of the data and let P be a special probability distribution for the data, both of which will be discussed later. Here, T is called the *test statistic* and P is called the *null distribution*. For any potential data set x , define

$$p(x) = \text{Prob}(T(Y) \geq T(x)) \text{ when } Y \text{ has distribution } P. \quad (2)$$

In words, $p(x)$ gives the probability that a random data set Y would have a test statistic T at least as large as x has, if Y was chosen according to the null distribution P . (When computing the probability, only Y is random; x is held fixed. See section “[Heuristic Resampling](#)” for additional intuition.) In certain special cases, using Eq. 2 to define $p(X)$ creates a p-value, meaning that it satisfies property (1) for an appropriate null hypothesis. For instance, if the null hypothesis is simply that the data have distribution P , then $p(X)$ is a p-value for this null hypothesis. In many cases, p-values cannot be created using Eq. 2, but a discussion of these cases is beyond the scope of this entry.

Example 1 Let $X = (X_1, \dots, X_n)$ be a sequence of n independent coin flips with common probability θ of heads. Let $T = \#\text{heads}$. Let P correspond to the case $\theta = 0.5$ and let the null hypothesis be the same, namely, $H_0: \theta = 0.5$. Using Eq. 2 in this case gives

$$\begin{aligned} p(x) &= \text{Prob}(T(Y) \geq T(x)) \\ &= \sum_{k=T(x)}^n \text{Prob}(T(Y) = k) \\ &= \sum_{k=T(x)}^n \binom{n}{k} 0.5^n, \end{aligned}$$

where $\binom{n}{k} = n!/(k!(n-k)!)$ is the number of distinct ways to have k heads in a sequence of n coin flips and where the computation is done for Y having probability distribution P . Then $p(X)$ is a p-value for H_0 . (To compute $p(X)$, we substitute the observed value of X for the variable x on the right side of the derived formula for $p(x)$ above.) If we observe 7 heads in 10 flips, then the p-value is 0.172. If we had decided to reject H_0 when the p-value was less than 0.2, then we would reject. If instead we had chosen a threshold of 0.1, then we would not reject. This p-value is designed to be used when we anticipate that the coin might favor heads in cases where the null is false. For example, if we observe 3 heads in 10 flips, then the p-value is 0.945 and we would normally not reject, even though there is a sense in which 3 heads and 7 heads are equally extreme observations for a fair coin. By changing the test statistic, T , we could create a p-value that was more symmetric in its behavior or one that tended to be small for large numbers of tails. The choice depends on the scientific context and on the desired error performance. Finally, we note that the original p-value is also a p-value for the null hypothesis $H_0 : \theta \leq 0.5$, illustrating that this method of constructing p-values based on a single null distribution P can sometimes be used even when the null hypothesis includes many distributions. ■

This method in Eq. 2 of constructing a p-value based on a test statistic T and a null distribution P maps closely onto what is normally done with resampling methods in neuroscience. Within this context, there are several important issues:

- Choice of the null hypothesis H_0
 - Choice of the null distribution P
 - Choice of the test statistic T
 - Computation of the p-value $p(X)$
 - Adjustments for multiple hypothesis tests
- We will discuss each of these in the remainder of this entry.

Choice of H_0 and P

The choice of the null hypothesis, including the choice of the underlying statistical model, is arguably the most important choice among the items listed in the previous paragraph. The null hypothesis needs to be appropriate for the scientific question and the available data. Despite its centrality, there is little to say here about H_0 , because it is so context dependent. Perhaps the best guidance is to *always clearly state the complete statistical model and the null hypothesis*. Only when H_0 is clearly stated can one interpret the conclusion of a hypothesis test and judge its scientific relevance.

Given H_0 , the next step is to choose a null distribution P under which a p-value can be computed. If H_0 is a *simple null hypothesis*, meaning that it consists of a single hypothesized probability distribution for the data, then we can take P to be this unique distribution specified by H_0 . If H_0 is a *composite null hypothesis*, meaning that it consists of many possible probability distributions for the data, then it may be difficult to find an appropriate P or one may not even exist. Example 1 above illustrates both a simple null hypothesis ($H_0 : \theta = 0.5$) and a composite null hypothesis ($H_0 : \theta \leq 0.5$) and a corresponding null distribution P (which happens to be the same for each, in this case).

Example 2 Let $X' = (X'_1, \dots, X'_n)$ be a sequence of n independent coin flips with a fixed, but unknown, common probability v' of

heads. Let $X'' = (X_1'', \dots, X_n'')$ be another sequence of n independent coin flips with a fixed, but unknown, common probability v'' of heads. In this case, the data are $X = (X', X'')$. The null hypothesis H_0 is that X' and X'' are independent. H_0 is a composite null hypothesis because v' and v'' are not specified by H_0 and are unknown. The unknown parameters $v = (v', v'')$ are often called *nuisance parameters*, because they are necessary to specify the probability distribution but are otherwise unrelated to the target statistical question – in this case, a question about independence.

Let $T = T(X) = \#\{i : X'_i = X''_i = \text{heads}\} = \#\text{aligned heads}$, which we might expect to be large if X' and X'' are positively correlated. The distribution of T depends heavily on the unknown parameters v and is not uniquely specified if these parameters are not known. Hence, a null distribution P for computing p-values is not apparent. For example, T could be large because the sequences are correlated or because v' and v'' are both large, resulting in many heads, some of which are likely to align by chance. Bootstrap approximation and conditional inference are two common approaches for specifying a null distribution P in situations like this with nuisance parameters. Each is considered below in the continuation of this example.

This example is stereotypical of early frameworks for testing for synchronization between two simultaneously recorded neural spike trains, modeled by X' and X'' , with heads denoting a spike (an action potential) in a small time bin and tails denoting no-spike. The unknown parameters v' and v'' are often called the theoretical firing rates of the respective neurons, and $N(X')$ and $N(X'')$ correspond to the observed spike counts, where $N = \#\text{heads}$. T is the number of precisely synchronous spikes. This simple framework is no longer thought to be appropriate, particularly when recording *in vivo*, because, among other things, the underlying modeling assumption that v' and v'' are constant in time is usually a very poor description of the data. More recent approaches improve on this simple framework

both by making the underlying modeling assumptions more believable and by aligning the null hypotheses more closely with the scientific questions of interest (Amarasingham et al. 2012; Harrison et al. 2013, “► Surrogate Data for Evaluation of Spike Correlation” in this encyclopedia). ■

Bootstrap Approximation

Consider a composite null hypothesis H_0 that would admit a null distribution if we happened to know the value of some nuisance parameter v . The null distribution might be different for each v , say $P = P_v$, which, using Eq. 2, would give rise to a different p-value for each v , say $p(X) = p_v(X)$. One possibility is to use the observed data to obtain an estimate \hat{v} for v and then use the approximate p-value $p_{\hat{v}}(X)$ in place of the true p-value $p_v(X)$. It is an approximate p-value, because the true unknown value of v is replaced with an approximation \hat{v} estimated from data. Usually, Eq. 1 will not hold exactly for an approximate p-value.

Example 2 Part II: Bootstrap Approximation Continuing Example 2, suppose for the moment that we happen to know the true values of v' and v'' . Then the null hypothesis becomes a simple null hypothesis, namely, that X' and X'' are sequences of independent coin flips with probability of heads given by the known values of v' and v'' , respectively. Using Equation 2 gives

$$\begin{aligned} p_v(x) &= p(x) = \text{Prob}(T(Y) \geq T(X)) \\ &= \sum_{i=0}^n \sum_{j=0}^n \sum_{k=T(x)}^n \text{Prob}(N(Y') = i, N(Y'') = j, T(Y) = k) \\ &= \sum_{i=0}^n \sum_{j=0}^n \sum_{k=T(x)}^n \binom{n}{i} \binom{i}{k} \binom{n-i}{j-k} \\ &\quad (v')^i (1-v')^{n-i} (v'')^j (1-v'')^{n-j}, \end{aligned} \tag{3}$$

where $x = (x', x'')$, where $N = \#\text{heads}$, where we take $\binom{a}{b} = 0$ if $a < b$ or $b < 0$, and where the computation is done for $Y = (Y', Y'')$ satisfying

the null hypothesis for parameters $v = (v', v'')$. The specific formula for this p-value is not the main point. The key observation is that we could compute $p(X)$, at least in principle, if we knew the values of the test statistic $T = T(X)$ and the parameters v . For instance, if $n = 10$, $v' = 0.3$, $v'' = 0.5$, and we observe $T = 5$, then the p-value is 0.0099. Note that we have emphasized this dependence on the parameters by writing

$$p(x) = p_v(x).$$

But what if v' and v'' are unknown, as originally stipulated in Example 2? One possibility is to estimate their values from the observed data, pretend that their estimated values are correct, and then use the p-value derived above for the case where the parameters are known. If $\hat{v} = (\hat{v}', \hat{v}'')$ are the estimated values, then we would use the approximate p-value

$$p_{\hat{v}}(X)$$

as given by Eq. 3. For instance, if $n = 10$ and we observe $N(X') = 5$ and $N(X'') = 6$, then we might estimate $\hat{v}' = 0.5$ and $\hat{v}'' = 0.6$ (these are the maximum likelihood estimates). If we additionally observe $T = 5$, then the approximate p-value is 0.1503. It is only an approximate p-value, because the true v' and v'' are replaced by estimates from the data. As n gets large, the approximation will improve and the approximate p-value will come closer and closer to being a true p-value in the sense of Eq. 1. ■

The substitution of the unknown nuisance parameters with their estimates from the data is sometimes called the *substitution method* (or *substitution principle*). Here we use the term *bootstrap approximation*, because it is the first and most important step in bootstrap and because this type of substitution arises almost exclusively in connection with bootstrap in resampling methods for neuroscience. Bootstrap approximations are easy to use and easy to

misuse. In Example 2 part II above, the null hypothesis only had two nuisance parameters that needed to be estimated from the data. A more modern example from neuroscience might have hundreds or thousands or even infinitely many nuisance parameters. Estimating a large number of parameters from data is fraught with difficulty and the estimation errors are essentially guaranteed to be large in some respects. For bootstrap approximations to work well in these situations, the p-value itself must be fairly insensitive to certain types of large approximation errors. Even in cases with only a single nuisance parameter, bootstrap approximations can fail (meaning that they perform poorly no matter how much data is available), usually in cases where the p-value in Eq. 2 is unusually sensitive to tiny changes in the nuisance parameter. There is a substantial literature about both the theoretical properties of bootstrap approximations and their practical use (Davison and Hinkley 1997).

Conditional Inference

Consider a composite null hypothesis H_0 that would admit a null distribution if we happened to condition on the value c of some statistic C , which we call a *conditioning statistic* (and is different from the test statistic). The null distribution might be different for different values of c , say $P = P^c$, which, using Eq. 2, would give rise to a different p-value for each c , say $p(X) = p^c(X)$. Since we can directly observe $c = C(X)$, however, this causes no difficulties, and $p^{C(X)}(X)$ is a valid p-value for the null hypothesis. The most common situation where we can use conditioning to create a null distribution is when $\text{Prob}(X = x|C(X) = c)$ is the same function of x and c regardless of the specific distribution of X , as long as X satisfies the null hypothesis. In this case, we can take $P^c(x) = \text{Prob}(X = x|C(X) = c)$.

Example 2 Part III: Conditional Inference Continuing Example 2, if we use the conditioning statistic $C(X) = (N(X'), N(X''))$,

which is the total number of heads for each of the two coins and assume the null hypothesis is true,

$$\begin{aligned}
 & \text{Prob}(X = x | C(X) = c) \\
 &= \frac{\text{Prob}(X' = x', X'' = x'', N(X') = c', N(X'') = c'')}{\text{Prob}(N(X') = c', N(X'') = c'')} \\
 &= \frac{\left[\prod_{i=1}^n (v')^{x'_i} (1-v')^{1-x'_i} (v'')^{x''_i} (1-v'')^{1-x''_i} \right] I(N(x') = c') I(N(x'') = c'')}{\binom{n}{c'} (v')^{c'} (1-v')^{n-c'} \binom{n}{c''} (v'')^{c''} (1-v'')^{n-c''}} \\
 &= \frac{I(N(x') = c') I(N(x'') = c'')}{\binom{n}{c'} \binom{n}{c''}}, \tag{4}
 \end{aligned}$$

where $x = (x, x')$, where $c = (c, c')$, and where I denotes the indicator function having $I(A) = 1$ if A is true and $I(A) = 0$ if A is false. In words, it says that if the two coins are independent, then the conditional distribution of the arrangement of heads and tails, given the number of heads for each coin, does not depend on the unknown probability of heads for each coin. Furthermore, the common conditional distribution is *uniform* meaning that all possible arrangements of heads and tails are equally likely, subject to having the correct numbers of heads. Since this conditional distribution does not depend on the unknown nuisance parameters v' and v'' , we can use it as a null distribution for the null hypothesis of independence, namely,

$$P(x) = P^c(x) = \frac{I(N(x') = c') I(N(x'') = c'')}{\binom{n}{c'} \binom{n}{c''}}. \tag{5}$$

The (conditional) null distribution in Eq. 5 does not depend on the unknown parameters v' and v'' , but it does depend on the observed number of heads c' and c'' . This presents no difficulties, though, since we can directly observe these values from data. Using the test statistic $T = \#\text{aligned heads}$ as before and using Eq. 2 to compute the p-value give

then the conditional distribution of the data given the conditioning statistic is

$$\begin{aligned}
 p^c(x) &= \sum_{k=T(x)}^n \text{Prob}(T(Y) = k) \\
 &= \sum_{k=T(x)}^n \frac{\binom{n}{c'} \binom{c'}{k} \binom{n-c'}{c''-k}}{\binom{n}{c'} \binom{n}{c''}}, \tag{6}
 \end{aligned}$$

where we take $\binom{a}{b} = 0$ if $a < b$ or $b < 0$ and where $Y = (Y', Y'')$ has the joint pmf P^c given in Eq. 5. Again, the specific form of the p-value is not the main point. We can observe $c = (c', c'') = (N(X'), N(X''))$ and, at least in principle, compute the valid p-value $p^c(x)$. For instance, if $n = 10$ and we observe $N(X') = 5$, $N(X'') = 6$ and $T(X) = 5$, then the p-value is 0.0238. ■

Conditional inference creates a null distribution without needing to use a bootstrap approximation. This can be an advantage in settings with many nuisance parameters, where the bootstrap approximation may be poor. Conditional inference can also be robust to modeling assumptions about the conditioning statistic, C , which is desirable in many contexts. Conditional inference is more limited than bootstrap approximation, however, since many examples do not have an appropriate conditioning statistic, C . The two approaches can also be combined if conditioning still leaves some unknown parameters that need to be estimated.

It is important to note that bootstrap approximation and conditional inference usually lead to different types of p-values. For example, the same data at the ends of Example 2 parts II and III gives an approximate p-value of 0.1503 using a bootstrap approximation and a p-value of 0.0238 using conditional inference. The difference between the two is not a result of approximation errors from the bootstrap approximation. Rather, the two methods lead to fundamentally different types of p-values. Both control the type-I error rate in the usual way (only approximately so for bootstrap), but each will have different type-II error profiles. One is not necessarily better than the other. The bootstrap approximate p-value is larger in this case because it accounts for the fact that T could be large by seeing an unusually large number of heads, whereas conditional inference uses knowledge about the observed number of heads and notes that T is unusually large (in fact, it is as large as possible) given the number of heads. The scientific context will dictate which of these is preferable.

Heuristic Resampling

The intuition behind the p-value in Eq. 2 is straightforward. If we repeatedly generate surrogate data sets Y according to some probability distribution P and see what fraction of them gives test statistics that are at least as extreme as the original data (if we did this infinitely many times, then the fraction would match the p-value formula), then we can gauge how unusual the original data are with respect to P . There are many examples in the literature where this intuition is implemented directly with some choice of P that makes intuitive sense, but that has not been derived directly from a well-formulated null hypothesis. These heuristic procedures can lead to revealing exploratory analyses, but the “p-values” obtained from them are rarely valid p-values for any null hypothesis. A “rejection” is particularly difficult to interpret, since there is no clear null hypothesis that is being rejected and since the numerical value of the “p-value” cannot be interpreted in the usual manner in terms of type-I error rates. Whenever possible, it is preferable to develop a proper null

hypothesis and communicate the results with a valid p-value.

Choice of T and the Alternative Hypothesis

Much like the choice of H_0 , the choice of T is critical but also highly problem-dependent. The choice of T is closely related to the concept of an alternative hypothesis. In most cases, investigators not only formulate a null hypothesis, but they also have rough expectations about how the data will appear if the null hypothesis is false. For example, when testing the null hypothesis of independence between two spike trains, in some settings, one might expect that a lack of independence will manifest itself as an abundance of synchronous spiking at some time scale. Usually T is chosen to capture this anticipated departure from the null behavior. The more precisely the alternative hypothesis is formulated, the more precisely T can be tailored to detect differences between the null and alternative hypotheses in the data.

Perhaps the most important guidance is *to avoid unscrutinized acceptance of the alternative hypothesis* after rejecting the null hypothesis. Usually, the alternative hypothesis is only one of many ways for the null hypothesis to be wrong. Careful choice of T can help ensure that the alternative hypothesis is detected, if it happens to be true, but for any choice of T , there are often many other distributions (not in the null or alternative hypotheses) that are also well detected. For example, suppose we reject the null hypothesis of independence between two spike trains using a test statistic that involves precise (millisecond-precision) synchronous spiking. While it is true that we can conclude that the neurons are dependent (this is the rejection of the null hypothesis), we should be careful not to immediately assume the existence of processes that create fine-precision spike timing (which would be acceptance of some specific alternative hypothesis that we have in mind, usually the one that motivated our choice of test statistic). There are many ways to be dependent that may create excess amounts of precise synchrony without involving precise spike timing.

Another important point is that *changing T changes the p-value and its properties*. Consequently, T cannot be chosen after inspecting the data or the resulting p-value will not be valid (cf., Kriegeskorte et al. 2009). Simple choices of T are easier to interpret and also less likely to raise concerns that T was tailored to the data.

Multiple Hypothesis Tests

Many experiments lead to multiple hypothesis tests. These could be different null hypotheses and/or different p-values for the same null hypothesis but tailored to different alternative hypotheses (typically created by using different test statistics). For example, when testing for differences between experimental conditions, there may be different hypothesis tests for each of many different spike trains, or different brain regions, or different time intervals. There are two key issues to keep in mind when performing multiple hypothesis tests.

First, the pattern of accepted and rejected hypotheses may not correspond to the underlying pattern of true and false null hypotheses.

There are many influences on the *power* of a test to detect violations of the null hypothesis, including the amount and quality of the data, the strength of the signal, the appropriateness of the test statistic, and so on. The pattern of rejections may reflect underlying fluctuations in power resulting from processes that are scientifically unrelated to those which are being studied by the hypothesis tests. For example, rejecting a null hypothesis of independence between spike trains in one experimental condition, but not another, is not necessarily strong evidence that the dependence structure has changed across conditions. Perhaps the firing rates changed across conditions and this influenced the power of the hypothesis test to detect dependence?

Second, large numbers of hypothesis tests will lead to some false rejections unless p-values are adjusted for multiple tests. For example, suppose that we simultaneously record spike trains from 100 neurons in each of two experimental conditions and then, for each neuron separately, construct a p-value to test whether the neuron's response distribution differed

across conditions. If we reject the null hypothesis of no difference across conditions whenever a p-value is less than 0.05, then (assuming the p-values are not overly conservative) we can expect roughly 5 rejections even if all 100 null hypotheses are true. If, further, the p-values are not overly correlated, then the probability of at least one false rejection among these 100 tests is close to one. The basic interpretation of a p-value has apparently been diluted by performing multiple hypothesis tests.

There is a vast and active literature about methods for adjusting p-values so that they maintain various interpretations in the presence of multiple tests (Farcomeni 2008; Nichols and Hayasaka 2003). A common approach is to adjust p-values so that they control the *family-wise error rate (FWER)*, which is the probability of one or more false rejections among all hypothesis tests in the family (regardless of the actual pattern of true and false null hypotheses). Defining this formally requires some care. Let $H_0^{(1)}, \dots, H_0^{(h)}$ be the collection of h null hypotheses and let $V \subseteq \{1, \dots, h\}$ denote the (unknown) indices of the true null hypotheses. We say that $\tilde{p}^{(1)}(X), \dots, \tilde{p}^{(h)}(X)$ are FWER-adjusted p-values for these null hypotheses if

$$\begin{aligned} \text{Prob}\left(\tilde{p}^{(k)}(X) \leq \alpha \text{ for one or more } k \in V\right) \\ \leq \alpha \text{ for all } 0 \leq \alpha \leq 1, \end{aligned}$$

for every possible distribution of X . Now, if we only reject those null hypotheses where the adjusted p-values are 0.05 or less, then our probability of falsely rejecting even a single true null hypothesis is at most 0.05. The Bonferroni correction is the simplest method to create FWER-adjusted p-values. Beginning with a collection of p-values, $p^{(1)}, \dots, p^{(h)}$, we simply multiply the original p-values by the number of tests, h , to get the adjusted p-values, i.e.,

$$\tilde{p}^{(k)}(x) = hp^{(k)}(x) \quad (k = 1, \dots, h).$$

Although the Bonferroni correction appropriately controls the type-I error rates (in the sense

of FWER), it can have poor type-II error rate performance. In particular, if the number of tests is large, then unadjusted p-values must be very small in order to reject using the Bonferroni-adjusted p-values. There exist improvements to the Bonferroni correction that provide the same FWER guarantees.

For situations with very large numbers of tests, controlling the FWER may be a too stringent goal, and statisticians have defined a variety of more relaxed criteria. For example, the *false discovery rate (FDR)* is the expected proportion of rejections that are false rejections (defining the proportion to be zero if there are no rejections), and methods that control the FDR bound this expected proportion. Loosely speaking, controlling the FDR allows there to be some false rejections, but hopefully not too many. Like the Bonferroni procedure for FWER, there are simple procedures for controlling the FDR, such as the Benjamini-Hochberg-Yekutieli correction, that require only a collection of unadjusted p-values.

Procedures for adjusting for multiple hypothesis tests require the original, uncorrected p-values to be actual *valid* p-values in the sense of Eq. 1. Using multiple testing adjustments on approximate p-values (such as approximate p-values resulting from bootstrap or from asymptotic approximations) requires great care. Multiple testing adjustments tend to amplify approximation errors, and errors that are insignificant for single hypothesis tests can easily corrupt multiple testing interpretations. For example, uncorrected p-values of 10^{-5} and 10^{-10} are essentially equivalent if we are testing a single null hypothesis at level 0.05, and a procedure that could approximate p-values to within 10^{-5} would be more than adequate for most purposes. But if this is one of a million different p-values, then 10^{-5} and 10^{-10} are quite different – only the latter would be unusual to see somewhere among the million p-values (consider a Bonferroni correction with $h = 10^6$) – and even tiny approximation errors could drastically alter our final conclusions.

Monte Carlo Approximation of p-Values

The examples above are special in that the p-values have a simple closed-form expression that is easy to compute. In many practical settings, there may be no practical methods for exactly computing the p-value in Eq. 2: $p(x) = \text{Prob}(T(Y) \geq T(x))$ when Y has distribution P . It is easy to approximate the p-value, however, as long as we can sample from the null distribution P . Loosely speaking, if we generate many random observations from P , then the p-value is closely approximated by the fraction of those observations that have test statistics at least as large as the original data. This is called *Monte Carlo* approximation. Furthermore, we can engineer our Monte Carlo p-value to actually be a valid p-value in sense of Eq. 1. As mentioned in section “[Multiple Hypothesis Test](#)”, using valid p-values is especially important in the context of multiple hypothesis testing.

Let $Y^{(1)}, \dots, Y^{(m)}$ be a random sample from the null distribution P . (Using superscripts to index the observations in the Monte Carlo sample will be convenient later.) The Monte Carlo p-value is

$$\hat{p}(x) = \hat{p}\left(x; Y^{(1)}, \dots, Y^{(m)}\right) \\ = \frac{\#\{k : T(Y^{(k)}) \geq T(x)\} + 1}{m + 1}. \quad (7)$$

Without the 1 in the numerator and denominator, this is simply the fraction of the $Y^{(k)}$ ’s with $T(Y^{(k)}) \geq T(x)$. Including the 1 is like including a copy of x among the $Y^{(k)}$ ’s when computing this fraction, and it ensures that $\hat{p}(X; Y^{(1)}, \dots, Y^{(m)})$ is a valid p-value for the original null hypothesis. Validity means that the type I error is controlled appropriately. As the Monte Carlo sample size, m , gets large, $\hat{p}(X)$ will be a better and better approximation of the target p-value, $p(X)$. Consequently, for large m , both p and \hat{p} control the type II error in similar ways.

Example 2 Part IV: Monte Carlo p-Values Revisiting Example 2, look again at the bootstrap approximate p-value formula in

Eq. 3 and the conditional inference p-value formula in Eq. 6. What if these formulas were not available or too difficult to compute? Monte Carlo approximation is often a good alternative.

Consider first the bootstrap approximation from Example 2 part II. We first estimate the unknown nuisance parameters from the observed data using $\hat{v} = (\hat{v}', \hat{v}'')$, and we hold these parameters fixed throughout the rest of the procedure. Now, we artificially generate a random data set that satisfies the null hypothesis using the parameters \hat{v} . There is no ambiguity about which distribution to use for the random data set, because once the nuisance parameters are specified, the null hypothesis contains only a single distribution $P = P_{\hat{v}}$. For this example, to generate a random data set $Y = (Y', Y'')$, we first sample $Y' = (Y'_1, \dots, Y'_n)$ independently from a coin with probability of heads \hat{v}' . Then, independently from Y' , we sample $Y'' = (Y''_1, \dots, Y''_n)$ independently from a coin with probability of heads \hat{v}'' . $Y = (Y', Y'')$ is a single random data set from the (bootstrap approximate) null distribution P . Let us call this data set $Y^{(1)}$. Now, using the same \hat{v} , we independently repeat this procedure many times to get a collection of Monte Carlo data sets $Y^{(1)}, \dots, Y^{(m)}$, which is a random sample of size m from the (bootstrap approximate) null distribution $P = P_{\hat{v}}$. We can compare the observed number of aligned heads $T(X)$ to the collection of numbers of aligned heads from the Monte Carlo data $T(Y^{(1)}), \dots, T(Y^{(m)})$ to get a Monte p-value $\hat{p}(X)$, as defined in Eq. 7. For large m , $\hat{p}(X) \approx p_{\hat{v}}(X)$ from Eq. 3 (with v replaced by \hat{v}). Note that $\hat{p}(X)$ would itself be a valid p-value if the Monte Carlo sample came from P_v , but it does not. It comes from $P_{\hat{v}}$, which, if our bootstrap approximation is good, will be very close to P_v . The combination of a bootstrap approximation and Monte Carlo approximation is called **bootstrap**, and in this case, it would be called *parametric bootstrap hypothesis testing* – parametric, because our bootstrap approximation involves the estimation of a fixed and finite number of parameters (in this case, two parameters: v', v''). It is important to remember that the bootstrap

approximation is the key approximation in bootstrap. Monte Carlo approximation is only done for computational convenience, and usually m can be chosen sufficiently large that the Monte Carlo approximation error is negligible.

Now consider conditional inference from Example 2 part III. We first observe the numbers of heads $c = C(X) = (N(X'), N(X'')) = (c', c'')$ coming from the two coins in the original data, and we define the null conditional distribution $P = P^c$ as in Eq. 5. To generate a random data set $Y = (Y', Y'')$ from P , we first generate $Y' = (Y'_1, \dots, Y'_n)$ by choosing c' of flips to be heads, $n - c'$ of the flips to be tails, and uniformly shuffling the order, so that each of the $\binom{n}{c'}$ possibilities is equally likely. Another way of thinking about this is to randomly and uniformly shuffle the order of the flips in the original sequence X' , which automatically has c' heads. Then we independently do the same thing for $Y'' = (Y''_1, \dots, Y''_n)$, but using c'' heads and $n - c''$ tails. Calling this shuffled data set $Y^{(1)} = Y$, we can repeat this process independently, each time using the same $c = (c', c'')$, to get a Monte Carlo random sample $Y^{(1)}, \dots, Y^{(m)}$ from the null conditional distribution P . Exactly like the bootstrap sample, we compute $\hat{p}(X)$ using Eq. 7. For large m , $\hat{p}(X) \approx p^c(X)$. Furthermore, $\hat{p}(X)$ is itself a valid p-value. ■

Example 3: Permutation Tests Let S_k denote the spike train data collected on trial k and let $E_k \in \{1, 2\}$ denote which of two experimental conditions was in effect during trial k . The complete data set of n trials (each of the same duration) is $X = (S, E)$, where $S = (S_1, \dots, S_n)$ and $E = (E_1, \dots, E_n)$. We assume that E_1, \dots, E_n are *exchangeable*, which means that every possible ordering of experimental conditions was, in principle, equally likely to occur. (Usually, this is easy to ensure as part of the overall experimental design.) We want to test whether the experimental condition is related to the spiking data. The formal null hypothesis is that S and E are independent, that is, the experimental condition has no effect on spiking. We conjecture that if the

null hypothesis is false (i.e., if there is a difference across conditions), then it will be reflected in the distribution of total spike counts over a trial, namely, $N(S_k) = \# \text{ spikes in } S_k = \# \text{ spikes on trial } k$. In particular, we expect the average spike count in condition 1 to be different from the average spike count in condition 2, quantified by the absolute difference:

$$\begin{aligned} T(X) &= T(S, E) \\ &= \left| \frac{\sum_{k:E_k=1} N(S_k)}{\#\{k : E_k = 1\}} - \frac{\sum_{k:E_k=2} N(S_k)}{\#\{k : E_k = 2\}} \right|. \end{aligned}$$

This will be our test statistic.

The null hypothesis of independence is a very large composite null hypothesis. Without further assumptions, there are infinitely many nuisance parameters needed to specify the distribution of S . We will use conditional inference to specify a unique null distribution P . Let $D = D(E) = \#\{k : E_k = 1\}$ be the number of trials in experimental condition 1. Our conditioning statistic will be $C = C(X) = (S, D)$, that is, we will condition on all of the spike train data, including the order of the trials, and we will also condition on the number of trials in experimental condition 1 (and, consequently, the number of trials in experimental condition 2, which is $n - D$). The only uncertainty remaining is the ordering of E , that is, the pairing of experimental condition with trial. Under the null hypothesis of independence (and assuming E was constructed to be exchangeable), then every possible ordering of E is equally likely. The null conditional distribution is just the uniform distribution over all possible $\binom{n}{D}$ pairings of trials with condition labels. Since this conditional distribution is the same for all possible distributions in the null hypothesis, we can use it as our null distribution without needing to estimate any nuisance parameters or to introduce additional modeling assumptions. To sample from this distribution, we simply shuffle, or permute, the experimental condition

labels relative to the trials. We can do this many times, each time computing the test statistic T . (Note that T will change because we are changing which trials are assigned to the different experimental conditions.) Equation 7 gives a valid Monte Carlo p-value for this hypothesis test, which is called a Monte Carlo *permutation test*. ■

Example 4: Trial Shuffling This is similar to Example 3, except that now E_k is spike train data from another neuron recorded simultaneously with S_k . The null hypothesis is still independence – in this case, independence between neurons. We change the test statistic to be the absolute correlation coefficient (Pearson's r) between spike counts:

$$\begin{aligned} T(X) &= T(S, E) \\ &= |\text{corr-coef}((N(S_k), N(E_k)) : k = 1, \dots, n)|. \end{aligned}$$

To create a unique null distribution, we condition on all of S , as before, and we condition on all of E except for the specific order of the trials in E . The null hypothesis of independence, combined with the assumption that E is exchangeable, gives the uniform conditional null distribution over the ordering of the trials for E . To sample from this null distribution, we simply shuffle the order of E 's trials. Monte Carlo p-values are computed in the usual way.

Scientifically, interpreting a rejected null hypothesis in this case requires some care. For instance, unlike Example 3, where we could design E to be exchangeable, here we must assume that E is exchangeable. In some experiments, this may not be true. For example, if the neurons are modifying their response functions over trials (because of, say, habituation or learning or fatigue or metabolic changes), then trials are not exchangeable. When this modification affects both neurons, then it may be detectable using the correlation coefficient test statistic. It likely depends on the experimental context whether this type of co-modulation reflects the underlying mechanisms the investigator was

intending to detect with a test of independence. This final caution holds more generally. There are many mechanisms, including experimental artifacts, such as misaligned trials, that can create dependence between spike trains. With sufficient data and an appropriate test statistic, trial shuffling can detect these dependencies, but it cannot determine which mechanisms created the dependencies. ■

Summary

The perspective of this entry is that spike train resampling is best viewed as Monte Carlo hypothesis testing. More specifically, the procedure of using surrogate data created by resampling spike trains for the purpose of evaluating the significance of patterns observed in the data is best viewed as Monte Carlo sampling from a null hypothesis that admits a unique null distribution for the purpose of numerically approximating a p-value. The key concepts underlying this view are reviewed above, along with some standard guidance about the use and misuse of hypothesis testing. The entry “► [Surrogate Data for Evaluation of Spike Correlation](#)” in this encyclopedia describes many of the commonly used methods for resampling spike trains.

Cross-References

- [Correlation Analysis of Parallel Spike Trains](#)
- [Decision-Making, Threshold](#)
- [Estimation of Neuronal Firing Rate](#)
- [Neural Coding](#)
- [Neural Decoding](#)
- [Population Encoding/Decoding](#)
- [Spatial Temporal Spike Pattern Analysis](#)
- [Spike Train Analysis: Overview](#)
- [Statistical Analysis of Neuroimaging Data](#)
- [Surrogate Data for Evaluation of Spike Correlation](#)
- [Unitary Event Analysis](#)

References

- Amarasingham A, Harrison M, Hatsopoulos N, Geman S (2012) Conditional modeling and the jitter method of spike re-sampling. *J Neurophysiol* 107:517–531
- Casella G, Berger RL (2002) Statistical inference, 2nd edn. Duxbury Press, Pacific Grove
- Davison AC, Hinkley DV (1997) Bootstrap methods and their application. Cambridge University Press, Cambridge
- Farcomeni F (2008) A review of modern multiple hypothesis testing, with particular attention to the false discovery proportion. *Stat Methods Med Res* 17:347–388
- Harrison MT, Amarasingham A, Kass RE (2013) Statistical identification of synchronous spiking. In: DiLorenzo PM, Victor JD (eds) Spike timing: mechanisms and function. Taylor & Francis, Boca Raton, pp 77–120
- Kass RE, Eden U, Brown EN (2014) Analysis of neural data. Springer, New York
- Kriegeskorte N, Simmons WK, Bellgowan PS, Baker CI (2009) Circular analysis in systems neuroscience: the dangers of double dipping. *Nat Neurosci* 12:535–540
- Lehmann EL, Romano JP (2005) Testing statistical hypotheses, 3rd edn. Springer, New York
- Nichols T, Hayasaka S (2003) Controlling the familywise error rate in functional neuroimaging: a comparative review. *Stat Methods Med Res* 12:419–446

Silicon Cochleas

- [Neuromorphic Sensors, Cochlea](#)

Simple-to-Complex Hierarchy

- [Hierarchical Models of the Visual System](#)

Simplified Conductance-Based Models

- [Reduced Morphology Models](#)

Simulation Experiment Description Markup Language (SED-ML)

Dagmar Waltemath¹ and Nicolas Le Novère^{2,3}

¹Systems Biology and Bioinformatics,
University of Rostock, Rostock, Germany

²Babraham Institute, Babraham Research
Campus, Cambridge, UK

³EMBL European Bioinformatics Institute,
Cambridge, UK

Definition

The Simulation Experiment Description Markup Language is an XML-based exchange format for the encoding of simulation experiments mainly in the field of computational biology. It stores the simulation recipe, including the models used in the experiment, the pre- and post-processing procedures, and the instructions for how to generate the simulation output.

Detailed Description

Overview

The Simulation Experiment Description Markup Language (SED-ML) encodes simulation setups in XML. Thereby it provides a means to exchange simulation descriptions in standard format. SED-ML respects the Minimum Information Guidelines for Simulation Experiments (Minimum Information About a Simulation Experiment, MIASE (Waltemath et al. 2011a)). Following these recommendations, the first version of SED-ML has been published in March 2011 (Waltemath et al. 2011b). It covers the description of time-course simulations and consists of five major building blocks:

1. The **Model** entity contains references to the models used in the simulation experiment and pre-processing procedures on these models before simulation. Models must be in standard representation formats (e.g., SBML, CellML, NeuroML). Examples for pre-processing are, e.g., changing the value of an observable,

computing the change of a value using mathematics, or general changes on any XML element of the model representation.

2. The **Simulation** entity contains all information about the simulation settings and the steps taken during simulation, e.g., the particular type of simulation and the algorithm used for the execution of the simulation.
3. The **Task** entity applies one of the defined simulations on one of the referenced models at a time.
4. The **DataGenerator** entity encodes post-processing procedures which need to be applied to the simulation result before output, e.g., normalization of data.
5. The **Output** entity specifies the simulation output, e.g., the particular plots to be shown.

Structure of SED-ML

Model Elements

The SED-ML model elements define the identity and location of the model(s) to be simulated and specify the model's native encoding format. The location is to be given as a Uniform Resource Identifier (URI), which enables software interpreting SED-ML to retrieve the model. In case of a relative URI, the base is the location of the referring SED-ML file. The SED-ML archive format can furthermore be used to share model and simulation descriptions together (see the specification (Waltemath et al. 2011b)). In addition to defining the source model's location and encoding, SED-ML model elements can also list changes to be applied to a model before simulation. Such changes could be altering attribute values (e.g., a parameter value in an SBML model or the initial_value of a CellML variable) or changing the model structure. Attribute values may undergo a simple substitution or more complex calculation using content MathML 2.0 (<http://www.w3.org/Math/>). The model structure may be changed by adding or removing XML elements.

Simulation Elements

The SED-ML simulation elements define the simulation algorithms to be used in the experiment and their configuration. Simulation

algorithms are specified using terms from the Kinetic Simulation Algorithm Ontology (KiSAO, <http://biomodels.net/kisao/>). KiSAO classifies and characterizes kinetic simulation algorithms. Furthermore, configuration details of the simulation can be described in SED-ML, such as the start and end times or the number of time points to output. The current implementation supports the description of time-course simulation setups. Extensions towards further experiment types are already being discussed and will be available in the next versions, including the description of steady-state analyses and nested simulations, such as parameter scans.

Task Elements

The SED-ML task elements apply a particular simulation algorithm to a specific model. Because simulations and models are described independently, they can be combined in diverse ways. Tasks allow for this flexibility. For example, a simulation can be applied to different versions of a model with varying parameterization.

DataGenerator Elements

The SED-ML dataGenerators define transformations of raw simulation output (as generated by a task) into the desired numerical form. They can simply be references to a model variable but may also be defined through complex mathematical expressions encoded using content MathML. Some variables used in an experiment are not explicitly defined in the model, but may be implicitly contained and can be addressed using SED-ML-specific constructs. The SED-ML website provides a mapping of these SED-ML symbols onto possibly existing concepts in the individual languages.

Output Elements

The SED-ML output elements describe how numerical data from the data generators are grouped together. SED-ML allows to generate 2D and 3D plots or sets of unrelated arrays.

SED-ML Development

SED-ML is a community-driven project that is part of the COmputational Modeling in BIology

NEtwork (COMBINE, <http://co.mbine.org>). SED-ML development is coordinated by five elected editors. Format extensions are discussed on the SED-ML mailing list and on annual meetings. Simulation descriptions in SED-ML are currently provided for SBML and CellML models. The adoption of SED-ML for NeuroML models is ongoing.

Software Support

SED-ML files can be created and read using software libraries and tools (Waltemath et al. 2011c). The libSedML (<http://libsedml.sf.net/>) is a set of .NET libraries for reading, validating, and writing SED-ML descriptions, along with all necessary utility functions for resolving models and XPath expressions. The libSedMLScript, which is part of libSedML, provides a script-based language for defining SED-ML experiments. Alternatively, jlibsedml (<http://sourceforge.net/projects/jlibsedml/>) is a Java library for creating, manipulating, validating, and working with SED-ML documents. The jlibsedml application programming interface (API) follows a similar organization to that of libSBML, a successful and popular library for manipulation of SBML documents. SProS (the SED-ML Processing Service) is an API for creating, reading, and manipulating SED-ML documents. It is integrated in the CellML API. Future versions of SProS will also provide support for running simulations described in SED-ML and involving CellML models (using the simulation facilities already present in the CellML API).

An up-to-date list of software supporting SED-ML is available from the Showcases on the SED-ML web page (<http://sed-ml.org>).

Cross-References

- ▶ [CellML](#)
- ▶ [neuroConstruct](#)
- ▶ [NeuroML](#)
- ▶ [Systems Biology Markup Language \(SBML\)](#)

References

- Waltemath D, Adams R, Beard DA, Bergmann FT, Bhalla US, Britten R, Chelliah V, Cooling MT, Cooper J, Crampin EJ, Garny A, Hoops S, Hucka M, Hunter P, Klipp E, Laibe C, Miller AK, Moraru I, Nickerson D, Nielsen P, Nikolski M, Sahle S, Sauro HM, Schmidt H, Snoep JL, Tolle D, Wolkenhauer O, Le Novère N (2011a) Minimum information about a simulation experiment (MIASE). *PLoS Comput Biol* 7(4): e1001122
- Waltemath D, Bergmann FT, Adams R, Le Novère N (2011b) Simulation experiment description markup language (SED-ML): level 1 version 1. <http://sed-ml.org/documents/sed-ml-L1V1.pdf>. Accessed 28 Sept 2013
- Waltemath D, Adams R, Bergmann FT, Hucka M, Kolpakov F, Miller AK, Moraru II, Nickerson D, Snoep JL, Le Novère N (2011c) Reproducible computational biology experiments with SED-ML: the simulation experiment description markup language. *BMC Syst Biol* 5:198

Further Readings

- Adams RA (2012) SED-ED, a workflow editor for computational biology experiments written in SED-ML. *Bioinformatics* 28(8):1180–1181
- Courtot M, Juty N, Knüpfer C, Waltemath D, Zhukova A, Dräger A, Dumontier M, Finney A, Golebiewski M, Hastings J, Hoops S, Keating S, Kell DB, Kerrien S, Lawson J, Lister A, Lu J, Machne R, Mendes P, Pocock M, Rodriguez N, Villeger A, Wilkinson DJ, Wimalaratne S, Laibe C, Hucka M, Le Novère N (2011) Controlled vocabularies and semantics in systems biology. *Nat Mol Syst Biol* 7:543
- Waltemath D, Henkel R, Winter F, Wolkenhauer O (2013) Reproducibility of model-based results in systems biology. In: Prokop A, Csukas B (eds) *Systems biology: integrative biology and simulation tools*, vol 1. Springer (in press)

SK Channels (KCa2.x)

- Calcium-Dependent Potassium Channels

Skill Acquisition in Stick Balancing

- Human Balancing Tasks: Power Laws, Intermittency, and Lévy Flights

Sleep

- Low Frequency Oscillations (Anesthesia and Sleep): Overview

Sleep Oscillations

- Low Frequency Oscillations (Anesthesia and Sleep): Overview

Sleep Spindles

- Low Frequency Oscillations (Anesthesia and Sleep): Overview

Sleep, Neural Population Models of

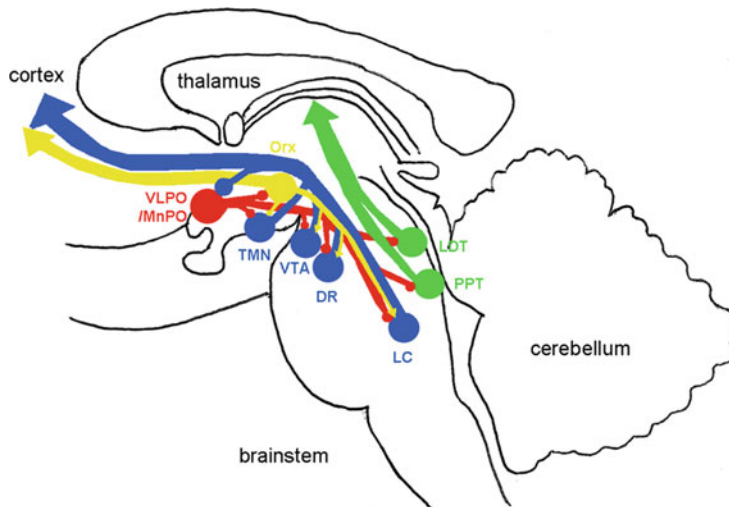
Andrew J. K. Phillips
Division of Sleep Medicine, Brigham and Women's Hospital, Harvard Medical School, Boston, MA, USA

Definition

A neural population model of sleep is a mathematical model of neural populations that regulate the timing and expression of sleep/wake patterns. Specific circuits and nuclei have been identified in the mammalian brainstem and hypothalamus that play a key role in modulating the brain's overall arousal state with a circadian (daily) rhythm. These neural populations have been the focus of most sleep modeling.

Detailed Description

Sleep is an arousal state characterized by physical inactivity, reduced sensitivity to environmental stimuli, and a range of characteristic



Sleep, Neural Population Models of, Fig. 1 The brain's overall arousal state is modulated by ascending projections to the cortex and thalamus from nuclei in the brainstem and hypothalamus. These include (i) wake-promoting nuclei that release monoaminergic neurotransmitters (blue), the tuberomammillary nucleus (TMN), the ventral tegmental area (VTA), the dorsal raphe (DR), and the locus coeruleus (LC); (ii) wake-promoting and REM sleep-promoting nuclei that release acetylcholine (green), the laterodorsal tegmentum (LDT) and the

pedunculopontine tegmentum (PPT); and (iii) wake-promoting neurons in the lateral hypothalamus (yellow) that release orexin (Orx). These nuclei are all GABAergically inhibited by sleep-promoting neurons (red) in the ventrolateral preoptic area (VLPO) and median preoptic area (MnPO). Excitatory (pointed arrows) and inhibitory (rounded arrows) interactions between nuclei are indicated. Mutual inhibition between sleep-promoting and wake-promoting nuclei forms the basis for the sleep/wake switch

physiological changes, including changes to the EEG associated with rapid eye movement (REM) and non-REM (NREM) sleep in mammals. Sleep is regulated by a variety of physiological and biochemical processes (Krueger et al. 2008; Saper et al. 2010), including specific neural populations in the brainstem and hypothalamus. Various mathematical models have now been developed, providing a conduit between the underlying physiology and the sleep/wake dynamics observed at the behavioral level.

The Sleep/Wake Switch

The arousal states of sleep and wakefulness typically manifest as global patterns of brain activity; notable exceptions to this rule are unihemispheric sleep (sleeping with one brain hemisphere) and local sleep (emergence of sleep-like activity patterns in overworked neural assemblies while the rest of the brain is awake),

which demonstrate that sleep can in principle be regulated on more local scales. Global synchronization of sleep and wake states across brain regions is achieved by control systems in the brainstem and hypothalamus. As shown in Fig. 1, a group of monoaminergic, cholinergic, and orexinergic neural populations projects diffusely to the cortex and thalamus. The coherent activation of these populations modulates corticothalamic activity, so as to promote and sustain wakefulness.

A population of sleep-promoting neurons in the ventrolateral preoptic area (VLPO) and median preoptic area (MnPO) of the hypothalamus GABAergically inhibits the wake-promoting monoaminergic, cholinergic, and orexinergic neural populations. Interestingly, the wake-promoting monoaminergic populations in turn inhibit the sleep-promoting VLPO/MnPO populations. This mutual inhibition between sleep-promoting and wake-promoting neural populations provides a basis for a switch-like

system, with stable sleep and wake states, and relatively rapid transitions between states (Saper et al. 2010). This system is called the *sleep/wake switch*.

Sleep-Regulatory Processes

Prior to the recent detailed mapping of sleep-regulatory circuits in the brain, mathematical models of sleep were developed. In the absence of physiological data, these models were phenomenological rather than physiological. The most influential of these models was the two-process model of sleep (Daan et al. 1984), which provided the conceptual basis for most subsequent models of sleep and human performance (Van Dongen 2004). The two-process model assumes that sleep can be understood in terms of two key sleep-regulatory processes: the circadian process and the sleep homeostatic process. The circadian process represents an approximately 24-h biological rhythm in sleepiness and alertness, typically described by a periodic function or nonlinear oscillator. The sleep homeostatic process represents the increasing need to sleep the longer one is awake and the dissipation of this need the longer one is asleep, typically described by exponentially saturating functions.

The physiological basis for the circadian process has now been well elucidated. Circadian rhythms are generated endogenously on a molecular level by virtually all mammalian cells. These cellular rhythms are synchronized by a master circadian clock that resides in the suprachiasmatic nucleus (SCN) of the hypothalamus. SCN neurons act as tightly coupled circadian pacemaker cells, sending a robust circadian signal to many other brain regions. The SCN receives direct input from the retina, allowing it to entrain to the daily light/dark cycle (Foster and Kreitzman 2005).

The physiological basis for the sleep homeostatic process is still not well understood, but evidence points towards the accumulation of certain sleep-promoting factors in the brain during wakefulness. These substances include adenosine, nitric oxide, TNF- α , Interleukin-1, and prostaglandin D2 (Krueger et al. 2008).

Both the circadian and sleep homeostatic processes have been found to act on the neural populations in the sleep/wake switch (Pace-Schott and Hobson 2002). The SCN has multiple relays to both the sleep-promoting and wake-promoting neural populations. The sleep-promoting factor adenosine has also been found to have effects on the VLPO. The sleep/wake switch therefore provides a neural basis for the integration of the circadian and sleep homeostatic processes.

Neural Population Models of Sleep

In order to test the theoretical value of the sleep/wake switch theory of sleep regulation, and to link the dynamics of underlying neural systems to behavioral manifestations, various mathematical models of the neural populations in the sleep/wake switch have recently been developed (Tamakawa et al. 2006; Phillips and Robinson 2007; Behn et al. 2007; Behn and Booth 2010; Rempe et al. 2010; Kumar et al. 2012; Sedigh-Sarvestani et al. 2012). These models have included different levels of detail in terms of the neural populations included, as well as slightly different mathematical formalisms, including neural mass, single neuron, and neural mass/neurotransmitter concentration implementations. Central to all of these models is mutual inhibition between sleep-promoting and wake-promoting neural populations, i.e., the sleep/wake switch.

Here, we present a simplified mathematical description of the core dynamics of these neural population models of the sleep/wake switch. We base our equations on the Phillips–Robinson model, since it is the simplest and most widely used of the models (Robinson et al. 2011).

We model two neural populations: a wake-promoting population (subscript w) and a sleep-promoting population (subscript s). Each population has a mean firing rate, Q_j , and a mean cell body voltage relative to resting, V_j . We assume that the firing rate is a sigmoidal function of voltage, $Q_j = S(V_j)$. We also assume that the postsynaptic effects on voltage for each population are proportional to the presynaptic firing

rates. The dynamics can then be represented by a pair of coupled first-order differential equations,

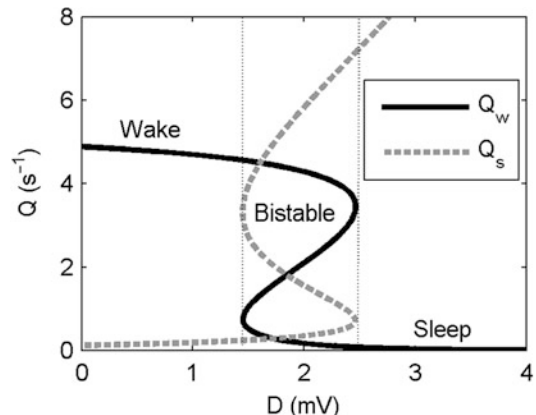
$$\begin{aligned}\tau_w dV_w/dt + V_w &= v_{ws}Q_s + A, \quad \tau_s dV_s/dt + V_s \\ &= v_{sw}Q_w + D(t),\end{aligned}$$

where τ_j is a time constant for the saturation time constant; $v_{ws} < 0$ and $v_{sw} < 0$ represent the strengths of the inhibitory synaptic connections between the two populations; A represents any constant net input to the wake-promoting population; and $D(t)$ represents the net drive to the sleep-promoting population from circadian and sleep homeostatic processes. In general, the circadian and sleep homeostatic processes could also have a direct effect on the wake-promoting population. Here, we consider the most simple case for analysis.

The dynamics of the neural populations occur on a timescale of milliseconds to minutes (determined by the τ_j parameters), whereas $D(t)$ varies on a daily timescale by definition. A timescale separation can therefore be performed, treating D as approximately constant on timescales relevant to neural dynamics (Fulcher et al. 2008). The system dynamics can then be summarized by the reduced manifold of equilibrium values for various fixed values of D , as shown in Fig. 2.

For reasonable parameter values, the reduced system has two stable states, corresponding to sleep and wake. For a certain intermediate range of values for D , the system is bistable. As D oscillates with a period of ~ 24 h, the system is dragged back and forth across the bistable region, resulting in daily transitions between sleep and wake. The model exhibits hysteresis, because the thresholds for sleep-to-wake and wake-to-sleep transitions are different, as shown in Fig. 2.

This hysteresis behavior describes the most basic, reduced dynamics of most neural population models of the sleep/wake switch. Interestingly, these physiologically based models recapitulate the basic assumptions of the phenomenological two-process model: two separate thresholds for sleep-to-wake and wake-to-sleep



Sleep, Neural Population Models of, Fig. 2 If the sleep drive, D , is assumed to be slowly varying, the model dynamics can be visually summarized in terms of the equilibrium values for the wake-promoting population firing rate, Q_w , and the sleep-promoting population firing rate, Q_s . When the drive for sleep is low, the model has a stable wake state, with high Q_w and low Q_s . When the drive for sleep is high, the model has a stable sleep state with low Q_w and high Q_s . For an intermediate range of drive values, the model is bistable, with stable sleep and wake states. Saddle node bifurcations occur at critical thresholds (dotted lines). The stable wake and sleep branches are linked by an unstable equilibrium branch within the bistable zone. As D slowly oscillates on a daily timescale, the model therefore undergoes hysteresis as it is dragged across the thresholds where sleep and wake states become unstable

transitions (Phillips and Robinson 2008; Rempe et al. 2010). In other words, these models provide a physiological justification for the two-process model, as well as providing new insights by explicitly modeling the underlying physiological dynamics.

Neural population models of the sleep/wake switch have been highly successful in reproducing and predicting many aspects of human sleep and circadian rhythms (Robinson et al. 2011). In addition, mathematical models have been developed to describe how modulation of the corticothalamic system can give rise to the neural activity patterns associated with sleep and wakefulness, as well as transitions between arousal states (Robinson et al. 2002; Hill and Tononi 2005; Steyn-Ross et al. 2005; Deco et al. 2013). Linking corticothalamic and subcortical models poses a significant theoretical and numerical challenge due to their inherently

different spatiotemporal scales, but such models are on the horizon (Robinson et al. 2010).

Recent Findings

Neural population models of the sleep/wake switch have been highly successful in reproducing and predicting many aspects of human sleep and circadian rhythms. Specifically, models of the sleep/wake switch have been used to understand the physiological mechanisms that underlie interindividual (Phillips et al. 2010a; Robinson et al. 2011) and interspecies (Phillips et al. 2010b, 2013) differences in sleep timing and duration. They have been used to reproduce normal human sleep (Phillips and Robinson 2007) and mouse sleep (Behn et al. 2007), as well as the effects of neurotransmitter microinjections (Behn and Booth 2010). They have also been applied to predicting human performance, including the effects of sleep deprivation (Fulcher et al. 2010) and caffeine on subjective fatigue (Puckeridge et al. 2010) and the effects of shiftwork on performance (Postnova et al. 2012).

Given the current uncertainty regarding the physiological mechanisms that underlie the REM/REM sleep cycle, neural population models have also been used to probe the possible dynamics of the system. This has led to concrete hypotheses regarding physiological mechanisms and circuits that could potentially generate the REM/NREM sleep cycle (Rempe et al. 2010; Behn and Booth 2012; Behn et al. 2013). Sleep/wake switch models have also recently been applied to reproducing the desynchronization of sleep/wake cycles from the circadian process that can occur when individuals are completely isolated from environmental time cues and are free to self-select their sleep/wake timings (Phillips et al. 2011; Gleit et al. 2013).

In addition, mathematical models have been developed to describe how modulation of the corticothalamic system can give rise to the neural activity patterns associated with sleep and wakefulness, as well as transitions between arousal states (Robinson et al. 2002; Hill and Tononi 2005; Steyn-Ross et al. 2005; Deco et al. 2013). Linking

corticothalamic and subcortical models poses a significant theoretical and numerical challenge due to their inherently different spatiotemporal scales, but such models are on the horizon (Robinson et al. 2010).

Cross-References

- [Anesthesia, Neural Population Models of](#)
- [Bifurcations, Neural Population Models and](#)
- [Down Under Neural Population Models](#)
- [Neural Population Model](#)
- [Neuroimaging, Neural Population Models for](#)
- [Phase Response Curves: Overview](#)
- [Wilson-Cowan Model](#)

References

- Behn CGD, Booth V (2010) Simulating microinjection experiments in a novel model of the rat sleep-wake regulatory network. *J Neurophysiol* 103:1937–1953
- Behn CGD, Booth V (2012) A fast-slow analysis of the dynamics of REM sleep. *SIAM J Appl Dyn Syst* 11:212–242
- Behn CGD, Brown EN, Scammell TE, Kopell NJ (2007) Mathematical model of network dynamics governing mouse sleep–wake behavior. *J Neurophysiol* 97:3828–3840
- Behn CGD, Ananthasubramaniam A, Booth V (2013) Contrasting existence and robustness of REM/non-REM cycling in physiologically based models of REM sleep regulatory networks. *SIAM J Appl Dyn Syst* 12:279–314
- Daan S, Beersma DG, Borbély AA (1984) Timing of human sleep: recovery process gated by a circadian pacemaker. *Am J Physiol* 246:R161–R183
- Deco G, Hagmann P, Hudetz AG, Tononi G (2013) Modeling resting-state functional networks when the cortex falls sleep: local and global changes. *Cereb Cortex* (in press)
- Foster RG, Kreitzman L (2005) *Rhythms of life*. Yale University Press, New Haven
- Fulcher BD, Phillips AJK, Robinson PA (2008) Modeling the impact of impulsive stimuli on sleep-wake dynamics. *Phys Rev E Stat Nonlin Soft Matter Phys* 78:051920
- Fulcher BD, Phillips AJK, Robinson PA (2010) Quantitative physiologically based modeling of subjective fatigue during sleep deprivation. *J Theor Biol* 264:407–419
- Gleit RD, Behn CGD, Booth V (2013) Modeling interindividual differences in spontaneous internal desynchrony patterns. *J Biol Rhythms* 28:339–355

- Hill S, Tononi G (2005) Modeling sleep and wakefulness in the thalamocortical system. *J Neurophysiol* 93:1671–1698
- Krueger JM, Rector DM, Roy S, Van Dongen HPA, Belenky G, Panksepp J (2008) Sleep as a fundamental property of neuronal assemblies. *Nat Rev Neurosci* 9:910–919
- Kumar R, Bose A, Mallick BN (2012) A mathematical model towards understanding the mechanism of neuronal regulation of wake-NREMS-REMS states. *PLoS One* 7:e42059
- Pace-Schott EF, Hobson JA (2002) The neurobiology of sleep: genetics, cellular physiology and subcortical networks. *Nat Rev Neurosci* 3:591–605
- Phillips AJK, Robinson PA (2007) A quantitative model of sleep-wake dynamics based on the physiology of the brainstem ascending arousal system. *J Biol Rhythms* 22:167–179
- Phillips AJK, Robinson PA (2008) Sleep deprivation in a quantitative physiologically based model of the ascending arousal system. *J Theor Biol* 255:413–423
- Phillips AJK, Chen PY, Robinson PA (2010a) Probing the mechanisms of chronotype using quantitative modeling. *J Biol Rhythms* 25:217–227
- Phillips AJK, Robinson PA, Kedziora DJ, Abeysuriya RG (2010b) Mammalian sleep dynamics: how diverse features arise from a common physiological framework. *PLoS Comput Biol* 6:e1000826
- Phillips AJK, Czeisler CA, Klerman EB (2011) Revisiting spontaneous internal desynchrony using a quantitative model of sleep physiology. *J Biol Rhythms* 26:441–453
- Phillips AJK, Fulcher BD, Robinson PA, Klerman EB (2013) Mammalian rest/activity patterns explained by physiologically based modeling. *PLoS Comput Biol* 9: e1003213
- Postnova S, Layden A, Robinson PA, Phillips AJK, Abeysuriya RG (2012) Exploring sleepiness and entrainment on permanent shift schedules in a physiologically based model. *J Biol Rhythms* 27:91–102
- Puckeridge M, Fulcher BD, Phillips AJK, Robinson PA (2010) Incorporation of caffeine into a quantitative model of fatigue and sleep. *J Theor Biol* 273:44–54
- Rempe MJ, Best J, Terman D (2010) A mathematical model of the sleep/wake cycle. *J Math Biol* 60:615–644
- Robinson PA, Rennie CJ, Rowe DL (2002) Dynamics of large-scale brain activity in normal arousal states and epileptic seizures. *Phys Rev E Stat Nonlin Soft Matter Phys* 65:041924
- Robinson PA, Rennie CJ, Phillips AJK, Kim JW, Roberts JA (2010) Phase transitions in physiologically-based multiscale mean-field brain models. In: Steyn-Ross DA, Steyn-Ross ML (eds) *Modeling phase transitions in the brain*. Springer, New York, pp 179–201
- Robinson PA, Phillips AJK, Fulcher BD, Puckeridge M, Roberts JA, Rennie CJ (2011) Quantitative modeling of sleep dynamics. In: Hutt A (ed) *Sleep and anesthesia*. Springer, New York, pp 45–68
- Saper CB, Fuller PM, Pedersen NP, Lu J, Scammell TE (2010) Sleep state switching. *Neuron* 68:1023–1042
- Sedigh-Sarvestani M, Schiff SJ, Gluckman B (2012) Reconstructing mammalian sleep dynamics with data assimilation. *PLoS Comput Biol* 8:e1002788
- Steyn-Ross DA, Steyn-Ross ML, Sleigh JW, Wilson MT, Gillies IP, Wright JJ (2005) The sleep cycle modelled as a cortical phase transition. *J Biol Phys* 31(3–4):547–569
- Tamakawa Y, Karashima A, Koyama Y, Katayama N, Nakao M (2006) A quartet neural system model orchestrating sleep and wakefulness mechanisms. *J Neurophysiol* 95:2055–2069
- Van Dongen HPA (2004) Comparison of mathematical model predictions to experimental data of fatigue and performance. *Aviat Space Environ Med* 75:A15–A36

Further Reading

Books

- Hutt A (2011) *Sleep and anesthesia*. Springer, New York
- Steyn-Ross DA, Steyn-Ross ML (2010) *Modeling phase transitions in the brain*. Springer, New York

Scholarpedia

- Neurobiology of sleep and wakefulness
Sleep homeostasis

Wikimedia

- Circadian rhythm
Neuroscience of sleep
Sleep
Suprachiasmatic nucleus

Slow Feature Analysis

Laurenz Wiskott

Institut für Neuroinformatik, Ruhr-Universität Bochum, Bochum, Germany

S

Definition

Slow feature analysis (SFA) is an unsupervised learning algorithm for extracting slowly varying features from a multidimensional input signal in time. It is not based on low-pass filtering, i.e., temporal averaging, but combines input components of single time steps into temporally stable features. SFA can be used for nonlinear dimensionality reduction and learning of invariant representations. Algorithmically, it is closely related to principal component analysis (PCA).

Detailed Description

Slowness Principle

The slowness principle is based on the observation that different representations of a sensorial input vary on different time scales. For instance, a zebra grazing in the savanna is a scene that changes slowly. This scene is represented in the eyes of an observer in terms of activities of retinal receptors, which, due to the black-and-white stripes of the zebra, change quickly between high and low values whenever the zebra moves or the gaze of the observer changes. However, in higher brain areas of the observer, there is a high-level representation of the zebra grazing, which changes slowly again. This difference in time scales is true for most dynamic scenes. The slowness principle therefore states that high-level representations can be learned from the receptor activities simply by extracting features that vary slowly over time (without using the trivial option of low-pass filtering).

The idea of the slowness principle has probably first been mentioned by Geoffrey Hinton in 1989; early algorithms were presented by Peter Földiák and by Graeme Mitchison, both in 1991; slow feature analysis (SFA) has first been introduced by Laurenz Wiskott in 1998; see (Wiskott et al. 2011) for references.

Slow Feature Analysis

Most learning algorithms based on the slowness principle are online learning rules, i.e., they improve the extracted features incrementally with each time step of the training data. Slow feature analysis (SFA) (Wiskott et al. 2011) in contrast is an algorithm that takes all training data into account at once.

SFA first uses PCA to normalize the input signal such that it has zero mean and unit variance in all directions, which is also known as whitening or spherling. It then calculates the time derivative (in the discrete case the difference between successive time points) of the whitened signal and uses PCA again to find the directions of smallest variance, which are the directions of slowest variation and correspond to the slow features to be extracted.

As SFA is based on PCA, it is basically a linear algorithm. However, one typically applies a predefined set of nonlinear functions to the input signal first, which is known as nonlinear expansion, and then applies SFA to this expanded input signal. Thus, SFA learns linear combinations of fixed nonlinear functions, which results in nonlinear functions to extract features from the input.

It has been shown analytically that SFA is closely related to spike-timing-dependent plasticity (STDP) (Sprekeler et al. 2007).

Applications in Computational Neuroscience

SFA has been developed for learning invariant representations of moving objects in a feedforward model of the visual system. It has been shown that a hierarchical network of SFA nodes extracts features from a video signal of moving objects that permit invariant object recognition with a simple classifier and also extraction of positional and pose information with linear regression (Wiskott et al. 2011). Interestingly, on the first SFA layer units share many properties with complex cells in the primary visual cortex, such as phase invariance, orientation selectivity, and frequency tuning. One also finds end- and side-inhibited units there. Complex cell-like units emerge also if learning is based on simulated retinal waves rather than moving objects (Dähne et al. 2014).

If combined with independent component analysis, an SFA network trained with input from a simulated rat running around in a static environment develops units that behave like place cells and others that behave like head-direction cells in the hippocampal formation of rats (Wiskott et al. 2011). Place cells fire if a rat is at a particular location independently of its head direction; head-direction cells fire if a rat is oriented in a particular direction independently of its location. SFA can extract location and head direction because these variables vary slowly compared to individual pixel values of the visual input sequence as the rat runs through the environment.

SFA has also been used for technical applications (Escalante-B and Wiskott 2012).

References

- Dähne S, Wilbert N, Wiskott L (2014) Slow feature analysis on retinal waves leads to VI complex cells. PLoS Comput Biol, in press
- Escalante-B AN, Wiskott L (2012) Slow feature analysis: perspectives for technical applications of a versatile learning algorithm. Künstliche Intell [Artif Intell] 26(4):341–348
- Sprekeler H, Michaelis C, Wiskott L (2007) Slowness: an objective for spike-timing-dependent plasticity? PLoS Comput Biol 3(6):e112
- Wiskott L, Berkes P, Franzius M, Sprekeler H, Wilbert N (2011) Slow feature analysis. Scholarpedia 6(4):5282

Slow Oscillation

► Delta Rhythms: Models and Physiology

Slow Oscillations

► Low Frequency Oscillations (Anesthesia and Sleep): Overview

Slow Oscillations and Epilepsy: Network Models

Alain Destexhe

Unit of Neuroscience Information and Complexity (UNIC), Centre National de la Recherche Scientifique (CNRS), Gif-sur-Yvette, France

Definition

Network models are very useful tools to investigate the genesis of oscillatory behavior such as epileptic seizures. During many types of seizures, the brain produces oscillatory spike-and-wave discharges, which are particularly prominent for absence seizures. It was found that the thalamocortical mechanisms leading to spindle oscillations and their large-scale synchrony can explain spike-and-wave oscillations, if the excitability of the cerebral cortex is augmented. These

pathological oscillations can be reproduced by network models involving the reciprocal interaction between thalamus and cortex.

Detailed Description

Introduction

Many types of epileptic seizures display very synchronized oscillations producing a typical electroencephalogram (EEG) pattern consisting of one or several sharp deflections (“spikes”) followed by a surface-positive “wave.” Spike-and-wave patterns of similar characteristics are also seen in a number of experimental models in cats, rats, mice, and monkeys, as well as in many other types of epilepsies. In some of these experimental models, it was shown that the critical regions involved are the thalamus and neocortex and that the genesis of spike-and-wave activity shares common mechanisms with sleep spindle oscillations, which are generated in the thalamus. Computational models have explored mechanisms for such spike-and-wave activity, as reviewed here.

The Cellular Bases of Spike-and-Wave Discharges in Cortex

Computational models have first explored the cellular pattern needed to generate spike-and-wave EEG or local-field potentials. Using a simple biophysical model of cortical network with excitatory and inhibitory neurons (Destexhe 1998), it was found that spike-and-wave LFP patterns can be generated if all cells fire in synchrony (“spike” component), followed by a hyperpolarization mediated by K^+ conductances (“wave” component). The synchronized discharge during the “spike” was indeed found in many different experimental models of seizures (reviewed in Destexhe 2013), while the hyperpolarization during the “wave” remains poorly studied. Intracellular recordings during spike-and-wave seizures showed that the “wave” is correlated by hyperpolarization, which was interpreted as due to a mixture of disinhibition and K^+ currents (Neckelmann et al. 2000). The model suggests that this slow K^+ conductance can be due to two different

mechanisms: either it can be generated by the slow voltage-dependent K⁺ conductances responsible for spike-frequency adaptation in pyramidal neurons. In this case, the strong firing during the “spike” maximally activates these adapting currents, which then produce the slow hyperpolarization. Another possible origin is synaptic; the strong firing may massively activate the slow type of GABAergic inhibition, acting on GABA_B receptors, which also cause a slow activation of K⁺ channels.

Hypersynchronized Slow Oscillations in the Thalamus

Many experimental evidences show that thalamic circuits are implicated in seizure generation (reviewed in Gloor and Fariello 1988; Crunelli and Leresche 2002). It was found that if convulsants are applied to the thalamus *in vitro*, blocking GABA_A receptors, they induce the production of a slow and synchronized oscillation at around 3 Hz and are dependent on GABA_B receptors (von Krosigk et al. 1993). Although it is tempting to associate the origin of the seizure and the spike-and-wave oscillation to the thalamus, it is not the case, because this slow oscillation was shown to be different from spike-and-wave oscillations *in vivo* (Steriade and Contreras 1998). This slow oscillation was simulated by network models of thalamic circuits (Destexhe et al. 1993, 1996; Golomb et al. 1996) and was due to the mutual interaction between thalamic relay and reticular neurons, involving GABA_B receptors.

Model of Spike-and-Wave Discharges in the Thalamocortical System

Experimentally, it was shown that the cerebral cortex is the key to the induction of seizures. In cats, different experimental manipulations of cortical excitability lead to spike-and-wave seizures, but the *physiologically intact* thalamus is necessary (Gloor and Fariello 1988). In rat models of absence seizures, a focus of increased excitability was found in cortex (Meeren et al. 2002; Polack et al. 2007), but the thalamus was also necessary for seizure generation (Vergnes and Marescaux 1992). These results were replicated by

computational models of thalamic and cortical networks, endowed with the different receptor type present as well as the intrinsic cellular properties of thalamic and cortical cells (Destexhe 1998, 1999). This model is explained below.

The main hypothesis explored by this model was that seizure generation uses the oscillatory-generating mechanisms present in the thalamus but with an over-excitable cortex. In “control” conditions, the network model generates spindle oscillations. As shown in detail in another entry (“► [Spindle Oscillations: Models](#)”), spindle oscillations are generated by thalamic circuits and can be modeled by thalamic networks. In the thalamocortical system, the cortex plays an essential role in synchronizing the thalamic-generated oscillations, as also described in detail in another entry (“► [Corticothalamic Feedback: Large-Scale Synchrony](#)”). In this case, the models established that the most efficient way for the cortex to control the thalamic oscillation and organize its large-scale synchrony is to evoke strong inhibition in the thalamus (Destexhe et al. 1998).

This “inhibitory dominant” character of the corticothalamic interaction is fundamental to explain seizures. While this cortically evoked thalamic inhibition is mostly mediated by GABA_A receptors in normal conditions, it may be different in pathological conditions. If the cortex is hyperexcitable, the exaggerated corticothalamic feedback will be strong enough to activate GABA_B receptors (due to their nonlinear activation properties – see Destexhe and Sejnowski 1995). This activation of slow GABA_B inhibition will “force” the thalamus, although physiologically intact, to oscillate at a slower and more synchronized frequency around 3 Hz (Destexhe 1998).

This mechanism was tested by simulating networks of thalamic and cortical cells, with the different receptor types present, and the system was able to generate hypersynchronized oscillations at 3 Hz when solely the cortex was affected (its excitability was augmented by diminishing intracortical inhibition). Remarkably, this model generated 2–3 Hz oscillations with spike-and-wave patterns in the calculated LFPs (Destexhe 1998).

A very similar mechanism was found for faster oscillation frequencies typically observed in rodents (Destexhe 1999). In this case, the total conductance of GABA_B inhibition in the thalamus had to be weaker, preventing the thalamus to oscillate at 3 Hz. Thus, this model predicts that the ~3 Hz spike-and-wave of cats, monkey, and man and the ~8 Hz spike-and-wave seizures of rats and mice have a common cellular mechanism but different respective conductances of GABA_A and GABA_B receptor-mediated inhibition in the thalamus. This prediction still awaits to be tested.

Testing the Mechanism in Thalamic Slices

The main prediction of this thalamocortical model of seizures is that a too-strong corticothalamic feedback should be able to switch the *intact* thalamus to oscillate at 3 Hz (Destexhe 1998), a frequency which is not normally seen in the physiologically intact thalamus. This prediction was tested in thalamic slices, where the corticothalamic fibers can be stimulated electrically. It was found by two independent studies (Bal et al. 2000; Blumenfeld and McCormick 2000) that, indeed, strong stimulation of corticothalamic fibers can “force” the thalamus to oscillate at 3 Hz and that this forcing is dependent on GABA_B receptors. It was also shown that the “forced” 3 Hz oscillations are more synchronized than the natural 10 Hz spindle rhythm produced by the same thalamic circuits. These findings are all in agreement with the predictions of the model and therefore support the view that 3 Hz hypersynchronized oscillations can be generated by the thalamus subject to a hyperexcitable cortex.

Discussion

In conclusion, computational models have provided a plausible explanation for a number of contrasting experimental results. First, the thalamus can produce a slow oscillation around 3 Hz, where GABA_B receptors are important, but this oscillation is not the primary cause for ~3 Hz spike-and-wave discharges seen in epileptic seizures. The model can reproduce the experiments

showing that the disinhibited thalamus does not produce spike-and-wave in cortex.

Second, seizures can be generated by a hyperexcitable cortex, but the intact thalamus is necessary. The generation of seizures depends on an interaction between cortex and thalamus. An essential ingredient in this interaction is that the corticothalamic feedback must be very efficient in evoking inhibition in the thalamus. If this is the case, the models show that a hyperexcitable cortex will generate a feedback strong enough to recruit GABA_B receptors in the thalamus and “force” the slow oscillatory mode (although the thalamus is physiologically intact).

If these ingredients are assembled in a thalamocortical model, ~3 Hz spike-and-wave oscillations can be generated if the cortex alone is made hyperexcitable, but the thalamus is kept physiologically intact (Destexhe 1998). This thalamocortical mechanism is dependent on the presence of GABA_B receptors in the thalamus, which are responsible for the ~3 Hz oscillation of the entire system. If the thalamus has weak GABA_B-mediated inhibition, then the hyperexcitable system oscillates at a faster frequency, around 8 Hz, as found in rodents. Thus, the models predict that a common mechanism underlies absence seizures in all mammals but that the exact oscillation frequency will be dependent on the balance between GABA_A and GABA_B receptors in the thalamus (Destexhe 1999).

Finally, this model is compatible with the finding that a focus in cerebral cortex is associated to absence seizures in rats (Meeren et al. 2002). It was found that deep (layers 5–6) cortical neurons are hyperexcitable and seem to lead the discharges during ictal activity (Polack et al. 2007). As layer 6 neurons project to thalamus, this finding is consistent with the idea that an excessive corticothalamic feedback may be a primary cause for absence seizures.

Cross-References

- [Corticothalamic Feedback: Large-Scale Synchrony](#)
- [Spindle Oscillations: Models](#)

References

- Bal T, Debay D, Destexhe A (2000) Cortical feedback controls the frequency and synchrony of oscillations in the visual thalamus. *J Neurosci* 20:7478–7488
- Blumenfeld H, McCormick DA (2000) Corticothalamic inputs control the pattern of activity generated in thalamocortical networks. *J Neurosci* 20:5153–5162
- Crunelli V, Leresche N (2002) Childhood absence epilepsy: genes, channels, neurons and networks. *Nat Rev Neurosci* 3:371–382
- Destexhe A (1998) Spike-and-wave oscillations based on the properties of GABA_B receptors. *J Neurosci* 18:9090–9111
- Destexhe A (1999) Can GABA_A conductances explain the fast oscillation frequency of absence seizures in rodents? *Eur J Neurosci* 11:2175–2181
- Destexhe A (2013) Network models of absence seizures. In: Faingold CL, Blumenfeld H (eds) *Neuronal networks in brain function, CNS disorders and therapeutics*. Elsevier, Amsterdam (in press)
- Destexhe A, Sejnowski TJ (1995) G-protein activation kinetics and spill-over of GABA may account for differences between inhibitory responses in the hippocampus and thalamus. *Proc Natl Acad Sci U S A* 92:9515–9519
- Destexhe A, McCormick DA, Sejnowski TJ (1993) A model for 8–10 Hz spindling in interconnected thalamic relay and reticularis neurons. *Biophys J* 65:2474–2478
- Destexhe A, Bal T, McCormick DA, Sejnowski TJ (1996) Ionic mechanisms underlying synchronized oscillations and propagating waves in a model of ferret thalamic slices. *J Neurophysiol* 76:2049–2070
- Destexhe A, Contreras D, Steriade M (1998) Mechanisms underlying the synchronizing action of corticothalamic feedback through inhibition of thalamic relay cells. *J Neurophysiol* 79:999–1016
- Gloor P, Fariello RG (1988) Generalized epilepsy: some of its cellular mechanisms differ from those of focal epilepsy. *Trends Neurosci* 11:63–68
- Golomb D, Wang XJ, Rinzel J (1996) Propagation of spindle waves in a thalamic slice model. *J Neurophysiol* 75:750–769
- Meeren HK, Pijn JP, Van Luijtelaar EL, Coenen AM, Lopes da Silva FH (2002) Cortical focus drives widespread corticothalamic networks during spontaneous absence seizures in rats. *J Neurosci* 22:1480–1495
- Neckelmann D, Amzica F, Steriade M (2000) Changes in neuronal conductance during different components of cortically generated spike-wave seizures. *Neuroscience* 96:475–485
- Polack PO, Guillemaud I, Hu E, Deransart C, Depaulis A, Charpier S (2007) Deep layer somatosensory cortical neurons initiate spike-and-wave discharges in a genetic model of absence seizures. *J Neurosci* 27:6590–6599
- Steriade M, Contreras D (1998) Spike-wave complexes and fast components of cortically generated seizures. I. Role of neocortex and thalamus. *J Neurophysiol* 80:1439–1455
- Vergnes M, Marescaux C (1992) Cortical and thalamic lesions in rats with genetic absence epilepsy. *J Neural Transm* 35(Suppl):71–83
- von Krosigk M, Bal T, McCormick DA (1993) Cellular mechanisms of a synchronized oscillation in the thalamus. *Science* 261:361–364

Further Reading

- Destexhe A (2007) Spike-and-wave oscillations. *Scholarpedia* 2:1402, http://www.scholarpedia.org/article/Spike-and-Wave_Oscillations
- Destexhe A, Sejnowski TJ (2001) Thalamocortical assemblies. Oxford University Press, Oxford

Slow Oscillations: Models

Albert Compte

Systems Neuroscience, IDIBAPS, Barcelona, Spain

Synonyms

[Up and down state models](#)

Definition

Several computational models have been proposed to describe the generation of spontaneous slow oscillations, or up and down state dynamics, in neuronal circuits of the cerebral cortex. Most models rely on strong excitatory feedback to generate reverberatory dynamics in the up state, which are then quenched by some negative feedback mechanism to form down states. The specific mechanisms responsible for triggering the transitions between up and down states distinguish these models. In addition, some models have been proposed that emphasize the role of thalamocortical loops in generating this spontaneous activity.

Detailed Description

During non-REM sleep and under most anesthetics, cortical network dynamics exhibit slow

oscillations or up and down state switching (see ► [Slow Oscillations: Physiology](#)). This pattern of activity has been the subject of numerous computational models, which have formulated quantitative accounts of the possible mechanisms that participate in their generation.

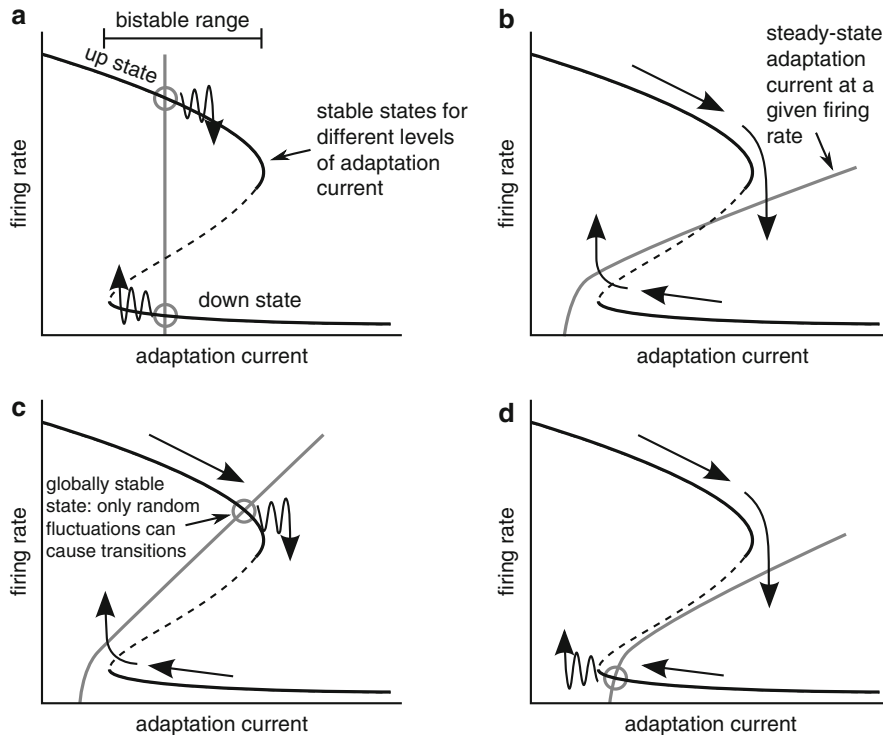
The models contemplate two main mechanisms to ignite up states. One set of models proposes that down states end as a result of the recovery of a fatigue mechanism accumulated during up states, such as some activity-dependent potassium current (Compte et al. 2003; Destexhe 2009), or short-term synaptic depression (Mejias et al. 2010). Spontaneously active excitatory neurons, possibly in specific layers (Destexhe 2009), are then responsible for starting a new up state. This links down state duration to the time constant of recovery of such fatigue mechanism. On the other hand, up states could be started by input fluctuations that impose a transition from a stable down state to the up state. Mechanistically, these fluctuations could be due to spontaneous synaptic release (Timofeev et al. 2000; Holcman and Tsodyks 2006; Mejias et al. 2010) or to external fluctuating inputs (Kepcs and Raghavachari 2007; Hughes et al. 2002; Mattia and Sanchez-Vives 2012). Down state duration in these scenarios is highly variable.

Similarly, the extinction of up states has also been modeled through either deterministic or stochastic processes. Mechanisms relying on activity-dependent negative feedback bring the up state deterministically to the point of sudden transition to the down state (Fig. 1b, d). Such negative feedback can be due to activity-dependent potassium currents (Compte et al. 2003; Hill and Tononi 2005), short-term synaptic depression (Holcman and Tsodyks 2006), short-term synaptic facilitation to interneurons (Melamed et al. 2008), or slow GABA_B feedback inhibition (Parga and Abbott 2007). On the other hand, endogenous fluctuations can also induce transitions from the up to the down state (Fig. 1a, c), in the form of stochastic inputs nonlinearly gated by NMDA receptors (Kepcs and Raghavachari 2007) or as a result of the stochastic dynamics of the firing rate in small populations (Mattia and Sanchez-Vives 2012).

Note, however, that these recurrent networks impose complex interdependencies between all these mechanisms: as an example, short-term depression promotes up-to-down transitions on its own (Holcman and Tsodyks 2006), but prevents them when combined with adaptation currents (Benita et al. 2012).

All the models proposed share a common mechanistic substrate: up and down dynamics emerge from an underlying bistability between these states that gets perturbed by additional slow or episodic mechanisms. This general dynamic picture can be illustrated graphically for a network with recurrent excitation and slow rate adaptation mechanisms (Fig. 1; Latham et al. 2000), from which it can be generalized to other mechanisms. The bistability condition implies that two stable states are accessible for a range of values for the adaptation current (bistable range, Fig. 1a). Thus, for a fixed level of adaptation (gray line in Fig. 1a), only random occasional fluctuations in excitability can impose a transition between the stable states (Fig. 1a). Adaptation mechanisms, however, can modify the system so that it no longer has stable fixed points but exhibits an oscillatory behavior. During this oscillation the network shows slow drifts along the up and down branches as adaptation builds up and decays, respectively (Fig. 1b). Depending on the magnitude of adaptation and the level of external drive to the network, transitions may occur deterministically due to the slow dynamics of adaptation (Fig. 1b, down-to-up in Fig. 1c and up-to-down in Fig. 1d), or they may be induced by episodic fluctuations that trigger transitions to escape from a stable state (Fig. 1a, up-to-down in Fig. 1c and down-to-up in Fig. 1d).

The mechanism by which bistability is achieved in the cortical network is generally assumed to be excitatory synaptic reverberation within the local circuit (Timofeev et al. 2000; Compte et al. 2003; Bazhenov et al. 2002; Hill and Tononi 2005; Holcman and Tsodyks 2006; Melamed et al. 2008; Mejias et al. 2010; Mattia and Sanchez-Vives 2012). Indeed, the bistable range of the cubic nullcline in Fig. 1 grows larger with stronger recurrent connections. This is consistent with the strong and dense connectivity in



Slow Oscillations: Models, Fig. 1 Mechanistic scenarios for up and down state switching in a bistable recurrent network with adaptation currents. (a) For fixed values of the adaptation current, the recurrent network stabilizes at firing rates that trace a cubic nullcline with a stable upper branch (up states) and a stable lower branch (down states). Unstable solutions are marked with a dashed line. In a range of values of adaptation (bistable range), the system features bistability between the two states. For very weak or absent adaptation dynamics, the systems sit at a fixed value of adaptation current (gray line) giving rise to two stable states. In this scenario, transitions between states can only occur if external fluctuations arrive that impose

a change of state (wiggled arrows). (b) For strong adaptation, the nullcline defining the values of adaptation current that are steadily maintained at a given neuronal firing rate (gray line) does not intersect the network stability nullcline (black cubic line), and the system cycles periodically between up and down states. (c) Weaker adaptation makes the adaptation nullcline intersect the network nullcline in the upper branch and up states become stable. Only strong fluctuations will induce an up-to-down transition. (d) Starting from the condition in b, a slight hyperpolarization to all neurons in the network makes the down state stable, and down-to-up transitions now depend on strong episodic fluctuations

cortical circuits and explains parsimoniously the sensitivity of up states to excitatory synaptic blockers and the resilience of up-and-down membrane voltage dynamics to the hyperpolarization of individual neurons. Alternative mechanisms for such bistability are nonlinearities in NMDA receptors (Kepes and Raghavachari 2007) or interactions between intrinsic ionic channels in individual neurons (Hughes et al. 2002; Parga and Abbott 2007). Also, intrinsic mechanisms such as persistent sodium currents have been invoked to achieve and maintain reverberatory

activity in the up state (Timofeev et al. 2000; Bazhenov et al. 2002; Hill and Tononi 2005).

Several mechanisms have been proposed to explain that firing rates during up states remain low despite strong excitatory feedback in the network. Here, the most common mechanism invoked is inhibitory feedback from the local microcircuitry. A strong coupling with a local inhibitory population can control firing rates while recurrent excitation maintains up states. Consistent with this, blockers of inhibitory synaptic transmission increase the firing rates in up

states (Sanchez-Vives et al. 2010). It has been argued that short-term synaptic depression can also counteract strong excitation and maintain low firing rates in up states (Holcman and Tsodyks 2006).

Finally, computational models have also addressed the role of the thalamocortical loop in slow oscillations. While thalamocortical neurons can modulate cortically generated slow oscillations (Bazhenov et al. 2002; Hill and Tononi 2005), some computational studies attribute an active role of thalamocortical neurons in maintaining these dynamics. In particular, intrinsic oscillatory mechanisms in thalamocortical neurons may take part in up state initiation in cortical networks (Hughes et al. 2002).

- Latham PE, Richmond BJ, Nelson PG, Nirenberg S (2000) Intrinsic dynamics in neuronal networks. I. Theory. *J Neurophysiol* 83:808–827
- Mattia M, Sanchez-Vives MV (2012) Exploring the spectrum of dynamical regimes and timescales in spontaneous cortical activity. *Cogn Neurodyn* 6:239–250
- Mejias JF, Kappen HJ, Torres JJ (2010) Irregular dynamics in up and down cortical states. *PLoS One* 5:e13651
- Melamed O, Barak O, Silberberg G, Markram H, Tsodyks M (2008) Slow oscillations in neural networks with facilitating synapses. *J Comput Neurosci* 25:308–316
- Parga N, Abbott LF (2007) Network model of spontaneous activity exhibiting synchronous transitions between up and down states. *Front Neurosci* 1(1):57–66
- Sanchez-Vives MV, Mattia M, Compte A, Perez-Zabalza M, Winograd M, Descalzo VF, Reig R (2010) Inhibitory modulation of cortical up states. *J Neurophysiol* 104:1314–1324
- Timofeev I, Grenier F, Bazhenov M, Sejnowski TJ, Steriade M (2000) Origin of slow cortical oscillations in deafferented cortical slabs. *Cereb Cortex* 10:1185–1199

Cross-References

► Slow Oscillations: Physiology

References

- Bazhenov M, Timofeev I, Steriade M, Sejnowski TJ (2002) Model of thalamocortical slow-wave sleep oscillations and transitions to activated states. *J Neurosci* 22:8691–8704
- Benita JM, Guillamon A, Deco G, Sanchez-Vives MV (2012) Synaptic depression and slow oscillatory activity in a biophysical network model of the cerebral cortex. *Front Computat Neurosci* 6:64
- Compte A, Sanchez-Vives MV, McCormick DA, Wang X-J (2003) Cellular and network mechanisms of slow oscillatory activity (<1 Hz) in a cortical network model. *J Neurophysiol* 89:2707–2725
- Destexhe A (2009) Self-sustained asynchronous irregular states and up-down states in thalamic, cortical and thalamocortical networks of nonlinear integrate-and-fire neurons. *J Comput Neurosci* 27:493–506
- Hill S, Tononi G (2005) Modeling sleep and wakefulness in the thalamocortical system. *J Neurophysiol* 93:1671–1698
- Holcman D, Tsodyks M (2006) The emergence of up and down states in cortical networks. *PLoS Comput Biol* 2:e23
- Hughes SW, Cope DW, Blethyn KL, Crunelli V (2002) Cellular mechanisms of the slow (<1 Hz) oscillation in thalamocortical neurons in vitro. *Neuron* 33:947–958
- Kepcs A, Raghavachari S (2007) Gating information by two-state membrane potential fluctuations. *J Neurophysiol* 97(4):3015–3023

Slow Oscillations: Physiology

Maria Victoria Sanchez-Vives
ICREA and Systems Neuroscience, IDIBAPS,
Barcelona, Spain

Synonyms

Slow waves; Up and down states

Definition

Slow oscillations are the coordinated activity of large populations of neurons consisting of an alternation of active periods (Up states) and silent periods (Down states). These oscillations occur with a slow frequency (≤ 1 Hz) in the corticothalamicocortical network during slow-wave sleep and deep anesthesia, and they spontaneously occur also in cortical slices. This rhythmic activity emerges in the cortical network when there are no other driving inputs, and it can be considered its default activity. During the active periods, or Up states, neocortical neurons (both excitatory

and inhibitory) are depolarized, receive barrages of synaptic inputs, and fire action potentials. During Down states neurons remain hyperpolarized and the synaptic activity is almost nonexistent. This “on-and-off” synaptic activity results in a bimodal distribution of the membrane potential values, an intracellular signature of slow oscillations. During the active or Up states, the activity expresses coherent oscillations at high frequencies in the beta (15–30 Hz) and gamma (30–90 Hz) range.

Detailed Description

Background

Slow waves during quiescent sleep have been recorded since the early days of electroencephalogram (EEG) in the 1930s. However, the first detailed characterization of the cortical slow oscillation was published by Steriade and collaborators in 1993 (Steriade et al. 1993a; Steriade et al. 1993b; Steriade et al. 1993c). In these studies, the frequency of the slow oscillation was described to be between 0.2 and 0.5 Hz, and generally below 1 Hz in the cat.

Origin

Slow oscillations are prominent in the corticothalamic loop, and they originate in the cortical recurrent connectivity. The initial observation that slow oscillations persisted in the cortex after destruction of the connected thalamus (Steriade et al. 1993c) while the opposite was not true (Timofeev and Steriade 1996) was strongly suggestive of their cortical origin. The fact that cortical slices *in vitro* spontaneously generate slow oscillations highly similar to the ones in the whole brain is also a strong evidence in favor of their cortical origin (Sanchez-Vives and McCormick 2000; McCormick et al. 2003). *In vivo* cortical slabs (Timofeev et al. 2000), disconnected from the surrounding tissue, can as well generate slow oscillations. However, the cortex is reciprocally connected to subcortical structures, and the emergent pattern recorded *in vivo* is shaped as a result of this interaction. The interaction with the thalamus is especially

relevant, since it also displays slow oscillations coordinated with the cortical ones (Steriade et al. 1993b; Crunelli and Hughes 2010). Detailed analysis has revealed that the inactivation of the thalamus results in a decreased frequency of the cortical slow oscillations (David et al. 2013).

Mechanisms of Initiation of the Up States

Simultaneous recordings from different cortical layers provide a layer profile of activation during Up states. Cortical recordings from different species (cats, ferrets, rodents) both *in vivo* and *in vitro* agree on the leading role of infragranular layers – in particular layer 5 – in the initiation of Up states (Sanchez-Vives and McCormick 2000; Sakata and Harris 2009; Chauvette et al. 2010). Layer 5 neurons not only lead Up states, but also have a more intense and longer discharge during each Up state, while layer 2/3 neurons display a weaker and shorter firing (Sanchez-Vives and McCormick 2000; Sakata and Harris 2009). Furthermore, optogenetic activation of layer 5 – but not of layer 2/3 neurons – is enough to initiate Up states and entrain slow oscillations (Beltramo et al. 2012; Stroh et al. 2013).

Different mechanisms have been proposed for layer 5 neurons to initiate the firing that by reverberation in close loops results in the initiation of new waves. A larger intrinsic excitability of layer 5 neurons drives them to start firing during Down states (Sanchez-Vives and McCormick 2000; Compte et al. 2003; Sakata and Harris 2009), stochastic release of synaptic vesicles (Timofeev et al. 2000) and specific pacemaker cells (Le Bon-Jego and Yuste 2007).

Only in human cortex Up states are reported to start in supragranular layers (Cserecsa et al. 2010), a critical difference in cortical function that requires further study.

Excitatory/Inhibitory Balance During Up States

A key element in the balance and control of either spontaneous emergent or evoked cortical activity is the relation between excitation and inhibition. Both excitatory and inhibitory neurons fire during Up states (Steriade et al. 1993c). Conductance measurements during Up states reveal that the

weights of excitation and inhibition are well balanced *in vivo* (Haider et al. 2006) and similarly *in vitro* (Shu et al. 2003) as argued theoretically (Compte et al. 2003). Changes in excitatory and inhibitory conductance *in vitro* reveal that both increase and decrease at the beginning/end of Up states occur in close association with each other (Shu et al. 2003). The timing of individual excitatory and inhibitory synaptic events also reveals a remarkable coincidence in the accumulation of both excitatory and inhibitory synaptic events during the rise of an Up state both *in vitro* and *in vivo*, although it is 1.4 times faster *in vivo* (Compte et al. 2009). A similar coincidence also occurs at the termination of the Up state. Such interlocking in time of excitation and inhibition is also found in simultaneous recordings of nearby pairs of cortical neurons (Okun and Lampl 2008).

Both the excitatory and the inhibitory synaptic conductances are high at the beginning of the Up state, and they tend to progressively decrease, but their ratio remains constant and close to 1 in anesthetized and *in vitro* preparations (Shu et al. 2003; Haider et al. 2006). Other studies report that the inhibitory conductance is much larger than the excitatory conductance during Up states in natural sleep (Rudolph et al. 2007).

Mechanisms of Termination of the Up States

Several mechanisms have been proposed that could account for the termination of Up states. They include arrival of excitation (Shu et al. 2003; Haider et al. 2006), synaptic depression (Bazhenov et al. 2002), thalamic disinhibition (Contreras et al. 1996), activation of K⁺ currents (Sanchez-Vives and McCormick 2000; Compte et al. 2003), or extracellular K⁺ dynamics (Frohlich et al. 2006). The time course of the slow afterhyperpolarization observed in intracellular recordings during Down states (e.g., Fig. 7c in Sanchez-Vives and McCormick 2000; Contreras et al. 1996) suggests that slow K⁺ currents can be contributing to the termination of Up states and maintenance of Down states. Different mechanisms involving K⁺ currents have been proposed, including ATP-dependent K⁺ current (Cunningham et al. 2006), GABA_B receptor-mediated responses (Mann et al. 2009),

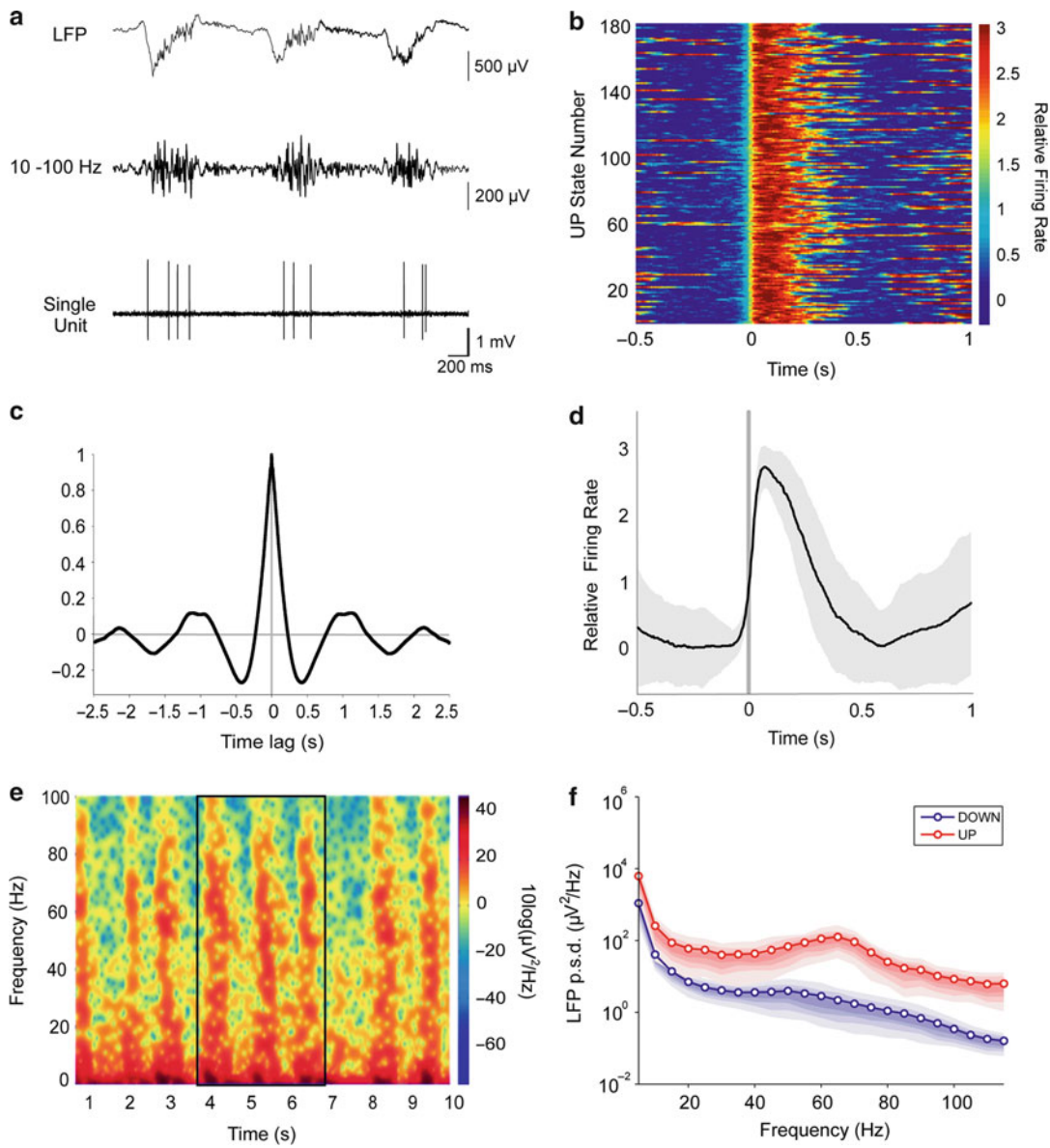
and Ca²⁺- and Na⁺-dependent K⁺ currents (Sanchez-Vives and McCormick 2000). Slow K⁺-mediated afterhyperpolarizations are blocked by neurotransmitters (acetylcholine, noradrenaline) that control the transition from sleep to awake (Schwindt et al. 1988; Brumberg et al. 2000), providing a mechanism for stopping the bistability when entering the awake state.

Propagation

Slow waves propagate along the cortical network. Propagation occurs both *in vivo* during slow-wave sleep or anesthesia and also in the cortex *in vitro*. During wave propagation, infragranular layers lead the front of the wave, although columnar interactions between supragranular and infragranular layers are required for maintaining correct propagation speed (Wester and Contreras 2012). The propagation is continuous, and locally generated Up states can be recorded along the propagation in all cortical layers. The reported values of the propagation speed vary across species and conditions: 1.2–7 m/s in humans during slow-wave sleep (Massimini et al. 2004), 100 mm/s in the anesthetized cat (Steriade et al. 1993c), around 30 mm/s in the anesthetized mouse (Ruiz-Mejias et al. 2011; Stroh et al. 2013), and 10 mm/s in the neocortical slices *in vitro* (Sanchez-Vives and McCormick 2000). In paleocortex *in vitro*, such as the olfactory cortex, propagation is an order of magnitude faster (114 mm/s) (Sanchez-Vives et al. 2008). Cortical inhibition slows down propagation (Trevelyan et al. 2007), and the gradual blockade of GABA_A-mediated inhibition progressively increases the propagation speed (Sanchez-Vives et al. 2011). Once the wave is transformed into an epileptiform discharge due to inhibition removal, propagation speed increases by one order of magnitude (Sanchez-Vives et al. 2011).

Fast Rhythms During Up States

During Up states the *in vivo* network activity is temporally structured in fast oscillations in the beta (15–30 Hz) and gamma (30–90 Hz) range (Steriade et al. 1996; Hasenstaub et al. 2005; Ruiz-Mejias et al. 2011). Inhibitory synaptic



Slow Oscillations: Physiology, Fig. 1 Slow oscillations and fast frequencies during Up states. (a) Slow oscillations in the mouse prefrontal cortex under ketamine anesthesia. *Upper trace:* Unfiltered LFP (local field potential). *Middle trace:* Filtered LFP between 10 and 100 Hz. *Lower trace:* Single-unit recording obtained in the vicinity of the LFP recording (<200 μ m apart). For details see Ruiz-Mejias et al. 2011. (b) Raster plot of the relative firing rate in the local population (color scale) obtained from 200 s recording and corresponding to 180 Up states.

Up states are aligned at the onset. For methodological details see Reig et al. 2010. (c) Waveform autocorrelation of the same 200 s period of LFP shown in B. (d) Waveform average of the raster plot in b. Gray shade correspond to the SD. (e) Spectrogram of the same LFP recording. The central three Up states in the black box correspond to the traces illustrated in a. (f) Power spectral density plots of the LFP during Up and Down states, where a resonant peak appears in the gamma band during Up states

potentials carry the great majority of power in this high-frequency range, often synchronously inhibiting nearby pyramidal cells (Hasenstaub et al. 2005).

The emergent activity of the cortical network *in vitro* can also be synchronized in these high frequencies as a result of pharmacological activation, typically with cholinergic or metabotropic agonists, kainate, or electrical tetanic stimulation of the tissue (Buhl et al. 1998; Cunningham et al. 2003; Hasenstaub et al. 2005; Traub et al. 2005). Although these neuromodulators potently modulate high frequencies, robust beta/gamma oscillations emerge already during physiological network function *in vitro* in the absence of externally applied neuromodulatory agents and without any particular stimulation pattern (Compte et al. 2008). The systematic comparison across different cortical areas of beta and gamma power in the mouse *in vivo* reveals that prefrontal cortex Up-state activity presents significantly stronger fluctuations than in motor, somatosensory, and visual cortex, in particular in the gamma range (one order of magnitude larger power) (Ruiz-Mejias et al. 2011; Fig. 1).

References

- Bazhenov M, Timofeev I, Steriade M, Sejnowski TJ (2002) Model of thalamocortical slow-wave sleep oscillations and transitions to activated states. *J Neurosci* 22:8691–8704
- Beltramo R, D’Urso G, Dal Maschio M, Farisello P, Bovetti S, Clovis Y, Lassi G, Tucci V, De Pietri TD, Fellin T (2012) Layer-specific excitatory circuits differentially control recurrent network dynamics in the neocortex. *Nat Neurosci* 16:227–234
- Brumberg JC, Sanchez-Vives MV, McCormick DA (2000) Waking up the sleeping slice. *Proc Soc Neurosci* 26:1966
- Buhl EH, Tamas G, Fisahn A (1998) Cholinergic activation and tonic excitation induce persistent gamma oscillations in mouse somatosensory cortex *in vitro*. *J Physiol* 513(Pt 1):117–126
- Chauvette S, Volgshev M, Timofeev I (2010) Origin of active states in local neocortical networks during slow sleep oscillation. *Cereb Cortex* 20(11):2660–2674
- Compte A, Sanchez-Vives MV, McCormick DA, Wang XJ (2003) Cellular and network mechanisms of slow oscillatory activity (<1 Hz) and wave propagations in a cortical network model. *J Neurophysiol* 89:2707–2725
- Compte A, Reig R, Descalzo VF, Harvey MA, Puccini GD, Sanchez-Vives MV (2008) Spontaneous high-frequency (10–80 Hz) oscillations during up states in the cerebral cortex *in vitro*. *J Neurosci* 28:13828–13844
- Compte A, Reig R, Sanchez-Vives MV (2009) Timing excitation and inhibition in the cortical network. In: Josic K, Rubin J, Matias M, Romo R (eds) *Coherent behavior in neuronal networks*, vol 3. Springer, New York
- Contreras D, Timofeev I, Steriade M (1996) Mechanisms of long-lasting hyperpolarizations underlying slow sleep oscillations in cat corticothalamic networks. *J Physiol* 494(Pt 1):251–264
- Crunelli V, Hughes SW (2010) The slow (<1 Hz) rhythm of non-REM sleep: a dialogue between three cardinal oscillators. *Nat Neurosci* 13:9–17
- Csercsa R, Dombovari B, Fabo D, Wittner L, Eross L, Entz L, Solyom A, Rasonyi G, Szucs A, Kelemen A, Jakus R, Juhos V, Grand L, Magony A, Halasz P, Freund TF, Magloczky Z, Cash SS, Papp L, Karmos G, Halgren E, Ulbert I (2010) Laminar analysis of slow wave activity in humans. *Brain* 133:2814–2829
- Cunningham MO, Davies CH, Buhl EH, Kopell N, Whittington MA (2003) Gamma oscillations induced by kainate receptor activation in the entorhinal cortex *in vitro*. *J Neurosci* 23:9761–9769
- Cunningham MO, Pervouchine DD, Racca C, Kopell NJ, Davies CH, Jones RS, Traub RD, Whittington MA (2006) Neuronal metabolism governs cortical network response state. *Proc Natl Acad Sci U S A* 103:5597–5601
- David F, Schmidt JT, Taylor HL, Orban G, Di Giovanni G, Uebel VN, Renger JJ, Lambert RC, Leresche N, Crunelli V (2013) Essential thalamic contribution to slow waves of natural sleep. *J Neurosci* 33:19599–19610
- Frohlich F, Bazhenov M, Timofeev I, Steriade M, Sejnowski TJ (2006) Slow state transitions of sustained neural oscillations by activity-dependent modulation of intrinsic excitability. *J Neurosci* 26:6153–6162
- Haider B, Duque A, Hasenstaub AR, McCormick DA (2006) Neocortical network activity *in vivo* is generated through a dynamic balance of excitation and inhibition. *J Neurosci* 26:4535–4545
- Hasenstaub A, Shu Y, Haider B, Kraushaar U, Duque A, McCormick DA (2005) Inhibitory postsynaptic potentials carry synchronized frequency information in active cortical networks. *Neuron* 47:423–435
- Le Bon-Jego M, Yuste R (2007) Persistently active, pacemaker-like neurons in neocortex. *Front Neurosci* 1:123–129
- Mann EO, Kohl MM, Paulsen O (2009) Distinct roles of GABA(A) and GABA(B) receptors in balancing and

- terminating persistent cortical activity. *J Neurosci* 29:7513–7518
- Massimini M, Huber R, Ferrarelli F, Hill S, Tononi G (2004) The sleep slow oscillation as a traveling wave. *J Neurosci* 24:6862–6870
- Mccormick DA, Shu Y, Hasenstaub A, Sanchez-Vives M, Badoual M, Bal T (2003) Persistent cortical activity: mechanisms of generation and effects on neuronal excitability. *Cereb Cortex* 13:1219–1231
- Okun M, Lampl I (2008) Instantaneous correlation of excitation and inhibition during ongoing and sensory-evoked activities. *Nat Neurosci* 11:535–537
- Reig R, Mattia M, Compte A, Belmonte C, Sanchez-Vives MV (2010) Temperature modulation of slow and fast cortical rhythms. *J Neurophysiol* 103:1253–1261
- Rudolph M, Pospisichl M, Timofeev I, Destexhe A (2007) Inhibition determines membrane potential dynamics and controls action potential generation in awake and sleeping cat cortex. *J Neurosci* 27:5280–5290
- Ruiz-Mejias M, Ciria-Suarez L, Mattia M, Sanchez-Vives MV (2011) Slow and fast rhythms generated in the cerebral cortex of the anesthetized mouse. *J Neurophysiol* 106(6):2910–2921
- Sakata S, Harris KD (2009) Laminar structure of spontaneous and sensory-evoked population activity in auditory cortex. *Neuron* 64:404–418
- Sanchez-Vives MV, McCormick DA (2000) Cellular and network mechanisms of rhythmic recurrent activity in neocortex. *Nat Neurosci* 3:1027–1034
- Sanchez-Vives MV, Descalzo VF, Reig R, Figueroa NA, Compte A, Gallego R (2008) Rhythmic spontaneous activity in the piriform cortex. *Cereb Cortex* 18:1179–1192
- Sanchez-Vives MV, Mattia M, Compte A, Perez-Zabalza M, Winograd M, Descalzo VF, Reig R (2011) Inhibitory modulation of cortical up states. *J Neurophysiol* 104:1314–1324
- Schwindt PC, Spain WJ, Foehring RC, Chubb MC, Crill WE (1988) Slow conductances in neurons from cat sensorimotor cortex in vitro and their role in slow excitability changes. *J Neurophysiol* 59:450–467
- Shu Y, Hasenstaub A, McCormick DA (2003) Turning on and off recurrent balanced cortical activity. *Nature* 423:288–293
- Steriade M, Amzica F, Nunez A (1993a) Cholinergic and noradrenergic modulation of the slow (approximately 0.3 Hz) oscillation in neocortical cells. *J Neurophysiol* 70:1385–1400
- Steriade M, Contreras D, Curro Dossi R, Nunez A (1993b) The slow (<1 Hz) oscillation in reticular thalamic and thalamocortical neurons: scenario of sleep rhythm generation in interacting thalamic and neocortical networks. *J Neurosci* 13:3284–3299
- Steriade M, Nunez A, Amzica F (1993c) A novel slow (<1 Hz) oscillation of neocortical neurons in vivo: depolarizing and hyperpolarizing components. *J Neurosci* 13:3252–3265
- Steriade M, Contreras D, Amzica F, Timofeev I (1996) Synchronization of fast (30–40 Hz) spontaneous oscillations in intrathalamic and thalamocortical networks. *J Neurosci* 16:2788–2808
- Stroh A, Adelsberger H, Groh A, Ruhlmann C, Fischer S, Schierloh A, Deisseroth K, Konnerth A (2013) Making waves: initiation and propagation of corticothalamic Ca²⁺ waves in vivo. *Neuron* 77:1136–1150
- Timofeev I, Steriade M (1996) Low-frequency rhythms in the thalamus of intact-cortex and decorticated cats. *J Neurophysiol* 76:4152–4168
- Timofeev I, Grenier F, Bazhenov M, Sejnowski TJ, Steriade M (2000) Origin of slow cortical oscillations in deafferented cortical slabs. *Cereb Cortex* 10:1185–1199
- Traub RD, Bibbig A, LeBeau FE, Cunningham MO, Whittington MA (2005) Persistent gamma oscillations in superficial layers of rat auditory neocortex: experiment and model. *J Physiol* 562:3–8
- Trevelyan AJ, Sussillo D, Yuste R (2007) Feedforward inhibition contributes to the control of epileptiform propagation speed. *J Neurosci* 27:3383–3387
- Wester JC, Contreras D (2012) Columnar interactions determine horizontal propagation of recurrent network activity in neocortex. *J Neurosci* 32:5454–5471

Further Reading

Scholarpedia

- Bazhenov M, Timofeev I (2006) Thalamocortical oscillations. *Scholarpedia* 1(6):1319
- Okun M, Lampl I (2009) Balance of excitation and inhibition. *Scholarpedia* 4(8):7467
- Wilson C (2008) Up and down states. *Scholarpedia* J 3(6):1410

Slow Rhythms

- [Low Frequency Oscillations \(Anesthesia and Sleep\): Overview](#)

Slow Waves

- [Slow Oscillations: Physiology](#)

Slowness of Movement Model

- [Bradykinesia Models](#)

Slow-Wave Oscillation (SWO)

- ▶ [Delta Rhythms: Models and Physiology](#)

Smoluchowski Equation

- ▶ [Fokker-Planck Equation](#)

Sodium Channels

Dominique Engel

GIGA-Neurosciences, University of Liège,
Liège, Belgium

Synonyms

[Na⁺ channels](#); [Voltage-gated Na⁺ channels](#)

Definition

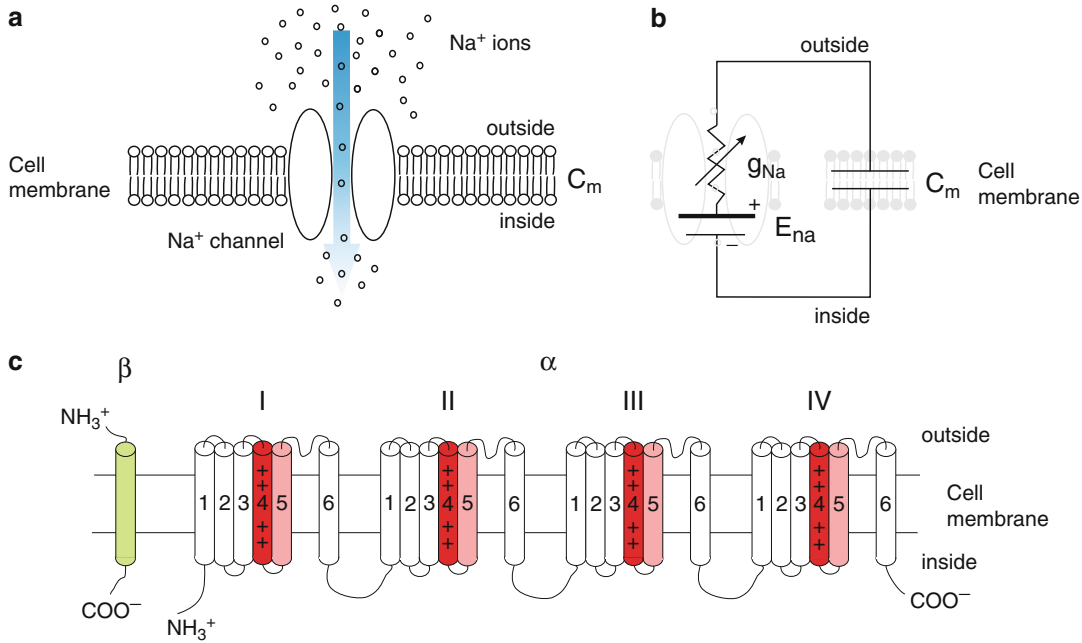
Sodium channels are proteins enmeshed in the cell membrane of both excitable and nonexcitable cells. They are in general composed of two different types of proteins, termed subunits, an alpha (α) and two beta (β) subunits. The arrangement of the α subunit across the cell's membrane enables the formation of an aqueous tunnel termed channel linking the cell's interior and the extracellular space. Changes in the transmembrane voltage govern channel gating. When the channel is open, almost exclusively sodium (Na⁺) ions flow through the channel (Fig. 1a). The Na⁺ ion flow through the channel can be blocked by tetrodotoxin (TTX), a specific and widely used puffer fish toxin.

Functional properties of sodium channels can be translated into an electrical conductance model consisting of a battery in series with a resistor and an arrow indicating a time- and voltage-dependent conductance (Johnston and Wu 1995; Hille 2001; Fig. 1b).

Detailed Description

Structure and Function of Sodium Channels

Sodium channels are proteins enmeshed in the cell membrane of different excitable cell types including neurons of the central and peripheral nervous system and muscle cells including skeletal, smooth, and cardiac muscle cells but also in various nonexcitable cells (Black and Waxman 2013). They are composed of a principal alpha subunit responsible for the formation of the pore and beta auxiliary subunits implicated in the regulation of channel function (Johnston and Wu 1995; Hammond 2001; Catterall 2012; Fig. 1c). The alpha subunit exists in distinct isoforms (Table 1) and consists of a long chain of about 2000 amino acids arranged in four repetitions of a specific sequence of amino acids termed homologous domain (I, II, III, and IV). Within each domain, the sequence forms six transmembrane segments (S1–S6). The four homologous domains are presumably arranged across the membrane to form a central pore bordered by S6 segments. S4 segments are important for the gating as they are composed by positively charged amino acids and thereby are believed to represent the voltage sensor of the channel (Johnston and Wu 1995; Hammond 2001; Hille 2001; Catterall 2012). In neurons, sodium channels are present generally in each subcellular compartment (soma, axon, and dendrites). But a nonhomogeneous distribution of the channels may exist in the different neuronal compartments (Magee 2008; Vacher et al. 2008). The function of Na⁺ channels in excitable cells is to permit an entry of positive charges into the cell in order to depolarize the membrane and to generate action potentials (APs). Na⁺ channel permeability is essential for the initiation and the propagation of APs in excitable cells, and their open probability increases largely during the upstroke of APs. Na⁺ channels mentioned above and in the two following paragraphs have fast activation and inactivation and are therefore termed transient Na⁺ channels. Two additional Na⁺ currents may be expressed by excitable cells, termed "resurgent" and "persistent," passing current during membrane potential repolarization after brief



Sodium Channels, Fig. 1 Structure and function of sodium channels. (a) Schematic representation of a sodium channel embedded in the plasmic membrane of a cell. When the membrane potential is close to rest, Na⁺ ions are flowing inside the cell due to the driving force of Na⁺ ($V_m - E_{Na}$). (b) Conductance model for sodium channels. E_{Na} is the equilibrium potential for Na⁺ represented

by the battery and g_{Na} is the variable conductance of Na⁺ channels which depends on time and potential represented by the arrow. C_m is the capacitance of the membrane. (c) Transmembrane organization of the α and β subunits of the sodium channel. Modified from Catterall W (2001) with permission

Sodium Channels, Table 1 Mammalian sodium channel properties

Conventional name	Original name	Corresponding gene	TTX sensitivity	Predominant location
Na _v 1.1	Type I, rat I, Scn1a	SCN1A	Yes	CNS, PNS
Na _v 1.2	Type II, rat II,	SCN2A	Yes	CNS
Na _v 1.3	Type III, rat III	SCN3A	Yes	Embryonic CNS
Na _v 1.4	SkM, μ1	SCN4A	Yes	skeletal muscle
Na _v 1.5	SkM2, rH1, H1	SCN5A	No	Heart muscle
Na _v 1.6	Type IV, NaCh6, Na6, Scn8a	SCN8A	Yes	CNS, PNS, axons
Na _v 1.7	PN1, hNE, Nas	SCN9A	Yes	PNS, Schwann cells
Na _v 1.8	SNS, PN3, NaNG	SCN10A	No	PNS, sensory neurons
Na _v 1.9	SNS2, NaN, SCN12A	SCN11A	No	PNS
Na _x	Nav2.1, Nav2.2	SCN6A	No	Heart, uterus, glia
	Nav2.3, SCL11, NaG	SCN7A	No	PNS smooth muscle

CNS: central nervous system, PNS: peripheral nervous system, TTX: tetrodotoxin (specific blocker of sodium channels). A more detailed description of the diversity of Na⁺ channels is reviewed in (Goldin, 2002). A detailed analysis of the localization of Na⁺ channels is reviewed in (Vacher et al. 2008).

depolarizations (Cruz et al. 2011) and passing noninactivating current, respectively (Kiss 2008). Dysfunctions of sodium channels (sodium “channelopathies”) cause a variety of diseases among which are epileptic syndromes and muscle diseases (Waxman 2001; Savio-Galimberti et al. 2012).

Patch-Clamp Recordings of Single-Channel and Macroscopic Sodium Currents

The development of the patch-clamp technique gave the opportunity to measure directly the unitary Na^+ current flowing through a single sodium channel (Sakmann and Neher 1995). Unitary Na^+ currents have a typical rectangular time course representing transitions between open and closed states of the channel. Unitary currents are therefore all-or-none events, and their peak amplitude is voltage-dependent according to Ohm’s law:

$$i_{\text{Na}} = \gamma_{\text{Na}}(V_m - E_{\text{Na}})$$

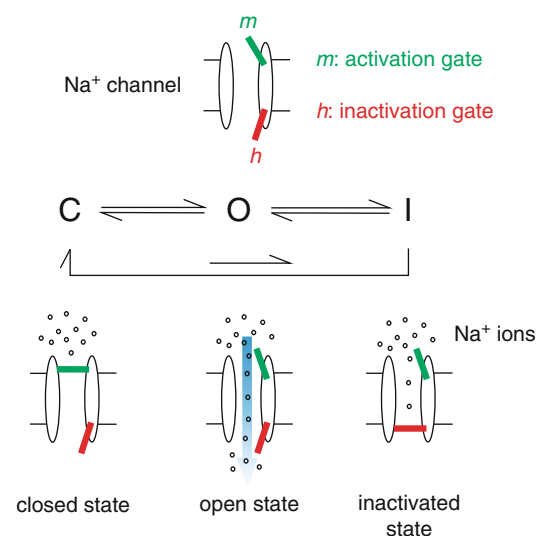
where i_{Na} is the unitary Na^+ current, γ_{Na} is the single-channel conductance, V_m is the membrane potential, and E_{Na} is the reversal potential of Na^+ ions.

The summation of a large number of unitary Na^+ currents results in a macroscopic Na^+ current which corresponds nearly to the “whole-cell” current recorded in a cell. Unitary and macroscopic Na^+ currents are proportional and related by the following equation:

$$I_{\text{Na}} = N p_{(t)} i_{\text{Na}}$$

where I_{Na} is the macroscopic current, N is the number of Na^+ channels, and $p_{(t)}$ is the open probability at a time t . Mechanistically, the behavior of Na^+ channels is characterized by transitions between three distinct states, an open state (O), a closed state (C), and an inactivated state (I). Transitions are illustrated by the scheme in Fig. 2.

Typically, the sodium channel switches from C to O on depolarization and rapidly back from O to C with repolarization when the depolarization time is very short. On sustained depolarization, the sodium channel closes more slowly and switches from O to I . The latter transition is termed



Sodium Channels, Fig. 2 Conformational states in the Hodgkin Huxley formalism. Sequence of transitions of sodium channels through C, O and I states illustrated with the movement of the gating particles (m and h)

inactivation and corresponds to a refractory state of the channel characterized by a non-passing ion state (Ulbricht 2005; Catterall et al. 2012). The probability of the Na^+ channels being open increases with depolarization and the duration of the open state varies around a mean value termed mean open time. To be able to reopen after inactivation, sodium channels need to transit through the C state for a certain period of time, and this is achieved with membrane hyperpolarization (Hammond 2001). With fundamental work published in 1952, Hodgkin and Huxley interpreted the transitions between the conformational states of sodium channels with the movement of activation (m) and inactivation (h) gates regulating the permeability of the channel (Fig. 2; Johnston and Wu 1995; Koch 1999). In the Hodgkin–Huxley (HH) formalism, permeability changes are described by ionic conductance which is voltage- and time-dependent:

$$g_{\text{Na}} = \bar{g}_{\text{Na}} m^3 h$$

from which the right side of the equation can be implemented in the equation describing the macroscopic Na^+ current:

$$I_{Na} = \bar{g}_{Na} m^3 h (V_m - E_{Na})$$

where \bar{g}_{Na} (g_{Na} “bar”) is the maximal value of the conductance and m , h represent the fraction of two distinct type of gating particles in the inside of the membrane.

Modeling Sodium Channel Conductance to Estimate Membrane Potential Changes

A detailed functional analysis of sodium channel properties is fundamental to understand the generation of APs in excitable cells. With their pioneer study, Hodgkin and Huxley proposed a quantitative model describing the permeability of sodium channels in terms of ionic conductance changes using experimental data. With this model, they could also predict the time course of APs. Without any knowledge about the structure of an ion channel, they predicted that sodium channels are gated by gating variables which are dependent on time and voltage and postulated that the transitions between open and closed states obey first-order kinetics (Johnston and Wu 1995; Destexhe and Huguenard 2001; Hille 2001; Koch 1999). While the HH formalism has still a large influence to describe channel functional properties and to predict AP time course, it is a macroscopic approximation (Catterall et al. 2012) and may have some limitations. For instance, the HH formalism is unable to describe the abrupt onset of APs of cortical neurons (Naundorf et al. 2006).

Alternatively, the gating of sodium channels in stochastic Markov models is described by transitions through a series of distinct conformational states. These models assume that the transitions between conformational states are memoryless and depend only on the current state (Destexhe and Huguenard 2001; Kispersky and White 2008). Markov models are thereby more precise to describe conformational changes of single channels (Destexhe and Huguenard 2001).

Cross-References

► [Hodgkin-Huxley Model](#)

References

- Black J, Waxman S (2013) Noncanonical roles of voltage-gated sodium channels. *Neuron* 80:280–291
- Catterall W (2001) A 3D view of sodium channels. *Nature* 409:988–991
- Catterall W (2012) Voltage-gated sodium channels at 60: structure, function and pathophysiology. *J Physiol* 590:2577–2589
- Catterall W, Raman I, Robinson H, Sejnowski T, Paulsen O (2012) The Hodgkin-Huxley heritage: from channels to circuit. *J Neurosci* 32:14064–14073
- Cruz JS, Silva DF, Ribeiro LA, Araujo IGA, Magalhaes N, Medeiros A, Freitas C, Araujo I, Oliviera FA (2011) Resurgent Na^+ current: a new avenue to neuronal excitability control. *Life Sci* 89:564–569
- Destexhe A, Huguenard J (2001) Which formalism to use for modeling voltage-dependent conductances. In: De Schutter E (ed) Computational neuroscience. Realistic modeling for experimentalists. CRC Press, Boca Raton, pp 129–157
- Goldin A (2002) Evolution of voltage-gated Na^+ channels. *J Exp Biol* 205:575–584
- Hammond C (2001) Cellular and molecular neurobiology, 2nd edn. Academic, San Diego
- Hille B (2001) Ion channels of excitable membranes, 3rd edn. Sinauer Associates, Sunderland
- Johnston D, Wu MS (1995) Foundation of cellular neurophysiology. The MIT Press, Cambridge, MA
- Kispersky T, White J (2008) Stochastic models of ion channel gating. *Scholarpedia* 3(1):1327
- Kiss T (2008) Persistent Na -channels: origin and function. A review. *Acta Biol Hungarica* 59(Suppl):1–12
- Koch C (1999) Biophysics of computation. Oxford University Press, New York
- Magee J (2008) Dendritic voltage-gated ion channels. In: Stuart G, Spruston N, Häusser M (eds) Dendrites, 2nd edn. Oxford University Press, New York, pp 225–250
- Naundorf B, Wolf F, Volgshev M (2006) Unique features of action potential initiation in cortical neurons. *Nature* 440:1060–1063
- Sakmann B, Neher E (1995) Single-channel recording. Plenum, New York
- Savio-Galimberti E, Gollob M, Darbar D (2012) Voltage-gated sodium channels: biophysics, pharmacology, and related channelopathies. *Front Pharmacol* 3:1–19
- Ulbricht W (2005) Sodium channel inactivation: molecular determinants and modulation. *Phys Rev* 85:1271–1301
- Vacher H, Mohapatra D, Trimmer J (2008) Localization and targeting of voltage-dependent ion channels in mammalian central neurons. *Physiol Rev* 88:1407–1447
- Waxman S (2001) Transcriptional channelopathies: an emerging class of disorders. *Nature Rev Neurosci* 2:652–659

Further Reading

- Carnevale N, Hines M (2005) The neuron book. Cambridge University Press, New York
- Jack J, Noble D, Tsien R (1983) Electric current flow in excitable cells. Oxford University Press, Oxford
- Scholarpedia. www.scholarpedia.org. (conductance-based models, gating currents, ion channels, electrical properties of cell membranes)

Software for Neuroimaging Data Analysis

Jean Baptiste Poline¹ and David Kennedy²

¹Henry H. Wheeler, Jr. Brain Imaging Center, Helen Wills Neuroscience Institute, University of California, Berkeley, CA, USA

²Department of Psychiatry, Division of Neuroinformatics, University of Massachusetts Medical Center, Worcester, MA, USA

Definition

Software is defined by as “a plan specification composed of a series of instructions that can be interpreted by or directly executed by a processing unit.” We define Software for Neuroimaging Data Analysis as software whose primary goal is to support the extraction of information, and ultimately knowledge, from data acquired by an imaging device used on the brain (of human or animal subjects).

Detailed Description

Introduction

Tell us what you think about neuroimaging software, and we will tell you who you are. To some, using software to analyze data is little more than a technical step that stands between data acquisition and publishing. Doctoral students, postdocs, or technical assistants only need to operate the appropriate software, i.e., the script to run or the right sequence of buttons to press. To others, choosing, adapting, running, or developing the right software code is critical and requires investing significant time and resources.

Data analysis is one of the most time-consuming parts of neuroimaging research. While it can take, in general, months to acquire a small to medium dataset, it often takes years before the data are fully analyzed. It is not rare that specific software or methods have to be developed for a specific question or dataset. Data are typically reanalyzed several times in different ways, using different inputs or software options, influencing the interpretation or the type I error rate (Simmons et al. 2011). With the perspective of efficiency, if most of the time is spent on data analysis, sharpening these tools should be a priority. In addition, errors are ubiquitous in data analysis, and software bugs or misuses are a major contributor to this (Donoho 2010). To take a classic example, a source of error was (and probably still is) the handling of the left versus right hemisphere identification in neuroimaging data, which very likely led to many erroneous publications. Finally, software tools are strongly influencing – and limiting – the type of questions that are put to the data. These factors should place a thorough understanding of one’s analysis software in a predominant place in the research process.

While no neuroimaging research would be done without software, few articles are dedicated to the description of their development and capability. Partly, this is due to the nature of the software description that does not lend itself very well to a static written description; this is better seen through example of use and documentation. Partly, this reflects the somewhat distorted nature of the publication process in neuroimaging (as well as in other scientific fields) that puts too much emphasis on the interpretation (the “story”) and less on the facts (and, inherent to the scientific process, how these were obtained). Donoho famously paraphrased Claerbout (https://en.wikipedia.org/wiki/Jon_Claerbout) stating that “*an article about computational science in a scientific publication is not the scholarship itself, it’s merely scholarship advertisement. The actual scholarship is the complete software development environment and the complete set of instructions which generated the figures*” (Donoho et al. 2009). There is little doubt that

neuroimaging is a computational science and that Donoho and Claerbout's point applies to our field.

In this encyclopedia entry, we lay out the neuroimaging software analysis landscape in section “[Detailed Description](#),” then consider the problems we face currently in section “3,” and suggest directions for solutions in section “4.” We last review some of the future challenges in this field. There will be no attempt to make an even non-exhaustive list of the software currently in use in neuroimaging although we cite some software to illustrate our text. Our purpose is to reflect and inform on some sociological aspects of the brain imaging field related to data analysis software which are likely less ephemeral than current software. We will use examples that are related to the research community from MRI (magnetic resonance imaging) and more rarely EEG-MEG (electro- and magnetoencephalography), but most of the ideas can be extrapolated to other brain imaging modalities (positron-emission tomography, near-infrared spectroscopy, etc.).

Emergence Mechanisms and Taxonomy

We start by reviewing a few mechanisms by which neuroimaging software emerge. We take a few examples to illustrate these mechanisms and then propose a few major criteria for software classification.

Emergence Mechanisms

A Data Analysis Method Developed in a Lab This mechanism is simple and often observed. A good method to analyze data has been developed in a lab and has produced interesting results and led to (possibly high-profile) publications. Other researchers in the same lab, or in other labs, would like to use the same technique, but it is not easily recoded because of its mathematical or algorithmic complexity. There is a pressure to share the software with colleagues attracted by the technique, as well as reward since ensuing collaborations will lead to authorship for the developer. More rarely, the author believes that scientific work requires that colleagues can check and reproduce one's work. The software

may get used locally for a while and then distributed under more or less lenient terms of use and license.

This mechanism is close to what happens for SPM, for instance, started by Karl Friston (Ashburner 2012). SPM is an interesting example because of its predominance in positron-emission tomography and functional magnetic resonance imaging data analysis for a long time. The early distribution of the code, the fact that the software was solving for both spatial normalization and the multiple comparison statistical aspects, and the use of a high-level language (Matlab) were key aspects of its success. To some degree, this is also the story of software such as Brainstorm, MLE, fieldtrip, or others in the EEG-MEG field (see the special issue of Baillet et al. 2011).

The Methodological Lab Development Receptacle

More a communal than a single researcher enterprise, laboratories which are mainly dedicated to developing methods are almost systematically developing the software tools to consolidate their research. This often takes the form of a software library, maintained so that research work can build on the previous methods without having to restart coding from scratch with every new student. But many groups have also developed full-fledged applications to demonstrate their research to a wider, more application-oriented community. For instance, the Oxford group, led by S. Smith, was predominantly developing methods to analyze MRI and fMRI data and developed FLS (Jenkinson et al. 2012) to propose an alternative to SPM. It took a few years for the software to establish itself as a valid alternative, but key methodological components and a coding language that did not require buying a license (Matlab can be a significant budget for a lab) and led to faster execution were important aspects of the initial success. Later, FSL developed methods in diffusion imaging, while SPM developed the “Dynamical Causal Models” techniques, differentiating the two software suites for some applications. Many other examples can be found, such as the Montreal Neurological Institute (MNI) Brain Imaging Center ([MNI Software Tools n.d.](#)).

The Commercial Enterprise The transformation of a research software to a commercial product is not an easy enterprise, given the competition of freely available tools. BrainVoyager (Goebel 1996) is a remarkable example of success in this category. The incentive here is clearly to generate revenues, as well as having the means to easily incorporate a new method in one's preferred and controlled environment. BrainVoyager has in particular good visualization components as well as an interface adapted to end users which made for some of its success. More commercial software are used for EEG because of its strong link to the medical community (e.g., Besa <http://www.besa.de>).

Software Evolution Most software platforms that have been around for numerous years undergo an evolution in the set of functions that they perform. SPM started in support of PET imaging and evolved to handle functional and anatomical MRI, EEG, and MEG and more over the years. FreeSurfer (Fischl 2012) initially handles cortical surface extraction and quantification and evolved to include intersubject registration and subcortical segmentation, as well as adapt to numerous cortical parcellations schemes. These developments clearly follow the laboratories scientific directions, but students who are responsible for developing part of the code eventually leave the laboratories and this often lead to code base difficult to refactor and maintain.

One key for the success of all these tools is they are developed by or closely associated with a neuroscience/brain imaging laboratory that publicize the software through publications, talks, or teaching.

What's the Difference? Taxonomy of Software

While criteria for classifications are numerous and often nonindependent, we briefly review four possible criteria.

Application Domain and Scope This is probably the clearest and easiest of these criteria. Eight large categories dominate: (i) anatomical structures, (ii) diffusion imaging, (iii) functional (time-domain) data (PET or fMRI), (iv) electric

and magnetic encephalography, (v) visualization tools, (vii) infrastructure software such as pipelining and databasing systems, and (viii) other more specialized software such as imaging genetics, PET modeling, etc. Many of the most used neuroimaging packages include several components, for instance, some visualization aspects and some scripting or pipelining capabilities. Other categories continue to emerge, such as the software for the connectome (e.g., Gray 2011) or "brain reading" (e.g., MVP <http://www.pymvpa.org>).

Intended Users Part of the neuroimaging community has trained in psychology, neuroscience, or medicine; others may be trained in computer science, physics, or statistics. Some of software are clearly targeting the former part of the community (e.g., Toussaint et al. 2007), with easy installation and graphical interfaces, while others are at the stage of libraries and require programming skills to be used (e.g., the nipy suites: www.nipy.org).

Code Openness and Licensing These aspects are also critical for adoption in particular by method-oriented researchers. Many of the research software are open source with GPL-/BSD-/MIT-/CECILL-like licenses (e.g., SPM, many of the MEG tools such as Brainstorm or MNE, Baillet et al. 2012). While the code may be open, only a few however have open-source developing modes, where contributors propose changes through the mechanism of "pull requests" and decisions on whether to include or not a change are discussed on mailing lists. Some have licenses that distinguish the commercial and academic uses such as FSL.

Licensing of software remains a problematic in terms of the proliferation of different licensing terms. While the development of the Creative Commons suite of selectable options is a great advance, much software has been released prior to the development of that licensing strategy, and a majority of the software has been developed by investigators working at various academic institutions with specific intellectual property that have been felt to require university-specific

terms. As an example, the Neuroimaging Informatics Tools and Resources Clearinghouse (NITRC) hosts over 640 neuroimaging resources, and these require the listing of over 120 separate licenses.

Development Language This may not seem a major criterion at first sight for many. However, the readability of the code, its maintainability, and the flexibility with which the code source can be extended and refactored are major aspects for both maintenance and extension of a software platform. A strong attractive aspect of SPM is that it is written in Matlab, a high-level language that is particularly well suited for matrix algebra, which is at the heart of many of the data analysis methods. This makes it possible for a neuroscientist to adapt the code to develop his or her own ideas. Other high-level languages of the kind are Octave (Matlab clone), Python, and R.

The Problems with Software

There are a number of issues that are associated with the current state of brain imaging regarding software for data analysis. We list below these issues from the most practical to the most general/sociological aspects.

Proliferation: Finding the Right Software

The proliferation of myriad software solutions poses a number of practical issues that researchers or practitioners have to face. As an image processing need becomes more mature, more software has been developed to attempt to deal with it, and the user tends to be faced with more options about how to solve this task in their ongoing studies. Let us take individual image registration to a template image to illustrate this. In 1990, you either wrote the software yourself or accessed AIR (Woods et al. 1992); today, there are over 10 (AIR, FSL (FLIRT, FNIRT), DRAMS (Ou et al. 2011), SPM-LDDMM, ANTS (Avants et al. 2010), CIVET (Ad-Dab'bagh et al. 2006), nipy (nipy.org)) different major software solutions to such a task, spanning linear and nonlinear techniques, varying registration cost functions and different degrees of freedom in

the fit, etc. (Klein et al. 2009). Where there are multiple “major” software options, you can be sure that there are many more options that have been developed that you just might not know about. This is not limited to the registration problem. For instance, fMRI had more than two decades to investigate various ways of extracting neuroscience or clinical results from data. To name a few, with fMRI, one can work on the cortical surface or on the volume data and apply dozens of preprocessing steps; MEG data can be analyzed using coherency or with evoked potential and led to many tools (Baillet et al. 2012), in diffusion imaging one can extract individual fibers or work with probabilistic models, etc. The complexity is exponentially increasing when data are combined. To add to the issue, software are constantly evolving, augmented with new functionality and debugged.

While the neuroimaging community may already be facing too many choices, the computer science and engineering literature are rife with algorithms and techniques that just are not commonly investigated by most neuroscience researchers. The main reason is that making these algorithms available to a wide audience requires software development skills that are not always available in methodological research teams. The “cost” to develop, distribute, and maintain a large or complex code and user base software is typically high, although underestimated in the research community.

Given multiple options to choose from, how does the investigator find all the options and choose the best option? Equally importantly, what are the practical differences between the different options?

There are many metrics and proxy metrics for “best” software solution for a given task. Ideally, one would like to know that the software is validated and that it produces the “correct” answer in testing on when the solution is known. This can include simulation data. However simulation data when computationally known “ground truth” is designed into the data very often cannot mimic complete set of nuances of real data. Similarly, the performance of software under different input conditions (signal to noise ratio,

contrast to noise ratio, etc.) is an important characteristic. Traditionally, patient and extreme populations are susceptible to more artifacts (motion) than healthy controls, so how well software performs in the presence of some degree of acquisition imperfections is also critical. It is not uncommon to find that the “best” software in perfect conditions may not be the “best” under more practical, real-world scenarios. Software that is designed and deployed with unit testing and that has been validated and profiled relative to all the available software options is to be preferred.

Popularity is a common criterion for selection of the “best” software option for a researcher. The argument is simple: reviewers will not – or rarely – question a method that has been used in published literature. Similarly, many research laboratories have developed a “culture” of using specific platforms; that’s what the current personnel are used to using, so that’s what they pass on to new investigators. Legacy of analyses performed in a specific way can span decades. Popularity can be quantitatively assessed by metrics like download count and number of publications. However, *popularity, correctness, and usefulness are notions that are far from being fully aligned*.

A last important factor is the documentation and available help with the software. All major software have forums and diffusion lists that often are critical for solving a particular question.

Software Testing

Testing whether the outcome of software is producing the right result is no simple task. This is particularly true for software that offer a high-level graphical interface to the user. One specific issue is that there is yet a lack of quality checking tools embedded in the software most commonly used, such that if, for some reason, part of the analysis fails (entry error, implementation bug or not covering the use case, etc.), it is hard to find if anything went wrong at all, especially if the results “look” all right. One reason for this, in fMRI, is that although the field has more than twenty years of experience, almost any pattern of activity can be explained in a cognitive task.

At the implementation levels, although the outcome of example dataset or simulations is generally checked to provide reasonable results, the software rarely implement unit and integration testing procedure. This makes the code base fragile to any change. There are famous example of bugs in neuroimaging, and one of the most confusing and leading to a large number of erroneous publications was the left versus right issue (neurological vs. radiological display) as some early image formats did not allow code properly for this information. This was corrected in the NIfTI format (as long as the DICOM to NIfTI conversion is correct – which is not a small assumption). Other examples exist where software has implemented an incorrect statistical correction technique, for instance. Until a more careful and principled approach is taken by the developers of neuroimaging software, we are unclear on the error rate. Note that many of the mistakes may not be due to a specific faulty routine or method, but done during collecting and formatting all the auxiliary information (response time, paradigm sequence, etc.) necessary to launch an analysis. The example of the Duke University scandal (and other such examples) should be kept vivid in the mind of the research community, not as an exception but as a situation that can easily occur (Baggerly and Coombes 2009).

Analyses Reproducibility

A critical aspect to neuroimaging analysis lies in their reproducibility. This is a software issue in the sense that some software platforms will make it almost impossible to reproduce an analysis, for instance, when there is no other option than clicking on graphical interfaces, and detailed graphical logging options are not available. Many software platforms, however, do provide some solutions to this with the ability to script the analysis. This is of utmost importance. The mechanism is simple: if it takes a few days to set up and run an analysis, and if the results “look all right,” there will be a very strong resistance to start over again in case of doubt. This will also prevent experimenters from checking that results are similar with trivial change of parameters.

For instance, if changing a filter value by a small amount changes very significantly the results, these results are not robust, and unless there is a clear way to choose this filter value, the scientific community should not trust the findings. Interestingly, this ability also provides scientists with a way of trying out many filter values and selecting the best results, which poses some other issues addressed later in this entry.

Provenance

Even when scriptable, very few software platforms track and report their complete provenance of operation and attach it to the derived data; and those that do, do not necessarily do it in a standard fashion. First, this is important when software goes through major revisions and the nature of the results and methods can evolve substantially. When it comes to comparing the resultant data with other results, even from the same software system, version information (and computer operating system) can influence the results (Gronenschild et al. 2012). Second, when there is doubt on how the data have been generated within a lab, since there is no way to check their provenance, the only solution is to regenerate the results. This happens relatively frequently when a new student or postdoctoral fellow has to work on previously analyzed data. A third point is that if provenance data existed and were included in the supplementary material or better available digitally, reviewers could check the validity of the computations described in articles.

Data Management and Sharing Capacity

Just as shared raw imaging data is becoming increasingly important, so is the sharing of derived results. Most software do not integrate data management and sharing capacity. This prevents researchers to easily collaborate and build on the work of each other with more direct and effective ways than with the publications. The data organization impacts in part of the effectiveness (and therefore lower cost) of the research performed and in part the rate of error and provenance tracking capacity.

One of the factors that make raw data sharing work is the existence of standards for data

description. Image data formats, such as DICOM and NIFTI, are understood by scanner manufacturers and analysis software platforms alike. When it comes to the derived data however, there is yet neither the culture nor the infrastructure (standards or repositories) to promote widespread sharing of derived data. Standards for the representations of common derived results need to be adopted by a broad set of software developers and derived databases in order to fully promote the sharing of derived data.

Software Installation and Interoperability

A final factor that integrates a number of the aforementioned issues relates to promotion and “marketing” of a software system. There is little incentive and mechanisms so far in the community to establish and use a standard application program interface (API) to help software interact easily. *This is because software are rarely developed across laboratories.* Developers have therefore little interest at easing the interactions with other software and often tend to promote their tools even when it is demonstrated that other solutions may lead to better results. As a number of software packages become more mature, and the development and support infrastructure behind them becomes more complex and expensive, the need to develop continued funding to support the infrastructure is magnified. A laboratory may choose to continue developing some software to have some internal cohesion, or because large resources have been invested (“too big to fail”) despite evidence that more adequate solutions exist or more useful scientific results may be obtained with other software. This points to the immaturity of the scientific community which can act in a competing and individualistic mode when efficiency would require collaboration.

A second aspect is that it can be expected that significant improvements in processing methods have been developed by smaller, more transient software efforts, but it can be very hard to compete with the established providers to distribute the method. This is because groups controlling which methods are to be integrated in most popular software are also the ones developing

methods. There will be a strong resistance to implement a “competing” method in an in-house software. Methodological improvements that are embraced by the field may become adopted and incorporated into the major developers’ packages eventually, but these improved methods have to reach a level of adoption that is not easy to obtain given the established tools.

This may be less the case when software are the products of large consortiums (for instance, from the BIRN, INCF, etc.), often also working on standardization of formats or meta-information. Pipelining systems such as nipype are to some extend breaking these barriers, but they require good knowledge of the pipelining system as well as of the individual software.

Solutions

Some solutions to the issues listed in the previous section are emerging in the neuroimaging community. We list the ones that seem most promising.

Neuroimaging Informatics Tools and Resources Clearinghouse

The host of “problems” introduced above is not new or specific to the neuroimaging software community, and “solutions” to many of them are in place. One important tool in the handling of a rich and diverse set software options is an independent “clearinghouse” of information about all of the software relevant to a particular field. As a clearinghouse, such a resource supports the needs of the software developers to make consumers aware of their software’s availability and supports the needs of users to be able to find all the potential software solutions to a particular problem. For the neuroimaging community, such a resource exists in the Neuroimaging Informatics Tools and Resources Clearinghouse (NITRC – nitrc.org). Funded by the National Institutes of Health Blueprint for Neuroscience Research in 2006, the Neuroimaging Informatics Tools and Resources Clearinghouse (NITRC) is the go-to website for neuroinformatics software, tools, data, and other resources for an ever-broadening set of imaging domains (Kennedy et al. 2009). Starting with

structural and functional MRI, NITRC catalogs virtually every resource in the domain to promote discovery and dissemination. The scope of resources covered by NITRC has expanded to include EEG/MEG/eCoG, PET/SPECT, CT, optical imaging tools, and, most recently, imaging genomics and clinical informatics. NITRC provides three types of services: NITRC Resources Repository (NITRC-R), the collaboration environment hub that enables the distribution, enhancement, and adoption of neuroimaging tools and resources (Luo and Kennedy 2009); NITRC Image Repository (NITRC-IR), a curated repository (developed from the XNAT open-source framework, Marcus et al. 2007) of NIFTI-1 and DICOM images searchable by metadata such as handedness, gender, and group; and NITRC Computational Environment (NITRC-CE) and NITRC-CE for Cluster Compute Instances, virtual big-data compute services (using the Amazon EC2 ([Amazon. Amazon Elastic Compute Cloud \(EC2\)](#) n.d.) Cloud and NeuroDebian, Hanke and Halchenko 2011; Halchenko and Hanke 2012) pre-configured with popular neuroimaging software analysis tools using pay-as-you-go compute time on AWS ([Amazon. Amazon Web Service \(AWS\)](#) n.d.) Marketplace.

In addition, as an independent clearinghouse, all providers, commercial and academic, large and small, and mature and in development, can have exposure to the community. NITRC provides a forum where community dialog about best practices, optimal solutions, standards development, etc., can occur in a fashion that transcends the forums and resources of the myriad individual resource providers. As a data host with community engagement, test datasets can be hosted and standard validation and comparison protocols can be run, and dissemination of the comparative results supported.

The International Neuroinformatics Coordinating Facility

The International Neuroinformatics Coordinating Facility (INCF) develops collaborative neuroinformatics infrastructure and promotes the sharing of data and computing resources to

the international research community. The INCF achieves its mission, in part, through the conduct of “Scientific Programs,” which are long-term strategic undertakings to address issues of high importance to the neuroscience community. Each program provides tools for integrating research findings from different labs and multiple experimental techniques. One of these, the **Standards for Data Sharing** program, aims to develop generic standards and tools to facilitate the recording, sharing, and reporting of neuroscience metadata, in order to improve practices for the archiving and sharing of neuroscience data. Metadata define the methods and conditions of data acquisition and subsequent analytical processing. Within data sharing broadly is the NeuroImaging DAta SHaring (NI-DASH) task force. NI-DASH focuses on neuroimaging as a testbed for the development of specific tools and standards for data sharing within neuroimaging (Poline et al. 2012).

Along with the development of standards, INCF supports a number of data repositories designed to promote the adoption of the standards as they are developed. INCF XNAT is a neuroimaging archive that is supported by easy-to-use data sharing tools integrated with the delivery of quantitative feedback quality assurance measures to incentivize image data sharing. INCF Dataspace enables the collaboration between researchers through the sharing of a broad set of neuroscience data, including text, images, sounds, movies, models, and simulations.

Open Science and Open-Source Software Development

Open-source collaborative projects have proved that they can lead to very successful software and be major components in research or industry. Mozilla Firefox, LibreOffice, the Linux operating system, major databasing, and communication systems such as MySQL, PostgreSQL, Apache, etc., are only but a few examples of this. The software are developed by large distributed communities, with core team often scattered around the globe. They have along the years developed the tools and the know-how (the cultural rules) to

interact remotely and make the software evolve. They sometimes attract hundreds of developers whose interest may lie in the product itself, or sometimes just in being part of a community that produces useful software (see Raymond 1999 for a description of the open-source development history process).

Can neuroimaging software adopt this model? Contradicting the Betteridge’s law (http://en.wikipedia.org/wiki/Betteridge%27s_law_of_headlines), we believe that the answer is yes. An interesting example of this is the nipy libraries suite. Nipy started in Montreal with J. Taylor and then in France and in California (www.nipy.org) at the university of Berkeley and at Neurospin and was originally a library for functional MRI statistical analysis. Early on, the main developer (M. Brett) decided to apply the open-source development principles and constructed an adapted environment, using the most efficient collaborative tools (i.e., the git control version system, the github social coding platform, the python language, a suite of unit test with good coverage of the code base, a nightly building of the software, etc.). Although nipy itself has not made it the large brain imaging community, these working principles have fostered the emergence of multiple useful software projects (nibabel, nipype, dipy, nitime, etc.), and other solid projects are following the same principles (scikit-learn/nilearn, MNE, etc.).

Similarly, at the level of applications, a number of open science and software projects are modeled under the principles of open collaboration, meaning that any developer can propose code changes and the major direction of the software are discussed between developers. Neurosynth, Brainspell, and Neurovault are just a few of promising examples.

The New Challenges

The Reproducibility Problem

Neuroimaging is at a critical point in its sociological development. There are a few critical factors for this. First, many studies include a small number of subjects, and therefore the chance that the alternative hypothesis is true is low even when the statistical test leads to reject the null hypothesis (Button et al. 2012; Ioannidis 2005). In other words, most of the claims are likely to be false

because of power issues. Second, there is a strong sociological pressure to publish in the academic environment. It is clear that publication is the main assessment tool for grant attribution and renewal, as well as for granting tenure position. There are, therefore, very few imaging datasets that are acquired and not published, because the flexibility and multiplication of the analyses will almost certainly provide a significant test. The poor state of our knowledge will almost invariably provide a possible explanation for the results. Simmons et al. (2001) assessed a risk of type I error of about 60 % if flexible analyses are allowed in psychology. The flexibility of neuroimaging analyses is even larger, alimented by the publication pressure. Third, mistakes are ubiquitous, even within the most serious and careful individuals and laboratories (e.g., “anatomy of a coding error”; <http://www.russpoldrack.org/2013/02/anatomy-of-coding-error.html>). In this later case, the author provided a great service to the community in presenting the issue.

By combining these three factors, we conclude that there is a very high chance that many neuroimaging results (or neuroimaging genetics) are likely to be false. Clearly some results are reproduced, and meta-analyses are able to extract common results that are likely to be correct and will be found again. But extracting the solid results with large enough sample size – e.g., having the “big enough” data – or replicating across enough studies close enough in their goal remains a critical challenge of this field, and we suspect of others (see, for instance, an example in cancer research by Begley and Ellis 2012). From the above, we clearly see that neuroimaging has not been well served by our current publication paradigm. If one is interested in a result published in a journal, it is most often impossible to replicate the results, assess its validity, and link it to results of the same kind. The result – and the knowledge that we can extract from it – is in effect a sentence in a pdf file. Tools to mine text are being developed – but tools to link the scientific claim to the data and computation that have led to the claims are mostly to be developed.

The field needs to generate a framework for deploying reproducible and re-executable

neuroimage processing workflows to support the full connection between data, processing, results, and published claims so that the inference can persist and be dynamically assessed as the available data evolves over time. In addition to simply being able to re-execute a specifically published analysis (which by itself is significant and important), this will enable vastly new ways of querying data and performing analyses. One can take a publication perspective and from a result in one publication discover other publications that used similar data, found a similar finding, or used a similar analysis method. One can then explore all the parameters of an experiment. The primary authors of a paper may not be able to probe or explore all experimental factors, nor should they; but that does not mean that the stability of results relative to parameter settings, other data sources, is not important to explore. We cannot continue to assume that the one published set of observations from a particular set of data is the only interpretation. This “dynamic” nature needs to be exposed, so that all experimental parameters can be part of the ongoing dialog about what a set of observations mean and how they extend as the data available changes.

Computational Challenges

Virtualization Software deployment and utilization, for both the developer and user, is hampered by the proliferation of operating systems and hardware platforms. This places extra demands on developers to support the many platforms their users may be using and on users to deal with many software installation dependencies that may or may not be compatible with their existing hardware platform. This proliferation of platforms leads to increased variance in the results and provenance of ongoing neuroimaging studies and limiting data integration and aggregation. One major effort designed to alleviate some of these issues is NeuroDebian. The NeuroDebian project (<http://neuro.debian.net>; Halchenko and Hanke 2012) integrates many neuroimaging (and generic computing and neuroscience) software developments in a turnkey platform. Besides preparing, testing, and uploading software for inclusion into official

Debian GNU/Linux distribution immediately making those available to millions of users worldwide, NeuroDebian project provides a repository with backport builds of maintained software for all supported Debian and Ubuntu releases making them available on top of existing deployments of their stable and LTS releases. NeuroDebian virtual appliance provides users of other platforms (e.g., Windows or OS X) a seamless solution for deploying complex analysis environments for research, teaching, and collaboration. Integration of software within a uniform software and data deployment platform allows for a seamless installation and maintenance of computing environments staying at the frontier of methodological developments while also allowing for easy instrumentation of existing installations on bare metal, or automated Debian-based deployments locally (VirtualBox <https://virtualbox.org/> and Vagrant <http://www.vagrantup.com/> or Docker <http://www.docker.io/>), or cloud appliances.

Distributed Computation There is still a long way to go in the initiative to enable a comprehensive data sharing infrastructure for the neuroimaging community. Nevertheless, numerous successes in large-scale image data sharing have occurred (i.e., Alzheimer’s Disease Neuroimaging Initiative (Mueller et al. 2005), National Database for Autism Research (Hall et al. 2012), Autism Brain Data Exchange (Di Martino et al. 2013), 1,000 Functional Connections (Biswal et al. 2010), INDI http://fcon_1000.projects.nitrc.org/indi/IndiPro.html; Mennes et al. 2013; The ADHD-200 Consortium 2012, etc.). This means that researchers now have access to thousands of publically available neuroimaging cases. This blessing of data is matched with a curse of computation. As the available data grows and the complexities of processing and pooling data in specific domains increase, the demands on the availability of high-performance or large-scale computational resources skyrocket. The era of imaging analysis requiring processing workflows that operate on thousands of cases is upon us. While many universities are fortunate enough to host local high-performance

computational resources, not all investigators have access to such computational resources, and even those that do may or may not have these configured to handle the necessary neuroimaging processing software tools. In addition to local high-performance computing, the emergence of consumer-accessible cloud computing has brought the availability of scalable, on-demand computing to the community. Relatively simple configure of local and cloud-based neuroimaging systems is now easily deployed using such resources as NeuroDebian, VirtualBox, NITRC Computational Environment, and StarCluster. Thus, the acquisition of massive amounts of compute nodes is no longer rate limiting.

More limiting, at the moment, is the logistics and expense of moving the vast data resources to the processors. Now that net input data volumes to the workflows can be on the order of Terabytes, moving (or copying) this data to a local computer system will be intolerably slow (as well as relatively insecure). As data sources begin to reside on cloud-based storage facilities, and mirrored to multiple national and international sites, the financial and temporal pressures to move the computational processing to the cloud “nearby” will increase dramatically. This will usher in a completely new era in the design and financing of modern large-scale neuroimaging computational analysis.

Training and Collaboration

As the world of neuroimaging data analysis and software development complexifies, the need for training the new generations of researchers to the new collaborative tools is becoming clear. None will be able to be an expert in all the domains required by brain imaging (image acquisition physics, applied mathematics and statistics for data analysis, software development, and the application field of neuroscience, cognitive neuroscience, neurology, or psychiatry). The only practical solution is to train on how to collaborate efficiently between individuals with complementary expertise. This means learning the common language of collaboration through Internet, such as version control systems and collaborative

development tools. As neuroimaging has become a computational field, we need to respond to the new challenge of training researchers on how to collaborate on computational projects, as well as clarify how acknowledgments and credits are to be handled in groups of individuals originating from multiple institutions and countries. The new “brain imaging” curriculum should have a significant component on this as this critically impacts both the quality and the efficiency of the research performed.

Conclusion

The neuroimaging research community could gain both in efficiency and in correctness by focusing more on its basic tools. In the same way that a common image format facilitates greatly the adoption and use of software tools, common application program interfaces, provenance exchange formats standards, test datasets, and community platforms, linking data to publications and programming training would lead neuroimaging to another level of efficiency. This may have to be the tasks of an emerging research field: the brain imaging neuroinformatics – or brain informatics.

References

- Ad-Dab'bagh Y, Lyttelton O, Muehlboeck JS, Lepage C, Einarson D, Mok K, Ivanov O, Vincent RD, Lerch J, Fombonne E (2006) The CIVET image-processing environment: a fully automated comprehensive pipeline for anatomical neuroimaging research. In: Proceedings of the 12th annual meeting of the organization for human brain mapping, M. Corbetta, p S45
- Amazon. Amazon Elastic Compute Cloud (EC2) (n.d.) <http://aws.amazon.com/ec2>
- Amazon. Amazon Web Service (AWS) (n.d.) <http://aws.amazon.com/>.
- Ashburner J (2012) SPM: a history. *Neuroimage* 62(2):791–800. doi:10.1016/j.neuroimage.2011.10.025
- Avants BB, Yushkevich P, Pluta J, Minkoff D, Korczykowski M, Detre J, Gee JC (2010) The optimal template effect in hippocampus studies of diseased populations. *Neuroimage* 49(3):2457–2466. doi:10.1016/j.neuroimage.2009.09.062
- Baggerly KA, Coombes KR (2009) Deriving chemosensitivity from cell lines: forensic bioinformatics and reproducible research in high-throughput biology. *Ann Appl Stat* 3(4):1309–1334. doi:10.1214/09-AOAS291
- Baillet S, Karl F, Robert O (2011) Academic software applications for electromagnetic brain mapping using MEG and EEG. *Comput Intell Neurosci*. doi:10.1155/2011/972050
- Begley CG, Ellis LM (2012) Drug development: raise standards for preclinical cancer research. *Nature* 483(7391):531–533
- Biswal BB, Mennes M, Zuo XN, Gohel S, Kelly C, Smith SM, Beckmann CF et al (2010) Toward discovery science of human brain function. *Proc Natl Acad Sci* 107(10):4734–4739. doi:10.1073/pnas.0911855107
- Di Martino A, Yan C-G, Li Q, Denio E, Castellanos FX, Alaerts K, Anderson JS et al (2013) The autism brain imaging data exchange: towards a large-scale evaluation of the intrinsic brain architecture in autism. *Mol Psychiatry*. doi:10.1038/mp.2013.78
- Donoho DL (2010) An invitation to reproducible computational research. *Biostatistics* 11(3):385–388. doi:10.1093/biostatistics/kxq028
- Donoho DL, Maleki A, Rahman IU, Shahram M, Stodden V (2009) Reproducible research in computational harmonic analysis. *Comput Sci Eng* 11(1):8–18
- Ed Gronenschild HBM, Habets P, Jacobs HIL, Mengelers R, Rozendaal N, van Os J, Marcelis M (2012) The effects of FreeSurfer version, workstation type, and Macintosh operating system version on anatomical volume and cortical thickness measurements. *PLoS One* 7(6):e38234. doi:10.1371/journal.pone.0038234
- Fischl B (2012) FreeSurfer. *Neuroimage* 62(2):774–781. doi:10.1016/j.neuroimage.2012.01.021
- Goebel R (1996) BRAINVOYAGER: a program for analyzing and visualizing functional and structural magnetic resonance data sets. *Neuroimage* 3(3):S604. doi:10.1016/S1053-8119(96)80606-9
- Halchenko YO, Hanke M (2012) Open is not enough. Let's take the next step: an integrated, community-driven computing platform for neuroscience. *Front Neuroinf* 6:22. doi:10.3389/fninf.2012.00022
- Hall D, Huerta MF, McAuliffe MJ, Farber GK (2012) Sharing heterogeneous data: the national database for autism research. *Neuroinformatics* 10(4):331–339
- Hanke M, Halchenko YO (2011) Neuroscience runs on GNU/Linux. *Front Neuroinf* 5:8. doi:10.3389/fninf.2011.00008
- Ioannidis JP (2005) Why most published research findings are false. *PLoS Med* 2(8):e124. doi:10.1371/journal.pmed.0020124
- Jenkinson M, Beckmann CF, Behrens TEF, Woolrich MW, Smith SM (2012) FSL. *Neuroimage* 62(2):782–790. doi:10.1016/j.neuroimage.2011.09.015
- Kennedy DN, Haselgrave C, Buccigrossi R, Grethe J (2009) Software development for neuroimaging: promoting community access and best practices through NITRC. In: Biomedical imaging: from nano to macro, 2009. ISBI'09. IEEE international symposium on,

- IEEE, pp 1146–1149. http://ieeexplore.ieee.org/xpls/abs_all.jsp?arnumber=5193260
- Klein A, Andersson J, Ardekani BA, Ashburner J, Avants B, Chiang MC, Christensen GE et al (2009) Evaluation of 14 nonlinear deformation algorithms applied to human brain MRI registration. *Neuroimage* 46(3):786–802. doi:10.1016/j.neuroimage.2008.12.037
- Luo XZJ, Kennedy DN (2009) Neuroimaging informatics tools and resources clearinghouse (NITRC) resource announcement. *Neuroinformatics* 7:55–56. doi:10.1385/NI
- Marcus DS, Olsen TR, Ramaratnam M, Buckner RL (2007) The extensible neuroimaging archive toolkit. *Neuroinformatics* 5(1):11–33
- Mennes M, Biswal BB, Xavier Castellanos F, Milham MP (2013) Making data sharing work: the FCP/INDI experience. *Neuroimage* 82:683–691. doi:10.1016/j.neuroimage.2012.10.064
- MNI Software Tools (n.d.) <http://www.bic.mni.mcgill.ca/ServicesSoftware/HomePage>
- Mueller SG, Weiner MW, Thal LJ, Petersen RC, Jack CR, Jagust W, Trojanowski JQ, Toga AW, Beckett L (2005) Ways toward an early diagnosis in Alzheimer's disease: the Alzheimer's disease neuroimaging initiative (ADNI). *Alzheimer Dementia* 1(1):55–66
- Ou Y, Sotiras A, Paragios N, Davatzikos C (2011) DRAMMS: deformable registration via attribute matching and mutual-saliency weighting. *Med Image Anal* 15(4):622–639. doi:10.1016/j.media.2010.07.002
- Poline J-B, Breeze JL, Ghosh S, Gorgolewski K, Halchenko YO, Hanke M, Haselgrove C et al (2012) Data sharing in neuroimaging research. *Front Neuroinf* 6:1–13. doi:10.3389/fninf.2012.00009
- Raymond E (1999) The cathedral and the bazaar. *Knowl Technol Policy* 12(3):23–49. doi:10.1007/s12130-999-1026-0
- Simmons JP, Nelson LD, Simonsohn U (2011) False-positive psychology: undisclosed flexibility in data collection and analysis allows presenting anything as significant. *Psychol Sci* 22(11):1359–1366. doi:10.1177/0956797611417632
- The ADHD-200 Consortium (2012) The ADHD-200 consortium: a model to advance the translational potential of neuroimaging in clinical neuroscience. *Front Syst Neurosci* 6:62. doi:10.3389/fnsys.2012.00062
- Toussaint N, Souplet JC, Fillard P (2007) MedINRIA: medical image navigation and research tool by INRIA. In: Proceedings of MICCAI, vol 7. <http://med.inria.fr/>
- Woods RP, Cherry SR, Mazziotta JC (1992) Rapid automated algorithm for aligning and reslicing PET images. *J Comput Assist Tomogr* 16(4):620–633
- connectome automated pipeline: an overview. *IEEE Pulse* 3(2):42–48. doi:10.1109/MPUL.2011.2181023
- Johnson H, Harris G, Williams K (2007) BRAINSFit: mutual information rigid registrations of whole-brain 3D images, using the insight toolkit. <http://www.insight-journal.org/download/pdf/8169/BRAINSFit.pdf>

Somatosensory Cortex: Neural Coding of Motion

Yu-Cheng Pei

Chang Gung Memorial Hospital and University,
Taoyuan County, Taiwan

Synonyms

Aperture problem; Tactile motion; Tactile motion integration

Definition

The tactile perception of motion involves the perception of movement of an object across the skin. Neural processing in the somatosensory cortex transforms the information originating from populations of afferents into a percept of the direction and speed of the tactile motion.

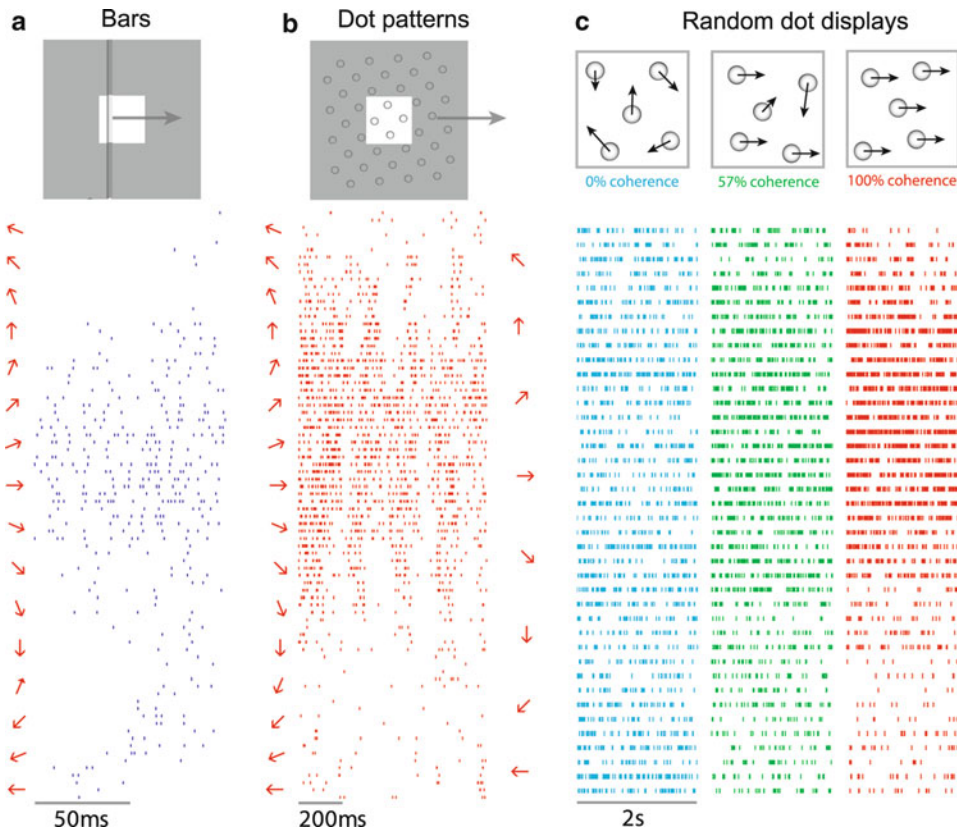
Detailed Description

Two Sources of Tactile Motion Information

The perception of tactile motion is thought to rely on two types of signals at the somatosensory periphery: the sequential activation of slowly adapting type 1 (SA1) (Johansson and Vallbo 1979) and rapidly adapting (RA) afferents (Kirman 1974; Sherrick and Rogers 1966) as an object moves across the skin and the activation of slowly adapting type 2 (SA2) afferents (Olausson et al. 2000) caused by friction-induced skin stretch resulting from motion (Olausson and Norrsell 1993).

Further Reading

Gray WR, Bogovic JA, Vogelstein JT, Landman BA, Prince JL, Vogelstein RJ (2012) Magnetic resonance



Somatosensory Cortex: Neural Coding of Motion,

Fig. 1 Responses of a neuron in area 1 to bars (a), dot patterns (b), and random dot displays (c) presented to the monkey's fingertip. The stimuli are illustrated as insets at the top: for bars and dot patterns, the white square shows the 1×1 cm area at which the stimuli were presented; the gray region illustrates the stimulus extending outside of the stimulation area. To the left of each raster is the

direction of motion of the stimulus. This neuron produced the most robust response to stimuli moving from left to right (with a slight slant outward), regardless of whether the stimuli were bars, dot patterns, or random dot displays. For random dot displays, the tuning response increased with increases in the motion coherence. Error bars denote mean \pm s.e.m (Reproduced from Pei et al. (2010) with permission from PLoS Biology (Pei et al. 2010))

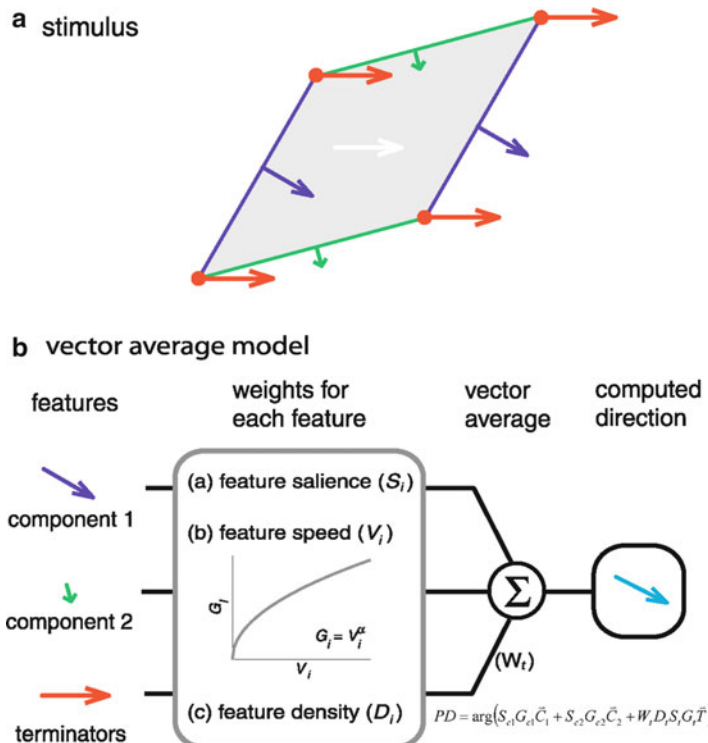
Direction Tuning Emerged in the Primary Somatosensory Cortex

SA1 and RA afferents encode stimulus motion in a pixel-wise manner, and each single afferent exhibits little to no direction tuning (Whitsel et al. 1972; Pei et al. 2010); that is, the responses of these afferents are not modulated by the direction in which an object moves across their receptive field. Direction tuning emerges in primary somatosensory cortex (S1), namely, in areas 3b, 1, and 2 (Werner and Whitsel 1970; Whitsel et al. 1972; Costanzo and Gardner 1980; Warren et al. 1986; Ruiz et al. 1995). The direction tuning of S1 neurons has been hypothesized to be shaped

by asymmetrical lateral inhibition in a feedforward neural circuit (Gardner and Costanzo 1980). Specifically, a cortical neuron receives inputs from subcortical neurons with adjacent receptive fields, and each input suppresses the input from an adjacent spatial location. If inhibition along one direction is stronger than along the opposite direction, the neuron would exhibit direction tuning.

Neurons in Primary Somatosensory Cortex Exhibit Shape-Invariant Direction Tuning

The preferred direction (*PD*) of neurons in S1 is invariant across stimulus types (including



Somatosensory Cortex: Neural Coding of Motion, Fig. 2 A terminator-mediated vector average model for tactile motion integration. (a) Breakdown of the stimulus features for input components into the VA model. Green and blue contours and arrows correspond to the component edges and their respective directions of motion; red vertices and arrows correspond to the terminators and their direction of motion. (b) Computation for the stimulus

direction based on the direction of its components. Each feature is weighted according to its density (length of the edges, density of the terminators), its amplitude, and its speed. Weighted unit direction vectors are then summed to compute the perceived direction (Reproduced from Pei et al. (2011) with permission from Neuron (Pei et al. 2011))

bars, dot patterns, and random dot displays), amplitudes, and motion speed (Fig. 1) (Pei et al. 2010). That is, they respond most strongly to motion across the skin in a given direction, regardless of the geometric properties of the object scanned across the skin. While neurons in area 3b exhibit some direction tuning, neurons in area 1, which is downstream to area 3b, produce responses that are more strongly dependent on motion direction. The responses of area 1 are highly predictive of the perceived direction of motion, suggesting that this population of neurons plays a causal role in tactile motion perception.

Motion Integration Is Mediated by a Terminator-Mediated Vector Average Model

Plaids, which are constructed by superimposing two moving gratings (Pei et al. 2008), can be used to understand how motion information is integrated across the sensory sheet. Based on the responses to these more complex stimuli, a model for tactile motion integration was developed that predicts both neuronal responses to and the perception of tactile motion across a variety of conditions (Pei et al. 2011). According to the model, the representation of motion is determined by the motion vectors of the component gratings, as well by the intersections of the

gratings (which constitute terminators, whose motion direction is unambiguous). Components and terminators are then weighted according to their speeds and amplitudes account for the *PDs* and combined using a vector average (Fig. 2).

Processing of Motion Speed in the Primary Somatosensory Cortex

Human subjects can scale the perceived speed of tactile motion stimuli (Essick et al. 1988; Bensmaia et al. 2006). The structure of scanned objects is essential for tactile speed perception as evidenced by the fact that speed information is unavailable for smooth surfaces (Depeault et al. 2008). Furthermore, the spatial characteristics of the surfaces – i.e., their texture – influence speed perception. A population of neurons in areas 1 and 2 exhibit a graded increase in discharge with increasing speed, and their responses are affected by spatial period, suggesting a role in tactile speed scaling (Depeault et al. 2013).

Cross-References

- ▶ [Somatosensory Cortex: Neural Coding of Shape](#)
- ▶ [Somatosensory Cortex: Organization](#)

References

- Bensmaia SJ, Killebrew JH, Craig JC (2006) The influence of visual motion on tactile motion perception. *J Neurophysiol* 96(3):1625–1637
- Costanzo RM, Gardner EP (1980) A quantitative analysis of responses of direction-sensitive neurons in somatosensory cortex of awake monkeys. *J Neurophysiol* 43:1319–1341
- Depeault A, Meftah E-M, Chapman CE (2008) Tactile speed scaling: contributions of time and space. *J Neurophysiol* 99(3):1422–1434
- Depeault A, Meftah EM, Chapman CE (2013) Neuronal correlates of tactile speed in primary somatosensory cortex. *J Neurophysiol* 110(7):1554–1566
- Essick GK, Franzén O, Whitsel BL (1988) Discrimination and scaling of velocity of stimulus motion across the skin. *Somatosens Motor Res* 6:21–40
- Gardner EP, Costanzo RM (1980) Neuronal mechanisms underlying direction sensitivity of somatosensory cortical neurons in awake monkeys. *J Neurophysiol* 43:1342–1354
- Johansson RS, Vallbo B (1979) Tactile sensibility in the human hand: relative and absolute densities of four types of mechanoreceptive units in glabrous skin. *J Physiol* 286:283–300
- Kirman JH (1974) Tactile apparent movement: the effects of interstimulus onset interval and stimulus duration. *Percept Psychophys* 15:1–6
- Olausson H, Norrsell U (1993) Observations on human tactile directional sensibility. *J Physiol* 464:545–559
- Olausson H, Wessberg J, Kakuda N (2000) Tactile directional sensibility: peripheral neural mechanisms in man. *Brain Res* 866:178–187
- Pei YC, Hsiao SS, Bensmaia SJ (2008) The tactile integration of local motion cues is analogous to its visual counterpart. *Proc Natl Acad Sci USA* 105:8130–8135
- Pei YC, Hsiao SS, Craig JC, Bensmaia SJ (2010) Shape invariant coding of motion direction in somatosensory cortex. *PLoS Biol* 8:e1000305
- Pei YC, Hsiao SS, Craig JC, Bensmaia SJ (2011) Neural mechanisms of tactile motion integration in somatosensory cortex. *Neuron* 69:536–547
- Ruiz S, Crespo P, Romo R (1995) Representation of moving tactile stimuli in the somatic sensory cortex of awake monkeys. *J Neurophysiol* 73:525–537
- Sherrick CE, Rogers R (1966) Apparent haptic movement. *Percept Psychophys* 1:175–180
- Warren S, Härmäläinen HA, Gardner EP (1986) Objective classification of motion- and direction-sensitive neurons in primary somatosensory cortex of awake monkeys. *J Neurophysiol* 56:598–622
- Werner G, Whitsel BL (1970) Stimulus feature detection by neurons in somatosensory areas I and II of primates. *IEEE Trans Man Mach Syst* 11:36–38
- Whitsel BL, Roppolo JR, Werner G (1972) Cortical information processing of stimulus motion on primate skin. *J Neurophysiol* 35:691–717

Somatosensory Cortex: Neural Coding of Shape

Jeffrey M. Yau

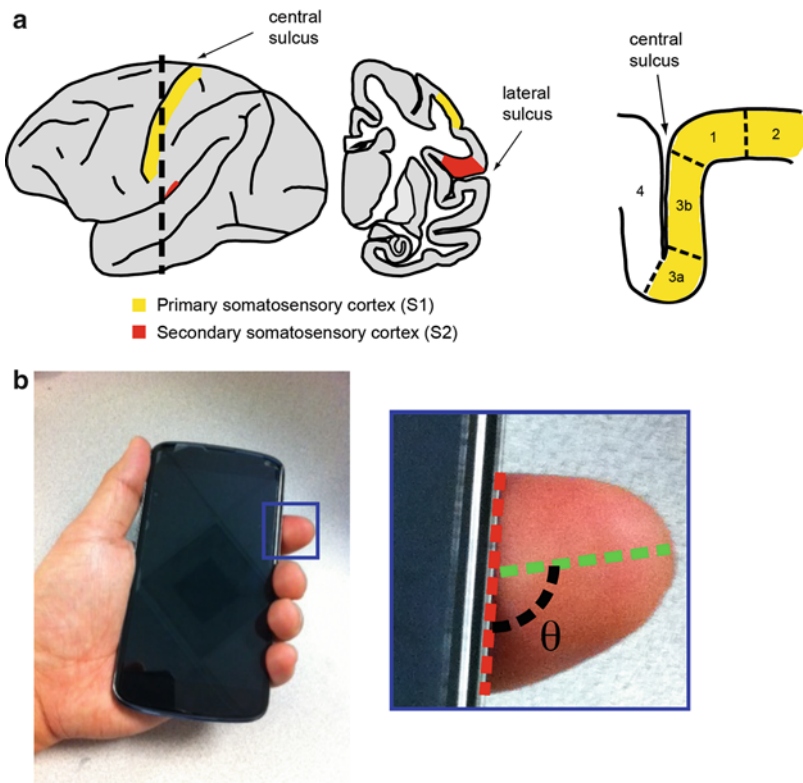
Johns Hopkins University, Baltimore, MD, USA

Definition

We appreciate object shape information by touch alone. Spatial feature representations, initially carried by populations of slowly adapting type I afferents (SA1s) in the peripheral nervous system, are centrally encoded by neural populations residing in the somatosensory cortex. Cortical neurons function as spatial filters that select out specific object features falling within their

Somatosensory Cortex: Neural Coding of Shape,

Fig. 1 Somatosensory system and shape perception. (a) The somatosensory cortical system in primates comprises primary (S1) and secondary (S2) somatosensory cortices. S1 consists of a densely interconnected set of regions: Brodmann areas 1, 2, and 3. (b) Tactile shape perception requires the integration of cutaneous and proprioceptive information. The phone's straight edge (red dashed line) is processed within each finger pad and is represented as an oriented edge feature in the activity of cortical neurons



receptive fields (RFs) on the skin. This neural selectivity, or tuning, changes across a hierarchy of processing stages spanning primary (S1) and secondary somatosensory (S2) cortices (Fig. 1a). While somatosensory neurons at the first cortical processing stage (area 3b in S1) have small receptive fields and respond to simple contour features like oriented bars and edges, neurons at intermediate and later processing stages (area 2 and S2) respond to stimulation of larger skin regions and are selective for more complex spatial features. In individual neurons and across neural populations, spatial tuning evolves in time, reflecting extensive and rapid network processing. Decoding of object shape information requires integrating activity over neural populations tuned for cutaneous and proprioceptive information.

Detailed Description

We rely on our sense of touch to perceive and manipulate objects. Consider the act of holding

a smartphone in one hand (Fig. 1b) – although much of the phone's body is cradled in the palm of your hand, notice how your fingers are deftly positioned around the phone's frame, allowing you to grip it easily and securely. If you gently adjust and tighten your grip, you may notice how the phone's frame presses into each individual finger, and you can focus your attention on how the frame passes over your skin along a single edge (Fig. 1b, red dashed line). Shape perception is based in part on this cutaneous information, and importantly, regardless of where your fingers and thumb fall on the phone as you adjust your grip, you maintain a stable perception of the object in your hand. This stable object representation is encoded in the distributed neural activity over shape-sensitive neurons in the somatosensory cortex.

To understand how shape information is represented in the brain, we must consider how this information is initially encoded at the hand. Specialized mechanoreceptors in the skin respond to different cutaneous aspects of object

contact (Johnson 2001). Note that separate afferent populations also carry proprioceptive information about hand conformation, which is necessary for stereognosis (i.e., haptic perception of objects) – this information is integrated with cutaneous shape information in the cortex (see below). Individual afferents display no spatial tuning and only respond when a stimulus impinges the afferent's small RF. In this manner, a shape's spatial profile is carried in the total activity over a population of afferents. Of the cutaneous afferents, SA1 fibers carry the most refined spatial information, and the SA1 population activity conveys a low-pass filtered neural image of a tactile stimulus that is isomorphic with respect to the contacted shape. Ultimately, information about object shape must be extracted from a pattern of activation across a two-dimensional sheet of receptors embedded in the skin. The challenge to characterizing somatosensory shape coding, then, is in understanding how cortical neurons process this two-dimensional spatial information conveyed by peripheral afferents.

Spatial Filtering

A large body of neurophysiological evidence implicates area 3b of S1 cortex as the primary cortical recipient of sensory input projecting from the afferent systems, sent via the dorsal column nuclei and the thalamus (Bensmaia and Yau 2011). Area 3b neurons function as linear spatial filters that cover small regions on a single finger pad: A neuron's RF is a linear approximation of the effects of stimulus elements inside the RF on the neuron's response. Stimulus contact in any single RF region can result in an increase or decrease in spiking activity, and a neuron's overall response to each stimulus pattern is given by the sum of the effects of the stimulus elements over all RF regions. This can be formalized as

$$r(t) = b_0 + b_1 \cdot 5emx_1(t) + b_2 \cdot 5emx_2(t) + \dots b_i x_i(t) \quad (1)$$

where $r(t)$ is the spiking activity predicted in response to the stimulus pattern at time t , b_0 is the baseline firing rate, b_i is the effect strength

(positive or negative) of a stimulus element in the i th region of the skin, and $x_i(t)$ is the stimulus value in the i th region of the skin (e.g., as in a bitmap, where a value of 1 indicates the presence of a stimulus element and 0 indicates no contact) at time t . The model can be rewritten in matrix form in order to solve for the set of weights defining the linear RF:

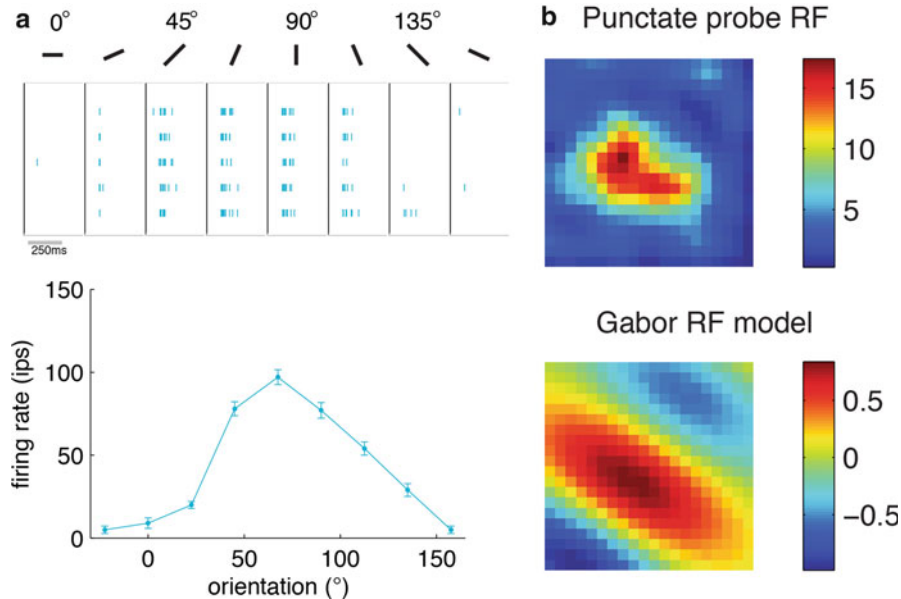
$$r = Xb \quad (2)$$

where r is a vector containing firing rates over all response times, X is the stimulus matrix, and b is a vector of weights (plus a constant term) describing the RF. The matrix equation can be solved for b :

$$b = (X^T X)^{(-1)} X^T r \quad (3)$$

where $X^T X$ is the stimulus autocorrelation matrix (which is an identity matrix when a white noise stimulus devoid of temporal and spatial correlation is employed). RF maps for cortical neurons recorded from area 3b, derived from linear regression or reverse correlation, display obvious structured organization and typically consist of a central excitatory field flanked by one or more inhibitory fields (DiCarlo et al. 1998).

The shape and arrangement of these RF structures, or kernels, clearly underlie the spatial tuning of area 3b neurons. Specifically, a neuron may respond vigorously to a small bar indented in its RF at a particular orientation, and its response strength will decrease as the bar's orientation deviates from this “preferred” orientation (Fig. 2a). The shape and orientation of the RF structures tend to match that of the “preferred” bar orientation. Because of the clear correspondence between RF composition and spatial selectivity, orientation tuning in area 3b neurons can also be parameterized with two-dimensional Gabor filter RF models (Bensmaia et al. 2008; Fig. 2b). Although the neural basis for the linear RF composition is unknown, such organization likely results from the patterned convergence of afferent inputs projecting through the medial lemniscal system. However, cortical response selectivity is likely also shaped by recurrent



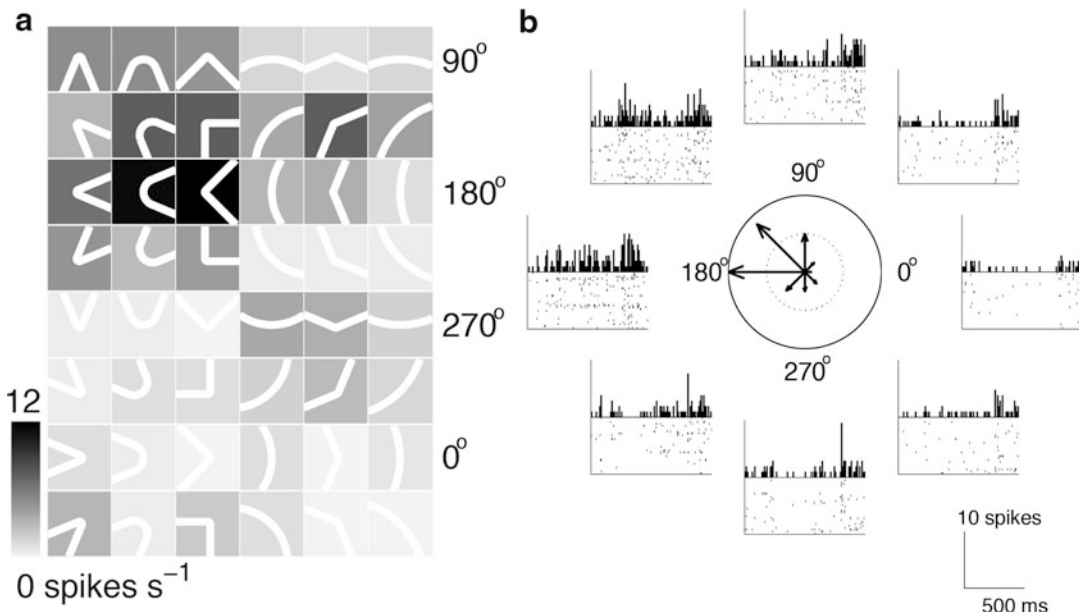
Somatosensory Cortex: Neural Coding of Shape, Fig. 2 Neural coding of bar orientation. **(a)** *Top*: spiking activity of an example somatosensory neuron to a bar stimulus presented briefly within the neuron’s RF at different orientations reveals clear response modulation that is consistent over repeated trials (*rows* in the raster plot). *Bottom*: orientation-tuning curve shows the neuron’s response as a function of bar orientation and a clear

preference for bars oriented near 67.5° . **(b)** *Top*: RF map for a different orientation-tuned cortical neuron computed by averaging responses (*scale bar*) to small punctate probes presented at each RF location. *Bottom*: RF map capturing orientation selectivity with a two-dimensional Gabor function (relative response weight for each pixel given by *scale bar*)

network interactions among cortical populations (see below).

Neural responses become more selective as one ascends the somatosensory processing pathway. As a result, while the responses of afferents and of neurons in area 3b can be accounted for effectively using linear models, the responses of neurons in area 1, the primary recipient of projections from area 3b, cannot. Indeed, neurons in area 1 exhibit many properties that are similar to their counterparts in area 3b (e.g., orientation tuning), but detailed RF comparisons consistently reveal more complex spatial selectivity in area 1. Response properties continue to grow more complex and nonlinear in area 2 (the most caudal S1 region in the postcentral gyrus) and in S2 (located in the superior bank of the lateral sulcus). RF size increases dramatically to span multiple fingers and even one or both hands in their entirety (in the case of S2 neurons). Linear RF models account for little response variance in

most neurons in these populations as shape coding transitions from orientation selectivity to curvature tuning (Yau et al. 2009): Individual neurons respond preferentially to curved and angled contour fragments pointing in narrow direction ranges (Fig. 3). Although these response patterns cannot be approximated with two-dimensional spatial filter models, they can be modeled explicitly with tuning functions in the curvature direction domain. Thus, we can consider transitions in shape coding within the somatosensory system as projections of shape representations from an initial two-dimensional skin-based coordinate space into orientation and curvature feature spaces. Neural computations that transform object information into higher-order contour derivatives (orientation is a first-order spatial derivative; curvature can be defined as the rate of change in orientation along a contour, a second-order derivative) may be especially efficient for building compact and



Somatosensory Cortex: Neural Coding of Shape,

Fig. 3 Neural coding of contour curvature. (a) Gray scale indicates average spiking activity of a neuron in area 2 responding to contour fragments indented into the skin at different curvature directions. (b) Raster plots and

peri-stimulus time histograms showed curvature responses sorted by direction (rows in a). Central bouquet plot depicts the same neuron's average responses as a function of direction and reveals its strong preference for *leftward* (180°) pointing curves

sparse shape representations. In other words, these transformations in shape representations can help minimize the number of active neurons required for coding shape, thereby reducing the metabolic demands related to shape processing.

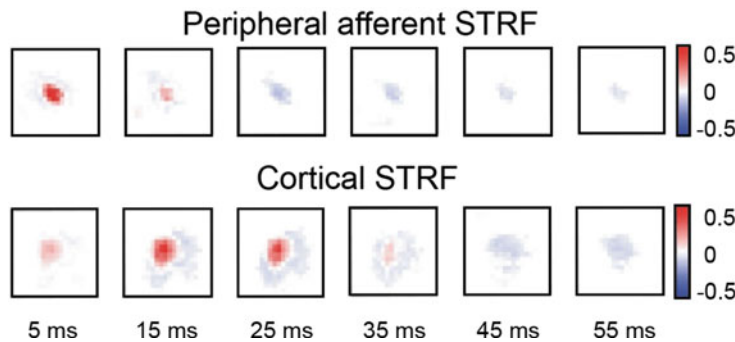
Position Tolerance

Shape-selective responses in many area 2 and S2 neurons exhibit position consistency: Tuning preferences are maintained even as stimulus features are moved over different RF locations. Although stimulus position changes can result in general response strength modulations, the relative preference for particular ranges of edge orientation or contour curvature direction is preserved regardless of where the stimulus is presented within and across finger pads (Fitzgerald et al. 2006). This position tolerance is computationally demanding and requires nonlinear shape coding mechanisms.

Temporal Dynamics

Shape coding in the somatosensory system is a dynamic process which takes place over tens

to hundreds of milliseconds after a stimulus contacts the skin. Dynamic shape coding in the peripheral afferent system and cortical neurons has been studied by characterizing selectivity using spatiotemporal receptive field (STRF) models, which capture the temporal modulation of neural RFs, in addition to their spatial tuning properties (Fig. 4). (These models are a temporal extension of the spatial filtering models described above.) Cortical neurons display a range of spatiotemporal response patterns, and the most common STRF (in areas 3b and 1) consists of initial excitation, flanked by inhibitory regions (“surround inhibition”) and followed by a long period of (“replacing”) inhibition (Sripati et al. 2006). Because of this composition, the majority of cortical STRFs are space-time inseparable: RFs cannot be decomposed into the product of a spatial kernel (excitatory region) and a temporal kernel (e.g., an exponential response decay or a difference of two exponential decays). (Note that some cortical STRFs lack surround inhibition, like afferent STRFs, making them



Somatosensory Cortex: Neural Coding of Shape, Fig. 4 Dynamic spatial response properties. Example spatiotemporal receptive field (STRF) for a peripheral afferent unit (*top*) and a cortical neuron (*bottom*). Pixel color (*scale bar*) indicates response contribution of each

RF location (spikes per second per micrometer). The majority of cortical STRFs in areas 3b and 1 comprise an excitatory center coupled with surround inhibition and trailed by replacing inhibition

space-time separable.) Although the neural basis for these dynamic response patterns is still unknown, there is little question that evolution of RF composition depends on rapid intracortical interactions. Importantly, particular aspects of dynamic shape coding, especially the spatiotemporal profile of inhibition, may play a critical role in establishing response properties like invariance to scanning velocity (DiCarlo and Johnson 1999), i.e., a preference for spatial patterns that is consistent across a range of scanning speeds. Moreover, recurrent network interactions likely also contribute to the dynamic feature selectivity observed in cortical neurons: Orientation selectivity builds gradually in areas 3b and 1, after population spiking activity peaks (Bensmaia et al. 2008), and curvature signaling similarly lags an initial buildup of spiking activity in areas 2 and S2 (Yau et al. 2013). Such response time courses may reflect the role of cortical inhibition in sculpting neural selectivity and sharpening shape representations over time.

Proprioception

Representation of three-dimensional object shape requires the integration of cutaneous and proprioceptive information. Consider again the act of holding and perceiving a smartphone in your hand: All of the cutaneous processing described above only accounts for your ability to perceive the phone's straight and curved boundary edges

in contact with your fingers. The exact computation used by somatosensory neurons to combine these cutaneous representations with hand conformation information is unknown, but neuroimaging and neurophysiological evidence implicate neural populations residing in area 2 (Mountcastle 2005). Indeed, area two neurons, while selective for cutaneous stimulus patterns, are additionally sensitive to the three-dimensional arrangement of the hand and fingers (Iwamura and Tanaka 1978). Accordingly, area 2 lesions result in clear haptic object perception deficits (Carlson 1981). There is also evidence that area two responses may be influenced by motor command signals in the context of active object exploration (London and Miller 2013): This proprioceptive feedback (which may be the result of efference copy) from the motor system could serve to gate self-generated sensory signals and to refine shape representations acquired during object manipulations.

Conclusion

Shape representations are carried in population activity of somatosensory cortical neurons. Across different levels of a cortical hierarchy, shape representations transition from occupying a skin-centered coordinate space to higher-order feature spaces. Response selectivity grows more

complex at successively higher processing stages in the somatosensory cortical pathway: Linear responses give way to nonlinear responses. Neural response patterns evolve rapidly in time, reflecting intracortical interactions that sharpen shape representations. In many respects, the principles of shape coding in the somatosensory system resemble those that apply to shape coding in the visual system (although equivalence may be restricted to two-dimensional shape representations). Despite our advancements in understanding neural shape coding in the somatosensory cortex, the computations underlying three-dimensional object representations, which require the integration of cutaneous and proprioceptive information, are not well understood. Similarly, whether and how haptic shape information interacts with other object characteristics like texture and temperature remains to be tested. Finally, the computations underlying the decoding of tactile shape representations for perceptual access and executive functioning remain to be characterized.

- DiCarlo JJ, Johnson KO, Hsiao SS (1998) Structure of receptive fields in area 3b of primary somatosensory cortex in the alert monkey. *J Neurosci* 18:2626–2645
- Fitzgerald PJ, Lane JW, Thakur PH, Hsiao SS (2006) Receptive field properties of the macaque second somatosensory cortex: representation of orientation on different finger pads. *J Neurosci* 26:6473–6484
- Iwamura Y, Tanaka M (1978) Postcentral neurons in hand region of area 2: their possible role in the form discrimination of tactile objects. *Brain Res* 150:662–666
- Johnson KO (2001) The roles and functions of cutaneous mechanoreceptors. *Curr Opin Neurobiol* 11:455–461
- London BM, Miller LE (2013) Responses of somatosensory area 2 neurons to actively and passively generated limb movements. *J Neurophysiol* 109:1505–1513
- Mountcastle VB (2005) The sensory hand. Neural mechanisms in somatic sensation. Harvard University Press, Cambridge
- Sripati AP, Yoshioka T, Denchev P, Hsiao SS, Johnson KO (2006) Spatiotemporal receptive fields of peripheral afferents and cortical area 3b and 1 neurons in the primate somatosensory system. *J Neurosci* 26:2101–2114
- Yau JM, Pasupathy A, Fitzgerald PJ, Hsiao SS, Connor CE (2009) Analogous intermediate shape coding in vision and touch. *Proc Natl Acad Sci U S A* 106:16457–16462
- Yau JM, Connor CE, Hsiao SS (2013) Representation of tactile curvature in macaque somatosensory area 2. *J Neurophysiol* 109:2999–3012

Cross-References

- ▶ [Emergence of Orientation Selectivity in the Cerebral Cortex, Modeling](#)
- ▶ [Receptive Field Modeling](#)
- ▶ [Somatosensory Cortex: Organization](#)
- ▶ [Somatosensory System: Overview](#)

References

- Bensmaia SJ, Yau JM (2011) The organization and function of somatosensory cortex. In: Hertenstein MJ, Weiss SJ (eds) *The handbook of touch*, 1st edn. Springer, New York, pp 161–187
- Bensmaia SJ, Denchev PV, Dammann JF III, Craig JC, Hsiao SS (2008) The representation of stimulus orientation in the early stages of somatosensory processing. *J Neurosci* 28:776–786
- Carlson M (1981) Characteristics of sensory deficits following lesions of Brodmann's areas 1 and 2 in the postcentral gyrus of *Macaca mulatta*. *Brain Res* 204:424–430
- DiCarlo JJ, Johnson KO (1999) Velocity invariance of receptive field structure in somatosensory cortical area 3b of the alert monkey. *J Neurosci* 19:401–419

Somatosensory Cortex: Organization

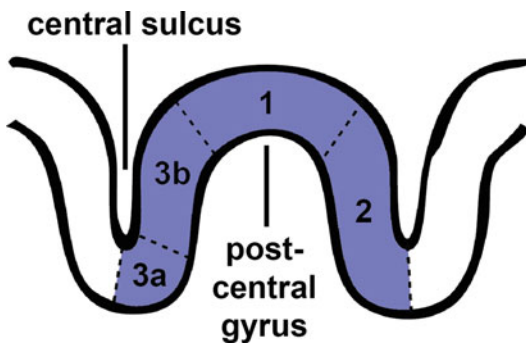
Gregg Tabot

Committee on Computational Neuroscience,
Somatosensory Research Lab, University of
Chicago, Chicago, IL, USA

Detailed Description

History

In 1909, Brodmann published maps of the different regions of cortex in humans and monkeys (Brodmann 1909). He partitioned the postcentral gyrus into three distinct areas based on cytoarchitecture and cell organization. From rostral to caudal, he designated these areas as areas 3, 1, and 2. Later studies showed that Brodmann's area 3 could be functionally and structurally divided into two distinct areas now labeled areas 3a and 3b (Vogt and Vogt 1919). Although all four brain



Somatosensory Cortex: Organization, Fig. 1 Primary somatosensory cortex comprises four brain areas: areas 3a, 3b, 1, and 2



Somatosensory Cortex: Organization, Fig. 2 A coronal view of primary somatosensory cortex from a single hemisphere of the brain. The size of the body part represents how much cortical volume is devoted to processing that part

areas are often together designated primary somatosensory cortex (S1) and to an extent respond to cutaneous stimulation, area 3b is most analogous to the other primary sensory cortices given its similarity in inputs and laminar structure. Area 3b is thus S1 proper.

Later, in 1940 Adrian discovered a second brain region, adjacent to S1, which contained representations of the forefoot and hindfoot in cats (Adrian 1940). Adrian initially thought this area to be a cortex dedicated to the cats' special ability to extend and retract their claws; however, Woolsey was able to show that this additional somatosensory area, now known as the secondary somatosensory cortex (S2), is shared by monkeys and other animals (Woolsey 1943).

Structural Organization

Area 3a is located in the fundus of the central sulcus, contiguous to primary motor cortex (area 4) on the rostral side and to area 3b on the caudal side. Area 3b lies on the rostral bank of the postcentral gyrus and, proceeding caudally, abuts area 1, located at the apex of the postcentral gyrus, followed by area 2, which lies on the apex and sometimes on the caudal bank of the postcentral gyrus (Fig. 1).

Each of the four brain areas comprises a distinct cortical representation of the contralateral body (Kaas et al. 1979) (Fig. 2). The representation of each body part in the cortex is not

proportional to its physical size or mass. Instead, the parts of the body with dense innervations (i.e., the hand or face) have larger cortical representations than do parts that are more sparsely innervated (i.e., the back or leg) and likely contribute to a richer sensory representation.

S2 is located in the parietal operculum on the upper bank and ceiling of the lateral sulcus (Woolsey et al. 1979). The structural organization of S2 is not as well characterized as is that of S1 but is thought to comprise at least two distinct cortical representation of the contralateral body (Krubitzer et al. 1995).

Functional Organization

Area 3a, considered a transitional zone between the motor and somatosensory cortices, receives and processes information about muscle stretch, joint movement, and posture from muscle receptors (Yumiya et al. 1974) and possibly other proprioceptors. Area 3a is thought to contribute to the sense of proprioception, the awareness of the position, and movements of one's body. Its dense

reciprocal connections with motor cortex (Zarzecki et al. 1978) suggest a role in the coordination of movements.

Tactile information is processed in areas 3b, 1, and 2 in a hierarchical fashion (Iwamura 1998). Cutaneous signals are first processed in area 3b (via projections from the ventral posterior nucleus of the thalamus) then are further elaborated in areas 1 and 2 (which also receive some thalamic input) before being sent to S2 or other associative areas for further processing. The hierarchical progression is observed in the increasing latencies of the responses to tactile stimuli (Lebedev and Nelson 1996) and in the response properties of neurons. Indeed, receptive fields (RFs) get larger as one ascends the processing pathway from area 3b to 2, and neurons exhibit increasingly complex response properties as one proceeds caudally (Iwamura et al. 1993), such as a selectivity for direction of motion (Pei et al. 2010) or the orientation of edges (Bensmaia et al. 2008). In addition to exhibiting complex cutaneous RFs, neurons in area 2 also receive proprioceptive input, suggesting that this area mediates the integration of cutaneous and proprioceptive information to achieve a three-dimensional percept of objects.

Cutaneous and proprioceptive neurons from S1 then project to S2, which is functionally divided into different fields: anterior, central, and posterior (Fitzgerald et al. 2004). Neurons in the central field are sensitive to cutaneous stimuli with RFs that often span multiple digits (Krubitzer et al. 1995). Some neurons exhibit orientation selectivity over their (large) RFs (Fitzgerald et al. 2006) and even more complex shape tuning properties such as a selectivity for orientation (Yau et al. 2009). In contrast, neurons in the anterior and posterior fields are more sensitive to proprioceptive stimuli than to cutaneous stimuli (Fitzgerald et al. 2004).

In addition to processing cutaneous and proprioceptive stimuli, both S1 and S2 process noxious stimuli (Treede et al. 1999): S1 neurons seem to encode pain intensity while S2 neurons may be involved in signaling the presence of any pain (Timmermann et al. 2001).

Cross-References

- [Proprioception](#)
- [Somatosensory Cortex: Neural Coding of Motion](#)
- [Somatosensory Cortex: Neural Coding of Shape](#)

References

- Adrian ED (1940) Double representation of the feet in the sensory cortex of the cat. *J Physiol* 98:16–18
- Bensmaia SJ, Denchev PV, Dammann JF, Craig JC, Hsiao SS (2008) The representation of stimulus orientation in the early stages of somatosensory processing. *J Neurosci* 28(3):776–786
- Brodmann K (1909) *Vergleichende Lokalisationslehre der Großen Hirnrinde*. Johann Ambrosius Barth
- Fitzgerald PJ, Lane JW, Thakur PH, Hsiao SS (2004) Receptive field properties of the macaque second somatosensory cortex: evidence for multiple functional representations. *J Neurosci* 24(49): 11193–11204
- Fitzgerald PJ, Lane JW, Thakur PH, Hsiao SS (2006) Receptive field properties of the macaque second somatosensory cortex: representation of orientation on different finger pads. *J Neurosci* 26(24): 6473–6484
- Iwamura Y (1998) Hierarchical somatosensory processing. *Curr Opin Neurobiol* 8(4):522–528
- Iwamura Y, Tanaka M, Sakamoto M, Hikosaka O (1993) Rostrocaudal gradients in the neuronal receptive field complexity in the finger region of the alert monkey's postcentral gyrus. *Exp Brain Res* 92:360–368
- Kaas JH, Nelson RJ, Sur M, Lin CS, Merzenich MM (1979) Multiple representations of the body within the primary somatosensory cortex of primates. *Science* 204:521–523
- Krubitzer L, Clarey J, Tweedale R, Elston G, Calford M (1995) A redefinition of somatosensory areas in the lateral sulcus of macaque monkeys. *J Neurosci* 348:55–72
- Lebedev MA, Nelson RJ (1996) High-frequency vibratory sensitive neurons in monkey primary somatosensory cortex: entrained and nonentrained responses to vibration during the performance of vibratory-cued hand movements. *Exp Brain Res* 111:313–325
- Pei YC, Hsiao SS, Craig JC, Bensmaia SJ (2010) Shape invariant coding of motion direction in somatosensory cortex. *PLoS Biol* 8(2):e1000305
- Timmermann L, Ploner M, Haucke K, Schmitz F, Baltissen R, Schnitzler A (2001) Differential coding of pain intensity in the human primary and secondary somatosensory cortex. *J Neurophysiol* 86(3): 1499–1503

- Treede RD, Kenshal DR, Gracely RH, Jones AKP (1999) The cortical representation of pain. *Pain* 79:105–111
- Vogt C, Vogt O (1919) Allgemeinere Ergebnisse unserer Hirnforschung. *J Psycho Neurol* 25:279–462
- Woolsey CN (1943) “Second” somatic receiving areas in the cerebral cortex of cat, dog and monkey. *Fed Proc* 2:55–56
- Woolsey CN, Erickson TC, Gilson WE (1979) Localization in somatic sensory and motor areas of human cerebral cortex as determined by direct recording of evoked potentials and electrical stimulation. *J Neurosurg* 51:476–506
- Yau JM, Pasupathy A, Fitzgerald PJ, Hsiao SS, Connor CE (2009) Analogous intermediate shape coding in vision and touch. *Proc Natl Acad Sci* 106(38): 16457–16462
- Yumiya H, Kubota K, Asanuma H (1974) Activities of neurons in area 3a of the cerebral cortex during voluntary movements in the monkey. *Brain Res* 78(2):169–177
- Zarzecki P, Shinoda Y, Asanuma H (1978) Projections from area 3a to the motor cortex by neurons activated from group I muscle afferents. *Exp Brain Res* 33(2):269–282

Somatosensory Neurons: Spike-Timing

Hannes Saal

Department of Organismal Biology and Anatomy, University of Chicago, Chicago, IL, USA

Synonyms

Entrainment; First-spike latency; Phase-locking; Temporal coding

Definition

A long-standing controversy in neural coding has been about whether the timing of individual action potentials (spikes) conveys information and is behaviorally relevant or whether information is instead transmitted simply by neurons’ firing rates. Both peripheral and cortical somatosensory neurons in primates can exhibit precisely

timed action potentials in response to tactile stimuli, and there is a growing consensus that not only is some tactile information exclusively represented by such temporal codes but also that spike timing can shape tactile perception.

Detailed Description

Precisely Timed Responses of Cutaneous Mechanoreceptors to Skin Vibrations

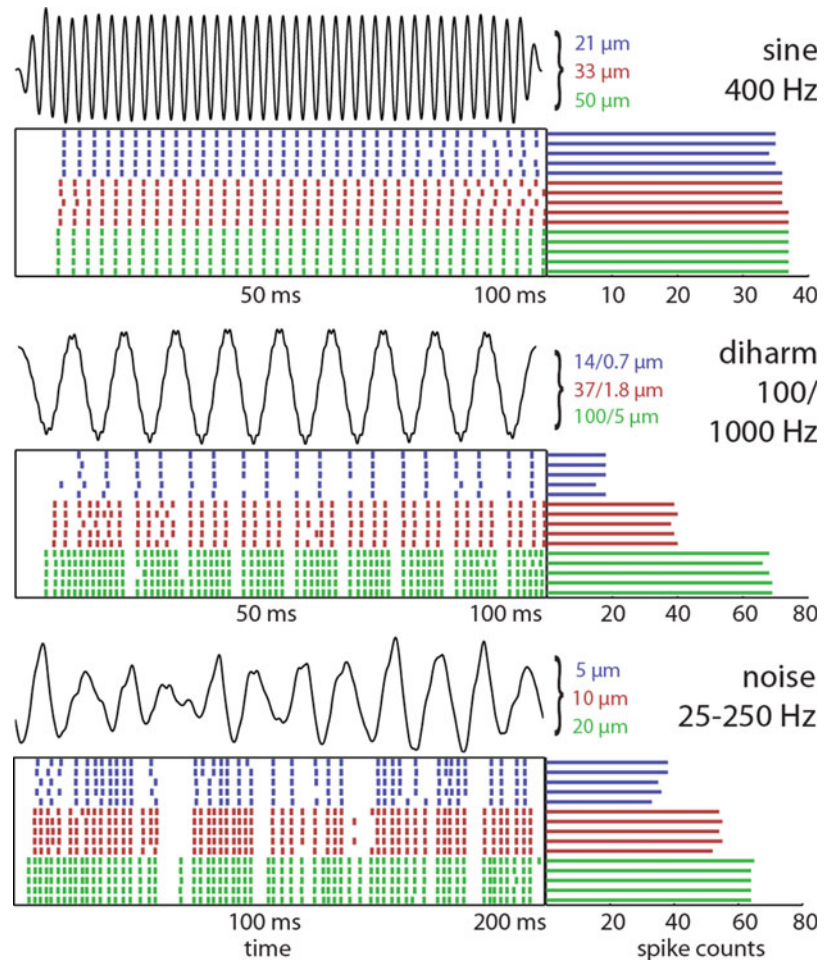
In primates, rapidly adapting (RA) and Pacinian (PC) afferents entrain to medium- and high-frequency vibrations, respectively, in that their action potentials occur precisely within a given phase of each stimulus cycle (Talbot et al. 1968). Such precise timing can also be seen in the responses to diharmonic and noise stimuli (Muniak et al. 2007, see Fig. 1). PC responses are generally more precise than RA responses. Slowly adapting type I (SA1) afferents only respond weakly to vibrations, and their spikes are not precisely timed. Finally, the temporal patterning has been shown to be behaviorally relevant at a fine temporal resolution, by presenting different stimuli that elicit similar or the same firing rates and then test whether those are perceptually discriminable (Mackevicius et al. 2012). One behavior where skin oscillations are especially relevant is texture perception, where RA and PC afferents respond with precise temporal spiking patterns to texture-elicited skin vibrations (Weber et al. 2013).

Peripheral Responses During Object Manipulation

Another temporal code might be active during object manipulation. When grasping an object, one needs to rapidly adapt grip forces depending on object properties to prevent slip or overgrasping. Information about object curvature and similar properties is encoded mostly by SA1 and RA afferents. It has been shown that in addition to firing rates, the first-spike latencies of SA1 and RA afferents are highly informative about object features. A neural code based on first-spike latencies could explain how tactile feedback is rapidly integrated into motor commands

Somatosensory Neurons: Spike-Timing,
Fig. 1 Responses of a PC afferent to sinusoidal, diharmonic, and bandpass noise stimuli. In each of the three panels, the top trace shows the time-varying position of the vibratory stimulus (with the three amplitudes marked to the right). The raster plots show the responses of a PC afferent to five repeated presentations of the stimulus at the three stimulus amplitudes. The bars to the right indicate the spike counts evoked on each stimulus presentation. While spike counts tend to change with stimulus amplitude, temporal patterning in the afferent response is more consistent across amplitudes.

(Adapted from Mackevicius et al. (2012))

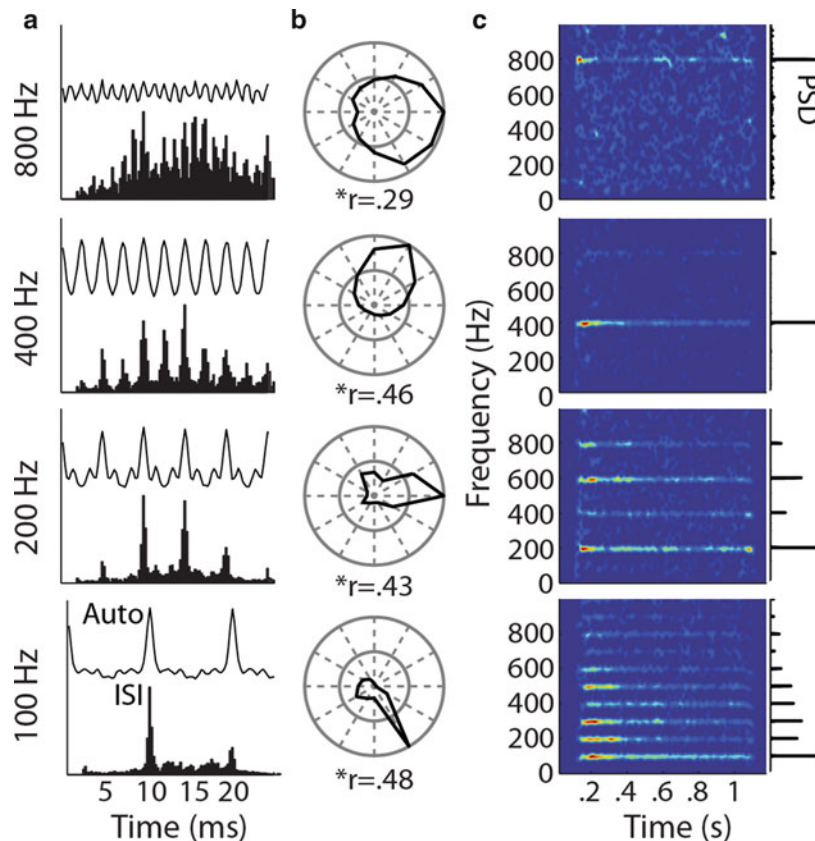


(grip force adjustments can occur within 100 ms) (Johansson and Birznieks 2004; Saal et al. 2009).

Spike Timing in Somatosensory Cortex

Whether spike timing matters in primate somatosensory cortex is more controversial. It is often assumed that even though peripheral afferents might exhibit precisely timed spikes, such temporal information might be converted into a rate code on the way to cortex. Thus, most work on somatosensory cortical neurons has focused on characterizing the makeup and extent of spatial receptive fields using firing rates. A notable exception concerns flutter stimuli (low-frequency vibrations in the range of 5–50 Hz), in response to which cortical somatosensory neuron both

exhibit entrainment (phase-locking) and modulate their firing rates. However, changes in the perception of flutter stimuli align more closely with changes in the firing rates of cortical neurons rather than changes in their temporal profile, which has led to the conclusion that spike timing plays no role in the perception of flutter stimuli (Luna et al. 2005; Salinas et al. 2000). For high-frequency texture-like vibrations, however, a different picture emerges. For such stimuli, their amplitude is signaled in the slowly time-varying firing rates of cortical neurons, while their frequency content is transmitted by precisely timed action potentials (Harvey et al. 2013, see Fig. 2). Such a code is an instance of multiplexing, where different kinds of



Somatosensory Neurons: Spike-Timing,

Fig. 2 Temporal patterning in cortical responses to sinusoidal stimulation. (a) Autocorrelations (top) and interspike interval histograms (bottom) for one neuron in area 3b, whose responses are entrained with the stimulus up to 800 Hz. (b) Phase histograms along with vector strength (r) for the same neuron as in (a) showing action potentials tended to occur during a restricted phase of each

stimulus cycle. (c) Spectrograms for the same neuron as in (a), with corresponding power spectral densities (PSD) in the insets to the right. Note that the temporal patterning begins almost immediately and lasts for the duration of the stimulus and that the fundamental frequency in the neural response reflects the frequency of the sinusoid. (Adapted from Harvey et al. (2013))

information are transmitted by different aspects of the neural response. Interestingly, information about amplitude and frequency is separated so well by these two different codes that some frequencies would be impossible to tell apart without, providing a strong argument that spike timing is indeed behaviorally relevant.

Spike Timing and Attention

Spike timing across a population of neurons can also carry information. Specifically, attention modulates the synchrony of spikes of cortical somatosensory neurons (Steinmetz et al. 2000). Such a mechanism might enhance the saliency of

attended stimuli by increasing the number of coincident spikes across the neural population.

Cross-References

- [Cutaneous Mechanoreceptive Afferents: Neural Coding of Texture](#)
- [Metric Space Analysis of Neural Information Flow](#)
- [Neural Coding](#)
- [Spike Train](#)
- [Tempotron Learning](#)
- [Time-Frequency Analysis](#)

References

- Harvey MA, Saal HP, Dammann JF 3rd, Bensmaia SJ (2013) Multiplexing stimulus information through rate and temporal codes in primate somatosensory cortex. *PLoS Biol* 11:e1001558
- Johansson RS, Birznieks I (2004) First spikes in ensembles of human tactile afferents code complex spatial fingertip events. *Nat Neurosci* 7:170–177
- Luna R, Hernandez A, Brody CD, Romo R (2005) Neural codes for perceptual discrimination in primary somatosensory cortex. *Nat Neurosci* 8:1210–1219
- Mackevicius EL, Best MD, Saal HP, Bensmaia SJ (2012) Millisecond precision spike timing shapes tactile perception. *J Neurosci* 32:15309–15317
- Muniak MA, Ray S, Hsiao SS, Dammann JF, Bensmaia SJ (2007) The neural coding of stimulus intensity: linking the population response of mechanoreceptive afferents with psychophysical behavior. *J Neurosci* 27:11687–11699
- Saal HP, Vijayakumar S, Johansson RS (2009) Information about complex fingertip parameters in individual human tactile afferent neurons. *J Neurosci* 29:8022–8031
- Salinas E, Hernandez A, Zainos A, Romo R (2000) Periodicity and firing rate as candidate neural codes for the frequency of vibrotactile stimuli. *J Neurosci* 20:5503–5515
- Steinmetz PN, Roy A, Fitzgerald PJ, Hsiao SS, Johnson KO, Niebur E (2000) Attention modulates synchronized neuronal firing in primate somatosensory cortex. *Nature* 404:187–190
- Talbot WH, Darian-Smith I, Kornhuber HH, Mountcastle VB (1968) The sense of flutter-vibration: comparison of the human capacity with response patterns of mechanoreceptive afferents from the monkey hand. *J Neurophysiol* 31:301–334
- Weber AI, Saal HP, Lieber JD, Cheng J, Manfredi LR, Dammann JF, Bensmaia SJ (2013) Spatial and temporal codes mediate the tactile perception of natural textures. *Proc Natl Acad Sci U S A* 10:17107–17112

Somatosensory Prosthesis

Sliman J. Bensmaia

Department of Organismal Biology and Anatomy, University of Chicago, Chicago, IL, USA

Detailed Description

Our ability to dexterously manipulate objects relies heavily on somatosensory signals from

the hand (Johansson and Flanagan 2009). Receptors embedded in the skin, joints and muscle convey information about the size, shape, and texture of grasped objects, and signal whether these are slipping from our grasp. The sensory experience of our hand also plays an important role in conferring to it embodiment, making it feel a part of us. Without these signals, using our hand to perform even the most rudimentary tasks would be slow, clumsy, and effortful. Given the importance of somatosensation in natural motor behavior, to achieve a clinically viable upper-limb neuroprosthesis will require that this sense be restored.

Sensory Substitution

There are a variety of approaches to conveying useful somatosensory feedback for use in upper-limb neuroprostheses. The least invasive approach consists of substituting lost sensation by mechanically stimulating – with vibratory motors, e.g., – regions of the sensory sheet that are still intact (the face, for example) (Stepp et al. 2012). In both amputees and individuals with upper spinal cord injury – the two patient populations that are targeted with these technologies – mechanical stimulation can be applied to signal movements of the hand and objects contacting it. While sensory substitution does not require surgical intervention, the patient must learn to associate patterns of skin stimulation with hand movements or with object contact, which may require extensive training. Furthermore, given spatial constraints, patients can only be instrumented with a relatively small number of stimulators, so sensory substitution can be used to convey only limited information compared to the high-bandwidth of the intact native hand.

Neural Interfaces

An alternative approach consists of interfacing directly with the nervous system. Indeed, in intact individuals, signals from the hand are carried via

nerve fibers that climb up the arm and the spinal cord before they synapse onto neurons in the brainstem (in the dorsal column nuclei). These secondary afferents then cross the midline and project to the ventroposterior nucleus thalamus, which in turn projects to primary somatosensory cortex. In principle, an interface can be developed to interact with any of these neuronal populations by developing the right type of implantable device (Weber et al. 2012), but the different potential interface sites vary in their accessibility. The neural interface approach consists of eliciting patterns of neuronal activation informative of the state of the limb and of events impinging upon it, typically through electrical stimulation of the neuronal tissue. Let us briefly compare and contrast interfaces with the nerve and with the brain, at the two anatomical extremes of the interface continuum.

Peripheral interfaces: Afferents can be accessed either in the residual nerve (Dhillon and Horch 2005) or in the dorsal root (Hokanson et al. 2011), where all of their cell bodies are located. Only a relatively small number of different types of mechanoreceptive afferents convey proprioceptive and cutaneous information, and the properties of these neurons are both highly stereotyped and well characterized. Furthermore, these neurons are not interconnected, so they essentially convey independent signals to the brain, which greatly simplifies stimulation strategies. The idea, then, is to attempt to reproduce natural patterns of activation in the nerve by strategically injecting small electrical currents into it, ideally through many independently controlled electrodes. The patterns of electrical stimulation can be modulated in space and time to produce naturalistic patterns of afferent activation. A variety of very powerful single input single output models have been developed to convert the output of sensors on the prosthesis into desired patterns of neuronal activation and these patterns can in theory be effected in the nerve through electrical stimulation (Dong et al. 2012; Kim et al. 2009, 2010), while other multi input multi output models have also been explored (Daly et al. 2012; Liu et al. 2011).

Cortical interfaces: A cortical interface has the advantage that it can be applied to patients with upper spinal cord injury, for whom the communication between the nerve and the brain has been severed. Another desirable feature of cortical interfaces is that sensory systems extract behaviorally relevant information from the relatively unelaborated representation in the nerve through successive stages of processing. Indeed, individual cortical neurons encode more complex stimulus features than do their peripheral counterparts. Furthermore, cortical neurons are organized topographically, such that nearby neurons tend to respond to similar stimulus features. This organizational scheme, largely absent in the nerve, may thus be exploited in attempting to elicit artificial percepts.

There are two general approaches to conveying sensory information through a cortical interface. The first, analogous to its peripheral counterpart, consists of attempting to reproduce naturalistic patterns of neuronal activation through electrical stimulation. To the extent that patterns of activation are naturalistic, the evoked percepts will be verisimilar and thus intuitive, requiring little training on the part of the patient. Within this approach, the functional topography of the brain can be exploited. For example, information about contact location – where is the object contacting the skin? – is important for object manipulation. In intact individuals, where we feel a poke on the skin is determined by which population of neurons gets activated. Thus, information about contact location might be conveyed by stimulating small populations of somatosensory neurons, thereby eliciting a percept that is localized to a small patch of skin (Tabot et al. 2013). In amputees, the sensation is projected to a phantom limb, in tetraplegic patients to their deafferented limb. Now imagine that anytime the prosthetic thumb touches an object, stimulation is triggered through electrodes that are implanted in the thumb representation of somatosensory cortex. The evoked sensation will be projected to the phantom or deafferented thumb, which will lead to an intuitive sense of where contact happened. In fact, studies suggest that, while stimulating the neuronal

representation of the thumb will be experienced on the phantom or deafferented thumb, if patients have consistent visual experience of contact with the thumb, paired with sensations experienced on the native thumb, the sensations will start to be experienced on the prosthesis (Marasco et al. 2011). Artificial touch may thus lead to embodiment of the robotic limb! While some degree of naturalism might be achieved with a brain interface, cortical neurons are embedded in highly complex networks, and electrical stimulation of cortical tissue leads to diffuse activation of neurons with very different response properties despite the spatial organization of the brain (Histed et al. 2009). Producing truly naturalistic patterns of activation through electrical stimulation is therefore an endeavor that is doomed to failure.

With this in mind, the so-called biomimetic approach – the exploitation of existing neuronal representations – may be unnecessary. Another approach to conveying sensory feedback through a cortical interface consists of exploiting the brain's ability to learn. Indeed, the brain is known to be highly adaptable, so it is not unreasonable to hypothesize that if a systematic mapping is created between patterns of sensory activation and patterns of intracortical microstimulation, patients will learn to use this artificial sensory feedback to control the limb. Indeed, animals are able to learn to use completely arbitrary but systematic artificial sensations to guide behavior (Thomson et al. 2013; O'Doherty et al. 2011). However, the space of possible sensations that were tested in these experiments is small relative to the almost infinite space of sensory events associated with the hand and it is unclear whether the adaptation-based approach will scale up sufficiently for use in upper-limb neuroprostheses. Most likely, biomimicry and adaptation will both play critical roles in successful attempts to convey sensory feedback.

Conclusions

Multielectrode arrays have been implanted in the brain of human patients, and algorithms have

been developed to decipher how these patients wish to move anthropomorphic robotic arms from signals in the motor parts of their brain (Hochberg et al. 2012; Collinger et al. 2013). In other words, these patients can control robotic limbs by thought alone. While these studies constitute staggering examples of scientific and technological achievement, the evoked movements are slow and inaccurate, and the neuroprostheses are only viable in a laboratory setting. Given its importance in guiding movement, the incorporation of somatosensory feedback in the next generation of prostheses may bring about a major improvement in the dexterity of these limbs, and perhaps eventually may lead to a clinically viable option to restore sensorimotor function in amputees and tetraplegic patients.

References

- Collinger JL et al (2013) High-performance neuroprosthetic control by an individual with tetraplegia. *Lancet* 381(9866):557–564
- Daly J, Liu J, Aghagolzadeh M, Oweiss K (2012) Optimal space-time precoding of artificial sensory feedback through multichannel microstimulation in bi-directional brain-machine interfaces. *J Neural Eng* 9(6):065004
- Dhillon GS, Horch KW (2005) Direct neural sensory feedback and control of a prosthetic arm. *IEEE Trans Neural Syst Rehabil Eng* 13(4):468–472
- Dong Y et al (2012) A simple model of mechanotransduction in primate glabrous skin. *J Neurophysiol* 109:1350–1359.
- Histed MH, Bonin V, Reid RC (2009) Direct activation of sparse, distributed populations of cortical neurons by electrical microstimulation. *Neuron* 63(4):508–522
- Hochberg LR et al (2012) Reach and grasp by people with tetraplegia using a neurally controlled robotic arm. *Nature* 485(7398):372–375
- Hokanson JA, Ayers CA, Gaunt RA, Bruns TM, Weber DJ (2011) Effects of spatial and temporal parameters of primary afferent microstimulation on neural responses evoked in primary somatosensory cortex of an anesthetized cat. In: Conference proceedings: ... Annual International Conference of the IEEE Engineering in Medicine and Biology Society, IEEE Engineering in Medicine and Biology Society, Boston, MA, pp 7533–7536
- Johansson RS, Flanagan JR (2009) Coding and use of tactile signals from the fingertips in object manipulation tasks. *Nat Rev Neurosci* 10(5):345–359

- Kim SS et al (2009) Conveying tactile feedback in sensorized hand neuroprostheses using a biofidelic model of mechanotransduction. *IEEE Trans BIOCAS* 3(6):398–404
- Kim SS, Sripathi AP, Bensmaia SJ (2010) Predicting the timing of spikes evoked by tactile stimulation of the hand. *J Neurophysiol* 104(3):1484–1496
- Liu JB, Khalil HK, Oweiss KG (2011) Neural feedback for instantaneous spatiotemporal modulation of afferent pathways in bi-directional brain-machine interfaces. *IEEE Trans Neural Syst Rehabil Eng* 19(5):521–533
- Marasco PD, Kim K, Colgate JE, Peshkin MA, Kuiken TA (2011) Robotic touch shifts perception of embodiment to a prosthesis in targeted reinnervation amputees. *Brain J Neurol* 134(Pt 3):747–758
- O'Doherty JE et al (2011) Active tactile exploration using a brain-machine-brain interface. *Nature* 479(7372):228–231
- Stepp CE, An Q, Matsuoka Y (2012) Repeated training with augmentative vibrotactile feedback increases object manipulation performance. *PLoS One* 7(2): e32743
- Tabot GA, Dammann III JF, Berg JA, Tenore FV, Boback JL, Vogelstein RJ, Bensmaia SJ (2013) Restoring the sense of touch with a prosthetic hand through a brain interface. *Proc Natl Acad Sci*, 110:18279–84
- Thomson EE, Carra R, Nicolelis MA (2013) Perceiving invisible light through a somatosensory cortical prosthesis. *Nat Commun* 4:1482
- Weber DJ, Friesen R, Miller LE (2012) Interfacing the somatosensory system to restore touch and proprioception: essential considerations. *J Mot Behav* 44(6):403–418

a degree of the original performance is regained, accompanied by various changes in auditory processing.

Detailed Description

Localizing sound sources in the external world requires the integration of multiple cues. The relative time of arrival and sound level across the two ears depend on which side of the head the sound originates from (azimuth) and frequency-dependent filtering by the head and ears that depends on the vertical angle of the sound source (elevation). For a given location these cues correspond, but not uniquely for a given frequency. Thus, information is integrated across different monaural and binaural cues and different frequency ranges. The correspondence of cue values also depends on individual's head and outer ear (pinna) size and shape and the relative state of their hearing at each ear, all of which change with age. Possibly as a consequence, the calibration of these cues in the auditory system is quite flexible. Flexibility may also be an advantage for dealing with different acoustic environments.

Experience-Dependent Changes in Sound Localization Ability

Manipulating of the cues for sound localization by altering the sound input to the ear immediately results in impaired sound localization ability. However, in most cases there is some subsequent recovery of sound localization ability over time.

Occlusion of one ear (typically with a removable ear plug) results in an immediate shift in free field azimuthal sound localization toward locations on the other side. In humans (Kumpik et al. 2010), ferrets (King et al. 2000), and owls (Knudsen 2002), sound localization ability improves over days and weeks of continued occlusion. Performance with the altered cues recovers completely in juveniles and is robust in experiments with adult ferrets and humans but does not occur in adult owls. However, even owls raised with altered cues can

Sound Localization and Experience-Dependent Plasticity

Christian J. Sumner and Robert Mill
MRC Institute of Hearing Research,
Nottingham, UK

Definition

The ability to localize sounds in space, and the way in which such a task is performed, is not fixed. If the physical cues for sound localization are altered, ability is initially disrupted. However, following experience with the new set of cues,

learn to localize correctly if normal hearing is reestablished in adulthood. Although differences in timing and level across the two ears are the dominant cues for azimuthal sound localization, in adult humans (Kumpik et al. 2010) and ferrets (Kacelnik et al. 2006), performance improvement in azimuthal sound localization appears to reflect an increased reliance on monaural spectral cues.

Modification of the vertical cues for sound localization also results in adaptation of behavioral responses. Ear molds that modify the elevation-dependent spectral filtering by the pinnae produce immediate deficits in the vertical plane. Performance is almost entirely recovered with experience (Hoffman et al. 1998). Explicit modification of binaural cues (e.g., interaural timing), azimuthal shifts, or nonlinear transforms also results in an immediate drop and subsequent improvement of localization ability, though recovery of unaltered performance is not generally complete and it is not possible to adapt to reversal of the inputs to each ear. Training also produces improvements on unaltered cues (see Wright and Zhang (2006) for a review). The immediate effect of monaural earplugging in adult humans suggests that sound localization in both azimuth and elevation relies on a rapidly updated weighting of all acoustic cues depending on their reliability (Van Wanrooij and Van Opstal 2007).

Reversal of cue manipulations generally results in recovery of the original sound localization behavior with only small aftereffects. Recovery is immediate in most cases in mammals (see Wright and Zhang 2006; Kacelnik et al. 2006) but only gradual in owls raised with monaural occlusion (Knudsen 2002). Improvement is often dependent on explicit training (Kumpik et al. 2010; Kacelnik et al. 2006) and has been observed when cues are only altered during testing sessions (see Wright and Zhang 2006).

Visual manipulations such as prism lenses that disrupt the correspondence between auditory and visual space also induce corrective changes in sound localization behavior (Knudsen 2002; Zwiers et al. 2003).

Mechanisms Underlying Changes in Perceptual Ability

Perceptual changes in sound localization have been shown to be associated with a range of different physiological changes that depend on experimental species and circumstances.

In the superior colliculus of the midbrain, there is a multisensory map of space, which plays an important role in orienting responses toward visual and auditory objects. In owls raised with one ear occluded, or with a visual displacement, a rewiring of the projection from the auditory midbrain (the inferior colliculus) occurs that ensures that spatial maps remained well aligned (Knudsen and Brainard 1991; Knudsen 2002). Realignment of space maps is also seen in the superior colliculus of ferrets raised with abnormal visual or auditory cues (King et al. 2000). However, realignment is not complete and alignment nevertheless improves once normal cues are reinstated. This is consistent with the rapid recovery of behavioral performance, as if the “default” map develops regardless. Even visual deprivation during development still results in a largely normal map. However, pinnae and conchae are required for the auditory space map to develop properly.

In purely auditory regions (inferior colliculus in the midbrain, primary auditory cortex), raising animals with a monaural hearing loss tends to result a change in binaural sensitivity in favor of the unaffected ear (see King et al. 2011). This suggests a shift toward monaural cues, rather than “rebalancing” the binaural cues.

Despite the ability of adult mammals to adapt perceptually in response to monaural occlusion, the auditory-visual space map of the midbrain does not realign in adulthood. However, there is considerable evidence that the auditory cortex and descending pathways in the auditory system are involved. Protracted deactivation of the auditory cortex which can affect sound localization often has a more profound effect on the ability to adapt behaviorally to altered localization cues (Nodal et al. 2012). The descending pathways also appear to mediate adaptation in mammals. Lesions to the descending pathway from the auditory cortex to the midbrain (Bajo et al. 2010) or

efferent connections (olivocochlear) from the brainstem to the cochlea (Irving et al. 2011) do not affect normal sound localization but impair the ability to adapt to monaural occlusion. These data are consistent with the idea that auditory spatial plasticity in adulthood reflects a change in the way different cues are used (choosing reliable ones) rather than change in the way any individual cue is computed. Possibly, the effort required to interpret altered cues places a greater reliance on the cortex and descending pathways.

References

- Bajo VM, Nodal FR, Moore DR, King AJ (2010) The descending corticocollicular pathway mediates learning-induced auditory plasticity. *Nat Neurosci* 13:253–260
- Hoffman PM, Van Riswick JGA, Van Opstal J (1998) Relearning sound localization with new ears. *Nat Neurosci* 1:417–421
- Irving S, Moore DR, Liberman MC, Sumner CJ (2011) Olivocochlear efferent control in sound localization and experience dependent learning. *J Neurosci* 31:2493–2501
- Kacelnik O, Nodal FR, Parsons CH, King AJ (2006) Training-induced plasticity of auditory localization in adult mammals. *PLoS Biol* 4(4):e71
- King AJ, Parsons CH, Moore DR (2000) Plasticity in the neural coding of auditory space in the mammalian brain. *Proc Natl Acad Sci U S A* 97:11821–11828
- King AJ, Dahmen JC, Keating P, Leach ND, Nodal FR, Bajo VM (2011) Neural circuits underlying adaptation and learning in the perception of auditory space. *Neurosci Biobehav Rev* 35:2129–2139
- Knudsen EI (2002) Instructed learning in the auditory localization pathway of the barn owl. *Nature* 417:322–328
- Knudsen EI, Brainard MS (1991) Visual instruction of the neural map of auditory space in the developing optic tectum. *Science* 253:85–87
- Kumpik D, Kacelnik O, King AJ (2010) Adaptive reweighting of localization cues in response to chronic unilateral earplugging in humans. *J Neurosci* 30:4883–4894
- Nodal FR, Bajo VM, King AJ (2012) Plasticity of spatial hearing: behavioural effects of cortical inactivation. *J Physiol* 15:3965–3986
- Van Wanrooij MM, Van Opstal AJ (2007) Sound localization under perturbed hearing. *J Neurophysiol* 97:615–726
- Wright BA, Zhang Y (2006) A review of learning with normal and altered sound-localization cues in human adults. *Int J Audiol* 45:S92–S98
- Zwiers MP, Van Opstal JA, Paige GD (2003) Plasticity in human sound localization induced by compressed spatial vision. *Nat Neurosci* 6:175–181

Sound Localization in Mammals, Models

J. Braasch

School of Architecture, Rensselaer Polytechnic Institute, Troy, NY, USA

Definition

Models of sound localization for mammals describe or simulate the process of how the mammalian auditory system determines the position and/or spatial extent of one or multiple sound sources from cues it extracts from signals captured at the eardrums.

Detailed Description

Historical Overview

The first theories describing how the human auditory system can determine the position of a sound source appeared in the late nineteenth century after W. Thompson (1877), S. P. Thompson (1882), and Steinhauser (1877) discovered that interaural time and level differences occur between both ear signals if a sound source arrives from the side. The focus continued to be on so-called lateralization models, which explain how a sound source is perceived to the left or right based on interaural cues. The first model that describes an actual physiological mechanism of how the central nervous system localizes sound is the Jeffress model, which proposes a combination of delay lines and coincidence detectors to estimate the lateral position of a sound source based on interaural time differences. Within the same time period, better electronic devices enabled psychophysicists to better understand how the auditory system extracts localization cues.

Devices like precise sine generators and circuits to produce interaural time and level differences made it possible to measure the performance of the auditory system in greater detail. One milestone was an experiment by

Mills (1958) to demonstrate that the auditory system cannot lateralize a signal based on the interaural time differences of the left and right signal carriers above 1.5 kHz, correctly assuming that the underlying physiological mechanism can no longer utilize phase locking above this threshold. Later it was shown that interaural time differences in the signals' envelopes can be extracted and used by the auditory system.

Another important factor in the development of localization models was advances in signal processing and communication theory. A milestone was reached, when Cherry and Sayers (1956) described a functional localization model using a cross-correlator. In his model cross-correlation is applied between the left and right ear signals to measure the delay and thus the ITD between both signals.

In the late 1970s, computers were powerful enough to develop computational models that predict the lateral position of an auditory event precisely for a given pair of ear signals by simulating the complete pathway from the eardrums to higher stages including band-pass filter banks to mimic the basilar membrane's separation of the signals in bands of approximately a third of an octave wide (auditory bands) and simulating the stochastic processes of hair cells.

Aside from models simulating the general functionality of the localization process, models exist to simulate the underlying physiological process in greater detail, often simulating the response of a certain cell type measured in electrophysiological animal experiments. The latter are frequently termed pink box models to separate them from the functional black box models. Cai et al. (1998a, b), and Stecker et al. (2005) are good examples of this type of approach.

Understanding the mechanisms of how the auditory system determines the elevation and front/back direction of sound sources was much more difficult than understanding how the auditory system estimates lateral positions due to the complexity of the involved monaural cues. Blauert (1969/1970) was able to demonstrate

that the auditory systems utilize characteristic, direction-dependent frequency boosts or reductions which occur when the pinnae alter the incoming sound waves. Zakarauskas and Cynader (1993) presented an early localization model based on spectral monaural cues using the second derivative of the frequency spectrum. Later, statistical methods such as a Bayes classifier were used to predict the three-dimensional location of auditory events by analyzing both interaural and monaural cues (e.g., see Hartung (1998) and Nix and Hohmann (2006)).

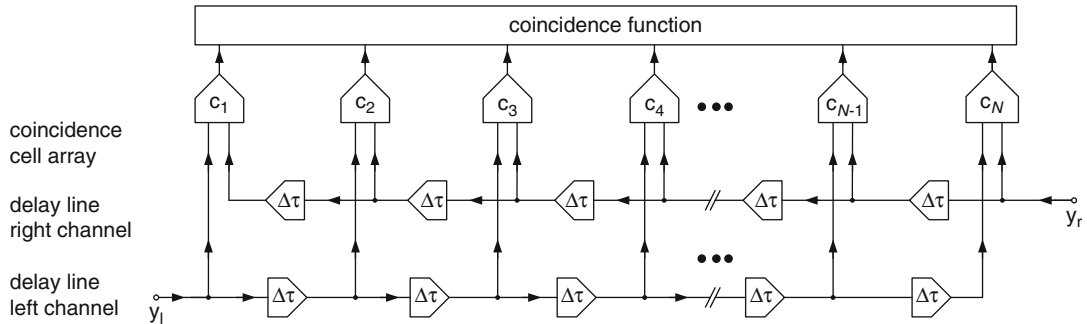
Jeffress Model

The Jeffress model (1948) was the first model to propose a physiological mechanism for mammalian sound localization. The core idea of the Jeffress model is the combination of delay lines and coincidence cells. In this model, two separate delay lines exist for each ear that run parallel. The signals propagate on each line in opposite direction as shown in Fig. 1. A signal arriving at the left ear, $y_{l(m)}$, with m being the index for time, has to pass the first delay line, $l(m, n)$, from left to right. The variable n is the index for the coincidence detectors at different internal delays. A signal arriving at the right ear, $y_{r(m)}$, travels on the other delay line, $r(m, n)$, in the opposite direction. The discrete implementation of the delay lines can be described as follows:

$$\begin{aligned} l(m+1, n+1) &= l(m, n); \\ 1 \leq n < N \wedge l(m, 1) &= y_{l(m)}, \end{aligned} \quad (1)$$

$$\begin{aligned} r(m+1, n-1) &= r(m, n); \\ 1 < n \leq N \wedge r(m, N) &= y_{r(m)}, \end{aligned} \quad (2)$$

with N being the number of implemented coincidence cells. The time, t , and the internal delay, τ , can be easily estimated from the indices, m and n , and the sampling frequency, f_s , as follows: $t = (m - 1)/f_s$ and $\tau = (n - (N + 1)/2)/f_s$. A coincidence detector, $c(m, n)$, is activated when it receives simultaneous inputs from both delay lines at the positions that it is connected to. Each of the coincidence detectors is adjusted



Sound Localization in Mammals, Models, Fig. 1 Coincidence mechanism as first proposed by Jeffress (1948)

to a different ITD, due to the limited velocity of propagation of the signals on the delay line. For example, a sound source located in the left hemisphere will arrive at the left ear first, and therefore the signal will travel a greater distance on the delay line than the signal for the right ear before both of them activate the coincidence detector for the corresponding ITD.

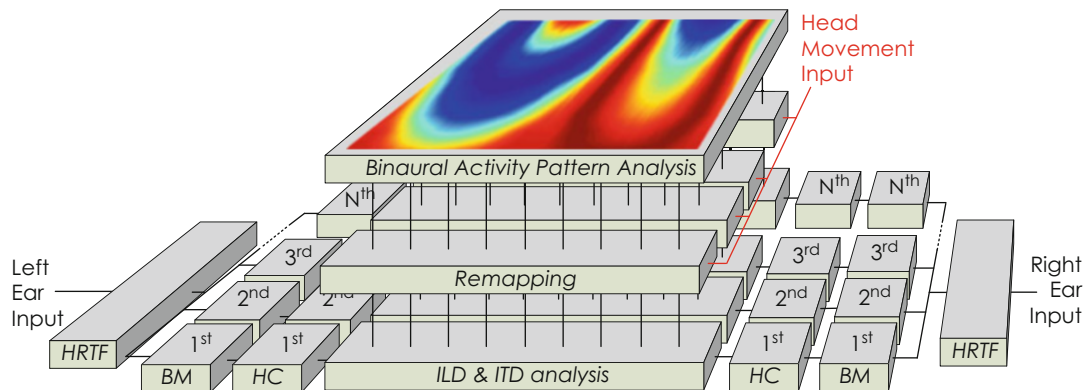
Interaural Cross-Correlation Models

Actually, Jeffress himself never specified explicitly how two spikes would coincide. Stern and Colburn (1978) later pointed out that the coincidence model can be considered to be an estimator for the interaural cross-correlation (IACC) function – which had been proposed earlier by Cherry and Sayers (1956) to estimate ITDs. To this end they assumed that many parallel coincidence detector cells exist which are tuned to the same ITD. Then, the probability that two spikes from two opposite channels will activate a specific coincidence cell is given by the product of the number of spikes in those left and right channels, the interaural delay of which matches the internal delay of the coincidence cell. This product also appears in the running cross-correlation function, which is defined for a discrete system as follows (Note that $l(m',n)$ and $r(m',n)$ have to be determined recursively from Eqs. 1 and 2. The classical continuous form of the running cross-correlation function is

$$\Psi_{y_l, r}(t, \tau) = \int_{t'=t}^{t+\Delta t} y_l(t' - \tau/2) \cdot y_r(t' + \tau/2) dt'.$$

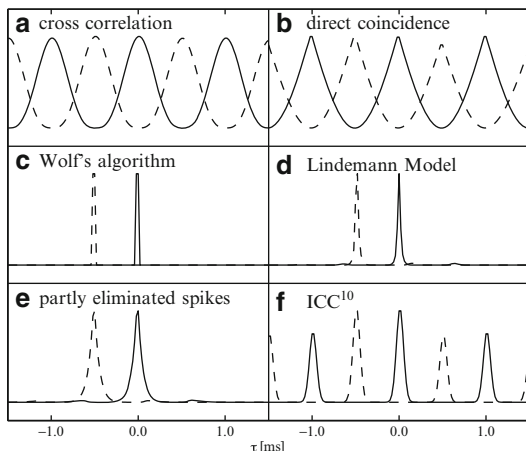
$$\begin{aligned} \Psi_{y_l, r}(m, n) &= \frac{1}{\Delta m} \sum_{m'=m}^{m+\Delta m} c(m', n) \\ &= \frac{1}{\Delta m} \sum_{m'=m}^{m+\Delta m} l(m', n) r(m', n), \quad (3) \end{aligned}$$

with $c(m, n) = l(m, n) r(m, n)$ and the assumption that the amplitudes in the left and right channels are proportional to the number of spikes. In Eq. 3 a rectangular window of the length, Δm , was chosen within which the cross-correlation function for each time interval is calculated. Often other window shapes, e.g., Hanning window, triangular window, and exponential window, are used. The duration of the time window, $\Delta t = \Delta m/f_s$, can be determined in psychoacoustical experiments measuring binaural sluggishness. Values come out to be on the order of tenths to hundreds of milliseconds depending on the listener and measurement method (Grantham and Wightman 1978, 1979; Grantham 1982, 1979; Kollmeier and Gilkey 1990). Sayers and Cherry (1957) used the interaural cross-correlation (IACC) to determine the ITDs, and in 1978 a computational lateralization model based on IACC and the simulation of the auditory periphery was introduced independently in Blauert and Cobben (1978) and Stern and Colburn (1978). The general structure of a common cross-correlation model is shown in Fig. 2. Besides the common cross-correlation function, there are alternative ways to implement the coincidence detectors. Figure 3 shows the results of different implementations, namely, the interaural cross-correlation functions of two 1-kHz



Sound Localization in Mammals, Models,
Fig. 2 General model structure of a binaural localization model utilizing head rotations according to Braasch et al. (2013). HRTF outer-ear simulation/HRTF filtering, BM basilar membrane/band-pass filtering, HC hair-cell/half-wave rectification, ITD and ILD analysis interaural time

difference (ITD) cue extraction/interaural cross-correlation and interaural level difference (ILD) cue analysis with EI cells; remapping to azimuth angles with head-rotation compensation; binaural activity pattern analysis to estimate the sound-source positions



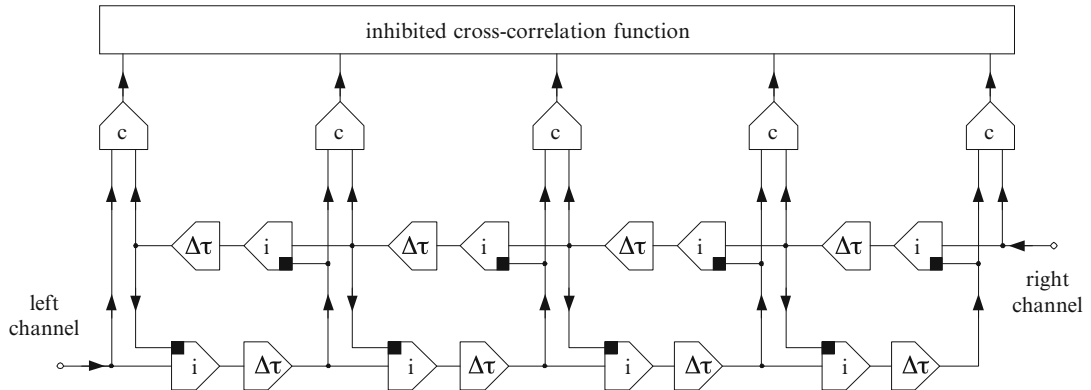
Sound Localization in Mammals, Models,
Fig. 3 Examples for the outputs of different coincidence detectors for a 500-Hz sinusoidal signal. (a) Cross-correlation algorithm; (b) direct coincidence algorithm, spikes always interact when passing each other; (c) Wolf's algorithm; (d) Lindemann's algorithm; (e) coincidence algorithm with partly eliminated spikes after coincidence; and (f) cross-correlation algorithm taken to the power of 10 (solid lines, 0-ms ITD; dashed lines, 0.5-ms ITD)

coincide when they pass by each other on the delay lines. In this case the output of the coincidence function is not the product of the amplitudes in the left and right channel for each delay time, but rather the minimum of those two amplitudes. The signal amplitude, then, correlates with the number of spikes within the time interval of Δt as follows:

$$c_d(m, n) = \min[l(m, n), r(m, n)]. \quad (4)$$

The output characteristics of this algorithm, Fig. 3b, are quite similar to the output characteristics of the cross-correlation algorithm, with the exception that the peaks are slightly narrower at the top. In his original work, Wolf further assumed that two spikes would be canceled out after they coincide. This approach, however, is very sensitive to interaural level differences and, thus, the signals in the left and right channels have to be compressed in amplitude beforehand. For this reason, Wolf used a hair-cell model (Duifhuis 1972) to transform the signal-level code into a rate code. The output of Wolf's algorithm is shown in Fig. 3c. In contrast to the cross-correlation algorithm, the peaks are very narrow and the side peaks have vanished. Lindemann achieved a similar effect a few years earlier by introducing contralateral inhibition elements into

sinusoidal tones with ITDs of 0 and 0.5 ms are depicted. In contrast to the models reported in Blauert and Cobben (1978) and Stern and Colburn (1978), Wolf (1991) assumed that two spikes from opposite channels would always



Sound Localization in Mammals, Models, Fig. 4 Structure of the Lindemann algorithm

his model. The implementation of the inhibition elements is achieved by modifying the computation of the delay lines from Eqs. 1 and 2 to

$$l(m+1, n+1) = l(m, n)[1 - c_s \cdot r(m, n)]; \quad (5)$$

$$0 \leq l(m, n) < 1,$$

$$r(m+1, n-1) = r(m, n)[1 - c_s \cdot l(m, n)]; \quad (6)$$

$$0 \leq r(m, n) < 1,$$

with c_s being the static inhibition constant, $0 \leq c_s < 1$. Now the signals in both delay lines inhibit each other before they meet and reduce the amplitude of the signal in the opposite channel at the corresponding delay unit as can be seen in Fig. 4. The side peaks that are found in the plain cross-correlation algorithm in Fig. 3a are eliminated in this way. Wolf's algorithm becomes more similar to Lindemann's algorithm, if only a certain percentage of the spikes is canceled in Fig. 3e. In this case, it is not even necessary to use a probabilistic hair-cell model. If only a smaller amount of the spikes is eliminated, there is, qualitatively spoken, only a little difference in whether the spikes are inhibited/canceled before or after they coincide. It should be noted that the outcome of these inhibitory algorithms is dependent on the ILDs.

In the simulation of binaural hearing, it is sometimes advantageous to reduce the peak widths of the cross-correlation curves when determining the position of the peak. Besides employing an inhibition stage, a peak reduction

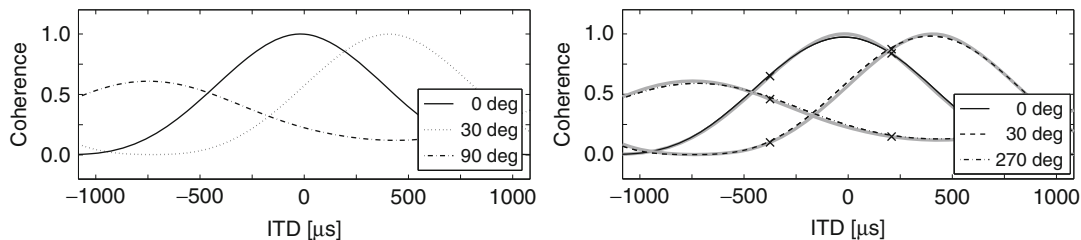
can be achieved by taking the signal to a power greater than one. Figure 3f shows this procedure for the power of 10. However, by this approach, the side peaks are hardly reduced.

When using the cross-correlation algorithm, not only the position of the cross-correlation peak but also its normalized height – the so-called interaural cross-correlation (IACC) coefficient or interaural coherence (IC) – can be used to gain information about the spaciousness of the environment, e.g., a room. It can be determined by taking the maximum of the normalized cross-correlation function,

$$\Psi_{y_l, r}(\tau) = \frac{\int_{t=-\infty}^{+\infty} y_l(t) \cdot y_r(t + \tau) dt}{\sqrt{\int_{t=-\infty}^{+\infty} y_l^2(t) dt \cdot \int_{t=-\infty}^{+\infty} y_r^2(t) dt}}, \quad (7)$$

with the internal delay, τ , and the left and right sound pressure signals, $y_l(t)$ and $y_r(t)$.

The left panel of Fig. 5 shows an example of an IACC function of a broadband noise signal for three different positions for a frequency band centered at 434 Hz. The peak of the solid cross-correlation function is located at 0 μ s which corresponds to the position at 0°. The peak of the dashed IACC function is located at 400 μ s, which indicates an azimuth of 30°. The height of the peak depicts the coherence, that is, the degree to



Sound Localization in Mammals, Models,
Fig. 5 *Left:* Interaural cross-correlation functions for a sound source at three different positions in the horizontal plane. The sound sources at 0° and 30° azimuth are fully correlated; the sound source at 270° is partly decorrelated. *Right:* Interaural cross-correlation functions for a sound source at three different positions in the horizontal plane. The same stimuli as in the left panel are used, but this time a two-channel model was applied with delay lines for

which both signals are similar when shifted by the corresponding internal delay, τ . In both cases, the signal is fully correlated. In the third example, depicted by a dash-dotted line, the signal is partly decorrelated as indicated by the lower peak height of 0.6. The peak location at $-600\ \mu\text{s}$ belongs to an azimuth angle of 270°.

The cross-correlation coefficient correlates strongly with “spaciousness” – or auditory source width – a psychoacoustical measure for the spatial extent of auditory events and an important parameter for room acousticians (Blauert and Lindemann (1986) and Okano et al. (1998)). Spaciousness decreases with an increasing correlation coefficient and, therefore, with the height of the cross-correlation peak (Fig. 5).

Two-Channel ITD Models

A few years ago the Jeffress model and with it the cross-correlation approach was challenged by physiological studies on gerbils and guinea pigs. McAlpine and Grothe (2003) and others (Grothe et al. 2010; McAlpine 2005; McAlpine et al. 2001; Pecka et al. 2008) have shown that the ITD cells for these species are not tuned evenly across the whole physiologically relevant range, but heavily concentrate on two phases of $\pm 45^\circ$.

Consequently, their absolute best-ITD values vary with the center frequency that the cells are

$\pm 45^\circ$. The actually measured values, x_- for the -45° -phase condition and x_+ for the $+45^\circ$ -phase condition, are shown by the “x” symbols. The simulated IACC curves were compensated for half-wave rectification. The gray curves show the actual IACC curves from the left panel. The normalized cross-correlation curves were estimated using standard trigonometric sine–cosine relationships for magnitude $A = \sqrt{x_-^2 + x_+^2}$ and phase $\phi = \arctan(x_-/x_+)$

tuned to. Dietz et al. (2011, 2008) and Pulkki and Hirvonen (2009) developed lateralization models that draw from McAlpine and Grothe’s (2003) findings. It is still under dispute whether the Jeffress delay-line model or the two-channel model correctly represents the human auditory system, since the human ITD mechanism cannot be studied directly on a neural basis. For other species, such as owls, a mechanism similar to the one proposed by Jeffress has been confirmed by Carr and Konishi (1990). For instance, opponents of the two-channel theory point out that the cross-correlation model has been tested much more rigorously than other ones and is able to predict human performance in great detail (Bernstein and Trahiotis 2002). From a practical standpoint, the result for both approaches is not as different as one might think. For the lower frequency bands, the cross-correlation functions always have a sinusoidal shape, due to the narrow width of the auditory bands – see the right panel of Fig. 5. Consequently, the whole cross-correlation function is more or less defined by two phase values 90° apart.

Models Utilizing Interaural Level Differences

Interaural level differences are the second major localization cue. They occur because of shadowing effects of the head, especially when a sound arrives sideways. For humans ILDs typically reach values of up to $\pm 30\ \text{dB}$ at frequencies

around 5 kHz and azimuth angles of $\pm 60^\circ$. At low frequencies the shadowing effect of the head is not very effective and ILDs hardly occur, unless the sound sources come very close to the ear canal entrance (Blauert 1997; Brungart and Rabinowitz 1999). This led Lord Rayleigh (1907) to postulate his *duplex theory*, which states that ILDs are the primary localization cue for high frequencies and ITDs for low frequencies. In the latter case, Lord Rayleigh assumed that unequivocal solutions for the ITDs can no longer exist for high frequencies. Then, the wavelength of the incoming sound is much shorter than the width of the head, which determines the physiological range for ITDs of approximately $\pm 800 \mu\text{s}$.

Mills (1958) later supported the duplex theory by demonstrating that the auditory system can no longer detect ITDs from the fine structure of signals above 1,500 Hz. This effect results from the inability of the human auditory system to phase lock the firing patterns of auditory cells with the waveform of the signal at these frequencies. Meanwhile, however, it has been shown that the auditory system can extract ITDs at high frequencies from the signals' envelopes (Joris

1996; Joris and Yin 1995), and the original duplex theory had to be revised accordingly.

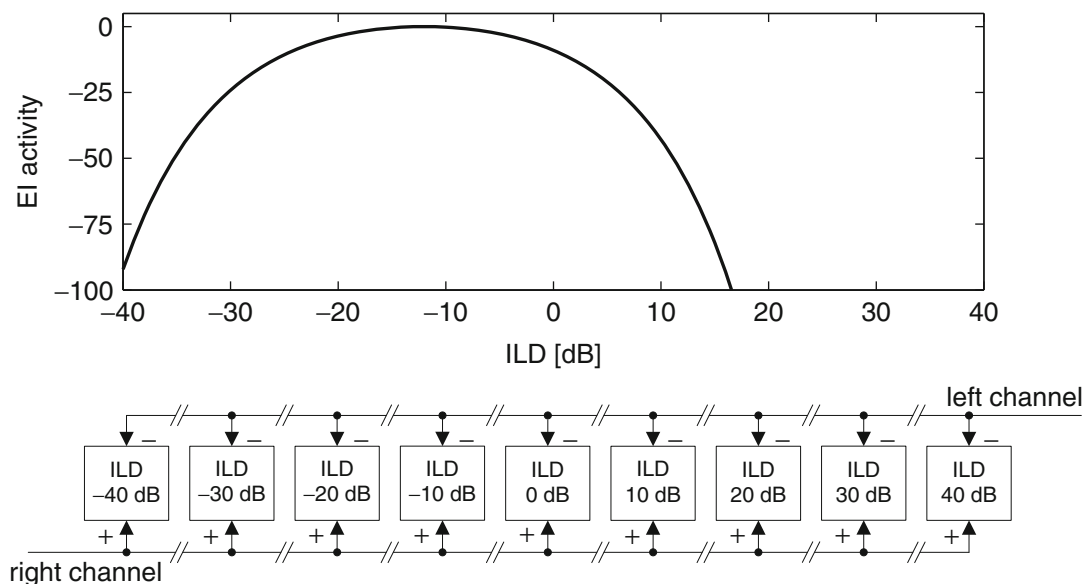
ILDs, denoted as α , can be computed directly from the left and right ear signals – which is typically done for individual frequency bands:

$$\alpha = 10\log_{10}(P_1) - 10\log_{10}(P_r), \quad (8)$$

with P_1 the power of the left and P_r the power of the right signal. Reed and Blum (1990) introduced a physiologically motivated algorithm to compute ILDs based on the activity, $E(\alpha)$, of an array of *excitation/inhibition* (EI) cells:

$$E(\alpha) = \exp \left[\left(10^{\alpha/\text{ILD}_{\max}} \sqrt{P_1} - 10^{-\alpha/\text{ILD}_{\max}} \sqrt{P_r} \right)^2 \right], \quad (9)$$

with P_1 and P_r being the power in the left and right channels, respectively, and ILD_{\max} the maximal ILD magnitude that the cells are tuned to. Each cell is tuned to a different ILD. Figure 6 shows an example for a sound with an ILD of -12 dB . The curve depicts how the response of each cell is reduced the further the applied ILD is away from the value the cell is tuned to.

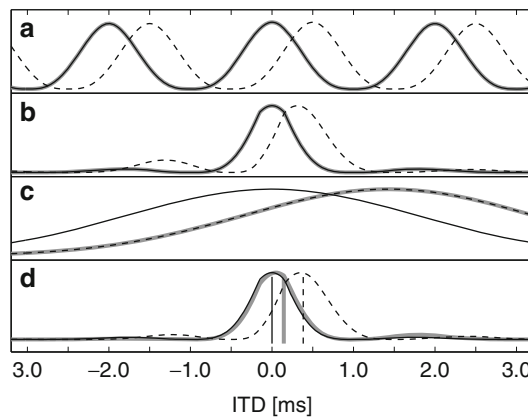


Sound Localization in Mammals, Models, Fig. 6 *Bottom:* EI-cell structure. *Top:* Output of the EI cells for a signal with an ILD of -12 dB .

Lateralization Models

Many models have been established to predict the perceived left/right lateralization of a sound which is presented to a listener through headphones with an ITD or an ILD or both. Usually, those sounds are perceived inside the head on the interaural axis with a distance from the center of the head. This distance, the so-called lateralization, is usually measured on an interval or ratio scale. The simplest implementation of a decision device is to correlate the perceived lateralization with the estimated value of a single cue, e.g., the position of the cross-correlation peak in one frequency band. This is possible, because the laterality, the perceived lateral position, is often found to be nearly proportional to the value of the analyzed cue.

The decision device has to be more complex if different cues are to be analyzed or if one cue under consideration is observed in different frequency bands. A very early model that integrates information from different cues, ITDs and ILDs, is the position-variable model of Stern and Colburn (1978). The authors were able to predict the perceived lateralization for a 500-Hz sinusoidal tone for all combinations of ITDs and ILDs. The left panels of Fig. 7 show the results of the position-variable model for three different combinations of ITDs and ILDs. The ITDs are measured using the cross-correlation algorithm of Fig. 7a. Afterward, the cross-correlation curve is multiplied by a delay-weighting function in order to enhance the output for small ITDs; see Fig. 7b. This is done to take into consideration that the number of neural fibers which are tuned to small ITDs is higher than those tuned to large ITDs. The delay-weighting function (Colburn 1977) is shown in Fig. 8, left panel, dotted curve. The influence of the ILDs is represented in a second function of Gaussian shape and constant width of 1,778 μ s, as depicted in Fig. 7c. The peak position of this second weighting is varied with the ILD of the signal. For this purpose, the signal's ILD, α , is calculated according to Eq. 8 and transferred into a corresponding ITD, τ , using a function which can be derived from psychoacoustical data as follows:



Sound Localization in Mammals, Models,

Fig. 7 Results for the position-variable model (Stern and Colburn 1978) for a 500-Hz sinusoidal signal with different combinations of ITD and ILD, namely, 0 ms/0 dB (black solid line), 0 ms/15 dB (gray solid line), and 0.5 ms/15 dB (black dashed line): (a) interaural cross-correlation functions, (b) delay-line weighted function of (a) to emphasize small ITD values, (c) ILD functions, and (d) combined ITD and ILD analysis by multiplying (b) with (c) and calculating the centroid as represented by the vertical lines

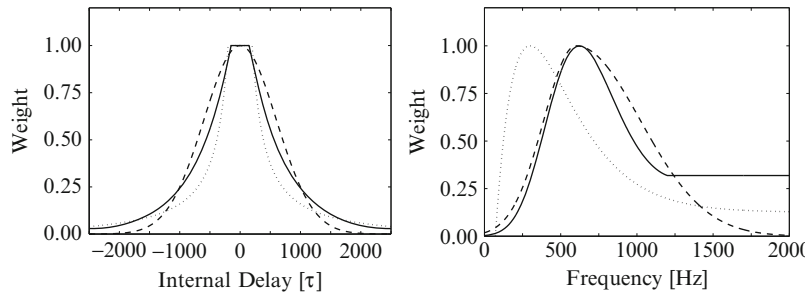
$$\tau = 0.1\alpha - 3.5 \cdot 10^{-5}\alpha^3[\text{ms}]. \quad (10)$$

Finally, this function is multiplied with the weighted cross-correlation function from Fig. 7b, and the centroid of the resulting function correlates with the perceived lateralization (Fig. 7d).

Localization in the Horizontal Plane

Several methods to calculate sound-source positions from the extracted binaural cues exist. One method of achieving this is to create a database to convert measured binaural cues, namely, ITDs and ILDs, into spherical coordinates.

Such a database or map can be derived from a measured catalog of *head-related transfer functions* (HRTFs) of a large number of sound-source directions. Here, the binaural cues are calculated frequency-wise from the left- and right-ear HRTFs of each position. Using this database, the measured binaural cues of a sound source with unknown positions can be mapped to spherical angles. The application of the remapping method to localize a signal in the horizontal



Sound Localization in Mammals, Models,

Fig. 8 Delay weighting (*left panel*): Colburn (1977), dotted line; Shackleton et al. (1992), solid line; and Stern and Shear (1996), dashed line. Frequency weighting (*right*

panel): Raatgever (1980), dotted line; Stern et al. (1988), solid line; and Akeroyd and Summerfield (1999), dashed line

plane is discussed in detail in Braasch et al. (2013). Figure 10 shows the results of remapped cross-correlation functions and ILD-based EI cell-array functions for different frequency bands. The results were obtained using a click source signal convolved with HRTFs from a human catalog at 0° elevation.

An ongoing challenge has been to figure out how the auditory system combines the individual cues to determine the location of auditory events – in particular to answer how the auditory system performs tasks to (i) combine different cue types, such as ILDs and ITDs, (ii) integrate information over time, (iii) integrate information over frequency, (iv) discriminate between concurrent sources, and (v) deal with room reflections.

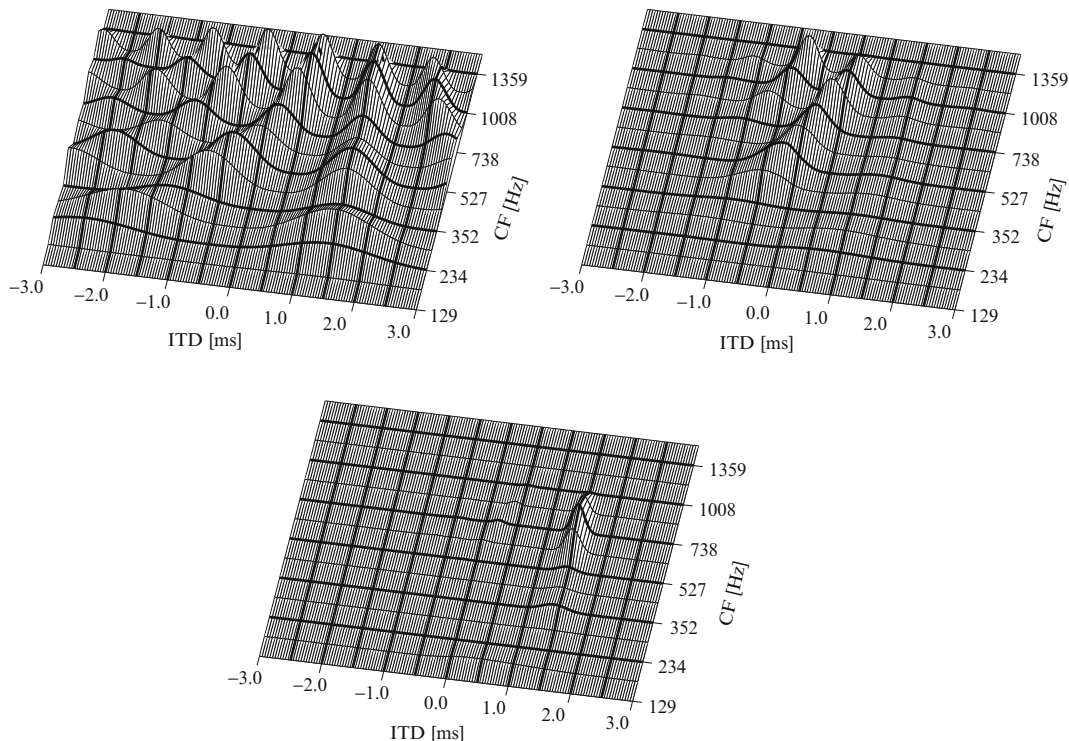
A number of detailed overviews (Stern and Trahiotis 1995; Stern et al. 2006; Braasch 2005) have been written on cue weighting, and only a brief introduction will be given here. One big question is how the auditory system weights cues temporally. The two opposing views are that the auditory system primarily focuses on the onset part of the signal versus the belief that the auditory system integrates information over a longer signal duration. Researchers have worked with conflicting cues – such as trade-off between early onset and later ongoing cues – and it is generally agreed upon that the early cues carry a heavier weight (Freyman et al. 1997; Haftor 1997; Zurek 1993). This phenomenon can be simulated with a temporal weighting function. More recently it was suggested that the auditory

system does not simply blindly combine these cues but also evaluates the robustness of these cues and discounts unreliable cues. A good example for this approach is a model by Faller and Merimaa (2004). In their model not only the positions of the cross-correlation peaks are calculated to determine the ITDs but also the coherence – as, for example, determined by the maximum value of the interaural cross-correlation function. Coherent time-frequency segments are considered to be more salient and weighted higher assuming that concurrent sound sources and wall reflections that can produce unreliable cues decorrelate the signal and thus show low coherence.

Frequency weighting also applies and, in fact, the duplex theory can be seen as an early model where ITD cues are weighted high at low frequencies, and ILD cues dominate at higher frequencies. Newer models have provided a more detailed view of how ITDs are weighted over frequency. Different curves have been obtained for different sound stimuli (Akeroyd and Summerfield 1999; Raatgever 1980) including straightness and centrality weighting (Stern et al. 1988, see Fig. 9).

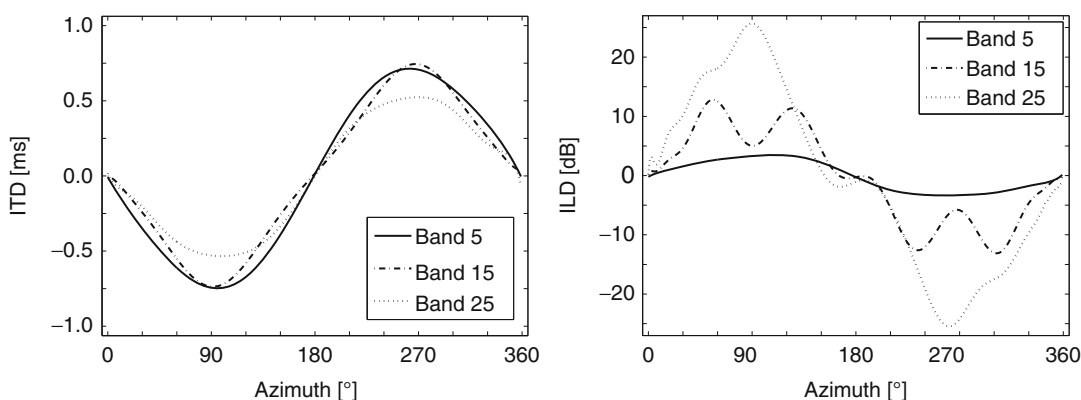
Localization Models Using Monaural Cues

A model proposed in 1969/1970 (Blauert 1969/1970) analyzes monaural cues in the median plane as follows. The powers in different frequency bands, the directional bands, are analyzed and compared to each other. Based on the signal's angle of incidence (front, above, or back),



Sound Localization in Mammals, Models,
Fig. 9 Output of Stern et al.'s model (Stern et al. 1988) to a band-pass noise, 700-Hz center frequency, 1,000-Hz bandwidth, 1.5-ms ITD. The *top-left panel* shows the

output without centrality and straightness weighting, the *top-right panel* with centrality weighting only, and the *bottom-left panel* with centrality and straightness weighting



Sound Localization in Mammals, Models,
Fig. 10 *Left:* Interaural time differences. *Right:* Interaural level differences. Plotted for different

frequency bands: Band 5, $f_c = 234$ Hz (*solid line*); Band 15, $f_c = 1,359$ Hz (*dashed line*); and Band 25, $f_c = 5,238$ Hz (*dotted line*)

the pinnae enhance or deemphasize the power in certain frequency regions, which are the primary localization cues for sound sources within the median plane. Building on this knowledge, Blauert's model uses a comparator to correctly predict the direction of the auditory event for narrowband signals.

Zakarauskas and Cynader (1993) developed an extended model for monaural localization, which is based on the assumption that the slope of a typical sound source's own frequency spectrum only changes gradually with frequency, while the pinnae-induced spectral changes vary more with frequency. The model primarily uses the second-order derivative of the spectrum in frequency to determine the elevation of the sound source – assuming that the sound source itself has a locally constant frequency slope. In this case, an internal, memorized representation of a sound source's characteristic spectrum becomes obsolete.

Baumgartner et al. (2013) created a probabilistic localization model that analyzes inter-spectral differences (ISDs) between the internal representations of a perceived sound and templates calculated for various angles. The model also includes listener-specific calibrations to 17 individual listeners. It had been shown earlier that, for some cases, ISDs can be a better predictor for human localization performance than the second-order derivative of the spectrum (Langendijk and Bronkhorst 2002). By finding the best ISD match between the analyzed sound and the templates, Baumgartner et al.'s model is able to demonstrate similar localization performance as human listeners.

In contrast to models which do not require a reference spectrum of a sound source before it is altered on the pathway from the source to the ear, it is sometimes assumed that listeners use internal representations of a variety of everyday sounds to which the ear signals are compared to in order to estimate the monaural cues. A database with the internal representations of a high number of common sounds has not been implemented in monaural model algorithms so far. Some models exist, however, that use an internal representation of a single reference

sound, e.g., for broadband noise (Hartung 1998) and for click trains (Janko et al. 1997).

Three-Dimensional Localization Models

In free field, the signals are filtered by the outer ears and the auditory events are, thus, usually perceived as externalized in three-dimensional space. One approach to estimate the position of a sound source is to train a neural network to estimate the auditory event from the interaural cues rather than to combine the cues analytically, e.g., Hartung (1998) and Janko et al. (1997). When applying such a method, the neuronal network has to be trained on test material. The advantage of this procedure is that often very good results are achieved for stimuli that are very similar to the test material. The disadvantages are, however, the long time necessary to train the neural network and that the involved processing cannot easily be described analytically.

The frequency-dependent relationship between binaural cues and the azimuth and elevation angles can be determined from a catalog of HRTFs which contains the HRTFs for several angles. Spatial maps of these relationships can be set up, using one map per analyzed frequency band. It should be noted at this point that, although neurons that are spatially tuned were found in the inferior colliculus of guinea pigs (Hartung 1998) and in the primary field of the auditory area of the cortex of cats (Middlebrooks and Pettigrew 1981; Imig et al. 1990), a topographical organization of those types of neurons could not be shown yet.

Those types of localization models that analyze both ITDs and ILDs either process both cues in a combined algorithm (e.g., Stern and Colburn 1978) or evaluate both cues separately and combine the results afterward, in order to estimate the position of the sound source (e.g., Janko et al. 1997; Nix and Hohmann 2000, 2006; Hartung 1998). In Janko et al. (1997) it is demonstrated that, for filtered clicks, both the ITDs and ILDs contribute very reliable cues in the left-right dimension, while in the front-back and the up-down dimensions, ILDs are more reliable than ITDs. The findings are based on

model simulations using a model that includes a neural network. The network was trained with a back-propagation algorithm on 144 different sound-source positions in the whole sphere, the positions being simulated using HRTFs. The authors could feed the neural network with either ITD cues, ILD cues, or both. Monaural cues could also be processed.

Precedence Effect Models

Dealing with room reflections remains to be one of the biggest challenges in communication acoustics across a large variety of tasks including sound localization, sound-source separation, as well as speech and other sound feature recognition. Typically, models use a simplified room impulse response, often only consisting of a direct sound and a single discrete reflection to simulate the precedence effect. Lindemann (1986a, b) took the following approach to the inhibition of location cues coming from reverberant information. Whenever his contralateral inhibition algorithm detects a signal at a specific interaural time difference, the mechanism starts to suppress information at all other internal delays or ITDs and thus solely focuses on the direct source signal component. The Lindemann model relies on onset cues to be able to inhibit reflections, but fairly recently Dizon and Colburn (2006) have shown that the onset of a mixture of an ongoing direct sound and its reflection can be truncated without affecting the precedence effect.

Based on their observation that human test participants can localize the on- and offset-truncated direct sound correctly in the presence of a reflection, Braasch and Blauert recently proposed an autocorrelation-based approach (Braasch and Blauert 2011). The model reduces the influence of the early specular reflections by autocorrelating the left and right ear signals. Separate autocorrelation functions for the left and right channels determine the delay times between the direct sound source and the reflection in addition to their amplitude ratios. These parameters are then used to steer adaptive deconvolution filters to eliminate each reflection separately. It is known from research on the *apparent source width* of auditory objects that our central nervous

system is able to extract information about early reflections (Barron and Marshall 1981), which supports this approach. The model is able to simulate the experiments from Dizon and Colburn's (2006) study.

Further it has been shown recently that for short test impulses such as clicks, localization dominance can be simulated using a simple cross-correlation algorithm without inhibition stages when a hair-cell model is included in the preprocessing stage (Hartung and Trahiotis 2001). To this end an adaptive hair-cell model (Meddis et al. 1990) was employed. Parts of the precedence effect are, thus, understood as results of sluggish processing in the auditory periphery. Further models to simulate the adaptive response of the auditory system to click trains, “buildup of the precedence effect,” can be found in Zurek (1987) and Djelani (2001).

Localization in Multiple-Sound-Source Scenarios

In general, physiologically motivated computational localization models have difficulties to localize two or more independent sound sources. A number of binaural localization models exist that are specialized to localize a test sound in the presence of distracting sound sources, but these models typically follow more traditional signal-processing methods and do not represent the neural mechanism with the same details some of the previously mentioned models do. In one class of models, termed “cocktail-party processors,” the information on the location of the sound sources is used to segregate them from each other (e.g., Bodden 1992; Lehn 2000). These algorithms can be used to improve the performance of speech recognition systems (Rateitschek 2000). For further improvement of binaural models, it has been proposed to implement an expert system, which completes the common signal-driven, bottom-up approach (Blauert 1999). The expert system should include explicit knowledge on the auditory scene and on the signals – and their history. This knowledge is to be used to set up hypotheses and to decide if they prove to be true or not. As an example, front-back differentiation can be named. The expert system could actively test

whether the hypothesis that the sound source is presented in the front is true or false, by employing “auditory scene analysis (ASA)” cues. It could further analyze the monaural spectrum of the sound source in order to estimate the influence of the room in which the sound source is presented, determine the interaural cues, and even evaluate cues from other modalities, for example, visual cues. The expert system would evaluate the reliability of the cues and weight them according to the outcome of the evaluation. In the future, once the computational power increases furthermore and more knowledge on the auditory system is gained, one can expect that binaural models will become more complex and include the simulation of several binaural phenomena rather than the simulation of only a few specific effects.

Matters become more complicated if it is not clear how many sound sources currently exist. Then the cues do not only have to be weighted properly but also assigned to the corresponding source. Here one can either take a target + background approach (Nix and Hohmann 2006), where only the target sound parameters are quantified and everything else is treated as noise, or one can attempt to determine the positions of all sound sources involved (Braasch 2002, 2003; Roman and Wang 2008). Often in models that segregate the individual sounds from a mixture, the positions of the sources are known a priori, such as in Bodden (1993) and Roman et al. (2006).

References

- Akeroyd MA, Summerfield Q (1999) A fully temporal account of the perception of dichotic pitches. *Br J Audiol* 33:106–107
- Barron M, Marshall AH (1981) Spatial impression due to early lateral reflections in concert halls: the derivation of a physical measure. *J Sound Vib* 77(2):211–232
- Baumgartner R, Majdak P, Laback B (2013) Assessment of sagittal-plane sound-localization performance in spatial-audio applications. In: Blauert J (ed) *The technology of binaural listening*, chapter 4. Springer, Berlin/Heidelberg/New York, pp 93–119
- Bernstein L, Trahiotis C (2002) Enhancing sensitivity to interaural delays at high frequencies by using “transposed stimuli”. *J Acoust Soc Am* 112:1026–1036
- Blauert J (1969/1970) Sound localization in the median plane. *Acustica*, 22:205–213
- Blauert J (1997) Spatial hearing: the psychophysics of human sound localization (2nd revised). MIT Press, Berlin/Heidelberg/New York
- Blauert J (1999) Spatial hearing (Revised edition). Massachusetts Institute of Technology, Boston
- Blauert J, Cobben W (1978) Some consideration of binaural cross correlation analysis. *Acustica* 39:96–104
- Blauert J, Lindemann W (1986) Auditory spaciousness: some further psychoacoustic analysis. *J Acoust Soc Am* 80:533–542
- Bodden M (1992) *Binaurale Signalverarbeitung: Modellierung der Richtungserkennung und des Cocktail-Party-Effektes* [Binaural signal processing: modelling the recognition of direction and the cocktail-party effect]. Ph.D. thesis, Ruhr-University Bochum, Bochum
- Bodden M (1993) Modeling human sound-source localization and the cocktail-party effect. *Act Acust/Acoustica* 1:43–55
- Braasch J (2002) Localization in the presence of a distracter and reverberation in the frontal horizontal plane: II. Model algorithms. *Act Acust/Acoustica* 88(6):956–969
- Braasch J (2003) Localization in the presence of a distracter and reverberation in the frontal horizontal plane: III. The role of interaural level differences. *Act Acust/Acoustica* 89(4):674–692
- Braasch J (2005) Modeling of binaural hearing. In: Blauert J (ed) *Communication acoustics*. Springer Verlag, Berlin, pp 75–108
- Braasch J, Blauert J (2011) Stimulus-dependent adaptation of inhibitory elements in precedence-effect models. In: *Proceeding Forum Acusticum 2011*. Aalborg, pp 2115–2120
- Braasch J, Clapp S, Parks A, Pastore T, Xiang N (2013) A Binaural Model that Analyses Acoustic Spaces and Stereophonic Reproduction Systems by Utilizing Head Rotations. In: Jens Blauert (ed) *The Technology of Binaural Listening*. Springer Berlin Heidelberg, pp 201–223
- Brungart D, Rabinowitz W (1999) Auditory localization of nearby sources. Head-related transfer functions. *J Acoust Soc Am* 106:1465–1479
- Cai H, Carney LH, Colburn HS (1998a) A model for binaural response properties of inferior colliculus neurons. I. A model with interaural time difference-sensitive excitatory and inhibitory inputs. *J Acoust Soc Am* 103:475–493
- Cai H, Carney LH, Colburn HS (1998b) A model for binaural response properties of inferior colliculus neurons. II. A model with interaural time difference-sensitive excitatory and inhibitory inputs and an adaptation mechanism. *J Acoust Soc Am* 103:494–506

- Carr CE, Konishi M (1990) A circuit for detection of interaural time differences in the brain stem of the barn owl. *J Neurosci* 10(10):3227–3246
- Cherry EC, Sayers BMA (1956) “Human ‘cross-correlator’” – a technique for measuring certain parameters of speech perception. *J Acoust Soc Am* 28(5):889–895
- Colburn HS (1977) Theory of binaural interaction based on auditory-nerve data. II. Detection of tones in noise. *J Acoust Soc Am* 61:525–533
- Dietz M, Ewert SD, Hohmann V, Kollmeier B (2008) Coding of temporally fluctuating interaural timing disparities in a binaural processing model based on phase differences. *Brain Res* 1220:234–245
- Dietz M, Ewert SD, Hohmann V (2011) Auditory model based direction estimation of concurrent speakers from binaural signals. *Speech Commun* 53(5):592–605
- Dizon RM, Colburn HS (2006) The influence of spectral, temporal, and interaural stimulus variations on the precedence effect. *J Acoust Soc Am* 119:2947–2964
- Djelani T (2001) Psychoakustische Untersuchungen und Modellierungsansätze zur Aufbauphase des auditiven Präzedenzeffektes. Ph.D. thesis, Ruhr-Universität Bochum
- Duijhuis H (1972) Perceptual analysis of sound. Ph.D. thesis, Techn Hogeschool Eindhoven, Eindhoven
- Faller C, Merimaa J (2004) Source localization in complex listening situations: SELECTION of binaural cues based on interaural coherence. *J Acoust Soc Am* 116:3075–3089
- Freyman RL, Zurek PM, Balakrishnan U, Chiang YC (1997) Onset dominance in lateralization. *J Acoust Soc Am* 101:1649–1659
- Grantham DW (1979) Discrimination of dynamic interaural intensity differences. *J Acoust Soc Am* 76:71–76
- Grantham DW (1982) Detectability of time-varying interaural correlation in narrow-band noise stimuli. *J Acoust Soc Am* 72:1178–1184
- Grantham DW, Wightman FL (1978) Detectability of varying interaural temporal differences. *J Acoust Soc Am* 63:511–523
- Grantham DW, Wightman FL (1979) Detectability of a pulsed tone in the presence of a masker with time-varying inter-aural correlation. *J Acoust Soc Am* 65:1509–1517
- Grothe B, Pecka M, McAlpine D (2010) Mechanisms of sound localization in mammals. *Physiol Rev* 90(3):983–1012
- Hafter E (1997) Binaural adaptation and the effectiveness of a stimulus beyond its onset. In: Gilkey RH, Anderson TR (eds) *Binaural and spatial hearing in real and virtual environments*. Lawrence Erlbaum, Mahwah, pp 211–232
- Hartung K (1998). Modellalgorithmen zum Richtungshören, basierend auf Ergebnissen psychoakustischer und neurophysiologischer Experimente mit virtuellen Schallquellen [Model algorithms regarding directional hearing, based on psychoacoustic and neurophysiological experiments with virtual sound sources]. Ph.D. thesis, Ruhr-University Bochum, Bochum
- Hartung K, Trahiotis C (2001) Peripheral auditory processing and investigations of the “precedence effect” which utilize successive transient stimuli. *J Acoust Soc Am* 110:1505–1513
- Imig TJ, Irons WA, Samson FR (1990) Single-unit selectivity to azimuthal direction and sound pressure level of noise bursts in cat high frequency auditory cortex. *J Neurophysiol* 63:1448–1466
- Jankó J, Anderson T, Gilkey R (1997) Using neural networks to evaluate the viability of monaural and interaural cues for sound localization. In: Gilkey RH, Anderson TR (eds) *Binaural and spatial hearing in real and virtual environments*. Lawrence Erlbaum Associates, Mahwah, pp 557–570
- Jeffress LA (1948) A place theory of sound localization. *J Comp Physiol Psychol* 41:35–39
- Joris P (1996) Envelope coding in the lateral superior olive. II. Characteristic delays and comparison with responses in the medial superior olive. *J Neurophysiol* 76:2137–2156
- Joris P, Yin T (1995) Envelope coding in the lateral superior olive. I. Sensitivity to interaural time differences. *J Neurophysiol* 73:1043–1062
- Kollmeier B, Gilkey RH (1990) Binaural forward and backward masking: evidence for sluggishness in binaural detection. *J Acoust Soc Am* 87:1709–1719
- Langendijk EHA, Bronkhorst AW (2002) Contribution of spectral cues to human sound localization. *J Acoust Soc Am* 112(4):1583–1596
- Lehn K (2000) Unscharfe zeitliche Clusteranalyse von monauralen und inter-auralen Merkmalen als Modell der auditiven Szenenanalyse [Fuzzy time-based cluster analysis of monaural and inter-aural cues as a model of auditory scene analysis]. Ph.D. thesis, Ruhr-University Bochum, Bochum
- Lindemann W (1986a) Extension of a binaural cross-correlation model by contralateral inhibition. I. Simulation of lateralization of stationary signals. *J Acoust Soc Am* 80:1608–1622
- Lindemann W (1986b) Extension of a binaural cross-correlation model by contralateral inhibition. II. The law of the first wave front. *J Acoust Soc Am* 80:1623–1630
- McAlpine D (2005) Creating a sense of auditory space. *J Physiol* 566(1):21–28
- McAlpine D, Grothe B (2003) Sound localisation and delay lines – do mammals fit the model? *Trend Neurosci* 26:347–350
- McAlpine D, Jiang D, Palmer AR (2001) A neural code for low-frequency sound localization in mammals. *Nat Neurosci* 4(4):396–401
- Meddis R, Hewitt MJ, Shakleton TM (1990) Implementation details of a computational model of the inner hair-cell auditory-nerve synapse. *J Acoust Soc Am* 87:1813–1816
- Middlebrooks JC, Pettigrew JD (1981) Functional classes of neurons in primary auditory cortex of the cat

- distinguished by sensitivity to sound localization. *J Neurophysiol* 1:107–120
- Mills AW (1958) On the minimum audible angle. *J Acoust Soc Am* 30:237–246
- Nix J, Hohmann V (2000) Robuste Lokalisation im Störgeräusch auf der Basis statistischer Referenzen. In: *Fortschr Akust DAGA* 2000, pp 474–475
- Nix J, Hohmann V (2006) Sound source localization in real sound fields based on empirical statistics of interaural parameters. *J Acoust Soc Am* 119:463–479
- Okano T, Beranek LL, Hidaka T (1998) Relations among interaural cross-correlation coefficient ($IACC_E$), lateral fraction (LF_E), and apparent source width (ASW) in concert halls. *J Acoust Soc Am* 104:255–265
- Pecka M, Brand A, Behrend O, Grothe B (2008) Interaural time difference processing in the mammalian medial superior olive: the role of glycinergic inhibition. *J Neurosci* 28(27):6914–6925
- Pulkki V, Hirvonen T (2009) Functional count-comparison model for binaural decoding. *Act Acust/Acoustica* 95(5):883–900
- Raatgever J (1980) On the binaural processing of stimuli with different interaural phase relations. Ph.D. thesis, Delft University of Technology, Delft
- Rateitschek K (2000) Ein binauraler Signalverarbeitungsansatz zur robusten maschinellen Spracherkennung in lärmfüllter Umgebung [A binaural signal processing approach to robust speech recognition in noisy environments]. Ph.D. thesis, Ruhr-University Bochum, Bochum
- Rayleigh L (1907) On our perception of sound direction. *Phil Mag* 13:214–232
- Reed M, Blum J (1990) A model for the computation and encoding of azimuthal information by the lateral superior olive. *J Acoust Soc Am* 88:1442–1453
- Roman N, Wang D (2008) Binaural tracking of multiple moving sources. *IEEE Trans Audio Speech Lang Processing* 16(4):728–739
- Roman N, Srinivasan S, Wang D (2006) Binaural segregation in multisource reverberant environments. *J Acoust Soc Am* 120(6):4040–4051
- Sayers BM, Cherry EC (1957) Mechanism of binaural fusion in the hearing of speech. *J Acoust Soc Am* 29:973–987
- Shackleton TM, Meddis R, Hewitt MJ (1992) Across frequency integration in a model of lateralization. *J Acoust Soc Am* 91:2276–2279
- Stecker GC, Harrington IA, Middlebrooks JC (2005) Location coding by opponent neural populations in the auditory cortex. *PLoS Biol* 3(3):520–528
- Steinhauser A (1877) The theory of binaural audition. *Phil Mag* 7(181–197):261–274
- Stern R, Colburn H (1978) Theory of binaural interaction based on auditory-nerve data. IV. A model for subjective lateral position. *J Acoust Soc Am* 64:127–140
- Stern RM, Shear GD (1996) Lateralization and detection of low-frequency binaural stimuli: effects of distribution of internal delay. *J Acoust Soc Am* 100:2278–2288
- Stern RM, Trahiotis C (1995) Models of binaural interaction. In: Moore BCJ (ed) *Hearing*. Academic Press, New York, pp 347–386
- Stern RM, Zeiberg AS, Trahiotis C (1988) Lateralization of complex binaural stimuli: a weighted-image model. *J Acoust Soc Am* 84:156–165
- Stern R, Wang D, Brown G (2006) Binaural sound localization. In: Wang D, Brown G (eds) *Computational auditory scene analysis*. Wiley Interscience, Hoboken, pp 147–186
- Thompson SP (1877) On binaural audition. *Phil Mag* 4:274–276
- Thompson SP (1882) On the function of the two ears in the perception of space. *Phil Mag* 13:406–416
- Wolf S (1991) Untersuchungen zur Lokalisation von Schallquellen in geschlossenen Räumen. Ph.D. thesis, Ruhr-University Bochum, Bochum
- Zakarauskas P, Cynader M (1993) A computational theory of spectral cue localization. *J Acoust Soc Am* 94:1323–1331
- Zurek PM (1987) The precedence effect. In: Yost WA, Gourevitch G (eds) *Directional hearing*. Springer, New York, pp 85–105
- Zurek PM (1993) A note on onset effects in binaural hearing. *J Acoust Soc Am* 93:1200–1201

Sound Source Identification

► Acoustic Timbre Recognition

Sound Source Separation

► Auditory Perceptual Organization

Space (Length) Constant, Lambda, in Neuronal Signaling

William R. Holmes

Department of Biological Sciences, Ohio University, Athens, OH, USA

Definition

The space (length) constant λ with $\lambda = (R_m d / (4R_a))^{1/2}$ is a measure of steady-state voltage

decay with distance in a cell. Quantitatively λ is the distance over which the steady-state voltage decays to $1/e$ or 37 % of its value at the origin in a semi-infinite cable.

Detailed Description

As given in the definition above, the space constant λ with $\lambda = (R_m d / (4R_a))^{1/2}$ is a measure of steady-state voltage decay in a cell. Quantitatively λ is the distance (usually expressed in cm or μm) over which the steady-state voltage decays to $1/e$ or 37 % of its value at the origin in a semi-infinite cable. This can be seen by solving the steady-state cable equation (Rall 1977)

$$\lambda^2 d^2 V / dx^2 - V = 0$$

with boundary conditions of voltage clamp to V_0 at the origin and voltage bounded at $x = \infty$ to get

$$V(x) = V_0 \exp(-x/\lambda).$$

The above equation is useful to describe voltage displacements from rest. A more general solution for voltage decay with distance that includes resting potential explicitly is

$$V(x) = V_{\text{rest}} - (V_{\text{rest}} - V_0) \exp(-x/\lambda)$$

where now V_0 is actual voltage instead of a difference from rest.

The importance of λ is that it determines how spatially separated inputs are integrated (spatial summation). If λ is small, then spatially separated inputs are unlikely to sum because voltage will decay significantly over the distance between the inputs, but if λ is large, inputs will not decay as much with distance allowing summation to occur. Given the formula for λ , spatial summation is more likely to occur when diameter or membrane resistivity is large or axial resistivity is small.

One must be careful not to equate quantitatively the steady-state voltage decrement with distance for the semi-infinite cylinder with

voltage decay in finite cylinders. For finite cylinders steady-state voltage decay with distance will depend strongly on both the boundary conditions and the length of the cylinders (see entry “► [Cable Equation](#)”), and for transient inputs voltage decay with distance will be very different. Conductance changes associated with transient inputs may make λ variable in time; depending on the level of background synaptic activity, λ may be large at one moment and small at another causing effective spatial integration to vary widely.

The definition of λ given above is for the special case where extracellular voltage is assumed to be isopotential. In the derivation of the cable equation, a generalized λ is defined as

$$\lambda = \sqrt{\frac{r_m}{r_i + r_e}}$$

where r_m is membrane resistance of a unit length of membrane in Ωcm and r_i and r_e are the intracellular and extracellular resistances per unit length in Ω/cm . In single cell models, it is usually appropriate to neglect r_e unless ephaptic interactions are a concern. If we neglect r_e then

$$\lambda = \sqrt{\frac{r_m}{r_i}} \text{ or in terms of specific resistivities}$$

$$\lambda = \sqrt{\frac{R_m d}{4R_a}}$$

Setting r_e to 0 in the above expression for λ leads to another insight when the equation is expressed as $\lambda r_i = r_m / \lambda$. What this equation says is that λ corresponds to the length of the core conductor for which the core resistance (λr_i) equals the resistance (r_m / λ) across the membrane.

References

- Rall W (1977) Core conductor theory and cable properties of neurons. In: *Handbook of physiology. The nervous system. Cellular biology of neurons*, sect 1, vol I, pt 1, chap 3. American Physiological Society, Bethesda, pp 39–97

Sparse Coding of Natural Images

- ▶ Independent Component Analysis of Images

Spatial Modeling

- ▶ Metabotropic Receptors (G Protein Coupled Receptors)

Spatial Spectral Analysis

Armin Fuchs

Center for Complex Systems and Brain Sciences,
Florida Atlantic University, Boca Raton, USA

Definition

Spatial spectral methods are extensions of the well-known Fourier transform in time into the spatial domain. Whereas the basis functions for the Fourier transform are sine and cosine or complex exponentials, the bases used in space often reflect a symmetry of the problem. Common basis sets are plane waves (Cartesian space), Bessel functions (circular and cylindrical symmetry), and spherical harmonics (sphere). Moreover, basis vectors can be derived from the dataset under consideration that are optimal with respect to certain criteria like mean squared error.

Detailed Description

Spectral methods are best known from the Fourier transform that decomposes a time series into its frequency components. Spectral methods in space are applied to datasets that are recorded at different locations in space like EEG (electroencephalography is recorded with up to several hundred electrodes attached to different locations on the scalp surface), MEG

(magnetoencephalography measures the magnetic field created by electric currents inside the brain at the locations of sensors surrounding the head), or even fMRI (functional magnetic resonance imaging, where brain activity is measured at locations inside a 3-dimensional volume).

In general, a spatial pattern that evolves in time is decomposed into a set of functions that depend only on space and corresponding time series representing their amplitudes. To be specific, one can think of an EEG experiment where the electric potential at the scalp surface is recorded at N different locations. Such a dataset can be written as a vector $\mathbf{H}(t)$, where component $H_i(t)$ is the time series from electrode i . On the other hand, for a given time point t , the N components of \mathbf{H} represent a discrete spatial pattern of activity on the scalp surface. If N is sufficiently large, the potential can be described as a continuous function of space and time $H(x, t)$. For the spatially discrete and continuous cases, the decompositions read

$$\mathbf{H}(t) = \sum_{i=1}^M \xi_i(t) \mathbf{v}^{(i)} \quad H(x, t) = \sum_{i=1}^M \eta_i(t) g^{(i)}(x) \quad (1)$$

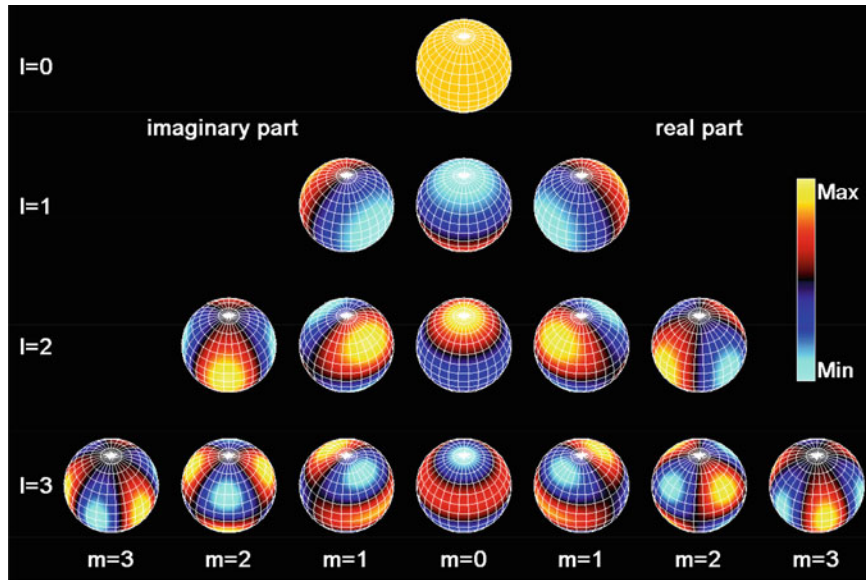
where $\xi_i(t)$ and $\eta_i(t)$ are the time-dependent amplitudes that correspond to the pattern vectors and functions $\mathbf{v}^{(i)}$ and $g^{(i)}(x)$, respectively.

One application of such decompositions is the reduction of the size of the dataset, i.e., the sums are truncated at a value $M \ll N$. How well such a truncated decomposition represents the original data obviously depends on the choice of the basis vectors $\mathbf{v}^{(i)}$ or basis functions $g^{(i)}(x)$.

One of the most popular function sets to describe scalp potentials is the spherical harmonics [Nunez and Srinivasan 2006] given by

$$Y_l^m(\theta, \phi) = \sqrt{\frac{(2l+1)}{4\pi} \frac{(l-m)!}{(l+m)!}} P_l^m(\cos \theta) e^{im\phi} \quad (2)$$

where θ and ϕ are the polar and azimuthal angle, respectively, and P_l^m are the associate Legendre polynomials of degree l and order m .



Spatial Spectral Analysis, Fig. 1 The spatial patterns for the spherical harmonics with $l = 0 \dots 3$ and $m = 0 \dots 3$ plotted on a sphere with the real parts of the

complex-valued functions on the *right* and the imaginary parts on the *left*

The spherical harmonics are orthogonal and normalized such that

$$\int_0^{2\pi} d\phi \int_0^\pi \sin \theta d\theta Y_l^{m'}(\theta, \phi) Y_l^{m*}(\theta, \phi) = \delta_{ll'} \delta_{mm'} \quad (3)$$

where the asterisk “*” denotes the complex conjugate and δ represents the Kronecker delta.

The spatial patterns on the sphere for $l = 0 \dots 3$ and $m = 0 \dots 3$ are shown in Fig. 1 with the real and imaginary parts of the complex-valued functions on the right and left. The value for m is the number of minima and maxima in the azimuthal direction and Y_0^0 is a constant with a value of $1/\sqrt{4\pi}$.

The spherical harmonics in space are closely related to the Fourier series in time as both are the eigenfunctions to an operator (The eigenfunctions of an operator are similar to the eigenvectors of a matrix. The application of a matrix to one of its eigenvectors simply scales the vector and nothing else, $Mv = \lambda v$, where λ is a scalar, the eigenvalue. In the same way, an operator applied to one of its eigenfunctions results in the same function times a scalar

$O(f(x) = \lambda f(x))$ that takes a second derivative. For the Fourier series in sine and cosine or complex exponentials, this takes the form

$$\begin{aligned} \frac{d^2}{dt^2} \cos \omega t &= -\omega^2 \cos \omega t \\ \frac{d^2}{dt^2} \sin \omega t &= -\omega^2 \sin \omega t \\ \frac{d^2}{dt^2} e^{i\omega t} &= -\omega^2 e^{i\omega t} \end{aligned}$$

In space, in Cartesian coordinates, the Laplace operator, Δ , is simply the sum of the second derivatives, whereas in spherical coordinates, its form is more complicated. Explicitly, on a unit sphere, the angular part, $\Delta_{\theta\phi}$, applied to the spherical harmonics reproduces these functions times a constant

$$\begin{aligned} \Delta_{\theta\phi} &= \frac{1}{\sin \theta} \frac{\partial}{\partial \theta} \sin \theta \frac{\partial}{\partial \theta} + \frac{1}{\sin^2 \theta} \frac{\partial^2}{\partial \phi^2} \\ \Delta_{\theta\phi} Y_l^m(\theta, \phi) &= m(m+1) Y_l^m(\theta, \phi) \end{aligned}$$

In other words, the spherical harmonics $Y_l^m(\theta, \phi)$ are the eigenfunctions to the angular part of the Laplacian in spherical coordinates with eigenvalues $m(m+1)$.

Data-Dependent Basis: PCA

Instead of using a system of predefined basis vectors or functions, there are ways to calculate a basis from the dataset itself that is optimal in a certain sense to the specific data under consideration [Johnson and Wichern 2007, Jolliffe 2002]. One such procedure is known as principal component analysis (PCA) (Other names for identical or very similar methods are Karhunen-Loëve transform (KLT) or singular value decomposition (SVD)), where the basis is obtained as the eigenvectors $\mathbf{v}^{(i)}$ of the covariance matrix, C . Specifically, assuming a dataset of time series from N electrodes in EEG, the covariance matrix is an $N \times N$ matrix and calculated as

$$C_{ij} = \frac{1}{T} \int_0^T dt \{H_i(t) - \bar{H}_i\} \{H_j(t) - \bar{H}_j\} \quad (4)$$

where \bar{H}_i and \bar{H}_j are the mean values over time of $H_i(t)$ and $H_j(t)$, respectively. The eigenvalues of C , λ_i are a measure of the contribution of the corresponding eigenvector to the dataset. In many applications 90–95% of the entire variance is represented by a few of the eigenvectors corresponding to the largest eigenvalues. The time series of the amplitudes for the eigenvectors are obtained as

$$\xi_i(t) = \mathbf{H}(t) \cdot \mathbf{v}^{(i)} = \sum_{n=1}^N H_n(t) v_n^{(i)} \quad (5)$$

As the covariance matrix is real, symmetric, and positive semi-definite, all eigenvalues are real and nonnegative, and the eigenvectors are mutually orthogonal. Moreover, the time series for the amplitudes $\xi_i(t)$ are also orthogonal and fulfill the relation

$$\int_0^T dt \xi_i(t) \xi_j(t) = \lambda_i \delta_{ij} \quad (6)$$

Principal component analysis is optimal in the sense that it minimizes the mean squared error between the dataset and its expansion for all truncation points. This means that if the

decomposition is taken up to a point M and $\mathbf{v}^{(m)}$ are the eigenvectors corresponding to the M largest eigenvalues, the error E_M defined as

$$E_M = \sum_{n=1}^N \int_0^T dt \left\{ H_n(t) - \sum_{i=1}^M \xi_i(t) v_n^{(i)} \right\}^2 = \text{Min} \forall M \quad (7)$$

is a minimum independent of M , i.e., there is no set of M basis vectors that carry more of the variance of the dataset than the eigenvectors $\mathbf{v}^{(m)}$ of the covariance matrix.

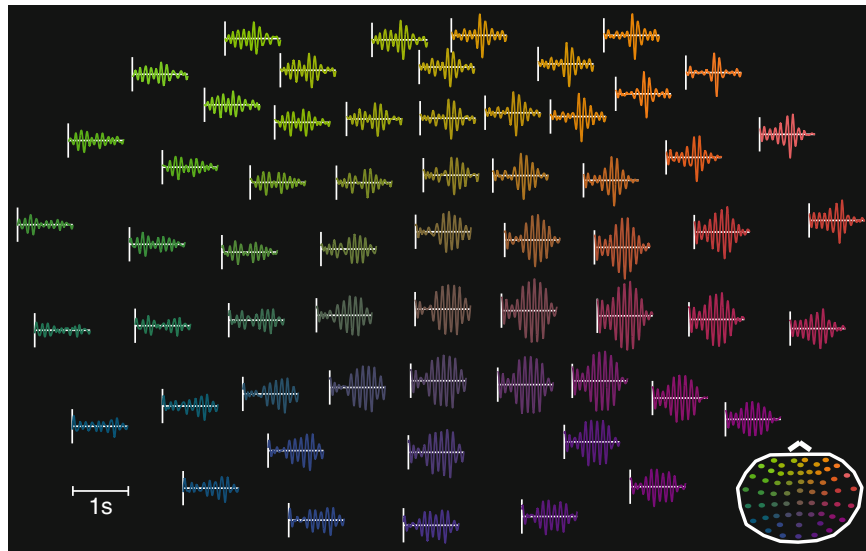
Explicit Example

A short dataset representing 1 s from an EEG recording using a montage with 60 electrodes is shown in Fig. 2. The time series are arranged and color-coded in a topological layout corresponding to the spatial locations of the electrodes on the scalp surface (also shown in the insert). The same color coding for the time series is used in the butterfly plot in Fig. 3a, which also shows the spatial pattern of the potential at the maxima and minima. This dataset is decomposed by calculating the 60×60 covariance matrix as in Eq. 4, finding its eigenvalues and eigenvectors, and determining the amplitudes of the spatial patterns according to Eq. 5.

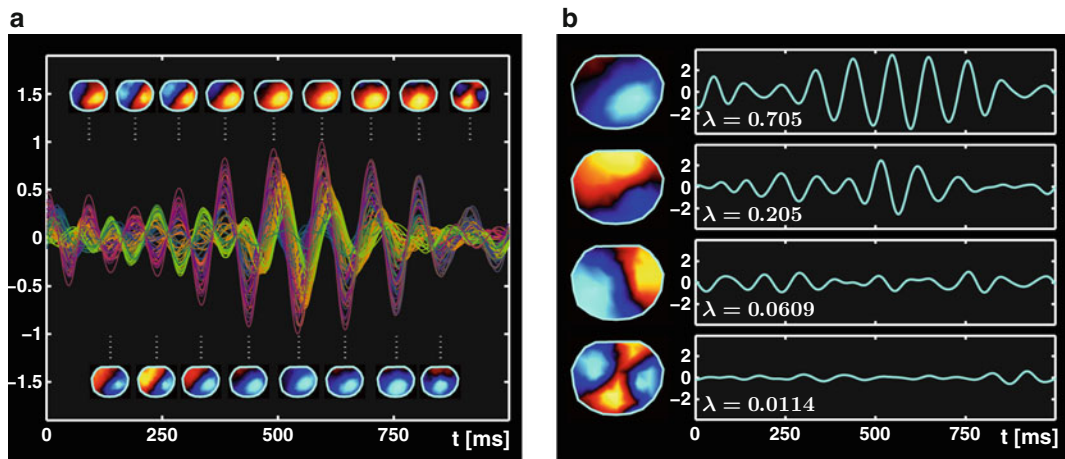
The results are shown in Fig. 3b with the four dominating spatial pattern, i.e., the eigenvectors corresponding to the four largest eigenvalues on the left and their time-dependent amplitudes on the right. The eigenvalues sum up to 0.9823, which means that more than 98 % of the total variance in the original 60-dimensional dataset is covered by these four patterns and their amplitudes.

Summary and Conclusions

Spatial spectral methods, in general, are used to perform a separation of a spatiotemporal signal into patterns that depend only on space and corresponding time-dependent amplitudes,



Spatial Spectral Analysis, Fig. 2 Sample dataset of an EEG recording of 1 s from 60 different locations on the scalp surface as shown in the insert



Spatial Spectral Analysis, Fig. 3 The dataset and its decomposition using PCA. (a) Superposition of the time series (butterfly plot) with the color coding used in Fig. 2 together with topographical plots showing the spatial

patterns at the maxima and minima. (b) Spatial patterns representing the eigenvectors $v^{(1-4)}$ that correspond to the four largest eigenvalues (left). Time-dependent amplitudes $\xi_{1-4}(t)$ and eigenvalues λ_{1-4} (right)

which may lead to a strong compression of the original dataset while keeping the relevant information. On the other hand, methods like PCA can also be used to detect artifacts (like bad electrodes in EEG) as they may get lumped into an individual pattern and can then be removed from the dataset. Aside from those representing artifacts, one should not attempt to interpret

individual spatial patterns obtained by PCA as a manifestation of underlying separate sources because due to the way they are obtained (as eigenvectors of a real, symmetric matrix), they are mutually orthogonal, a constraint that is in general incompatible with activity patterns originating from different sources inside the brain. There are other decomposition techniques

like independent component analysis (ICA) where the patterns do not have to be orthogonal but a further discussion of such methods is beyond the scope of this entry.

References

- Johnson RA, Wichern DW (2007) Applied multivariate statistical analysis, 7th edn. Prentice Hall, Upper Saddle River, NJ
- Jolliffe IT (2002) Principal component analysis, 2nd edn. Springer, Heidelberg
- Nunez PL, Srinivasan R (2006) Electric fields of the brain – the neurophysics of EEG, 2nd edn. Oxford University Press, Oxford

If t_1 and t_2 are taken at infinite resolution, the probability of observing it twice is zero. Therefore, some time accuracy (Δt) is associated with the pattern such that B occurred at $[t_1 \pm \Delta t/2]$ after A and C at $[t_2 \pm \Delta t/2]$ after A. Figure 1 illustrates such a precise spatiotemporal pattern.

Variations In some works the value of Δt was varied and allowed to become longer, the longer is the delay t_i . In some works, just the order of events (disregarding the exact time interval between successive events) was also considered as a spatiotemporal pattern.

Detailed Description

History

Numerous publications mentioned observing precise spatiotemporal patterns in neuronal data (see Abeles and Gat 2001 for a partial list). The first ones to make a systematic search for such patterns were Dayhoff and Gerstein (1983a, b), who looked for repeating sequences of inter-spike intervals in the recorded activity of a single unit in the cat cortex. The first to systematically search for such patterns in parallel spike trains were Abeles and Gerstein (1988). Both reported significant excess. However, their methods for evaluating significance were criticized (Oram et al. 1999; Baker and Lemon 2000).

Meaning of Finding Precise Patterns

Existence of significant precise spatiotemporal patterns is taken as evidence that there is some mechanism that precisely controls the timing of events in the involved point processes. That relates to the question of how information is coded and transmitted within the cortex. Is it by firing rate, oscillations, precise synchrony, or delayed synchrony (► Neural Coding)? For that the question whether there exists some mechanism that produces precise timing (and can read it) is so important. In a single neuron, precise firing patterns may be produced in a burst of spikes, and periodic oscillations may be produced by internal pacemaker mechanism or in an oscillating network. The main interest in repeating

Spatial Temporal Spike Pattern Analysis

Moshe Abeles

The Leslie and Susan Gonda(Goldschmied)
Multidisciplinary Brain Research Center, Bar-Ilan
University, Ramat-Gan, Israel

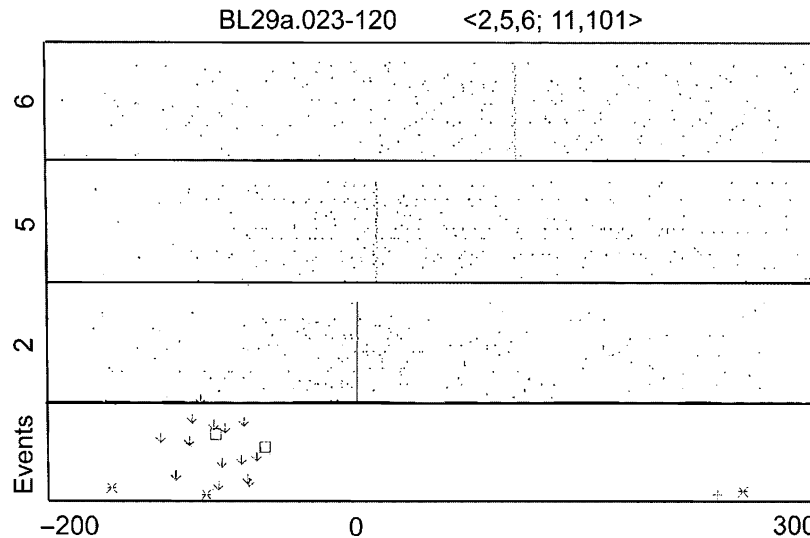
Definition

Sequences of events that repeat several times are called *precise spatiotemporal patterns*. The number of participating events is called the *complexity* of the patterns. The time precision with which the delays are measured is called the *time accuracy* of the pattern.

Examples Suppose we have three parallel point processes (e.g., times of spiking of three neurons), among them, we find repeatedly an event from process A followed after t_1 seconds by an event from B and after t_2 seconds by an event from C, then the composite event

A
| t_1 |B
| t_2 |C

is called a precise spatiotemporal pattern and may be coded $\langle A, B, C ; t_1, t_2 \rangle$. Its *complexity* is 3.



Spatial Temporal Spike Pattern Analysis,

Fig. 1 Example of a precise spatiotemporal pattern. Dot display of the pattern $<2,5,6; 11, 101>$ that repeated 31 times. The precision was 3 ms. All dot rasters are aligned on the first spike in the pattern. Recording from the frontal cortex of a monkey performing a localization task of visual and auditory stimuli. The patterns tend to

appear after a visual stimulus (*down pointing arrows*) but are not tightly locked in time to the stimulus. Each neuron fired also other (seemingly random) spikes during and around the time of the patterns. This suggests that the precise timing is a network property (and not due to any internal processes of each of the neurons)

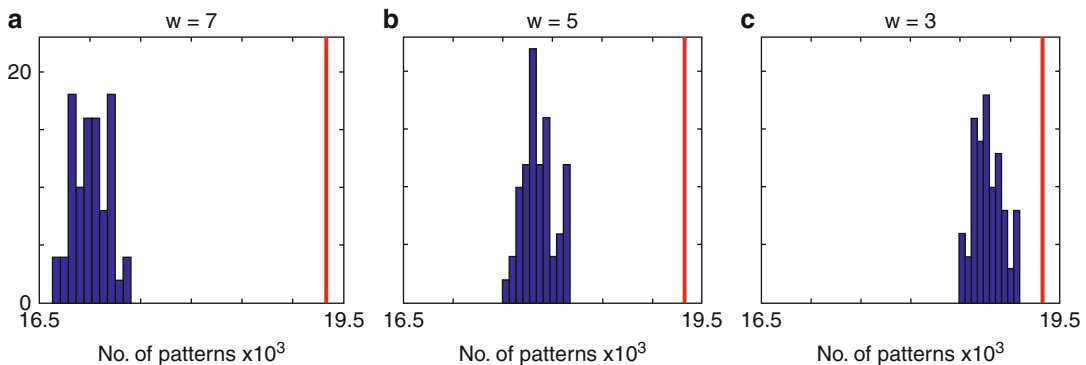
spatiotemporal patterns is directed to cases that cannot be explained by precise time relations of external events, by intrinsic mechanisms of a single neuron, or by close to periodic oscillations of a network. When the above simple explanations do not apply, then one should assume that the patterns are the expression of some special neural networks that can produce them. The synfire chain model (Abeles 1982) and the polychronization model (Izhikevich 2006) are two such models.

Statistical Significance

Given enough data and large enough Δt , one expects to see many precise spatiotemporal patterns by chance. How can one decide whether the number of repetitions exceeds chance? Typically, one generates surrogate spike trains and looks for patterns there. If the data contains many more, it is assumed that they are significant. Numerous proposals of surrogates for looking for patterns exist in the literature including the following: the individual point processes are inhomogeneous Poisson processes (Oram et al. 1999); they

behave like gamma processes (Baker and Lemon 2000); two successive intervals in the same point process are not independent (Gerstein 2004); and a particular pattern $<A_0, A_1, A_2, \dots, A_n; t_1, t_2, \dots, t_n>$ happens many more times when compared to patterns of the same events with slightly different times $<t_1, t_2, \dots, t_n>$ (Abeles and Gat 2001) (**► Surrogate Data for Evaluation of Spike Correlation**).

The good way to examine the existence of precise timing was suggested by Geman and Bienenstock (Date et al. 2000; Hastopoulos et al. 2003). According to their suggestion, the null hypothesis is that there is nothing that controls the event timing below some accuracy W . Therefore, randomly teetering the event timing within W seconds should not affect any statistics that is derived from the involved point processes. Thus, one teeters the timing by W and computes the same statistics again and again forming a probability density function of the statistic for teetered data. If the value of the data statistic falls in the tail of this pdf, one can estimate the



Spatial Temporal Spike Pattern Analysis,
Fig. 2 Distributions of patterns in randomly teetered data. Red bar, the number of repeating patterns in the data. Blue histogram, the distribution of the number of repeating patterns in data that was randomly teetered 100 times. The data is from the MEG recording of a subject that performed a task of following a musical

probability of the time accuracy of the data from the area of the tail. Figure 2 illustrates this process.

In theory, this idea is of limited usefulness. Any variation in the rate of events (e.g., a response of a neuron to a stimulus) will be “smeared” by such teetering. Thus, given enough data, it would be possible to detect significant variations by teetering. However, if the variations are slow relative to the window width W , it would take enormous amount of data to obtain significant differences. One should therefore be careful not to use this method when sharp transients of some property are expected. For example, interspike interval histograms may change abruptly from zero (during the refractory period) to some high level. Cross-correlations between pairs of spike trains may show a very sharp peak at zero lag ([► Unitary Event Analysis](#); [► Correlation Analysis of Parallel Spike Trains](#)). Teetering spike times within W is equivalent to convolving the histogram with a boxcar kernel of width W . If the transition is sharp relative to W , significance may be found. This suggests a way to evaluate how much data would be needed before these effects will be significant.

Therefore, this method should not be used to detect significance for precise spatiotemporal patterns when the same point process participates

meter. The MEG data was converted to current dipoles in the cortex. From these the position of sharp (20 ms) peaks was detected and presented as parallel point processes. Data was sampled at 508/s and the precision was three samples. The teetering windows were 7, 5, and 3 samples from left to right respectively

more than once or when near zero delays between events in two point processes are included. The work of Shmiel et al. (2006) illustrates finding accurate time relations between two spike trains even when W was 0.5 ms and all possible precautions were taken into considerations.

Cross-References

- [Correlation Analysis of Parallel Spike Trains](#)
- [Neural Coding](#)
- [Surrogate Data for Evaluation of Spike Correlation](#)
- [Unitary Event Analysis](#)

References

- Abeles M (1982) Local cortical circuits: an electrophysiological study. Springer, Berlin/Heidelberg/New York, pp 57–75
 Abeles M, Gat I (2001) Detecting precise firing sequences in experimental data. J Neurosci Meth 107:141–154
 Abeles M, Gerstein GL (1988) Detecting spatiotemporal firing patterns among simultaneously recorded single neurons. J Neurophysiol 60:909–924
 Baker S, Lemon RN (2000) Precise spatiotemporal repeating patters in monkey primary and supplementary motor areas occur at chance level. J Neurophysiol 84:1770–1780

- Date A, Bienenstock E, Geman S (2000) A statistical tool for testing hypothesis about the temporal resolution of neural activity. *Soc Neurosci Abstr* 26:828.6
- Dayhoff J, Gerstein GL (1983a) Favored patterns in spike trains. I. Detection. *J Neurophysiol* 49:1334–1348
- Dayhoff J, Gerstein GL (1983b) Favored patterns in spike trains. II. Application. *J Neurophysiol* 49:1349–1363
- Gerstein GL (2004) Searching for significance in spatiotemporal firing patterns. *Acta Neurobiol Exp* 64:203–307
- Hastopoulos NG, Geman S, Amarasingham A, Bienenstock E (2003) At what timescale does the nervous system operates? *Neurocomputing* 52–54:25–29
- Izhikevich EM (2006) Polychronization: computations with spikes. *Neural Comput* 18:245–282
- Oram MW, Wiener MC, Lestienne R, Richmond BJ (1999) Stochastic nature of precisely timed spike patterns in visual system neuronal responses. *J Neurophysiol* 81:3021–3033
- Shmuel T, Rotem D, Shmuel O, Ben-Shaul Y, Nadasdy Z, Shemesh M, Teicher M, Abeles M (2006) Temporally precise cortical firing patterns are associated with distinct action segments. *J Neurophysiol* 96:2645–2652

Further Reading

Abeles M (1991) *Corticonics: neural circuits of the cerebral cortex*. Cambridge University Press, Cambridge/New York/Port Chester/Melbourne/Sydney

Spatiotemporal Energy Models

Wyeth Bair

Department of Biological Structure, University of Washington, Seattle, WA, USA

Synonyms

[Disparity energy model](#); [Motion energy model](#)

Definition

Spatiotemporal energy models were developed to explain the physiological properties of a class of motion sensitive neurons known as complex direction selective (DS) cells in the primary visual cortex (V1). These models are tuned to respond to energy within the spatiotemporal frequency spectrum of time-varying imagery,

particularly to the spectral bands that are associated with specific directions of motion. This is accomplished using quadrature pairs of linear filters that are oriented both in space and in space-time. Spatiotemporal energy models are commonly used as the initial stages of higher-level models of motion, stereopsis, and form processing.

Detailed Description

Fundamental Example

The classical instance of a spatiotemporal energy model is the motion energy (ME) model (Adelson and Bergen 1985). It consists of two linear filters that have a quadrature phase relationship, meaning that one filter is shifted by ninety degrees with respect to the other. For example, if one filter is the product of a cosine function times a Gaussian, the other is the product of a sine times the same Gaussian, as follows:

$$h1(x, y, t) = \cos(f_s x + f_t t) e^{-[1/2((x^2+y^2)/\sigma_s^2 - 1/2t^2/\sigma_t^2)]}$$

$$h2(x, y, t) = \sin(f_s x + f_t t) e^{-[1/2((x^2+y^2)/\sigma_s^2 - 1/2t^2/\sigma_t^2)]}$$

where f_s , f_t , σ_s , and σ_t set the preferred spatial frequency (SF) and temporal frequency (TF) and the size of the filters in space and time, respectively. The output of the model is the sum of the squares of the two filter outputs.

Conceptual Development

Three insights were essential to the invention of spatiotemporal energy models. The first was that visual neurons could be modeled as linear filters and described in terms of their sensitivities to spatial and temporal frequencies within a sequence of images. By the end of the decade in which Hubel and Wiesel (1962) made the critical discovery that many V1 neurons were selective for the orientation, size, and direction of motion of simple bar stimuli, other experimentalists, in particular those using drifting sinewave grating stimuli, had begun theorizing that the visual system was in fact a spatial frequency

analyzer containing independent, narrowband channels (Campbell and Robson 1968; Campbell et al. 1969; Blakemore and Campbell 1969; Maffei and Fiorentini 1973). Ultimately, it was established that responses of simple cells in V1 could, under limited conditions, be well described by the outputs of linear filters (Movshon et al. 1978).

The second essential insight was that visual motion, particularly rigid translation, creates orientation in space-time and that this can be detected by oriented space-time filters (Fahle and Poggio 1981; Watson and Ahumada 1983; Adelson and Bergen 1985). Here, theory preceded experiment, as the first clear demonstrations of spatiotemporal orientation in the responses of V1 neurons appeared several years later (Reid et al. 1987; McLean and Palmer 1989). The third essential insight was the use of the squared outputs of a quadrature pair of filters to demodulate the temporal response to moving stimuli (Adelson and Bergen 1985). This is related to the fact that $\cos^2 + \sin^2$ is a constant, and it allows the ME model to respond to a moving grating with a constant positive response and to a moving bar with a unimodal positive response. This was important to capture the responses of complex, as opposed to simple, DS neurons.

Related Approaches

A contemporaneous approach to modeling DS neuronal responses began with the fundamentally nonlinear, correlation-style Reichardt motion detector (Reichardt 1957, 1961) and added appropriate linear filters at the front end, resulting in the elaborated Reichardt detector (ERD) model (van Santen and Sperling 1984, 1985). The ERD model has computational steps that are distinct from those of the ME model; nevertheless, in some forms, the final outputs of the two models are mathematically equivalent (Adelson and Bergen 1985). This demonstrates the close link between what are arguably the two historically most important models for direction selective neurons. An alternative approach that contrasts with the energy model was proposed by Watson and Ahumada (1985) in which the

temporal modulation of the response, rather than being removed by squaring the outputs of quadrature filters, is retained and used to encode information relevant for downstream velocity estimation.

More recently, the spatiotemporal energy model has been modified and generalized to account for the responses of neurons that are selective for binocular disparity. The first binocular disparity energy (BDE) model (Ohzawa et al. 1990; Ohzawa 1998) was strictly spatial and consisted of separate pairs of quadrature filters for the left and right eyes. The preferred disparity is determined by a parameter that controls the offset of the filters across the two eyes, and the quadrature pair, followed by squaring, maintains the complex cell behavior. The BDE model has been unified with the ME model (Chen et al. 2001) to produce a set of spatiotemporal energy models that can account for both disparity and direction selectivity. These models continue to be the subject of active development as researchers attempt to account more accurately for response properties to an ever increasing set of visual stimuli (Read et al. 2002; Chen and Qian 2004; Haefner and Cumming 2008; Peng and Shi 2010).

Cross-References

- [Emergence of Orientation Selectivity in the Cerebral Cortex, Modeling](#)
- [Hierarchical Models of the Visual System](#)
- [Receptive Field Modeling](#)
- [Spatiotemporal Receptive Fields](#)
- [Stereo Vision, Models of](#)

References

- Adelson EH, Bergen JR (1985) Spatiotemporal energy models for the perception of motion. *J Opt Soc Am A* 2:284–299
Blakemore C, Campbell FW (1969) On the existence of neurones in the human visual system selectively sensitive to the orientation and size of retinal images. *J Physiol* 203:237–260

- Campbell FW, Robson JG (1968) Application of fourier analysis to the visibility of gratings. *J Physiol* 197:551–566
- Campbell FW, Cooper GF, Enroth-Cugell C (1969) The spatial selectivity of the visual cells of the cat. *J Physiol* 203:223–235
- Chen Y, Qian N (2004) A coarse-to-fine disparity energy model with both phase-shift and position-shift receptive field mechanisms. *Neural Comput* 16:1545–1577
- Chen Y, Wang Y, Qian N (2001) Modeling V1 disparity tuning to time-varying stimuli. *J Neurophysiol* 86:143–155
- Fahle M, Poggio T (1981) Visual hyperacuity: spatiotemporal interpolation in human vision. *Proc R Soc London Ser B, Biol Sci* 213:451–477
- Haefner RM, Cumming BG (2008) Adaptation to natural binocular disparities in primate V1 explained by a generalized energy model. *Neuron* 57:147–158
- Hubel DH, Wiesel TN (1962) Receptive fields, binocular interaction and functional architecture in the cat's visual cortex. *J Physiol* 160:106–154
- Maffei L, Fiorentini A (1973) The visual cortex as a spatial frequency analyzer. *Vision Res* 13:1255–1267
- McLean J, Palmer LA (1989) Contribution of linear spatiotemporal receptive field structure to velocity selectivity of simple cells in area 17 of cat. *Vision Res* 29:675–679
- Movshon JA, Thompson ID, Tolhurst DJ (1978) Spatial summation in the receptive fields of simple cells in the cat's striate cortex. *J Physiol* 283:53–77
- Ohzawa I (1998) Mechanisms of stereoscopic vision: the disparity energy model. *Curr Opin Neurobiol* 8:509–515
- Ohzawa I, DeAngelis GC, Freeman RD (1990) Stereoscopic depth discrimination in the visual cortex: neurons ideally suited as disparity detectors. *Science* 249:1037–1041
- Peng Q, Shi BE (2010) The changing disparity energy model. *Vision Res* 50:181–192
- Read JCA, Parker AJ, Cumming BG (2002) A simple model accounts for the reduced response of disparity-tuned V1 neurons to anti-correlated images. *Vis Neurosci* 19:735–753
- Reichardt W (1957) Autokorrelationsauswertung als Funktionsprinzip des Zentralnervensystems. *Zeitschrift für Naturforschung, Teil B* 12:447–457
- Reichardt W (1961) Autocorrelation, a principle for the evaluation of sensory information by the central nervous system. In: Rosenblith WA (ed) *Sensory communication*. MIT Press, Cambridge, MA, pp 303–317
- Reid RC, Soodak RE, Shapley RM (1987) Linear mechanisms of directional selectivity in simple cells of cat striate cortex. *Proc Natl Acad Sci U S A* 84:8740–8744
- van Santen JPH, Sperling G (1984) Temporal covariance model of human motion perception. *J Opt Soc Am A* 1:451–473
- van Santen JPH, Sperling G (1985) Elaborated Reichardt detectors. *J Opt Soc Am A* 2:300–321
- Watson AB, Ahumada AJ Jr (1983) A look at motion in the frequency domain. In: Tsotsos JK (ed) *Motion: perception and representation*. NASA technical memorandum, vol 84352. Association for Computing Machinery, New York, pp 1–10
- Watson AB, Ahumada AJ Jr (1985) Model of human visual-motion sensing. *J Opt Soc Am A* 2:322–341

Specific Intracellular (or Cytoplasmic) Resistance

► Resistivity, Axial

Spectral Interdependency Methods

Mukesh Dhamala

Physics and Astronomy, Neuroscience Institute, Georgia State University, Atlanta, GA, USA

Synonyms

Coherence and Granger causality spectral analysis; Multivariate spectral analysis; Oscillatory network activity analysis

Definition

Spectral interdependency methods are a means of statistically quantifying the interrelationship between a pair of dynamic processes as a function of frequency or time period of oscillation. The measures of spectral interdependency are derived from the time series recordings of dynamic systems either by using autoregressive modeling (parametric method) or by using direct Fourier or wavelet transforms (nonparametric method). For a pair of multivariate stationary processes (1 and 2), there are three measures that characterize the spectral interdependency between these processes. They are total interdependence ($M_{1,2}$), Granger causality (one-way effect or directional influence from

the first process to the second process, $M_{1 \rightarrow 2}$, or from the second to the first, $M_{2 \rightarrow 1}$), and instantaneous causality (measure of reciprocity, $M_{1,2}$). In general, the total interdependence is the sum of directional influences and instantaneous causality frequency by frequency ($M_{1,2} = M_{1 \rightarrow 2} + M_{2 \rightarrow 1} + M_{1,2}$) and is related to coherence (C_{12}) as $M_{1,2} = -\ln(1 - C_{12})$. These measures can also be estimated for nonstationary processes by using moving time-windowed autoregressive modeling or Fourier transformations or wavelet transformations. Coherence and spectral Granger causality are well-accepted measures in neuroscience to characterize frequency-specific interdependence between multiple time series from multisite neurophysiological recordings.

Detailed Description

Many processes in nature, including brain processes, have oscillatory motion, and the time series measurements of their activity are rich in oscillatory content, lending them naturally to spectral analysis. Spectral interdependency methods are used to study the relationship in the frequency domain between multiple processes from their simultaneously recorded time series signals. Consider a pair of zero-mean, stationary processes (1 and 2) in which simultaneously measured time series at a sampling rate of f_s are represented as 1: $X_1(1), X_1(2), \dots, X_1(t), \dots$ and 2: $X_2(1), X_2(2), \dots, X_2(t), \dots$. The spectral interdependency measures as defined above are derived from the spectral matrix (S) and/or from the transfer function (H) and noise covariance matrix (Σ), which can be estimated by the parametric (Ding et al. 2006) or nonparametric approaches applied to these time series (Dhamala et al. 2008a, b). Brief mathematical derivations and descriptions of these interdependency measures (C_{12} , $M_{1,2}$, $M_{1 \rightarrow 2}$, $M_{2 \rightarrow 1}$, and $M_{1,2}$) are included below.

Directed transfer function (DTF) (Kaminski et al. 2001) and partial directed coherence (PDC) (Baccala and Sameshima 2001) are the accepted alternative measures of directional

influence, equivalent to the measures for $M_{1 \rightarrow 2}$ and $M_{2 \rightarrow 1}$ as defined above. DTF is obtained from H and PDC from the Fourier transform of model coefficients in the parametric approach.

Parametric Approach

Jointly, X_1 and X_2 series can be represented as the following bivariate autoregressive (AR) models:

$$\begin{aligned} X_1(t) &= \sum_{j=1}^{\infty} a_{11,j} X_1(t-j) + \sum_{j=1}^{\infty} a_{12,j} X_2(t-j) + \varepsilon(t) \\ X_2(t) &= \sum_{j=1}^{\infty} a_{21,j} X_1(t-j) + \sum_{j=1}^{\infty} a_{22,j} X_2(t-j) + \eta(t), \end{aligned} \quad (1)$$

where ε and η are residual (one-step-ahead prediction) errors and are uncorrelated over time. After Fourier transforming the bivariate AR representation Eq. 1 and applying proper ensemble average, we obtain the following spectral density matrix S as a function of frequency (f):

$$S(f) = H(f)\Sigma H^*(f), \quad (2)$$

where $*$ denotes the matrix adjoint. Here, the noise covariance matrix Σ is computed from the residual errors $\varepsilon(t)$, $\eta(t)$ and the transfer function matrix $H(f)$ is constructed from the matrix inverse of the Fourier transforms of the coefficients as

$$\begin{aligned} \Sigma &= \begin{pmatrix} \text{var}(\varepsilon) & \text{cov}(\varepsilon, \eta) \\ \text{cov}(\varepsilon, \eta) & \text{var}(\eta) \end{pmatrix} \\ H_{lm}(f) &= \left(\delta_{lm} - \sum_{k=1}^{\infty} a_{lm,k} e^{-i2\pi fk} \right)^{-1}, \end{aligned} \quad (3)$$

where δ_{lm} is the Kronecker delta function with the matrix element index lm .

Nonparametric Approach

S , H , and Σ can also be estimated by using the nonparametric spectral methods (Dhamala et al. 2008a, b) without explicitly fitting the time series $X_1(t)$ and $X_2(t)$ in autoregressive models. In this approach, S is constructed by Fourier transforming X_1 and X_2 and properly averaging over ensembles usually with multitapers (Mitra and Pesaran 1999):

$$S_{lm} = \langle x_l(f)x_m(f^*) \rangle, \quad (4)$$

where lm is the index for time series and matrix element, $\langle \rangle$ represents averaging over ensemble, and X 's are the direct Fourier transforms of X 's. H and Σ can be derived from the minimum-phase factors of S :

$$\begin{aligned} H &= \psi \zeta_0^{-1} \\ \Sigma &= A_0 A_0^T, \end{aligned} \quad (5)$$

where T stands for matrix transposition, $\psi(e^{i\theta}) = \sum_{k=0}^{\infty} A_k e^{ik\theta}$ defined on the unit circle and $A_k = \frac{1}{2\pi} \int_{-\pi}^{\pi} \psi(e^{i\theta}) e^{-ik\theta} d\theta$.

Spectral Interdependence

The coherence function $C(f)$ is derived from the cross spectra normalized by the product of the individual auto spectra and measures the amount of interdependence (synchrony) as a function of frequency:

$$C(f) = \frac{|S_{12}(f)|^2}{S_{11}(f)S_{22}(f)}. \quad (6)$$

$C(f)$ is sensitive to both amplitude and phase relationships between processes at f and its value ranges from 0 (no interdependence) to 1 (maximum interdependence). $C(f)$ is related to Geweke's measure of total interdependence ($M_{1,2}$) (Ding et al. 2006):

$$M_{1,2}(f) = -\ln(1 - C(f)), \quad (7)$$

whose value ranges from 0 to infinity. The total spectral interdependence ($M_{1,2}$) is equal to the sum of Granger causality or directional influences (one-way effects, $M_{1 \rightarrow 2}$ and $M_{2 \rightarrow 1}$) and instantaneous causality ($M_{1,2}$) (Geweke 1982):

$$M_{1,2} = M_{1 \rightarrow 2} + M_{2 \rightarrow 1} + M_{1,2} \quad (8)$$

Here, directional influences between 1 and 2 are given by (Geweke 1982)

$$\begin{aligned} M_{1 \rightarrow 2}(f) &= \ln \frac{S_{22}(f)}{\tilde{H}_{11}(f)\Sigma_{11}\tilde{H}_{11}^*(f)} \\ M_{2 \rightarrow 1}(f) &= \ln \frac{S_{11}(f)}{\tilde{H}_{22}(f)\Sigma_{22}\tilde{H}_{22}^*(f)}, \end{aligned} \quad (9)$$

where $\tilde{H}_{11} = H_{11} + \frac{\Sigma_{12}}{\Sigma_{11}}H_{12}$, $\tilde{H}_{22} = H_{22} + \frac{\Sigma_{12}}{\Sigma_{22}}H_{21}$, and

instantaneous causality $M_{1,2}$ is given by

$$M_{1,2}(f) = -\ln \frac{|S(f)|}{(\tilde{H}_{11}(f)\Sigma_{11}\tilde{H}_{11}^*(f))(\tilde{H}_{22}(f)\Sigma_{22}\tilde{H}_{22}^*(f))}. \quad (10)$$

Granger causality at low frequencies between a pair of cointegrated series depends only on a few statistically interpretable coefficients from the error correction model if Hosoya's spectral decomposition (Hosoya 1991) is used (Granger and Lin 1995).

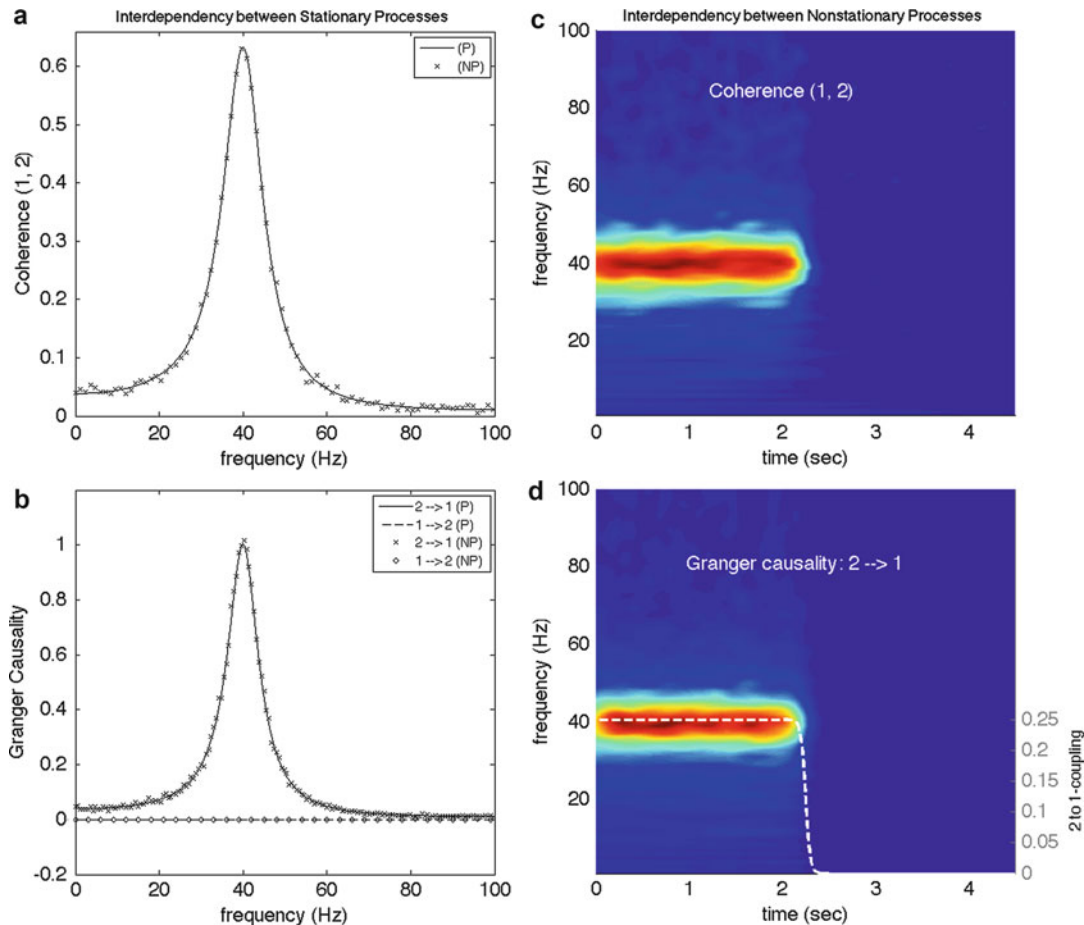
The time-domain counterparts of these spectral measures in Eq. 8 are obtained by integrating the spectral measures over the entire frequency range as $\frac{2}{f_s} \int_0^{\frac{f_s}{2}} M(f) df$. The integral of total interdependence measures the total amount of mutual information, and the other integrals are simply the respective time-domain measures of Granger causality.

Spectral Interdependence for Nonstationary Processes

The spectral interdependency measures can also be defined for nonstationary processes by treating their time series in sufficiently short windows as locally stationary processes. They can be estimated as a function of time and frequency by using moving time-windowed autoregressive modeling (Liang et al. 2000), moving time-windowed Fourier transformations (Shioigai et al. 2012), or wavelet transformations (Dhamala et al. 2008a, b).

Numerical Examples

Here, we generate time series (500 trials) from jointly stationary and nonstationary processes and illustrate the estimation of coherence and Granger causality spectra using the



Spectral Interdependency Methods,
Fig. 1 Coherence (a, c) and Granger causality (c, d) spectra between stationary (a, b) and nonstationary (c, d) processes (1 and 2). Parametric (*P*) and Fourier transform-based nonparametric (*NP*) methods are used here to

parametric (*P*) and nonparametric (*NP*) approaches. We consider two interacting autoregressive processes, 2: $\{X_2(t)\}$ driving 1: $\{X_1(t)\}$, similar to the network model considered in Dhamala et al. (2008b), where $X_1 = 0.55 X_1(t-1) - 0.8X_1(t-2) + C(t)X_2(t-1) + \varepsilon(t)$ and $X_2(t) = 0.55X_2(t-1) - 0.8X_2(t-2) + \eta(t)$. Here, $(\varepsilon(t), \eta(t))$'s are independent white noise processes with zero means and unit variances, the sampling rate is considered to be 200 Hz, and the coupling strength $C(t)$ remains 0.25 for time t in the stationary condition and slowly changes from 0.25 to 0 around $t = 2$ s in the case

evaluate these quantities (a, b) between the stationary processes. The wavelet transform-based time-frequency maps of coherence (c) and Granger causality (d) recover the time-varying nature of 2 to 1 coupling (shown on the right *y*-axis in d)

of nonstationary processes. *P* and *NP* approaches agree well in coherence and Granger causality spectra (Fig. 1a, b). Morlet wavelet transform-based method yields complete time-frequency maps of coherence (Fig. 1c) and Granger causality (Fig. 1d), consistent with the trend of the 2 to 1 coupling as shown on the right side of Fig. 1d.

Extensions of Spectral Interdependency Methods

As an extension of the ordinary coherence described above, block coherence (Nedungadi et al. 2011) can estimate coherence spectra

between pairs of nonoverlapping time series. Conditional Granger causality (Geweke 1984; Hosoya 2001) measures directional influences between two processes eliminating the effect of a third process, thereby distinguishing between direct and mediated causality (Ding et al. 2006; Dhamala et al. 2008b). The multivariate version of the spectral Granger causality between two processes makes use of this idea of eliminating the causal effect from all other interrelated processes as an extension of the conditional Granger causality defined for three processes.

Applications in Neuroscience

Spectral interdependency measures have been instrumental in attempts to understand the relationships between oscillatory brain processes at various spatial scales from multisite brain activity recordings. Coherence is widely used in neuroscience (Siegel et al. 2012; Roberts et al. 2013). The insights provided by this measure have even led to the “neuronal communication through coherence” hypothesis (Fries 2005; Roberts et al. 2013). Spectral Granger causality and equivalent directional measures have been used in a variety of brain signal recordings, such as local field potentials, EEG, MEG, and fMRI, in animals and humans (see Bressler and Seth 2011; Friston et al. 2012 for reviews). Because of the unknown theoretical distributions of coherence and spectral Granger causality, establishing statistical significance in these measures derived from experimental time series requires data resampling (surrogate) methods such as jackknifing (Bokil et al. 2010), bootstrapping, and random permutation (Seth 2010).

References

- Baccala LA, Sameshima K (2001) Partial directed coherence: a new concept in neural structure determination. *Biol Cybern* 84:463–474
- Bokil H, Andrews P, Kulkarni JE, Mehta S, Mitra PP (2010) Chronux: a platform for analyzing neural signals. *J Neurosci Methods* 192:146–151
- Bressler SL, Seth AK (2011) Wiener-Granger causality: a well established methodology. *Neuroimage* 58:323–329
- Dhamala M, Rangarajan G, Ding M (2008a) Estimating Granger causality from Fourier and wavelet transforms of time series data. *Phys Rev Lett* 100(018701):1–4
- Dhamala M, Rangarajan G, Ding M (2008b) Analyzing information flow in brain networks with nonparametric Granger causality. *Neuroimage* 41:354–362
- Ding M, Chen Y, Bressler SL (2006) Granger causality: basic theory and application to neuroscience. In: Schelter S, Winterhalder N, Timmer J (eds) *Handbook of time series analysis*. Wiley, Berlin, pp 437–459
- Fries P (2005) A mechanism for cognitive dynamics: neuronal communication through neuronal coherence. *Trends Cogn Sci* 9:474–480
- Friston K, Moran R, Seth AK (2012) Analysing connectivity with Granger causality and dynamic causal modeling. *Curr Opin Neurobiol* 23:172–178
- Geweke J (1982) Measurement of linear-dependence and feedback between multiple time-series. *J Am Stat Assoc* 77:304–313
- Geweke J (1984) Measures of conditional linear dependence and feedback between time series. *J Am Stat Assoc* 79:907–915
- Granger CWJ, Lin J-L (1995) Causality in the long run. *Econ Theory* 11:530–536
- Hosoya Y (1991) The decomposition and measurement of the interdependence between second-order stationary processes. *Prob Theory Relat Fields* 88:429–444
- Hosoya Y (2001) Elimination of third-series effect and defining partial measures of causality. *J Time Ser Anal* 22:537–554
- Kaminski M, Ding M, Truccolo WA, Bressler SL (2001) Evaluating causal relations in neural systems: Granger causality, directed transfer function and statistical assessment of significance. *Biol Cybern* 85:145–157
- Liang H, Ding M, Nakamura R, Bressler SL (2000) Causal influences in primate cerebral cortex during visual pattern discrimination. *Neuroreport* 11:2875–2880
- Mitra PP, Pesaran B (1999) Analysis of dynamic brain imaging data. *Biophys J* 76:691–708
- Nedungadi A, Ding M, Rangarajan G (2011) Block coherence: a method for measuring the interdependence between two blocks of neurobiological time series. *Biol Cybern* 104:197–207
- Roberts M, Lowet E, Brunet N, Ter Wal M, Tiesinga P, Fries P, De Weerd P (2013) Robust gamma coherence between macaque V1 and V2 by dynamic frequency matching. *Neuron* 78:523–536
- Seth AK (2010) A MATLAB toolbox for Granger causal connectivity analysis. *J Neurosci Methods* 186:262–273
- Shioigai Y, Dhamala M, Oshima K, Hasler M (2012) Cortico-cardio-respiratory network interactions during anesthesia. *PLoS One* 7:e44634
- Siegel M, Donner TH, Engel AK (2012) Spectral fingerprints of large-scale neuronal interactions. *Nat Rev Neurosci* 13:121–134

Spectrot temporal Analysis

► Time-Frequency Analysis

Spectrot temporal Receptive Fields

Shihab Shamma

Electrical and Computer Engineering
Department and Institute for System Research,
University of Maryland, College Park, MD, USA
École Normale Supérieure, Paris, France

Synonyms

Frequency tuning curves; Iso-intensity response curves; Spectrot temporal Response Fields

Definition

The spectrot temporal response field (STRF) of an auditory neuron is a time-frequency measure of the dynamic responses of an auditory neuron to impulsive energy delivered at various frequencies. As such, it gives simultaneously two types of information about the neuron. The first is its frequency tuning, or more specifically which frequencies excite the cell best and which inhibit it. The other is the nature of its temporal response, i.e., whether it is sustained in time or is rapidly adapting. This measure is linear and takes the stimulus spectrogram as its input and hence is often found to be useful in predicting responses of a neuron to unseen stimuli.

Detailed Description

The Value of the STRF

A key requirement in the study of sensory nervous systems is the ability to characterize effectively neuronal response selectivity. In the visual system, striving for this objective yielded remarkable progress in understanding the

functional organization of the visual cortex and its implications to perception. For instance, the discovery of ordered feature representations of retinal space, color, ocular dominance, orientation, and motion direction in various cortical fields has instigated vast studies into the anatomical bases of this organization, its developmental course, and the changes it undergoes during learning or following injury. In the primary auditory cortex (A1), response selectivity of the neurons (also called their *response fields*) is ordered topographically according to the frequency they are most tuned to, an organization inherited from the cochlea. Beyond their tuning, however, AI responses and response fields exhibit a bewildering variety of dynamics, frequency bandwidths, response thresholds, and patterns of excitatory and inhibitory regions. All this has been learned over decades of testing with a large variety of acoustic stimuli (tones, clicks, noise, and natural sounds) and response measures (tuning curves, rate-level functions, and binaural maps).

Distinguishing the STRF

A response measure that has proven particularly useful beyond the feature-specific measures enumerated earlier is the notion of a generalized *spatiotemporal*, or equivalently for the auditory system, the *spectrot temporal response field* (STRF). It is distinguished from other measures by its broader descriptive power (encompassing both dynamics and spectral selectivity) and its relatively noncommittal nature (not requiring too much prior knowledge such as frequency tuning or threshold). In the last two decades, the STRF has become widely employed in all sensory systems (Hochstein and Shapley 1976; De Valois and De Valois 1988; Arun et al. 2006; Aertsen and Johannesma 1981; DeAngelis et al. 1995; Gosselin and Schyns 2002), and especially in the auditory system where it had found its original promise, development, and examination of its value and liability (Arun et al. 2006; Aertsen and Johannesma 1981; de Boer 1967; de Boer and de Jongh 1978). The STRF has primarily been viewed as a linear characterization of the complex stimulus-response transformations seen

in sensory neurons. However, there are well-understood limitations of the STRF ability to capture all the essential details of a sensory neuron's response. These stem from the existence of a host of known nonlinearities such as spiking threshold, rate saturation, and synaptic depression that can complicate the interpretation of the STRF and render its representation stimulus dependent or meaningless. Nevertheless, the utility of the STRF has inspired deeper and broader examination of its constraints and pitfalls and ways to circumvent them (David et al. 2006; Christianson et al. 2008; Atencio et al. 2008; Nagel and Doupe 2008) or even exploit them to learn more about the nonlinearities in the system (Theunissen et al. 2000; Ahrens et al. 2008; Klein et al. 2006).

Using the STRF

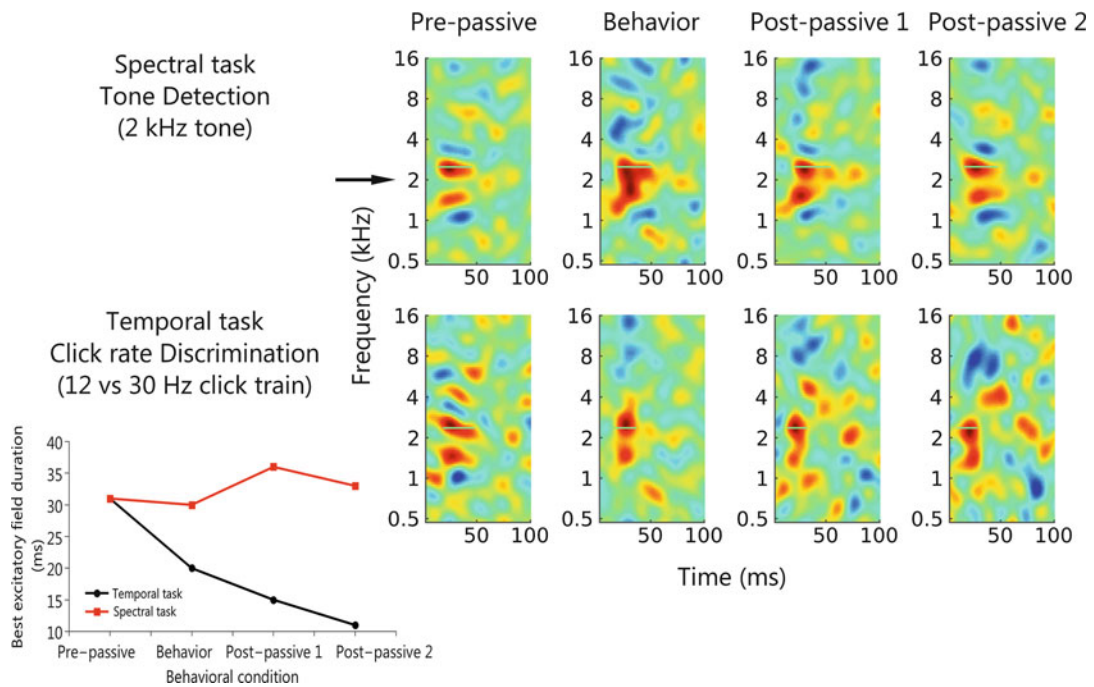
The STRF concept has proven valuable in the understanding of auditory cortical processing and its applications in audio systems ranging from speech and speaker recognition to enhancements of speech signals and cochlear implants. Their first valuable contribution has been to provide an effective summary of the representation of sound features in the primary auditory cortex (Theunissen et al. 2000; Atencio et al. 2008; Shamma et al. 1995). A key finding has been the realization that the huge variety of auditory cortical responses in frequency tuning, dynamics, and other features has inspired models of auditory processing that view the cortex as a "multiscale" spectrotemporal analyzer that decomposes the signal into a rich representation that can be effectively harnessed for a variety of applications (Chi et al. 2006). For example, complex signals such as speech and music can be analyzed in this cortical model to understand how phonetic information is represented (Mesgarani et al. 2008) or how timbres of different musical instruments are encoded (Patil et al. 2012). The uniqueness of the representation of the different types of signals allows us further to separate the speech from interfering noise, to detect the presence of speech compared to no speech (Massgarani et al. 2005), and to separate multiple speakers (Elhilali and Shamma 2008).

STRF and Plasticity

STRFs have proven valuable in plasticity and developmental studies as a summary of a neuron's response properties *even if incomplete*. The reason is that in many cases, it is not the completeness of the representation that is of interest but rather *how* the (admittedly incomplete) representation changes during behavior or learning. In this role, the STRF has demonstrated a robustness and versatility that was not initially appreciated. For instance, auditory cortical STRFs often provide an estimate of the *relative* sensitivity of a neuron to different frequencies and temporal dynamics. Therefore, when examining the effects of attention and learning, changes in neuronal responsiveness are often unpredictable in their dynamics or spectral configurations or are very small and augment already very noisy responses. The STRF counters both of these challenges. Thus, by virtue of its generalized nature (not being specific to a particular feature or response dimension), changes in the neuronal sensitivity in one of multiple dimensions can readily be spotted and characterized (Fritz et al. 2003). Furthermore, these response changes are often very difficult to discern or interpret (as spectral or temporal changes) in the firing rates themselves. STRFs by their nature are simultaneous *relative* measures of a neuron's responsiveness to many frequencies and dynamics. Consequently, the effect of attention and learning (and behavior in general) is often seen as changes in the STRF shape that can be readily interpreted as changes in the relative sensitivity of the neuron to different frequencies (Fritz et al. 2005a) or in the temporal parameters of the STRF such as its latency (Fritz et al. 2005b) (Fig. 1).

Forward and Inverse STRF

Another interesting use of the STRFs is in characterizing global response properties of a large population of cells or cortical areas for the purpose of summarizing its representational properties and how that may change due to learning and plasticity. Specifically, in many situations, cortical neurons encode considerable details about the underlying sensory stimuli, and the encoded



Spectrotemporal Receptive Fields, Fig. 1 Example of an STRF that showed spectral and temporal task-related plasticity in successive tasks. The spectral task was performed first, with a target tone of 2 kHz. The STRF obtained during spectral task behavior displayed an expansion of both excitatory fields towards the target frequency. The STRF returned to its original pre-passive shape following behavior. Shortly after the spectral task, the animal was presented with the temporal task, in which it had to discriminate reference click trains of 12 Hz from target click trains presented at 30 Hz. In contrast to the

plasticity observed during the spectral task, in the temporal task the excitatory field of the STRF became narrower. This narrowing of the STRF persisted following behavior. Persistent plasticity has also been described previously (Fritz et al. 2003) (From Abstract #377, ARO 2013, *Laminar Recordings of Task-Related Receptive Field Plasticity with Multisite Depth Electrodes in the Primary Auditory Cortex (AI) of the Behaving Ferret*, by Elgueda D., B Englitz, M Locastro, M Elhilali, S Shamma, and J Fritz)

information is likely to change with stimulus context and behavioral conditions in a manner that is difficult to discern across large sets of single neuron data because of the complexity of cortical receptive fields. STRFs help overcome this problem because they facilitate methods of stimulus *reconstruction* to study how complex sounds are encoded in AI. In such a method, measured STRFs are used to *invert* the responses and hence map population responses to an estimate of the stimulus spectrogram (Mesgarani et al. 2009). This enables one to perform a direct comparison between an original stimulus spectrogram and its reconstruction following learning or from responses during a behavioral paradigm. In fact, by estimating the fidelity of

such reconstructions using generalized spectrally and temporally modulated noise stimuli, one can determine the range over which AI neurons can faithfully encode such spectrotemporal features. Finally, contrasting stimulus reconstructions under different behavioral states can reveal a novel view of the rapid changes in spectrotemporal response properties induced by different attentional and motivational states.

Updating the STRF

There is much ongoing research to develop new STRF measurement procedures and structures and to combine them with new methodologies that go beyond the simple ways employed earlier. For instance, generalizing the STRFs to include

nonlinear phenomena (Atencio et al. 2008; Christianson et al. 2008; Nagel and Doupe 2008), inhibitory interactions (Schinkel-Bielefeld et al. 2012), and more flexible structures are among the goals being pursued. Also, STRFs are now being regularly estimated with a variety of specialized complex sounds such as bird vocalizations and speech (David et al. 2007; David et al. 2009; Theunissen et al. 2000), measurements that yield STRFs that are tailored to describe more faithfully cortical responses to these sounds. Furthermore, STRFs have now transcended their initial use in single unit recordings and are currently being widely used as a tool to summarize responses in human subjects recorded with fMRI (Zatorre and Belin 2001), MEG (Ding and Simon 2012), EEG (Power et al. 2011), and ECoG (Mesgarani and Chang 2012).

References

- Aertsen AMHJ, Johannesma PIM (1981) The spectro-temporal receptive field. *Biological cybernetics* 42(2):133–143
- Ahrens MB, Linden JF, Sahani M (2008) Nonlinearities and contextual influences in auditory cortical responses modeled with multilinear spectrotemporal methods. *J Neurosci* 28:1929–1942
- Arun P, Sripathi AP, Yoshioka T, Denchev P, Hsiao SS, Johnson KO (2006) Spatiotemporal receptive fields of peripheral afferents and cortical area 3b and 1 neurons in the primate somatosensory system. *J Neurosci* 26:2101–2114
- Atencio CA, Sharpee TO, Schreiner CE (2008) Cooperative nonlinearities in auditory cortical neurons. *Neuron* 58(6):956–966
- Chi T, Ru P, Shamma S (2006) Multiresolution spectrotemporal analysis of complex sounds. *J Acoust Soc Am* 118:887
- Christianson GB, Sahani M, Linden JF (2008) The consequences of response nonlinearities for interpretation of spectrotemporal receptive fields. *J Neurosci* 28:446–455
- David SV, Hayden BY, Gallant JL (2006) Spectral receptive field properties explain shape selectivity in area V4. *J Neurophysiol* 96:3492–3505
- David S, Mesgarani N, Shamma S (2007) Estimating sparse spectro-temporal receptive fields with natural stimuli. *Netw Comput Neural Syst* 18(3):191–212
- David S, Mesgarani N, Fritz JB, Shamma S (2009) Rapid synaptic depression explains nonlinear modulation of spectro-temporal tuning in primary auditory cortex by natural stimuli. *J Neurosci* 29:3374–3386
- De Boer E (1967) Correlation studies applied to the frequency resolution of the cochlea. *J Audit Res* 7:209–217
- de Boer E, de Jongh HR (1978) On cochlear encoding: potentialities and limitations of the reverse-correlation technique. *J Acoust Soc Am* 63:115–135
- De Valois RL, De Valois KK (1988) Spatial vision. Oxford University Press, New York
- DeAngelis GC, Ohzawa I, Freeman RD (1995) Receptive field dynamics in central visual pathways. *Trends Neurosci* 18:451–458
- Ding N, Simon JZ (2012) Emergence of neural encoding of auditory objects while listening to competing speakers. *Proc Natl Acad Sci U S A* 109(29):11854–11859
- Elhilali M, Shamma S (2008) The cocktail party problem – with a cortical twist. *J Acoust Soc Am* 124(6):3751–3771
- Fritz J, Shamma S, Elhilali M, Klein D (2003) Rapid task-dependent plasticity of spectrotemporal receptive fields in primary auditory cortex.” *Nat Neurosci* 6(11):1216–1223
- Fritz J, Shamma S, Elhilali M (2005a) Differential dynamic plasticity of A1 receptive fields during multiple spectral tasks. *J Neurosci* 25:7623–7635
- Fritz J, Shamma S, Elhilali M (2005b) Active listening: task-dependent plasticity of receptive fields in primary auditory cortex. *Hear Res* 206:159–176
- Gosselin F, Schyns P (2002) A new framework for visual categorization. *Trends Cog Neurosci* 6:70–76
- Hochstein S, Shapley RM (1976) Linear and nonlinear spatial subunits in Y cat retinal ganglion cells. *J Physiol* 262(2):265–284
- Klein DJ, Simon JZ, Depireux DA, Shamma SA (2006) Stimulus-invariant processing and spectrotemporal reverse-correlation in primary auditory cortex. *J Comput Neurosci* 20:111–136
- Mesgarani N, Slaney M, Shamma S (2005) Content-based audio classification based on multiscale spectro-temporal features. *IEEE Trans Audio Speech* 14(3):920–930
- Mesgarani N, Chang EF (2012) Selective cortical representation of attended speaker in multi-talker speech perception. *Nature* 485(7397):233–236
- Mesgarani N, David S, Fritz JB, Shamma SA (2008) Phoneme representation and classification in primary auditory cortex. *J Acoust Soc Am* 123:2433
- Mesgarani N, David S, Shamma S (2009) Influence of context and behavior on the population code in primary auditory cortex. *J Neurophysiol* 102:3329–3339
- Nagel KI, Doupe AJ (2008) Organizing principles of spectro-temporal encoding in the avian primary auditory area field L. *Neuron* 58(6):938–955
- Patil K, Pressnitzer D, Shamma S, Elhilali M (2012) Music in our ears: the biological bases of musical timbre perception. *PLoS computational biology* 8(11):e1002759
- Power AJ, Reilly RB, Lalor EC (2011) Comparing linear and quadratic models of the human auditory system using EEG. *Conf Proc IEEE Eng Med Biol Soc* 4:4171–4174

- Schinkel-Bielefeld N, David S, Shamma S, Butts D (2012) Inferring the roles of inhibition in auditory processing of complex natural stimuli. *J Neurophysiol* 107(12):3296–3307
- Shamma S, Versnel H, Kowalski N (1995) Ripple analysis in the ferret primary auditory cortex. I. Response characteristics of single units to sinusoidally rippled spectra. *J Audit Neurosci* 1:233–254
- Theunissen FE, Sen K, Doupe AJ (2000) Spectral-temporal receptive fields of nonlinear auditory neurons obtained using natural sounds. *J Neurosci* 20:2315–2331
- Zatorre R, Belin P (2001) Spectral and temporal processing in human auditory cortex. *Cereb Cortex* 11(10):946–953

Further Readings

- Fritz JB, Elhilali M, Shamma S (2007) Adaptive changes in cortical receptive fields induced by attention to complex sounds. *J Neurophysiol* 98:2337–2346
- Moller AR (1973) Statistical evaluation of the dynamic properties of cochlear nucleus units using stimuli modulated with pseudorandom noise. *Brain Res* 57:443–456

Spectrotemporal Response Fields

► Spectrotemporal Receptive Fields

Speech Sounds

► Pulse-Resonance Sounds

Speed-Accuracy Tradeoff

Rafal Bogacz

Department of Computer Science, University of Bristol, Bristol, UK

Definition

In many decision tasks, humans and animals cannot simultaneously improve both speed and accuracy of choices (Wickelgren 1977). If subjects are required to be faster, they become less accurate, and conversely, when they are more accurate, they become slower. This inverse relationship

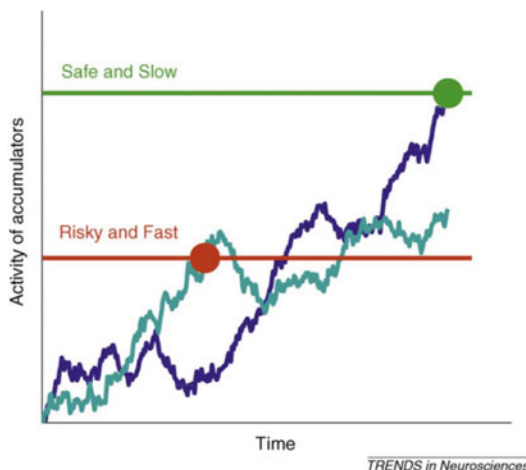
between the speed and the accuracy of choices is known as the speed-accuracy trade-off (SAT).

Detailed Description

SAT Results from the Accumulation of Noisy Information

SAT is produced in many models of decision making, but to motivate these models, it is helpful to first briefly review a specific example of a task used for studying the neurobiology of perceptual decision making. Neural bases of decision making have been studied in a simple task in which a subject is presented with a stimulus consisting of dots moving left or right and on each trial has to make an eye movement in the direction of the movement of the majority of dots. A brain area critical for this task is a part of visual cortex specialized in motion processing (known as V5 or MT), where different neurons are selective for different directions of motion and respond when motion in their preferred direction is present in their receptive field (Britten et al. 1992). These neurons provide information that could be used to make a decision, but the activity of these sensory neurons is noisy due to the noise present in the stimulus and the stochastic nature of neuronal firing. Experimental data suggest that to average out this noise, the output from sensory neurons selective for a particular stimulus is integrated by the frontoparietal neurons selective for a corresponding response (Gold and Shadlen 2007). This is suggested by an observation that the neurons selective for a particular response gradually increase their activity within a trial with a rate that depends on the activity of corresponding sensory neurons. It has been further observed that the movement is initiated whenever the activity of these integrator neurons reaches a certain threshold level (Gold and Shadlen 2007).

Computational models describing the above decision process range from abstract mathematical models, e.g., Ratcliff (1978), to detailed spiking models, e.g., Furman and Wang (2008).



Speed-Accuracy Tradeoff, Fig. 1 Simulated activity of accumulators in the race model. In the simulation the accumulator corresponding to *dark blue line* received input from a source with a higher mean than the accumulator corresponding to *light blue line*. *Green and red lines* indicate two possible positions of decision threshold and *circles* the times when the decision would be made (Reproduced from Bogacz et al. (2010) with permission from Cell Press)

The simplest of these models is an abstract race model in which two integrators accumulate independently sensory inputs from two corresponding sources, and the choice is made when the activity of any integrator reaches a threshold (Vickers 1970). The sources of input are noisy, but one of them provides an input with a higher mean, and the choice is considered correct, when the integrator accumulating the information from this source is the first to reach the threshold. The integration process averages out the noise present in the inputs; thus, the longer the period of integration, the higher the probability that the “correct” accumulator wins the race. The ability to trade speed for accuracy in the model arises due to the assumption that subjects are able to vary the distance between the baseline level of the integrators at the start of the trial and the threshold, as illustrated in Fig. 1. When this baseline to threshold distance is short, the decisions are on average faster but less accurate, whereas when the baseline to threshold distance is long, it takes

on average longer to reach the threshold, but the choice is made on the basis of a larger amount of input, so it is more likely to be correct.

Speed Emphasis Increases Baseline Activity

In many computational models, like the race model discussed above, speed and accuracy depend on the baseline to threshold distance: thus, faster choices may be achieved either by lowering the decision threshold or by increasing the initial level of activity of the integrator neurons. Experimental data suggest that the latter mechanism is employed by the brain. Increased baseline with speed emphasis was first suggested by imaging studies that observed higher activity in several decision-related areas before the onset of trials on which participants were required to be fast (Forstmann et al. 2008; Ivanoff et al. 2008; van Veen et al. 2008). More recently this suggestion was confirmed by a study (Heitz and Schall 2012) in which monkeys were trained to make saccadic choices in three conditions: fast, neutral, and accurate (in the fast condition they were rewarded only if the correct response was made before a certain deadline). Recordings of the activity of neurons from frontal eye field (FEF) in this task revealed that their activity before stimulus onset was indeed higher in the fast than in the neutral condition. Furthermore, a computational model of subcortical neurons receiving input from FEF, which was constrained by the data from the above experiment, suggested that the threshold activity these downstream neurons needed to reach for the response to be initiated was the same for all three conditions (Heitz and Schall 2012).

Control Over Speed and Accuracy

Several detailed theories have been proposed on how the speed and accuracy of choices are controlled in neural decision circuits in cortex (Furman and Wang 2008; Roxin and Ledberg 2008) and basal ganglia (Lo and Wang 2006; Frank et al. 2007; Forstmann et al. 2010). These models describe what inputs or plastic changes in the corticobasal-ganglia circuits could result in

the increased baseline activity of cortical integrators with speed emphasis (see previous section), and these theories have been reviewed in more detail by Bogacz et al. (2010). Although these proposed mechanisms are very different from one another, it is conceivable that multiple mechanisms operate in parallel.

Optimal Speed and Accuracy

The selected combination of speed and accuracy of choices influences the reward rate, i.e., the number of rewards per unit of time, in many natural foraging tasks and experimental paradigms. For example, consider a simple paradigm in which on each trial a subject has to judge the direction of movement of the majority of dots (as described earlier) and receives rewards for correct responses and no penalties for errors, and after each response there is a fixed delay until the beginning of the next trial. In this paradigm the optimal combination of speed and accuracy maximizing the reward rate depends on task parameters (Bogacz et al. 2006). For instance, when the dots move completely randomly, in order to maximize the reward rate, the subject should respond as quickly as possible (as the accuracy cannot be improved by inspecting the stimulus), whereas when substantial fraction of dots move coherently, the subject should take more time to respond more accurately. Experimental evidence suggests that humans indeed adapt their speed and accuracy to improve their reward rate (Simen et al. 2009), especially when given more practice (Balci et al. 2011).

In the above paradigm, if the difficulty of all trials is constant, reward rate is maximized in computational models by setting the baseline to threshold distance to an appropriate constant throughout the trial (Bogacz et al. 2006). However, when the difficulty varies between trials, the distance should change within a trial to maximize reward rate. For example, when a substantial amount of time has elapsed within a trial and the choice has still not been made, the subject may infer that this is a very difficult trial, so it is better to force a decision and move on to the next

trial. Methods for estimating the optimal time course of the threshold parameter of decision models have been described (Deneve 2012; Drugowitsch et al. 2012). However, recall that in mathematical models speed and accuracy can be adjusted by varying either the threshold or the baseline level of activity, and experimental data indicate that when difficulty varies between trials, the levels of activity of integrator neurons increase within a trial, eventually forcing a fixed decision threshold to be reached (Churchland et al. 2008).

References

- Balci F, Simen P, Niyogi R, Saxe A, Hughes JA, Holmes P, Cohen JD (2011) Acquisition of decision making criteria: reward rate ultimately beats accuracy. *Atten Percept Psychophys* 73:640–657
- Bogacz R, Brown E, Moehlis J, Holmes P, Cohen JD (2006) The physics of optimal decision making: a formal analysis of models of performance in two-alternative forced choice tasks. *Psychol Rev* 113:700–765
- Bogacz R, Wagenmakers EJ, Forstmann BU, Nieuwenhuis S (2010) The neural basis of the speed-accuracy tradeoff. *Trends Neurosci* 33:10–16
- Britten KH, Shadlen MN, Newsome WT, Movshon JA (1992) The analysis of visual motion: a comparison of neuronal and psychophysical performance. *J Neurosci* 12:4745–4765
- Churchland AK, Kiani R, Shadlen MN (2008) Decision-making with multiple alternatives. *Nat Neurosci* 11:693–702
- Deneve S (2012) Making decisions with unknown sensory reliability. *Front Neurosci* 6:75
- Drugowitsch J, Moreno-Bote R, Churchland AK, Shadlen MN, Pouget A (2012) The cost of accumulating evidence in perceptual decision making. *J Neurosci* 32:3612–3628
- Forstmann BU, Dutilh G, Brown S, Neumann J, von Cramon DY, Ridderinkhof KR, Wagenmakers EJ (2008) Striatum and pre-SMA facilitate decision-making under time pressure. *Proc Natl Acad Sci U S A* 105:17538–17542
- Forstmann BU, Anwander A, Schafer A, Neumann J, Brown S, Wagenmakers EJ, Bogacz R, Turner R (2010) Cortico-striatal connections predict control over speed and accuracy in perceptual decision making. *Proc Natl Acad Sci U S A* 107:15916–15920
- Frank MJ, Sherman SJ, Scheres A (2007) Understanding decision making deficits in neurological conditions: insights from models of natural action selection. *Philos Trans Roy Soc Ser B* 362:1641–1654

- Furman M, Wang XJ (2008) Similarity effect and optimal control of multiple-choice decision making. *Neuron* 60:1153–1168
- Gold JI, Shadlen MN (2007) The neural basis of decision making. *Annu Rev Neurosci* 30:535–574
- Heitz RP, Schall JD (2012) Neural mechanisms of speed-accuracy tradeoff. *Neuron* 76:616–628
- Ivanoff J, Branning P, Marois R (2008) fMRI evidence for a dual process account of the speed-accuracy tradeoff in decision-making. *PLoS One* 3:e2635
- Lo CC, Wang XJ (2006) Cortico-basal ganglia circuit mechanism for a decision threshold in reaction time task. *Nat Neurosci* 9:956–963
- Ratcliff R (1978) A theory of memory retrieval. *Psychol Rev* 83:59–108
- Roxin A, Ledberg A (2008) Neurobiological models of two-choice decision making can be reduced to a one-dimensional nonlinear diffusion equation. *PLoS Comput Biol* 4:e1000046
- Simen P, Contreras D, Buck C, Hu P, Holmes P, Cohen JD (2009) Reward rate optimization in two-alternative decision making: empirical tests of theoretical predictions. *J Exp Psychol Hum Percept Perform* 35:1865–1897
- van Veen V, Krug MK, Carter CS (2008) The neural and computational basis of controlled speed-accuracy tradeoff during task performance. *J Cogn Neurosci* 20:1952–1965
- Vickers D (1970) Evidence for an accumulator model of psychophysical discrimination. *Ergonomics* 13:37–58
- Wickelgren WA (1977) Speed-accuracy tradeoff and information processing dynamics. *Acta Psychol (Amst)* 41:67–85

Spike Initiation

- Action Potential Initiation

Spike Metric

- Spike Train Distance

Spike Rate

- Estimation of Neuronal Firing Rate

Spike Time Response Curve

Theoden I. Netoff

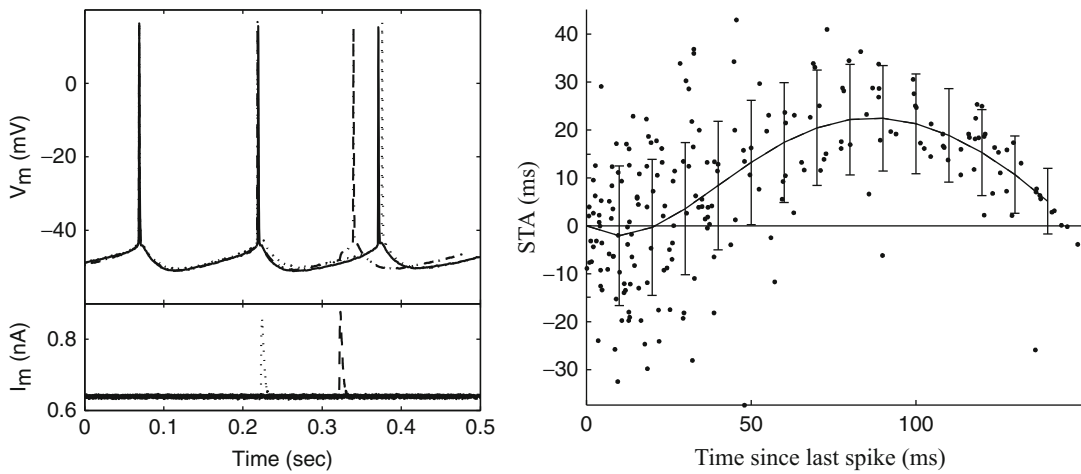
Department of Biomedical Engineering,
University of Minnesota, Minneapolis,
MN, USA

Definition

The spike time response curve (STRC) is a measure of how a stimulus affects the timing of a neuron's action potential. Specifically, in a periodically firing neuron, the STRC is a measure of the change in the interspike interval given the time of the stimulus pulse since the last action potential. An example of an STRC measured from a pyramidal neuron in the hippocampus is shown in Fig. 1. The STRC is closely related to the phase response curve (PRC); the difference is that the STRC is not normalized by the period of the neuron.

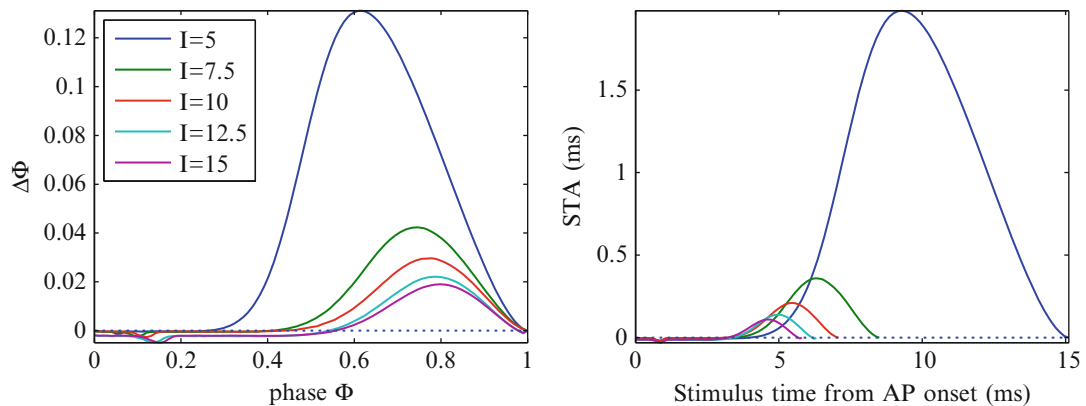
Detailed Description

An example where the PRC and the STRC provide different information is when comparing stimulus responses at different firing rates of the neuron. Figure 2 shows the same data plotted as a PRC and as an STRC from a model neuron, the $I_{NaP,K}$ model (Izhikevich 2007). As current applied to the neuron increases, the interspike interval shortens. It can be seen at higher current and shorter ISIs, the PRC peak of the PRC shifts to the right. However, when plotted as an STRC, the peak shifts earlier in time. The amplitude of the phase advance is also normalized by the interspike interval. It can be seen that the difference in the peak from the smallest to biggest PRC is about sixfold, while in the STRC, the difference between the smallest peak spike advance and the largest is a twenty-fold difference. As stated above, the STRC retains information



Spike Time Response Curve, Fig. 1 *Left* panel, a pyramidal neuron in the hippocampus is recorded and stimulated using whole-cell patch clamp. Voltage traces (*top*) and stimulus current (*below*) are plotted from three segments of data. The first interspike interval is unperturbed in all three traces, and interspike intervals are almost identical. In the second interval, a stimulus is applied. The *solid line* shows the unperturbed recording, and the *dotted* and *dashed* lines show recordings where

a synaptic-like stimulus waveform is applied, at a time just after the neuron spikes (*dotted*) and in the *middle* of the period (*dashed*). *Right* panel, the spike time response curve is generated by plotting spike time advance (STA) from the unperturbed interspike interval (150 ms in this case) against the time that the stimulus was applied since the last spike. A polynomial function is fit to the mean and the standard deviation of the data (This figure is modified from Netoff et al. (2005))



Spike Time Response Curve, Fig. 2 Phase response curve compared to STRC. A PRC (*left*) and an STRC (*right*) are measured from a computational model of a neuron at different amounts of applied current. As the

applied current increases, the interspike interval decreases. The PRC is normalized to the change in the unperturbed interspike interval, while the STRC is not. Both graphs represent the same data but with different axes

about time intervals, whereas the PRC is normalized by the intrinsic period. It is necessary to retain the information about time intervals in order to predict the synchronization properties of periodically driven or reciprocally coupled oscillatory neurons, as described in the entry on “► Pulse-Coupled Oscillators” (Netoff

et al. 2005; Oprisan et al. 2003; Glass and Mackey 1988).

Cross-References

► Pulse-Coupled Oscillators

References

- Glass L, Mackey MC (1988) From clocks to chaos: the rhythms of life. Princeton University Press, Princeton
- Izhikevich EM (2007) Dynamical systems in neuroscience: the geometry of excitability and bursting. MIT Press, Cambridge, MA
- Netoff TI et al (2005) Synchronization in hybrid neuronal networks of the hippocampal formation. *J Neurophysiol* 93:1197–1208
- Oprisan SA et al (2003) Dynamics from a time series: can we extract the phase resetting curve from a time series? *Biophys J* 84:2919–2928

Spike-Timing Dependent Plasticity (STDP), Biophysical Models

Thom Griffith¹, Jack Mellor² and Krasimira Tsaneva-Atanasova³

¹Department of Engineering Mathematics, University of Bristol, Bristol, UK

²School of Physiology and Pharmacology, University of Bristol, Bristol, UK

³Department Mathematics, College of Engineering, Mathematics and Physical Sciences, University of Exeter, Exeter, UK

Definition

A biophysical model of spike-timing-dependent plasticity (STDP) is one which converts time intervals, in a given firing pattern of synaptically coupled pre- and postsynaptic neurons, to modifications of the connecting synapse. This class of STDP model is defined by their mathematical representation of specific biophysical quantities, which have been shown to play a role in the intracellular mechanisms underlying synaptic plasticity.

Detailed Description

Within the STDP framework, models of synaptic plasticity are dependent on the precise relative timing of pre- and postsynaptic spikes and,

broadly speaking, utilize one, or a combination, of two modelling approaches. The first group of STDP models use phenomenological modelling to empirically describe the relationship between the model inputs (pre- and postsynaptic spike times) and the model output (synaptic weight modification). There is usually little or no attempt to represent the intracellular machinery governing synaptic plasticity in the model. The second group of STDP models use a *biophysical* modelling approach, which means that they include variables that represent specific biophysical species or quantities. The mathematical relationships between the variables in a biophysical model encapsulate our mechanistic understanding of the biochemical and electrophysiological processes that are being modelled. Predictions from biophysical STDP models can therefore offer insight into the mechanisms governing the induction of synaptic plasticity.

Ca²⁺-Based Models of STDP

The critical trigger for synaptic plasticity is a rise in intracellular Ca²⁺ concentration, [Ca²⁺], since synaptic long-term potentiation (LTP) and depression (LTD) are blocked by pharmacological buffering of Ca²⁺ (Malenka and Bear 2004; Graupner and Brunel 2010). The importance of intracellular Ca²⁺ is reflected in the fact that dynamic cytosolic Ca²⁺ levels, acting as intermediate signals for induction of plasticity, are a common feature of most biophysical models of STDP.

Ca²⁺-based biophysical models of STDP must include a description of the changes in [Ca²⁺] due to pre- and postsynaptic spiking. Ca²⁺ sources may depend on the particular synapse to be modelled but most frequently include influx via NMDA receptors (NMDARs), influx via Ca²⁺-permeable AMPA receptors (AMPARs), influx via voltage-gated Ca²⁺ channels (VGCCs), or Ca²⁺ release from intracellular stores. Since most modelling efforts are directed towards understanding NMDAR-dependent plasticity, NMDARs are the primary source of Ca²⁺ in the majority of biophysical STDP models. Entry of extracellular Ca²⁺ via postsynaptic membrane ion channels can be dependent on both the

postsynaptic membrane potential and the action of neurotransmitters in the synaptic cleft; therefore, biophysical models of STDP often contain descriptions of electrophysiological cell membrane phenomena and AMPAR/NMDAR ligand gating in response to neuron pair spiking. The sophistication of intracellular Ca^{2+} handling within the model can be further increased by the inclusion of Ca^{2+} buffers or plasma membrane ion pumps.

Simplified Intracellular Dynamics

Biophysical STDP models can be categorized according to their method of transposing postsynaptic Ca^{2+} signals into synaptic modifications. In one set of STDP models, simplifications of the forward-connected Ca^{2+} -dependent mechanisms underlying synaptic plasticity are used alongside a realistic biophysical treatment of Ca^{2+} dynamics within the postsynaptic neuron. Ca^{2+} signalling networks in these models are reduced to abstract Ca^{2+} -signal detection systems or simple algebraic equations, which introduce phenomenological variables relating postsynaptic $[\text{Ca}^{2+}]$ to synaptic weight changes. These types of STDP models vary in their consideration of the postsynaptic $[\text{Ca}^{2+}]$ transient, with some using peak magnitude only as their signal (e.g., Shouval et al. 2002; Rackham et al. 2010), while others consider the whole transient (e.g., Rubin et al. 2005). The Ca^{2+} detectors are designed to describe simplified kinase/phosphatase activity in dephosphorylation/phosphorylation cycles that are critical for synaptic plasticity induction and to capture the essential quality of the Ca^{2+} -control hypothesis, which states that high transient intracellular $[\text{Ca}^{2+}]$ leads to LTP, whereas moderate more prolonged increases in $[\text{Ca}^{2+}]$ result in LTD (Lisman 1989). Examples of models using this approach include Shouval et al. (2002), Abarbanel et al. (2003), Rubin et al. (2005), and Rackham et al. (2010).

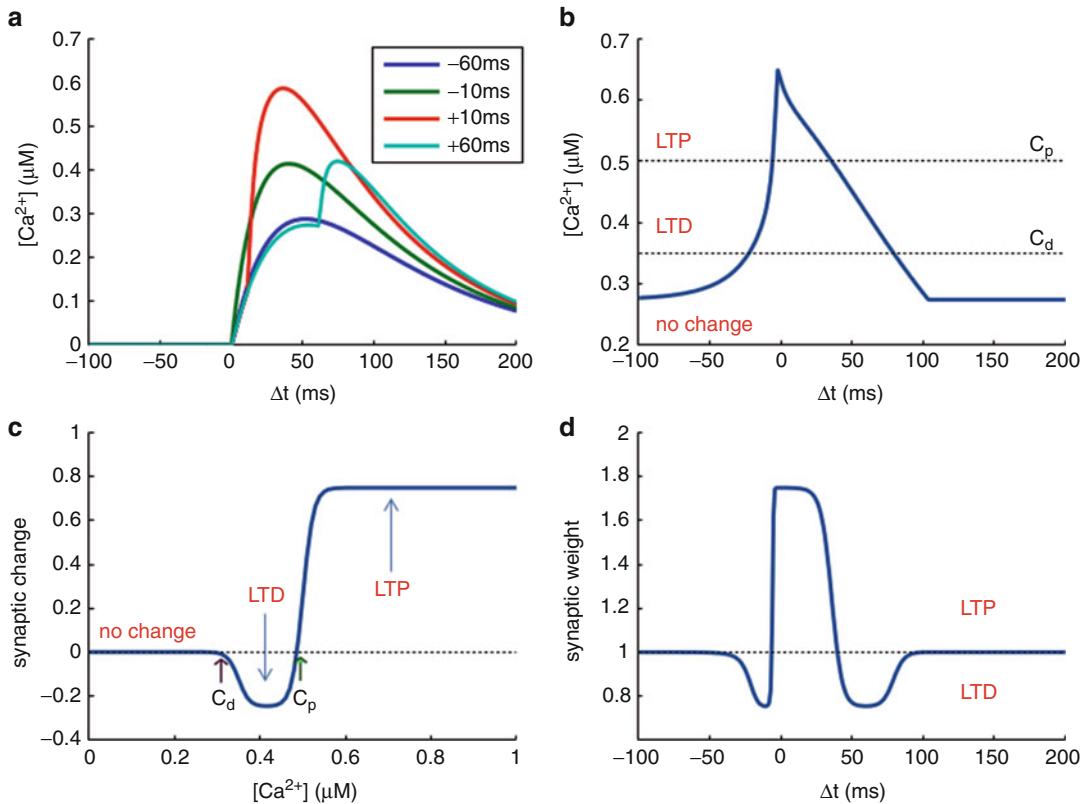
The simplest of these models (Shouval et al. 2002, Fig. 1) results in a second LTD window at large positive STDP time intervals between pre- and postsynaptic spikes, an effect that is not observed in the majority of

experimental STDP spike-pair studies. Conflicts with experimental data, such as this, can be remedied by the introduction of further phenomenological variables to “veto” LTD at positive time intervals (Rubin et al. 2005) or by including the stochastic properties of synaptic transmission in the model, a modification which significantly reduces the magnitude of the second LTD window (Shouval and Kalantzis 2005).

Modelling Signalling Pathways

A key signalling pathway that has been identified in the mediation of NMDAR-dependent synaptic plasticity is the Ca^{2+} /calmodulin-dependent protein kinase II (CaMKII) signalling cascade (Lisman et al. 2002). Phosphorylation of CaMKII is linked with increased synaptic AMPAR number and conductance. Models of the complex CaMKII signalling pathway use Ca^{2+} signals to regulate the phosphorylation state of CaMKII. These models can exhibit a bistable switch-like behavior in the phosphorylation state of CaMKII (Fig. 2). This is due to the combination of a CaMKII autophosphorylation-generated positive-feedback loop in the signalling network and CaMKII activity inhibition by Ca^{2+} /calmodulin-dependent protein phosphatase 1 (PP1). Bistable models result in a synapse that exists in one of two states: a baseline state with synaptic AMPAR conductance magnitude corresponding to low levels of postsynaptic CaMKII phosphorylation and a potentiated state corresponding to the second stable (high) phosphorylation level of CaMKII. The transition between the two states is triggered by intracellular $[\text{Ca}^{2+}]$, with moderate concentrations leading to low CaMKII phosphorylation states and high concentrations causing a transition to the highly phosphorylated state. This behavior corresponds with the Ca^{2+} -control hypothesis. A requirement for the maintenance of plasticity in CaMKII models is that the two CaMKII phosphorylation states must also be stable at baseline intracellular Ca^{2+} levels.

Castellani et al. (2005) is an example of a CaMKII-class, biophysical STDP model, describing induction of plasticity only since

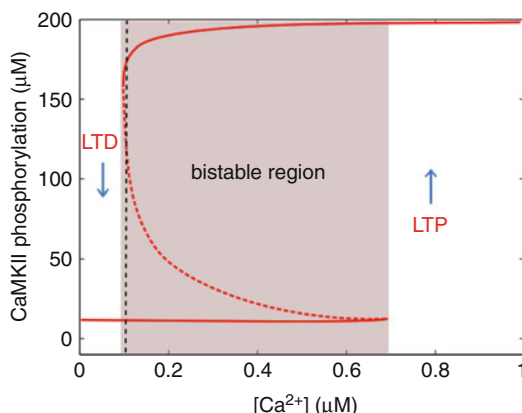


Spike-Timing Dependent Plasticity (STDP), Biophysical Models, Fig. 1 STDP according to Shouval et al. (2002). (a) $[Ca^{2+}]$ transients as described by Shouval et al. (2002) for four spike pairs. Presynaptic spike occurs at $t = 0$, and postsynaptic spike occurs at time interval as indicated in the legend. The only source of Ca^{2+} in the model is Ca^{2+} influx mediated by NMDARs. (b) Peak predicted $[Ca^{2+}]$ plotted against the spike-pair time interval. LTP and LTD peak $[Ca^{2+}]$ -signal threshold values, c_p and c_d , are illustrated showing plasticity outcomes for

spike-pair intervals from -100 ms to 200 ms. (c) The calcium-control hypothesis. Plot shows direction and magnitude of synaptic strength modification with $[Ca^{2+}]$ signal according to the calcium-control hypothesis (Shouval et al. 2002). LTD is predicted at moderate Ca^{2+} levels, and for large $[Ca^{2+}]$, LTP is the outcome. (d) STDP curve for spike pairs within range -100 ms to 200 ms as predicted by Shouval et al. (2002). Note the second LTD window at larger positive time intervals, an effect that is not observed in the majority of experimental STDP studies

bistability is absent from the model. An early mathematical model of the CaMKII system that exhibits bistability in the phosphorylation states of CaMKII is detailed by Lisman and Zhabotinsky (2001). Studies that have used similar CaMKII bistable switching models, with particular application to STDP, include Graupner and Brunel (2007) and Urakubo et al. (2008). A more complicated signalling network is described by Jain and Bhalla (2009), whose model incorporates transcription and protein synthesis for the maintenance of LTP/LTD.

There is still some uncertainty as to whether NMDAR-dependent LTD/LTP is the same process acting in opposing directions or whether NMDAR-dependent LTD induction proceeds via a separate molecular signalling pathway to LTP induction. Models of cerebellar, non-NMDAR-dependent LTD do use a separate signalling pathway, which proceeds in a metabotropic glutamate receptor (mGluR)-dependent manner, ultimately leading to removal of AMPARs from the postsynaptic membrane and, hence, a reduction in synaptic transmission efficiency (Ito 2001).



Spike-Timing Dependent Plasticity (STDP), Biophysical Models, Fig. 2 Bistable CaMKII switch. Concentration of phosphorylated CaMKII subunits as a function of the intracellular Ca^{2+} level. Stable states are indicated by *solid red line*, and unstable stationary states are indicated by *dashed red line*. Shaded region represents the $[\text{Ca}^{2+}]$ window within which both low and high CaMKII phosphorylation states are stable. Baseline $[\text{Ca}^{2+}]$ is indicated with *vertical dashed black line* showing stability of both high and low CaMKII phosphorylation states allowing maintenance of plasticity at normal intracellular levels of Ca^{2+} . LTP and LTD $[\text{Ca}^{2+}]$ signal windows are shown either side of the bistable region (Figure reproduced from Zhabotinsky (2000))

Modelling Approaches

Over 100 biophysical models for synaptic plasticity exist in publication, most of which bear a resemblance to the models described in the above sections (Manninen et al. 2010). These models can be classified according to the various methods used to create the model. For instance, many models have deterministic outcomes, while others include the stochasticity inherent in biochemical processes and have variable output. It is also possible to utilize a hybrid approach, incorporating stochastic and deterministic methods within the same model. Furthermore, some models take into account the spatial dependence of plasticity mechanisms since $[\text{Ca}^{2+}]$ signalling may be variable over the intracellular region to be modelled, whereas other models compress $[\text{Ca}^{2+}]$ signals to their time-dependent component only. Some biophysical STDP models include increased complexity, such that the outputs

include spatial resolution of biological signals, and also variability across synapse populations (Manninen et al. 2010).

References

- Abarbanel HDI, Gibb L, Huerta R, Rabinovich MI (2003) Biophysical model of synaptic plasticity dynamics. *Biol Cybern* 89(3):214–226
- Castellani GC, Quinlan EM, Bersani F, Cooper LN, Shouval HZ (2005) A model of bidirectional synaptic plasticity: from signaling network to channel conductance. *Learn Memory* (Cold Spring Harbor, NY) 12(4):423–432
- Graepel M, Brunel N (2007) STDP in a bistable synapse model based on CaMKII and associated signaling pathways. *PLoS Comput Biol* 3(11):e221
- Graepel M, Brunel N (2010) Mechanisms of induction and maintenance of spike-timing dependent plasticity in biophysical synapse models. *Front Comput Neurosci* 4:1–19
- Ito M (2001) Cerebellar long-term depression: characterization, signal transduction, and functional roles. *Physiol Rev* 81(3):1143–1195
- Jain P, Bhalla US (2009) Signaling logic of activity-triggered dendritic protein synthesis: an mTOR gate but not a feedback switch. *PLoS Comput Biol* 5(2): e1000287
- Lisman J (1989) A mechanism for the Hebb and the anti-Hebb processes underlying learning and memory. *Proc Natl Acad Sci USA* 86(23):9574–9578
- Lisman JE, Zhabotinsky AM (2001) A model of synaptic memory: viewpoint a CaMKII/PP1 switch that potentiates transmission by organizing an AMPA receptor anchoring assembly. *Neuron* 31:191–201
- Lisman J, Schulman H, Cline H (2002) The molecular basis of CaMKII function in synaptic and behavioural memory. *Nat Rev Neurosci* 3(3):175–190
- Malenka RC, Bear MF (2004) LTP and LTD: an embarrassment of riches. *Neuron* 44(1):5–21
- Manninen T, Hituri K, Kotaleski JH, Blackwell KT, Linne M-L (2010) Postsynaptic signal transduction models for long-term potentiation and depression. *Front Comput Neurosci* 4(December):1–29
- Rackham OJL, Tsaneva-Atanasova K, Ganesh A, Mellor JR (2010) A Ca-based computational model for NMDA receptor-dependent synaptic plasticity at individual post-synaptic spines in the hippocampus. *Front Synaptic Neurosci* 2(July):31
- Rubin JE, Gerkin RC, Bi G, Chow CC, Jonathan E (2005) Ca^{2+} Time course as a signal for spike-timing – dependent plasticity. *J Neurophysiol* 93:2600–2613
- Shouval HZ, Kalantzis G (2005) Stochastic properties of synaptic transmission affect the shape of spike time – dependent plasticity curves. *J Neurophysiol* 93:1069–1073

- Shouval HZ, Bear MF, Cooper LN (2002) A unified model of NMDA receptor-dependent bidirectional synaptic plasticity. *Proc Natl Acad Sci USA* 99(16): 10831–10836
- Urakubo H, Honda M, Froemke RC, Kuroda S (2008) Requirement of an allosteric kinetics of NMDA receptors for spike timing-dependent plasticity. *J Neurosci J Soc Neurosci* 28(13):3310–3323
- Zhabotinsky AM (2000) Bistability in the Ca(2+)/calmodulin-dependent protein kinase-phosphatase system. *Biophysical Journal* 79(5):2211–21

Spike Train

Robert E. Kass
Carnegie Mellon University, Pittsburgh, PA, USA

Definition

A spike train is a sequence of recorded times at which a neuron fires an *action potential*. When the voltage drop across a neural soma or axon membrane is recorded, intermittent pulses of roughly 100 mV over 1–2 ms are observed – these are action potentials or “spikes.” On a behavioral time scale of several hundred milliseconds, each spike may be considered to occur at a single point in time. Sequences of such spike times form spike trains. The total duration of a recorded spike train can range from less than a second to many minutes or even, in chronic recordings, to many days. Spike trains are considered to be the primary mode of information transmission in the nervous system.

Detailed Description

When action potentials are recorded repeatedly from a neuron in response to changing stimuli (or while an organism produces changing behaviors), they maintain a relatively consistent shape. However, the pattern of spike times varies as the stimulus changes. Most prominently, the rate at which spikes occur, the firing rate (FR), varies with conditions. When firing rate is defined in terms of the number of spikes that occur over

a time interval of length Δt (such as $\Delta t = 500$ ms), using

$$FR = \frac{\text{number of spikes}}{\Delta t}, \quad (1)$$

this phenomenon of firing rate varying with stimulus is called *rate coding*. While analysis of neural activity in terms of varying firing rates, as defined in Eq. 1, is useful in many contexts, more subtle alterations of the pattern of spike times also occur and these, too, may convey information. For example, the lengths of gaps between spikes, known as inter-spike intervals (ISIs), often vary substantially across an observed spike train. In principle, a neural communication “code” could carry enormous amounts of information in the specific patterns of spike times, but even in highly controlled *in vitro* preparations, repeated injection of the same time-varying current can lead to varying spike times, due to the stochastic behavior of ion channels and related sources of noise. Furthermore, synaptic noise is introduced at multiple connections across a neural network. Thus, a good deal of the irregularity of ISIs observed in many parts of the nervous system (especially, in cortex) may be unrelated to any stimulus or behavior. The problem of *neural coding* is to determine the ways that patterns of spike times convey information in particular contexts, possibly extending beyond rate coding. For this purpose, spike trains are subjected to statistical methods of data analysis.

In probability and statistics, irregular sequences of event times are modeled as *point processes*. If we start at time $t = 0$ and let X_1, X_2, \dots be a sequence of random variables representing the ISIs, then the time of the j th spike is given by $S_j = \sum_{i=1}^j X_i$ and the sequence S_1, S_2, \dots forms a point process. In practice, point processes representing spike trains are considered only over some finite interval of time $[0, T]$.

The oldest and most basic model for spike trains is the *integrate-and-fire model*, according to which a neuron is equivalent to an electrical circuit involving a resistor and a capacitor in parallel, together with an input current; the neuron fires whenever the voltage reaches a threshold, then it resets to a fixed resting

potential. A component of the input current may be used to represent stochastic synaptic activity. This idea, and many variations on it, is commonly used to generate artificial spike trains in computational studies (Gerstner and Kistler 2002). The resulting spike trains follow point processes and, under simplifying assumptions, can be subjected to theoretical analysis. For example, when excitatory and inhibitory inputs are conceptualized (in the theoretical limit) as Brownian motion, the ISI distribution may be derived analytically (Tuckwell 1988), and it turns out that certain features of this ISI distribution bear a striking qualitative resemblance to corresponding features of observed spike trains.

Point process representations of spike trains are governed by a theoretical instantaneous firing rate. If we replace the spike count in the numerator of Eq. 1 by its theoretical counterpart, the expected spike count, and then pass to the limit as $\Delta t \rightarrow 0$, we obtain

$$FR(t) = \lim_{\Delta t \rightarrow 0} \frac{P(\text{spike in } (t, t + \Delta t))}{\Delta t}. \quad (2)$$

(For small intervals Δt there is at most 1 spike and the expected count is equal to the probability of spiking.) However, the definition in Eq. 2 omits any mention of both the spiking behavior prior to time t and the experimental context. For instance, immediately after a neuron fires a spike, the probability of the neuron firing again is greatly reduced – this is known as the refractory period. If we write all relevant variables that affect the probability of a neuron firing (including the time of the most recent previous spike) as a vector x_t , we instead obtain the more explicit definition of neural firing rate:

$$FR(t|x_t) = \lim_{\Delta t \rightarrow 0} \frac{P(\text{spike in } (t, t + \Delta t)|x_t)}{\Delta t}. \quad (3)$$

Acknowledging that the numerator of Eq. 3 may involve complicated functions of stimuli, prior spiking patterns, and other variables, a statistical model for spike trains involves two things: (i) a simple, universal formula for the probability density of the spike train in terms of the instantaneous firing rate function defined in Eq. 3 and

(ii) a specification of the way the firing rate function depends on the variables x_t (the numerator of Eq. 3). This representation provides a framework that may be called *point process regression* because it relates the specific pattern of spike times, i.e., the spike train, to variables collected as x_t . The full battery of modern statistical machine learning methods may then be applied to the problem of neural coding.

The simplest point process regression models take a special form known in the statistics literature as *generalized linear models* (GLMs). In computational neuroscience the term GLM may refer to any type of point process regression model.

Cross-References

- ▶ [Estimation of Neuronal Firing Rate](#)
- ▶ [Generalized Linear Models for Point Process Analyses of Neural Spiking Activity](#)
- ▶ [Neural Coding](#)
- ▶ [Spike Train Analysis: Overview](#)

References

- Gerstner W, Kistler W (2002) Spiking neuron models: single neurons, populations, plasticity. Cambridge University Press, Cambridge
 Tuckwell H (1988) Introduction to theoretical neurobiology. Non linear and stochastic theories, vol 2. Cambridge University Press, Cambridge

Further Reading

- Kass RE, Eden UT, Brown EN (2014) Analysis of neural data. Springer, New York

Spike Train Distance

Jonathan D. Victor
 Brain and Mind Research Institute and
 Department of Neurology, Weill Cornell Medical College of Cornell University, New York, NY, USA

Synonyms

[Spike metric](#)

Definition

A “spike train distance” (or, equivalently, a “spike metric”) is a means for comparing two samples of stereotyped event sequences. While spike train distances can be applied to any kind of stereotyped event sequence, we focus here on their application to neuroscience, in which the event sequences represent the sequence of action potentials emitted by a neuron or a set of neurons.

Detailed Description

Overview

Spike train distances are “metrics,” namely, rules for assigning a notion of distance, or dissimilarity, to elements in a topological space. Two considerations give this general framework a special flavor when applied to neural data. The first consideration is mathematical: the topology of event sequences combines a discrete component with a continuous component. The discrete component is that the number of events in a spike train must be an integer; the continuous component is that each of these events can occur across a continuum of times. The second consideration is biological: much is known about the physiology of neurons and neural circuits, and spike train distances are typically designed with the goal of capturing the biologically significant aspects of neuronal activity.

As detailed below, two contrasting ideas concerning the biological meaning of a spike train serve as anchor points: (a) the firing events in a spike train might serve primarily as a means to represent an underlying firing rate versus (b) the times of these firing events might have individual significance, enabling neural computations to be based on coincident firing events across neurons and other aspects of fine temporal structure.

Notation

A spike train – the sequence of action potentials emitted by one or more neurons – is formalized as a sequence of stereotyped events, called

spikes, that occur during a fixed observation period $[0, T]$. That is, a spike train A is represented by an ascending sequence of real numbers $t_1^A, \dots, t_{M(A)}^A$ in $[0, T]$, where t_k^A (or simply t_k) is the time of occurrence of the k th spike and $M(A)$ is the total number of spikes (which may be 0).

The above applies to a setting in which all spikes originate from a single neuron or the identity of the neurons that generate the individual spikes is not distinguished. It is readily extended to a setting in which the neural activity arises from L different neurons, and the neuron of origin of each event is known: the sequence of times $t_1, \dots, t_{M(A)}$ is associated with a sequence of labels $a_1, \dots, a_{M(A)}$, each drawn from a set of tags $\{1, \dots, L\}$. Thus, spike trains are regarded as a sample drawn from a **point process** (activity of one neuron) or a **labeled point process** (activity of several neurons).

Formal Definition

A spike train distance is a mapping D from the set of spike trains to the nonnegative real numbers that meet the three requirements of a topological **metric**:

$$\begin{aligned} \text{Nonnegativity : } D(A, B) &\geq 0, \text{ and } D(A, B) = 0 \\ &\text{only if } A = B \end{aligned} \tag{1}$$

$$\text{Symmetry : } D(A, B) = D(B, A) \tag{2}$$

$$\begin{aligned} \text{Triangle inequality : } D(A, C) &\leq D(A, B) \\ &+ D(B, C) \end{aligned} \tag{3}$$

The nonnegativity property (3) is frequently relaxed to omit the “only if” clause, in which case, D is formally a **pseudometric**. In this case, the space of spike trains can be partitioned into equivalence classes of spike trains that are at distances of 0 from each other, and D acts as a metric on these equivalence classes. The “spike count distance,” formalized following Eq. 10, is a simple example of a pseudometric; spike trains with the same number of spikes fall into an equivalence class.

Constructing Spike Train Distances

There are two main families of spike train distances: embedding-based and cost-based. In the first approach, spike train distances are defined by embedding spike trains into a vector space and then adopting the vector space distance. In the second approach, a set of simple transformations of spike trains is specified, along with their (nonnegative) costs. The spike train distance is then defined as the minimal total cost of transforming one spike train into another.

Spike Train Distances Based on Embedding

In the embedding construction, spike trains are first mapped into a **normed vector space** V via a mapping f . Since the vector space norm $\|x\|$ provides a metric via $D(u, v) = \|u - v\|$, the vector space norm yields a metric on the spike trains:

$$D(A, B) = \|f(A) - f(B)\|. \quad (4)$$

The nature of the mapping f from the space of spike trains to the vector space is critical. Typically, this mapping respects an additive structure on the spike trains: that is, if $A + B$ denotes the spike train that results from superimposing A and B (with suitable provision made for coincident spikes), then $f(A + B) = f(A) + f(B)$. For such embeddings, then resulting metric is unchanged by parallel translation:

$$D(A + C, B + C) = D(A, B) \quad (5)$$

Spike train distances in this class generally emphasize either the continuous aspect of spike train topology or its discrete aspect. The family of distances introduced by (van Rossum 2001) is a prototypical example of the former. We consider first the case of an unlabeled spike train, which here is regarded as a sequence of delta functions. The target vector space consists of scalar functions of time (considered as a continuous variable), and the embedding f consists of a convolution by a kernel function $K(t)$:

$$f(A)(t) = \int_{-\infty}^{\infty} K(t - \tau) \sum_{j=1}^{M(A)} \delta(\tau - t_j^A) d\tau \quad (6)$$

Since the mapping Eq. 6 from the spike train A to the vector space element $f(A)$ is linear, it follows that the resulting metric, defined by Eq. 4, is unchanged by parallel translation (as in Eq. 5).

Typically, the kernel function K in Eq. 6 includes a parameter that expresses the temporal resolution of the comparison between two spike trains, e.g., $K(t) = \frac{1}{t_0} e^{-t/t_0}$ ($t \geq 0$). If spikes in train A and train B are matched within this resolution, i.e., if $|t_j^A - t_j^B| < t_0$, then the spike train distance between A and B will be small. Gaussians, boxcars, and similar nonnegative windowing functions are also reasonable choices for K . These embedding functions are conventionally used in conjunction with an L^p norm for the target vector space,

$$\|f(A)\| = \left(\int_{-\infty}^{\infty} |f(A)(t)|^p dt \right)^{1/p} \quad (7)$$

usually with $p = 2$ (the Euclidean norm). Thus, the net result of a linear embedding followed by the vector space norm provides a Euclidean geometry on spike trains.

To extend this kind of spike train distance to the multineuronal setting (L labeled neurons), the target vector space is taken to be vector-valued functions of time (Houghton and Sen 2008), and the norm is the L^2 -norm on the space of vector-valued functions. To define the embedding function f , vectors \vec{v}_l (typically, unit vectors) are assigned to each of the L labels. With this assignment,

$$f(A)(t) = \int_{-\infty}^{\infty} K(t - \tau) \sum_{j=1}^{M(A)} \vec{v}_{a(j)} \delta(\tau - t_j^A) d\tau \quad (8)$$

Thus, the j th event, a spike on neuron $a(j)$ at time t_j , is mapped to a bump (the kernel shape) “pointing” in the direction $\vec{v}_{a(j)}$ that has been

assigned to neuron $a(j)$. The angles between the vectors \vec{v}_l correspond to the extent to which the spike train distance is sensitive to the label associated with each spike.

In the above examples, the embeddings are linear, and, moreover, time reversal (formally, replacing each t_j with $T - t_{M(A)} - j$) has no effect on the resulting distances. Neither of these properties is needed for an embedding to yield a distance; in fact, there are biological motivations to consider distances that derive from embeddings that lack these properties. For example, as a consequence of synaptic facilitation and depression (Sen et al. 1996), the effect of a spike on a postsynaptic neuron depends on how much time has elapsed since the previous spike. This dependence can be incorporated into an embedding function (Houghton 2009), conferring on it both nonlinearities and time-reversal asymmetries.

Spike train distances based on an embedding can also emphasize their discrete aspect. Specifically, a spike train can be discretized into “bins” of width ΔT (typically chosen to be short enough so that no bin contains more than two spikes) and then regarded as a binary sequence. The Hamming distance between two discretized spike trains (i.e., an L^1 distance in a vector space of dimension $T/\Delta T$) is a spike train distance. The main distinction is that in contrast to the kernel-based distances discussed above, spike trains that have spikes in different bins are regarded as equally distant, regardless of whether the times of occurrence of the spikes are close.

Embeddings can also be used to construct measures of spike train *similarity* (i.e., measures that decrease as spike trains become more dissimilar), via the normalized inner product

$$\rho(A, B) = \frac{\langle f(A), f(B) \rangle}{\|f(A)\| \|f(B)\|}, \quad (9)$$

where $\langle u, v \rangle$ is the inner product in the vector space V and $\|v\| = \sqrt{\langle v, v \rangle}$ is the corresponding norm. These similarity measures have an exact correspondence to a spike train distance, as $\cos^{-1}(\rho(A, B))$ is a metric – namely, the geodesic distance between the unit vectors in the direction

of $f(A)$ and $f(B)$ on the unit sphere. The Haas and White measure (Haas and White 2002) uses an exponential kernel for the embedding Eq. 6; the Schreiber measure (Schreiber et al. 2003) uses a Gaussian kernel. Since these measures are normalized for spike count, they are only sensitive to temporal pattern, and a provision needs to be made for the empty spike train.

Cost-Based Distances

While distances constructed via vector space embeddings focus on either the continuous or discrete aspects of the topology of spike trains, cost-based distances attempt to combine these two facets.

The prototypical example was introduced by Victor and Purpura, the “spike time” distance (Victor and Purpura 1997). As is the case for the other distances in this class, the key ingredient is a set of elementary transformations between spike trains, each of which is assigned a cost. Once the elementary transformations have been specified, the distance between two spike trains is the minimal total cost required to transform one spike train into another. That is, the distance $D(A, B)$ is defined as

$$D(A, B) = \min \sum_{k=0}^K c(X_k, X_{k+1}), \quad (10)$$

where X_0, \dots, X_K is a sequence of spike trains with $X_0 = A$ and $X_K = B$, and each successive spike train is linked to the next by an elementary transformation of cost $c(X_k, X_{k+1}) = c(X_{k+1}, X_k)$. For the specific case of the spike time distance, the elementary transformations consist of (i) inserting a spike into a spike train, (ii) deleting a spike from a spike train, and (iii) shifting a spike in time. Inserting or deleting a spike is assigned a cost of 1; shifting a spike by an amount of time Δt is assigned a cost $q|\Delta t|$. The parameter q plays the same role as the parameter $1/t_0$ for the kernel-based distances: as q increases (or as t_0 decreases), the distance becomes progressively more sensitive to fine timing differences. For $q = 0$, the distance is entirely insensitive to timing differences (so, formally, it is a pseudometric), since spikes can be

moved “for free.” In this limit, the distance – which is often called the “spike count distance” – is simply the difference in spike counts $D(A, B) = |M(A) - M(B)|$.

The choice of elementary transformations determines the qualitative nature of the distance. An example of a contrasting cost-based distance is the “interspike interval” distance (Victor and Purpura 1997), in which the elementary transformations act on interspike intervals rather than on the spike times themselves. Since changing the length of one interspike interval shifts the time of all successive spikes, two spike trains can be close in terms of the spike interval distance, but not in terms of the spike time distance. Thus, these distances confer different topologies on the space of spike trains: the topology of the spike time distance is equivalent to that of the van Rossum distance (Eq. 6) with a typical kernel, but the topology of the spike interval distance is not. Additionally, the spike time distance is invariant under parallel translation (adding a common spike train to the spike trains being compared, as in Eq. 5), while the spike interval distance is not. Cost-based distances are typically non-Euclidean (Aronov and Victor 2004; Dubbs et al. 2010).

Cost-based distances are also applicable to the multineuron setting (Aronov et al. 2003). For the spike time distance, a straightforward approach is to include an elementary transformation that assigns a cost to changing the neuronal label associated with a spike. Parametric variation of this cost changes the character of the distance from one that is sensitive to overall population activity (low cost to change the label) to one that is sensitive to cross-population patterns (high cost to change the label).

For cost-based distances, the overall distance and the costs associated with elementary transformations can be interpreted in terms of a generative model for spike trains (Dauwels et al. 2009). Cost-based distances can also be formulated in terms of “alignments” between spikes rather than transformations (Dubbs et al. 2010).

The above constructions can be generalized in many ways. To name a few, normalization by

spike count can be applied; the costs of each transformation (Victor et al. 2007) or alignment (Dubbs et al. 2010) can be transformed by a power law prior to summation; elementary transformations sensitive to burst structure can be added (Victor and Purpura 1997); and different kinds of elementary transformations can be combined.

Other Spike Train Distances

There are several useful spike train distances that do not fall into either major category (Hunter and Milton 2003; Kreuz et al. 2007, 2012; Quian-Quiroga et al. 2002; Rusu and Florian 2014). Each of these measures compares spike times or intervals in one train with the nearest spike times or intervals in the other. For the Hunter-Milton measure (Hunter and Milton 2003), a choice of scale parameter is required; the event synchronization measure (Quian-Quiroga et al. 2002) and the ISI/SPIKE family (Kreuz et al. 2007, 2012) are normalized to the local firing rate and therefore scale-free. The main difference between the event synchronization measure (Quian-Quiroga et al. 2002) and the ISI/ SPIKE family (Kreuz et al. 2007, 2012) is that the latter includes an explicit comparison of local interspike intervals. The family of metrics recently introduced by Rusu and Florian(Rusu and Florian 2014) is also scale-free and is distinguished by being relatively more sensitive to large-scale temporal structure and less sensitive to spike counts and to fine structure within bursts.

The “coincidence factor,” while not a distance, has also been used to compare discretized spike trains based on a normalized count of coincidences (Jolivet et al. 2008; Kistler et al. 1997).

Applications

Spike train distances can be used to ask several kinds of questions about neural data. They provide a way to quantify neuronal variability: for this purpose, one determines the distances between members of a set of spike trains that represent samples of spontaneous activity or samples of responses to the same stimulus. They provide a way to measure the quality of

a model, by determining the distance between experimentally observed spike trains and models of them.

Spike train distances are also the starting point for strategies to analyze neural coding. They can be used as a way to estimate the **mutual information** between a set of stimuli and a set of responses, by determining the extent to which neural responses to a set of stimuli form reliable clusters. The dependence of this estimate on the kind of spike train distance used (e.g., one that is sensitive to spike times, vs. spike intervals, or the degree of temporal precision of the distance) points to the features of the neural response that carries the information (Victor and Purpura 1996, 1997). Spike train distances can also be used as a tool to visualize the geometry of the response distributions and the stimulus domain that they represent (Aronov et al. 2003), by taking them as the starting point for multidimensional scaling and related algorithms.

Finally, spike train distances can be used as a cost function to drive learning algorithms that shape artificial networks to process temporal patterns (Florian 2012).

For a more extensive review of many of these applications, see Houghton and Victor (2011), Victor (2005), and Victor and Purpura (2010).

Computational Methods

Computation of distances based on embeddings is straightforward, as the essential steps are convolution and pairwise multiplication. For cost-based distances, dynamic programming algorithms modeled after alignment algorithms for genetic sequences (Needleman and Wunsch 1970; Sellers 1974) provide an efficient way to identify the minimal-cost sequence of transformations in the single-neuron setting and for settings with a small number of neurons. The number of computations is approximately $O(N^2)$ for unlabeled spike trains containing N events and $O(N^{L+1})$ when L neurons (labels) are present. These algorithms extend to enable simultaneous computation of distances for all values of its parameters (cost to move a spike, cost to change a label) (Victor et al. 2007). For the single-neuron scenario and single values of the cost parameter,

a graph-theoretic approach based on the “Hungarian” algorithm may provide improved performance (Dubbs et al. 2010). For five or more neurons, an incremental matching algorithm (Diez et al. 2012) is the most efficient approach currently available; the computational complexity (specifically, the number of computations required) scales approximately as N^6 , independent of the number of neurons.

Acknowledgments The author thanks Conor Houghton and Thomas Kreuz for their very helpful comments on this entry. This work was supported by NIH NEI grant EY09314.

Cross-References

- ▶ [Correlation Analysis of Parallel Spike Trains](#)
- ▶ [Spike Train](#)
- ▶ [Spike Train Analysis: Overview](#)

References

- Aronov D, Victor JD (2004) Non-Euclidean properties of spike train metric spaces. *Phys Rev E Stat Nonlin Soft Matter Phys* 69(6 Pt 1):061905
- Aronov D, Reich DS, Mechler F, Victor JD (2003) Neural coding of spatial phase in V1 of the macaque monkey. *J Neurophysiol* 89:3304–3327
- Dauwels J, Vialatte F, Weber T, Cichocki A (2009) Quantifying statistical interdependence by message passing on graphs. Part I. One-dimensional point processes. *Neural Comput* 21:2203–2268
- Diez DM, Schoenberg FP, Woody CD (2012) Algorithms for computing spike time distance and point process prototypes with application to feline neuronal responses to acoustic stimuli. *J Neurosci Methods* 203(1):186–192
- Dubbs AJ, Seiler BA, Magnasco MO (2010) A fast L(p) spike alignment metric. *Neural Comput* 22(11): 2785–2808
- Florian RV (2012) The chronotron: a neuron that learns to fire temporally precise spike patterns [Research Support, Non-U.S. Gov't]. *PLoS ONE* 7(8):e40233. doi:10.1371/journal.pone.0040233
- Haas JS, White JA (2002) Frequency selectivity of Layer II stellate cells in the medial entorhinal cortex. *J Neurophysiol* 88:2422–2429
- Houghton C (2009) Studying spike trains using a van Rossum metric with a synapse-like filter. *J Comput Neurosci* 26:149–155

- Houghton C, Sen K (2008) A new multineuron spike train metric. *Neural Comput* 20:1495–1511
- Houghton C, Victor JD (2011) Measuring representational distances – the spike train metrics approach. In: Kriegeskorte N, Kreiman G (eds) *Understanding visual population codes – towards a common multivariate framework for cell recording and functional imaging*. MIT Press, Cambridge, MA
- Hunter JD, Milton G (2003) Amplitude and frequency dependence of spike timing: implications for dynamic regulation. *J Neurophysiol* 90:387–394
- Jolivet R, Kobayashi R, Rauch A, Naud R, Shinomoto S, Gerstner W (2008) A benchmark test for quantitative assessment of simple neuron models. *J Neurosci Method* 169(2):417–424
- Kistler WM, Gerstner W, van Hemmen JL (1997) Reduction of the Hodgkin-Huxley equations to a single-variable threshold model. *Neural Comput* 9(5):1015–1045
- Kreuz T, Haas JS, Morelli A, Abarbanel HD, Politi A (2007) Measuring spike train synchrony. *J Neurosci Method* 165:151–161
- Kreuz T, Chicharro D, Houghton C, Andrzejak RG, Mormann F (2012) Monitoring spike train synchrony. arXiv:1209.6604
- Needleman SB, Wunsch CD (1970) A general method applicable to the search for similarities in the amino acid sequence of two proteins. *J Mol Biol* 48(3):443–453
- Quiroga R, Kreuz T, Grassberger P (2002) Event synchronization: a simple and fast method to measure synchronicity and time delay patterns. *Phys Rev E Stat Phys Plasmas Fluids Relat Interdiscip Topics* 66:041904
- Rusu CV, Florian RV (2014) A new class of metrics for spike trains. *Neural Comput* 26(2):306–348. doi:10.1162/NECO_a_00545
- Schreiber S, Fellous JM, Whitmer D, Tiesinga P, Sejnowski TJ (2003) A new correlation-based measure of spike timing reliability. *Neurocomputing* 52–54:925–931
- Sellers P (1974) On the theory and computation of evolutionary distances. *SIAM J Appl Math* 26:787–793
- Sen K, Jorge-Rivera JC, Marder E, Abbott LF (1996) Decoding synapses. *J Neurosci* 16(19): 6307–6318
- van Rossum MC (2001) A novel spike distance. *Neural Comput* 13(4):751–763
- Victor JD (2005) Spike train metrics. *Curr Opin Neurobiol* 15(5):585–592
- Victor JD, Purpura KP (1996) Nature and precision of temporal coding in visual cortex: a metric-space analysis. *J Neurophysiol* 76(2):1310–1326
- Victor JD, Purpura KP (1997) Metric-space analysis of spike trains: theory, algorithms and application. *Network* 8:127–164
- Victor JD, Purpura KP (2010) Spike Metrics. In: Rotter S, Gruen S (eds) *Analysis of parallel spike trains*. Springer, New York/Heidelberg
- Victor JD, Goldberg DH, Gardner D (2007) Dynamic programming algorithms for comparing multineuronal spike trains via cost-based metrics and alignments. *J Neurosci Methods* 161(2):351–360

Further Reading

- Dubbs AJ, Seiler BA, Magnasco MO (2010) A fast L(p) spike alignment metric. *Neural Comput* 22(11):2785–2808
- Houghton C, Victor JD (2011) Measuring representational distances – the spike train metrics approach. In: Kriegeskorte N, Kreiman G (eds) *Understanding visual population codes – towards a common multivariate framework for cell recording and functional imaging*. MIT Press, Cambridge, MA
- Needleman SB, Wunsch CD (1970) A general method applicable to the search for similarities in the amino acid sequence of two proteins. *J Mol Biol* 48(3):443–453
- Van Rossum MC (2001) A novel spike distance. *Neural Comput* 13(4):751–763
- Victor JD, Purpura KP (1997) Metric-space analysis of spike trains: theory, algorithms and application. *Network* 8:127–164
- Victor JD, Purpura KP (2010) Spike Metrics. In: Rotter S, Gruen S (eds) *Analysis of parallel spike trains*. Springer, New York/Heidelberg

Spike-Dependent Synaptic Learning Rules

- [Spike-Timing Dependent Plasticity, Learning Rules](#)

Spike-Field Coherence

- [Spike Triggered Average](#)

Spike-Frequency Adaptation

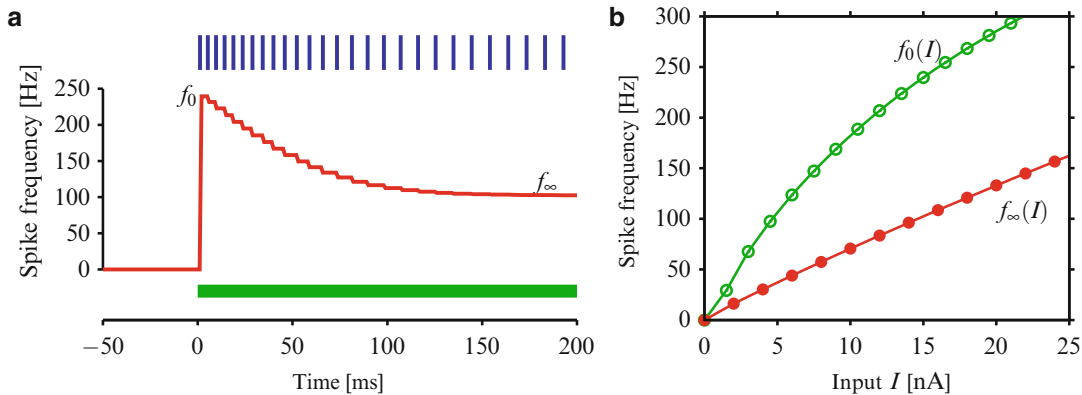
Jan Benda¹ and Joel Tabak²

¹Institute for Neurobiology, Eberhard Karls University, Tübingen, Germany

²Florida State University, Tallahassee, FL, USA

Definition

When stimulated with a constant stimulus, many neurons initially respond with a high spike



Spike-Frequency Adaptation, Fig. 1 Phenomenon spike-frequency adaptation. (a) Spike train (vertical strokes at the top) of an adapting neuron evoked by the onset of a constant stimulus (green bar at the bottom, $I = 15 \text{ nA}$). The spike frequency drops from an initially high onset rate, f_0 , in an approximately exponential way down to a lower steady-state rate, f_∞ . (b) Repeating the experiment shown in (a) for various stimulus intensities

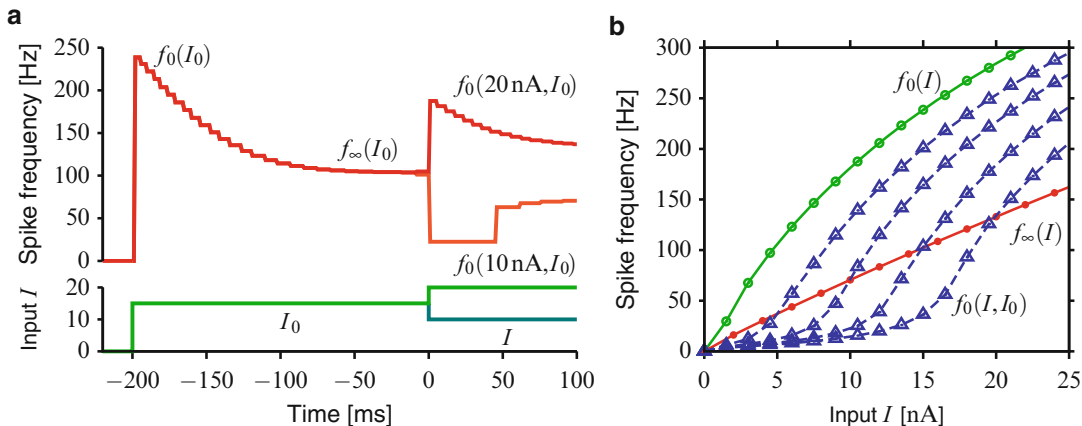
I (here an injected current) results in the onset f - I curve $f_0(I)$ and the steady-state f - I curve $f_\infty(I)$. Shown are simulations of a single-compartment conductance-based model with an M-type current (the Ermentrout model; Ermentrout 1998; Benda et al. 2010; with $\bar{g}_{\text{Ca}} = 0$, $\bar{g}_{\text{AHP}} = 0$, and $\bar{g}_M = 8 \mu\text{S}/\text{cm}^2$, the input current is scaled such that 1 nA equals $1 \mu\text{A}/\text{cm}^2$)

frequency that then decays down to a lower steady-state frequency (Fig. 1a). This dynamics of the spike-frequency response is referred to as “spike-frequency adaptation”. Spike-frequency adaptation is a process that is slower than the dynamics of action-potential generation. Spike-frequency adaptation by this definition is an aspect of the neuron’s super-threshold firing regime, although the mechanisms causing spike-frequency adaptation could also be at work in the neuron’s subthreshold regime.

Detailed Description

In the context of spike-frequency adaptation, spike frequency is often measured as the instantaneous rate, i.e., the averaged reciprocal interspike intervals at each time. This measures the inverse period of super-threshold firing. In contrast, the PSTH (peristimulus time histogram (► Estimation of Neuronal Firing Rate)) estimates the probability of a spike at a given time and therefore is also sensitive to variability of the response caused by intrinsic or external noise sources.

Important characteristics of a neuron with spike-frequency adaptation are its f - I curves (spike frequency f versus input strength I). Because of adaptation, a certain input intensity will not evoke a constant spike frequency. Instead, the initial response in spike frequency to the onset of a constant input will result in the so-called “onset f - I curve” (green curve in Fig. 1b). Later during the constant stimuli, the spike frequency reaches a steady state. Drawn as a function of input intensity, this forms the “steady-state f - I curve”, which usually lies below the onset f - I curve, because the spike frequency adapts from the onset down to the steady state (red curve in Fig. 1b). The third type of f - I curves is the “adapted f - I curves” (Benda and Herz 2003). For these the neuron is first adapted to some adaptation input of fixed intensity and then the onset responses to various test inputs are measured (Fig. 2). The adapted response curves indicate how the neuron being in a certain and fixed adaptation state will initially respond to new stimuli. While each neuron has exactly one onset and one steady-state f - I curve, it has for each adaptation stimulus a different adapted f - I curve.



Spike-Frequency Adaptation, Fig. 2 Adapted f - I curves. In addition to the onset and the steady-state f - I curves, the adapted f - I curves provide important information about the adaptation properties of a neuron. (a) In order to measure an adapted f - I curve for a specific adaptation state, the neuron is first adapted to its steady-state response $f_\infty(I_0)$ by stimulating it with a constant adapting stimulus I_0 (here 15 nA). Then, a test stimulus I is applied and the onset response $f_0(I, I_0)$ to this stimulus is

measured. In the figure, the responses (red and orange) to two different test stimuli ($I = 20 \text{ nA}$ in green and $I = 10 \text{ nA}$ in dark cyan) are shown. (b) Each adapting stimulus I_0 results in one adapted f - I curve $f_0(I, I_0)$. Shown are adapted f - I curves for $I_0 = 5, 10, 15, 20 \text{ nA}$. In this example the adaptation process mainly shifts the adapted f - I curves to the right. All curves together characterize the spike-frequency response of an adapting neuron. Same model neuron as in Fig. 1

Simple adaptation currents (see below) will shift the neuron's adapted f - I curves to higher input intensities. Other (less well-understood) mechanisms like presynaptic inhibition may also tilt the adapted f - I curves (Hildebrandt et al. 2011) or distort it in other ways (see also Fig. 5).

Spike-frequency adaptation is related to the classification of neurons into phasic, phasic-tonic, or tonic spiking neurons. Tonic spiking neurons are neurons that keep firing in response to a constant stimulus with an almost constant rate. Many neurons that are classified as tonic spiking, however, still show some weak spike-frequency adaptation. On the other hand, phasic spiking neurons only emit one or several spikes to the onset of the stimulus and then cease spiking. If this onset response consists of several spikes with a decreasing spike frequency, then the phasic response is probably caused by strong spike-frequency adaptation. With less or only a single spike and no clear decrease in spike frequency, this type of response can be that of a type III neuron (► Excitability: Types I, II, and III). The intermediate phasic-tonic responses exactly

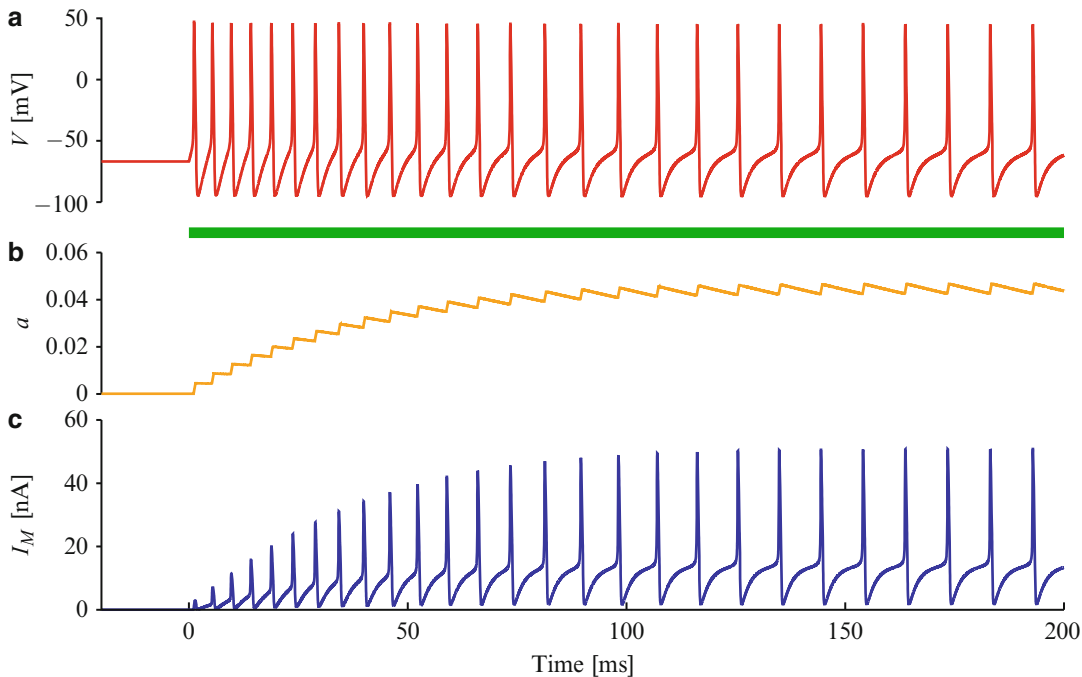
match the definition of spike-frequency adaptation.

Mechanisms

There are many different mechanisms that all cause a neuron to adapt its spike-frequency response. First, there are adaptation currents – ionic currents (► Biophysics of Adaptation in a Computational Model of the Leech T Neuron) that act together with the spike-generating currents (“output-driven adaptation”). Second, other mechanisms, such as fatigue of receptor currents, adapt the input a neuron receives (“input-driven adaptation”). And third, there are network effects that also can adapt the neuron’s response in both an input-driven or output-driven way.

Adaptation Currents

There exists a whole zoo of mechanisms based on ionic currents that are all directly or indirectly activated by the action potentials generated by the neuron – the output of the neuron – and have



Spike-Frequency Adaptation, Fig. 3 Dynamics of an adaptation current. (a) The membrane potential V in response to a step input ($I = 15$ nA, indicated by the green bar) simulated with the same model as in Fig. 1. As adaptation progresses the interspike intervals get longer. (b) The gating variable of the M-type current a is

increased by every action potential and decays slowly in between them. This way a slowly builds up during stimulation. (c) The adaptation current, here an M-type current, I_M , gets larger and larger as a increases and inhibits the input. This way it causes the neuron's response to adapt

at least one time scale involved that is slower than the dynamics of an action potential.

M-type currents are a simple example (Fig. 3; Brown and Adams 1980). These are voltage-gated potassium currents that are mainly activated at high voltages as they occur during an action potential and that deactivate with a slow time constant of about 100 ms. If the neuron initially fires with a frequency of say 200 Hz, then the activation of the M-type currents builds up from one action potential to the next, since there is not enough time for the current to completely deactivate between succeeding action potentials. As a potassium current, the activated M-type currents then counteract the input to the neuron and as a consequence the spike frequency is reduced – the neural response adapts.

An important class of adaptation currents are AHP-type currents, calcium-gated potassium currents, that enhance the after hyperpolarization

following an action potential (Sah 1996). Here, during each action potential, calcium enters the cell through voltage-gated calcium channels. Depending on the intracellular calcium concentration, the AHP-type currents are activated and as potassium currents inhibit the input to the neuron. Calcium is only slowly removed from the cytosol and this time scale is then reflected by the resulting spike-frequency adaptation.

Further ionic mechanisms that cause spike-frequency adaptation include sodium-activated potassium channels and slow inactivation of the sodium current (for details see “► Biophysics of Adaptation in a Computational Model of the Leech T Neuron”).

Input Adaptation

In receptor neurons the whole transduction process from the physical stimulus to the receptor current can adapt in different ways. These can be

mechanisms controlling the sensitivity of the receptor organ, like the pupillary light reflex. Within the receptor neuron itself, the transduction machinery may produce adapting receptor currents due to fatigue (e.g., bleaching of rhodopsin) or active adaptation to the intensity of the physical stimulus within a second messenger cascade (e.g., in photoreceptors) or by molecular motors (e.g., in mechanical transduction in hair cells (► [Cochlear Inner Hair Cell, Model](#))). All these and many other mechanisms eventually produce an adapting receptor current that then leads to spike-frequency adaptation in the receptor neuron. Gollisch and Herz (2004) demonstrated how to unmask input-driven adaptation from output-driven adaptation in auditory receptor neurons of locusts.

In all other neurons that receive their input through synapses on their dendrite, the input current reaching the site of action-potential generation can also be adapted. The various forms of synaptic dynamics, in particular short-term depression, are potential sources of spike-frequency adaptation. Also various ionic currents on the dendrite (► [Quasi-active Approximation of Nonlinear Dendritic Cables](#)) might potentially adapt the input.

Network Effects

In case the spiking activity of a neuron leads to the activation of recurrent inhibitory synapses, this might cause spike-frequency adaptation in a way quite similar as the adaptation currents (Sutherland et al. 2009). Here, the slow time scale would be introduced by the time scale of the postsynaptic current of the inhibitory synapse, by the delay introduced by wiring, and by the integration dynamics of the neurons participating in this negative feedback loop.

Similar to input-driven adaptation, some forms of feedforward input may also cause spike-frequency adaptation in the target neuron. In its simplest form, the presynaptic neuron already adapts, and thus, the postsynaptic neuron very likely will adapt as well. In addition, the synaptic transmission might adapt through synaptic plasticity (► [Short-Term Plasticity, Biophysical Models](#)) or by presynaptic inhibition, or delayed and slower inhibitory input can adapt the response of the target neuron.

Network and cell-intrinsic adaptation mechanisms shape in specific ways functionally different response properties of auditory interneurons in locusts (Hildebrandt et al. 2009).

Models of Spike-Frequency Adaptation

There are many ways to model spike-frequency adaptation. In the following overview, we focus on output-driven adaptation, i.e., adaptation currents that are activated by the neuron's output activity (membrane voltage with action potentials). In contrast, input-driven adaptation is activated by the input signal irrespective of the resulting output.

Conductance-Based Models

In conductance-based models like the Hodgkin-Huxley model (► [Short-Term Plasticity, Biophysical Models](#)), any ionic current of a neuron is modeled in detail. This requires exact knowledge of the specific type of adaptation current involved. For example, the M-type current I_M would be modeled as

$$I_M = \bar{g}_M a(V - E_K) \quad (1)$$

$$\tau_a(V) \frac{da}{dt} = a_\infty(V) - a \quad (2)$$

where E_K is the potassium reversal potential, \bar{g}_M is the maximum conductance, and a is the gating variable of this voltage-gated current. $\tau_a(V)$ and $a_\infty(V)$ are the voltage-dependent time constant and activation variable, respectively, that determine the (slow) temporal evolution of the gating variable. $a_\infty(V)$ is a sigmoidal function depending on the membrane potential V that is close to zero at the resting potential and about one during an action potential (Brown and Adams 1980; Benda and Herz 2003).

Integrate-and-Fire Models

As for conductance-based models, any adaptation current can also be simply added to the input of an integrate-and-fire model. The only difference is that the effect the action potential has on the

dynamics of the current has to be modeled explicitly, for example, by increasing a in Eq. 2 by a certain increment whenever there was a spike.

Often, however, a more generalized form of adaptation currents is used in (leaky, quadratic, exponential) integrate-and-fire neurons (Izhikevich 2003; Brette and Gerstner 2005). This has the advantage that the exact nature of the adaptation current in question does not have to be known. First, the electromotoric force $E_K - V$ is often approximated away, so that the gating variable a then becomes the (appropriately scaled) adaptation current A . Second, $a_\infty(V)$ is replaced by incrementing A by some appropriate value ΔA whenever an action potential occurs at time t_i . Between the action potentials, A decays exponentially with a fixed adaptation time constant τ_a :

$$I_M \approx A \quad (3)$$

$$\tau_a \frac{dA}{dt} = -A + \Delta A \sum_{i=-\infty}^{\infty} \delta(t - t_i) \quad (4)$$

The adaptation dynamics (4) can be extended by an additional term proportional to V in order to incorporate the fact that some adaptation currents are already activated by subthreshold membrane voltages.

Integrate-and-fire models with a dynamic threshold are another class of adapting neuron models, where the firing threshold is incremented by each action potential and follows a slow dynamics between the action potentials. Although this mechanism also produces spike-frequency adaptation (Liu and Wang 2001), the resulting adapted f - I curves do not only shift to higher inputs, as any adaptation current does, but also reduce their slopes (Benda et al. 2010).

Firing-Rate Models

By simply approximating the neuron's spike generator by its f - I curve $f_0(I)$ and using Kirchhoff's law that ionic currents over the cell's membrane add up yield the following equation for the spike frequency $f(t)$:

$$f = f_0(I - A) \quad (5)$$

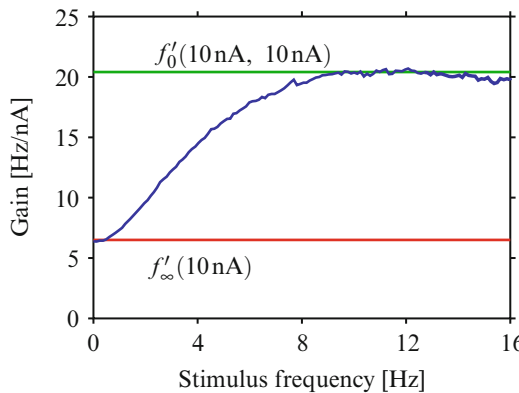
$$\tau_a \frac{dA}{dt} = -A + A_\infty(f) \quad (6)$$

(Benda and Herz 2003). Because the adaptation current acts inhibitory on the input current, it is subtracted from the input. The dynamics for A is the same as for the simplified integrate-and-fire neurons, but it is driven via the term $A_\infty(f)$ by the output spike frequency and not by individual spikes any more. This dependence on the spike frequency arises from averaging over the spike train in time (Wang 1998). This averaging procedure is possible if the spike frequency is higher than the reciprocal adaptation time constant. Only then the adaptation dynamics can be separated from the one of the membrane potential. Choosing $A_\infty(f)$ to be proportional to f often is a reasonable approximation. Then, the only nonlinearity remaining is the neuron's onset f - I curve. By linearizing the onset f - I curve around the current spike frequency, one can easily compute the neuron's filter properties that are introduced by the adaptation process.

Signal Processing

The slow adaptation variable (gating variable of M-type current, intracellular calcium concentration for AHP-type currents, etc.) is a low-pass filtered version of the output spike train (output-driven adaptation, Eqs. 4 or 6) or of the input to the neuron (in the case of input-driven adaptation). Since this low-pass filtered signal is then subtracted from the input current I , this basically (i.e., with linear f - I curves) results in a high-pass filter between the input to the neuron and the resulting output spike frequency. The spike frequency of an adapting neuron thus encodes the high-pass filtered input signal (Fig. 4; Benda and Herz 2003). For example, in electroreceptors, this high-pass filter resulting from adaptation processes enhances the response to fast stimulus components in communication signals (Benda et al. 2005).

The gain of the filter at low stimulus frequencies that are below the reciprocal adaptation time

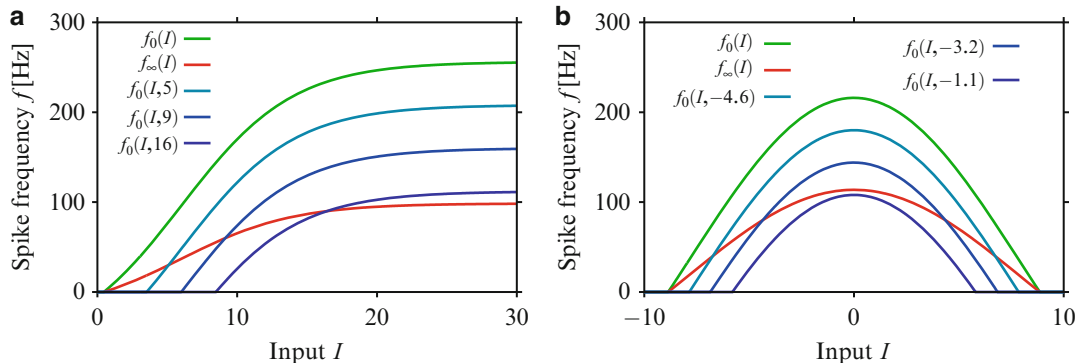


Spike-Frequency Adaptation, Fig. 4 High-pass filter of adapting neurons. Adaptation processes add high-pass filter characteristics to a neuron's transfer function between the input to the neuron (here, e.g., an injected current) and the resulting spike frequency. Shown is the gain, i.e., the amplitude of the modulation of the spike-frequency response divided by the amplitude of the injected current input as a function of the frequency of that input, obtained for the same model neuron as in Fig. 1. As a stimulus a low-pass filtered Gaussian white noise with cutoff frequency at 16 Hz, mean 10 nA, and standard deviation 2 nA was used. The slopes of the steady-state f - I curve (red) at 10 nA and the one of the adapted f - I curve (green) for $I_0 = 10$ nA are plotted for comparison

constant is given by the slope of the steady-state f - I curve. The gain of stimulus frequencies faster than the reciprocal adaptation time constant is given by the slope of the adapted f - I curves. In the case of purely subtractive adaptation, the latter equals the slope of the onset f - I curve.

It follows that neurons with flat steady-state f - I curves (zero slope) implement perfect intensity invariance (zero gain at low stimulus frequencies), i.e., no matter on what mean intensity a certain input waveform is delivered, the output spike-frequency will always be the same, since the mean intensity is completely filtered out by the adaptation process (Benda and Hennig 2008).

The high-pass filter effect of spike-frequency adaptation considers the linear aspects of spike-frequency adaptation only. At least the steady-state f - I curve is indeed linearized by adaptation currents (as shown in Ermentrout 1998, and also illustrated in Fig. 1b). In addition, the nonlinear shape of a neuron's f - I curves (e.g., rectification at zero firing rate and saturation) together with the high-pass filter introduces additional aspects. For example, the subtractive shift of the adapted f - I curves to higher input intensities might be accompanied by a reduction in their maximum firing rate and/or by a reduction of their slope (see Fig. 5 for



Spike-Frequency Adaptation, Fig. 5 Nonlinearities and adaptation. Simple subtractive adaptation can have unexpected effects when it occurs after a nonlinearity. The examples show two simple scenarios where the firing rate f of a neuron is directly proportional to the input current J , and an adaptation current A acts subtractive on the current, as in Eq. 5: $f = c \cdot (J - A)$, with $c > 0$, and $f = 0$ if $J < A$. The input current, however, depends nonlinearly on some (sensory) input I : $J(I)$. (a) The input nonlinearity

is a sigmoidal function of the sensory input: $J(I) = (1 + \exp(-(J - 6)/4))^{-1} - 0.2$ ($c = 320$ Hz). This is the case, for example, in auditory or olfactory receptor neurons. Although the adaptation acts subtractive on the input current, the resulting adapted f - I curves appear to be shifted to the right as well as downward. (b) $J(I) = \cos(0.2I) + 0.2$ ($c = 180$ Hz). This models, for example, an orientation-selective cell in the visual system. Here, the adapted f - I curves appear to be shifted downward

simple examples) and thereby influence the filter properties of a neuron in a nonlinear way.

The various forms of this interplay of adaptation dynamics and the resulting high-pass characteristics with nonlinearities lead to diverse functional consequences. For example, in the auditory system of crickets, the slow calcium dynamics leads to forward masking of weaker stimuli (Sobel and Tank 1994). A collision-detecting neuron in the visual system of locusts responds very selectively to looming stimuli because of spike-frequency adaptation (Peron and Gabbiani 2009).

Adaptation currents can even alter the type of action-potential dynamics ([► Excitability: Types I, II, and III](#)). A type I neuron where repetitive firing occurs via a saddle-node bifurcation on an invariant cycle can switch into a type II neuron where the resting potential loses stability via a Hopf bifurcation by the activation of an M-type adaptation current (Ermentrout et al. 2001; Prescott et al. 2006).

Multiple Adaptation Time Scales

Usually, spike-frequency adaptation occurs not only on a single but on several time scales. The shortest time scales of spike-frequency adaptation are in the range of 10–100 ms. This at the same time usually also is the strongest adaptation process in the neuron. Additional slower adaptation processes are weaker and have time constants of seconds, 10 s and slower. Adaptation on several time scales could resemble power-law adaptation (Clarke et al. 2013) or logarithmic adaptation (Xu et al. 1996) in contrast to the single adaptation process showing exponential adaptation of the firing rate.

Noise

Adaptation currents are a potential source of ion channel noise. Since these ionic currents are characterized by their slow adaptation dynamics, the resulting channel noise is a colored noise with correlation time given by the adaptation time constant. Such a noise results in positive correlations between successive interspike intervals and

in interspike-interval histograms with a sharper peak and heavier tail in comparison to the ones obtained with white noise (Fig. 6d–f; Schwalger et al. 2010).

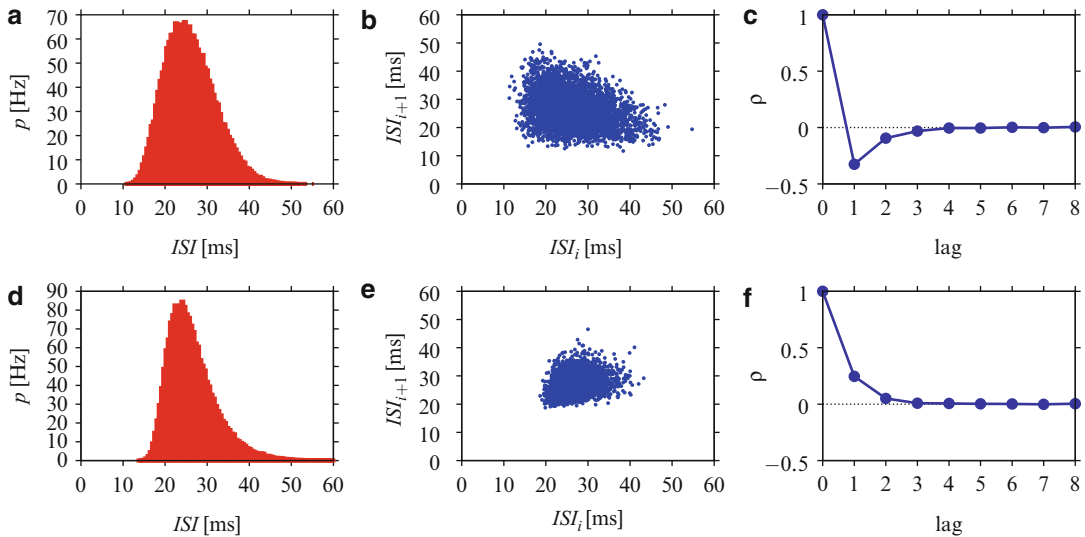
Output-driven adaptation also interacts with white noise, e.g., generated by ion channel noise from fast spike-generating currents. In this case, adaptation introduces negative serial correlations between successive interspike intervals (Fig. 6a–c; Chacron et al. 2000; Benda et al. 2010) that improve information transmission at low frequencies (Chacron et al. 2001). The interspike-interval statistics of auditory receptor neurons in locusts have been shown to be shaped by both white noise sources and colored noise presumably generated by an adaptation current (Fisch et al. 2012).

Rhythmogenesis in Neural Networks

The slow decrease in firing frequency due to adaptation currents provides delayed negative feedback that can result in the production of oscillations by excitatory neural networks. The population activity of an excitatory neural network can be roughly described by its mean firing rate, which varies according to

$$\tau \frac{df}{dt} = f_0(I) - f \quad (7)$$

(Wilson and Cowan 1972). Here, the firing frequency f is averaged spatially (over the population) and temporally (over the synaptic integration time scale). It is assumed that the neurons fire asynchronously. f_0 is the steady-state firing rate that will be reached with a network integration time constant τ . It is similar to the function f_0 in Eq. 5, but is not strictly the firing rate of one neuron, as it also incorporates information about synaptic dynamics, heterogeneity in the neuron population, etc. Because of the recurrent excitatory connectivity, the input I to the network is given by $I = wf$, where f is the output firing rate of the network, and w is a connectivity parameter akin to synaptic weight or the number of connections per neuron.



Spike-Frequency Adaptation, Fig. 6 Spike-frequency adaptation and noise. (a–c) Interspike-interval (ISI) histogram (a), return map (b), and ISI correlations (c) for the conductance-based model with an M-type adaptation current (same model as in Fig. 1) driven with white noise (mean $I = 10$ nA, noise strength

$D = 1$ nA 2 /Hz). (d–f) The same measures for colored noise arising from the stochasticity of the adaptation current. Noise strength was scaled to result in the same standard deviation of the ISI s ($D = 30$ nA 2 /Hz). Note the more peaked shape of the ISI distribution as well as the positive ISI correlations

If neurons are adapting, the effective input becomes $I = wf - A$, where A is the average adaptation current in the population. This description is valid as long as adaptation is much slower than network integration ($\tau_a > \tau$).

The population firing rate equilibrates to

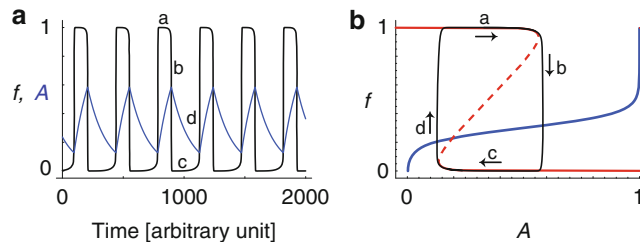
$$f = f_0(wf - A) \quad (8)$$

and A varies according to Eq. 6. Note that Eq. 8 can have two stable solutions over a range of A values. This bistability, due to the fast positive feedback provided by excitatory connections, together with the slow A dynamics produce relaxation oscillations as illustrated in Fig. 7 (Tabak et al. 2000; van Vreeswijk and Hansel 2001; Giugliano et al. 2004; Gigante et al. 2007).

Note that the exact dependence of adaptation on frequency (here given by Eq. 6 and represented as the blue curve in Fig. 7b) may affect the type of bifurcation that occurs between a silent and an oscillatory network as a source of excitation is increased (Nesse et al. 2008), but it does not change the fundamental mechanism of the oscillations. So the excitatory network can oscillate whether

adaptation is input- or output-driven (Nesse et al. 2008). Synaptic adaptation (often called short-term synaptic depression (► [Synaptic Dynamics: Overview](#))) also produces oscillations in excitatory networks, through the same mechanism as the intrinsic adaptation mechanisms described here (Tabak et al. 2000; Tsodyks et al. 2000; Wiedman and Luthi 2003). Note, however, that the two types of adaptation (intrinsic or synaptic) can be distinguished in models (even in firing rate models) as well as in experiments based on the models' predictions (Tabak et al. 2000, 2010; Wiedman and Luthi 2003). Thus, it is important to pay careful attention to what adaptation model is most appropriate in a particular modeling context.

In addition to its rhythmogenic properties in excitatory networks, activity-dependent adaptation facilitates network-based oscillations due to the interaction of excitatory and inhibitory populations (Augustin et al. 2013). The rhythmogenic mechanism based on excitatory connectivity and slow activity-dependent adaptation may underlie various types of network activity such as episodic activity in developing



Spike-Frequency Adaptation, Fig. 7 Oscillatory activity in an excitatory network with adaptation. (a)

Time courses of f , the average firing rate (black), and A , the average adaptation current (blue) in the population. During an episode of activity ($f \approx 1$), A is increasing, until activity drops to ≈ 0 . During the inter-episode interval, A decreases until the network is excitable enough to start a new high-activity episode. (b) The two time courses from (a) describe a closed trajectory in the (A , f) plane. The red curve is the curve of steady states of f , solutions of Eq. 8 at each value of A . There is an interval of A over which there are two stable steady states for f , one high and

one low (and an intermediate, unstable steady state, dashed). The blue curve represents $A_\infty(f)$; when the phase point (A , f) is above this curve, A increases; below this curve A decreases, according to Eq. 6. During an episode of network activity (a), f is high so A increases, moving the trajectory to the right. After the point where the high steady state meets the unstable steady state, the only available steady state is at low f . The trajectory jumps down (b), starting the inter-episode interval (c), during which A decreases. When A is low enough, the lower steady state disappears and the trajectory jumps up (d), beginning a new high-activity episode

networks (Butts et al. 1999; Tabak et al. 2000), respiratory rhythms (Kosmidis et al. 2004), or slow oscillations between up and down states in cortex (Compte et al. 2003).

Cross-References

- Biophysics of Adaptation in a Computational Model of the Leech T Neuron
- Cochlear Inner Hair Cell, Model
- Estimation of Neuronal Firing Rate
- Excitability: Types I, II, and III
- Quasi-active Approximation of Nonlinear Dendritic Cables
- Short-Term Plasticity, Biophysical Models
- Synaptic Dynamics: Overview

References

- Augustin M, Ladenbauer J, Obermayer K (2013) How adaptation shapes spike rate oscillations in recurrent neuronal networks. *Front Comput Neurosci* 7:9
- Benda J, Hennig RM (2008) Dynamics of intensity invariance in a primary auditory interneuron. *J Comput Neurosci* 24:113–136
- Benda J, Herz AVM (2003) A universal model for spike-frequency adaptation. *Neural Comput* 15:2523–2564
- Benda J, Longtin A, Maler L (2005) Spike-frequency adaptation separates transient communication signals from background oscillations. *J Neurosci* 25:2312–2321
- Benda J, Maler L, Longtin A (2010) Linear versus nonlinear signal transmission in neuron models with adaptation-currents or dynamic thresholds. *J Neurophysiol* 104:2806–2820
- Brette R, Gerstner W (2005) Adaptive exponential integrate-and-fire model as an effective description of neuronal activity. *J Neurophysiol* 94:3637–3642
- Brown DA, Adams PR (1980) Muscarinic suppression of a novel voltage-sensitive K^+ current in a vertebrate neuron. *Nature* 183:673–676
- Butts D, Feller M, Shatz C, Rokhsar D (1999) Retinal waves are governed by collective network properties. *J Neurosci* 19:3580–3593
- Chacron MJ, Longtin A, Maler L (2001) Negative interspike interval correlations increase the neuronal capacity for encoding time-dependent stimuli. *J Neurosci* 21:5328–5343
- Chacron MJ, Longtin A, St-Hilaire M, Maler L (2000) Suprathreshold stochastic firing dynamics with memory in P-type electroreceptors. *Phys Rev Lett* 85:1576–1579
- Clarke SE, Naud R, Longtin A, Maler L (2013) Speed-invariant encoding of looming object distance requires power law spike rate adaptation. *Proc Natl Acad Sci U S A* 110:13624–13629
- Compte A, Sanchez-Vives M, McCormick D, Wang XJ (2003) Cellular and network mechanisms of slow oscillatory activity (<1 Hz) and wave propagations in a cortical network model. *J Neurophysiol* 89:2707–2725
- Ermentrout B (1998) Linearization of f - I curves by adaptation. *Neural Comput* 10:1721–1729

- Ermentrout B, Pascal M, Gutkin B (2001) The effects of spike frequency adaptation and negative feedback on the synchronization of neural oscillators. *Neural Comput* 13:1285–1310
- Fisch K, Schwalger T, Lindner B, Herz AVM, Benda J (2012) Channel noise from both slow adaptation currents and fast currents is required to explain spike-response variability in a sensory neuron. *J Neurosci* 32:17332–17344
- Gigante G, Mattia M, Giudice PD (2007) Diverse population-bursting modes of adapting spiking neurons. *Phys Rev Lett* 98:148101
- Giugliano M, Darbon P, Arsiero M, Lüscher HR, Streit J (2004) Single-neuron discharge properties and network activity in dissociated cultures of neocortex. *J Neurophysiol* 92:977–996
- Gollisch T, Herz AVM (2004) Input-driven components of spike-frequency adaptation can be unmasked in vivo. *J Neurosci* 24:7435–7444
- Hildebrandt KJ, Benda J, Hennig RM (2009) The origin of adaptation in the auditory pathway of locusts is specific to cell type and function. *J Neurosci* 29:2626–2636
- Hildebrandt KJ, Benda J, Hennig RM (2011) Multiple arithmetic operations in a single neuron: the recruitment of adaptation processes in the cricket auditory pathway depends on sensory context. *J Neurosci* 31:14142–14150
- Izhikevich EM (2003) Simple model of spiking neurons. *IEEE Trans Neural Netw* 14:1569–1572
- Kosmidis E, Pierrefiche O, Vibert JF (2004) Respiratory-like rhythmic activity can be produced by an excitatory network of non-pacemaker neuron models. *J Neurophysiol* 92:686–699
- Liu YH, Wang XJ (2001) Spike-frequency adaptation of a generalized leaky integrate-and-fire model neuron. *J Comput Neurosci* 10:25–45
- Nesse W, Borisyuk A, Bressloff P (2008) Fluctuation-driven rhythmogenesis in an excitatory neuronal network with slow adaptation. *J Comput Neurosci* 25:317–333
- Peron S, Gabbiani F (2009) Spike frequency adaptation mediates looming stimulus selectivity in a collision-detecting neuron. *Nat Neurosci* 12:318–326
- Prescott SA, Ratté S, Sejnowski TJ (2006) Nonlinear interaction between shunting and adaptation controls a switch between integration and coincidence detection in pyramidal neurons. *J Neurosci* 26:9084–9097
- Sah P (1996) Ca^{2+} -activated K^+ currents in neurones: types, physiological roles and modulation. *Trends Neurosci* 19:150–154
- Schwalger T, Fisch K, Benda J, Lindner B (2010) How noisy adaptation of neurons shapes interspike interval histograms and correlations. *PLoS Comput Biol* 6: e1001026
- Sobel EC, Tank DW (1994) In vivo Ca^{2+} dynamics in a cricket auditory neuron: an example of chemical computation. *Science* 263:823–826
- Sutherland C, Doiron B, Longtin A (2009) Feedback-induced gain control in stochastic spiking networks. *Biol Cybern* 100:475–489
- Tabak J, Mascagni M, Bertram R (2010) Mechanism for the universal pattern of activity in developing neuronal networks. *J Neurophysiol* 103:2208–2221
- Tabak J, Senn W, O'Donovan M, Rinzel J (2000) Modeling of spontaneous activity in the developing spinal cord using activity-dependent depression in an excitatory network. *J Neurosci* 20:3041–3056
- Tsodyks M, Uziel A, Markram H (2000) Synchrony generation in recurrent networks with frequency-dependent synapses. *J Neurosci* 20:RC50
- van Vreeswijk C, Hansel D (2001) Patterns of synchrony in neural networks with spike adaptation. *Neural Comput* 13:959–992
- Wang XJ (1998) Calcium coding and adaptive temporal computation in cortical pyramidal neurons. *J Neurophysiol* 79:1549–1566
- Wiedman U, Luthi A (2003) Timing of network synchronization by refractory mechanisms. *J Neurophysiol* 90:3902–3911
- Wilson H, Cowan J (1972) Excitatory and inhibitory interactions in localized populations of model neurons. *Biophys J* 12:1–24
- Xu Z, Payne JR, Nelson ME (1996) Logarithmic time course of sensory adaptation in electrosensory afferent nerve fibers in a weakly electric fish. *J Neurophysiol* 76:2020–2032

Spike-Rate Neural Networks

► Large-Scale Neural Networks: Vision

Spike-Timing Dependent Plasticity, Learning Rules

Walter Senn¹ and Jean-Pascal Pfister^{1,2}

¹Department of Physiology, University of Bern, Bern, Switzerland

²Theoretical Neuroscience Group, Institute of Neuroinformatics, University of Zürich and ETH Zürich, Zürich, Switzerland

Synonyms

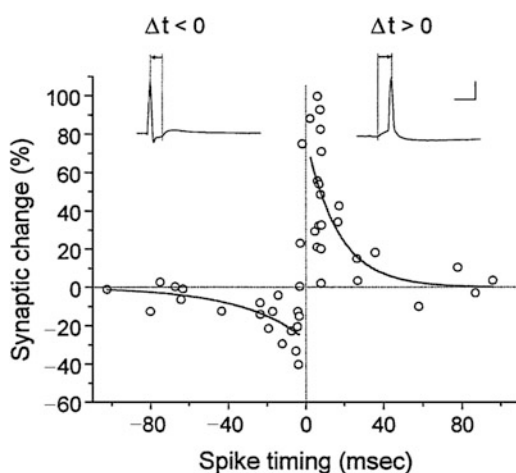
Spike-dependent synaptic learning rules; Spike-timing dependent synaptic plasticity; STDP

Definition

Biological phenomenon. Spike-timing-dependent plasticity (STDP) in its narrow sense refers to the change in the synaptic strength as a result of repeatedly triggering pairs of action potentials (“spikes”) with a fixed time difference between the pre- and postsynaptic action potentials (Markram et al. 1997; Bi and Poo 1998; Sjöström et al. 2001). STDP is typically observed for synapses between hippocampal or cortical pyramidal neurons in slices of juvenile rodents, and the spike pairings are repeated 50–100 times with various frequencies, e.g. 1 or 10 Hz. This protocol induces a change in the amplitude of a single excitatory postsynaptic potential (EPSP) which is plotted against the spike time difference $\Delta t = t_{\text{post}} - t_{\text{pre}}$ between the postsynaptic spike and the presynaptic spike (Fig. 1). The change takes in many cases a few minutes to be expressed and lasts at least for the duration of the experiment. Typically, when the presynaptic spike precedes the postsynaptic spike by roughly 10 ms, the synapse is potentiated; if the

presynaptic spike follows the postsynaptic spike, the synapse is depressed (for reviews, see Bi and Poo (2001); Senn (2002); Sjöström et al. (2008); Sjöström and Gerstner (2010)).

Learning rules. In a computational context, STDP refers to plasticity rules that depend on the timing of pre- and postsynaptic spikes and that are involved in various learning scenarios for neuronal networks. These learning rules either emphasize the link to the biophysics underlying the synaptic modification (Senn et al. 2001; Shouval et al. 2002; Karmarkar and Buonomano 2002; Rubin et al. 2005; Graupner and Brunel 2012), or are minimalistic with respect to a biological implementation (Kempter et al. 2001; Song and Abbott 2001), or are derived from the maximization of a utility function (Pfister et al. 2006; Toyoizumi et al. 2007; Florian 2007; Urbanczik and Senn 2009; Friedrich et al. 2011). The learning rules are studied in the context of supervised, unsupervised, or reinforcement learning. When evaluated from the performance point of view, learning rules that are mathematically derived from an optimization principle are superior over STDP rules designed to fit a given set of experimental data (Frémaux et al. 2010). Interestingly, biological plausibility and computational relevance may go together when considering 2-compartment neurons with synapses on a dendritic tree (Urbanczik and Senn 2014).



Spike-Timing Dependent Plasticity, Learning Rules,
Fig. 1 Change of the EPSP amplitudes as a function of the time difference $\Delta t = t_{\text{post}} - t_{\text{pre}}$ between the post- and presynaptic spike. Time constants for LTP and LTD fits are $\tau_{\text{pre}} \approx 17$ ms and $\tau_{\text{post}} \approx 34$ ms, respectively (for an interpretation, see Fig. 2). Pairing protocol: 60 spike pairs at 1 Hz. Inset: postsynaptic action potential, relative to the time of the presynaptic spike (*vertical line*). Scale bars: 10 ms, 50 mV (Figure from Bi and Poo (2001))

Detailed Description

STDP models come in different flavors, emphasizing more the phenomenology, the biophysics, or the computational aspects. As learning rules, their primary focus is on doing computations rather than on reproducing synaptic plasticity data. An excellent and comprehensive review to STDP models, starting with the basic pair-based STDP models (Fig. 2A) and including also functional consequences, is found in the Scholarpedia article by Sjöström and Gerstner (2010). Here we highlight the properties of third-order STDP models and focus on gradient rules.

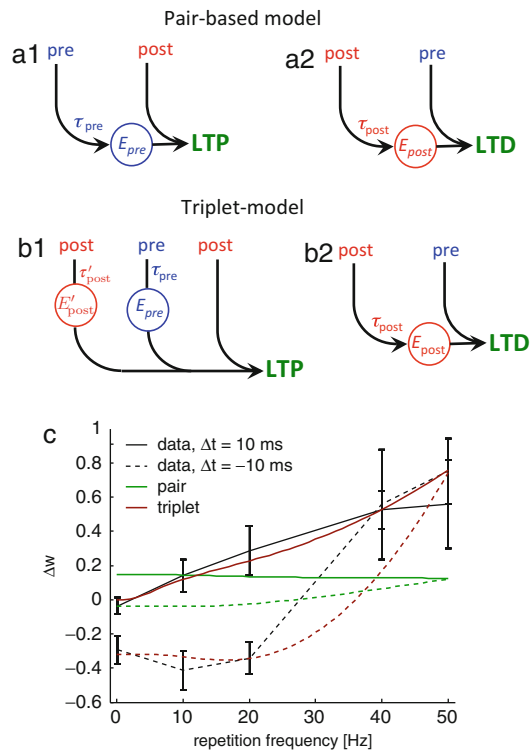
Phenomenological STDP Models

The simplest online model that phenomenologically reproduces the basic STDP curve (Fig. 1) separately induces long-term potentiation (LTP) or long-term depression (LTD), by either a pre-post or post-pre-coincidence detector, respectively. The key feature is that pre- and postsynaptic spikings are each tracked by leaky integrators, the so-called synaptic eligibility traces, while LTP and LTD are triggered proportionally to these traces at the times of the post- and presynaptic spikes, respectively (Fig. 2a, see also Sjöström and Gerstner (2010)).

The triplet model The simple STDP model which depends on pairs of spikes (pre-post and post-pre) correctly predicts the weight change only for a restricted number of protocols. If potentiation is assumed to be governed by triplets of spikes (pre-post-post) instead of pairs of spikes, a much broader class of experimental data can be captured (Pfister and Gerstner 2006). This so-called triplet model can be expressed as a sum of a depression term (Fig. 2B2) and a triplet term where at the time of the postsynaptic spike the weight change is proportional to the product of a postsynaptic and a presynaptic eligibility trace (Fig. 2B1).

The triplet model becomes especially relevant when the repetition frequency of the pre-post pairs increases. The pair-based model predicts a decrease of potentiation as a function of the pairing frequency. But in the visual cortex (L5 → L5 pyramidal neurons, Sjöstrom et al. (2001)), potentiation increases with increasing repetition frequency, and this is well reproduced by the triplet model (Fig. 2c; it is also qualitatively captured by the Senn-Markram-Tsodyks model; see Senn (2002)).

This triplet model has also interesting computational properties. Under the assumption of independent pre- and postsynaptic Poisson firing rate (Pfister and Gerstner 2006), the expected weight change predicted by the triplet model is consistent with the Bienenstock-Cooper-Munro (BCM) learning rule (Bienenstock et al. 1982) which elicits input selectivity, i.e., the output neuron becomes strongly responsive to one given (rate-based) input pattern and much less to all the other



Spike-Timing Dependent Plasticity, Learning Rules, Fig. 2 Phenomenological STDP models. (a) Simplest model reproducing Fig. 1. (A1) Each presynaptic spike stepwise increases a presynaptic eligibility trace E_{pre} that otherwise exponentially decays to 0 with time constant τ_{pre} (Eq. 1). LTP is induced by each postsynaptic spike proportionally to the amount of E_{pre} available at that time. (A2) LTD is induced by each presynaptic spike proportionally to E_{post} that low-pass filters the postsynaptic spiking. Note that the post-pre-chain is itself acausal and does not appear in the gradient-based learning schemes represented in the subsequent figures. (b) Triplet rule. (B1) In the triplet model, LTP is induced at the time of the postsynaptic spike and is proportional to the product $E_{\text{pre}}E'_{\text{post}}$. (B2) In the triplet model, LTD is induced by pairs of spikes as in B1. (c) Weight change as a function of the repetition frequency of the pre-post pairs (solid lines, $t_{\text{post}} - t_{\text{pre}} = 10 \text{ ms}$) and the post-pre pairs (dashed lines, $t_{\text{post}} - t_{\text{pre}} = -10 \text{ ms}$). The triplet model (brown) fits well the data from (Sjöström et al. 2001) (black) while the pair-based model (green) cannot

ones. Furthermore, if the independent Poisson assumption is relaxed such that output firing rate depends on the presynaptic spike timings, the triplet rule becomes sensitive to third-order spiking correlations in the input, thereby generalizing the BCM learning rule to spiking-correlated patterns (Gjorgjieva et al. 2011).

Extended models A next important extension of STDP models takes account of the modulation of plasticity by the postsynaptic voltage (Clopath et al. 2010; Clopath and Gerstner 2010). This unifying model is formulated in terms of the postsynaptic voltage time course and presynaptic spikes. It can explain the widest set of STDP experiments, including burst-induced synaptic plasticity and those experiments that reveal the dependence on the postsynaptic voltage, as e.g. in Artola et al. (1990) and Sjöström et al. (2001). This voltage-dependent model can also be seen as an extension of the triplet model where the postsynaptic eligibility trace in the potentiation term is replaced by a low-pass filter of the postsynaptic voltage. The triplet model, in turn, can be seen as a simplified version of the model by Senn et al. (2001). This latter model also depends on triple events (pre-post-post) for the induction of long-term potentiation, but the pre-post-post ordering is important while in the triplet model both pre-post-post as well as post-pre-post events lead to potentiation.

Biophysical STDP models Another class of STDP models explains the synaptic modifications as a nonlinear function of the postsynaptic calcium concentration. The question whether the postsynaptic calcium alone can capture the characteristical STDP curve of Fig. 1 (see Shouval et al. (2002) versus Karmarkar and Buonomano (2002)) has been affirmed by taking into account the calcium dynamics (Rubin et al. 2005) or additional nonlinearities (Graupner and Brunel 2012). Functionally, these threshold nonlinearities are very similar to the ones imposed on the pre- and postsynaptic eligibility traces introduced in the phenomenological models (Senn et al. 2001; Clopath et al. 2010). Yet, by starting with individual protein kinetics, a biophysical model may explain how these nonlinearities arise (Rubin et al. 2005), see also “► Spike-Timing Dependent Plasticity (STDP), Biophysical Models.”

Gradient-Based STDP Learning Rules

By their nature, the phenomenological and biophysical STDP models are not directly designed

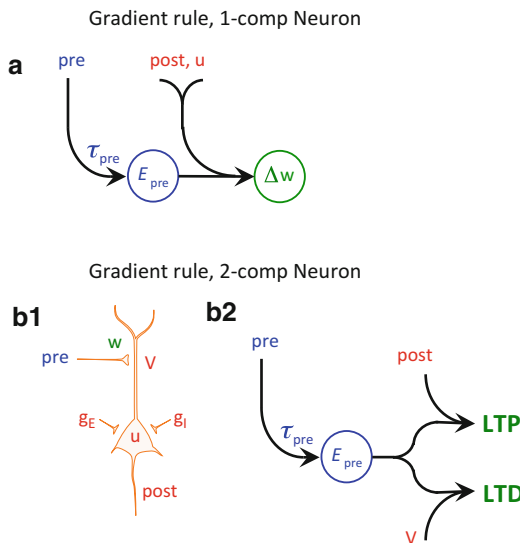
as synaptic learning rules that solve an explicit learning task. When canonical target functions for the learning can be defined, such as in the supervised and reinforcement learning scenario, spike-timing-dependent learning rules can be derived from gradient procedures that maximize/minimize these functions. A very convenient neuron model suited for a theory of learning is the escape rate neuron. Indeed since it allows to explicitly quantify the probability for a given postsynaptic spike train as a function of the afferent synaptic strengths w_j , the likelihood of a given spike train is differentiable (w.r.t to w_j) (Pfister et al. 2006). This neuron stochastically emits spikes with instantaneous firing rate $\rho(u)$ that is an increasing function of the instantaneous membrane potential $u(t)$. The latter is itself a sum of the postsynaptic potentials (PSPs) weighted by the synaptic strengths, $u(t) = \sum_j w_j \text{PSP}_j(t)$, optionally subtracted with a reset kernel after a postsynaptic spike.

Supervised learning In the supervised learning scenario, the target function can be defined as a distance between the desired postsynaptic spike train, $S_{\text{post}}^{\text{cl}}(t) = \sum_i \delta(t - t_i^{\text{post}})$, that is clamped as an output to the neuron and the spike trains that would be generated by the neuron itself. If we pick out a specific synapse, the presynaptic eligibility trace $E_{\text{pre}}(t)$ is again obtained by the leaky integration of the presynaptic spike train $S_{\text{pre}}(t) = \sum_i \delta(t - t_i^{\text{pre}})$. Typically, the integration time constant τ_{pre} is equal to the membrane time constant, and hence this trace can also be identified with the postsynaptic potential induced by that synapse, $E_{\text{pre}}(t) = \text{PSP}(t)$. The gradient rule that maximizes the log-likelihood of reproducing the clamped target spike trains is then obtained as (Pfister et al. (2006); see Fig. 3a)

$$E_{\text{pre}}(t) = \int_{-\infty}^t S_{\text{pre}}(\tilde{t}) e^{-\frac{t-\tilde{t}}{\tau_{\text{pre}}}} d\tilde{t} \quad (1)$$

$$\dot{w}(t) = \eta \frac{\rho'}{\rho} \left(S_{\text{post}}^{\text{cl}}(t) - \rho(u(t)) \right) E_{\text{pre}}(t), \quad (2)$$

where η is some small learning rate. Here, $\rho' = \rho'(u(t))$ is the derivative of the escape rate ρ with respect to u , evaluated at t . Interestingly,



Spike-Timing Dependent Plasticity, Learning Rules, Fig. 3 Gradient-based SDTP for supervised learning (a, b) and unsupervised learning (b). (a) An optimal learning rule that reproduces the timing of a given (“clamped”) output spike needs to take account of the postsynaptic membrane potential u beside the pre- and postsynaptic spikes (Eqs. 1 and 2). (B1) In a biological version, u is only slightly “nudged” by excitatory and inhibitory conductances g_E and g_I . The strength of synapses on the dendrites is adapted such that the dendritic potential V converges to the nudged somatic potential u . (B2) The corresponding gradient rule yields LTP that does only depend on the pre-post spike timings and LTD that depends only on the presynaptic spike time (captured by E_{pre}) and the local dendritic voltage (V ; see Eqs. 1 and 3)

by expressing Eq. 2 as a sum of a potentiation and a depression term, we note that potentiation depends on three factors (the postsynaptic spike, the presynaptic eligibility trace, and a nonlinear function of the postsynaptic membrane potential $\rho'(u)/\rho(u)$) and depression on two factors (the presynaptic eligibility trace and $\rho'(u)$). This learning rule is reminiscent of the voltage-triplet rule discussed above (Clopath and Gerstner (2010); see also Brea et al. (2013) for a detailed discussion of the mapping between those two learning rules).

Arguably, clamping the postsynaptic spike train $S_{\text{post}}^{\text{cl}}$ is biologically unfeasible as it would require that the membrane potential u is ∞ at the time of a target spike and $-\infty$ else, conflicting

with the evaluation of ρ and ρ' at the synaptically generated value of u . An alternative is to separate the spike-generating voltage from the synaptically induced voltage and consider a somatic and dendritic membrane potential, u and V , that are interpreted as a “teacher” (u) and “student” (V) potential, respectively (Fig. 2B1; Urbanczik and Senn (2014)). The soma receives conductance-based synaptic input that represents a teaching signal, and the postsynaptic spike train S_{post} is stochastically generated in the “free” run, i.e., according to a firing intensity $\rho(u)$ that is affected by this teaching input. Without teaching input, the somatic membrane potential is just the attenuated dendritic voltage, $u = \alpha V$, where α represents some dendritic attenuation factor and the instantaneous somatic firing is therefore $\rho(\alpha V)$. But if the somatic teaching input is turned on, the somatic voltage typically differs from the “dendritic prediction,” $u \neq \alpha V$. Learning is driven by the “prediction error” measured in terms of the firing rates, $\rho(u) - \rho(\alpha V)$. It reduces this error by adapting the synaptic strengths of the dendritic “student inputs.” At the synaptic location on the dendrite, the somatic rate $\rho(u)$ can be sampled by the backpropagating spikes S_{post} . The learning rule (Eq. 2) now translates to the biological version

$$\dot{w}(t) = \eta \frac{\rho'}{\rho} (S_{\text{post}}(t) - \rho(\alpha V(t))) E_{\text{pre}}(t), \quad (3)$$

that can operate all the time, without need for clamping (Fig. 2B2).

Crucially, after learning the teaching input driving, the synaptic plasticity (Eq. 3) can be turned off or on, without affecting the somatic voltage and hence without inducing additional weight changes. This is a consequence of the conductance-based teacher input that itself only changes the membrane potential if it deviates from the reversal potential defined that teaching input (Urbanczik and Senn 2014). The rule shares other interesting biological features. When the backpropagation is hampered, say due to insufficient dendritic depolarization, S_{post} is thinned out at the synaptic site and a putative LTP turns

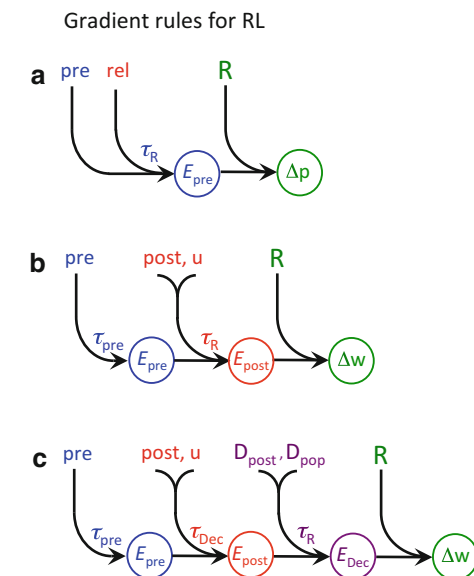
into LTD, as observed for synapses on the distal apical tree of cortical pyramidal neurons (Sjöström and Häusser 2006). Similarly, when the dendritic depolarization V is enhanced without additional postsynaptic spikes, LTD dominates as observed for these same cells (Sjöström et al. 2004).

Unsupervised learning The learning rule (Eq. 2) in the free run is itself not suited for unsupervised learning since averaging \dot{w} across trials cancels out to 0 at each point in time. However, if we consider a 2-dimensional sheet of 2-compartmental neurons as described in Fig. 2b, with Mexican-hat shaped somatosomatic connections, the somatic potential u is nudged away from V^* and the somatic firing in average does not anymore reflect the dendritic drive, $\langle S_{\text{post}} \rangle \neq \rho(V^*)$. In this case, the lateral connectivity induces a soft winner-take-all dynamics in the network that becomes a spike-based self-organizing feature map (Urbanczik and Senn 2014). When the dendrites of these neurons are supplied by spatiotemporal spike patterns via plastic synapses governed by the rule (Eq. 3), the feature map learns to cluster the spike patterns according to their similarity.

Another form of a gradient-based unsupervised learning that maximizes the mutual information between the pre- and postsynaptic spike trains was also shown to share classical STDP features while being able to develop receptive field properties (Toyoizumi et al. 2007). In the unsupervised setting, functional properties have also been shown for phenomenological STDP models in forming auditory maps (Gerstner et al. 1996), cortical columns (Song and Abbott 2001), direction-selective neurons in the visual cortex (Buchs and Senn 2002), or receptive fields similarly as described in the BCM theory (Gjorgjieva et al. 2011).

Reinforcement learning In reinforcement learning (RL), the putative synaptic weight changes induced by the pre- and postsynaptic activities are first low-pass filtered, and when a binary reward signal $R = \pm 1$ is applied, the changes accumulated until this time are multiplicatively modulated by R and turned into a real synaptic weight change. The phenomenological

STDP model shown in Fig. 2 has also been adapted to this reinforcement learning scenario where it is referred to as R-STDP (Izhikevich 2007; Legenstein et al. 2008). However, R-STDP is shown to be problematic since for each stimulus class the expected reward must be 0 (Frémaux et al. 2010). This is because the integral over the STDP curve (Fig. 1) in general deviates from 0, and hence learning with $\langle R \rangle \neq 0$ would cause a weight drift. This is not the case for Eq. 2 in the free run, nor for Eq. 3 without somatic teaching conductances. These latter rules translate to the RL rule schematized in Fig. 4b:



Spike-Timing Dependent Plasticity, Learning Rules, Fig. 4 Gradient-based STDP for reinforcement learning (RL). With incorporating downstream quantities into the synaptic plasticity, learning becomes faster. (a) The simplest spike-based RL rule changes the presynaptic release probability p (a proxy for the synaptic strength w) as a function of the presynaptic spike and the release, low-pass filtered with a time constant τ_R corresponding to the typical reward delay (Seung 2003). (b) The same synaptic modifications for supervised learning (Fig. 3) yields RL when low-pass filtered with τ_R and modulated with the delayed reward R (Eqs. 1, 4, and 5). (c) As a decision is made by a population of neurons, synaptic updates should take account of the population decision signal D_{pop} , compare it with the single neuron decision D_{post} , low-pass filter the correlation between the two decision signals with τ_R , and only then implement the resulting weight change modulated by R (Eqs. 1, 6, 7, and 8)

$$E_{\text{post}}(t) = \int_{-\infty}^t \frac{\rho'}{\rho} (S_{\text{post}}(\tilde{t}) - \rho(u(\tilde{t}))) E_{\text{pre}}(\tilde{t}) e^{-\frac{t-\tilde{t}}{\tau_R}} d\tilde{t} \quad (4)$$

$$\Delta w(T) = \eta R E_{\text{post}}(T), \quad (5)$$

where E_{pre} is given in (Eq. 1) and for the 2-compartmental model, the argument u of ρ and ρ' is replaced by V^* . The rule is shown to perform stochastic gradient ascent on the expected reward and has been studied in different applications (Xie and Seung 2004; Pfister et al. 2006; Florian 2007; Frémaux et al. 2010).

Stochastic gradient rules are not unique since the same gradient can be obtained from different estimators. The rule in Eq. 5, for instance, represents an estimator of the gradient of the expected reward, $\frac{\partial}{\partial w} \langle R \rangle = \langle R \frac{\partial}{\partial w} \log P_w(y|x) \rangle$, averaged across stimuli x , network activity y , time and reward. The reward R may depend on quantities downstream of x and y like the decision (or action) D that itself may stochastically depend on y . The reward $R(x, y)$ therefore is a stochastic function of (x, y) with conditional expectation $\langle R | x, y \rangle = \sum D R(x, D) P(D|x, y)$. For a synapse that has only access to the pre- and postsynaptic activities (components of x and y), the samples $R(x, y)$ have a large variance and so will the samples $R(x, y) \frac{\partial}{\partial w} \log P_w(y|x)$ of the gradient estimate have. In contrast, $R(x, D)$ may be a deterministic function (or again a stochastic function with smaller variance) and the samples $R(x, D) \frac{\partial}{\partial w} \log P_w(D|x)$ of the same reward gradient $\frac{\partial}{\partial w} \langle R \rangle$ show a smaller variance. To calculate $\frac{\partial}{\partial w} \log P_w(D|w)$, however, a synapse needs to have access to D (beside the pre- and postsynaptic activities).

Instead of considering $R(x, y)$, the reward can even be seen as a stochastic function of only the presynaptic spikes and the synaptic releases, $R(x, \text{rel})$. This leads to a learning rule where synaptic releases that are correlated with subsequent rewards are made more likely by enhancing the corresponding release probability (Seung, 2003). But the variance of this reward gradient estimator can be reduced by taking account of the postsynaptic activity. In this way, more and more

downstream information can be taken into account in the synaptic update, leading to learning rules that consider (A) only presynaptic spikes/releases and reward, (B) presynaptic spikes/releases, postsynaptic activity and reward, and (C) presynaptic spikes/releases, postsynaptic activities, single neuron and network decisions, and reward (Fig. 4). In these gradient estimators, the correlation between the synaptic parameter change and reward is progressively increased the more reward-relevant information the synapse exploits. In the case of only evaluating presynaptic spikes and releases, learning was claimed to mimic song acquisition in the zebra finch (Seung, 2003). When additionally evaluating the postsynaptic spikes and the membrane potential, the rule was shown to learn motor trajectories (Frémaux et al. 2010). When further evaluating the population decision the rule was shown to be successful in a complex sequential association task with delayed and scrambled rewards that is even hard to be learned by humans (Friedrich et al. 2011).

In population RL, the synaptic plasticity is modulated by the population decision that ultimately leads to the reward signal (Urbanczik and Senn 2009). The sign of the weight change should depend on whether the decision of the individual postsynaptic neuron D_{post} coincides with population decision D_{pop} formed by the majority of population neurons. These signals intrinsically depend on the neuronal code with which neurons and populations represent the possibly multivalued decisions and actions (Friedrich et al. 2014). In the simplest case of binary decisions, these signals may be set to 1 or -1, depending on whether the neuronal or population activity, low-pass filtered by τ_{Dec} , is above or below the corresponding decision threshold (Friedrich et al. 2011). The gradient rule emerging from this reasoning reads as (cf. Fig. 4c)

$$E_{\text{post}}(t) = \int_{-\infty}^t \frac{\rho'}{\rho} (S_{\text{post}}(\tilde{t}) - \rho(u(\tilde{t}))) E_{\text{pre}}(\tilde{t}) e^{-\frac{t-\tilde{t}}{\tau_{\text{Dec}}}} d\tilde{t} \quad (6)$$

$$E_{\text{Dec}}(t) = \int_{-\infty}^t D_{\text{post}}(\tilde{t}) D_{\text{pop}}(\tilde{t}) E_{\text{post}}(\tilde{t}) e^{-\frac{t-\tilde{t}}{\tau_{\text{Dec}}}} d\tilde{t} \quad (7)$$

$$\Delta w(T) = \eta R E_{\Delta \varepsilon \zeta}(T). \quad (8)$$

Intracellular recordings from dendrites during plasticity induction protocols have shown that SDTP also depends on dendritic NMDA spikes (Gordon et al. 2006). This raises the question whether there are spike-timing-dependent plasticity rules that take account of such dendritic spikes as well. There is in fact a class of gradient-based RL rules that incorporate the “triple-spike timing” among the presynaptic, dendritic, and postsynaptic spike sequence, including the dendritic and somatic voltage and the reward modulation, analogously to the four-step cascade schematized in Fig. 4c (Schiess et al. 2012).

Cross-References

- ▶ [Learning Rules: Overview](#)
- ▶ [Long Term Plasticity, Biophysical Models](#)
- ▶ [Reinforcement Learning in Cortical Networks](#)
- ▶ [Reward-Based Learning, Model-Based and Model-Free](#)
- ▶ [Spike-Timing Dependent Plasticity \(STDP\), Biophysical Models](#)
- ▶ [Tempotron Learning](#)

References

- Artola A, Bröcher S, Singer W (1990) Different voltage-dependent thresholds for inducing long-term depression and long-term potentiation in slices of rat visual cortex. *Nature* 347:69–72
- Bi G, Poo M (1998) Synaptic modifications in cultured hippocampal neurons: dependence on spike timing, synaptic strength, and postsynaptic cell type. *J Neurosci* 18:10464–10472
- Bi G, Poo M (2001) Synaptic modification by correlated activity: Hebb’s postulate revisited. *Annu Rev Neurosci* 24:139–166
- Bienenstock EL, Cooper LN, Munro PW (1982) Theory for the development of neuron selectivity: orientation specificity and binocular interaction in visual cortex. *J Neurosci* 2:32–48
- Brea J, Senn W, Pfister JP (2013) Matching recall and storage in sequence learning with spiking neural networks. *J Neurosci* 33:9565–9575
- Buchs NJ, Senn W (2002) Spike-based synaptic plasticity and the emergence of direction selective simple cells: simulation results. *J Comput Neurosci* 13:167–168
- Clopath C, Gerstner W (2010) Voltage and Spike Timing Interact in STDP – a unified model. *Front Synaptic Neurosci* 2:25
- Clopath C, Büsing L, Vasilaki E, Gerstner W (2010) Connectivity reflects coding: a model of voltage-based STDP with homeostasis. *Nat Neurosci* 13:344–352
- Florian RV (2007) Reinforcement learning through modulation of spike-timing-dependent synaptic plasticity. *Neural Comput* 19:1468–1502
- Frémaux N, Sprekeler H, Gerstner W (2010) Functional requirements for reward-modulated spike-timing-dependent plasticity. *J Neurosci* 30:13326–13337
- Friedrich J, Urbanczik R, Senn W (2011) Spatio-temporal credit assignment in neuronal population learning. *PLoS Comput Biol* 7:e1002092
- Friedrich J, Urbanczik R, Senn W (2014) Code-specific learning rules improve action selection by populations of spiking neurons. *Int J Neural Syst* 24:1–17
- Gerstner W, Kempter R, van Hemmen JL, Wagner H (1996) A neuronal learning rule for sub-millisecond temporal coding. *Nature* 383:76–81
- Gjorgjieva J, Clopath C, Audet J, Pfister JP (2011) A triplet spike-timing-dependent plasticity model generalizes the Bienenstock-Cooper-Munro rule to higher-order spatiotemporal correlations. *Proc Natl Acad Sci U S A* 108:19383–19388
- Gordon U, Polksy A, Schiller J (2006) Plasticity compartments in basal dendrites of neocortical pyramidal neurons. *J Neurosci* 26:12717–12726
- Graupner M, Brunel N (2012) Calcium-based plasticity model explains sensitivity of synaptic changes to spike pattern, rate, and dendritic location. *Proc Natl Acad Sci U S A* 109:3991–3996
- Izhikevich EM (2007) Solving the distal reward problem through linkage of STDP and dopamine signaling. *Cereb Cortex* 17:2443–2452
- Karmarkar UR, Buonomano DV (2002) A model of spike-timing dependent plasticity: one or two coincidence detectors? *J Neurophysiol* 88:507–513
- Kempter R, Gerstner W, van Hemmen JL (2001) Intrinsic stabilization of output rates by spike-based Hebbian learning. *Neural Comput* 13:2709–2741
- Legenstein R, Pecevski D, Maass W (2008) A learning theory for reward-modulated spike-timing-dependent plasticity with application to biofeedback. *PLoS Comput Biol* 4:e1000180
- Markram H, Lübke J, Frotscher M, Sakmann B (1997) Regulation of synaptic efficacy by coincidence of postsynaptic APs and EPSPs. *Science* 275:213–215
- Pfister JP, Gerstner W (2006) Triplets of spikes in a model of spike timing-dependent plasticity. *J Neurosci* 26:9673–9682
- Pfister J, Toyoizumi T, Barber D, Gerstner W (2006) Optimal spike-timing-dependent plasticity for precise action potential firing in supervised learning. *Neural Comput* 18:1318–1348

- Rubin JE, Gerkin RC, Bi GQ, Chow CC (2005) Calcium time course as a signal for spike-timing-dependent plasticity. *J Neurophysiol* 93:2600–2613
- Schiess M, Urbanczik R, Senn W (2012) Gradient estimation in dendritic reinforcement learning. *J Math Neurosci* 2:2
- Senn W (2002) Beyond spike timing: the role of nonlinear plasticity and unreliable synapses. *Biol Cybern* 87:344–355
- Senn W, Markram H, Tsodyks M (2001) An algorithm for modifying neurotransmitter release probability based on pre- and postsynaptic spike timing. *Neural Comput* 13:35–67
- Seung HS (2003) Learning in spiking neural networks by reinforcement of stochastic synaptic transmission. *Neuron* 40:1063–1073
- Shouval HZ, Bear MF, Cooper LN (2002) A unified model of NMDA receptor-dependent bidirectional synaptic plasticity. *Proc Natl Acad Sci U S A* 99:10831–10836
- Sjöström J, Gerstner W (2010) Spike-timing dependent plasticity. *Scholarpedia* 5:1362
- Sjöstrom PJ, Häusser M (2006) A cooperative switch determines the sign of synaptic plasticity in distal dendrites of neocortical pyramidal neurons. *Neuron* 51:227–238
- Sjöstrom PJ, Turrigiano GG, Nelson SB (2001) Rate, timing, and cooperativity jointly determine cortical synaptic plasticity. *Neuron* 32:1149–1164
- Sjöstrom PJ, Turrigiano GG, Nelson SB (2004) Endocannabinoid-dependent neocortical layer-5 LTD in the absence of postsynaptic spiking. *J Neurophysiol* 92:3338–3343
- Sjöstrom PJ, Rancz EA, Roth A, Häusser M (2008) Dendritic excitability and synaptic plasticity. *Physiol Rev* 88:769–840
- Song S, Abbott LF (2001) Cortical development and remapping through spike timing-dependent plasticity. *Neuron* 32:339–350
- Toyoizumi T, Pfister JP, Aihara K, Gerstner W (2007) Optimality model of unsupervised spike-timing-dependent plasticity: synaptic memory and weight distribution. *Neural Comput* 19:639–671
- Urbanczik R, Senn W (2009) Reinforcement learning in populations of spiking neurons. *Nat Neurosci* 12:250–252
- Urbanczik R, Senn W (2014) Learning by the dendritic prediction of somatic spiking. *Neuron* (in press)
- Xie X, Seung HS (2004) Learning in neural networks by reinforcement of irregular spiking. *Phys Rev E Stat Nonlin Soft Matter Phys* 69:041909

Spike-Timing Dependent Synaptic Plasticity

► [Spike-Timing Dependent Plasticity, Learning Rules](#)

Spike Triggered Average

Junji Ito

Institute of Neuroscience and Medicine (INM-6) and Institute for Advanced Simulation (IAS-6), Jülich Research Centre and JARA, Jülich, Germany

Synonyms

Reverse correlation; SFC; Spike-field coherence; STA

Definition

The spike-triggered average (STA) is a measure to relate a continuous signal and a simultaneously recorded spike train. It represents the average signal taken at the times of spike occurrences and with proper normalization is equivalent to the cross-correlation between the continuous signal and the spike train.

Detailed Description

The STA is widely used to study the temporal relationship between a spike train and a simultaneously recorded continuous signal, such as the local field potential (Eckhorn et al. 1988; Gray and Singer 1989; Murthy and Fetz 1996; Fries et al. 2001; Okun et al. 2010; Denker et al. 2011), membrane potential (Matsumura et al. 1996; Lampl et al. 1999; Poulet and Petersen 2008), synaptic conductance (under dynamic clamp, Gauck and Jaeger 2000) and electromyogram (McKiernan et al. 1998). Even non-physiological signals, such as electric stimulation to a single neuron (Mainen and Sejnowski 1995) or visual (Ringach and Shapley 2004) and auditory (Eggermont et al. 1983) stimulation, have been related to a spike train via the STA. In such cases the STA is commonly referred to as reverse correlation.

Here we introduce the STA in relation to the local field potential (LFP). The LFP signal is obtained as a low-frequency component, typically below approximately 100 Hz, of extracellular recordings of neuronal electric activity. Its physiological origin is the transmembrane current of neurons in the vicinity of the recording electrode (Mitzdorf 1985; Nunez and Srinivasan 2006). Theoretical considerations and experimental observations have elucidated that the strongest contribution to the LFP is from the currents caused by postsynaptic potentials, while the influence of action potentials on the LFP is weak (Mitzdorf 1985; Logothetis 2003; Buzsaki et al. 2012). Therefore, the LFP predominantly reflects the synaptic inputs to the local neuronal circuit around the tip of the recording electrode (including the recurrent inputs due to internal processing of the circuit) (Logothetis 2003). This view is further strengthened by the observation that temporal modulations of the (intracellularly recorded) somatic membrane potential of a single cell, which represent net synaptic input to the cell, are tightly correlated with modulations of the (extracellularly recorded) LFP in the vicinity of that same cell (Poulet and Petersen 2008; Okun et al. 2010). Given that spikes are the output of single neurons, the relationship between simultaneously recorded spikes and LFPs could be interpreted as reflecting the input–output relation of the local brain area [cross-ref: Local Field Potential, Relationship to Unit Activity].

It has been shown in various species and various cortical/subcortical brain regions that LFPs exhibit distinct oscillations in a wide range of frequencies (Buzsaki 2006). Previous studies have identified modulations of these oscillatory activities as reflecting changes in the functional states of perceptual, cognitive, and motor processes in the brain. An important question about the spike-LFP relation would therefore be whether, and if so how, temporal modulations of spiking activity are related to LFP oscillations or, more concretely, how the timings of spike occurrences correlate with the phase of LFP oscillations.

The spike-triggered average (STA) is a commonly used measure for assessing the

temporal relation between a spike train and an LFP signal. Assume simultaneous recordings of a spike train, represented as time points t_i ($1 \leq i \leq N$; N , total number of spikes) of spike occurrences, and an LFP signal, represented by $X(t)$, where t is time. For simplicity, also assume that the recording time is sufficiently long. The STA is defined as

$$STA(\tau) = \frac{1}{N} \sum_{i=1}^N X(t_i + \tau), \quad (1)$$

i.e., the average value of $X(t)$ at a given time lag τ in relation to the spike time t_i . This is equivalent to the cross-correlation (with normalization by the number of spikes) between the LFP signal and the spike train:

$$STA(\tau) = \frac{1}{N} \int_{-\infty}^{\infty} X(t + \tau) Y(t) dt,$$

with $Y(t) = \sum_{i=1}^N \delta(t - t_i)$ representing the spike train as a sum of Dirac delta functions $\delta(\cdot)$. Typically the STA is computed for a range of lags τ around the spike times, so that the waveform of the STA as a function of the lag illustrates the average modulation of the LFP around the occurrences of spikes. The STA obtained in this manner is widely used as a measure of the temporal locking of spikes to oscillatory LFP modulations (Eckhorn et al. 1988; Gray and Singer 1989; Murthy and Fetz 1996; Fries 2001; Okun et al. 2010; Denker et al. 2011).

When spikes occur preferentially at a specific phase of LFP oscillations, the summation in the right-hand side of Eq. 1 accumulates LFP values at similar phases of the oscillation for each lag τ , resulting in the STA having an oscillatory waveform with the preferred phase represented at $\tau = 0$. Thus, the degree of temporal spike-to-LFP locking can be evaluated by the strength of oscillatory modulations of the STA, i.e., the greater the modulation, the stronger the locking. A caveat is, however, that the strength of modulation depends not only on the degree of locking but also on the amplitudes of the oscillatory

components of the LFP signal. One way to quantify the degree of locking in spite of this amplitude dependence is to estimate the significance of the oscillatory modulation in the obtained STA by use of a bootstrap method. Commonly used methods include trial shuffling, spike randomization, and spike dithering [cross-ref: Surrogate Data for Evaluation of Spike Correlation]. A proper use of bootstrap significance tests also enables rejection of artificial locking due to non-stationarities in the firing rate of the spike train (Grün 2009; Louis et al. 2010).

The oscillatory power of LFP signals typically shows a strong dependence on frequency. Therefore, the amplitude dependence causes another concern when the LFP signal contains oscillatory components at multiple frequencies and one wishes to compare the strengths of the spike-to-LFP locking at different frequencies. To normalize for the difference in power at different frequencies, it is possible to move from the time domain to the frequency domain. Spike-field coherence (SFC) is a measure derived from the STA through such normalization. It is defined as

$$SFC(f) = \left| \tilde{STA}(f) \right|^2 / \left| \tilde{X}(f) \right|^2,$$

where

$$\tilde{STA}(f) = \int_{-\infty}^{\infty} STA(\tau) e^{-2\pi if\tau} d\tau, \quad \tilde{X}(f) = \int_{-\infty}^{\infty} X(t) e^{-2\pi ift} dt,$$

i.e., the power spectrum of the STA normalized by the power spectrum of the LFP signal used to compute the STA (Fries et al. 2002). For each frequency, f , the SFC takes on a value between 0 and 1, which corresponds to independence and to perfect locking, respectively, between the spike train and the corresponding spectral component of the LFP. Owing to the normalization by the LFP power, SFC serves as a proper measure for comparison of the degree of spike-to-LFP locking at different frequencies. Studies have shown that the modulation of SFC is related to various aspects of brain function such as sensory processing (Womelsdorf et al. 2006), attention

(Chalk et al. 2010), working memory (Pesaran et al. 2002), and decision making (Pesaran et al. 2008).

Cross-References

- ▶ [Auditory Nerve Response, Afferent Signals](#)
- ▶ [Dynamic Clamp Technique](#)
- ▶ [Gamma and Theta Oscillations, Hippocampus: Overview](#)
- ▶ [Local Field Potential, Relationship to Unit Activity](#)
- ▶ [Local Field Potentials \(LFP\)](#)
- ▶ [Low Frequency Oscillations \(Anesthesia and Sleep\): Overview](#)
- ▶ [Significance Evaluation](#)
- ▶ [Spike Train](#)
- ▶ [Surrogate Data for Evaluation of Spike Correlation](#)

References

- Buzsaki G (2006) Rhythms of the brain. Oxford University Press, New York
- Buzsaki G, Anastassiou CA, Koch C (2012) The origin of extracellular fields and currents – EEG, ECoG, LFP and spikes. *Nat Rev Neurosci* 13:407–420
- Chalk M, Herrero JL, Gieselmann MA, Delicato LS, Gotthardt S, Thiele A (2010) Attention reduces stimulus-driven gamma frequency oscillations and spike field coherence in V1. *Neuron* 66:114–125
- Denker M, Roux S, Lindén H, Diesmann M, Riehle A, Grün S (2011) The local field potential reflects surplus spike synchrony. *Cereb Cortex* 21:2681–2695
- Eckhorn R, Bauer R, Jordan W, Brosch M, Kruse W, Munk M, Reitboeck HJ (1988) Coherent oscillations: a mechanism of feature linking in the visual cortex? Multiple electrode and correlation analyses in the cat. *Biol Cybern* 60:121–130
- Eggermont JJ, Johannesma PM, Aertsen AM (1983) Reverse-correlation methods in auditory research. *Q Rev Biophys* 16:341–414
- Fries P, Reynolds JH, Rorie AE, Desimone R (2001) Modulation of oscillatory neuronal synchronization by selective visual attention. *Science* 291:1560–1563
- Fries P, Schröder J-H, Roelfsema PR, Singer W, Engel AK (2002) Oscillatory neuronal synchronization in primary visual cortex as a correlate of stimulus selection. *J Neurosci* 22:3739–3754
- Gauck V, Jaeger D (2000) The control of rate and timing of spikes in the deep cerebellar nuclei by inhibition. *J Neurosci* 20:3006–3016

- Gray CM, Singer W (1989) Stimulus-specific neuronal oscillations in orientation columns of cat visual cortex. *Proc Natl Acad Sci U S A* 86:1698–1702
- Grün S (2009) Data-driven significance estimation for precise spike correlation. *J Neurophysiol* 101:1126–1140
- Lampl I, Reichova I, Ferster D (1999) Synchronous membrane potential fluctuations in neurons of the cat visual cortex. *Neuron* 22:361–374
- Logothetis NK (2003) The underpinnings of the BOLD functional magnetic resonance imaging signal. *J Neurosci* 23:3963–3971
- Louis S, Borgelt C, Grün S (2010) Generation and selection of surrogate methods for correlation analysis. In: Grün S, Rotter S (eds) *Analysis of parallel spike trains*, Series in computational neuroscience. Springer, New York
- Mainen ZF, Sejnowski TJ (1995) Reliability of spike timing in neocortical neurons. *Science* 268:1503–1506
- Matsumura M, Chen D, Sawaguchi T, Kubota K, Fetz EE (1996) Synaptic interactions between primate precentral cortex neurons revealed by spike-triggered averaging of intracellular membrane potentials in vivo. *J Neurosci* 16:7757–7767
- McKiernan BJ, Marcario JK, Karrer JH, Cheney PD (1998) Corticomotoneuronal postspike effects in shoulder, elbow, wrist, digit, and intrinsic hand muscles during a reach and prehension task. *J Neurophysiol* 80:1961–1980
- Mitzdorf U (1985) Current source-density method and application in cat cerebral cortex: investigation of evoked potentials and EEG phenomena. *Physiol Rev* 65:37–100
- Murthy VN, Fetz EE (1996) Synchronization of neurons during local field potential oscillations in sensorimotor cortex of awake monkeys. *J Neurophysiol* 76:3968–3982
- Nunez PL, Srinivasan R (2006) Electric fields of the brain: the neurophysics of EEG. Oxford University Press, New York
- Okun M, Naim A, Lampl I (2010) The subthreshold relation between cortical local field potential and neuronal firing unveiled by intracellular recordings in awake rats. *J Neurosci* 30:4440–4448
- Pesaran B, Pezaris JS, Sahani M, Mitra PP, Andersen RA (2002) Temporal structure in neuronal activity during working memory in macaque parietal cortex. *Nat Neurosci* 5:805–811
- Pesaran B, Nelson MJ, Andersen RA (2008) Free choice activates a decision circuit between frontal and parietal cortex. *Nature* 453:406–409
- Poulet JFA, Petersen CCH (2008) Internal brain state regulates membrane potential synchrony in barrel cortex of behaving mice. *Nature* 454:881–885
- Ringach D, Shapley R (2004) Reverse correlation in neurophysiology. *Cognit Sci* 28:147–166
- Womelsdorf T, Fries P, Mitra PP, Desimone R (2006) Gamma-band synchronization in visual cortex predicts speed of change detection. *Nature* 439:733–736

Spiking Cochleas

- Neuromorphic Sensors, Cochlea

Spinal Biomechanics

- Biomechanical Model of Low Back Pain

Spinal Control of Voluntary Movements

- Coordinate Transformations, Role of Spinal Circuitry in

Spinal Cord Stimulation

- Methodologies for the Treatment of Pain
- Spinal Stimulation for Parkinson Treatment

Spinal Cord, Integrated (Non CPG) Models of

Gerald E. Loeb

Department of Biomedical Engineering,
University of Southern California, Los Angeles,
CA, USA

S

Synonyms

Adaptive control; Motor control; Motor learning;
Reflex; Regulator; Segmental control; Servo control;
Voluntary behavior

Definition

Spinal cord refers to the central nervous system (CNS) in vertebrates below the foramen

magnus, between the brainstem and the peripheral nervous system, not including the autonomic ganglia.

Learned sensorimotor behavior refers to all types of voluntary musculoskeletal activation that accomplish a behavioral goal and that utilize sensory feedback during execution, but here excluding cyclical locomotor behaviors known to be generated and controlled autonomously by central pattern generators residing within the spinal cord itself (see “Cross-References”).

Detailed Description

The spinal cord is not part of the brain; together they constitute the central nervous system of vertebrates. The spinal cord alone is capable of controlling complete motor behaviors such as locomotion. It can generate complex sequences of muscle activation and alter them to ambient conditions detected by somatosensory afferents. The well-studied role of the spinal cord in locomotion is covered in other entries (“► [Vertebrate Pattern Generation: Overview](#)”); this article considers whether and how the same spinal circuits contribute to voluntary motor behavior that is ultimately controlled by the brain.

Historical and Methodological Perspective

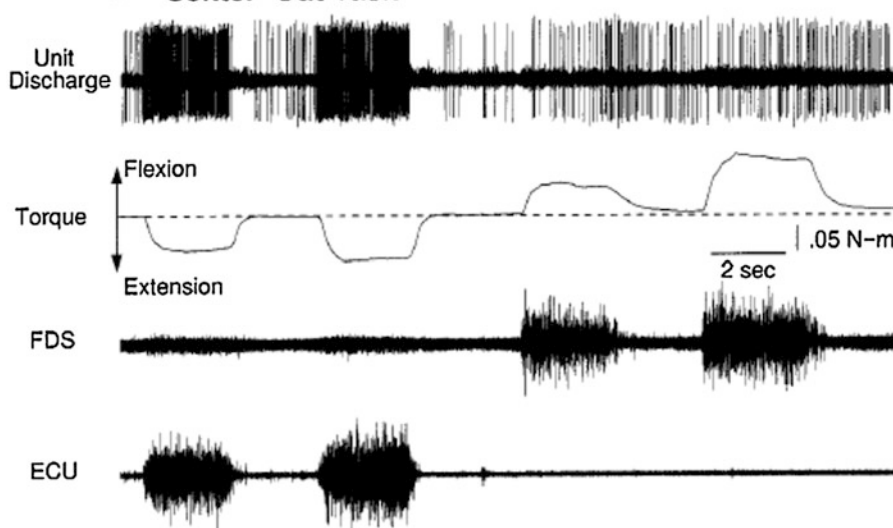
Several anatomical features of the spinal cord made it an attractive target for the earliest neurophysiological investigations. Its connections to and from the peripheral nervous system of the body are arranged in four laterally and dorsoventrally segregated and highly elongated rows of roots. These are divided and gathered into spinal nerves based on the openings between adjacent vertebrae. These roots and their associated peripheral nerves are readily traced by gross anatomical dissection to various target structures (individual muscles and regions of skin) whose function can be easily observed and manipulated. About 200 years ago, the anatomist Charles Bell and, separately, the physiologist Francois Magendie discovered that the ventral roots conveyed the motor commands to the muscles (Bell 1811) while the dorsal roots conveyed only

sensory information (Magendie 1822), respectively. This laid a foundation for the interpretation of clinical phenomena such as the knee-jerk reflex, well known to nineteenth-century neurology. At the turn of the twentieth century, Sir Charles Sherrington systematically extended the set of spinal reflexes to include both excitatory and inhibitory responses as well as interlimb effects and suggested that such reflexes constituted the building blocks of spinally mediated behaviors such as locomotion (Sherrington 1910).

As electrophysiological methodology developed during the middle of the twentieth century, it became possible to identify the individual neurons and circuits responsible for behavioral phenomena. The spinal interneurons came to be divided and identified by the nature of the input and output connections by which they were first identified. The newly discovered proprioceptors and spinal interneurons appeared to correspond to the feedback circuits utilized by the emerging field of servo control engineering to stabilize electrical and mechanical systems (including the instrumentation that those electrophysiologists generally had to build for themselves). This suggested that the reflexes might be just the most visible manifestations of continuous servo control, in which the spinal circuitry could simplify the problem of motor control by linearizing the complex mechanical properties of the musculoskeletal system (Houk 1979). It gradually became clear, however, that the actual input and output connections to spinal interneurons and motoneurons were far broader than predicted by servo control. The most local circuits were the easiest to find but the cumulative effects of the more widespread circuits are probably much larger. Furthermore, the strength and even the sign of many spinal reflexes were found to be modulated during both locomotor and voluntary motor behaviors (Burke 1999).

Neurophysiological studies of voluntary behaviors have focused mostly on the cerebral cortex of the brain, correlating neural activity recorded by chronically implanted microelectrodes with observable kinematics and/or muscle activity in the limb. However, the vast majority of

B Center-Out Task



Spinal Cord, Integrated (Non CPG) Models of
Fig. 1 Extracellularly recorded spikes from a spinal premotor interneuron recorded as monkey-generated isometric ramp-and-hold torques in flexion and extension at the wrist in order to match a visual cue; *FDS* = *EMG* from

flexor digitorum superficialis, *ECU* = *EMG* from *extensor carpi ulnaris*. Note strong correlation with *ECU* during extension torques but substantial activity during flexion torques that was not correlated with *FDS* modulation (From Perlmutter et al. 1998)

corticospinal projections end on spinal interneurons rather than the motoneurons that activate muscles directly (Rathelot and Strick 2009). These interneurons are vigorously active during learned, voluntary limb movements (see Fig. 1 below from Perlmutter et al. 1998). The threshold nonlinearity of spiking neurons implies that the cortical commands can be seen as enabling reflexive adjustments or, equally, that the ongoing somatosensory feedback enables the commanded behavior. Early attempts to tease this apart relied on the latencies of various responses to strong electrical stimuli, which depend on the physical lengths of the circuits and the conduction velocities of the axons. This can be used to compute the minimal latency of the fastest possible responses such as the monosynaptic stretch reflex, but it does not help with mechanical stimuli whose asynchronous afferent signals may undergo substantial temporospatial integration in the interneurons at every level before any response is seen.

This entry summarizes what is now known about the connectivity of the spinal circuits (for a detailed review, see Pierrot-Deseilligny and

Burke 2005). Much of that information comes from histological tracing and electrophysiological studies of the spinal cord of the cat, supplemented by clinical studies of human limb reflexes. There are substantial specializations in other species and other parts of the body such as the axial muscles of the neck and trunk (Richmond and Loeb 1992). This review also considers theories and models regarding how these spinal circuits could contribute to control of learned, voluntary limb movements. Other parts of the brain such as the cerebellum have equally well-developed connections to and from spinal cord (Spanne and Jörntell 2013) compared to the cerebral cortex. Damage to the cerebellum produces different but equally profound sensorimotor disorders, but its role in voluntary behavior is even less well understood. The actual functional relationships between the brain and the spinal cord remain contentious.

Basic Components

Somatosensory Afferents

A general review of somatosensation can be found elsewhere; this is a brief summary of the

afferents whose modalities and conduction velocities resulted in the naming conventions for the interneurons described below.

- **Spindle Primary Afferents (Ia):** Most muscles contain 20–500 elaborate sense organs attached in parallel with their muscle fibers. These muscle spindles each contain several specialized and separately innervated intrafusal muscle fibers. Each spindle is innervated by one rapidly conducting, primary afferent axon ($A\alpha$) whose local sensory endings consist of spirals wrapped around the middle of each of the intrafusal muscle fibers. These Ia afferents are exquisitely sensitive to stretch of the muscle (and hence of the spindle and its intrafusal muscle fibers). The absolute and relative sensitivities of the Ia afferents to length versus velocity are modulated over a wide dynamic range by centrally controlled activation of their various types of intrafusal muscle fibers (Loeb 1984).
- **Golgi Tendon Organ (GTO) Afferents (Ib):** Most muscles contain 20–200 simple sense organs attached in series with various subsets of their muscle fibers, making them sensitive to active muscle force. Each GTO is innervated by one rapidly conducting primary afferent axon ($A\alpha$). The random sampling of muscle fibers makes the response of a given GTO somewhat idiosyncratic, but the generally orderly recruitment of motor units results in ensemble activity of the Ib afferents that accurately reflects total muscle force (Mileusnic and Loeb 2009).
- **Group II Afferents:** The smaller and slower conducting myelinated axons ($A\beta$) in peripheral nerves are designated as Group II. They include both cutaneous mechanoreceptors with a wide range of sensitivities in both glabrous and hairy skin plus secondary spindle afferents attached to a subset of the intrafusal muscle fibers and sensitive mostly to absolute length. Some cutaneous stretch sensors contribute to the sense of body posture and motion in combination with the spindle afferents (Gandevia 1996); others are better suited to detecting intermittent contact with external objects.

• **Group III and IV Afferents:** The smallest myelinated ($A\delta$) and unmyelinated (C) sensory nerve fibers innervate a wide range of specialized receptors for strain, temperature, pain, and metabolic products. Their signals are processed locally by dorsal horn interneurons, many of which project to some of the spinal interneurons or their presynaptic inputs. Their slow conduction velocities lead to the presumption that they do not contribute importantly to moment-to-moment coordination but they probably modulate the state of the system in response to fatigue and injury (Martin et al. 2006).

• **Recurrent Motoneuron Collaterals:** Most alpha motoneurons give off collateral branches before leaving the spinal cord en route to the muscles. While not truly sensory, these efference copy signals provide feedback regarding important state variables of the system, contributing to both the reflexive behavior of the spinal cord itself and the ascending information that is conveyed to the brain (Windhorst 1990).

Presynaptic Modulation

An important feature of many spinal circuits is the presence of synaptic triads, in which the synaptic boutons of one neuron (modulator) end on the boutons of another neuron (transmitter) rather than on the cell body or dendrites of the receiver neuron. These presynaptic pathways may exert either depolarizing or hyperpolarizing effects on the resting membrane potential of the transmitter boutons. When a spike arrives at the transmitter bouton, the amplitude of the voltage excursion depends on this resting potential; the amount of transmitter that is released depends strongly on the voltage excursion. A depolarizing presynaptic modulation thus has the effect of inhibiting the efficacy of the transmitter; a hyperpolarizing modulation facilitates the transmitter. The presynaptic inhibitory effects of many cutaneous afferents have been particularly well described (Rudomin and Schmidt 1999). The monosynaptic stretch reflex is also presynaptically inhibited by descending cortical pathways (Meunier and Pierrot-Deseilligny 1998) and in fatigued

muscles (Baudry et al. 2010). The full extent of sources and recipients of presynaptic inhibition and facilitation is not known.

Limb Dynamics

Physiologists look for ways to simplify complex musculoskeletal anatomy and mechanics in order to identify organizing principles of control. By focusing on one axis of motion of one joint (e.g., dorsiflexion/extension of the ankle joint), it is possible to describe all the muscles that create a positive moment as synergists and all that create a negative moment as antagonists. Activation of the muscles in each group will have opposite effects on the joint torque, and motion of the joint in this axis will have opposite effects on the stretch receptors in these two groups of muscles. Unsurprisingly, the reflexes elicited by afferents from synergistic muscles are substantially different and often opposite in sign from those elicited by the same types of afferents from the antagonist muscles (Sherrington 1908). Much of the terminology below reflects this natural reciprocity of function and connectivity.

Unfortunately, most musculoskeletal anatomy and dynamics are not well described by simple reciprocity. Most joints have more than one axis of motion and the majority of mammalian muscles cross more than one joint. The lengths of the muscles and their moment arms on each axis of motion depend on the posture and motion of all the axes of all the joints that they cross. Muscles that are synergists for the restricted motion described above may be undergoing length changes that are opposite in sign and generating torques in other axes that are opposite in sign. Furthermore, a skeleton consisting of a series of linked inertial masses is subject to intersegmental dynamics, sometimes summarized as Coriolis effects. Acceleration induced by a muscle crossing one joint results in angular accelerations at distant joints, similar to the complex sequence of motion induced by cracking a whip from its proximal end (Zajac and Gordon 1989). The idealized classical circuits described below use the terminology of synergist and antagonist, but most muscles relate to most other muscles via combinations of both types of circuitry (designated as a “partial synergist” relationship).

The net effects depend on the gains in the competing pathways, which are strongly modulated by both descending and local pathways, as discussed in Coordination and Regulation.

Spinal Circuits

Ia Monosynaptic Stretch Reflex

The tendon jerk reflexes (e.g., knee, ankle) are the fastest and most reliable responses because they involve only one synapse between a rapidly conducting Ia spindle afferent and an alpha motoneuron. The Ia afferents from a given muscle project to most or all of the motoneurons that control that muscle (homonymous projection; HOM in Fig. 2) and to many of the motoneurons of synergist (SYN) muscles (Eccles et al. 1957a). Nevertheless, the strength of the observable response can be substantially modulated by postsynaptic polarization of the receiving pool of motoneurons via other synaptic inputs and by presynaptic inhibition or facilitation of the Ia synapse itself. The brain can learn to change the gain of even this direct connection (Wolpaw 2010).

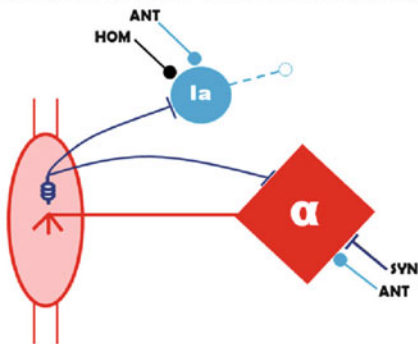
Ia Inhibitory Interneurons

Spindle Ia afferents excite a class of inhibitory interneurons that project to the motoneurons of antagonist muscles (Eccles and Lundberg 1958). Thus, stretching one muscle tends to inhibit activity that may be occurring in the antagonist muscles and that would otherwise oppose the excitatory stretch reflex described above. It is important to remember that the spindle receptors of both the synergist and antagonist muscles are generally biased by their respective fusimotor efferents so that they are generating continuous activity. Sudden perturbations that give rise to excitatory and inhibitory reflexes are just the most obvious manifestation of a continuous push-pull servo control system. These reciprocal circuits work continuously to maintain stable body posture and minimize energetically wasteful cocontraction of mutually antagonistic muscles.

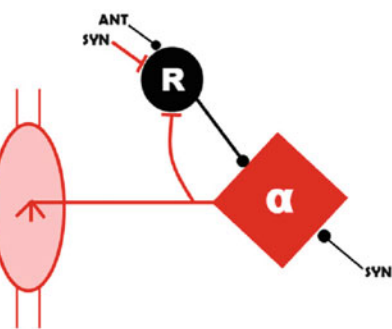
Ib Inhibitory Interneurons

The force-sensitive Golgi tendon organs excite a class of inhibitory interneurons that project to

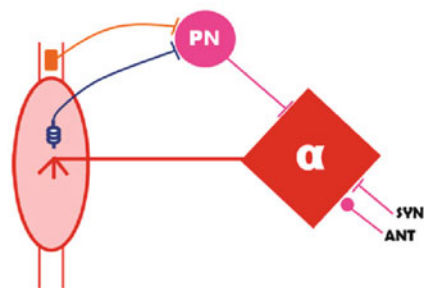
Stretch reflex and Ia inhibitory



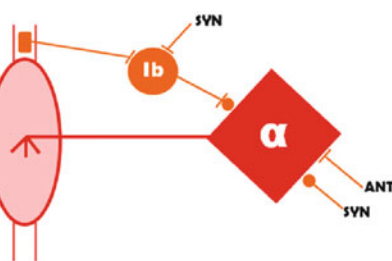
Renshaw



Propriospinal



Ib



Spinal Cord, Integrated (Non CPG) Models of
Fig. 2 Five classical interneuronal pathways that comprise the model from the perspective of a single muscle. Projections from neural elements associated with self (*HOM*) as well as synergist (*SYN*) and antagonist (*ANT*)

muscles are shown with color codes: Ia inhibitory interneurons are *blue*, Ib inhibitory interneurons are *orange*, and Renshaw inhibitory interneurons are *black* (Illustration from Tsianos et al. 2011)

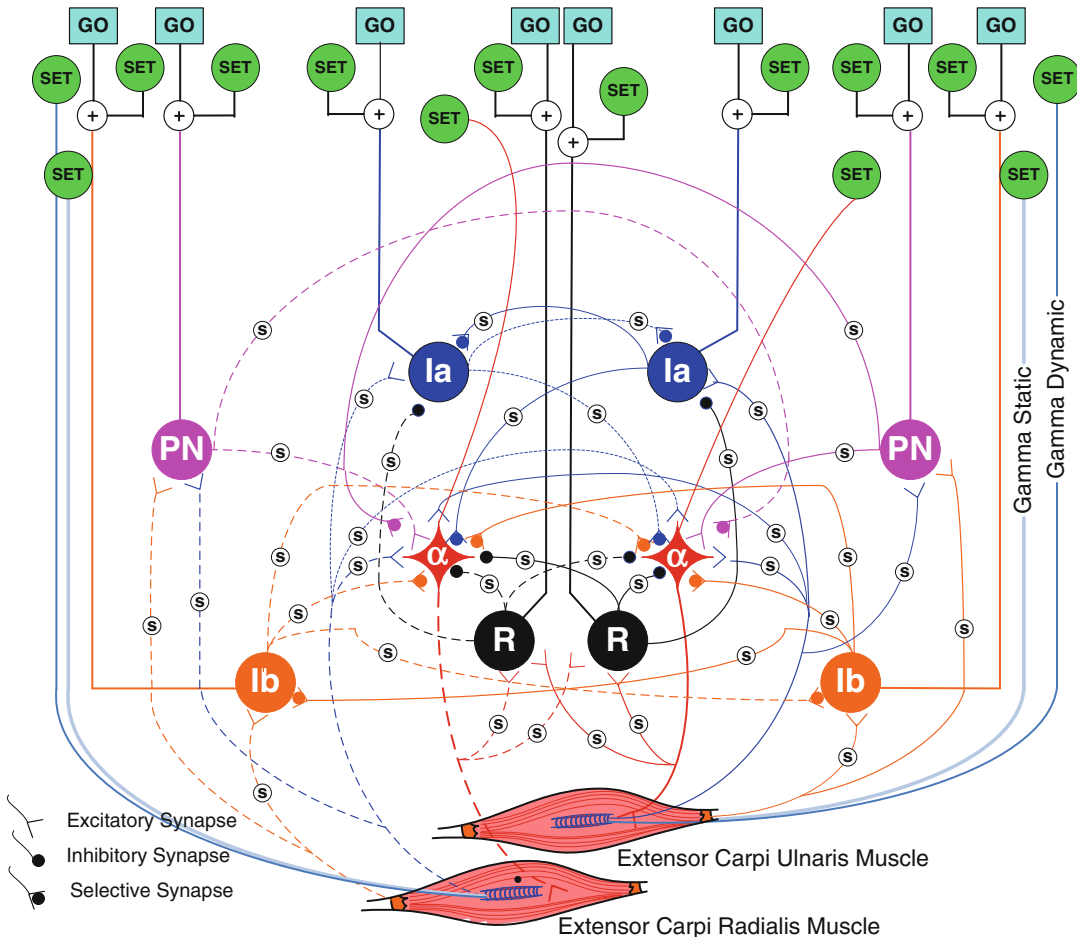
their own and synergist motoneurons (Eccles et al. 1957b). This results in a simple servo controller that tends to stabilize fluctuations in force. The story does not end there, however. The Ib inhibitory interneurons actually receive inputs from a wide range of cutaneous and proprioceptive afferents, and they project widely to both synergistic and antagonistic motoneurons. Furthermore, Ib inhibitory interneurons project to each other, resulting in disinhibition whereby force feedback can actually result in positive, self-reinforcing feedback loops (McCrea 1986). This complexity is summarized in Fig. 2 (Ib, bottom right) and Fig. 3 with a symbol denoting the selectability of both excitatory and inhibitory effects between the Ib inhibitory interneuron and homonymous alpha motoneuron.

Renshaw Inhibitory Interneurons

The recurrent motoneuron collaterals excite an interneuron that inhibits the homonymous motoneurons and their synergists, in the manner of a servo control governor preventing runaway activation of the muscles. These Renshaw inhibitory interneurons also project to the Ia inhibitory neurons of the same muscle, resulting in a disinhibition of the antagonist motoneurons (Windhorst 1990).

Propriospinal Excitatory Interneurons

There are clusters of excitatory spinal interneurons located just rostral to both the cervical and lumbar enlargements wherein the limb motor nuclei are located. These interneurons receive direct excitatory projections from both Ia and Ib



Spinal Cord, Integrated (Non CPG) Models of
Fig. 3 The major proprioceptive feedback circuits between two wrist muscles that are synergists for some tasks (e.g., extension) and antagonists for others (e.g., radioulnar deviation); color code is the same as in Fig. 1.

Tasks were controlled by learning a background pattern of *SET* signals to designated spinal neurons and presynaptic gains (*S* in circles) and a *GO* pattern to initiate the task via only the spinal interneurons (Figure from Raphael et al. 2010)

afferents as well as strong descending control from the brain (Jankowska et al. 1973). They have been implicated in the initiation of voluntary limb movements via their excitatory and inhibitory effects on synergist and antagonist motoneurons, respectively (Lundberg 1992).

Cutaneous Reflex Interneurons

Activity in cutaneous afferents can produce strong and widely distributed excitation and inhibition of motoneurons. The pathways all go through chains of at least two interneurons, however, each of which is subject to modulation by

other afferents, other interneurons, and descending signals from the brain. The functional contribution of cutaneous feedback is obvious from studies of dexterous manipulation of objects (Johansson and Flanagan 2009), but specific circuit models are not available.

Spindle Secondary Interneurons (Group II)

The tonic stretch reflex and perhaps some of the knee-jerk reflex may be generated by disynaptic excitation arising from Group II muscle afferents. These same interneurons also receive input from Flexor Reflex Afferents (see below). It has been

proposed that these Group II interneurons and others resulting in disynaptic inhibition contribute to voluntary behaviors (Lundberg et al. 1987), but there is little direct evidence as yet.

Flexor Reflex Afferents

Nociceptive cutaneous afferents (Group III = A δ fibers, Group IV = C fibers) give rise to the flexion reflex, consisting of coordinated activation of ipsilateral limb flexors and often accompanied by contralateral limb extension (Anden et al. 1964; Duysens et al. 2013). It is prominent during locomotion, enabling the limb to withdraw from an obstructive or aversive stimulus to get around an obstacle. Specific models of these oligosynaptic circuits are not available.

Commissural Interneurons

Interneurons that project across the midline appear to be useful for interlimb coordination during locomotion (Jankowska 2008). Specific circuit models are not available and their role in learned motor behaviors is unknown.

Central Pattern Generators (CPG)

As discussed elsewhere (McCrea and Rybak 2008), the spinal cord contains reciprocally inhibited groups of interneurons that function as self-sustaining oscillators for cyclical behaviors such as locomotion. Their relatively simple, alternating rhythms are converted into the more subtly phased activation of individual muscles by the interneuronal circuits listed above and perhaps unknown others. Their rhythms can be altered or even reset by somatosensory feedback and descending control. It is unknown whether these CPG circuits are utilized for learned motor behaviors that have similar oscillatory patterns.

Decision and Command Versus Coordination and Regulation

The general notion is that the brain is strategic, deciding what voluntary movement should be executed and when, while the spinal cord is tactical, dealing with the details of apportioning the physical work among various muscles and making reflexive adjustments to cope with local conditions. Most of the theories described below

were motivated by the desire to simplify these problems, both so that the process could be understood by researchers and so that the brain could actually solve them. Nevertheless, from the relatively slow rate at which infants develop motor coordination, it is apparent that this is a very hard problem requiring a great deal of adaptive learning by the brain. Simple and intuitive theories may not be consistent with reality.

Fusimotor Servo Control

If the brain plans movements according to the desired trajectory of limb postures, then there has to be a computation to convert that plan into the net drive to each of the muscles required to stay on that trajectory. The complex mechanical dynamics of a multiarticulate limb plus the highly nonlinear force-generating properties of muscle make such a calculation difficult, to say the least. Servo control offers a way out of this dilemma. Muscle activation could be commanded (or at least assisted) by first activating fusimotor neurons, thereby turning on muscle spindle afferents, and then allowing the excitatory reflexes from those afferents to turn on the motoneurons until the muscle shortened to the point where the fusimotor effects were negated (Merton 1953).

These ideas have fallen out of favor for two reasons. One is the lack of evidence for sufficiently high gains in these pathways or for fusimotor drive and spindle afferent activity that clearly leads the alpha motoneuron activity. The second is the recognition that the spindle afferents are responsible for much of the senses of posture and kinesthesia (Scott and Loeb 1994), which must be independent of muscle activation. It seems more likely that the fusimotor system is used to optimize the sensitivity of the spindle afferents to the expected range of voluntary movements, thereby improving rather than degrading these critical senses (Loeb and Marks 1985).

Reciprocal and Equilibrium Control

Another way to solve the above-stated problem of getting a complex musculoskeletal system into the desired posture is to take advantage of the springlike properties of mutually antagonistic

sets of muscles at each joint. Active muscles themselves tend to behave like springs, increasing their force output when stretched and decreasing it when shortened. Simply coactivating mutually antagonistic muscles at different levels necessarily results in various postures (Bizzi et al. 1993); perturbations away from those postures are automatically resisted by the effective mechanical impedance of the system (which includes springlike terms related to joint angle plus terms related to joint velocity and acceleration (Hogan 1984)). The ability of such a control system to follow dynamic trajectories can be greatly enhanced by including the reciprocal reflexes mediated by spindle afferents, and they can be more subtly modulated by further including fusimotor control. This is the so-called gamma equilibrium-point hypothesis (Feldman 1966; Feldman et al. 1998). A more general model of how the brain could utilize the reciprocally organized spindle feedback was presented by Maier et al. (2005).

While these muscle properties and reflexes certainly affect the properties of the system that the brain must control, they do not by themselves seem to account well for many observed behaviors (Kistemaker et al. 2007). Equilibrium control predicts more inefficient and undesirable cocontraction of muscles than is generally observed. It has difficulty with highly dynamic movements or when the goal is to control force on an object or surface rather than position. Finally, it is difficult to extend these schemes to account for the many multiarticular muscles and for the intersegmental dynamics of limbs.

Inverse Dynamics Models

Presumably the brain generates the command signals to the spinal cord that will result in the desired limb trajectory. If the brain were sending signals directly to the motoneurons, it could learn an inverse model of the musculoskeletal mechanics and then employ an optimization scheme to compute an effective and efficient pattern of commands (Kawato 1999; Scott and Norman 2003). It would also have to monitor the sensory feedback and compute the necessary adjustments (Scott 2004), suppressing or taking into account

any reflexes that would be occurring simultaneously in the autonomous circuits of the spinal cord (and probably other lower centers). But the brain is largely sending signals to the spinal interneurons themselves. In order to compute those commands, the brain would require an inverse model that included also the connectivity of the interneurons plus a forward model of the sensory afferents that project to those interneurons. It is unclear how the brain could learn such a complex model.

Regulator Models

Rather than trying to assign specific roles to each individual reflex or circuit, it may be more productive to look at the emergent properties of the complete spinal cord network. One approach is to ask what sorts of connections between afferents and efferents would be useful for solving typical problems in motor control. Given certain constraints, it is possible to apply an engineering tool for designing a linear quadratic regulator (LQR), which is essentially a matrix of excitatory and inhibitory gains between all possible pairs of input and output signals. The solution minimizes a cost function that reflects both the deviations from the desired state of the system and the expense of efforts to correct such deviations. When such a matrix was computed for maintaining stable standing posture in the hindlimb of a cat, the patterns of connections bore a striking resemblance to the patterns of connectivity in the major known interneuronal circuits listed above (Loeb et al. 1990; He et al. 1991). The matrix computed for a different mechanical state such as when freely moving through space would be substantially different, similar to the changes in reflex gains known to occur for such state changes. The methods used by engineers to compute such LQRs are unlikely to be employed by the brain, but it is possible that they could be approximated by trial-and-error iteration over the lifetime of the animal.

While LQR analysis provides some insights into the general utility of the spinal cord for responding to perturbations, it does not provide a way to generate the desired states or trajectories in the first place. The general absence of direct

cortical drive to the alpha motoneurons and the targeting of that drive onto the interneurons that mediate the reflexes suggest that the brain must plan simultaneously both the nominal behavior and desirable responses to anticipated perturbations (Loeb et al. 1999). The difficulty of computing such plans from inverse models suggests that they must be learned and stored as lookup tables and then replayed whenever the brain is called on to perform a familiar or at least similar task. Given the very large number of different interneuronal drives and synaptic gains in the spinal circuitry, is it feasible for solutions to be learned by trial-and-error exploration of this huge hyperspace?

Reasonably complete models of the classical spinal circuits that employ proprioceptive feedback (for the first five spinal circuits above, see Figs. 2 and 3) were constructed for an idealized 2DOF, 4-muscle wrist model (Raphael et al. 2010) and for a 2DOF, 6-muscle planar elbow-shoulder system (Tsianos et al. 2011). In both cases, simple trial-and-error adjustment from initially random states of the spinal cord resulted in kinematically successful and energetically efficient performance of a wide range of typical behaviors (resisting perturbations, rapid reaching to precise postures, compensation for viscous curl-fields, generating precise end-point forces). Success was attributed to the large number of “good-enough” solutions offered by the spinal circuitry, which seems to have little tendency to become entrapped in poor local minima. Solutions to one task provided useful starting points to learn new tasks, and sparse sets of such sequentially learned tasks could be interpolated to achieve intermediate behaviors despite the nonlinearity of the underlying neuromusculoskeletal system Tsianos et al. (in press). Somewhat disconcertingly, this implies that the internal representations of and strategies for a given motor behavior may differ substantially among individuals. That would be consistent with the differences that emerge when physically “normal” individuals try to learn a new and unusual sport, but it makes it difficult to design and interpret experiments that usually require pooling data from many individuals.

Conclusions

The role of the spinal cord in learned sensorimotor behaviors remains contentious and may be shifting as animals evolve toward a wider repertoire of learned rather than instinctive behaviors. The propriospinal interneurons provide a case in point. In cats, these interneurons and their contribution to reaching movements are relatively easily demonstrated. In nonhuman primates, they are difficult to excite and, therefore, to find at all in anesthetized preparations (Alstermark et al. 2007). One possibility is that the resting bias of the spinal interneurons and perhaps other subcortical circuits may become hyperpolarized to suppress their reflexive responses until the cortex decides what combination of those reflexes will generate a more reasoned response. Another possibility is that the cortical systems that presumably subserve learned behaviors may simply overwhelm the other inputs to the spinal circuitry to take fairly direct control of the musculature, including the responses to perturbations (Kurtzer et al. 2008). Ignoring the phylogenetically old but sophisticated coordination provided by spinal interneurons might make sense if the brain needs to develop an internal model of the plant in order to compute motor programs de novo. Conversely, these circuits may be very useful if the brain must learn, store, and recall its repertoire without such online computation. Newly evolved musculoskeletal systems and functions such as dexterous manipulation of objects and vocalized speech may have no choice but to rely on newly evolved direct corticomotoneuronal projections, whether they are computing or recalling motor programs, but even these undergo substantial modulation by spinal circuits (Petersen et al. 2010).

Nevertheless, it is worth remembering that the first problem faced by a newborn brain is system identification. It does not “know” that the external world and its own body exist, much less what effects its various output axons will have on that body. In the process of self-organizing that knowledge, the brain will discover and learn to cope with whatever musculoskeletal apparatus and local neural circuitry exist. Learning a new task must inevitably involve decisions about

which components of the apparatus and the circuitry appear to be useful and which need to be ignored or suppressed. The challenge to the developing organism is to learn those tasks as quickly as possible, not to conform to abstract theories of how those tasks might be learned or performed.

References

- Alstermark B, Isa T, Pettersson LG, Sasaki S (2007) The C3–C4 propriospinal system in the cat and monkey: a spinal pre-motoneuronal centre for voluntary motor control. *Acta Physiol* 189:123–140
- Anden NE, Jukes MG, Lundberg A, Vyklicky L (1964) A new spinal flexor reflex. *Nature* 202:1344–1345
- Baudry S, Maerz AH, Enoka RM (2010) Presynaptic modulation of Ia afferents in young and old adults when performing force and position control. *J Neurophysiol* 103:623–631
- Bell SC (1811) Idea of a new anatomy of the brain: submitted for the observations of his friends. Strahan and Preston, London
- Bizzi E, Hogan N, Mussa-Ivaldi F, Giszter S (1993) Does the nervous system use equilibrium-point control to guide single and multiple joint movements? *Behav Brain Sci* 15:603–613
- Burke RE (1999) The use of state-dependent modulation of spinal reflexes as a tool to investigate the organization of spinal interneurons. *Exp Brain Res* 128:263–277
- Duyse J, De Groote F, Jonkers I (2013) The flexion synergy, mother of all synergies and father of new models of gait. *Front Comput Neurosci* 7, doi:10.3389/fncom.2013.00014
- Eccles RM, Lundberg A (1958) Integrative pattern of Ia synaptic actions on motoneurones of hip and knee muscles. *J Physiol* 144:271–298
- Eccles JC, Eccles RM, Lundberg A (1957a) The convergence of monosynaptic excitatory afferents on to many different species of alpha motoneurons. *J Physiol* 137:22–50
- Eccles JC, Eccles RM, Lundberg A (1957b) Synaptic actions on motoneurons caused by impulses in Golgi tendon organ afferents. *J Physiol* 138:227–253
- Feldman AG (1966) Functional tuning of the nervous system with control of movement or maintenance of a steady posture. II. Controllable parameters of the muscles. *Biophys J* 11:565–578
- Feldman AG, Ostry DJ, Levin MF, Gribble PL, Mitnitski AB (1998) Recent tests of the equilibrium-point hypothesis (lambda model). *Motor Control* 2:26–42
- Gandevia SC (1996) Kinesthesia: roles for afferent signals and motor commands. In: Rowell LB, Shepherd JT (eds) *Handbook of physiology*, Section 12. Oxford University Press, London, pp 128–172
- He J, Levine WS, Loeb GE (1991) Feedback gains for correcting small perturbations to standing posture. *IEEE Trans Autom Control* 36:322–332
- Hogan N (1984) An organising principle for a class of voluntary movements. *J Neurosci* 4:2745–2754
- Houk JC (1979) Regulation of stiffness by skeleto-motor reflexes. *Annu Rev Physiol* 41:99–114
- Jankowska E (2008) Spinal interneuronal networks in the cat: elementary components. *Brain Res Rev* 57:46–55
- Jankowska E, Lundberg A, Stuart D (1973) Propriospinal control of last order interneurones of spinal reflex pathways in the cat. *Brain Res* 53:227–231
- Johansson RS, Flanagan JR (2009) Coding and use of tactile signals from the fingertips in object manipulation tasks. *Nat Rev Neurosci* 10:345–359
- Kawato M (1999) Internal models for motor control and trajectory planning. *Curr Opin Neurobiol* 9:718–727
- Kistemaker DA, Van Soest AJ, Bobbitt MF (2007) Equilibrium point control cannot be refuted by experimental reconstruction of equilibrium point trajectories. *J Neurophysiol* 98:1075–1082
- Kurtzer IL, Pruszynski JA, Scott SH (2008) Long-latency reflexes of the human arm reflect an internal model of limb dynamics. *Curr Biol* 18:449–453
- Loeb GE (1984) The control and responses of mammalian muscle spindles during normally executed motor tasks. *Exerc Sport Sci Rev* 12:157–204
- Loeb GE, Marks WB (1985) Optimal control principles for sensory transducers. In: Boyd IA, Gladden MH (eds) *Proceedings of the international symposium: the muscle spindle*. MacMillan, London, pp 409–415
- Loeb GE, Levine WS, He J (1990) Understanding sensorimotor feedback through optimal control. *Cold Spring Harbor Symp Quant Biol* 55:791–803
- Loeb GE, Brown IE, Cheng EJ (1999) A hierarchical foundation for models of sensorimotor control. *Exp Brain Res* 126:1–18
- Lundberg A (1992) To what extent are brain commands for movements mediated by spinal interneurons? *Behav Brain Sci* 15:775–776
- Lundberg A, Malmgren K, Schomburg ED (1987) Reflex pathways from group II muscle afferents. 3. Secondary spindle afferents and the FRA: a new hypothesis. *Exp Brain Res* 65:294–306
- Magendie F (1822) Experiences sur les fonctions des racines des nerfs rachidiens. *J Physiol Exp* 2:276–279
- Maier MA, Shupe LE, Fetz EE (2005) Dynamic neural network models of the premotoneuronal circuitry controlling wrist movements in primates. *J Comput Neurosci* 19:125–146
- Martin PG, Smith JL, Butler JE, Gandevia SC, Taylor JL (2006) Fatigue-sensitive afferents inhibit extensor but not flexor motoneurons in humans. *J Neurosci* 26:4796–4802
- McCrea DA (1986) Spinal cord circuitry and motor reflexes. *Exerc Sport Sci Rev* 14:105–141
- McCrea DA, Rybak IA (2008) Organization of mammalian locomotor rhythm and pattern generation. *Brain Res Rev* 57:134–146

- Merton PA (1953) Speculations on the servo-control of movement. In: Wolstenholme GEW (ed) *The spinal cord*. Churchill, London, pp 247–255
- Meunier S, Pierrot-Deseilligny E (1998) Cortical control of presynaptic inhibition of Ia afferents in humans. *Exp Brain Res* 119:415–426
- Mileusnic MP, Loeb GE (2009) Force estimation from ensembles of Golgi tendon organs. *J Neural Eng* 6:1–15
- Perlmutter SI, Maier MA, Fetz EE (1998) Activity of spinal interneurons and their effects on forearm muscles during voluntary wrist movements in the monkey. *J Neurophysiol* 80:2475–2494
- Petersen NC, Butler JE, Taylor JL, Gandevia SC (2010) Probing the corticospinal link between the motor cortex and motoneurones: some neglected aspects of human motor cortical function. *Acta Physiol* 198:403–416
- Pierrot-Deseilligny E, Burke DC (2005) *The circuitry of the human spinal cord: its role in motor control and movement disorders (vol Illustrated)*. Cambridge University Press, Cambridge, UK
- Raphael G, Tsianos GA, Loeb GE (2010) Spinal-like regulator facilitates control of a two-degree-of-freedom wrist. *J Neurosci* 30:9431–9444
- Rathelot JA, Strick PL (2009) Subdivisions of primary motor cortex based on cortico-motoneuronal cells. *Proc Natl Acad Sci U S A* 106:918–923
- Richmond FJ, Loeb GE (1992) Electromyographic studies of neck muscles in the intact cat. II. Reflexes evoked by muscle nerve stimulation. *Exp Brain Res* 88:59–66
- Rudomin P, Schmidt RF (1999) Presynaptic inhibition in the vertebrate spinal cord revisited. *Exp Brain Res* 129:1–37
- Scott SH (2004) Optimal feedback control and the neural basis of volitional motor control. *Nat Rev Neurosci* 5:532–546
- Scott SH, Loeb GE (1994) The computation of position sense from spindles in mono-and multiarticular muscles. *J Neurosci* 14:7529–7540
- Scott SH, Norman KE (2003) Computational approaches to motor control and their potential role for interpreting motor dysfunction. *Curr Opin Neurol* 16:693–698
- Sherrington CS (1908) On reciprocal innervation of antagonistic muscles. Eleventh note. Further observations on successive induction. *Proc R Soc Lond Ser B Biol Sci* 80:53–71
- Sherrington CS (1910) Flexion-reflex of the limb, crossed extension-reflex and reflex stepping and standing. *J Physiol* 40:28–121
- Spanne A, Jörntell H (2013) Processing of multidimensional sensorimotor information in the spinal and cerebellar neuronal circuitry: a new hypothesis. *PLoS Comp Biol* 9:e1002979
- Tsianos GA, Raphael G, Loeb GE (2011) Modeling the potentiality of spinal-like circuitry for stabilization of a planar arm system. *Prog Brain Res* 194:203–213
- Tsianos GA, Goodner J, Loeb GE (in press) Useful Properties of Spinal Circuits for Learning and Performing Planar Reaches. *J Neural Engineering* (in press)
- Windhorst U (1990) Activation of renshaw cells. *Prog Neurobiol* 35:135–179
- Wolpaw JR (2010) What can the spinal cord teach us about learning and memory? *Neuroscientist* 16: 532–549
- Zajac FE, Gordon ME (1989) Determining muscle's force and action in multi-articular movement. *Exerc Sport Sci Rev* 17:187–230

Spinal Electrical Stimulation

► Epidural Stimulation

Spinal Electromagnetic Stimulation

► Paraspinal Magnetic and Transcutaneous Electrical Stimulation

Spinal Locomotor Network

► Locomotor Pattern Generation in the Rodent Spinal Cord

Spinal Neuromagnetic Stimulation

► Paraspinal Magnetic and Transcutaneous Electrical Stimulation

Spinal Root Stimulation

► Paraspinal Magnetic and Transcutaneous Electrical Stimulation

Spinal Stimulation for Parkinson Treatment

Romulo Fuentes

Edmond and Lily Safra International Neuroscience Institute, Natal, Brazil

Synonyms

Dorsal column stimulation; Epidural stimulation; Spinal cord stimulation

Definition

Spinal stimulation for Parkinson treatment is a neuromodulation procedure proposed as therapy for alleviating the motor symptoms of Parkinson's disease. It requires the epidural implant of bipolar electrodes in the dorsal portion of the spinal cord to deliver electrical pulses at specific frequencies.

Detailed Description

Spinal cord stimulation is a technique used for treating chronic pain conditions which are refractory to pharmacological therapies. In 2009 it was proposed that spinal cord stimulation could be used for treating the motor symptoms of Parkinson's disease (PD). PD is characterized by a lack of dopamine due to the death of the dopaminergic neurons of the substantia nigra. It interferes with the normal functioning of the corticobasal ganglia causing the classical symptoms of hypokinesia and rigidity, that is, slow movements and stiffness of the joints.

Patients and animal models of PD exhibit characteristic low-frequency, high-amplitude synchronic neural activity at the corticobasal ganglia loop. The rationale behind using spinal cord stimulation for PD was that high-frequency stimulation of spinal sensory afferents will convey to the supraspinal structures a signal capable of disrupting the low-frequency pathological

rhythms, thus restoring normal functioning of the circuit.

The first experiments showed that dopamine-depleted mice showing strong akinesia would have their locomotion capability restored when receiving spinal cord stimulation. Further, rats with bilateral striatal 6-OHDA lesions, another model of PD, would exhibit the same effect. Electrophysiological recording in the mice showed that spinal cord stimulation caused dramatic changes in the synchrony pattern of the striatum and primary motor cortex, decreasing the low-frequency synchronization (<25 Hz) and increasing the synchronization at higher frequencies (>30 Hz).

The first report of spinal cord stimulation used in two PD patients failed to show any alleviation of motor symptoms. Four additional reports from different clinical groups over the world show that spinal cord stimulation used in PD patients who also suffer chronic pain, primary or secondary to PD, will experience significant improvement of motor symptoms related to gait, locomotion speed, and posture.

Further Reading

- Agari T, Date I (2012) Spinal cord stimulation for the treatment of abnormal posture and gait disorder in patients with Parkinson's disease. *Neurol Med Chir* 52:470–474
- Fénelon G, Goujon C, Gurruchaga J-M, Cesaro P, Jarraya B, Palfi S, Lefaucheur J-P (2011) Spinal cord stimulation for chronic pain improved motor function in a patient with Parkinson's disease. *Parkinsonism Relat Disord* 18:1–2
- Fuentes R, Petersson P, Siesser WB, Caron MG, Nicolelis MAL (2009) Spinal cord stimulation restores locomotion in animal models of Parkinson's disease. *Science* 323(5921):1578–1582
- Fuentes R, Petersson P, Nicolelis MAL (2010) Restoration of locomotive function in Parkinson's disease by spinal cord stimulation: mechanistic approach. *Eur J Neurosci* 32(7):1100–1108
- Hassan S, Amer S, Alwaki AR, Elborno A (2013) A patient with Parkinson's disease benefits from spinal cord stimulation. *J Clin Neurosci* 20:1155–1156
- Landi A, Trezza A, Pirillo D, Vimercati A, Antonini A, Sganzerla EP (2012) Spinal cord stimulation for the treatment of sensory symptoms in advanced Parkinson's disease. *Neuromodul J Int Neuromodul Soc* 2012:276–279

Thevathasan W, Mazzone P, Jha A, Djamshidian A, Dileone M, Di Lazzaro V, Brown P (2010) Spinal cord stimulation failed to relieve akinesia or restore locomotion in Parkinson disease. *Neurology* 74(16):1325–1327

Spindle Oscillations: Models

Alain Destexhe

Unit of Neuroscience Information and Complexity (UNIC), Centre National de la Recherche Scientifique (CNRS), Gif-sur-Yvette, France

Definition

Sleep spindles appear during the early phases of sleep in all mammals. These 7–14 Hz oscillations are generated by the thalamus, but their triggering and large-scale synchrony depends on the cerebral cortex and thalamocortical interactions. Computational models have been designed to study how these oscillations are generated, what type of intrinsic currents and synaptic receptors are implicated, and how their synchrony is organized in the thalamocortical system.

Detailed Description

Introduction

The mammalian brain generates various types of slow oscillations during slow-wave sleep, such as spindle waves, delta oscillations, and slower oscillations (Steriade 2003). Spindle oscillations, which are mostly visible in the early stages of sleep (stage II in humans), are the best studied sleep oscillation because it is present in all mammals during sleep or anesthesia. Spindles are generated by thalamic circuits under physiological conditions, in contrast to delta and slow oscillations, for which cortical generators also exist. We focus here on sleep spindles, their genesis by thalamic networks, how these oscillations are distributed across the entire thalamocortical system.

Thalamic Pacemakers for Spindle Oscillations

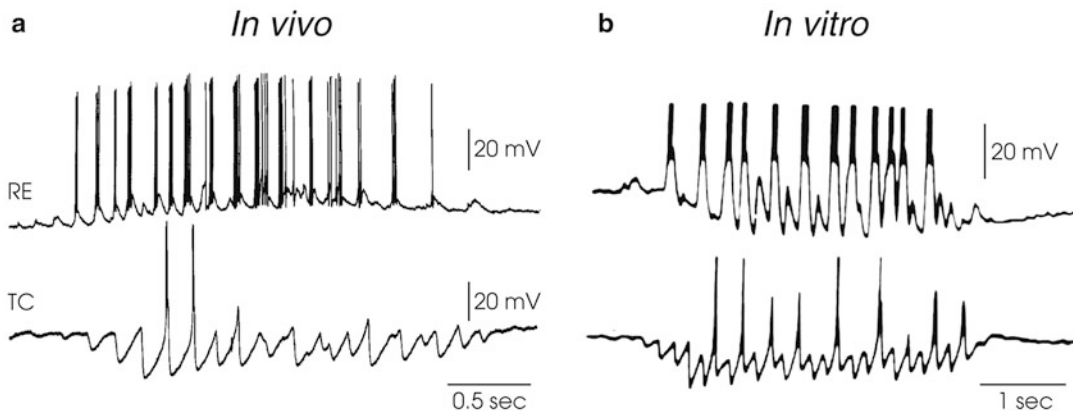
Spindles are visible in the electroencephalogram (EEG), in which they consist of short 1–3 s

periods of 7–14 Hz oscillations, organized within a waxing-and-waning envelope, that recur periodically every 10–20 s. In cats and rodents, spindle waves of similar characteristics appear during slow-wave sleep and are typically more prominent at sleep onset. They are enhanced by some anesthetics, such as barbiturates, which, when administered at an appropriate dose, generate an EEG dominated by spindles.

The first indication that spindles could originate outside the cerebral cortex was from Bishop in 1936, who showed that rhythmical activity was suppressed in the cerebral cortex following destruction of its connections with the thalamus. In 1938, Bremer showed that rhythmical activity is still present in the white matter following destruction of the cortical mantle. Later, Adrian in 1941, and Morison and Bassett in 1945, observed that spindle oscillations persist in the thalamus upon removal of the cortex, providing firm experimental evidence that these oscillations originate in the thalamus. These experiments led to the development of the “thalamic pacemaker” hypothesis (Steriade and Deschênes 1984), according to which rhythmic activity is generated in the thalamus and communicated to the cortex, where it entrains cortical neurons and is responsible for the rhythmical activity observed in the EEG. The more recent discovery of spontaneously occurring spindles in ferret thalamic slices (von Krosigk et al. 1993) confirmed the thalamic pacemaker hypothesis. Furthermore, this *in vitro* model of spindle waves has made it possible to precisely characterize the ionic mechanisms and synaptic receptors involved in spindle oscillations.

Cellular Mechanisms of Spindle Oscillations

The first cellular mechanism to explain the genesis of spindle oscillations was proposed by Andersen and Eccles in 1962. From intracellular recordings from thalamocortical (TC) relay neurons during spindles, they reported that TC cells fired bursts of action potentials interleaved with inhibitory postsynaptic potentials (IPSPs). They suggested that TC cells fire in response to IPSPs (post-inhibitory rebound), which was later demonstrated to be a characteristic



Spindle Oscillations: Models, Fig. 1 Spindle oscillations in thalamic circuits. (a) *In vivo* intracellular experiments realized in cats under barbiturate anesthesia, showing the activity of thalamocortical (TC) and thalamic reticular (RE) cells during spindle waves (modified from

Steriade and Deschênes 1984). (b) *In vitro* intracellular experiments realized in ferret visual thalamic slices, showing the activity of the same type of thalamic neurons during spindle waves (modified from von Krosigk et al. 1993)

electrophysiological feature of thalamic cells by Jahnsen and Llinas. Andersen and Eccles suggested that the oscillations arose from the reciprocal interactions between TC cells and inhibitory local-circuit interneurons. This mechanism was later incorporated into a computational model that included a phenomenological description of the inhibitory rebound.

The mechanism proposed by Andersen and Eccles was seminal but was not entirely correct because reciprocal connections between TC cells and thalamic interneurons have never been observed in anatomical studies. It was later found by Scheibel and Scheibel (1966a, b, 1967) that the thalamic reticular (RE) nucleus, a sheetlike structure of inhibitory neurons surrounding the thalamus, could provide the inhibition of TC cells and that “TC-RE” loops could underlie recruitment phenomena and spindle oscillations. They predicted that the output of the RE nucleus should be inhibitory and that the inhibitory feedback from RE cells onto TC cells should be critical for the genesis of thalamic rhythmicity. This hypothesis was supported by the observation that the pattern of firing of RE neurons was tightly correlated with IPSPs in TC neurons.

The involvement of the thalamic RE nucleus in the generation of spindles was firmly

established by a series of critical experiments by the group of Steriade in cats *in vivo*. The typical intracellular features of spindle oscillations in the two thalamic cell types are shown in Fig. 1a. By using intracellular or extracellular experiments, Steriade and collaborators have shown that, first, cortically projecting thalamic nuclei lose their ability to generate spindle oscillations if deprived of input from the RE nucleus (Steriade et al. 1985). Second, the isolated RE nucleus can itself generate rhythmicity in the spindle frequency range (Steriade et al. 1987).

Thus, three different mechanisms were proposed to explain thalamic rhythmicity: the “TC-interneuron” loops of Andersen and Eccles, the “TC-RE” loops of Scheibel and Scheibel, and the “RE pacemaker” hypothesis of Steriade (although Steriade’s work also demonstrated the importance of the cortex – see next section). The introduction of an *in vitro* model of spindle waves in young ferrets by McCormick’s group (Fig. 1b; von Krosigk et al. 1993) supported the second of these mechanisms. Slices of the visual thalamus that contain the dorsal (lateral geniculate nucleus or LGN) and reticular nuclei (perigeniculate nucleus or PGN), as well as the interconnections between them, generated spindles spontaneously, confirming earlier experimental evidence for the genesis of spindles in the thalamus.

The great advantage of the *in vitro* preparation is that it allowed a detailed pharmacological investigation of the ionic currents and synaptic receptors underlying the spindle oscillations. The spindle waves disappeared after the connections between TC and RE cells were severed, consistent with the mechanism based on intrathalamic TC-RE loops proposed by Scheibel and Scheibel. This *in vitro* experiment also confirmed the observation that the input from RE neurons is necessary to generate spindles (Steriade et al. 1985). However, the RE nucleus maintained *in vitro* did not generate oscillations without connections from TC cells, in contrast with the observation of spindle rhythmicity in the isolated RE nucleus *in vivo* (Steriade et al. 1987).

Thus, *in vitro* experiments appear to support a mechanism by which oscillations are generated by the TC-RE loop, in contrast with the “RE pacemaker” hypothesis. Computational models are needed to investigate which of these mechanisms are plausible biophysically, as shown in the next section.

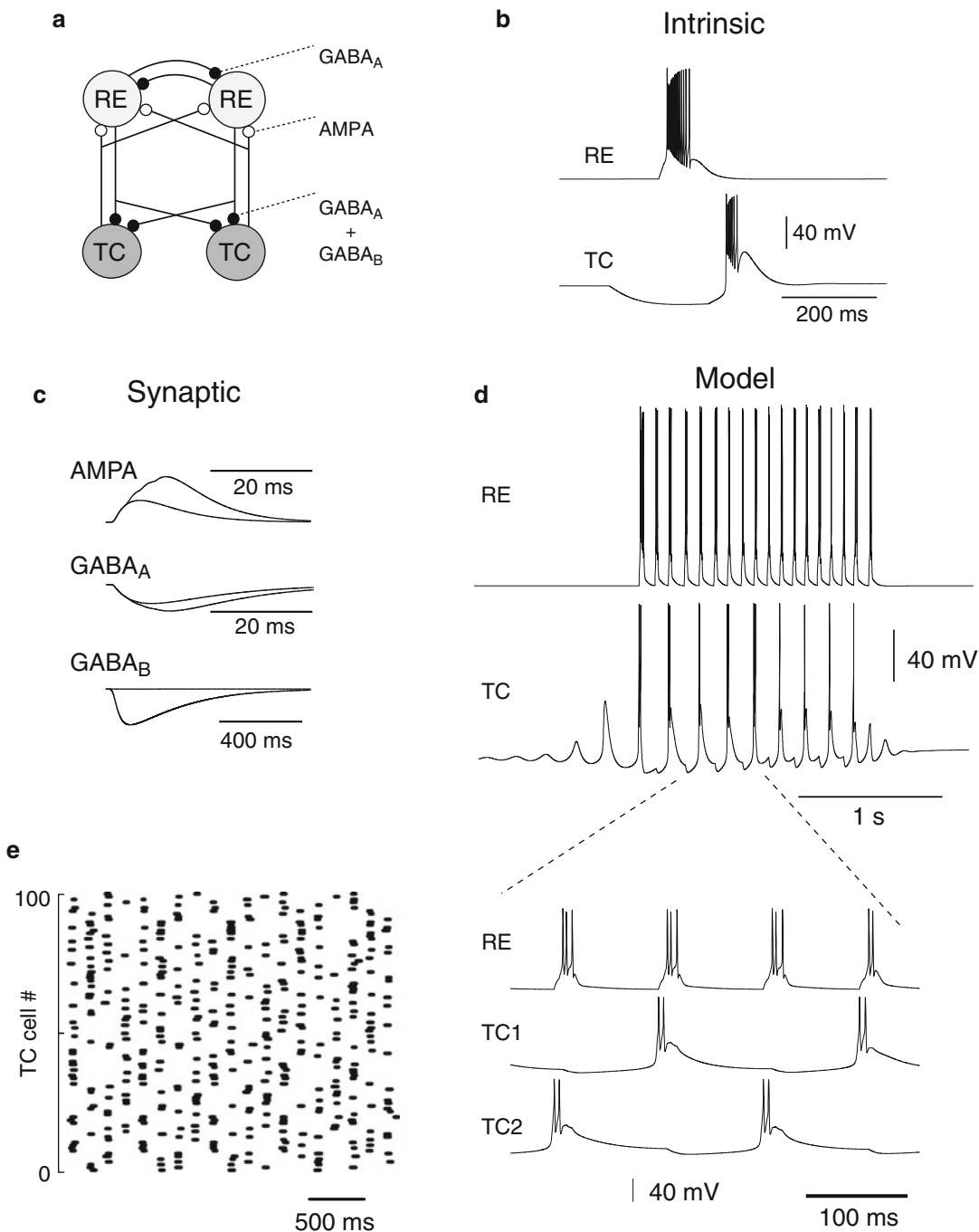
Models of Spindle Oscillations

Computational models investigated different cellular mechanisms of spindle oscillations, to attempt clarifying these contrasting experimental results. First, models investigated whether the RE nucleus is capable of displaying oscillations consistent with experiments. Models found that RE neurons interacting through GABAergic synapses can generate spindle rhythmicity (Wang and Rinzel 1993; Destexhe et al. 1994a; Bazhenov et al. 1999; reviewed in Destexhe and Sejnowski 2001, 2003) and proposed different mechanisms. GABAergic interactions between RE neurons can make them oscillate synchronously through mutual inhibitory-rebound interactions, either with slow GABAergic synapses (Wang and Rinzel 1993) or with fast (GABA_A receptor mediated) GABAergic synapses with extended connectivity (Destexhe et al. 1994a). Synchronized oscillations can also be generated from RE neurons connected with depolarizing GABAergic synapses (Bazhenov et al. 1999). The presence of gap junctions in the reticular nucleus (Landisman et al. 2002) was also incorporated

in models (Fuentealba et al. 2004) and reinforced its propensity to oscillate in the spindle frequency range. Thus, models suggest that the intrinsic properties of thalamic RE neurons, combined with their synaptic or electrical interactions, support the RE pacemaker hypothesis.

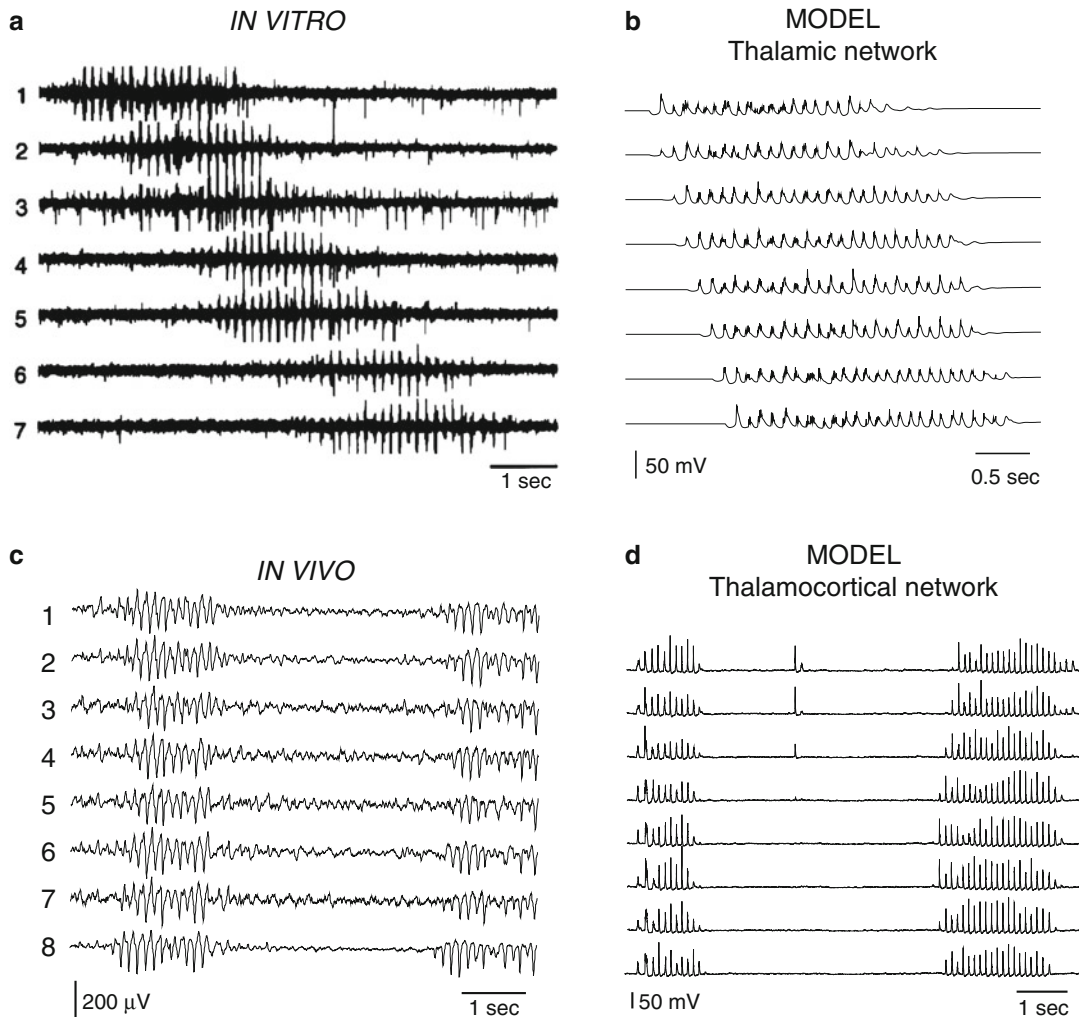
Second, models also investigated the TC-RE loop hypothesis for spindle generation (Destexhe et al. 1996; Golomb et al. 1996). This TC-RE loop model is shown in Fig. 2d. Neurons were modeled using Hodgkin-Huxley (1952)-type representations of Na^+ , K^+ , and Ca^{2+} voltage-dependent currents, which were based on voltage-clamp data on thalamic neurons (see details in Destexhe et al. 1996). These models reproduced the most salient intrinsic properties of thalamic neurons, such as the production of bursts of action potentials (Fig. 2b). Synaptic interactions were modeled using conductance-based kinetic models (► **Kinetic Models of Postsynaptic Currents**) which were used to simulate the main receptor types (AMPA , GABA_A , and GABA_B) identified in thalamic circuits (Fig. 2b, right). Under these conditions, the circuit generated 7–14 Hz spindle oscillations with the typical features identified intracellularly in the different thalamic neuron types. The model reproduced the typical mirror image between TC and RE cells during spindles, as well as the phase relations between cells (see Fig. 2d). In particular, TC cells produced bursts once every 2–3 cycles, a feature consistently observed experimentally (compare with Fig. 2c). More irregular behavior, similar to the experiments, was obtained in larger networks (Fig. 2e) or in the presence of the cortex (see below). The oscillations also showed the typical waxing-and-waning envelope of spindles; this property was due in the model to Ca^{2+} -mediated slow regulation of the I_h current (Destexhe et al. 1993), a prediction that was later verified experimentally (Lüthi and McCormick 1998).

Thus, models show that taking into account the complex bursting properties of thalamic neurons, combined with their interactions through well-defined types of synaptic receptors, can account for both RE pacemaker oscillations and spindle oscillations arising from TC-RE loops



Spindle Oscillations: Models, Fig. 2 Modeling the interactions between intrinsic and synaptic properties to generate spindle oscillations. (a) Circuit of interconnected thalamocortical (TC) and thalamic reticular (RE) neurons with different receptor types. (b) Models of the intrinsic properties of thalamic neurons. (c) Models of the synaptic receptor types mediating their interactions.

(d) Computational model of spindle oscillations in circuits of interconnected TC and RE cells. The expanded trace below shows the phase relations of the two cell types. (e) Phase relations of TC cells during spindle oscillations in a different computational model (a, b, c, d from Destexhe et al. 1996; e From Wang et al. 1995)



Spindle Oscillations: Models, Fig. 3 Control of spindle oscillations by the cerebral cortex. (a) Multisite extracellular recordings *in vitro* showing the propagating activity of spindle waves in the visual thalamic slice (modified from Kim et al. 1995). (b) Model of propagating spindle wave activity in thalamic networks with topographic connectivity (modified from Destexhe

et al. 1996). (c) Multisite extracellular recordings in the thalamus of cats *in vivo* showing the large-scale synchrony of spindle waves in the intact thalamocortical system (modified from Contreras et al. 1996). (d) Large-scale synchrony obtained in a thalamocortical model (modified from Destexhe et al. 1998)

without assuming pacemaker activity in the RE nucleus. How to resolve such an apparent inconsistency? This question was addressed by a computational model of the RE nucleus which took into account the action of neuromodulators (such as noradrenaline) in depolarizing RE cells. This model produced oscillations only when a sufficient level of neuromodulator was present (Destexhe et al. 1994b). The difference between *in vivo* and *in vitro* preparations may therefore be

explained by the limited connectivity between the RE neurons in the slice and/or by the fact that slices lack the necessary level of neuromodulation to maintain isolated RE oscillations (Destexhe et al. 1994b). The main prediction from this model is that applying neuromodulators to slices of the RE nucleus should induce oscillations similar to those observed *in vivo*. This prediction still awaits to be tested.

Dialogue Between the Thalamus and Cortex: Emergence of Large-Scale Synchrony

The large-scale properties of initiation and distribution of spindle oscillations were investigated more recently by using multiple recordings *in vivo* and *in vitro* (Fig. 3a, c). Spindle oscillations *in vitro* show traveling wave patterns, with the oscillation typically starting on one side of the slice and propagating to the other side, at a constant propagation velocity (Fig. 3a). In contrast to thalamic slices, the intact thalamocortical system *in vivo* does not display such clear-cut propagation, but spindle oscillations are remarkably synchronized over extended thalamic regions and show very limited traveling wave activity (Fig. 3c), in agreement with early observations. Moreover, a study by Contreras et al. in 1996 showed that large-scale synchrony was lost when the cortex was removed, suggesting that although the oscillation is generated by the thalamus, its synchrony depends on the cortex. However, cutting intracortical connections has no effect on large-scale synchrony, so cortical connections are not responsible for organizing the synchrony of sleep spindles.

Computational models were designed to explore mechanisms to explain the large-scale synchrony of sleep spindles, as shown in detail in another chapter (“► [Corticothalamic Feedback: Large-Scale Synchrony](#)”). Models first simulated the propagating properties found in slices (Fig. 3b). These models assumed a topographic connectivity between TC and RE layers and could generate traveling spindle waves consistent with *in vitro* data. Second, a thalamocortical model (Destexhe et al. 1998) simulated large networks with bidirectional interactions between cortex and thalamic layers and showed that all experiments could be reproduced under one assumption: that the cortex recruited TC cells primarily through inhibition. This “inhibitory dominant” cortical feedback to the thalamus is consistently observed experimentally and can explain large-scale synchrony by mutual recruitment of thalamic and cortical networks (Fig. 3d). The same mechanism can also explain the genesis of absence type of epileptic seizures when the excitability of cortical neurons is too

high. These points were developed in more detail in another chapter (“► [Slow Oscillations and Epilepsy: Network Models](#)”). The concept of cortical control of thalamic spindle oscillations can be generalized to other oscillation types, and it was proposed by Steriade that the slow oscillation organizes spindle, delta oscillations and more complex patterns such as K-complexes (Steriade 2003).

Cross-References

- [Corticothalamic Feedback: Large-Scale Synchrony](#)
- [Kinetic Models of Postsynaptic Currents](#)
- [Slow Oscillations and Epilepsy: Network Models](#)

References

- Adrian ED (1941) Afferent discharges to the cerebral cortex from peripheral sense organs. *J Physiol* 100:159–191
- Andersen P, Eccles JC (1962) Inhibitory phasing of neuronal discharge. *Nature* 196:645–647
- Bazhenov M, Timofeev I, Steriade M, Sejnowski TJ (1999) Self-sustained rhythmic activity in the thalamic reticular nucleus mediated by depolarizing GABA_A receptor potentials. *Nature Neurosci* 2:168–174
- Bishop GH (1936) The interpretation of cortical potentials. *Cold Spring Harbor Symp Quant Biol* 4:305–319
- Bremer F (1938) Effets de la déafférentation complète d'une région de l'écorce cérébrale sur son activité électrique. *CR Soc Biol Paris* 127:355–359
- Contreras D, Destexhe A, Sejnowski TJ, Steriade M (1996) Control of spatiotemporal coherence of a thalamic oscillation by corticothalamic feedback. *Science* 274:771–774
- Destexhe A, Sejnowski TJ (2001) Thalamocortical assemblies. Oxford University Press, Oxford
- Destexhe A, Sejnowski TJ (2003) Interactions between membrane conductances underlying thalamocortical slow-wave oscillations. *Physiological Reviews* 83:1401–1453
- Destexhe A, Babloyantz A, Sejnowski TJ (1993) Ionic mechanisms for intrinsic slow oscillations in thalamic relay neurons. *Biophys J* 65:1538–1552
- Destexhe A, Bal T, McCormick DA, Sejnowski TJ (1996) Ionic mechanisms underlying synchronized oscillations and propagating waves in a model of ferret thalamic slices. *J Neurophysiol* 76:2049–2070

- Destexhe A, Contreras D, Sejnowski TJ, Steriade M (1994a) A model of spindle rhythmicity in the isolated thalamic reticular nucleus. *J Neurophysiol* 72:803–818
- Destexhe A, Contreras D, Sejnowski TJ, Steriade M (1994b) Modeling the control of reticular thalamic oscillations by neuromodulators. *Neuro Report* 5:2217–2220
- Destexhe A, Contreras D, Steriade M (1998) Mechanisms underlying the synchronizing action of corticothalamic feedback through inhibition of thalamic relay cells. *J Neurophysiol* 79:999–1016
- Fuentelba P, Crochet S, Timofeev I, Bazhenov M, Sejnowski TJ, Steriade M (2004) Experimental evidence and modeling studies support a synchronizing role for electrical coupling in the cat thalamic reticular nucleus *in vivo*. *Eur J Neurosci* 20:111–119
- Golomb D, Wang XJ, Rinzel J (1996) Propagation of spindle waves in a thalamic slice model. *J Neurophysiol* 75:750–769
- Hodgkin AL, Huxley AF (1952) A quantitative description of membrane current and its application to conduction and excitation in nerve. *J Physiol* 117:500–544
- Kim U, Bal T, McCormick DA (1995) Spindle waves are propagating synchronized oscillations in the ferret LGNd *in vitro*. *J Neurophysiol* 74:1301–1323
- Landisman CE, Long MA, Beierlein M, Deans MR, Paul DL, Connors BW (2002) Electrical synapses in the thalamic reticular nucleus. *J Neurosci* 22:1002–1009
- Lüthi A, McCormick DA (1998) Periodicity of thalamic synchronized oscillations: the role of Ca^{2+} -mediated upregulation of I_h . *Neuron* 20:553–563
- Morison RS, Bassett DL (1945) Electrical activity of the thalamus and basal ganglia in decorticate cats. *J Neurophysiol* 8:309–314
- Scheibel ME, Scheibel AB (1966a) The organization of the nucleus reticularis thalami: a Golgi study. *Brain Res* 1:43–62
- Scheibel ME, Scheibel AB (1966b) Patterns of organization in specific and nonspecific thalamic fields. In: Purpura DP, Yahr M (eds) *The thalamus*. Columbia University Press, New York, pp 13–46
- Scheibel ME, Scheibel AB (1967) Structural organization of nonspecific thalamic nuclei and their projection toward cortex. *Brain Res* 6:60–94
- Steriade M (2003) Neuronal substrates of sleep and epilepsy. Cambridge University Press, Cambridge, UK
- Steriade M, Deschênes M (1984) The thalamus as a neuronal oscillator. *Brain Res Reviews* 8:1–63
- Steriade M, Deschênes M, Domich L, Mulle C (1985) Abolition of spindle oscillations in thalamic neurons disconnected from nucleus reticularis thalami. *J Neurophysiol* 54:1473–1497
- Steriade M, Domich L, Oakson G, Deschênes M (1987) The deafferented reticular thalamic nucleus generates spindle rhythmicity. *J Neurophysiol* 57:260–273
- von Krosigk M, Bal T, McCormick DA (1993) Cellular mechanisms of a synchronized oscillation in the thalamus. *Science* 261:361–364
- Wang XJ, Rinzel J (1993) Spindle rhythmicity in the reticularis thalami nucleus – synchronization among inhibitory neurons. *Neurosci* 53:899–904
- Wang XJ, Golomb D, Rinzel J (1995) Emergent spindle oscillations and intermittent burst firing in a thalamic model: specific neuronal mechanisms. *Proc Natl Acad Sci USA* 92:5577–5581

Further Reading

Steriade M, Jones EG, McCormick DA (eds) (1997) *Thalamus*, vol 2. Elsevier, Amsterdam/Holland

Spontaneous Activity, Models of

Joana Cabral¹ and Gustavo Deco^{1,2}

¹Theoretical and Computational Neuroscience Group, Center for Brain and Cognition, Universitat Pompeu Fabra, Barcelona, Spain

²ICREA, Institució Catalana de Recerca i Estudis Avançats, Barcelona, Spain

Synonyms

Models of ongoing activity; Models of resting-state activity

Definition

Whole-brain computational models of the spontaneous dynamics of coupled brain areas. These models are useful to investigate the origin of ongoing fluctuations observed in brain activity during rest and their correlation structure.

Detailed Description

A growing body of neuroimaging research has revealed that during rest the brain exhibits spontaneous fluctuations in neural activity. These fluctuations emerge spontaneously during quiet wakeful rest and vanish either when triggered by a task or when falling asleep. This type of spontaneous activity has been mostly detected in the blood-oxygen level-dependent (BOLD) signal

using functional magnetic resonance imaging (fMRI) (Biswal et al. 1995). Explorations into the spatial organization of these spontaneous activations have revealed the existence of correlated activity (or *functional connectivity*) between spatially segregated brain areas. These functional connections appear closely related to the underlying map of white matter neuroanatomical connections. However, to understand spontaneous activity from a mechanistic perspective, anatomical information is not sufficient, and it is important to consider the way brain areas interact when they are in the spontaneous state. This is where bottom-up computational models of spontaneous activity come forward, since they allow testing potential theoretical scenarios by comparing the numerical simulation with real resting-state signals in health and disease (Ritter et al. 2013; Deco et al. 2013a; Cabral et al. 2014). In general, models of spontaneous activity consist in a whole-brain network model, where the nodes represent brain areas and the links represent the structural connections between them. Differences between models consist essentially on the equations used to describe the dynamics at the node level, i.e., the behavior of a brain area in the spontaneous state, and the way brain areas interact.

Models of Spontaneous Activity

Anatomical Connectivity

One main component of models of spontaneous activity is the anatomical connectivity matrix, which expresses the coupling weights between brain areas. Typically, these coupling weights are scaled in proportion to the number of white matter fiber tracts connecting each pair of brain areas. The first models of spontaneous activity (Honey et al. 2007; Ghosh et al. 2008; Deco et al. 2009) have used the anatomical connectivity between 38 brain areas from one hemisphere of the macaque brain (Kötter 2004). More recent models (Honey et al. 2009; Cabral et al. 2011; Deco and Jirsa 2012; Deco et al. 2013b) have used the human anatomical connectome derived *in vivo* from diffusion MRI between 66 brain areas covering the whole cortical surface (Hagmann et al. 2008) or 90 brain areas defined

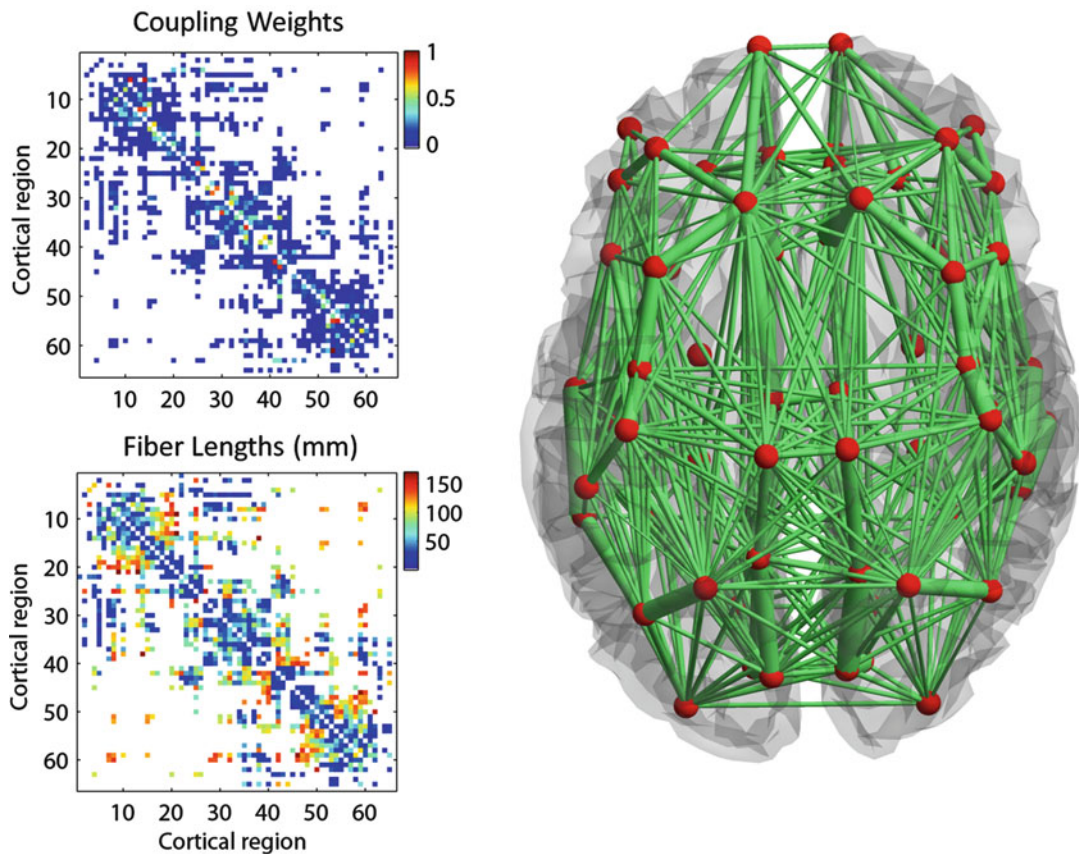
according to the AAL template (Cabral et al. 2012). In some models, the structural distance between brain areas is also taken into account, as it induces time-delayed interactions between brain areas (Ghosh et al. 2008; Deco et al. 2009; Cabral et al. 2011, 2012) (Fig. 1).

Local Node Model

Another main component of the models is the type of dynamics assumed at the node level, i.e., the intrinsic behavior of brain areas when they are in the spontaneous state. Assuming that each brain area consists in a system of densely interconnected neurons, the population dynamics can be represented, in a reduced manner, by a small set of differential equations. Existing models of spontaneous activity represent the dynamics of a local brain area in the following ways:

- Conductance-based biophysical neural mass model (Honey et al. 2007, 2009)
- ► **Fitzhugh–Nagumo Model** neural mass model (Ghosh et al. 2008)
- ► **Wilson–Cowan Model** of excitatory and inhibitory neural pools (Deco et al. 2009)
- Coupled oscillator using an extended version of the Kuramoto model (Cabral et al. 2011)
- Node model in an asynchronous state (Cabral et al. 2012)
- Attractor network of spiking neurons (Deco and Jirsa 2012)
- Dynamic mean field model (Deco et al. 2013b)

Depending on the models, coupled brain areas may display different dynamical regimes, namely, a fixed-point attractor, a limit-cycle attractor, or a chaotic attractor. In the first case, all neurons in a brain area fire irregularly, and the system tends to a stable asynchronous state. In this case, oscillations are damped and manifest as resonances in the network response (Ghosh et al. 2008; Deco and Jirsa 2012; Deco et al. 2013b; Cabral et al. 2012). On the other hand, when the neurons in a brain area fire synchronously with rhythmic periodicity due to recurrent excitation and inhibition, then neural populations display self-sustained oscillations, and the dynamics is approximated to a limit-cycle



Spontaneous Activity, Models of, Fig. 1 Anatomical network. Anatomical connectivity between with 66 brain areas derived using DSI averaged over five healthy subjects (Hagmann et al. 2008). (Top-left) The coupling weights are proportional to the number of tracts detected. Weights were normalized so that $0 \leq C_{np} \leq 1$. White = no connection. (Bottom-left) Distance between regions

attractor (Deco et al. 2009; Cabral et al. 2011). Finally, when the local network exhibits intrinsic instabilities where nonperiodic intermittent oscillations occur due to nonlinear interactions between neurons, then a chaotic dynamics is instantiated (Honey et al. 2007, 2009). Although there is a qualitative difference between models, all scenarios are plausible in the light of the current knowledge in spontaneous neural dynamics.

Systems of Coupled Brain Areas

Coupling local node models according to the whole-brain anatomical network structure, it is possible to simulate the behavior of coupled

given as the average length of the fibers connecting a pair of regions. (Right) Schematic representation of the anatomical network, where regions (red spheres) are placed at their center of gravity and the link's thickness is proportional to the number of fiber tracts detected in each connection

brain areas at a global scale. In the models, each brain area receives excitatory input from anatomically connected brain areas. In general, the main parameter of the models is the global coupling weight, which scales the anatomical connectivity matrix. When the distance between brain areas is considered, a finite (typically homogeneous) transmission speed is assumed resulting in time-delayed inputs (Ghosh et al. 2008; Deco et al. 2009; Cabral et al. 2011). In addition, some models include an external noisy input (Ghosh et al. 2008; Deco et al. 2009; Deco and Jirsa 2012; Cabral et al. 2012). Depending on the model, delays and/or noise may – or not – play a role in shaping the dynamics of the brain at rest.

Simulated BOLD Functional Connectivity

To compare the simulated neural activity with data from resting-state fMRI functional connectivity, it is necessary to estimate the BOLD signal changes associated with the simulated signals. Existing models of resting-state activity have used the Balloon-Windkessel hemodynamic model (Friston et al. 2003) to estimate the BOLD signal from simulations. Subsequently, the simulated spontaneous functional connectivity is computed by calculating the correlation matrix between the simulated BOLD signals in all brain areas. For a range of parameters (generally the global coupling weight but also the transmission speed and the noise level when these are considered), the system displays slow BOLD signal fluctuations with a correlation structure that fairly approximates the empirical BOLD functional connectivity. Importantly, for all models, the optimal fit with the empirical data is found for a set of parameters where the system operates at the edge of an instability, i.e., at the critical point of a bifurcation. This intrinsic instability of the system leads to the amplification of the underlying anatomical structure. In other words, at that critical bifurcation point, the global network dynamics reveals correlation patterns that are spatially shaped by the underlying anatomical structure, leading to an optimal fit with the empirical BOLD functional connectivity.

Discussion and Future Directions

Existing models of spontaneous activity point to the direction that the brain during rest reflects an intrinsically unstable regime, where a repertoire of different functional network configurations is temporary activated. However, the dynamics occurring at time scales faster than the hemodynamic response, as well as the nonstationarity of resting-state functional connectivity, has not been adequately addressed in computational models. To provide a global picture of the dynamics occurring in the brain at rest, existing and future models need to go beyond reproducing fMRI functional connectivity matrices and explore the nonstationary connectivity dynamics, as well as the faster oscillatory dimension, revealed with other neuroimaging modalities,

such as EEG, intracranial recordings, and MEG. Going beyond the BOLD signal, these methods provide pictures of resting-state dynamics from new perspectives, which must be taken into account in future models to deepen our understanding on resting-state activity.

References

- Biswal B, Yetkin FZ, Haughton VM, Hyde JS (1995) Functional connectivity in the motor cortex of resting human brain using echo-planar MRI. *Soc Magn Reson Med* 34(4):537–541
- Cabral J, Hugues E, Sporns O, Deco G (2011) Role of local network oscillations in resting-state functional connectivity. *Neuroimage* 57:130–139
- Cabral J, Hugues E, Kringelbach ML, Deco G (2012) Modeling the outcome of structural disconnection on resting-state functional connectivity. *Neuroimage* 62:1342–1353
- Cabral J, Kringelbach ML, Deco G (2014) Exploring the network dynamics underlying brain activity during rest. *Progress in Neurobiology* 114:102–131
- Deco G, Jirsa VK (2012) Ongoing cortical activity at rest: criticality, multistability, and ghost attractors. *J Neurosci* 32:3366–3375
- Deco G, Jirsa VK, McIntosh AR, Sporns O, Kötter R (2009) Key role of coupling, delay, and noise in resting brain fluctuations. *Proc Natl Acad Sci U S A* 106:10302–10307
- Deco G, Jirsa VK, McIntosh AR (2013a) Resting brains never rest: computational insights into potential cognitive architectures. *Trends Neurosci* 36:268–274
- Deco G, Ponce-Alvarez A, Mantini D, Romani GL, Hagmann P, Corbetta M (2013b) Resting-state functional connectivity emerges from structurally and dynamically shaped slow linear fluctuations. *J Neurosci* 33(27):11239–11252
- Friston KJ, Harrison L, Penny W (2003) Dynamic causal modelling. *Neuroimage* 19:1273–1302
- Ghosh A, Rho Y, McIntosh AR, Kotter R, Jirsa VK (2008) Cortical network dynamics with time delays reveals functional connectivity in the resting brain. *Cogn Neurodyn* 2:115–120
- Hagmann P, Cammoun L, Gigandet X, Meuli R, Honey CJ, Wedeen VJ, Sporns O (2008) Mapping the structural core of human cerebral cortex. *PLoS Biol* 6:e159
- Honey CJ, Kötter R, Breakspear M, Sporns O (2007) Network structure of cerebral cortex shapes functional connectivity on multiple time scales. *Proc Natl Acad Sci U S A* 104:10240–10245
- Honey CJ, Sporns O, Cammoun L, Gigandet X, Thiran JP, Meuli R, Hagmann P (2009) Predicting human resting-state functional connectivity from structural connectivity. *Proc Natl Acad Sci U S A* 106:2035–2040

- Kötter R (2004) Online retrieval, processing, and visualization of primate connectivity data from the CoCoMac database. *Neuroinformatics* 2:127–144
- Ritter P, Schirner M, McIntosh AR, Jirsa VK (2013) The virtual brain integrates computational modeling and multimodal neuroimaging. *Brain Connect* 3:121–145

Spreading Depolarizations

- ▶ [Migraines and Cortical Spreading Depression](#)

Squid Axon Model

- ▶ [Hodgkin-Huxley Model](#)

STA

- ▶ [Spike Triggered Average](#)

Stability and Homeostasis in Small Network Central Pattern Generators

Jorge Golowasch

Federated Department of Biological Sciences,
New Jersey Institute of Technology/Rutgers
University, Newark, NJ, USA

Synopsis

All animals contain circuits in their central nervous system that produce rhythmic activity. The circuits, often referred to as central pattern generators (CPGs), typically underlie vital activities or behaviors, such as locomotion, respiration, heartbeat, digestion, circadian activity, etc. (Marder et al. 2005). By the very nature of these behaviors, they require a certain degree of stability of the individual parameters or features that characterize the activity to ensure the survival of the individual. In patterned activity, a key

activity feature is the relative timing of activation (phase) of different components of the network. On the other hand, the nervous system is best known for its plasticity and capacity to change in response to many types of inputs. Thus, how stability of activity is ensured is the subject of intense research. In order to attain a stable state, the neurons in these circuits need mechanisms that monitor the state of the system to homeostatically adjust parameters that bring the system to within operational limits. Here, we discuss conditions and likely mechanisms that participate in this process. It is important to note that this field is, as of early 2014, in its early stages of development and much remains to be discovered and understood.

Central pattern generators (CPGs). Networks (or parts of networks) that autonomously produce patterned activity, without requiring timing cues from external sources to the network.

Model Systems

Species with anatomically simple nervous systems that include small CPG-containing networks are among the ones that offer the best opportunities for understanding the basic mechanisms in operation. Such species (and small neuronal networks) include crabs and lobsters (pyloric, gastric, and cardiac networks), leech (heartbeat network), nudibranchs such as *Tritonia* and *Clione* (swimming network), snails such as *Aplysia* and *Lymnaea* (feeding network), etc. (Marder et al. 2005). The simplicity of the networks involved lies primarily in their low number of neurons, of which the majority are identified, large, and often found in low copy number, thus ensuring unequivocal identification of the component neurons involved in the CPG. Modern molecular and optogenetic methods are bringing us closer to the possibility of manipulating large numbers of identified neurons in more complex networks, but identification challenges remain a problem (Carroll et al. 2013).

When working with model systems with large numbers of neurons, great care needs to be exercised to ensure that a subclass within a large neuronal class does not express a gene or protein different enough to determine a distinct function, while expressing the marker that characterizes the broader class. If this latter marker is used to identify the class, one may be wrong in assuming that all cells belong to the same class.

What Is Stable?

In principle, any feature by which network activity may be characterized could be a target for homeostatic mechanisms that stabilize activity. Here, we will focus on network properties primarily but will describe some cases in which the properties of individual cells of small networks are found to be conserved. Additionally, two very different types of stability, likely to depend on distinct types of homeostatic mechanisms, are observed: one is the consistency of activity patterns over many individuals, which we will refer to as *population stability*. Another is the consistency of activity patterns over time within an individual, which we will refer to as *individual stability*.

In pattern generators, it is frequently the case that the phases of activities of the neurons in the network need to be stabilized. This ensures that different segments in the body, for example, bend in the correct sequence to ensure propulsion when swimming (Varkonyi et al. 2008) and that the contraction of agonistic and antagonistic muscle occurs in the appropriate temporal relationship to enable walking instead of hopping or trotting (Kiehn 2011) or to enable the correct sequence of inspiratory and expiratory muscle contractions in the respiratory system (Carroll et al. 2013). In the pyloric network of crustaceans, several neuronal types fire in a specific order and drive the contractions of the about 40 muscles found on the pyloric sac. The phase at which each of the participating neurons starts and ends their bursts of activity is extremely well conserved across individuals (Bucher et al. 2005; Goaillard et al. 2009). A similar example of stability has

been observed in the leech heart network, a network of neurons spanning several ganglia along the length of the animal, whose relative order of activity is essential to ensure the proper order of muscle contraction of the heart muscles that spans the length of the animal (Roffman et al. 2012). Thus, it can probably be safely concluded that phase control and stabilization under certain conditions is a general requirement for pattern generating networks.

Phase. A fraction that an event in a pattern takes relative to the duration of one cycle. Thus, the fraction of time during which a neuron is active (e.g., spiking) is its active phase; the onset phase is the point in a cycle when activity begins, etc.

Another feature of small pattern generating networks that has been found to be conserved in some systems is the ability to restore the pattern to a state that is similar to the natural, unperturbed state after it is disrupted by external perturbations. This individual stability property has been observed in a number of different systems and in response to different perturbations, including stroke, spinal cord injury, deafferentation, temperature changes, etc. Although this type of feature has been widely studied at the level of individual synapses or intrinsic properties (and termed homeostatic plasticity in general (Williams et al. 2013)), we will discuss some of the cases that are relevant to small, pattern generating networks in some detail below.

The requirement to stabilize phase of activity is challenged by two different sources of variability in the system. One is the varying nature of the inputs that the nervous system receives and to which it must respond adaptively in a moment-by-moment basis to maintain phase constant. This is, therefore, an issue that applies at the level of individuals and will here be referred to as *individual stability*. Another challenge that has been observed in uniquely identified neurons across animals is the high degrees of variability with which both synaptic and intrinsic ionic currents (which generate the activity of the CPGs) are expressed while maintaining the activity

strikingly similar across the population. This issue will here be referred to as *population stability*.

Population Stability

The best known examples of population stability are found in the pyloric network activity of crustaceans, namely, lobsters and crabs, and the heartbeat activity of leeches. When recorded over a large population of unrelated animals, the activity of pyloric network neurons shows large variability in frequency, yet remarkable phase constancy, with each neuron activating and terminating its bursts of activity at a phase that is nearly completely independent of frequency (Bucher et al. 2005; Goaillard et al. 2009). A very similar phenomenon occurs in the network that controls the leech heartbeat (Norris et al. 2006). Phase constancy across individuals is also observed in lampreys and fish, where very precise phase shifts in the contraction of adjacent body segments during swimming are highly conserved across animals and independent of frequency (Lansner et al. 1998). The advantage in studying crustaceans and leeches is that the neurons involved in the generation of the rhythmic pattern are so few that we can be certain to identify each player. Moreover, in each one of these uniquely identified neurons, it has been possible to measure the amplitudes and properties of each of the ionic currents they express. The interplay of synaptic and intrinsic ionic currents is what determines the excitability and overall electric properties of the neurons in a network. Thus, it came as a surprise when a few years ago reports began to appear that showed that these currents are expressed at severalfold different levels between animals whose phase relationships were almost identical (Liu et al. 1998; Schulz et al. 2006; Goaillard et al. 2009; Roffman et al. 2012). Two alternatives can be envisaged to explain such independence of a crucial functional trait (phase) from the amplitudes, and probably also other parameters, of the currents that generate that activity: one is that the variable currents do not play a significant role in

determining phase relationships. That is unlikely to be the case since even the synaptic currents that most influence phasing are highly variable (Goaillard et al. 2009; Roffman et al. 2012). The other alternative is that somehow the ionic currents involved compensate for each other in their effects on phase and other activity features. What compensations are likely to be observed? An intuitively easy relationship to understand is the amplitude of an inward and an outward current. They can in principle be functional antagonists even though their specific kinetic and voltage-dependent properties will determine how complementary they actually are. MacLean et al. showed that this was the case, for example, between the hyperpolarization-activated inward current (I_h) and the transient K⁺ current (I_A) in lobster neurons that lead to the constancy of delay to first spike among neurons with different but compensating levels of these currents (MacLean et al. 2003, 2005).

The phenomenon of currents compensating for each other to stabilize an activity feature translates at the population level into the observation of the correlated expression of such ionic currents or conductances between individuals. In other words, correlated currents are currents whose amplitudes track each other, either positively (one grows proportionally to the growth of another) or negatively. This has now been shown in several cases, both in the small networks discussed here (Khorkova and Golowasch 2007; Schulz et al. 2007; Goaillard et al. 2009; Zhao and Golowasch 2012) and in vertebrate neurons from much more complex networks (Amendola et al. 2012; Unal et al. 2012). A growing body of both experimental and theoretical evidence indicates that the correlated expression of different ionic currents, including voltage-gated conductances as well as synaptic conductances, may be required to ensure stability of function (MacLean et al. 2003; Schulz et al. 2006, 2007; Khorkova and Golowasch 2007; Hudson and Prinz 2010; Temporal et al. 2012). In the pyloric network, for example, it has been shown that loss of rhythmic activity is accompanied by the loss of the correlated expression of certain voltage-gated currents, such as I_h and the high-threshold K⁺

current, I_{HTK} , in one cell type (Khorkova and Golowasch 2007; Temporal et al. 2012). It has also been observed that a number of activity properties in this network are correlated with more than one conductance (Goaillard et al. 2009; Zhao and Golowasch 2012). This indicates that the maintenance of constant phase relationships in a population of animals can be achieved in principle if neurons simultaneously control multiple conductances in a coordinated manner.

A similar situation can be observed in the leech heartbeat system. Here, we observe phase relationships between adjacent segments of the animal that are highly preserved across individuals (Norris et al. 2006). Underlying this, we find a wide range of synaptic conductances (Norris et al. 2011; Roffman et al. 2012). Thus, the question of how phases are maintained when synaptic currents are highly variable comes up here again. It had been hypothesized that the relative strengths of the synaptic inputs that the heart motor neurons receive from its presynaptic interneurons would determine the stable output of the network (Norris et al. 2007). However, extensive testing of this hypothesis did not clearly confirm that prediction (Norris et al. 2011), even though recent theoretical work indicates that synaptic conductance correlations are to be expected (Lamb and Calabrese 2013). Instead, it is now suggested that a more complex set of compensatory (or tuning) interactions between intrinsic and synaptic conductances may be responsible for the consistent phase relationships of the motor output (Norris et al. 2011).

Mechanisms

How can ionic currents be linked in a way that correlations appear at the population level? Several possibilities can be envisaged: (1) sets of ion channels are transcriptionally linked by common transcription regulation factors; (2) co-expression of, or co-assembly into, ribosomes (or ribosome granules), of sets of ion channel mRNAs; and (3) shared posttranslational modification or co-localization of distinct ion channels in macromolecular assemblies. A very interesting recent theoretical study showed that ionic conductance

correlations will result when a set of correlated ionic currents are all regulated in an activity-dependent manner, with the actual relationship that describes the coupling determined by the relative rates of regulation (O'Leary et al. 2013). Thus, if a target activity trait is regulated in an activity-dependent manner, coupled conductances across a population of cells will naturally arise from a set of random initial conditions. Furthermore, the relationships that characterize this coupling can be linear (O'Leary et al. 2013), which is fully consistent with a growing number of observations of such relationships, both theoretical and experimental (Burdakov 2005; Schulz et al. 2006, 2007; Khorkova and Golowasch 2007; Ball et al. 2010; Temporal et al. 2012).

Individual Stability

At the individual level, two distinct types of stabilization of phase relationships in CPGs have been described. One is the immediate regulation of phase in response to changing inputs to the CPG and to which it responds quickly to maintain phase constant. Another is the much slower response to drastic perturbation that may be described as recovery of function.

Phase Control

In many systems, phase maintenance depends on mechanisms operating at the level of the synaptic connectivity (circuitry) of the networks. Thus, different synaptic strengths along a gradient of body segments (Williams 1992) or the strength or number of excitatory or inhibitory connections between segments (Skinner and Mulloney 1998) can account for the different types of phase relationships in multisegmented animals (fish, lampreys, etc.). A different mechanism was proposed for the phase maintenance in networks consisting of follower neurons inhibited by oscillating or pacemaker neurons, a case commonly found among CPGs (Manor et al. 2003). Using computational and analytical tools the authors showed that short-term synaptic depression of the inhibitory synapse can create phase maintenance.

The idea behind this mechanism is that synaptic depression is dependent on frequency: the longer the synapse is active (such as when rhythm frequency is low), the more it depresses and thus the less effective the synapse becomes. With appropriate parameters, the synaptic delay can be nearly proportional to the change in cycle frequency and thus phase be well maintained (Manor et al. 2003). A related study shows that the interaction of synaptic depression and the properties of inactivating K⁺ currents could further contribute to phase constancy (Greenberg and Manor 2005). These mechanisms act with time constants close to the time constants of synaptic depression and current inactivation, both of which are close to the cycling frequencies of networks. They therefore function to maintain phase constancy at short time scales that are commensurate with the frequency of the network patterns.

Recovery of Function

Several small neuronal networks exhibit robust but much slower compensatory responses to perturbations than those described in the previous section. The responses lead to recovery of function and can bring the entire network back to a state similar to that prior to receiving the perturbation. In the mollusk *Tritonia diomedea*, for example, the escape swimming pattern can be characterized by a series of body flexions induced by sensory stimuli. A fictive motor pattern that underlies this behavior can also be elicited in preparations of the isolated brain *in vitro* (Katz 2009). When the connections between two of the key components of the swimming CPG are broken, the entire swimming pattern is disrupted and escape responses can no longer be elicited. However, within 1 day after the lesion, the escape responses are restored to levels almost indistinguishable from the control without reconnection of the severed connection (Sakurai and Katz 2009). This recovery of function is driven by a reconfiguration of the dendritic tree whereby one neuropilar region of the cell takes over the function of the dominant one located in the severed region. What molecular mechanism accounts for this is unknown.

In the pyloric network of crustaceans, we observe a similar phenomenon. The pyloric network resides in the stomatogastric ganglion (STG), and its activity is generated in a manner that depends on the uninterrupted release of neuromodulators from projecting neurons whose cell bodies are found in ganglia adjacent to the STG (Selverston and Moulins 1986). When these axons are severed or their action potential transmission is blocked (a process described as decentralization), pyloric activity rapidly ceases. However, within several hours to a few days, depending on the species, certain aspects of the pyloric rhythm (notably the phase relationships between the members of the network) return to control levels (Thoby-Brisson and Simmers 1998; Luther et al. 2003). What is particularly interesting about this recovery is that the phase relationships in the preparations whose pyloric rhythm has fully recovered are nearly indistinguishable from those observed before decentralization even though the frequency of the rhythm is typically slower. This is reminiscent of the population stability features observed in intact preparations in which phase relationships are tightly maintained but frequency is much more variable (Bucher et al. 2005; Goaillard et al. 2009). Before the recovery has reached its near control levels, however, the phase relationships as well as the frequency are significantly different from the final stable state (Luther et al. 2003). At the same time, ionic conductance amplitudes and their correlation levels change dramatically (Khorkova and Golowasch 2007; Temporal et al. 2012). One possible explanation for this is that whatever mechanisms that keep current amplitudes tied to one another under control conditions (during which neuromodulator levels are relatively high) are released. With this, amplitudes and correlations become free to change within a wide parameter space, perhaps different from the one normally visited by the cells under the normal neuromodulatory state. This may be necessary to find a new set of values for each of the conductances that can sustain stable activity again but now in the continuous absence of neuromodulators. Such robustness of the activity of this network is further revealed in

response to temperature changes. Temperature shifts induce large and significant changes in pyloric rhythm frequency, but the network remains capable of maintaining a remarkably stable set of phase relationships even when the temperature changes (and consequently, the frequency) are made quite rapidly (minutes) and over a wide range (Tang et al. 2010). Thus, here again we find that the relative timing of activity between the component neurons is a crucial parameter that is conserved or stabilized over very different conditions.

What mechanisms may be responsible for these effects? Different mechanisms of homeostatic regulation are found, even though a full picture has not yet emerged. Synaptic plasticity is clearly involved in several of these cases. For instance, the stabilization of phase relationships within the pyloric network when the temperature of the network is changed is accompanied by synaptic strength changes among several of the synaptic connections, as well as intrinsic ionic current modifications (Tang et al. 2010). The recovery of the pyloric rhythm after decentralization also appears to involve synaptic strength changes as well as changes to voltage-gated ionic conductances (Thoby-Brisson and Simmers 2002; Khorkova and Golowasch 2007), perhaps via changes in intracellular calcium regulation mechanisms (Yang and Golowasch 2011). Interestingly, changes induced by decentralization on the correlation between ionic currents have also been observed, indicating that conductance correlations are somehow under neuromodulatory control (Khorkova and Golowasch 2007).

References

- Amendola J, Woodhouse A, Martin-Eauclaire MF, Goaillard JM (2012) Ca(2)(+)/cAMP-sensitive covariation of I(A) and I(H) voltage dependences tunes rebound firing in dopaminergic neurons. *J Neurosci* 32:2166–2181
- Ball JM, Franklin CC, Tobin AE, Schulz DJ, Nair SS (2010) Coregulation of ion channel conductances preserves output in a computational model of a crustacean cardiac motor neuron. *J Neurosci* 30:8637–8649
- Bucher D, Prinz AA, Marder E (2005) Animal-to-animal variability in motor pattern production in adults and during growth. *J Neurosci* 25:1611–1619
- Burdakov D (2005) Gain control by concerted changes in I(A) and I(H) conductances. *Neural Comput* 17:991–995
- Carroll MS, Viemari JC, Ramirez JM (2013) Patterns of inspiratory phase-dependent activity in the *in vitro* respiratory network. *J Neurophysiol* 109:285–295
- Goaillard J-M, Taylor AL, Schulz DJ, Marder E (2009) Functional consequences of animal-to-animal variation in circuit parameters. *Nat Neurosci* 12:1424–1430
- Greenberg I, Manor Y (2005) Synaptic depression in conjunction with A-current channels promote phase constancy in a rhythmic network. *J Neurophysiol* 93:656–677
- Hudson AE, Prinz AA (2010) Conductance ratios and cellular identity. *PLoS Comput Biol* 6:e1000838
- Katz PS (2009) *Tritonia* swim network. *Scholarpedia* 4(5):3638
- Khorkova O, Golowasch J (2007) Neuromodulators, not activity, control coordinated expression of ionic currents. *J Neurosci* 27:8709–8718
- Kiehn O (2011) Development and functional organization of spinal locomotor circuits. *Curr Opin Neurobiol* 21:100–109
- Lamb DG, Calabrese RL (2013) Correlated conductance parameters in leech heart motor neurons contribute to motor pattern formation. *PLoS One* 8:e79267
- Lansner A, Kötaleksi JH, Grillner S (1998) Modeling of the spinal neuronal circuitry underlying locomotion in a lower vertebrate. *Ann N Y Acad Sci* 860:239–249
- Liu Z, Golowasch J, Marder E, Abbott LF (1998) A model neuron with activity-dependent conductances regulated by multiple calcium sensors. *J Neurosci* 18:2309–2320
- Luther JA, Robie AA, Yarotsky J, Reina C, Marder E, Golowasch J (2003) Episodic bouts of activity accompany recovery of rhythmic output by a neuromodulator- and activity-deprived adult neural network. *J Neurophysiol* 90:2720–2730
- MacLean JN, Zhang Y, Johnson BR, Harris-Warrick RM (2003) Activity-independent homeostasis in rhythmically active neurons. *Neuron* 37:109–120
- MacLean JN, Zhang Y, Goeritz ML, Casey R, Oliva R, Guckenheimer J, Harris-Warrick RM (2005) Activity-independent coregulation of IA and Ih in rhythmically active neurons. *J Neurophysiol* 94:3601–3617
- Manor Y, Bose A, Booth V, Nadim F (2003) Contribution of synaptic depression to phase maintenance in a model rhythmic network. *J Neurophysiol* 90:3513–3528
- Marder E, Bucher D, Schulz DJ, Taylor AL (2005) Invertebrate central pattern generation moves along. *Curr Biol* 15:R685–R699
- Norris BJ, Weaver AL, Morris LG, Wenning A, Garcia PA, Calabrese RL (2006) A central pattern generator producing alternative outputs: temporal pattern of premotor activity. *J Neurophysiol* 96:309–326

- Norris BJ, Weaver AL, Wenning A, Garcia PS, Calabrese RL (2007) A central pattern generator producing alternative outputs: pattern, strength, and dynamics of premotor synaptic input to leech heart motor neurons. *J Neurophysiol* 98:2992–3005
- Norris BJ, Wenning A, Wright TM, Calabrese RL (2011) Constancy and variability in the output of a central pattern generator. *J Neurosci* 31:4663–4674
- O’Leary T, Williams AH, Caplan JS, Marder E (2013) Correlations in ion channel expression emerge from homeostatic tuning rules. *Proc Natl Acad Sci USA* 110:E2645–E2654
- Roffman RC, Norris BJ, Calabrese RL (2012) Animal-to-animal variability of connection strength in the leech heartbeat central pattern generator. *J Neurophysiol* 107:1681–1693
- Sakurai A, Katz PS (2009) Functional recovery after lesion of a central pattern generator. *J Neurosci* 29:13115–13125
- Schulz DJ, Goaillard JM, Marder E (2006) Variable channel expression in identified single and electrically coupled neurons in different animals. *Nat Neurosci* 9:356–362
- Schulz DJ, Goaillard JM, Marder EE (2007) Quantitative expression profiling of identified neurons reveals cell-specific constraints on highly variable levels of gene expression. *Proc Natl Acad Sci USA* 104:13187–13191
- Selverston AI, Moulins M (1986) The Crustacean stomatogastric system: a model for the study of central nervous systems. Springer, Berlin/New York
- Skinner FK, Mulloney B (1998) Intersegmental coordination in invertebrates and vertebrates. *Curr Opin Neurobiol* 8:725–732
- Tang LS, Goeritz ML, Caplan JS, Taylor AL, Fisek M, Marder E (2010) Precise temperature compensation of phase in a rhythmic motor pattern. *PLoS Biol* 8(8): e1000469
- Temporal S, Desai M, Khorkova O, Varghese G, Dai A, Schulz DJ, Golowasch J (2012) Neuromodulation independently determines correlated channel expression and conductance levels in motor neurons of the stomatogastric ganglion. *J Neurophysiol* 107:718–727
- Thoby-Brisson M, Simmers J (1998) Neuromodulatory inputs maintain expression of a lobster motor pattern-generating network in a modulation-dependent state: evidence from long-term decentralization in vitro. *J Neurosci* 18:2212–2225
- Thoby-Brisson M, Simmers J (2002) Long-term neuromodulatory regulation of a motor pattern-generating network: maintenance of synaptic efficacy and oscillatory properties. *J Neurophysiol* 88:2942–2953
- Unal CT, Golowasch JP, Zaborszky L (2012) Adult mouse basal forebrain harbors two distinct cholinergic populations defined by their electrophysiology. *Front Behav Neurosci* 6:21
- Varkonyi PL, Kiemel T, Hoffman K, Cohen AH, Holmes P (2008) On the derivation and tuning of phase oscillator models for lamprey central pattern generators. *J Comput Neurosci* 25:245–261
- Williams TL (1992) Phase coupling by synaptic spread in chains of coupled neuronal oscillators. *Science* 258:662–665
- Williams AH, O’Leary T, Marder E (2013) Homeostatic regulation of neuronal excitability. *Scholarpedia* 8(1):1656
- Zhang Y, Golowasch J (2011) Recovery of rhythmic activity in a central pattern generator: analysis of the role of neuromodulator and activity-dependent mechanisms. *J Comput Neurosci* 31:685–699
- Zhao S, Golowasch J (2012) Ionic current correlations underlie the global tuning of large numbers of neuronal activity attributes. *J Neurosci* 32:13380–13388

State-Dependent Networks

► Recurrent Network Models, Reservoir Computing

State-Space Models for the Analysis of Neural Spike Train and Behavioral Data

Zhe Chen^{2,4} and Emery N. Brown^{1,2,3}

¹Institute for Medical Engineering and Science, Massachusetts Institute of Technology, Cambridge, MA, USA

²Department of Brain and Cognitive Sciences, Massachusetts Institute of Technology, Cambridge, MA, USA

³Department of Anesthesia, Critical Care and Pain Medicine, Massachusetts General Hospital, Harvard Medical School, Boston, MA, USA

⁴Department of Psychiatry, Neuroscience and Physiology, New York University School of Medicine, New York, NY, USA

Definition

An adaptation of the state-space paradigm to the analysis of neuroscience data in which the observation model is either a point process or a time series of binary observations and the state model is typically a linear Gaussian process. The paradigm has been applied to a number of problems including neural spike train decoding, analysis of receptive field dynamics, analyses of learning,

neural prosthetic control, and control of brain states under anesthesia.

The state-space paradigm for analyses of point processes and time series of discrete binary observations has been developed for the analysis of neural spike train and behavioral data (Brown et al. 1998; Smith and Brown 2003). The state-space point process (SSPP) paradigm has two standard components. The state equation defines the system dynamics. The observation equation defines how the system is measured. For the SSPP system the observations can be point processes or time series of discrete binary responses. Point processes are binary (0–1) events defined in continuous time. They are an ideal framework for analyzing series of neuronal action potentials where the binary events are defined as 1 if there is an action potential or spike and 0 otherwise. Data in behavioral studies commonly consist of time series of binary responses such as in a learning experiment where 1 is given for a correct response and 0 is given for an incorrect response. In system neuroscience experiments, the state equation defines the signal, stimulus, or brain state that is being represented by the neural activity or the behavior.

Detailed Description

Derivation of the State-Space Point Process Filter Algorithm

The use of the state-space paradigm to analyze neural spiking activity was introduced by Brown and colleagues, using an inhomogeneous Poisson observation model and a linear Gaussian state model to study the decoding of position from ensemble neural spiking activity in rodents (Brown et al. 1998; see ► [Neural Coding](#); ► [Population Encoding/Decoding](#)). The objective of the state-space analysis is to estimate the state at time t , given the data, up through time t (Brown et al. 1998; Smith and Brown 2003). The solution to this prediction problem is defined recursively by the associated Bayes' rule Chapman-Kolmogorov (BCK) system (see ► [Bayesian Approaches in Computational Neuroscience: Overview](#)). Bayes' rule defines the posterior density of the state at time t given all of the

observations from the start of the experiment up through time c . The Chapman-Kolmogorov, or one-step prediction equation, defines the probability density of the state at time t given the observations up through time $t - 1$ (Chen et al. 2010). This probability density is computed by integrating the product of the posterior density at time $t - 1$ and the state model that is typically Markov and defines the probability density of the states at time t given the state at time $t - 1$. Brown and colleagues showed that the state estimation from point process observations could be efficiently conducted by deriving a nonlinear recursive filter (NRF) algorithm to solve the associated BCK system (Brown et al. 1998; see ► [Digital Filtering](#)). The derivation used two approximations to derive the algorithm. First, it approximated continuous time as discrete time in small intervals and assumed a single (0 or 1) Poisson observation in each interval. Second, the NRF algorithm is derived by using a Gaussian approximation to integrate the BCK system and a second Gaussian approximation to compute the *maximum-a-posteriori* state estimate and its covariance matrix. The NRF algorithm becomes the Kalman filter algorithm when the observation equation is a linear function of the state and the observation noise is Gaussian and additive.

Extensions of the State-Space Point Process Theory

Brown and colleagues demonstrated that a point process adaptive filter algorithm is a special case of the NRF algorithm (Brown et al. 2001). They next developed an expectation-maximization algorithm to conduct simultaneous state and static model parameter estimation from general point process (non-Poisson) or time series of binary observations (Smith and Brown 2003; see ► [Generalized Linear Models for Point Process Analyses of Neural Spiking Activity](#)) and an augmented adaptive filter algorithm to conduct simultaneous state and dynamic model parameter estimation (Eden et al. 2004). The general point process paradigm improved the previously developed decoding algorithms (Brown et al. 1998) and defined explicitly the relationship between decoding the representation of a signal in an

ensemble of neurons and measuring dynamically the mutual information between the signal and the ensemble spiking activity (Barbieri et al. 2004; see ► [Information Theory: Overview](#)) The SSPP paradigm also provides a principled approach to analyzing binary data series recorded in learning experiments and explicit criteria to define when learning occurs (Wirth et al. 2003; Smith et al. 2004).

Brown and colleagues extended the SSPP algorithms to derive the exact state estimation algorithms for point processes using sequential Monte Carlo methods (Ergun et al. 2007), conduct state estimation from simultaneously observed point process and binary and continuous observations, (Prerau et al. 2008, 2009; Coleman et al. 2010) and implement deterministic and stochastic control systems (Ching and Liberman 2013; Shanechi et al. 2013a, b, c). Extensions of the state-space point process framework include the use of Markov chain Monte Carlo computations (Ahmadian et al. 2011; Yuan et al. 2012) and the analysis of interactions among simultaneously recorded neural spike trains using information geometry concepts (Shimazaki et al. 2012; see ► [Information Geometry as Applied to Neural Spike Data](#)).

Applications of the State-Space Point Process Paradigm

The first application of the SSPP was as a new paradigm to decode spatial information from ensembles of the hippocampal place cell neurons (Brown et al. 1998; see ► [Efficient Population Coding](#); ► [Estimation of Neuronal Firing Rate](#)). This analysis showed how ensembles of the hippocampal neurons maintained precise, dynamic representations of a rat's spatial location during foraging (Brown et al. 1998). The SSPP algorithms outperformed by an order of magnitude ad hoc algorithms in decoding spatial information from ensembles of the hippocampal neurons (Brown et al. 1998). The adaptive filter algorithm special case of the SSPP algorithm was used to study receptive field plasticity in the hippocampal neurons (Brown et al. 2001; Frank et al. 2004). An SSPP analysis showed that rodent hippocampal neurons can form new spatial receptive fields in 5–6 min (Frank

et al. 2004) and that in monkeys, hippocampal neuronal activity changes are tightly coupled to the acquisition of newly learned behaviors (Wirth et al. 2003). The SSPP algorithm applied to binary data established a new paradigm for dynamic analysis of behavior in learning experiments (Wirth et al. 2003; Smith et al. 2004; Prerau et al. 2008; Prerau et al. 2009; see ► [Behavioural Analysis, Bayesian](#)).

The SSPP algorithm accurately decoded motor cortex representations of hand positions (Truccolo et al. 2005). SSPP algorithms have been used to track heart rate variability, (Barbieri and Brown 2006) to track brain states under general anesthesia, (Chemali et al. 2013) and to precisely define anesthesia-induced loss and recovery of consciousness (Purdon et al. 2013; Wong et al. 2014). The SSPP algorithms established that during motor learning different groups of neurons can represent different movement components (Shanechi et al. 2012). SSPP algorithms have been used to implement stochastic and deterministic control paradigms: linear-quadratic regulatory algorithms for motor neural prostheses (Shanechi et al. 2013a, b; see ► [Brain-Machine Interface: Overview](#)) and proportional-integral, (Ching and Liberman 2013) linear-quadratic regulator and model predictive control algorithms (Shanechi et al. 2013c) to precisely maintain the brain in a medically induced coma. For motor prosthetic control, Carmena and colleagues recently showed that the SSPP paradigm outperforms by 30 % the widely used Kalman filter control paradigm (Shanechi et al. 2013d; see ► [Brain-Machine Interface: Overview](#)).

Cross-References

- [Bayesian Approaches in Computational Neuroscience: Overview](#)
- [Behavioural Analysis, Bayesian](#)
- [Brain-Machine Interface: Overview](#)
- [Digital Filtering](#)
- [Efficient Population Coding](#)
- [Estimation of Neuronal Firing Rate](#)
- [Generalized Linear Models for Point Process Analyses of Neural Spiking Activity](#)

- ▶ [Information Geometry as Applied to Neural Spike Data](#)
- ▶ [Information Theory: Overview](#)
- ▶ [Neural Coding](#)
- ▶ [Population Encoding/Decoding](#)

References

- Ahmadian Y, Pillow JW, Paninski L (2011) Efficient Markov chain Monte Carlo methods for decoding neural spike trains. *Neural Comput* 23:46–96
- Barbieri R, Brown EN (2006) Analysis of heartbeat dynamics by point process adaptive filtering. *IEEE Trans Biomed Eng* 53:4–12
- Barbieri R, Frank LM, Nguyen DP et al (2004) Dynamic analyses of information encoding in neural ensembles. *Neural Comput* 16:277–307
- Brown EN, Frank LM, Tang D, Quirk MC, Wilson MA (1998) A statistical paradigm for neural spike train decoding applied to position prediction from ensemble firing patterns of rat hippocampal place cells. *J Neurosci* 18:7411–7425
- Brown EN, Nguyen DP, Frank LM, Wilson MA, Solo V (2001) An analysis of neural receptive field plasticity by point process adaptive filtering. *Proc Natl Acad Sci U S A* 98:12261–12266
- Chemali J, Ching S, Purdon PL, Solt K, Brown EN (2013) Burst suppression probability algorithms: state-space methods for tracking EEG burst suppression. *J Neural Eng* 10:056017
- Chen Z, Barbieri R, EN Brown (2010) State-space modeling of neural spike train and neural behavioral data. In: *Statistical signal processing for neuroscience*: Oweiss. Oxford Press, Amsterdam, pp 161–200
- Ching S, Liberman MY, Chemali JJ et al (2013) Real-time closed-loop control in a rodent model of medically induced coma using burst suppression. *Anesthesiology* 119(4):848–860
- Coleman TP, Yanike M, Suzuki WA, Brown EN (eds) (2010) A mixed filter algorithm for dynamically tracking learning from multiple behavioral and neurophysiological measures. In: Glanzman DL, Ding M (eds) *Neuronal variability and its functional significance*. Oxford University Press, New York, pp 3–28
- Eden UT, Frank LM, Barbieri R, Solo V, Brown EN (2004) Dynamic analysis of neural encoding by point process adaptive filtering. *Neural Comput* 16:971–998
- Ergun A, Barbieri R, Eden UT, Wilson MA, Brown EN (2007) Construction of point process adaptive filter algorithms for neural systems using sequential Monte Carlo methods. *IEEE Trans Biomed Eng* 54:419–428
- Frank LM, Stanley GB, Brown EN (2004) Hippocampal plasticity across multiple days of exposure to novel environments. *J Neurosci* 24:7681–7689
- Prerau MJ, Smith AC, Eden UT, Yanike M, Suzuki WA, Brown EN (2008) A mixed filter algorithm for cognitive state estimation from simultaneously recorded continuous and binary measures of performance. *Biol Cybern* 99:1–14
- Prerau MJ, Smith AC, Eden UT et al (2009) Characterizing learning by simultaneous analysis of continuous and binary measures of performance. *J Neurophysiol* 102:3060–3072
- Purdon PL, Pierce ET, Mukamel EA et al (2013) Electroencephalogram signatures of loss and recovery of consciousness from propofol. *Proc Natl Acad Sci U S A* 110:E1142–E1151
- Shanechi MM, Hu RC, Powers M, Wornell GW, Brown EN, Williams ZM (2012) Neural population partitioning and a concurrent brain-machine interface for sequential motor function. *Nat Neurosci* 15:1715–1722
- Shanechi MM, Wornell GW, Williams ZM, Brown EN (2013a) Feedback-controlled parallel point process filter for estimation of goal-directed movements from neural signals. *IEEE Trans Neural Syst Rehabil Eng* 21:129–140
- Shanechi MM, Williams ZM, Wornell GW, Hu RC, Powers M, Brown EN (2013b) A real-time brain-machine interface combining motor target and trajectory intent using an optimal feedback control design. *PLoS One* 8:e59049
- Shanechi M, Chemali JJ, Liberman M, Solt K, Brown EN (2013) A brain-machine interface for control of medically-induced coma. *PLoS Comput Biol*: e1003284
- Shanechi MM, Orsborn A, Gowda S, Carmena JM (2013) Proficient BMI control enabled by closed-loop adaptation of an optimal feedback-controlled point process decoder. In: *Translational and computational motor control meeting*, San Diego, 8 Nov 2013
- Shimazaki H, Amari S, Brown EN, Grun S (2012) State-space analysis of time-varying higher-order spike correlation for multiple neural spike train data. *PLoS Comput Biol* 8:e1002385
- Smith AC, Brown EN (2003) Estimating a state-space model from point process observations. *Neural Comput* 15:965–991
- Smith AC, Frank LM, Wirth S et al (2004) Dynamic analysis of learning in behavioral experiments. *J Neurosci* 24:447–461
- Truccolo W, Eden UT, Fellows MR, Donoghue JP, Brown EN (2005) A point process framework for relating neural spiking activity to spiking history, neural ensemble, and extrinsic covariate effects. *J Neurophysiol* 93:1074–1089
- Wirth S, Yanike M, Frank LM, Smith AC, Brown EN, Suzuki WA (2003) Single neurons in the monkey hippocampus and learning of new associations. *Science* 300:1578–1581
- Wong KF, Smith AC, Pierce ET et al (2014) Statistical modeling of behavioral dynamics during propofol-induced loss of consciousness. *J Neurosci Methods* 227c: 65–74
- Yuan K, Girolami M, Nirajan M (2012) Markov chain Monte Carlo methods for state-space models with point process observations. *Neural Comput* 24:1462–1486

Statistical Analysis of Neuroimaging Data

Tohru Ozaki

Institute of Statistical Mathematics, Tokyo, Japan

Definition

The main goal of “statistical analysis of neuroimaging data” is to use statistical methods to extract useful neuroscientific information, from neuroimaging data such as fMRI, EEG, and MEG, which are derived from measurement of the dynamics of electrical and magnetic activity generated from the neural and vascular activities inside the live brain.

Detailed Description

A typical example is the statistical analysis of fMRI data, where the activation and deactivation of voxels (as measured by the BOLD signal) in response to some specific task of interest may be elucidated in a map called the activation map. Similarly for EEG/MEG data analysis, one of the main interests of statistical analysis is to estimate the activation of areas in response to specific stimuli to the live brain. It provides the basis for further elaborate statistical analysis, such as the analysis of dynamic causalities between the activated voxels in the estimated activation map.

“The statistical methods used in data analysis” very much depend on the type of available data. In neuroscience, the data are often (1) temporally correlated time series data and (2) multidimensional data, with dimension as large as 10–100 for EEG/MEG data and as large as 10,000 for fMRI data. Historically, statistical methods for neuroimaging data have been introduced using mostly those methods developed for identically distributed (i.i.d.) data. Direct application of conventional statistical methods to the analysis of high-dimensional temporally correlated neuroscience data often leads to difficulties precisely because the data is very far from

satisfying the i.i.d assumptions. The “time series modeling approach” has been specifically designed to take temporal correlations and multidimensionality into account and so is much more appropriate for application to the analysis of neuroscience data than the conventional i.i.d. approach.

An important and critical point for the statistical analysis of neuroimaging data is not the algorithm we use for computing the activation map, nor is it whether the activation map looks attractive. The most important point is whether the “assumptions” employed for computing and producing the map are statistically valid and appropriate for the observed time series data.

One of the most widely used statistical methods for the analysis of fMRI data is the statistical parametric mapping (SPM) developed by Friston et al. (1995). In the first stage of SPM, the dynamic characteristic of the BOLD signal is identified using a deterministic dynamical system (the hemodynamic response function) embedded in the statistical framework of the general linear model (GLM). Here the model parameters are estimated under the assumption that the GLM errors are i.i.d. and normally distributed. An additional assumption is that the high-dimensional fMRI data is assumed to be spatially independent, meaning that no spatial dynamic interaction is allowed, considered, or tested between the voxels.

In the second stage of SPM, the estimated parameters for each voxel are used to check whether the voxel is activated or not using conventional hypothesis testing methods. The validity of the hypothesis testing approach depends critically on the assumptions behind the models used for evaluating the null and alternative hypotheses. The activated areas judged to be significant by the testing method are often plotted as an activation map on each slice of the scanned MRI figures. The guidelines for producing an activation map are somewhat arbitrary and depend on whether the researcher needs a simple picture of the functioning of the brain or something more complex. However, the use of the deterministic hemodynamic function, the reliance on required assumptions such as

normal i.i.d. errors, and the spatial independence are rather too strong and make SPM rather controversial. Unfortunately the checking of the validity of the assumptions is not provided in the paradigm of the hypothesis testing procedure, and it appears that many analysts may be ignoring this issue.

A less well-known but a rather more orthodox approach to the statistical characterization of the dynamics of the neuroimaging data such as fMRI and EEG/MEG time series data is the direct time series modeling approach (Riera et al. 2004; Galka et al. 2004; Friston et al. 2003). In this approach, the dynamic characteristics of the stimulus-activation relation in the brain function are directly specified by a time series model (or a dynamical system model) with exogenous inputs. A typical example is to use an autoregressive model with an exogenous variable (ARX model), where the activation effect dynamically caused by the exogenous input (i.e., a stimulus) is specified by the exogenous terms. Plotting the activation map is, again, quite arbitrary and depends on the scientists' objectives. Some researchers may plot the exogenous terms (which could sometimes be negative according to whether the vascular flow in the voxel increases or decreases) and some people may prefer to plot the significance of the exogenous terms (i.e., the difference of the log-likelihood of the full model (including exogenous variables) and the sub-model (excluding the exogenous variables)).

There are many other methods developed for the statistical analysis of neuroimaging data (see Poldrack et al. 2011; Ozaki 2012; Li 2014). Some methods employ dynamical system models where the models are assumed, *a priori*, to be deterministic (e.g., DCM (dynamic causal modeling) in Friston et al. (2003)) Most of the methods rely on the techniques developed in multivariate analysis such as GLM, PLS (partial least squares), SEM (structural equation model), ICA (independent component analysis), PCA (principal component analysis), etc. Here important dynamic information, contained in the data as temporal correlations, is neglected in the i.i.d. assumptions.

The validity of the results of statistical analysis and imaging depends critically on the model

identified from the data, where each model stands on its own assumptions (i.i.d., temporally correlated, deterministic, and stochastic Bayesian or non-Bayesian). In the statistical modeling approach, the most critical issue is how to find the best model using appropriate assumptions for the given data. In contrast to the hypothesis testing case, we can consider more than a hundred candidate models using different assumptions and lag orders. For the identification of the best model among these candidate models, several approaches are available in time series analysis. "The innovation approach" is known to be especially powerful and easy to use in situations where we need to choose the best model among many candidate dynamic models representing the same data. This is because it stands on a very simple principle, i.e., "Choose, among the finite set of candidate models, a model which can predict the future time series best." This principle is essentially equivalent to Akaike's information criterion (AIC) minimization principle which was introduced from the idea of maximizing the expected Boltzmann entropy. By including lagged variables and spatial variables into the model, the prediction error variance is substantially minimized and statistical validity may be achieved, since in the time series case, the temporal independence and the normality of the prediction errors are guaranteed for stationary continuous Markov processes (Doob 1953).

Cross-References

- ▶ [Brain Imaging: Overview](#)
- ▶ [BrainMap](#)
- ▶ [Forward and Inverse Problems of MEG/EEG](#)
- ▶ [Imaging Analysis, Bayesian](#)
- ▶ [Independent Component Analysis of Images](#)

References

- Akaike H (1973) Information theory and an extension of maximum likelihood principle. In: Petrov BN, Csaki F (eds) Proceeding of 2nd international symposium on information theory. Akademiai-Kiado, Budapest, pp 267–281

- Doob JL (1953) Stochastic processes. Wiley, New York
- Friston KJ, Holmes AP, Worsley KJ, Poline JB, Frith C, Frackowiak RSJ (1995) Statistical parametric maps in functional imaging: a general linear approach. *Hum Brain Mapp* 2:189–210
- Friston KJ, Harrison L, Penny W (2003) Dynamic causal modelling. *Neuroimage* 19:1273–1303
- Galka A, Yamashita O, Ozaki T, Biscay R, Valdes-Sosa P (2004) A solution to the dynamical inverse problem of EEG generation using spatiotemporal Kalman filtering. *Neuroimage* 23:435–453
- Li X (2014) Functional magnetic resonance processing. Springer, Dordrecht
- Ozaki T (2012) Time series modeling of neuroscience data. Chapman & Hall/CRC Interdisciplinary Statistics
- Poldrack RA et al (2011) Handbook of functional MRI data analysis., Cambridge University Press
- Riera J, Yamashita O, Kawashima R, Sadato N, Okada T, Ozaki T (2004) fMRI activation maps based on the NN-ARX model. *Neuroimage* 23:680–697

networks. STEPS simulates such systems to a high level of detail by supporting complex morphology, stochastic kinetics, spatial concentration gradients, and diffusion. For reasons of efficiency STEPS employs the subvolume discretization approach based on Gillespie's stochastic simulation algorithm (Gillespie 1977), rather than particle-tracking methods.

Since version 2.0 STEPS also supports accurate computation of local membrane potentials Hepburn et al. (2013). Tight integration with the reaction-diffusion calculations allows detailed, accurate, and relatively efficient coupling between the molecular and the electrical components of cell signaling.

Binaries and source code are released under the GNU General Public License (version 3) and are available at <http://steps.sourceforge.net>.

Statistical Significance

► Significance Evaluation

STDP

► Spike-Timing Dependent Plasticity, Learning Rules

STEPS: STochastic Engine for Pathway Simulation

Iain Hepburn
Computational Neuroscience Unit, Okinawa Institute of Science and Technology, Onna-son, Okinawa, Japan
Theoretical Neurobiology, University of Antwerp, Antwerp, Belgium

Definition

STEPS (Hepburn et al. 2012) is a molecular simulator designed to simulate neuronal signaling pathways in dendrites and around synapses but can also be applied to other biochemical

Detailed Description

Python Interface

STEPS takes advantage of the benefits of a Python interface (Wils and De Schutter 2009) such as flexibility, easy integration with analysis tools, and even potentially other neuroscience software, yet the background computations are coded in C++ for high efficiency.

Biochemical Reactions

At the core of STEPS capabilities is the simulation of biochemical reactions. STEPS takes into account the inherent probabilistic nature of molecular interactions in small cellular volumes by solving reactions using a variant of Gillespie's stochastic simulation algorithm (Gillespie 1977), although deterministic solutions are also available. STEPS supports the Systems Biology Markup Language (Hucka et al. 2003) to aid biochemical model development.

Complex Morphology

A standout feature for STEPS over many other stochastic reaction-diffusion simulators is the support for complex cellular boundaries (Fig. 1) that have been shown to play an important role in neuronal signaling systems themselves (Santamaria et al. 2006).

STEPS: STochastic Engine for Pathway Simulation,

Fig. 1 Realistic morphology supported in STEPS. A section of spiny dendrite reconstructed from a surface triangular mesh available at <http://synapses.clm.utexas.edu/anatomy/Ca1pyrmd/radiatum/K24/K24.stm>. The tetrahedral mesh allows very accurate morphological resolution. © Hepburn et al. 2012; licensee BioMed Central Ltd

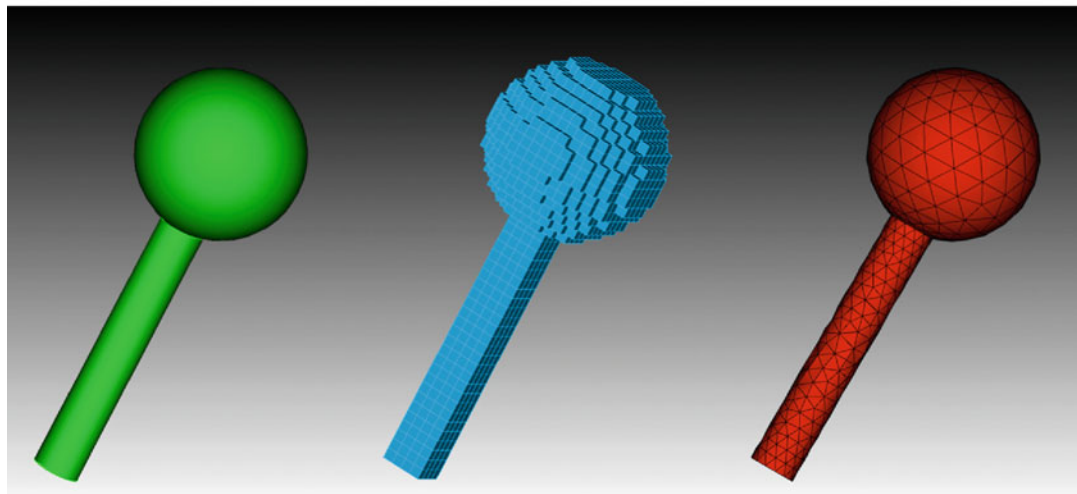
**a****b****c****STEPS: STochastic Engine for Pathway Simulation,**

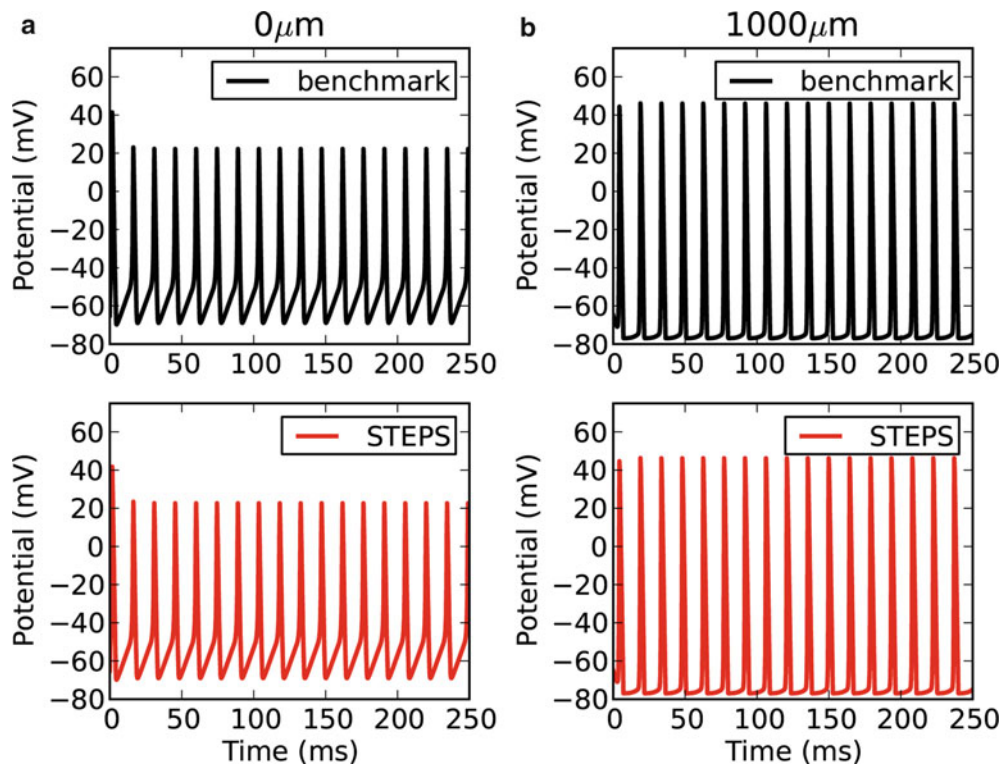
Fig. 2 High morphological accuracy with tetrahedral meshes. (a) Simple geometry consisting of a sphere connected to a cylinder represented by (b) a cubic mesh

and (c) a tetrahedral mesh, demonstrating that tetrahedral meshes are far more suitable for representing curved cellular membrane surfaces. © Hepburn et al. 2012; licensee BioMed Central Ltd

STEPS achieves this by supporting tetrahedral volume discretizations that allow very close approximations to curved surfaces and therefore true cellular morphology (Hepburn et al. 2012), far more so than cubic meshes (Fig. 2).

Spatial Gradients and Diffusion

Spatial concentration gradients and diffusion are known to be important considerations in neuronal signaling systems (Berridge et al. 2000; Augustine et al. 2003; Rizzuto and Pozzan 2006; Santamaria



STEPS: STochastic Engine for Pathway Simulation,
Fig. 3 Hodgkin-Huxley model in STEPS and comparison to NEURON benchmark (Rallpack3). STEPS 2.0 solves electrical potential on a tetrahedral mesh with a cylindrical boundary of 1 μm diameter and 1 mm length. A Hodgkin-Huxley implementation in STEPS with

et al. 2006), and these features are supported in STEPS. Complex multi-compartmental initial conditions can be achieved within the Python interface, with detailed spatial descriptions of the molecular players and their transporting channels. Diffusion of molecules can occur between groups of tetrahedrons comprising volumes such as cytoplasmic compartments and is also solved as a stochastic process. Since version 2.0 “surface diffusion” is also supported, which is a diffusion process transporting molecules between groups of triangles that form cellular membranes. This can be used to model mobility of molecular complexes within the membrane.

Validation

The STEPS developers place a firm emphasis on ensuring the accuracy of the software, and all

deterministic solutions (*lower panels*) demonstrates the high accuracy of the method in comparison to the cable equation solution benchmark in NEURON (*upper panels*) shown at both the 0 μm (a) and 1,000 μm (b) ends of the cylinder. © Hepburn et al. 2013

versions of STEPS are rigorously tested with an extensive set of reaction-diffusion systems against analytical or numerical solutions (Hepburn et al. 2012).

Membrane Potential and Voltage-Gated Channels

An extension to STEPS since version 2.0 allows accurate computation of electrical potential on tetrahedral meshes Hepburn et al. (2013). This approach ensures that potential is solved accurately in complex, irregular cellular morphologies where application of the 1-D cable equation would introduce errors (Lindsay et al. 2004), although comparisons to cable equation benchmarks in regular geometries are useful for validation by the Rallpacks (Fig. 3; Bhalla et al. 1992).

Tight integration occurs between local membrane excitability and reaction-diffusion computations, now extended to include voltage-gated channels and channel currents. All processes are solved stochastically for a detailed integration between the molecular systems and the electrical excitability of the cell, although deterministic solutions are also possible.

Cross-References

- ▶ [Biochemical Signaling Pathways and Diffusion: Overview](#)
- ▶ [Systems Biology Markup Language \(SBML\)](#)

References

- Augustine GJ, Santamaria F, Tanaka K (2003) Local calcium signaling in neurons. *Neuron* 40:331–346
- Berridge MJ, Lipp P, Bootman MD (2000) The versatility and universality of calcium signaling. *Nat Rev Mol Cell Bio* 1:11–21
- Bhalla US, Bilitch DH, Bower JM (1992) Rallpacks: a set of benchmarks for neuronal simulators. *Trends Neurosci* 15:453–458
- Gillespie DT (1977) Exact stochastic simulation of coupled chemical-reactions. *J Phys Chem-US* 81:2340–2361
- Hepburn I, Chen W, Wils S, De Schutter E (2012) STEPS: efficient simulation of stochastic reaction-diffusion models in realistic morphologies. *BMC Syst Biol* 6:36
- Hepburn I, Cannon R and De Schutter E (2013) Efficient calculation of the quasi-static electrical potential on a tetrahedral mesh and its implementation in STEPS. *Front Comput Neurosci* 7:129
- Hucka M, Finney A, Sauro HM, Bolouri H, Doyle JC, Kitano H, Arkin AP, Bornstein BJ, Bray D, Cornish-Bowden A, Cuellar AA, Dronov S, Gilles ED, Ginkel M, Gor V, Goryanin II, Hedley WJ, Hodgman TC, Hofmeyr JH, Hunter PJ, Juty NS, Kasberger JL, Kremling A, Kummer U, Le Novère N, Loew LM, Lucio D, Mendes P, Minch E, Mjolsness ED, Nakayama Y, Nelson MR, Nielsen PF, Sakurada T, Schaff JC, Shapiro BE, Shimizu TS, Spence HD, Stelling J, Takahashi K, Tomita M, Wagner J, Wang J (2003) The systems biology markup language (SBML): a medium for representation and exchange of biochemical network models. *Bioinformatics* 19:524–531
- Lindsay KA, Rosenberg JR, Tucker G (2004) From Maxwell's equations to the cable equation and beyond. *Prog Biophys Mol Bio* 85:71–116
- Rizzuto R, Pozzan T (2006) Microdomains of intracellular Ca^{2+} : molecular determinants and functional consequences. *Physiol Rev* 86:369–408
- Santamaria F, Wils S, De Schutter E, Augustine GJ (2006) Anomalous diffusion in Purkinje cell dendrites caused by spines. *Neuron* 52:635–648
- Wils S, De Schutter E (2009) STEPS: modeling and simulating complex reaction-diffusion systems with Python. *Front Neuroinform* 3:15

Stereo Vision, Models of

Jenny Read
Institute of Neuroscience, Newcastle University,
Newcastle-upon-Tyne, UK

Synonyms

[Models of 3D vision; Models of stereopsis](#)

Definition

Due to the different location of the eyes in the head, objects at different distances from the observer project to slightly different locations in the two eyes. Stereo vision refers to the perception of depth based on these slight disparities between the images seen by the two eyes (Freeman 2009). This entry reviews models of stereo vision based on the real nervous systems. Stereo vision algorithms have also been developed independently within the machine vision literature, sometimes biologically inspired, but these are not within the scope of this entry.

Detailed Description

Stereo vision has two main steps: (1) extracting disparity from the retinal images and (2) perceiving depth structure from disparity. Although psychophysics experiments have probed both aspects, much more is known about the neuronal mechanisms supporting the extraction of disparity than about how and where in the brain disparity is converted into a perception of depth. This

entry therefore concentrates on the first step. It seems that binocular disparity is initially encoded in the primary visual cortex (V1), which therefore acts as the “cyclopean retina” (Julesz 1971), that is, the first neural area which is able to detect features based purely on the differences between the two eyes images. There has been much work in recent years on how to model the response of disparity-selective neurons in V1 and how to decode this population activity in order to arrive at an estimate of the disparity at each point in the visual scene. In this entry, I aim to review this work.

Extracting Disparity from the Retinal Images

In primates, the first processing supporting specifically stereo vision is believed to occur in the primary visual cortex (V1). V1 is the first visual area to contain the neurons which receive inputs from both eyes and to be tuned to binocular disparity (Poggio et al. 1985). The most influential model of disparity tuning in V1 is the stereo energy model, put forward by Izumi Ohzawa et al. (1990) and based in turn on similar models in the motion literature (Adelson and Bergen 1985).

Stereo Energy Model: Basic Unit

The basic idea behind the stereo energy model is a binocular neuron with a receptive field in each eye (Fig. 1). The input from each eye depends on the inner product of each eye’s image with the

corresponding receptive field. For example, the input from the left eye is

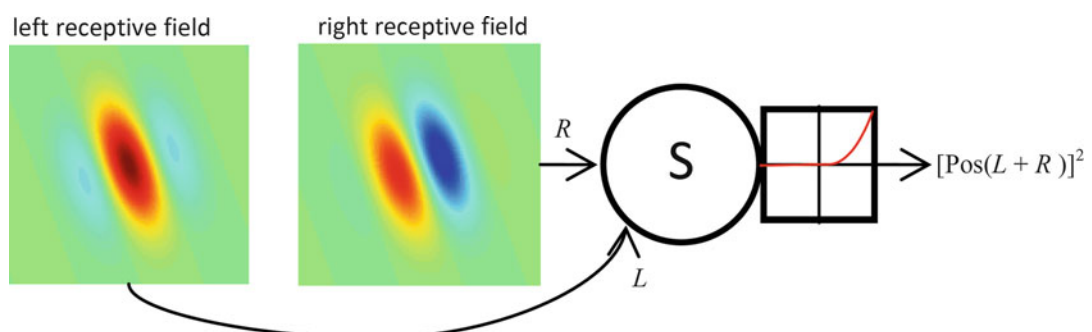
$$L = \int_{\text{retina}} dx dy I_L(x, y) \rho_L(x, y)$$

The function $I_L(x, y)$ represents the retinal image in the left retina, with luminance expressed relative to the mean, e.g., +1 = white, -1 = black, and 0 = gray. The function $\rho_L(x, y)$ represents the classical receptive field in the left retina, with 0 = no response (i.e., areas of the retina that are outside the receptive field), positive values corresponding to ON regions (areas where light stimulation tends to increase the cell’s firing rate and dark suppresses it), and negative values to OFF regions (where dark features tend to increase the cell’s firing and light suppresses it).

The energy model assumes that inputs from each eye are summed linearly. If the result is negative, the neuron is inhibited and does not fire. If positive, the neuron fires at a rate proportional to the square of the inputs:

$$S = [\text{Pos}(L + R)]^2 \quad (1)$$

where the notation $\text{Pos}(x)$ means half-wave rectification: $\text{Pos}(x) = x$ when $x > 0$, and $\text{Pos}(x) = 0$ otherwise. This model neuron is tuned to disparity both in monocularly visible features, e.g., the bar stimuli used in Ohzawa et al. (1990) and also in “cyclopean” stimuli such as dynamic random-



Stereo Vision, Models of, Fig. 1 Basic unit of the stereo energy model, after Ohzawa (1998). The graph on the right represents the squaring output nonlinearity. ON and OFF subregions of the receptive fields are shown in

red and blue, respectively. The receptive fields have the same orientation and spatial frequency but different phase. This cell would therefore be tuned to nonzero disparity

dot patterns (Julesz 1971). Cyclopean stimuli contain features such as depth edges which are not visible monocularly but are revealed only by comparing the two eyes' images. A detailed analysis shows that the cyclopean disparity tuning is due to the output nonlinearity (Read 2005). A unit which simply summed left and right inputs linearly ($L+R$) would be tuned to the disparity of a bar stimulus, but only as a side-effect of its tuning to the position of monocular features. It would respond equally well, on average, to broadband noise images with any disparity. Thus, a nonlinearity is essential to produce cyclopean disparity tuning, i.e., to ensure that the cell responds more on average to broadband noise images with its preferred disparity. The threshold-and-squaring nonlinearity in Eq. 1 is used in many models of V1 neurons because it describes their responses well. However, from a mathematical point of view, almost any nonlinearity would suffice to produce cyclopean disparity tuning.

The receptive fields are often represented by Gabor functions. Empirically, the spatial frequency and orientation tuning is similar between the eyes (Bridge and Cumming 2001; Read and Cumming 2003) and is usually modeled as being identical.

Position and Phase Disparity

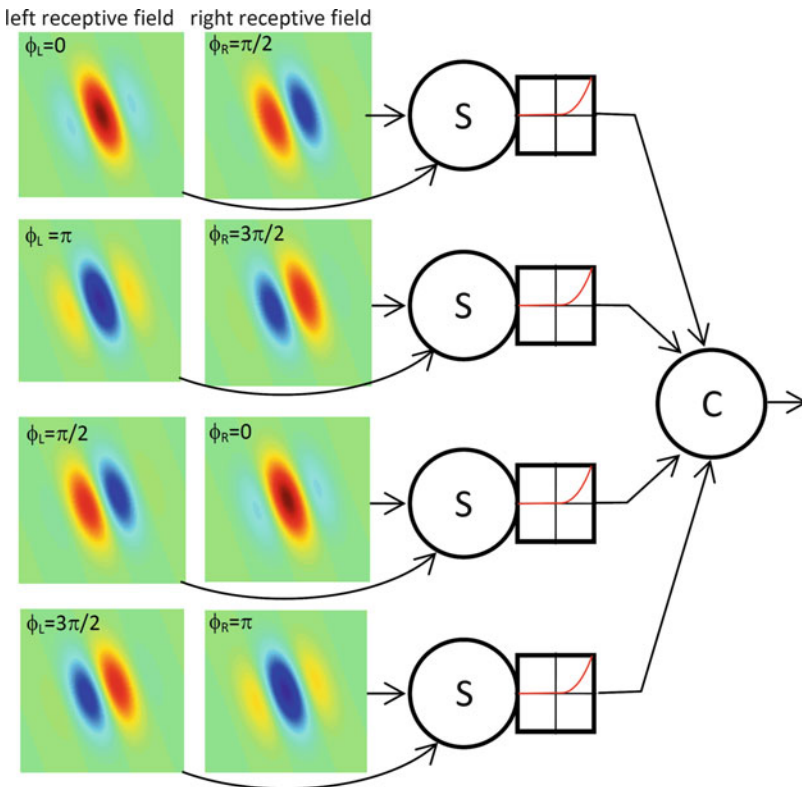
The spatial location and phase (i.e., the location of ON and OFF subregions) of the two receptive fields may vary. These determine the preferred disparity of the unit. Position disparity shifts the disparity curve without altering its shape; phase disparity alters the shape. A phase disparity of 0 produces a curve which is symmetrical about a central peak, known as tuned excitatory. A phase disparity of π inverts this to give a curve with a central trough (tuned inhibitory). A phase disparity of $\pm\pi/2$ produces odd-symmetric curves with equally large peaks and troughs. Several models have been built using pure phase disparity (Sanger 1988; Fleet et al. 1991; Qian 1994; Qian and Mikaelian 2000). However, V1 contains cells with both position and phase disparity (Anzai et al. 1997; Prince et al. 2002). Several models therefore incorporate both position and phase (Chen and Qian 2004; Read and Cumming 2007).

Complex Cells

The unit in Eq. 1 is a simple cell, in that it is tuned to the phase of a grating stimulus (Movshon et al. 1978a). To build a complex cell, which is insensitive to grating phase (Hubel and Wiesel 1962; Movshon et al. 1978b), we can sum many such units with different receptive-field phases (Qian and Zhu 1997). A common computational shortcut is to sum just four such units, whose receptive fields differ in phase by multiples of $\pi/2$ (Fig. 2). This produces a complex cell whose response is perfectly independent of grating phase. Note that this difference in phase must not be confused with the phase disparity discussed above. Phase disparity refers to a difference between the left- and right-eye receptive fields of a given energy-model unit ($\phi_R - \phi_L$ for each unit in Fig. 2). Here, we are talking about a difference in phase between receptive fields of different units, in the same eye (the four different ϕ_L in Fig. 2).

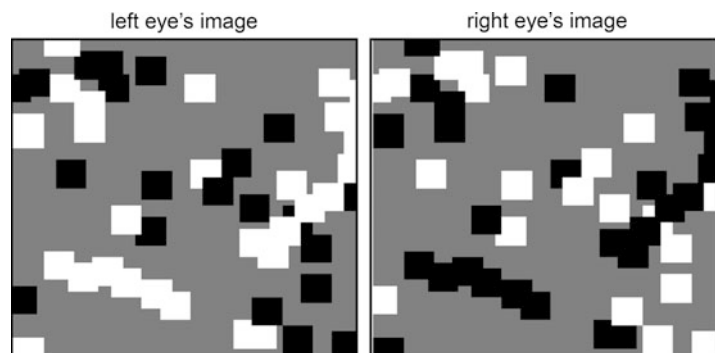
Modifications of the Energy Model

Several modifications have been proposed to the original energy model outlined above. One problem with the original energy model is that it responds equally strongly to disparity in anticorrelated random-dot patterns. These are nonphysical stimuli in which one eye's image is the photographic negative of the other (Fig. 3). This manipulation all but destroys depth perception (Cogan et al. 1993; Cumming et al. 1998; Read and Eagle 2000). Since this corresponds to changing the sign of I_R relative to I_L , it simply inverts the disparity tuning of an energy-model unit (Eq. 1). However, the response of real V1 neurons is attenuated as well as inverted (Cumming and Parker 1997). To capture the attenuation, Read et al. (2002) proposed thresholding the inner products L and R before summing them in Eq. 1. A similar approach was also proposed by Tanaka and Ohzawa (2006) to explain second-order stereopsis. Lippert and Wagner (2001) proposed changing the squaring nonlinearity. Adding an expansive nonlinearity to tuned-excitatory cells, or a compressive nonlinearity to tuned-inhibitory cells, can produce the desired effect. Haefner and Cumming



Stereo Vision, Models of, Fig. 2 Stereo energy-model complex cell, after Ohzawa (1998). The complex cell C represents the summed output of 4 of the basic units shown in Fig. 1, with different phases ϕ as labeled. The top two units have receptive fields which are the opposites of one another (π out of phase). This has the effect of removing the threshold before the squaring. To see why, let us call the output of the top S cell $[Pos(L_1 + R_1)]^2$. This is $(L_1 + R_1)^2$ when $(L_1 + R_1) > 0$, and 0 otherwise. Since

the second S cell has the same RFs, only inverted, its output will be $[Pos(-L_1 - R_1)]^2$. This is $(L_1 + R_1)^2$ when $(L_1 + R_1) \leq 0$, and 0 otherwise. Together, the sum of the two S cells is therefore $(L_1 + R_1)^2$. The bottom pair of cells is $\pi/2$ out of phase with the top pair, an arrangement known as *in quadrature*. This makes the response of the complex cell independent of the phase of the stimulus, essentially due to the trigonometric identity $\cos^2 + \sin^2 = 1$



Stereo Vision, Models of, Fig. 3 Anticorrelated random-dot stereogram. Note that black dots in the left eye are white in the right, and vice versa

(2008) showed that a similar approach captures the response of V1 cells to a wide range of nonphysical stimuli. Samonds et al. (2013) incorporated recurrent connections within V1 to account for the temporal dynamics of disparity tuning, as well as the attenuated response to anticorrelated images.

All these versions of the energy model predict a strong relationship between a cell's preferred orientation with grating stimuli and its tuning to 2D disparity. Binocular disparity is in principle 2D since the two eyes' images can be offset both horizontally and vertically, although in normal viewing the horizontal component is much larger (Read et al. 2009). The energy model predicts that cells should be more sensitive to disparities perpendicular to their preferred orientation than to those parallel to it. This prediction is borne out in the peripheral visual field in monkey (Durand et al. 2007) and in cat (Sasaki et al. 2010) and represents another success for the energy model. Matthews et al. (2003) exploited this property of the energy model, along with the radial bias of preferred orientations in the visual cortex, in order to develop a model of depth perception from vertical disparity. However, in the central visual field, Cumming (2002) reported that V1 neurons tend to be more sensitive to vertical than to horizontal disparity, irrespective of their orientation. One way to modify the energy model to account for this property is to include multiple subunits scattered more widely horizontally than vertically (Read and Cumming 2004).

The Energy Model and Time

The original energy model included no dependence on time. A more realistic model would include receptive fields whose response depends on time as well as on spatial location. This is important for capturing effects such as our poor temporal resolution for disparity (Norcia and Tyler 1984) or the Pulfrich illusion (Morgan 1976). Qian and Andersen (1997) were the first to modify the energy model to include time. Their model is tuned to both direction and disparity, which is relatively unusual experimentally: many V1 neurons are tuned to disparity but not direction (Read and Cumming 2005). Additionally,

in many V1 neurons, interocular delay simply reduces the amplitude of disparity tuning without shifting the preferred disparity (Read and Cumming 2005). It is difficult to reconcile this with the temporally band-pass tuning that V1 neurons typically show to luminance, i.e., they respond better to flickering than to constant stimuli. If one simply adds temporally band-pass receptive fields to the energy model, the model predicts that disparity tuning will invert for certain interocular delays. This is rarely observed (Read and Cumming 2005). Accordingly, work remains to be done on producing a model which captures the disparity response of real V1 neurons in the time domain.

Solving the Correspondence Problem

V1 cells are local, seeing only a small region of each retina. They respond to "false matches," image features which look similar but are caused by different objects in space, as well as to corresponding views of the same object. To disambiguate these, it is necessary to solve the "correspondence problem," correctly matching up image features in both eyes' images (Ohzawa 1998). This process is not completed in V1. Anticorrelated stereograms are one piece of evidence for this. As noted, V1 cells continue to respond to these nonphysical stimuli, albeit with attenuation, whereas cortical areas further down the processing pathway, for example, IT, do not (Janssen et al. 2003).

Models of stereo correspondence predate detailed knowledge of disparity encoding in V1 (Marr and Poggio 1979; Pollard et al. 1985). More recently, modelers have sought to understand how the correspondence problem could be solved by appropriately combining populations of V1-like neurons (Qian 1994, 1997).

One approach is to consider a population of cells which differ only in their tuning to disparity and take the stimulus disparity to be the preferred disparity of the maximally responding V1 cell (Qian 1994). However, often this will not be the correct answer, for two main reasons. First, the energy model is not sensitive to the precise arrangement of luminance within the receptive field; this information is lost when the inner

product is computed (Eq. 1), and its response depends on image contrast. Therefore, an energy-model unit will respond well to a false match which happens to stimulate the left and right receptive fields strongly, even if the image within each receptive field is quite different. To overcome these problems, it helps first to normalize out the cell's response to contrast (Sanger 1988; Read and Cumming 2006; Read 2010), e.g.:

$$C = \frac{2LR}{L^2 + R^2} \quad (2)$$

Such divisive normalization has been found in many brain areas and is so widespread that it has been proposed as a canonical computation of the cortex (Carandini and Heeger 2012). In the present case, the division transforms unnormalized energy, similar to a cross-correlation function (Qian and Zhu 1997), to a normalized correlation, bounded between -1 and $+1$. Now, the preferred disparity of the maximally responding C unit is guaranteed to be the correct stimulus disparity, if the stimulus disparity is exactly constant over the cells' receptive fields (Read and Cumming 2007). However, for more realistic situations, where disparity varies across the image, this approach too can fail.

Greater robustness is obtained by expanding the population under consideration to include cells tuned to a range of orientations and spatial frequencies/spatial scales as well as to a range of disparities. Fleet and colleagues (Fleet 1994; Fleet et al. 1996) proposed a linear pooling of neuronal responses across orientations and scales. Allenmark and Read (2011) showed that by pooling across orientations and spatial frequencies and then normalizing as in Eq. 2, one effectively computes the cross-correlation of the left and right retinal image patches. This linked the physiologically based stereo energy model to a class of more abstract models based on windowed cross-correlation of the retinal images, which had successfully captured several aspects of human vision (Tyler 1974, 1975, 1978; Banks et al. 2004; Nienborg et al. 2004, 2005; Filippini and Banks 2009).

Tsai and Victor (2003) used a template-matching approach pioneered in this area by Lehky and Sejnowski (1990). Their population includes neurons tuned to a range of spatial frequency and phase disparities. They compute the mean response of this population to "template" noise stimuli with uniform disparity. The disparity in any given stimulus is taken to be that of the template which best matches the population response. Their model also allows for the perception of *transparency* (multiple planes at different depths) when multiple templates match similarly well, capturing several aspects of human perception (McKee and Verghese 2002). Other aspects of transparency appear to require excitatory and inhibitory interactions between disparity-tuned neurons (Tsirlin et al. 2012)

Monocular Occlusions

A feature of binocular vision first studied by Leonardo da Vinci is that some image features may be visible to only one eye. These monocular occlusions present a special challenge for establishing correspondence. A few biologically inspired models suggest how these regions may be handled in the brain (Watanabe and Fukushima 1999; Hayashi et al. 2004; Assee and Qian 2007).

Perceiving Depth Structure from Disparity

Once the stereo correspondence problem has been solved, we have a "disparity map" specifying image disparity at every point in the visual field. This must then be converted into a perception of depth. Relative depth (i.e., "object A is in front of object B") can be deduced immediately from the relative disparity between them. Humans are much more sensitive to the relative disparity between objects or surfaces than to the absolute disparity of an isolated object (Westheimer 1979; Parker 2007).

Further evidence that neurons in the primary visual cortex (V1) do not directly support depth perception is provided by the fact that their response is determined by the absolute disparity of the stimulus within their receptive field, not by the disparity relative to other objects in the scene (Cumming and Parker 2000). The extraction of

relative disparity appears to begin in the cortical area V2, where neurons that are found are sensitive to relative disparity and are specifically tuned for disparity edges (von der Heydt et al. 2000; Thomas et al. 2002; Bredfeldt and Cumming 2006). These neurons' responses can be modeled by combining the output of different energy-model units (Bredfeldt et al. 2009).

For metric depth (i.e., "object A is 10 cm in front of object B"), disparity must be calibrated by a knowledge of the eye position. In theory, this can be obtained from extra-retinal signals (proprioception, efference copy) or from purely retinal signals if 2D disparity is available. As noted above, disparity in natural viewing is overwhelmingly horizontal, but vertical disparities also occur, in a pattern which is dependent on the eye position and largely independent of the scene viewed. In theory, therefore, the eye position can be recovered from the 2D disparity map (Longuet-Higgins 1982). There is psychophysical evidence that vertical disparity is indeed detected by the human visual system and used to guide perception (Rogers and Bradshaw 1993, 1995; Garding et al. 1995; Backus et al. 1999). However, little is known about the underlying neuronal mechanisms or the cortical areas involved. Detailed neuronally based models have therefore not been constructed.

Cross-References

► Large-Scale Neural Networks: Vision

References

- Adelson EH, Bergen JR (1985) Spatiotemporal energy models for the perception of motion. *J Opt Soc Am A* 2(2):284–299
- Allenmark F, Read JCA (2011) Spatial stereoresolution for depth corrugations may be set in primary visual cortex. *PLoS Comput Biol* 7(8):e1002142
- Anzai A, Ohzawa I, Freeman RD (1997) Neural mechanisms underlying binocular fusion and stereopsis: position vs. phase. *Proc Natl Acad Sci U S A* 94:5438–5443
- Assee A, Qian N (2007) Solving da Vinci stereopsis with depth-edge-selective V2 cells. *Vision Res* 47(20):2585–2602
- Backus BT, Banks MS, van Ee R, Crowell JA (1999) Horizontal and vertical disparity, eye position, and stereoscopic slant perception. *Vision Res* 39(6):1143–1170
- Banks MS, Gepshtein S, Landy MS (2004) Why is spatial stereoresolution so low? *J Neurosci* 24(9):2077–2089
- Bredfeldt CE, Cumming BG (2006) A simple account of cyclopean edge responses in macaque V2. *J Neurosci* 26(29):7581–7596
- Bredfeldt CE, Read JC, Cumming BG (2009) A quantitative explanation of responses to disparity defined edges in macaque V2. *J Neurophysiol* 101(2):701–713
- Bridge H, Cumming BG (2001) Responses of macaque V1 neurons to binocular orientation differences. *J Neurosci* 21(18):7293–7302
- Carandini M, Heeger DJ (2012) Normalization as a canonical neural computation. *Nat Rev Neurosci* 13(1):51–62
- Chen Y, Qian N (2004) A coarse-to-fine disparity energy model with both phase-shift and position-shift receptive field mechanisms. *Neural Comput* 16(8):1545–1577
- Cogan AI, Lomakin AJ, Rossi AF (1993) Depth in anticorrelated stereograms: effects of spatial density and interocular delay. *Vision Res* 33(14):1959–1975
- Cumming BG (2002) An unexpected specialization for horizontal disparity in primate primary visual cortex. *Nature* 418(6898):633–636
- Cumming BG, Parker AJ (1997) Responses of primary visual cortical neurons to binocular disparity without depth perception. *Nature* 389:280–283
- Cumming B, Parker A (2000) Local disparity not perceived depth is signaled by binocular neurons in cortical area V1 of the Macaque. *J Neurosci* 20(12):4758–4767
- Cumming BG, Shapiro SE, Parker A (1998) Disparity detection in anticorrelated stereograms. *Perception* 27(11):1367–1377
- Durand JB, Celebrini S, Trotter Y (2007) Neural bases of stereopsis across visual field of the alert macaque monkey. *Cereb Cortex* 17:1260–1273
- Filippini HR, Banks MS (2009) Limits of stereopsis explained by local cross-correlation. *J Vis* 9(1):8.1–18
- Fleet DJ (1994) Disparity from local weighted phase-correlation. *Systems, man, and cybernetics, 1994. 'Humans, information and technology', 1994 I.E. international conference on*, San Antonio
- Fleet DJ, Jepson AD, Jenkin MRM (1991) Phase-based disparity measurement. *Comput Vis Gr Image Process Image Underst* 53(2):198–210
- Fleet D, Wagner H, Heeger D (1996) Neural encoding of binocular disparity: energy models, position shifts and phase shifts. *Vision Res* 36:1839–1857
- Freeman R (2009) Binocular vision. In: Binder M, Hirokawa N, Windhorst U (eds) *Encyclopedia of neuroscience*. Springer, Berlin/Heidelberg
- Garding J, Porrill J, Mayhew JE, Frisby JP (1995) Stereopsis, vertical disparity and relief transformations. *Vision Res* 35(5):703–722

- Haefner RM, Cumming BG (2008) Adaptation to natural binocular disparities in primate V1 explained by a generalized energy model. *Neuron* 57(1):147–158
- Hayashi R, Maeda T, Shimojo S, Tachi S (2004) An integrative model of binocular vision: a stereo model utilizing interocularly unpaired points produces both depth and binocular rivalry. *Vision Res* 44(20):2367–2380
- Hubel DH, Wiesel TN (1962) Receptive fields binocular interaction and functional architecture in the cat's visual cortex. *J Physiol* 160:106
- Janssen P, Vogels R, Liu Y, Orban GA (2003) At least at the level of inferior temporal cortex, the stereo correspondence problem is solved. *Neuron* 37(4):693–701
- Julesz B (1971) Foundations of cyclopean perception. University of Chicago Press, Chicago
- Lehky SR, Sejnowski TJ (1990) Neural model of stereoacluity and depth interpolation based on a distributed representation of stereo disparity [published erratum appears in *J Neurosci* 1991;11(3): following Table of Contents]. *J Neurosci* 10(7): 2281–2299
- Lippert J, Wagner H (2001) A threshold explains modulation of neural responses to opposite-contrast stereograms. *Neuroreport* 12(15):3205–3208
- Longuet-Higgins HC (1982) The role of the vertical dimension in stereoscopic vision. *Perception* 11(4):377–386
- Marr D, Poggio T (1979) A computational theory of human stereo vision. *Proc R Soc Lond B Biol Sci* 204(1156):301–328
- Matthews N, Meng X, Xu P, Qian N (2003) A physiological theory of depth perception from vertical disparity. *Vision Res* 43(1):85–99
- McKee SP, Verghese P (2002) Stereo transparency and the disparity gradient limit. *Vision Res* 42(16):1963–1977
- Morgan MJ (1976) Pulfrich effect and the filling in of apparent motion. *Perception* 5(2):187–195
- Movshon J, Thompson I, Tolhurst DJ (1978a) Spatial summation in the receptive fields of simple cells in the cat's striate cortex. *J Physiol* 283:53–77
- Movshon JA, Thompson ID, Tolhurst DJ (1978b) Receptive field organization of complex cells in the cat's striate cortex. *J Physiol* 283:79–99
- Nienborg H, Bridge H, Parker AJ, Cumming BG (2004) Receptive field size in V1 neurons limits acuity for perceiving disparity modulation. *J Neurosci* 24(9):2065–2076
- Nienborg H, Bridge H, Parker AJ, Cumming BG (2005) Neuronal computation of disparity in V1 limits temporal resolution for detecting disparity modulation. *J Neurosci* 25(44):10207–10219
- Norcia AM, Tyler CW (1984) Temporal frequency limits for stereoscopic apparent motion processes. *Vision Res* 24(5):395–401
- Ohzawa I (1998) Mechanisms of stereoscopic vision: the disparity energy model. *Curr Opin Neurobiol* 8(4):509–515
- Ohzawa I, DeAngelis GC, Freeman RD (1990) Stereoscopic depth discrimination in the visual cortex: neurons ideally suited as disparity detectors. *Science* 249:1037–1041
- Parker AJ (2007) Binocular depth perception and the cerebral cortex. *Nat Rev Neurosci* 8(5):379–391
- Poggio GF, Motter BC, Squatrito S, Trotter Y (1985) Responses of neurons in visual cortex (V1 and V2) of the alert macaque to dynamic random-dot stereograms. *Vision Res* 25(3):397–406
- Pollard SB, Mayhew JE, Frisby JP (1985) PMF: a stereo correspondence algorithm using a disparity gradient limit. *Perception* 14(4):449–470
- Prince SJ, Cumming BG, Parker AJ (2002) Range and mechanism of encoding of horizontal disparity in macaque V1. *J Neurophysiol* 87(1):209–221
- Qian N (1994) Computing stereo disparity and motion with known binocular cell properties. *Neural Comput* 6:390–404
- Qian N (1997) Binocular disparity and the perception of depth. *Neuron* 18(3):359–368
- Qian N, Andersen RA (1997) A physiological model for motion-stereo integration and a unified explanation of Pulfrich-like phenomena. *Vision Res* 37(12): 1683–1698
- Qian N, Mikaelian S (2000) Relationship between phase and energy methods for disparity computation. *Neural Comput* 12(2):279–292
- Qian N, Zhu Y (1997) Physiological computation of binocular disparity. *Vision Res* 37(13): 1811–1827
- Read JCA (2005) Early computational processing in binocular vision and depth perception. *Prog Biophys Mol Biol* 87:77–108
- Read JCA (2010) Vertical binocular disparity is encoded implicitly within a model neuronal population tuned to horizontal disparity and orientation. *PLoS Comput Biol* 6(4):e1000754
- Read JCA, Cumming BG (2003) Testing quantitative models of binocular disparity selectivity in primary visual cortex. *J Neurophysiol* 90(5):2795–2817
- Read JCA, Cumming BG (2004) Understanding the cortical specialization for horizontal disparity. *Neural Comput* 16:1983–2020
- Read JCA, Cumming BG (2005) The effect of interocular delay on disparity selective V1 neurons: relationship to stereoacluity and the Pulfrich effect. *J Neurophysiol* 94:1541–1553
- Read JCA, Cumming BG (2006) Does visual perception require vertical disparity detectors? *J Vis* 6(12): 1323–1355
- Read JCA, Cumming BG (2007) Sensors for impossible stimuli may solve the stereo correspondence problem. *Nat Neurosci* 10(10):1322–1328
- Read JCA, Eagle RA (2000) Reversed stereo depth and motion direction with anti-correlated stimuli. *Vision Res* 40(24):3345–3358

- Read JCA, Parker AJ, Cumming BG (2002) A simple model accounts for the reduced response of disparity-tuned V1 neurons to anti-correlated images. *Vis Neurosci* 19:735–753
- Read JCA, Phillipson GP, Glennerster A (2009) Latitude and longitude vertical disparities. *J Vis* 9(13):11.1–37
- Rogers BJ, Bradshaw MF (1993) Vertical disparities, differential perspective and binocular stereopsis. *Nature* 361(6409):253–255
- Rogers BJ, Bradshaw MF (1995) Disparity scaling and the perception of frontoparallel surfaces. *Perception* 24(2):155–179
- Samonds JM, Potetz BR, Tyler CW, Lee TS (2013) Recurrent connectivity can account for the dynamics of disparity processing in v1. *J Neurosci* 33(7):2934–2946
- Sanger T (1988) Stereo disparity computation using Gabor filters. *Biol Cybern* 59:405–418
- Sasaki KS, Tabuchi Y, Ohzawa I (2010) Complex cells in the cat striate cortex have multiple disparity detectors in the three-dimensional binocular receptive fields. *J Neurosci* 30(41):13826–13837
- Tanaka H, Ohzawa I (2006) Neural basis for stereopsis from second-order contrast cues. *J Neurosci* 26(16):4370–4382
- Thomas OM, Cumming BG, Parker AJ (2002) A specialization for relative disparity in V2. *Nat Neurosci* 5(5):472–478
- Tsai JJ, Victor JD (2003) Reading a population code: a multi-scale neural model for representing binocular disparity. *Vision Res* 43(4):445–466
- Tsirlin I, Allison RS, Wilcox LM (2012) Perceptual asymmetry reveals neural substrates underlying stereoscopic transparency. *Vision Res* 54:1–11
- Tyler CW (1974) Depth perception in disparity gratings. *Nature* 251(5471):140–142
- Tyler CW (1975) Spatial organization of binocular disparity sensitivity. *Vision Res* 15(5):583–590
- Tyler CW (1978) Binocular cross-correlation in time and space. *Vision Res* 18(1):101–105
- von der Heydt R, Zhou H, Friedman HS (2000) Representation of stereoscopic edges in monkey visual cortex. *Vision Res* 40(15):1955–1967
- Watanabe O, Fukushima K (1999) Stereo algorithm that extracts a depth cue from interocularly unpaired points. *Neural Netw* 12(4–5):569–578
- Westheimer G (1979) Cooperative neural processes involved in stereoscopic acuity. *Exp Brain Res* 36(3):585–597

Steyn-Ross Model

- Down Under Neural Population Models

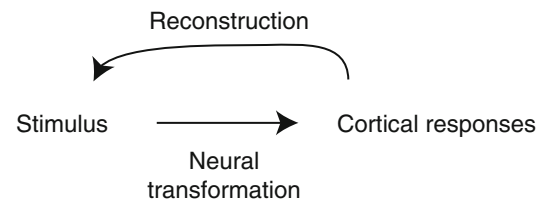
Stimulus Reconstruction from Cortical Responses

Nima Mesgarani

Department of Electrical Engineering,
The Fu Foundation School of Engineering
and Applied Science, Columbia University,
New York, NY, USA

Definition

Reconstruction is a technique used to recreate a stimulus from its corresponding neural responses. By projecting the cortical representation of stimulus in the neural space back to the physical domain where it is usually better understood, reconstruction provides a straightforward and direct method to study the stimulus features encoded by the population neural data. Reconstruction has also been used to decode the perceived or imagined stimuli from the measurements of brain activity.



Detailed Description

Background

Cortical neurons encode considerable details about stimuli which could be difficult to discern because of the complexity and diversity of cortical receptive fields. The typical approaches used to understand the cortical representation of stimuli include examining the distribution of tuning properties for a population of neurons (De Valois et al. 1982; Ferragamo et al. 1998; Woolley et al. 2005) and pre-stimulus time histogram

sorted with respect to selectivity to various stimulus parameters (Sachs et al. 1983; Mesgarani et al. 2008). Although useful, these methods are limited in their scope, especially when not all the relevant parameters of the neural space are understood and when dealing with complex stimuli that vary along numerous, possibly correlated dimensions. Stimulus reconstruction is an alternative for studying what aspects of the stimuli are encoded in the cortical responses and provide a direct comparison with the original signal.

Methods

Estimating the stimulus from responses can be done in various ways, including linear or nonlinear transformations applied to the population of neural data (Bialek et al. 1991; Rieke et al. 1995; Warland et al. 1997; Haag and Borst 1998; Stanley et al. 1999; Shpigelman et al. 2005; Mesgarani et al. 2009) or formulating this problem in a statistical inference framework (Pillow et al. 2005; Paninski et al. 2007).

Stimulus Statistics

It has been shown that imposing known stimulus structures and its prior distribution can significantly improve the accuracy of reconstruction (Mesgarani et al. 2009; Pillow et al. 2011; Ramirez et al. 2011). This is particularly useful if the reconstruction is used to approximate the best possible stimulus from cortical activity. However, if the reconstruction is used to examine stimulus features that are explicitly encoded in the neural data, inclusion of stimulus correlations may result in misleading conclusions. For example, if a correlated feature is not explicitly encoded in the neural data, it can still be reconstructed from its co-occurrence with another aspect of stimulus that is encoded [see Fig. 3 in (Mesgarani et al. 2009) for a simulation explaining this idea].

Applications

Stimulus reconstruction has been used in a variety of contexts, from decoding perceived or imagined information in the brain (Thirion et al. 2006; Naselaris et al. 2011; Pasley et al. 2012) to studying how the dynamic internal

state of an organism changes the population encoding of stimulus in the cortex (Ding and Simon 2012; Mesgarani and Chang 2012).

References

- Bialek W, Rieke F, de Ruyter van Steveninck RR, Warland D (1991) Reading a neural code. *Science* 252:1854–1857
- De Valois RL, Yund EW, Hepler N (1982) The orientation and direction selectivity of cells in macaque visual cortex. *Vision Res* 22:531–544
- Ding N, Simon JZ (2012) Emergence of neural encoding of auditory objects while listening to competing speakers. *Proc Natl Acad Sci* 109:11854–11859
- Ferragamo MJ, Haresign T, Simmons JA (1998) Frequency tuning, latencies, and responses to frequency-modulated sweeps in the inferior colliculus of the echolocating bat, *Eptesicus fuscus*. *J Comp Physiol A* 182:65–79
- Haag J, Borst A (1998) Active membrane properties and signal encoding in graded potential neurons. *J Neurosci* 18:7972–7986
- Mesgarani N, Chang EF (2012) Selective cortical representation of attended speaker in multi-talker speech perception. *Nature* 485:233–236
- Mesgarani N, David SV, Fritz JB, Shamma SA (2008) Phoneme representation and classification in primary auditory cortex. *J Acoust Soc Am* 123:899–909
- Mesgarani N, David SV, Fritz JB, Shamma SA (2009) Influence of context and behavior on stimulus reconstruction from neural activity in primary auditory cortex. *J Neurophysiol* 102:3329–3339
- Naselaris T, Kay KN, Nishimoto S, Gallant JL (2011) Encoding and decoding in fMRI. *Neuroimage* 56:400–410
- Paninski L, Pillow J, Lewi J (2007) Statistical models for neural encoding, decoding, and optimal stimulus design. *Prog Brain Res* 165:493–507
- Pasley BN, David SV, Mesgarani N et al (2012) Reconstructing speech from human auditory cortex. *PLoS Biol* 10(1):e1001251
- Pillow JW, Paninski L, Uzzell VJ et al (2005) Prediction and decoding of retinal ganglion cell responses with a probabilistic spiking model. *J Neurosci* 25:11003–11013
- Pillow JW, Ahmadian Y, Paninski L (2011) Model-based decoding, information estimation, and change-point detection techniques for multineuron spike trains. *Neural Comput* 23:1–45
- Ramirez AD, Ahmadian Y, Schumacher J et al (2011) Incorporating naturalistic correlation structure improves spectrogram reconstruction from neuronal activity in the songbird auditory midbrain. *J Neurosci* 31:3828–3842
- Rieke F, Bodnar DA, Bialek W (1995) Naturalistic stimuli increase the rate and efficiency of information

- transmission by primary auditory afferents. Proc Biol Sci 262:259–265
- Sachs MB, Voigt HF, Young ED (1983) Auditory nerve representation of vowels in background noise. J Neurophysiol 50:27
- Shpigelman L, Singer Y, Paz R, Vaadia E (2005) Spikernels: predicting arm movements by embedding population spike rate patterns in inner-product spaces. Neural Comput 17:671–690
- Stanley GB, Li FF, Dan Y (1999) Reconstruction of natural scenes from ensemble responses in the lateral geniculate nucleus. J Neurosci 19:8036–8042
- Thirion B, Duchesnay E, Hubbard E et al (2006) Inverse retinotopy: inferring the visual content of images from brain activation patterns. Neuroimage 33:1104–1116
- Warland DK, Reinagel P, Meister M (1997) Decoding visual information from a population of retinal ganglion cells. J Neurophysiol 78:2336–2350
- Woolley SM, Fremouw TE, Hsu A, Theunissen FE (2005) Tuning for spectro-temporal modulations as a mechanism for auditory discrimination of natural sounds. Nat Neurosci 8:1371–1379

Stimulus-Specific Adaptation, Models

Robert Mill
MRC Institute of Hearing Research,
Nottingham, UK

Definition

Stimulus-specific adaptation (SSA) refers to a reduction in neural activity due to the repeated presentation of a stimulus, which does not generalize to other stimuli (Ulanovsky et al. 2003). SSA is present in auditory cortex (Ulanovsky et al. 2003), thalamus (Antunes et al. 2010), and inferior colliculus (IC) (Malmierca et al. 2009), but not the cochlear nucleus (Ayala et al. 2013). SSA has attracted interest on account of its similarity to mismatch negativity (MMN) in human auditory evoked potentials (Nelken and Ulanovsky 2007; cf. Farley et al. 2010). Computer models of SSA aim to capture the main features of single and multiunit responses to sequences of stimuli containing rare, or novel, events.

Detailed Description

Measuring SSA

Several methods exist for measuring SSA. In the simplest case, one can measure the effect of one or more *conditioner tones* on the neural response to a *probe tone* with respect to some feature, e.g., frequency (Fig. 1a). Other studies measure the average adaptation to long patterns of tones (Fig. 1b). In this case, each tone in the sequence effectively serves as both a conditioner and a probe.

SSA is most commonly investigated using *oddball sequences*, in which a rare tone (*deviant*) is presented in the context of a common tone (*standard*) (Fig. 1c). Oddball sequences are typically presented twice, with the deviant and standard features exchanged on the second presentation. A *specificity index* (SI) provides a normalized measure of the degree of SSA:

$$SI = \frac{d_A - s_A + d_B - s_B}{d_A + s_A + d_B + s_B}$$

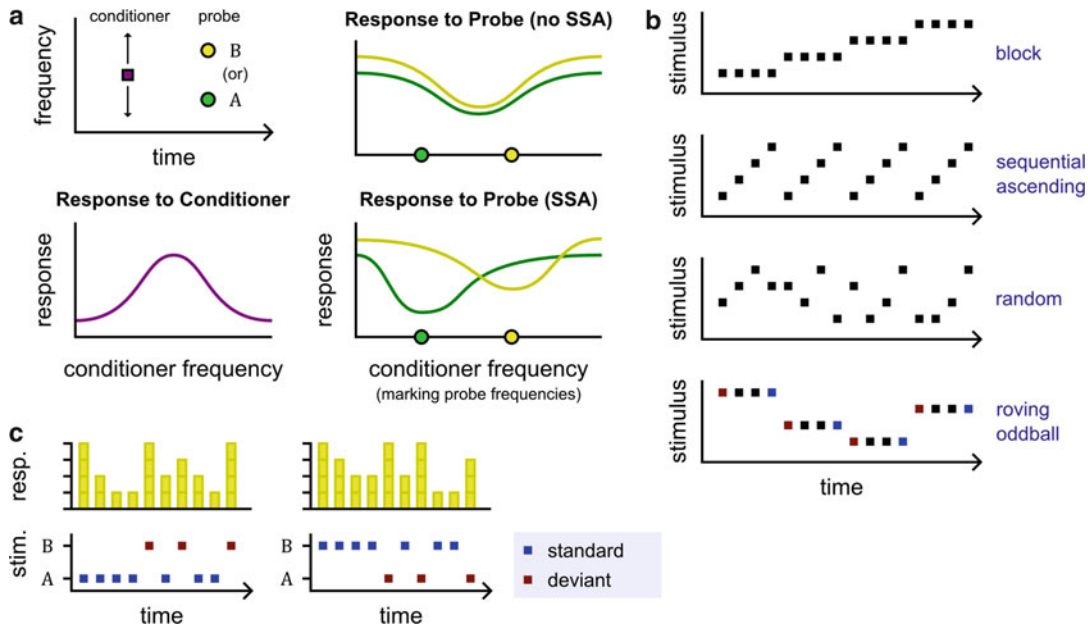
Here, s_X and d_X measure the activity evoked by tone X in the standard and deviant context, respectively. SSA is indicated when the SI significantly exceeds zero. Oddball sequences typically comprise several hundred tones.

Principal Results from SSA Studies

Most SSA studies use oddball sequences containing two frequencies and vary the frequency difference (Δf), the time difference between consecutive tones (Δt), and the probability of the deviant tone (p_{dev}). SI increases monotonically as:

- Δf increases
- Δt decreases
- p_{dev} decreases

How SSA elicited by other deviant features, such as intensity, duration, and amplitude modulation, should be interpreted remains a matter of contention.



Stimulus-Specific Adaptation, Models,

Fig. 1 Experiments used to explore SSA. (a) Cartoon showing how a conditioner tone (*purple*) affects the response to a probe tone (*yellow* and *green*). The adaptation of the probe may depend only on the response to the conditioner (no SSA, *top right*) or a combination of the probe and conditioner frequencies (SSA, *bottom right*) (Brosch and Schreiner 1997; Scholes et al. 2011). (b) Stimuli configurations used in other SSA experiments. The average response to a tone in the *block*, *sequential*,

Local History Models

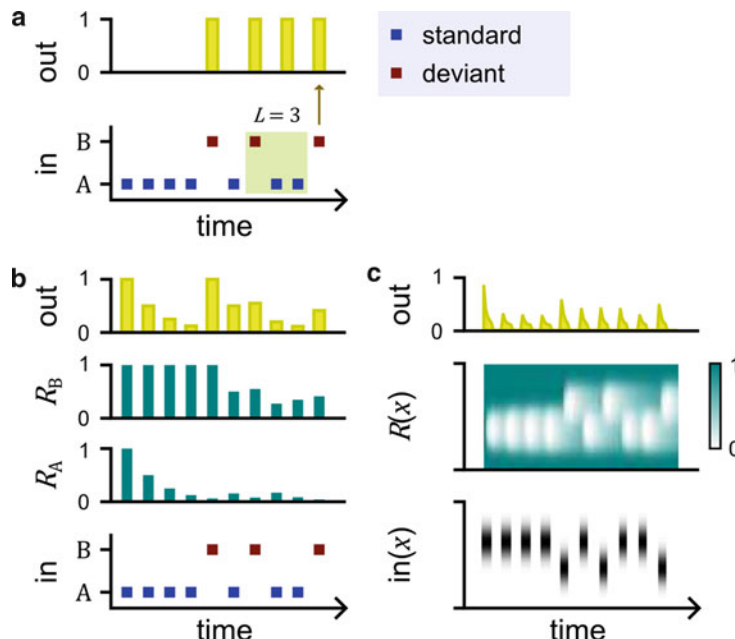
Local history models of SSA attempt to account for the response to a tone solely in terms of the tones preceding it (Ulanovsky et al. 2004). For instance, if a tone A presented in the context . . .ABAAX, then SSA neurons fire more vigorously when $X = B$ than when $X = A$. An explicit local history model stores recent tones in a finite memory of length L and responds only when this memory indicates that the incoming tone is deviant (Mill et al. 2011a). This type of model is illustrated in Fig. 2a for $L = 3$. Provided that A and B are confusable on the basis of their similarity, the model can account for the Δf and p_{dev} relations described above. However, the observation that more recent tones exert a stronger suppressive influence on the incoming tone lends greater support to a *decaying memory* model.

random configurations is smallest for the block stimulus and largest for the random stimulus (Pérez-González et al. 2005). In the *roving oddball* paradigm, the first and last tones are treated as standards and deviants, respectively (Bäuerle et al. 2011). (c) Schematic responses (*above*) to oddball stimuli (*below*). In the first presentation (*left*), tone B is the oddball. In the second presentation (*right*), tone A is the oddball. For these example sequences and measurements, SI ≈ 0.29

Decaying memory models assign to each stimulus X a resource, R_X , possibly corresponding to synaptic neurotransmitter (Taaseh et al. 2011). The activity elicited by X is then proportional to R_X . The resource decays following presentations of stimuli similar to X and undergoes a steady recovery in the meantime. A basic example is a model which, when presented with tone X , first responds with R_X and then updates for R_Y , $Y = \{A, B\}$, according to

$$\begin{aligned} R_Y &\leftarrow \alpha R_Y && \text{if } Y = X \\ R_Y &\leftarrow R_Y + \beta(1 - R_Y) && \text{if } Y \neq X. \end{aligned}$$

Figure 2b shows the output of this model using $\alpha = 0.5$, $\beta = 0.1$ for a short example oddball sequence. A model this simple can account for the p_{dev} relation.



Stimulus-Specific Adaptation, Models

Fig. 2 Output from simple SSA models. (a) In a two-tone oddball condition, a deviant response is generated to an incoming tone if it represents less than half of the items in a trailing memory of length $L = 3$. The computation of the deviant response to the last tone is highlighted in the figure (see Mill et al. 2011a). (b)

Response exemplifying a decaying memory model (see text). The top row shows the response; the middle rows show the resource state; the bottom row shows the stimulus pattern. (c) Response from the model described by Mill et al. (2012) ($SI \approx 0.04$). Inputs and resources are described in spatially continuous, rather than categorical, terms

In order to also explain the Δf relation, it must be modified so that similar stimuli either consume overlapping resources (Mill et al. 2011b, 2012; Taaseh et al. 2011) or are liable to be confused with each other (Mill et al. 2011a). Figure 2c shows an example output from the model described in Mill et al. (2012), in which resources, $R(x)$, are distributed along a continuous feature axis, x , and are consumed and recovered in continuous time. Inputs are modeled as pulses, separated by Δt in time and Δf in feature space.

Global History Models

Besides the short-term effects captured by a decaying memory model (~ 1 s), neurons exhibit additional decay components in their response to both standards and deviants that span longer time scales ($\sim 10\text{--}100$ s) (Ulanovsky et al. 2004; Zhao et al. 2011; Bäuerle et al. 2011; Pérez-González et al. 2012). Whereas

the depression of the thalamocortical synapses provide a plausible mechanism for the rapid time course (e.g., Ulanovsky et al. 2004), the biophysical mechanisms responsible for the slower time courses remain obscure.

Global dependence on the deviant probability, p_{dev} , is captured by a phenomenological regression model (Ulanovsky et al. 2004; Zhao et al. 2011), which fits the response to the n th tone according to the linear combination:

$$y_n = c_0 + c_1 M_n + c_2 p_{\text{dev}}$$

Here the coefficients c_0 , c_1 , and c_2 are free parameters, and M_n is a recent memory term computed using

$$M_n = \left(\frac{1}{\gamma} - 1 \right) \sum_{i=1}^{\infty} \gamma^i S_{n-i}$$

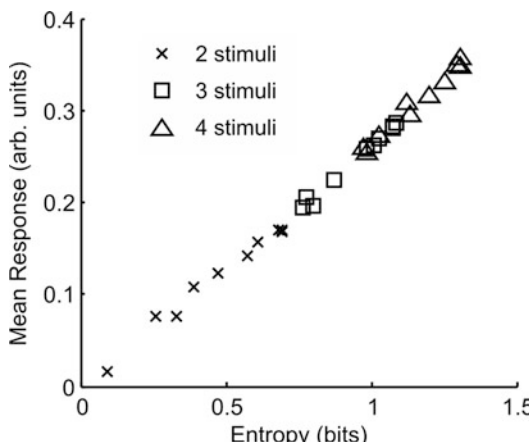
where γ is a decay parameter and $S_i = 1$ if the $(n - i)$ th tone identical to the n th tone and $S_i = 0$ otherwise.

Information Transmission

Ulanovsky et al. (2004) showed that auditory cortical responses to tones in an oddball sequence are proportional to their *unexpectedness*, defined in terms of the regression model described above. Mill et al. (2011a) reinforced this conclusion by demonstrating that a decaying memory model with rapid adaptation and slow recovery, when presented with a sequence containing multiple stimuli (e.g., $X \in \{X_1, X_2, \dots\}$), responds approximately in proportion to the stimulus entropy, i.e., $E\{-\ln P(X_i)\}$, provided that the stimuli adapt distinct channels (Fig. 3). SSA may thus constitute a mechanism to reduce redundancy in the neural signal as it ascends the auditory pathway (cf. Chechik et al. 2006).

Rarity Versus Novelty

SSA can be interpreted within the oddball paradigm as *novelty detection*: deviant stimuli are



Stimulus-Specific Adaptation, Models, Fig. 3 Decaying memory model response versus entropy. Mean response of the decaying memory model ($\alpha = 0.5$, $\beta = 0.1$; see “Local History Models”) to sequences containing 2 (oddball), 3, or 4 stimuli plotted against the entropy of the sequence. Note that the entropy of an oddball sequence in bits is $-p_{dev} \log_2 p_{dev} - (1-p_{dev})\log_2(1-p_{dev})$ (Adapted from Mill et al. (2011a))

conspicuous against the background of a common standard. This prompts a concern that SSA may reflect only rarity and not novelty per se (Fig. 4a). In response, researchers have devised a control condition, in which the deviant tone is presented among many standards, such that it is equally rare but otherwise unremarkable (see Fig. 4b) (Jacobsen and Schröger 2001; Farley et al. 2010; Taaseh et al. 2011).

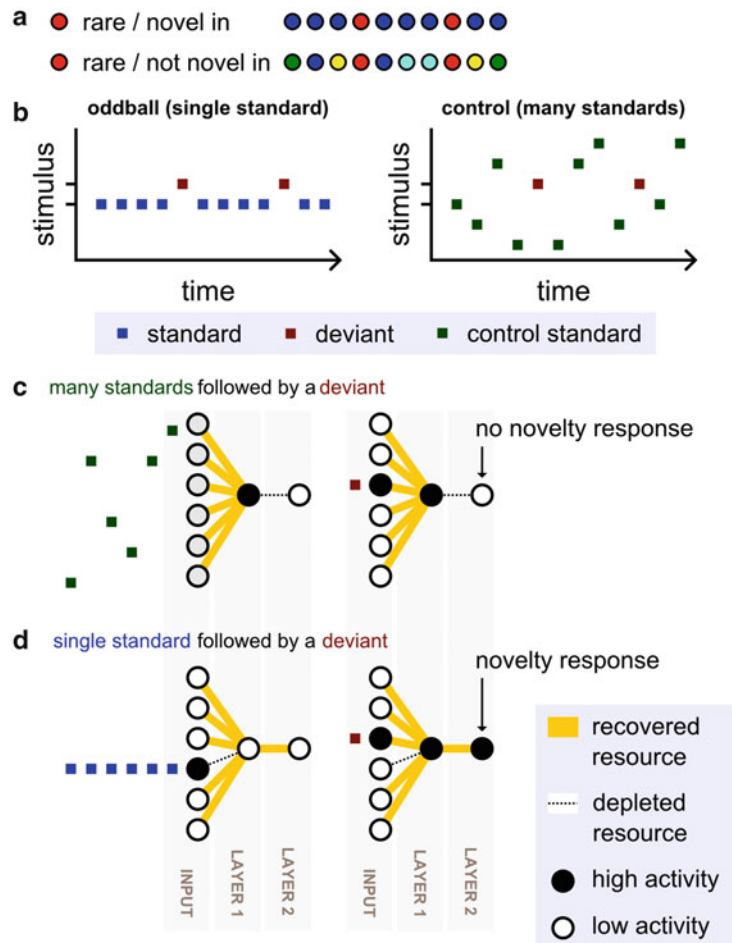
Single-cell recordings in auditory cortex have revealed both enhanced responses to stimuli presented in the single-standard context (Ulanovsky et al. 2003) and near-equal responses (Farley et al. 2010; Taaseh et al. 2011). This inconsistency has been attributed to differences in cross-adaptation resulting from the spacing of control standards. Moreover, an equal response in the two conditions fails to demonstrate insensitivity to novelty conclusively. Taaseh et al. (2011) show that a decaying memory model actually predicts appreciably smaller responses to deviants in the single-standard condition than in the many-standards condition. Consequently, an excess in the response to novel stimuli remains to be explained.

Mill et al. (2011b) have proposed a model containing two layers of adaptation in series that enhances responses to genuinely novel stimuli. The model is illustrated in Fig. 4c, d. In this model, adaptation to individual frequencies occurs at the first layer. The outputs from this layer are then subject to further adaptation at the second layer. When many standards are presented, the (representative) unit in the first layer is highly responsive (see “Information Transmission” above) and the unit in the second layer is adapted (Fig. 4c). Conversely, when a single standard is presented, the unit in the first layer undergoes adaptation, and the unit in the second layer recovers (Fig. 4d). Novelty responses are coded in the second layer.

Modulation of SSA by Inhibition

A convergence of depressing synapses conveying specific-stimulus signals suffices to explain many aspects of SSA (see above). However, recent

Stimulus-Specific Adaptation, Models,
Fig. 4 Control conditions and models of the novelty response. (a) Diagram contrasting rarity versus novelty. The *red* stimulus appears 20 % of the time but is only novel in the *top row*. (b) Illustration of the single-standard condition (*left*) and multiple-standard control condition (*right*). (c) Response of a two-layer model to multiple standards (*left*) followed by a deviant (*right*), which generates little or no novelty response. (d) Response of a two-layer model to a single standard (*left*) followed by a deviant (*right*), which generates a stronger novelty response (Mill et al. 2011b, Adapted from Fig. 2c, d)



studies have highlighted the contribution of inhibition in shaping the adaptation. Blocking inhibitory ($GABA_A$) receptors increases the responsiveness of IC neurons to both standards and deviants, but alters the overall response ratio such that the SI is smaller (Pérez-González et al. 2012). Furthermore, examining the difference between the poststimulus time histograms for deviant and standard tones reveals a subpopulation of cells that respond more vigorously to the standard than to the deviant after the stimulus onset. This tendency becomes more widespread following the application of the inhibitory blocker gabazine (Pérez-González and Malmierca 2012). Inhibition has to date assumed a marginal role in SSA modeling

(e.g., Mill et al. 2011b); it is clear, however, that inhibition strongly modulates SSA, and future detailed models must account for it.

References

- Antunes FM, Nelken I, Covey E, Malmierca MS (2010) Stimulus-specific adaptation in the auditory thalamus of the anesthetized rat. PLoS One 5(11):e14071
- Ayala YA, Pérez-González D, Duque D, Nelken I, Malmierca MS (2013) Frequency discrimination and stimulus deviance in the inferior colliculus and cochlear nucleus. Front Neural Circuits 6(119)
- Bäuerle P, von der Behrens W, Kössl M, Gaese BH (2011) Stimulus-specific adaptation in the gerbil primary auditory thalamus is the result of a fast frequency-specific habituation and is regulated by the corticofugal system. J Neurosci 31(26):9708–9722

- Brosch M, Schreiner CE (1997) Time course of forward masking tuning curves in cat primary auditory cortex. *J Neurophysiol* 77:923–943
- Chechik G, Anderson MJ, Bar-Yosef O, Young ED, Tishby N, Nelken I (2006) Reduction of information redundancy in the ascending auditory pathway. *Neuron* 51:358–368
- Farley BJ, Quirk MC, Doherty JJ, Christian EP (2010) Stimulus-specific adaptation in auditory cortex is an NMDA-independent process distinct from the sensory novelty encoded by the mismatch negativity. *J Neurosci* 30(49):16475–16484
- Jacobsen T, Schröger E (2001) Is there pre-attentive memory-based comparison of pitch? *Psychophysiol* 38:723–727
- Malmierca MS, Cristando S, Pérez-González D, Covey E (2009) Stimulus-specific adaptation in the inferior colliculus of the anesthetized rat. *J Neurosci* 29(17):5483–5493
- Mill R, Coath M, Wennekers T, Denham SL (2011a) Abstract stimulus-specific adaptation models. *Neural Comput* 23:435–476
- Mill R, Coath M, Wennekers T, Denham SL (2011b) A neurocomputational model of stimulus-specific adaptation to oddball and Markov sequences. *PLoS Comput Biol* 7(8):e1002117
- Mill R, Coath M, Wennekers T, Denham SL (2012) Characterising stimulus-specific adaptation using a multi-layer field model. *Brain Res* 1434:178–188
- Nelken I, Ulanovsky N (2007) Mismatch negativity and stimulus-specific adaptation in animal models. *J Psychophysiol* 21(3–4):214–223
- Pérez-González D, Malmierca MS (2012) Variability of the time course of stimulus-specific adaptation in the inferior colliculus. *Front Neural Circuits* 6(107)
- Pérez-González D, Malmierca MS, Covey E (2005) Novelty detector neurons in the mammalian auditory midbrain. *Eur J Neurosci* 22:2879–2885
- Pérez-González D, Hernández O, Covey E, Malmierca MS (2012) GABA_A-mediated inhibition modulates stimulus-specific adaptation in the inferior colliculus. *PLoS One* 7(3):e34297
- Scholes C, Palmer AR, Sumner CJ (2011) Forward suppression in the auditory cortex is frequency-specific. *Eur J Neurosci* 33:1240–1251
- Taaseh N, Yaron A, Nelken I (2011) Stimulus-specific adaptation and deviance detection in the rat auditory cortex. *PLoS One* 6(8):e23369
- Ulanovsky N, Las L, Nelken I (2003) Processing of low-probability sounds by cortical neurons. *Nat Neurosci* 6(4):391–398
- Ulanovsky N, Las L, Farkas D, Nelken I (2004) Multiple time scales of adaptation in auditory cortex neurons. *J Neurosci* 24(46):10440–10453
- Zhao L, Liu L, Feng L, Hong B (2011) Stimulus-specific adaptation and its dynamics in the inferior colliculus of rat. *Neuroscience* 181:163–174

Stimulus-Specific Information

Michael Wehr

Institute of Neuroscience, University of Oregon,
Eugene, OR, USA

Definition

Stimulus-specific information is an information-theoretic measure of how much information the responses of a neuron convey about a particular stimulus. It is closely related to specific information, which is a measure of the information that a given neuronal response provides about which stimuli were presented. The stimulus-specific information is the average of the specific information across all the responses that occur when a particular stimulus is presented.

Detailed Description

Stimulus-specific information (SSI) (Butts 2003; Butts and Goldman 2006) is typically computed for sensory neurons that selectively respond to sensory stimuli, such that their selectivity can be characterized by a tuning curve or receptive field. For example, auditory neurons are typically tuned to sound frequency. SSI is given by

$$SSI(f) = \sum_r p(r|f) i_{sp}(r)$$

where f is sound frequency (or, equivalently, any stimulus dimension, such as orientation), r is the neuronal response, and i_{sp} is the specific information (DeWeese and Meister 1999), which is given by

$$i_{sp} = -\sum_f p(f) \log_2 p(f) + \sum_f p(f|r) \log_2 p(f|r)$$

Note that $p(f) \log_2 p(f)$ is the entropy $H(f)$, so the specific information can also be written as

$$i_{sp} = H(f) - H(f|r)$$

Here, $H(f)$ is the entropy of the stimulus ensemble, which can also be thought of as the

number of possible stimuli and therefore also as the amount of uncertainty about the stimulus. $H(f|r)$ is this uncertainty given that a particular response r occurred. Thus, $i_{sp}(r)$ measures the reduction in uncertainty about the stimulus that is provided by response r or, in other words, the amount of information provided by the response r . Note that the choice for how to quantify the neuronal response r is not specified. For example, it could be firing rate, spike latency, or any arbitrary temporal code.

$SSI(f)$ is the i_{sp} averaged over all the responses r that occur when stimulus f is presented. It therefore represents how much information a neuron provides, on average, about that stimulus.

An important detail to remember when computing SSI is that information measures are subject to bias. This bias comes from the limited number of trials in experiments, which causes undersampling of the probability distributions in the above equations (for review, see Panzeri et al. 2007). There are several methods that attempt to correct for this bias. Probably, the simplest one is to compute SSI as above, but with all stimulus-response combinations randomly shuffled. In this case, the true SSI is zero, but the calculation will produce some positive value, which is caused by the bias. This value can be averaged and used as an estimate of the bias and subtracted from the raw SSI calculated above:

$$SSI_{\text{corrected}} = SSI - \langle SSI_{\text{shuffled}} \rangle$$

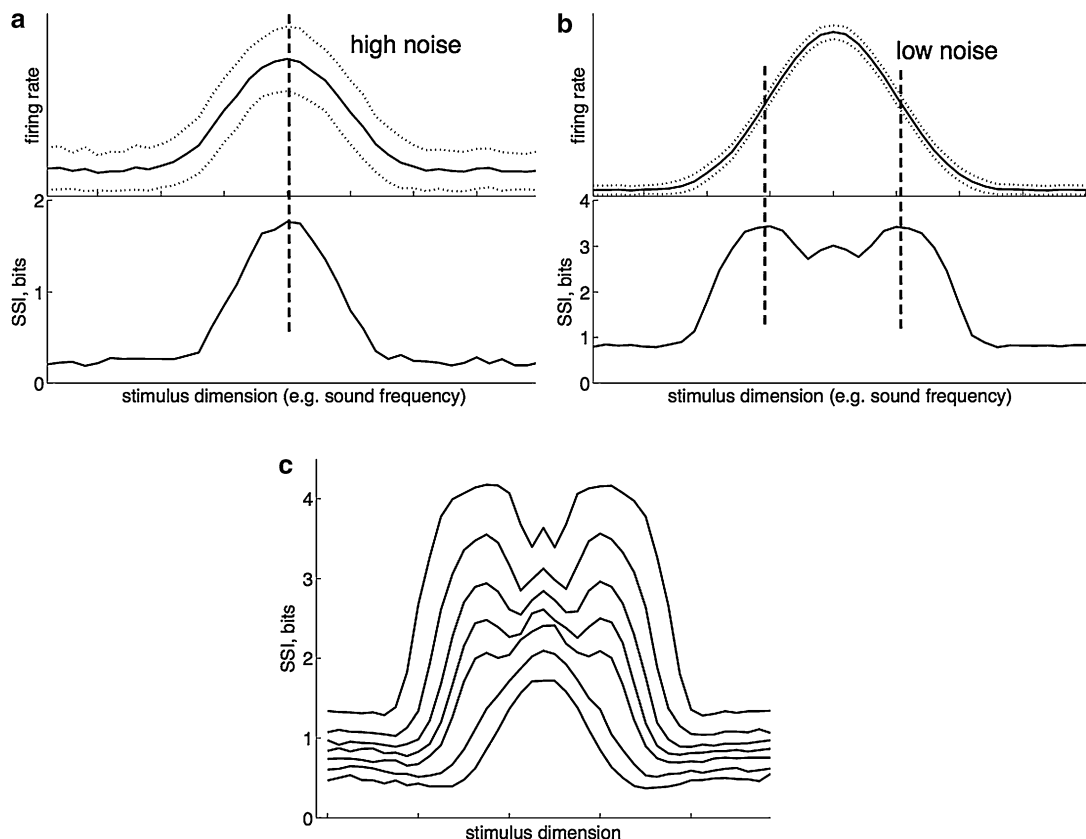
Note that some response types (such as temporal codes) have many more possible values than others (such as firing rates). The probability distributions for such codes therefore require correspondingly more data to sample and, for a given data set, would therefore be more susceptible to bias.

SSI can also be computed for a population of neurons, in a similar fashion to that for individual neurons. In this case, the response r is replaced by a vector of responses $\vec{r} = [r_1, r_2, \dots, r_N]$ for the population of N neurons (Butts and Goldman 2006). Again note the expected combinatorial increase in data requirements for sampling the response probability distributions.

Variability and Information

High SSI for a stimulus means that the stimulus is well encoded. This happens when uncertainty about the stimulus is reduced by the response. This hinges on the reliability of the response, and SSI is therefore strongly influenced by variability in neuronal responses. Variability in the response to a given stimulus (many different r s evoked by a single f) will reduce the amount of SSI.

The effect of variability on SSI leads to an intriguing tuning curve phenomenon that has important implications for neural coding (Butts and Goldman 2006). Sensory neurons are often thought of as feature detectors, whose responses signal how close a stimulus is to the preferred stimulus of the neuron. In this view, one would expect maximal SSI for the preferred stimulus, at the peak of the tuning curve. However, the flanks of the tuning curve, which have the steepest slope, also convey information about the stimulus. In the steep flanks, small changes in the stimulus produce large changes in the firing rate. Because the slope of the tuning curve is flat near its peak, responses to neighboring stimuli will be similar, and neurons may therefore be less able to discriminate stimuli near their best stimulus, compared to those in the flanks. In this view, one would expect maximal SSI in the flanks of the tuning curve, not the peak. Thus, these two intuitive views of neuronal tuning make quite different predictions about the most informative region of the receptive field. The dependence of SSI on response variability reconciles these different predictions, so that both interpretations can be correct depending on neuronal variability (Butts and Goldman 2006). When trial-to-trial variability is high, a model neuron conveys maximal stimulus-specific information at the peak of its tuning curve (Fig. 1a). As trial-to-trial variability is reduced, the maximal information gradually shifts to the steep flanks of the tuning curve (Fig. 1b, c). This unified framework suggests that neural coding strategies depend critically on the level of neuronal variability. A recent study of neurons encoding sound frequency in auditory cortex demonstrated that maximal SSI was always at the best frequency and never in the



Stimulus-Specific Information, Fig. 1 The effect of variability on SSI. (a), Top, Tuning curve of a model neuron with a high level of additive Gaussian noise (generating high response variability). Dotted lines indicate one SD. Bottom, SSI across stimuli. Maximal SSI was aligned with peak of the tuning curve (vertical dashed

line). (b), Same tuning curve but with low noise (and low response variability). Maximal SSI has now shifted to the points of steepest slope in the tuning curve (vertical dashed lines). (c), SSI curves across a range of variability levels, showing the transition of maximal SSI from peak to slope of the tuning curve

tuning curve flanks (Montgomery and Wehr 2010). This suggests that despite the high reliability of auditory cortical neurons, they are too variable to be most informative at the flanks of their tuning curves and instead act as feature detectors for their best frequency.

Cross-References

- [Emergence of Orientation Selectivity in the Cerebral Cortex, Modeling](#)
- [Information Theory: Overview](#)
- [Neuronal Population Vector](#)

References

- Butts DA (2003) How much information is associated with a particular stimulus? *Network* 14:177–187
- Butts DA, Goldman MS (2006) Tuning curves, neuronal variability, and sensory coding. *PLoS Biol* 4:e92
- DeWeese MR, Meister M (1999) How to measure the information gained from one symbol. *Network* 10:325–340
- Montgomery N, Wehr M (2010) Auditory cortical neurons convey maximal stimulus-specific information at their best frequency. *J Neurosci* 30(40):13362–13366
- Panzeri S, Senatore R, Montemurro MA, Petersen RS (2007) Correcting for the sampling bias problem in spike train information measures. *J Neurophysiol* 98:1064–1072

Stochastic Hopfield Network

► Boltzmann Machine

Stochastic Neural Field Theory

Paul Bressloff

Department of Mathematics, University of Utah,
Salt Lake City, UT, USA

Definition

One of the major challenges in neuroscience is to determine how noise that is present at the molecular and cellular levels affects dynamics and information processing at the macroscopic level of synaptically coupled neuronal populations. Often noise is incorporated into deterministic neural network models using extrinsic noise sources. An alternative approach is to assume that noise arises intrinsically as a collective population effect, which has led to a master equation formulation of stochastic neural networks. Stochastic neural fields are obtained by taking a continuum limit of a stochastic neural network with spatially structured synaptic weights.

Detailed Description

The spike trains of individual cortical neurons *in vivo* tend to be very noisy, having interspike interval (ISI) distributions that are close to Poisson (Softky and Koch 1993). The main source of intrinsic fluctuations at the single-cell level is channel noise, which arises from the variability in the opening and closing of a finite number of ion channels (Faisal et al. 2008). On the other hand, extrinsic fluctuations in membrane voltage are predominantly due to synaptic noise. That is, cortical neurons are bombarded by thousands of synaptic inputs, many of which are not correlated with a meaningful input and can

thus be treated as background synaptic noise (Brunel 2000). It is not straightforward to determine how noise at the single-cell level translates into noise at the population or network level. Neural field equations can be derived under two basic assumptions: (i) the spike trains of individual neurons are decorrelated (asynchronous) so that the total synaptic input to a neuron is slowly varying and deterministic and (ii) there exists a well-defined continuum limit of the resulting network rate equations. So far there has been no rigorous proof that either of these assumptions hold in large-scale spiking network models of cortex. In particular, there has been no systematic scaling up of spiking networks to derive continuum neural field models that take proper account of noise-induced fluctuations and statistical correlations between neurons at multiple spatial and temporal scales. Consequently, current formulations of stochastic neural field theory tend to be phenomenologically based. One approach is to consider a Langevin version of deterministic neural field equations involving some form of extrinsic spatiotemporal noise (Hutt et al. 2008; Faugeras et al. 2009; Bressloff 2012; Bressloff and Webber 2012a), whereas another is to treat the neural field equations as the thermodynamic limit of an underlying master equation (Buice and Cowan 2007; Bressloff 2009; Buice et al. 2010). In the latter case, a diffusion approximation leads to an effective Langevin equation with multiplicative noise. In order to develop the theory of stochastic neural fields, it is useful to consider discrete network models first (Bressloff 2012).

Langevin Equation Formulation

Consider a set of P homogeneous populations labeled $i = 1, \dots, P$. Suppose that population activity is given by a stochastic variable $A_j(t)$ evolving according to a Langevin equation (stochastic differential equation) of the form

$$\hat{\tau} dA_j(t) = [-A_j(t) + F(U_j(t))] dt + \sigma_j dW_j(t), \quad (1)$$

where F is a population rate function and $U_j(t)$ is a stochastic synaptic current satisfying the integral equation

$$U_j(t) = \sum_{k=1}^P \int_{-\infty}^t \Phi_{jk}(t-t') A_k(t') dt'. \quad (2)$$

Here $\Phi_{jk}(t)$ represents the temporal filtering effects of synaptic and dendritic processing of inputs from any neuron of population k to any neuron of population j . In Eq. 1, $W_j(t)$, $j = 1, \dots, P$, denotes a set of P -independent Wiener processes with

$$\langle dW_j(t) \rangle = 0, \quad \langle dW_j(t)dW_k(t) \rangle = C_{ij}dt. \quad (3)$$

Here C_{ij} incorporates any spatial correlations and σ_j is the strength of noise in the j th population. In general, the resulting stochastic model is non-Markovian. However, if we take $\Phi_{jk}(t) = w_{jk}\Phi(t)$ with $\Phi(t) = \tau^{-1}e^{-t/\tau}$ (exponential synapses), then we can convert the latter equation to the form

$$\tau dU_j(t) = \left[-U_j(t) + \sum_{k=1}^P w_{jk}A_k(t) \right] dt. \quad (4)$$

It is important to note that the time constant $\hat{\tau}$ cannot be identified directly with membrane or synaptic time constants. Instead, it determines the relaxation rate of a local population to the mean-field firing rate. In the limit $\hat{\tau} \rightarrow 0$, Eqs. 1 and 4 reduce to a *voltage-based* rate model perturbed by additive noise:

$$\tau dU_j(t) = \left[-U_j(t) + \sum_{k=1}^P w_{jk}F(U_k(t)) \right] dt + d\tilde{W}_j(t). \quad (5)$$

Here $\tilde{W}_j(t) = \sum_{k=1}^P w_{jk}\sigma_k W_k(t)$ so that

$$\begin{aligned} \langle d\tilde{W}_j(t) \rangle &= 0, \quad \langle d\tilde{W}_j(t)d\tilde{W}_k(t) \rangle \\ &= \left[\sum_l C_{ll'} w_{jl} w_{kl'} \sigma_l \sigma_{l'} \right] dt. \end{aligned} \quad (6)$$

On the other hand, in the limit $\tau \rightarrow 0$, we obtain a stochastic *activity-based* model

$$\hat{\tau} dA_j(t) = \left[-A_j(t) + F\left(\sum_k w_{jk}A_k(t)\right) \right] dt + \sigma_j dW_j(t). \quad (7)$$

Master Equation Formulation

An alternative approach to incorporating noise into the population firing rate has been developed in terms of a jump Markov process (Buice and Cowan 2007; Bressloff 2009, 2010; Buice et al. 2010). Such a description is motivated by the idea that each local population consists of a discrete number of spiking neurons and that finite-size effects are a source of intrinsic rather than extrinsic noise (Soula and Chow 2007; El Boustani and Destexhe 2009). The stochastic output activity of a local population of N neurons is now expressed as $A_j(t) = N_j(t)/(N\Delta t)$ where $N_j(t)$ is the number of neurons in the j th population that fired in the time interval $[t - \Delta t, t]$, and Δt is the width of a sliding window that counts spikes. Suppose that the discrete stochastic variables $N_j(t)$ evolve according to a one-step jump Markov process:

$$N_j(t) \rightarrow N_j(t) \pm 1 : \quad \text{transition rate } \Omega_j^\pm(t), \quad (8)$$

in which $\Omega_j^\pm(t)$ are functions of $N_j(t)$ and $U_j(t)$ with $U_j(t)$ evolving according to the integral equation 2 or its differential version (4). Thus, synaptic coupling between populations occurs via the transition rates. The transition rates are chosen in order to yield a deterministic rate-based model in the thermodynamic limit $N \rightarrow \infty$. One such choice is

$$\Omega_j^+(t) = \frac{N\Delta t}{\hat{\tau}} F(U_j(t)), \quad \Omega_j^-(t) = N_j(t)\hat{\tau}. \quad (9)$$

A further simplification is obtained in the limit $\tau \rightarrow 0$, since the continuous variables $U_j(t)$ can be eliminated to give a pure birth-death process for the discrete variables $N_j(t)$. Let $P(\mathbf{n}, t) = \text{Prob}[N(t) = \mathbf{n}]$ denote the probability that the network of interacting populations has configuration $\mathbf{n} = (n_1, n_2, \dots, n_P)$ at time t , $t > 0$, given some initial distribution $P(\mathbf{n}, 0)$. The probability distribution then evolves according to the birth-death master equations 8–10

$$\frac{dP(\mathbf{n}, t)}{dt} = \sum_{\alpha} \left[(\mathbb{E}_j - 1) \left(\Omega_j^-(\mathbf{n}) P(\mathbf{n}, t) \right) + (\mathbb{E}_j^{-1} - 1) \left(\Omega_j^+(\mathbf{n}) P(\mathbf{n}, t) \right) \right], \quad (10)$$

where $\Omega_j^+(\mathbf{n}) = (N\Delta/\hat{\tau})F\left[\sum_k w_{jk}n_k/(N\Delta t)\right]$, $\Omega_j^-(\mathbf{n}) = n_j//\hat{\tau}$ and \mathbb{E}_j are translation operators: $\mathbb{E}_j^{\pm 1}F(\mathbf{n}) = F(\mathbf{n}_{j\pm})$ for any function F with $\mathbf{n}_{j\pm}$ denoting the configuration with n_j replaced by $n_j \pm 1$. Equation 10 is supplemented by the boundary conditions $P(\mathbf{n}, t) = 0$ if $n_j = N+1$ or $n_j = -1$ for some j . The birth-death master equation 10 has been the starting point for a number of studies of the effects of intrinsic noise on neural fields, which adapt various methods from the analysis of chemical master equations including system-size expansions and path integral representations (Buice and Cowan 2007; Bressloff 2009; Buice et al. 2010). For large N the master equation can be approximated by a Langevin equation with multiplicative noise and thus reduces to the previous class of stochastic neural field model (Bressloff 2009).

Continuum Limit

A stochastic neural field equation can be obtained from either formulation by taking an appropriate continuum limit. For simplicity, we will focus on the simplest stochastic rate model given by Eqs. 1

and 4. The continuum limit of Eq. 4 proceeds heuristically as follows. First, set $U_j(t) = U(j\Delta d, t)$, $A_j(t) = A(j\Delta d, t)$, and $w_{jk} = \rho\Delta d w(j\Delta d, k\Delta d)$ where ρ is a synaptic density and Δd is an infinitesimal length scale. Taking the limit $\Delta \rightarrow 0$ and absorbing ρ into w gives

$$\tau dU(x, t) = \left[-U(x, t) + \int_{-\infty}^{\infty} w(x-y)A(y)dy \right] dt. \quad (11)$$

We also assume that the noise strength $\sigma_j = \sigma/\sqrt{\Delta d}$ and define $W_j(t)/\sqrt{\Delta d} = W(j\Delta d, t)$. Taking the limit $\Delta d \rightarrow 0$ in Eq. 1 gives

$$\hat{\tau} dA(x, t) = [-A(x, t) + F(U(x, t))]dt + \sigma dW(x, t) \quad (12)$$

With

$$\langle dW(x, t) \rangle = 0, \quad \langle dW(x, t)dW(y, t) \rangle = C(x-y)dt, \quad (13)$$

where we have assumed that C_{ij} depends on $|i-j|$. In the limit $\hat{\tau} \rightarrow 0$ we obtain a stochastic version of a voltage-based neural field equation, namely,

$$\begin{aligned} \tau dU(x, t) = & \left[-U(x, t) + \int_{-\infty}^{\infty} w(x-y)F(U(y, t))dy \right] dt \\ & + \sigma d\tilde{W}(x, t) \end{aligned} \quad (14)$$

with $\langle d\tilde{W}(x, t) \rangle = 0$

$$\begin{aligned} \langle d\tilde{W}(x, t)d\tilde{W}(y, t) \rangle = & dt \int_{-\infty}^{\infty} C(Z-Z')w(x-z) \\ & w(y-z')dz dz' \end{aligned} \quad (15)$$

Similarly, in the limit $\tau \rightarrow 0$ we have a stochastic version of an activity-based neural field equation

$$\begin{aligned}\hat{\tau}dA(x, t) = & \left[-A(x, t) + F\left(\int_{-\infty}^{\infty} w(x-y)A(y, t)\right)dy \right] dt \\ & + dW(x, t).\end{aligned}\quad (16)$$

From a numerical perspective, any computer simulation would involve rediscretizing space and then solving a time-discretized version of the resulting stochastic differential equation. On the other hand, in order to investigate analytically the effects of noise on spatiotemporal dynamics, it is more useful to work directly with stochastic neural fields. One can then adapt various PDE methods for studying noise in spatially extended systems (Sagues et al. 2007).

Applications

One application of stochastic neural field theory is to binocular rivalry waves (Bressloff and Webber 2012b). The basic model consists of two voltage-based excitatory neural fields of the form (14), which represent right and left eye networks, respectively. The neural fields mutually inhibit each other and also undergo some form of slow adaptation such as synaptic depression. It can be shown that the deterministic model supports a composite traveling front, in which the activity of one network advances while the other retreats – this represents the spatiotemporal switch in eye dominance that has been observed experimentally (Wilson et al. 2001). When multiplicative extrinsic noise is added to the model, one finds that the noise generates two distinct phenomena that occur on different time scales: a diffusive-like displacement of the binocular rivalry wave from its uniformly translating position at long time scales and fluctuations in the wave profile around its instantaneous position at short time scales. Moreover, one can use perturbation methods to calculate the diffusion coefficient characterizing the wandering of the front (Bressloff and Webber 2012b).

Another application of stochastic neural field theory is to modeling spontaneous cortical activity *in vitro* and *in vivo* (Beggs and Plenz 2004;

Plenz and Thiagarajan 2007). Buice and Cowan (Plenz and Thiagarajan 2007) have used path integral methods and renormalization group theory to establish that a stochastic neural field model based on a continuum version of a birth-death master equation belongs to the universality class of directed percolation and consequently exhibits power law behavior consistent with measurements of neuronal avalanches *in vitro* and *in vivo* (Beggs and Plenz 2004; Plenz and Thiagarajan 2007).

Cross-References

- [Neural Field Model, Continuum](#)
- [Neural Mass Action](#)
- [Neural Population Model](#)
- [Pattern Formation in Neural Population Models](#)
- [Population Density Model](#)

References

- Beggs JM, Plenz D (2004) Neuronal avalanches are diverse and precise activity patterns that are stable for many hours in cortical slice cultures. *J Neurosci* 24:5216–5229
- Bressloff PC (2009) Stochastic neural field theory and the system-size expansion. *SIAM J Appl Math* 70:1488–1521
- Bressloff PC (2010) Metastable states and quasicycles in a stochastic Wilson-Cowan model of neuronal population dynamics. *Phys Rev E* 85:051903
- Bressloff PC (2012) Spatiotemporal dynamics of continuum neural fields. *J Phys A* 45:033001 (109pp)
- Bressloff PC, Webber MA (2012a) Front propagation in stochastic neural fields. *SIAM J Appl Dyn Syst* 11:708–740
- Bressloff PC, Webber M (2012b) Neural field model of binocular rivalry waves. *J Comput Neurosci* 32:233–252
- Brunel N (2000) Dynamics of sparsely connected networks of excitatory and inhibitory spiking neurons. *J Comput Neurosci* 8:183–208
- Buice M, Cowan JD (2007) Field-theoretic approach to fluctuation effects in neural networks. *Phys Rev E* 75:051919
- Buice M, Cowan JD, Chow CC (2010) Systematic fluctuation expansion for neural network activity equations. *Neural Comp* 22:377–426

- El Boustani S, Destexhe A (2009) A master equation formalism for macroscopic modeling of asynchronous irregular activity states. *Neural Comput* 21:46–100
- Faisal AA, Selen LPJ, Wolpert DM (2008) Noise in the nervous system. *Nat Rev Neurosci* 9:292
- Faugeras O, Touboul J, Cessac B (2009) A constructive mean-field analysis of multi-population neural networks with random synaptic weights and stochastic inputs. *Front Comp Neurosci* 3:1–28
- Hutt A, Longtin A, Schimansky-Geier L (2008) Additive noise-induced Turing transitions in spatial systems with application to neural fields and the Swift-Hohenberg equation. *Physica D* 237:755–773
- Plenz D, Thiagarajan TC (2007) The organizing principles of neuronal avalanches: cell assemblies in the cortex? *Trends Neurosci* 30:101–110
- Sagues F, Sancho JM, Garcia-Ojalvo J (2007) Spatiotemporal order out of noise. *Rev Mod Phys* 79:829–882
- Softky WR, Koch C (1993) The highly irregular ring of cortical cells is inconsistent with temporal integration of random EPSPS. *J Neurosci* 13:334–350
- Soula H, Chow CC (2007) Stochastic dynamics of a finite-size spiking neural network. *Neural Comput* 19:3262–3292
- Wilson HR, Blake R, Lee SH (2001) Dynamics of traveling waves in visual perception. *Nature* 412:907–910

that, in the absence of noise, it is below the threshold of detection. A low-amplitude added noise contributes jitter to the weak periodic signal, but is not sufficient to ever push the signal over the detection threshold. A large-amplitude noisy input, in contrast, adds so much jitter that, while the weak signal plus noise does often exceed the threshold, the signal is not separable from the noise (Jung and Hänggi 1991; Dykman et al. 1992). An intermediate-amplitude noisy input allows the weak signal plus noise to cross the detection threshold sufficiently often that, upon sampling the threshold-crossing events, the original periodicity of the weak signal can be detected. The signal-to-noise ratio exhibits a characteristic peak when plotted as a function of the input noise. For comprehensive reviews of the phenomenon, see Moss and Wiesenfeld (1995), Wiesenfeld and Moss (1995), and Gammaitoni et al. (1998).

Detailed Description

Because of the periodic firing of neurons (and the periodicity of many other biological rhythms), biological physicists and neuroscientists have searched for evidence of stochastic resonance in various neural domains. Stochastic resonance has indeed been observed in a wide range of neural systems in many species, from the crayfish mechanosensory system (Pei et al. 1996) to the human visual system (Simonotto et al. 1997).

One of the areas where a stochastic resonance-like effect has been investigated with most relevance to the clinical treatment of human disorders has been that of balance control. A pioneering set of studies in this area was initiated by James Collins's research group in the Center for Biodynamics at Boston University. In a 2002 paper in *Physical Review Letters* (Priplata et al. 2002), they tested a feedback system in which the (roughly periodic) postural sway of humans during quiet standing could be significantly reduced by adding a small amount of mechanical noise to the subjects' feet. The subjects stood on a platform that contained actuators to provide input noise, with the frequency range

Stochastic Resonance: Balance Control and Cochlear Implants

Sonya Bahar

Center for Neurodynamics, University of Missouri at St. Louis, St. Louis, MO, USA

Synonyms

Noise enhancement of weak subthreshold signals

Definition

Originally discovered in climate data (Nicolis and Nicolis 1981; Nicolis 1982), the phenomenon of stochastic resonance occurs when an intermediate (i.e., neither too large nor too small) amount of noise enhances the transmission of a weak periodic signal (McNamara and Wiesenfeld 1989). More specifically, the signal-to-noise ratio of the weak *periodic* signal is increased by the added noise; the signal is “weak” in the sense

and amplitude of the noise controlled by the experimenters. The authors suggested that this approach could lead to the development of vibrating shoe insoles that could enhance balance in the elderly and successfully implemented this idea (Priplata et al. 2003). The underlying dynamics of this process can be related to the familiar task of trying to balance a meterstick on a finger or palm. The task proves far easier when one's hand is moving underneath the stick. Milton et al. (2009a) combined these two processes in a study of stick balancing by subjects on a vibrating platform and interpreted the vibration-enhanced balance control as a "time-delayed drift and act" effect. In this experiment, the subjects stood on a vibrating platform that produced vertical vibrations in their fingertips. These vibrations reduced the amplitude of fluctuations (in relative horizontal plane position) between the fingertip and the tip of the stick. A nonlinear dynamic-based exploration of the phenomenon can be found in Milton et al. (2009b).

The neural pathways involved in noise-enhanced human balance have not yet been completely elucidated. However, stochastic resonance has already been applied in a variety of clinical situations. A pilot study has been conducted to explore the possibility of using whole-body vibration to enhance chair rising in the elderly (Rogan et al. 2012) and as a possible therapy for Parkinsonian tremor (Kaut et al. 2011). Vibration-enhanced stability studies have been conducted in subjects with ankle instability (Ross and Guskiewicz 2006; Ross 2007; Ross et al. 2013) and with osteoarthritic knees (Collins et al. 2012) and to reduce musculoskeletal stress in metal manufacturing workers (Burger et al. 2012). Stochastic resonance has also been recently explored in the context of enhancing sensorimotor performance with noise added as a tactile stimulus to the subjects' fingers (Mendez-Balbuena et al. 2012).

Perhaps one of the most intriguing clinical applications of stochastic resonance is in the area of hearing impairment. After showing that the addition of actual auditory noise to a vowel coded in a cochlear implant enhanced the neural

evoked response, Morse and Evans (1999a, b) suggested that stochastic resonance techniques could be applied in the design of cochlear implants. The design of stochastic resonance-based cochlear implants has become an active area of research (Chatterjee and Robert 2001; Stocks et al. 2002; Zeng et al. 2000; Benham and Zeng 2003; Chatterjee and Oba 2005). Recent work is focused on optimizing methods to make the added noise truly independent across the array of nerve fibers (Stocks et al. 2009). It has been suggested that stochastic resonance may play a role in enhancing unimpaired hearing as well, with the Brownian motion of cochlear fluids providing a natural source of noise for the optimization of hair cell response (Ehrenberger et al. 1999).

References

- Benham SE, Zeng F-G (2003) Noise improves suprathreshold discrimination in cochlear-implant listeners. *Hear Res* 186:91–93
- Burger C, Schade V, Lindner C, Radlinger L, Elfering A (2012) Stochastic resonance training reduces musculoskeletal symptoms in metal manufacturing workers: a controlled preventive intervention study. *Work* 42:269–278
- Chatterjee M, Oba SI (2005) Noise improves modulation detection by cochlear implant listeners at moderate carrier levels. *J Acoust Soc Am* 118:993–1002
- Chatterjee M, Robert ME (2001) Noise enhances modulation sensitivity in cochlear implant listeners: stochastic resonance in a prosthetic sensory system? *J Assoc Res Otolaryngol* 2:159–171
- Collins AT, Blackburn JT, Olcott CW, Jordan JM, Yu B, Weinhold PS (2012) The assessment of postural control with stochastic resonance electrical stimulation and a neoprene knee sleeve in the osteoarthritic knee. *Arch Phys Med Rehabil* 93:1123–1128
- Dykman MI, Mannella R, McClintock PV, Stocks NG (1992) Phase shifts in stochastic resonance. *Phys Rev Lett* 68:2985–2988
- Ehrenberger K, Felix D, Svozil K (1999) Stochastic resonance in cochlear signal transduction. *Acta Otolaryngol* 119:166–170
- Gammaitoni L, Hänggi P, Jung P, Marchesoni F (1998) Stochastic resonance. *Rev Mod Phys* 70:223–287
- Jung P, Hänggi P (1991) Amplification of small signals via stochastic resonance. *Phys Rev A* 44:8032–8042
- Kaut O, Allert N, Coch C, Paus S, Grzeska A, Minnerop M, Wüllner U (2011) Stochastic resonance therapy

- in Parkinson's disease. *NeuroRehabilitation* 28:353–358
- McNamara B, Wiesenfeld K (1989) Theory of stochastic resonance. *Phys Rev A* 39:4854–4868
- Mendez-Balbuena I, Manjarrez E, Schulte-Mönting J, Huethe F, Tapia JA, Hepp-Reymond MC, Kristeva R (2012) Improved sensorimotor performance via stochastic resonance. *J Neurosci* 32:12612–12618
- Milton JG, Ohira T, Cabrera JL, Fraiser RM, Gyorffy JB, Ruiz FK, Strauss MA, Balch EC, Marin PJ, Alexander JL (2009a) Balancing with vibration: a prelude for “drift and act” balance control. *PLOS One* 4:e7427
- Milton J, Cabrera JL, Ohira T, Tajima S, Tonusaki Y, Eurich CW, Campbell SA (2009b) The time-delayed inverted pendulum: implications for human balance control. *Chaos* 19:026110
- Morse RP, Evans EF (1999a) Additive noise can enhance temporal coding in a computational model of analogue cochlear implant stimulation. *Hear Res* 133:107–119
- Morse RP, Evans EF (1999b) Preferential and non-preferential transmission of formant information by an analogue cochlear implant using noise: the role of the nerve threshold. *Hear Res* 133:120–132
- Moss F, Wiesenfeld K (1995) The benefits of background noise. *Sci Am* 273:66–69
- Nicolis C (1982) Stochastic aspects of climatic transitions – response to a periodic forcing. *Tellus* 34:1–9
- Nicolis C, Nicolis G (1981) Stochastic aspects of climatic transitions – additive fluctuations. *Tellus* 33:225–231
- Pei X, Wilkens LA, Moss F (1996) Light enhances hydrodynamic signaling in the multimodal caudal photoreceptor interneurons of the crayfish. *J Neurophysiol* 76:3002–3011
- Priplata A, Niemi J, Salen M, Harry J, Lipsitz LA, Collins JJ (2002) Noise-enhanced human balance control. *Phys Rev Lett* 89:238101
- Priplata AA, Niemi JB, Harry JD, Lipsitz LA, Collins JJ (2003) Vibrating insoles and balance control in elderly people. *Lancet* 362:1123–1124
- Rogan S, Hilfiker R, Schmid S, Radlinger L (2012) Stochastic resonance whole-body vibration training for chair rising performance on untrained elderly: a pilot study. *Arch Gerontol Geriatr* 55:468–473
- Ross SE (2007) Noise-enhanced postural stability in subjects with functional ankle instability. *Br J Sports Med* 41:656–659
- Ross SE, Guskiewicz KM (2006) Effect of coordination training with and without stochastic resonance stimulation on dynamic postural stability of subjects with functional ankle instability and subjects with stable ankles. *Clin J Sport Med* 16:323–328
- Ross SE, Linens SW, Wright CJ, Arnold BL (2013) Customized noise-stimulation intensity for bipedal stability and unipedal balance deficits associated with functional ankle instability. *J Athl Train* 48:463–470
- Simonotto E, Riani M, Seife C, Roberts M, Twitty J, Moss F (1997) Visual perception of stochastic resonance. *Phys Rev Lett* 78:1186–1189
- Stocks NG, Allingham D, Morse RP (2002) The application of suprathreshold stochastic resonance to cochlear implant coding. *Fluct Noise Lett* 2:L169–L181
- Stocks NG, Shulgin B, Holmes SD, Nikitin A, Morse RP (2009) Cochlear implant coding with stochastic beamforming and suprathreshold stochastic resonance. In: Applications of nonlinear dynamics. Springer, pp 237–248
- Wiesenfeld K, Moss F (1995) Stochastic resonance and the benefits of noise: from ice ages to crayfish and SQUIDS. *Nature* 373:33–36
- Zeng F-G, Fu Q-J, Morse R (2000) Human hearing enhanced by noise. *Brain Res* 869:251–255

Stochastic Simulation Algorithm (SSA)

► [Gillespie Algorithm for Biochemical Reaction Simulation](#)

Stochastic Simulators

Wonryull Koh¹ and Kim T. Blackwell²

¹School of Computing, College of Science and Technology, University of Southern Mississippi, Hattiesburg, MS, USA

²Molecular Neuroscience Department, Krasnow Institute for Advanced Study, George Mason University, Fairfax, VA, USA

Definition

A stochastic simulator for reaction-diffusion systems is a computer simulation tool that uses the Monte Carlo method to generate the time evolution of a spatially inhomogeneous chemically reacting system. The stochastic simulation algorithm (SSA) formulated by Dan Gillespie in 1976 numerically simulates the time evolution of a well-stirred chemically reacting system in a thermal equilibrium by defining the state of the system to be the integer numbers of molecular

populations. The SSA has been extended to incorporate diffusion, usually called the spatial SSA, by dividing the spatial domain into a collection of well-stirred subvolumes and treating diffusion between neighboring subvolumes as a set of first-order reactions. This entry focuses on stochastic simulators that use the spatial SSA.

Detailed Description

The small numbers and heterogeneous distribution of molecular species in biological cells give rise to stochastic variations in intracellular microdomains and diffusional gradients. These stochastic variations affect the behavior of biochemical network components, such as oscillators, switches, and positive and negative feedback loops, and play a significant role in the spatiotemporal activity and behavior of cells, such as cell differentiation, gene regulatory networks, and synaptic plasticity (e.g., see the reviews by Shahrezaei and Swain 2008; Andrews et al. 2009; Korteski and Blackwell 2010; and the references within). Computer simulations enable computational investigation of the stochastic and spatial effects in neuron behavior and activity that may be difficult to monitor in detail experimentally (Boulian et al. 2008), thereby providing a more amenable investigative platform to test hypotheses and gain further insights.

Traditionally, computer simulation of biochemical networks has involved deterministic simulations that represent molecular populations as continuous concentration variables. Systems of ordinary differential equations are used to describe the time evolution of concentrations when they are assumed to be spatially homogeneous. On the other hand, when the concentrations are assumed to be spatially heterogeneous, systems of partial differential equations are used. Deterministic models and simulations are valid in the thermodynamic limit of large numbers of molecules to study the average behavior of the modeled system. However, when the discreteness and stochasticity rather than the mean behavior

need to be examined, stochastic simulations are necessary.

Stochastic simulation methods are categorized as either spatial or nonspatial methods (Takahashi et al. 2005; Andrews et al. 2009). Nonspatial stochastic simulators (Alves et al. 2006) assume that the system to be modeled is well-stirred, that is, nonreactive collisions between molecules occur much more frequently than reactive collisions such that the molecules become uniformly randomly distributed in thermal equilibrium (Gillespie 1976, 2007). However, many cellular processes are influenced by not only the stochastic nature of molecular interactions but also the spatial heterogeneity of those molecules, which necessitates spatial stochastic simulations (Bhalla 2004a, b; Takahashi et al. 2005; Lemerle et al. 2005).

Spatial stochastic simulation methods are further categorized as particle-based or population-based (also known as voxel-based or subvolume-based) methods (Takahashi et al. 2005; Andrews et al. 2009). Particle-based spatial stochastic simulators use a variety of methods, including molecular dynamics, Brownian dynamics, Green's function reaction dynamics, and lattice-based approaches, to model the system at a single particle detail (Le Novere and Shimizu 2001; Stiles and Bartol 2001; Plimpton and Slepnev 2003; Ramsey et al. 2005; Takahashi et al. 2005; Alves et al. 2006; Azuma et al. 2006; Boulian et al. 2008; Andrews et al. 2009, 2010; Tolle and Le Novere 2010; Resasco et al. 2012). With these simulators, the location and reactions of individual molecules are tracked. Particle-based methods offer high spatial resolution and simulation detail at the single particle level; however, because they track individual molecules, they incur a high computational cost as the number of particles increases. Population-based stochastic simulation methods are about a factor of two faster than particle-based simulation methods (Dobrzynski et al. 2007; Andrews et al. 2010). Population-based spatial stochastic simulators subdivide the simulation volume into a collection of well-stirred subvolumes, and reactions are simulated in each subvolume by using a variant of Gillespie's stochastic simulation

algorithm (Gillespie 1976, 1977, 2001; Gibson and Bruck 2000), whereas diffusions are simulated as diffusion jumps between neighboring subvolumes as a set of first-order reactions. Population-based simulators keep track of the population number of each molecular species in each subvolume thereby providing the time evolution of the system state at mesoscopic detail.

Particle-based simulators keep track of every individual molecule in the system thereby providing the time evolution of the system state at microscopic detail. One type of particle-based simulator subdivides the cell into a two- or three-dimensional lattice (Azuma et al. 2006; Boulian et al. 2008). Diffusion of individual molecules is simulated as hopping to the neighboring unoccupied lattice sites. Reactions are effected with a specified probability when appropriate reactant molecules collide. Another type of particle-based simulator does not subdivide the simulation volume and instead uses Brownian motion, which allows particles to diffuse to arbitrary locations (Stiles and Bartol 2001; Andrews et al. 2009, 2010). If the trajectory of two diffusing molecules intersects during a diffusion time step, then those two molecules may react, depending on the probability of reaction. Molecular dynamics is a simulation method typically used to understand the behavior of a small number of molecules, e.g., the reaction energetics or protein conformation. Often, these simulations compute the forces between atoms within a single molecule, or between molecules, in order to determine which protein conformations or binding conformations are energetically most favorable. Of all these particle-based approaches, the Brownian motion simulators, such as MCell and smoldyn, have been used most commonly to study signaling pathways in neurons.

In this entry, we focus on population-based spatial stochastic simulation methods. In general, population-based spatial stochastic simulators have three common components: model input, numerical simulation, and simulation output for data analyses. Model input includes subdividing the simulation volume into a collection of well-stirred subvolumes and specifying initial

conditions of molecular species in each subvolume. Starting from the initial condition, the system is numerically simulated until the desired end time by using the specific simulation approach employed by the simulator. Usually, many simulation runs are made from the same initial condition with different random seeds for later analyses of the probability distribution, average, and/or variance of the system trajectories.

Here, we categorize population-based spatial stochastic simulation methods by the numerical simulation approach they take: exact and approximate. We first briefly explain the extension of Gillespie's stochastic simulation algorithm (SSA) for well-stirred systems to spatial systems with well-stirred subvolumes. We then describe stochastic simulation methods that utilize an exact SSA approach. We describe stochastic simulation methods that utilize approximate SSA approaches to ameliorate the heavy computational burden placed by the exact approach. We conclude with discussion of limitations and advantages of the current population-based spatial stochastic simulation methods.

Spatial Extension of Gillespie's Stochastic Simulation Algorithm

Gillespie's SSA is extended to include diffusion by relaxing the well-stirred requirement. For the spatial SSA, the system volume Ω is partitioned into Q subvolumes $\{V_1, \dots, V_Q\}$, each of which is assumed to be well-stirred. There are N molecular species $\{S_1, \dots, S_N\}$ that are involved in M chemical reaction channels $\{R_1, \dots, R_M\}$ in each subvolume, and each molecular species has a diffusion coefficient $D_i (i = 1, 2, \dots, N)$ greater than or equal to zero. The state vector $X_k(t) = (X_{1k}(t), \dots, X_{Nk}(t))$ denotes the number of molecules of $S_i (i = 1, 2, \dots, N)$ in subvolume $V_k (k = 1, 2, \dots, Q)$ at time t . Then, $X(t) = (X_1(t); \dots; X_Q(t))$ denotes the Q by N state matrix of the system at time t . N molecular species in each subvolume V_k are involved in M chemical reaction channels $\{R_{1k}, \dots, R_{Mk}\}$ and $N \cdot B_k$ diffusion channels $\{R_{ikl}^d\}$ where B_k is the number of V_k 's neighboring subvolumes and l denotes the

index of each neighboring subvolume of V_k . The dynamics of each reaction channel R_{jk} ($j = 1, 2, \dots, M$; $k = 1, 2, \dots, Q$) is characterized by a propensity function a_{jk} and the state change vector v_j applied to X_k . Given $x = X(t)$, $a_{jk}(x)dt$ gives the probability that an R_{jk} reaction will occur in the next time interval $[t, t + dt]$ in subvolume V_k . The state change vector v_j gives the change in the molecular populations induced by one R_{jk} reaction such that $x_k \rightarrow x_k + v_j$. Diffusive transfers of a molecular species S_i from a subvolume V_k to a neighboring subvolume V_l are treated as unimolecular reactions, $S_{ik} \rightarrow S_{il}$ (Gillespie 1976; Hanusse and Blanche 1981; Baras and Mansour 1996; Stundzia and Lumsden 1996). The dynamics of each diffusion channel R_{ikl}^d is characterized by a propensity function $\kappa_{ikl}x_{ik}$ and state change matrix $E_i^l - E_i^k$, where κ_{ikl} is a constant relating to the diffusion rate constant D_i (e.g., when V_k and V_l are both cuboids with side length u , $\kappa_{ikl} = D_i/u^2$), $E_i^l - E_i^k$ gives the change in the molecular populations induced by one R_{ikl}^d diffusion, and E_i^k denotes the Q by N matrix whose entries are all zero except for the entry (k, i) . Therefore, whereas Gillespie's SSA has M total reaction channels in the system volume Ω , the spatial SSA has up to $M \cdot Q + \sum_{k=1}^Q (N \cdot B_k)$ reaction channels in the system volume Ω that is subdivided into Q subvolumes. Note that the total number of diffusive transfer reaction channels is less than $\sum_{k=1}^Q (N \cdot B_k)$ when the diffusion coefficient of one or more molecular species S_i ($i = 1, 2, \dots, N$) is zero.

Starting from an initial condition, the spatial SSA proceeds by generating the time step τ to the next reaction and determining which reaction occurs in that next time interval and then affecting the reaction by updating the time and the state matrix. Gillespie gave two implementations of his SSA: the direct method and the first-reaction method.

With the first-reaction method, the next time step τ and the next reaction μ are determined by generating up to $M \cdot Q + \sum_{k=1}^Q (N \cdot B_k)$ random numbers r_{jk} ($j = 1, 2, \dots, M$; $k = 1, 2, \dots, Q$) and r_{ibk} ($i = 1, 2, \dots, N$; $b_k = 1, \dots, B_k$) where

$k = 1, \dots, Q$) from the uniform distribution in the unit interval and calculating

$$\tau_{jk} = \frac{1}{a_{jk}(x)} \ln \frac{1}{r_{jk}}$$

and

$$\tau_{ibk} = \frac{1}{\kappa_{ikl}x_{ik}} \ln \frac{1}{r_{ibk}}$$

and then selecting τ to be the smallest and μ to be the reaction R_{jk} or diffusion R_{ikl}^d of the chosen τ .

The spatial SSA generates a trajectory of the corresponding reaction-diffusion master equation (RDME), which describes the time evolution of the spatially varying probability density functions of molecular populations (Baras and Mansour 1996; Isaacson and Peskin 2006).

Exact Spatial Stochastic Simulation Methods

There have been several extensions of the exact stochastic simulation algorithm for spatial stochastic simulation. Gillespie's direct method (Gillespie 1976) was extended to include diffusion and to simulate calcium wave propagation by Stundzia and Lumsden (1996). SmartCell (Ander et al. 2004) extended Gibson and Bruck's next reaction method (Gibson and Bruck 2000), an optimized version of Gillespie's first-reaction method (Gillespie 1976, 1977), for spatial stochastic simulation. Bernstein (2005) extended the direct method (Gillespie 1976) with the use of a binary tree data structure. Isaacson and Peskin (2006) used the next reaction method (Gibson and Bruck 2000) to simulate a model of transcription, translation, and nuclear membrane transport in a spatial domain with multiple complex boundaries. URDME (Drawert et al. 2012) uses the next subvolume method (Elf and Ehrenberg 2004) with unstructured tetrahedral meshes. MesoRD (Hattne et al. 2005; Fange et al. 2012) uses the next subvolume method (Elf and Ehrenberg 2004) that combines the direct method (Gillespie 1976) and the next reaction method (Gibson and Bruck 2000) to determine the time step for the next reaction or

diffusion event in each subvolume and to keep track of the subvolume in which the next event occurs, respectively. MesoRD has been used to investigate the spatiotemporal oscillations of the MinD and MinE proteins in *Escherichia coli* (Fange and Elf 2006) but has not yet been applied to neuroscience investigations. MesoRD supports scale-dependent reaction rates to deal with diffusion-controlled reactions with finer spatial discretization (Fange et al. 2010, 2012). STEPS (Hepburn et al. 2012) extends the direct method with the use of a k-ary tree data structure and the composition and reject method (Slepoy et al. 2008) to optimize updating of the propensity values and finding the next reaction, respectively, at each time step. STEPS also uses tetrahedral meshes instead of cuboids, which allows STEPS to simulate more realistic geometries. STEPS has been used to investigate the interaction between a positive feedback loop and glutamate receptor trafficking in cerebellar LTD in a single spine (Antunes and De Schutter 2012).

Even with the use of efficient data structures and optimization strategies to minimize the number of computations at each time step, exact methods are too slow for many practical applications because they must simulate every single reaction and diffusion event in the system (Gillespie 2007). For spatial stochastic simulations, the slowness of exact simulation is exacerbated by the fact that the subdivision of the system volume into subvolumes and diffusive transfers between neighboring subvolumes increases the computational burden significantly. This has led to development of approximate spatial stochastic simulation methods to achieve greater simulation speed by sacrificing some of the exactness, which we describe in the next section.

Approximate Spatial Stochastic Simulation Methods

For simulating well-stirred systems, one of the most accurate (Andrews et al. 2009) and generally applicable approximate methods is the nonnegative Poisson τ -leaping method (Cao et al. 2005b). The nonnegative Poisson τ -leaping method tries to advance the state of the system by the largest value of the leap time τ while simultaneously allowing

multiple reaction events to occur and satisfying the leap condition (Gillespie 2001; Gillespie and Petzold 2003), which states that no propensity function is likely to change its value by a significant amount during $[t, t + \tau]$. With the leap condition that bounds the relative change in each propensity function $a_j(x)$ during the leap, the state vector is updated as

$$X(t + \tau) \dot{=} x + \sum_{j=1}^M P_j(a_j(x)\tau)v_j$$

where $P_j(a_j(x)\tau)$ is a statistically independent Poisson random variable, and a control strategy is in place to prevent any of the population of reactant species becoming negative due to the unboundedness of the Poisson random numbers (Cao et al. 2005b). When τ is both small enough to satisfy the leap condition and large enough such that the expected number of firings of each reaction channel R_j during τ is much greater than one, the τ -leaping strategy is equivalent to the chemical Langevin equation (Gillespie 2007).

Unlike some other approximate methods that introduce new mathematical strategies to make approximations to a portion of the corresponding CME to deal with a wide range of timescales (Haseltine and Rawlings 2002; Rao and Arkin 2003; Rathinam et al. 2003; Burrage et al. 2004; Cao et al. 2005a; Haseltine and Rawlings 2005; Srivastava et al. 2011), the τ -leaping method approximates the entire CME. This makes it relatively straightforward to extend the τ -leaping method to spatial stochastic simulations (Rossinelli et al. 2008) with confidence in accuracy. However, selecting the next leap time τ requires a larger computational overhead (Cao et al. 2006; Chatterjee and Vlachos 2007) than selecting the next event time with the exact algorithm. The added computational overhead accumulates especially when the leap time τ is repeatedly rejected to prevent potential negative populations, and the system must evolve following the exact algorithm, which sometimes makes a τ -leaping simulation slower than an exact simulation (Koh and Blackwell 2011).

Although the approximate strategies developed for well-stirred systems do not necessarily easily translate to spatial stochastic simulations, approximate methods have been developed to take advantage of the fact that, in spatial stochastic simulations, diffusive events between neighboring subvolumes occur much more frequently than reaction events within the subvolumes. The Gillespie multiparticle method (Rodriguez et al. 2006) simulates diffusion by randomly distributing diffusing molecules from a subvolume among its neighbors at predetermined intervals and simulates reactions in each subvolume by using the direct method in between the predetermined intervals. The binomial τ -leaping spatial simulation algorithm (Marquez-Lago and Burrage 2007) uses the next subvolume method (Elf and Ehrenberg 2004) to choose the subvolume with the smallest next event time, uses the binomial τ -leaping method (Tian and Burrage 2004) to calculate the next leap time τ in the chosen subvolume, and advances the subvolume with either the smallest next event time or the leap time. The hybrid τ -leaping method (Rossinelli et al. 2008) simulates diffusion deterministically with the time step chosen for simulating reactions stochastically with the τ -leaping method. The multinomial simulation algorithm (Lampoudi et al. 2009) simulates diffusion by distributing diffusing molecules from a subvolume among its neighbors with multinomial probabilities until the time to the next reaction event is reached while simulating reactions with the direct method. The diffusive finite state projection method (Drawert et al. 2010) simulates reactions with the direct method (Gillespie 1976) while simulating diffusion based on the finite state projection method (Munsky and Khammash 2006) that provides the exact or approximate solution of the CME for a given time. The adaptive hybrid method (Ferm et al. 2010) simulates reactions with the next subvolume method (Elf and Ehrenberg 2004) while simulating diffusion in three different ways – exact, τ -leaping, and deterministic – depending on the number of diffusing molecules. The spatial partitioned leaping algorithm (Iyengar et al. 2010) extends the partitioned leaping algorithm (Harris and Clancy

2006) to calculate the next leap time τ with the nonnegative Poisson τ -leaping method (Cao et al. 2006). It then classifies each reaction and diffusion in the system into one of four categories – exact stochastic, Poisson, Langevin, and deterministic – and advances the system based on τ and the category. The spatial direct method with gradient-based diffusion (Koh and Blackwell 2011, 2012) uses the direct method but approximates diffusion processes by using diffusion propensities that are based on the net movement of molecules from higher to lower concentration gradients rather than sampling all diffusion events regardless of local concentration gradients. This method also allows the user to control the degree of exactness in simulation with a control parameter.

All of the above approximate methods use adaptive time steps and need to calculate the next leap or event time at each simulation time step, which is time-consuming especially when the system volume comprises a complex geometry, such as a neuron, that requires very many subvolumes for representation. To circumvent this problem, NeuroRD (Oliveira et al. 2010) uses a predetermined time step. At each time step, it determines the number of reactions and diffusions from tabulated binomial distributions if the number of reactants in a subvolume is below a threshold; otherwise, it uses Poisson or Gaussian distributions depending on whether the propensities are below or above, respectively, another threshold. It distributes diffusing molecules from a subvolume among its neighbors with multinomial probabilities. NeuroRD has been used to investigate the role of anchoring proteins in synaptic plasticity (Kim et al. 2011; Oliveira et al. 2012). It has also been used to investigate how different spatiotemporal patterns of synaptic input determine the direction of synaptic plasticity (Kim et al. 2013). Because of the computational efficiency of NeuroRD, it has been used to simulate over 100 species and over 100 reactions in a dendrite with multiple spines.

Advantages and Challenges

Spatial stochastic simulators enable researchers to quantitatively investigate spatially varying

discrete and stochastic molecular interactions in a greater detail (Rao et al. 2002; Turner et al. 2004; Lemerle et al. 2005; Takahashi et al. 2005; Andrews and Arkin 2006; Andrews et al. 2009). Population-based spatial stochastic simulators are especially advantageous in allowing quantitative investigation at a mesoscopic detail between the microscopic detail provided by the particle-based stochastic simulators (Le Novere and Shimizu 2001; Stiles and Bartol 2001; Ramsey et al. 2005; Takahashi et al. 2005; Alves et al. 2006; Azuma et al. 2006; Boulian et al. 2008; Andrews et al. 2009, 2010; Tolle and Le Novere 2010) and the macroscopic detail provided by the partial-differential-equation-based simulators (Resasco et al. 2012). The mesoscopic approximation by subdividing the system volume into subvolumes is both an advantage and a limitation of the population-based spatial stochastic simulation methods.

The subdivision of the system volume into subvolumes must satisfy the assumption that each subvolume is well-stirred. The subvolume sizes must not be too small as in being smaller than the size of reacting and/or diffusing molecules. At the same time, the subvolume sizes must not be too large as in having concentration gradients within the subvolume. When the subvolume sizes are either too small or too large, it leads to unrealistic and/or inaccurate simulation results (Isaacson and Peskin 2006; Erban and Chapman 2009). For the well-stirred assumption to be physically valid, it was shown that the width of the subvolume must satisfy $\tau_R \gg \tau_D$, where τ_R and τ_D denote the typical time interval between reaction events and the typical time interval between diffusion events, respectively, and also that the width must be less than the reactant correlation length, which is difficult to predict (Baras and Mansour 1996; Bernstein 2005; Isaacson 2009).

In order to obtain more accurate detail at the microscopic level, particle-based stochastic simulation methods are preferred. On the other hand, in order to reduce the computational cost of simulation, macroscopic methods are preferred. There also have been attempts to use graphics processing units (GPUs) to speed up stochastic simulations although the GPU implementation

required a common global time step to avoid synchronization issues (Vigelius et al. 2011; Vigelius and Meyer 2012). For a systematic investigation of cellular processes spanning different spatial and temporal scales at various levels of detail, a remaining challenge is for a simulator to seamlessly and accurately transition among microscopic, mesoscopic, and macroscopic levels of detail. Meanwhile, population-based spatial stochastic simulators provide a good balance between sufficient stochastic and spatial details in simulation output and practical simulation speed.

Cross-References

- [Gillespie Algorithm for Biochemical Reaction Simulation](#)

References

- Alves R, Antunes F, Salvador A (2006) Tools for kinetic modeling of biochemical networks. *Nat Biotech* 24:667–672
- Ander M, Beltrao P, Di Ventura B, Ferkinghoff-Borg J, Foglierini M et al (2004) SmartCell, a framework to simulate cellular processes that combines stochastic approximation with diffusion and localisation: analysis of simple networks. *Syst Biol* 1:129–138
- Andrews SS, Arkin AP (2006) Simulating cell biology. *Curr Biol* 16:R523–R527
- Andrews S, Dinh T, Arkin A (2009) Stochastic models of biological processes. In: Meyers RA (ed) Encyclopedia of complexity and systems science. Springer, New York, pp 8730–8749
- Andrews SS, Addy NJ, Brent R, Arkin AP (2010) Detailed simulations of cell biology with smoldyn 2.1. *PLoS Comput Biol* 6:e1000705
- Antunes G, De Schutter E (2012) A stochastic signaling network mediates the probabilistic induction of cerebellar long-term depression. *J Neurosci* 32:9288–9300
- Azuma R, Kitagawa T, Kobayashi H, Konagaya A (2006) Particle simulation approach for subcellular dynamics and interactions of biological molecules. *BMC Bioinform* 7:S20
- Baras F, Mansour MM (1996) Reaction–diffusion master equation: a comparison with microscopic simulations. *Phys Rev E* 54:6139
- Bernstein D (2005) Simulating mesoscopic reaction–diffusion systems using the Gillespie algorithm. *Phys Rev E* 71:041103

- Bhalla US (2004a) Signaling in small subcellular volumes. I. Stochastic and diffusion effects on individual pathways. *Biophys J* 87:733–744
- Bhalla US (2004b) Signaling in small subcellular volumes. II. Stochastic and diffusion effects on synaptic network properties. *Biophys J* 87:745–753
- Boulianne L, Al Assaad S, Dumont M, Gross W (2008) GridCell: a stochastic particle-based biological system simulator. *BMC Syst Biol* 2:66
- Burrage K, Tian T, Burrage P (2004) A multi-scaled approach for simulating chemical reaction systems. *Prog Biophys Mol Biol* 85:217–234
- Cao Y, Gillespie DT, Petzold LR (2005a) The slow-scale stochastic simulation algorithm. *J Chem Phys* 122:014116
- Cao Y, Gillespie DT, Petzold LR (2005b) Avoiding negative populations in explicit Poisson tau-leaping. *J Chem Phys* 123:054104
- Cao Y, Gillespie DT, Petzold LR (2006) Efficient step size selection for the tau-leaping simulation method. *J Chem Phys* 124:044109
- Chatterjee A, Vlachos D (2007) An overview of spatial microscopic and accelerated kinetic Monte Carlo methods. *J Comput Aided Mater Des* 14:253–308
- Dobrzynski M, Rodriguez JV, Kaandorp JA, Blom JG (2007) Computational methods for diffusion-influenced biochemical reactions. *Bioinformatics* 23:1969–1977
- Drawert B, Lawson MJ, Petzold L, Khammash M (2010) The diffusive finite state projection algorithm for efficient simulation of the stochastic reaction-diffusion master equation. *J Chem Phys* 132:074101
- Drawert B, Engblom S, Hellander A (2012) URDME: a modular framework for stochastic simulation of reaction-transport processes in complex geometries. *BMC Syst Biol* 6:76
- Elf J, Ehrenberg M (2004) Spontaneous separation of bi-stable biochemical systems into spatial domains of opposite phases. *Syst Biol* 1:230–236
- Erban R, Chapman SJ (2009) Stochastic modelling of reaction-diffusion processes: algorithms for bimolecular reactions. *Phys Biol* 6:046001
- Fange D, Elf J (2006) Noise-induced min phenotypes in *E. coli*. *PLoS Comput Biol* 2:e80
- Fange D, Berg OG, Sjöberg P, Elf J (2010) Stochastic reaction-diffusion kinetics in the microscopic limit. *Proc Natl Acad Sci* 107:19820–19825
- Fange D, Mahmutovic A, Elf J (2012) MesoRD 1.0: Stochastic reaction-diffusion simulations in the microscopic limit. *Bioinformatics* 28:3155–3157
- Ferm L, Hellander A, Lötstedt P (2010) An adaptive algorithm for simulation of stochastic reaction-diffusion processes. *J Comput Phys* 229:343–360
- Gibson MA, Bruck J (2000) Efficient exact stochastic simulation of chemical systems with many species and many channels. *J Phys Chem A* 104:1876–1889
- Gillespie DT (1976) A general method for numerically simulating the stochastic time evolution of coupled chemical reactions. *J Comput Phys* 22:403–434
- Gillespie DT (1977) Exact stochastic simulation of coupled chemical reactions. *J Phys Chem* 81:2340–2361
- Gillespie DT (2001) Approximate accelerated stochastic simulation of chemically reacting systems. *J Chem Phys* 115:1716
- Gillespie DT (2007) Stochastic simulation of chemical kinetics. *Annu Rev Phys Chem* 58:35–55
- Gillespie DT, Petzold LR (2003) Improved leap-size selection for accelerated stochastic simulation. *J Chem Phys* 119:8229
- Hanssle P, Blanche A (1981) A Monte Carlo method for large reaction-diffusion systems. *J Chem Phys* 74:6148
- Harris LA, Clancy P (2006) A “partitioned leaping” approach for multiscale modeling of chemical reaction dynamics. *J Chem Phys* 125:144107
- Haseltine EL, Rawlings JB (2002) Approximate simulation of coupled fast and slow reactions for stochastic chemical kinetics. *J Chem Phys* 117:6959
- Haseltine EL, Rawlings JB (2005) On the origins of approximations for stochastic chemical kinetics. *J Chem Phys* 123:164115
- Hattne J, Fange D, Elf J (2005) Stochastic reaction-diffusion simulation with MesoRD. *Bioinformatics* 21:2923–2924
- Hepburn I, Chen W, Wils S, De Schutter E (2012) STEPS: efficient simulation of stochastic reaction-diffusion models in realistic morphologies. *BMC Syst Biol* 6:36
- Isaacson S (2009) The reaction-diffusion master equation as an asymptotic approximation of diffusion to a small target. *SIAM J Appl Math* 70:77–111
- Isaacson SA, Peskin CS (2006) Incorporating diffusion in complex geometries into stochastic chemical kinetics simulations. *SIAM J Sci Comput* 28:47–74
- Iyengar KA, Harris LA, Clancy P (2010) Accurate implementation of leaping in space: the spatial partitioned-leaping algorithm. *J Chem Phys* 132:094101
- Kim M, Park AJ, Havekes R, Chay A, Guercio LA et al (2011) Colocalization of protein kinase A with adenylyl cyclase enhances protein kinase A activity during induction of long-lasting long-term potentiation. *PLoS Comput Biol* 7:e1002084
- Kim B, Hawes SL, Gillani F, Wallace LJ, Blackwell KT (2013) Signaling pathways involved in striatal synaptic plasticity are sensitive to temporal pattern and exhibit spatial specificity. *PLoS Comput Biol* 9: e1002953
- Koh W, Blackwell KT (2011) An accelerated algorithm for discrete stochastic simulation of reaction-diffusion systems using gradient-based diffusion and tau-leaping. *J Chem Phys* 134:154103
- Koh W, Blackwell KT (2012) Improved spatial direct method with gradient-based diffusion to retain full diffusive fluctuations. *J Chem Phys* 137:154111
- Kotaleski JH, Blackwell KT (2010) Modelling the molecular mechanisms of synaptic plasticity using systems biology approaches. *Nat Rev Neurosci* 11:239–251
- Lampoudi S, Gillespie DT, Petzold LR (2009) The multinomial simulation algorithm for discrete stochastic

- simulation of reaction–diffusion systems. *J Chem Phys* 130:094104
- Le Novère N, Shimizu TS (2001) STOCHSIM: modelling of stochastic biomolecular processes. *Bioinformatics* 17:575–576
- Lemerle C, Di Ventura B, Serrano L (2005) Space as the final frontier in stochastic simulations of biological systems. *FEBS Lett* 579:1789–1794
- Marquez-Lago TT, Burrage K (2007) Binomial tau-leap spatial stochastic simulation algorithm for applications in chemical kinetics. *J Chem Phys* 127:104101
- Munsky B, Khammash M (2006) The finite state projection algorithm for the solution of the chemical master equation. *J Chem Phys* 124:044104
- Oliveira RF, Terrin A, Di Benedetto G, Cannon RC, Koh W et al (2010) The role of type 4 phosphodiesterases in generating microdomains of cAMP: large scale stochastic simulations. *PLoS One* 5:e11725
- Oliveira RF, Kim M, Blackwell KT (2012) Subcellular location of PKA controls striatal plasticity: stochastic simulations in spiny dendrites. *PLoS Comput Biol* 8: e1002383
- Plimpton SJ, Slepoy A (2003) ChemCell: a particle-based model of protein chemistry and diffusion in microbial cells. Sandia National Laboratories technical report 2003–45
- Ramsey S, Orrell D, Bolouri H (2005) Dizzy: Stochastic simulation of large-scale genetic regulatory networks. *J Bioinform Comput Biol* 03:415–436
- Rao CV, Arkin AP (2003) Stochastic chemical kinetics and the quasi-steady-state assumption: application to the Gillespie algorithm. *J Chem Phys* 118:4999
- Rao CV, Wolf DM, Arkin AP (2002) Control, exploitation and tolerance of intracellular noise. *Nature* 420:231–237
- Rathinam M, Petzold LR, Cao Y, Gillespie DT (2003) Stiffness in stochastic chemically reacting systems: the implicit tau-leaping method. *J Chem Phys* 119:12784
- Resasco DC, Gao F, Morgan F, Novak IL, Schaff JC et al (2012) Virtual cell: computational tools for modeling in cell biology. *Wiley Interdiscip Rev Syst Biol Med* 4:129–140
- Rodriguez JV, Kaandorp JA, Dobrzynski M, Blom JG (2006) Spatial stochastic modelling of the phosphoenolpyruvate-dependent phosphotransferase (PTS) pathway in Escherichia coli. *Bioinformatics* 22:1895–1901
- Rossinelli D, Bayati B, Koumoutsakos P (2008) Accelerated stochastic and hybrid methods for spatial simulations of reaction–diffusion systems. *Chem Phys Lett* 451:136–140
- Shahrezaei V, Swain PS (2008) The stochastic nature of biochemical networks. *Curr Opin Biotechnol* 19:369–374
- Slepoy A, Thompson AP, Plimpton SJ (2008) A constant-time kinetic Monte Carlo algorithm for simulation of large biochemical reaction networks. *J Chem Phys* 128:205101
- Srivastava R, Haseltine EL, Mastny E, Rawlings JB (2011) The stochastic quasi-steady-state assumption: reducing the model but not the noise. *J Chem Phys* 134:154109
- Stiles JR, Bartol TM Jr (2001) Monte Carlo methods for simulating realistic synaptic microphysiology using MCell. In: De Schutter E (ed) Computational neuroscience: realistic modeling for experimentalists. CRC Press, Boca Raton, pp 87–127
- Stundzia AB, Lumsden CJ (1996) Stochastic simulation of coupled reaction–diffusion processes. *J Comput Phys* 127:196–207
- Takahashi K, Arjunan SNV, Tomita M (2005) Space in systems biology of signaling pathways – towards intra-cellular molecular crowding in silico. *FEBS Lett* 579:1783–1788
- Tian T, Burrage K (2004) Binomial leap methods for simulating stochastic chemical kinetics. *J Chem Phys* 121:10356
- Tolle D, Le Novère N (2010) Meredys, a multi-compartment reaction–diffusion simulator using multistate realistic molecular complexes. *BMC Syst Biol* 4:24
- Turner TE, Schnell S, Burrage K (2004) Stochastic approaches for modelling in vivo reactions. *Comput Biol Chem* 28:165–178
- Vigelius M, Meyer B (2012) Multi-dimensional, mesoscopic Monte Carlo simulations of inhomogeneous reaction-drift-diffusion systems on graphics-processing units. *PLoS One* 7:e33384
- Vigelius M, Lane A, Meyer B (2011) Accelerating reaction–diffusion simulations with general-purpose graphics processing units. *Bioinformatics* 27: 288–290

Striatal Models, Cellular Detail

Kim T, Blackwell¹, Sriraman Damodaran² and Rebekah Evans²

¹Molecular Neuroscience Department, Krasnow Institute for Advanced Study, George Mason University, Fairfax, VA, USA

²Krasnow Institute for Advanced Study, George Mason University, Fairfax, VA, USA

Definition

Models of neuron types of the striatum, which include details of ion channels and neuron morphology.

Detailed Description

Striatal Function in Disease and Health

The striatum is the main input structure of the basal ganglia and is implicated in habit learning, addiction, and neuropathologies such as Parkinson's disease and Huntington's disease. Parkinson's disease is a motor dysfunction caused by degeneration of dopaminergic neurons that project strongly to the striatum. Huntington's disease is another motor dysfunction caused by degeneration of a subset of the neurons in the striatum. Experiments in both humans and animals have demonstrated that normal habit learning involves the striatum, and changes in striatal neural activity are observed consequent to cortical glutamatergic activity (in response to environmental stimuli or motor activity) and dopamine release in response to reward.

Cell Classes in the Striatum

The projection neurons of the striatum are the medium spiny neurons (MSNs) which make up the majority (90–95 %) of the neurons and are subdivided into two classes: those with dopamine D1 receptors which co-release substance P and dynorphin and those with dopamine D2 receptors which co-release mu-opioids. Three other classes of interneurons have been extensively studied: the GABAergic fast-spiking interneurons (FSIs) which are connected by gap junctions, the GABAergic neuropeptide Y-positive (NPY^+) interneurons which also produce nitrous oxide, and the acetylcholinergic (ACh) interneuron, also called the tonically active neuron because of its spontaneous and regular firing pattern. More recently, it has been possible to characterize a set of tyrosine hydroxylase neurons using transgenic expression systems. These neurons exhibit four different firing patterns, but their role in striatal circuits remains to be elucidated. The GABAergic interneurons are in a position to modulate the timing and pattern of firing of the projection neurons of the striatum. In addition, their interconnections via both chemical and electrical synapses may play a role in synchronization. The acetylcholinergic neurons modulate dopamine release from the substantia

nigra and modulate striatal neuron properties through pre- and postsynaptic metabotropic receptors.

One of the compelling questions about striatal function is the role of the D1 versus D2 MSNs. The prevalent theory regarding Parkinson's disease is that dopamine increases excitability of D1 MSNs and decreases excitability of D2 MSNs. This leads to overactivity of the D2 MSNs which tend to inhibit motor movement. Thus, some striatal models have been developed to evaluate which characteristics of MSNs can explain the difference between D1 and D2 neurons and the effect of dopamine. Both neuron classes exhibit a characteristic bimodal membrane potential distribution during anesthesia and sleep, known as up states and down states. Though the significance of this activity is still unclear, several models have investigated which neuron mechanisms underlie this activity. Both normal habit learning and the overly strong habit learning of drug addiction likely involve synaptic plasticity of the MSNs; thus, several models have investigated the control of calcium concentration during synaptic and neuronal activity, which are essential for synaptic plasticity.

Simple MSN Models

Some models contain only a subset of cellular components and attempt to reproduce a specific cellular phenomenon. The purpose of these types of models is to explain cellular behavior using the smallest possible subset of mechanisms. This has the dual advantage of minimizing the number of free parameters and also demonstrating that specific channels/interactions are required. It has the disadvantage of being unable to demonstrate possible alternative mechanisms which might explain the data just as well. An example of this approach is Gruber et al. (2003) which uses two potassium channels and one calcium channel to test whether the known effects of dopamine on these channels affect membrane bistability. Another model (Koos et al. 2004) represents the complete morphology but contains no voltage-dependent channels. This model shows that morphological characteristics, such as electrotonic distance, can account for the difference in

amplitude of inhibitory postsynaptic potentials (IPSPs) produced by FSIs compared to MSNs.

Complex MSN Models

Another class of striatal models includes the complex models. These contain a large number of cellular features and attempt to reproduce many characteristics of voltage and/or calcium waveforms. The advantage of this approach is being able to isolate specific channels or morphological characteristics within the context of many cellular characteristics to demonstrate the necessity or sufficiency of a mechanism in replicating an experimental finding. In addition, these models can be used to evaluate interactions between mechanisms and whether the proposed mechanism exhibits the same function or characteristics in a different context, e.g., *in vivo* versus *in vitro*, or when more channels are added. Ideally, these models can be reused to explain new data with minimal change. The disadvantage of this approach is having numerous free parameters, and the complexity can sometimes hinder the ability to illuminate concepts.

The first complete MSN model (Wolf et al. 2005) used the NEURON simulation software to model a neuron from the ventral striatum (also called the nucleus accumbens). It contains two types of sodium channel, six types of potassium channel, and six types of calcium channel, as well as synaptic channels (NMDA, AMPA, GABA). This model replicates many of the characteristics of MSNs such as the long delay to action potential at rheobase and the low frequency of spiking. The model was used to test the effects of the NMDA/AMPA ratio on entrainment to oscillation (Wolf et al. 2005) and later to test the effects of dopamine modulation on synaptic integration (Moyer et al. 2007). The inwardly rectifying potassium current (K_{ir}) was retuned (Stephen and Manchanda 2009) and implemented in this model to investigate the role of inactivating K_{ir} in MSN excitability. This model also was adapted by Spiga et al. (2010), who added morphology based on a digital reconstruction of an MSN and tested the effects of spine loss and AMPA current reduction on AP frequency during simulated up states.

Several other complex models of dorsal striatal MSNs have been developed. A NEURON model MSN by (Gertler et al. 2008) has one type of sodium channel, one type of calcium channel, and five types of potassium channels and synaptic channels (AMPA). The model was used to test the contribution of morphological differences between D1 and D2 MSNs in describing their different electrophysiological characteristics. This model was adapted by Plotkin et al. (2011) to test the ability of distal dendrites to evoke sustained somatic depolarizations. A similar model, by the same group (Day et al. 2008), was used to investigate the back propagation of the action potential into MSN dendrites.

Another NEURON model MSN by Flores-Barrera et al. (2009) has one type of sodium channel, two types of calcium channels, and five types of potassium channels as well as synaptic channels (NMDA, AMPA, GABA). This model is used to test whether GABAergic input, which is depolarizing below its reversal potential (roughly -60 mV), plays a role in maintaining the depolarization of an MSN during a cortico-striatal up state.

The most recent models (Evans et al. 2012; Evans et al. 2013) uses the GENESIS simulation software to model a dorsal striatum MSN containing one type of sodium channel, six types of potassium channels, five types of calcium channels, and four different NMDA receptor types as well as AMPA receptors. One of the models is used to test whether the NMDA receptor subtypes, based on the four GluN2 subunits, differentially affect the calcium influx into spines during closely timed pairings of pre- and postsynaptic activity (spike timing-dependent plasticity protocols). The other model implements explicit calcium diffusion, buffering, and pumps to investigate the mechanisms that control the calcium that is critical for synaptic plasticity.

Interneuron Models

Most striatal models focus on the spiny projection neurons, but there are several models of striatal interneurons.

The first complete model of a fast-spiking interneuron (FSI) (Kotaleski et al. 2006) contains three types of potassium channels, one type of sodium channel and synaptic channels (AMPA, GABA). This model replicated the observed spike latency and high firing frequency of striatal FSIs. This model was used to investigate how up state firing of FSIs is controlled by transient potassium currents and the contribution of these channels to enhancing signal detection. This model was further used to construct a network model (Hjorth et al. 2009) that investigated the contribution of gap junctions in FSI sensitivity to coincident input from the cortex.

Several simple models of acetylcholinergic neurons (Ach) have been developed. The goal of most of these models is to explain mechanisms underlying the rhythmic firing and burst firing observed in these neurons. Two models demonstrate two different sets of currents which can explain membrane potential oscillations in these models. The first model (Wilson 2005) demonstrates that Kir, HCN (hyperpolarization-activated and cyclic nucleotide-gated channel), and leak conductance in a single compartment could explain membrane potential oscillations in the voltage range of -80 to -60 mV. A second model investigates yet a different mechanism responsible for a slower time course of oscillations. This model (Wilson and Goldberg 2006) is implemented in XPPAUT and is also a single compartment. It contains an L-type calcium

channel, high-voltage-activated potassium channel, leak current, calcium-dependent potassium current, and calcium concentration calculated using a single time constant of decay. Simulations investigated why the slow afterhyperpolarization (sAHP) is activated by long depolarizations (even of small amplitude) but not activated by brief ones. Another model of ACh neurons (Goldberg et al. 2009) was used to investigate the role of calcium channel colocalization in mediating slow and fast afterhyperpolarizations. This model had a single electrical compartment that was subdivided into multiple concentric calcium compartments coupled by diffusion. Several calcium-binding proteins enabled the model to demonstrate that the transient calcium influx produced by an action potential preferentially binds to SK channels, whereas the lower but more prolonged calcium influx produced by subthreshold depolarization preferentially binds to the slower, higher-affinity-binding proteins.

Conclusion

There are several models of striatal neurons that contain cellular detail (Table 1). These models vary in complexity, morphology, and active channels. Each model is configured to test a specific aspect of striatal physiology as efficiently and accurately as possible, and therefore both the simple and the complex models are

Striatal Models, Cellular Detail, Table 1 Computational models of striatal neurons

Citation	Cell type	Simple/complex	Software	Available modelDB
Gruber et al. 2003	MSN	Simple	NEURON	Yes
Moyer et al. 2007; Wolf et al. 2005	MSN, N. Acc.	Complex	NEURON	Yes
Steephen and Manchanda 2009	MSN, N. Acc.	Complex	NEURON	Yes
Spiga et al. 2010	MSN, N. Acc.	Complex	NEURON	Yes
Koos et al. 2004	MSN	Simple	NEURON	No
Gertler et al. 2008	MSN	Complex	NEURON	No
Day et al. 2008	MSN	Complex	NEURON	No
Flores-Barrera et al. 2009	MSN	Complex	NEURON	No
Evans et al. 2012, 2013	MSN	Complex	Genesis	Yes
Kotaleski et al. 2006	FSI	Complex	Genesis	Yes
Wilson 2005	ACh	Simple	XPPAUT	No
Wilson and Goldberg 2006	ACh	Simple	XPPAUT	No
Goldberg et al. 2009	ACh	Simple	XPPAUT	No

valuable. With the increasing power of computers and tools for parameter optimization, the accuracy and complexity of models are likely to increase.

References

- Day M, Wokosin D, Plotkin JL, Tian X, Surmeier DJ (2008) Differential excitability and modulation of striatal medium spiny neuron dendrites. *J Neurosci* 28:11603–11614
- Evans RC, Morera-Herreras T, Cui Y, Du K, Sheehan T, Kotaleski JH, Venance L, Blackwell KT (2012) The effects of NMDA subunit composition on calcium influx and spike timing-dependent plasticity in striatal medium spiny neurons. *PLoS Comput Biol* 8: e1002493
- Evans RC, Maniar YM, Blackwell KT (2013) Dynamic modulation of spike timing-dependent calcium influx during corticostriatal upstates. *J Neurophysiol* 110(7): 1631–45
- Flores-Barrera E, Laville A, Plata V, Tapia D, Bargas J, Galarraga E (2009) Inhibitory contribution to suprathreshold corticostriatal responses: an experimental and modeling study. *Cell Mol Neurobiol* 29:719–731
- Gertler TS, Chan CS, Surmeier DJ (2008) Dichotomous anatomical properties of adult striatal medium spiny neurons. *J Neurosci* 28:10814–10824
- Goldberg JA, Teagarden MA, Foehring RC, Wilson CJ (2009) Nonequilibrium calcium dynamics regulate the autonomous firing pattern of rat striatal cholinergic interneurons. *J Neurosci* 29:8396–8407
- Gruber AJ, Solla SA, Surmeier DJ, Houk JC (2003) Modulation of striatal single units by expected reward: a spiny neuron model displaying dopamine-induced bistability. *J Neurophysiol* 90:1095–1114
- Hjorth J, Blackwell KT, Kotaleski JH (2009) Gap junctions between striatal fast-spiking interneurons regulate spiking activity and synchronization as a function of cortical activity. *J Neurosci* 29:5276–5286
- Koos T, Tepper JM, Wilson CJ (2004) Comparison of IPSCs evoked by spiny and fast-spiking neurons in the neostriatum. *J Neurosci* 24:7916–7922
- Kotaleski JH, Plenz D, Blackwell KT (2006) Using potassium currents to solve signal-to-noise problems in inhibitory feedforward networks of the striatum. *J Neurophysiol* 95:331–341
- Moyer JT, Wolf JA, Finkel LH (2007) Effects of dopaminergic modulation on the integrative properties of the ventral striatal medium spiny neuron. *J Neurophysiol* 98:3731–3748
- Plotkin JL, Day M, Surmeier DJ (2011) Synaptically driven state transitions in distal dendrites of striatal spiny neurons. *Nat Neurosci* 14:881–888
- Spiga S, Lintas A, Migliore M, Diana M (2010) Altered architecture and functional consequences of the mesolimbic dopamine system in cannabis dependence. *Addict Biol* 15:266–276
- Steephen JE, Manchanda R (2009) Differences in biophysical properties of nucleus accumbens medium spiny neurons emerging from inactivation of inward rectifying potassium currents. *J Comput Neurosci* 27:453–470
- Wilson CJ (2005) The mechanism of intrinsic amplification of hyperpolarizations and spontaneous bursting in striatal cholinergic interneurons. *Neuron* 45:575–585
- Wilson CJ, Goldberg JA (2006) Origin of the slow afterhyperpolarization and slow rhythmic bursting in striatal cholinergic interneurons. *J Neurophysiol* 95:196–204
- Wolf JA, Moyer JT, Lazarewicz MT, Contreras D, Benoit-Marand M, O'Donnell P, Finkel LH (2005) NMDA/AMPA ratio impacts state transitions and entrainment to oscillations in a computational model of the nucleus accumbens medium spiny projection neuron. *J Neurosci* 25:9080–9095

Structure-Aided Drug Design

- [Polypeptide and Protein Modeling for Drug Design](#)

Subcritical Bifurcation

- [Multistability in Neurodynamics: Overview](#)

Subjective Experience

- [Prosthetic Vision, Perceptual Effects](#)

Subthalamic Nucleus Cellular Models

Charles Wilson and Michael Farries
Department of Biology, University of Texas at San Antonio, San Antonio, TX, USA

Definition

The subthalamic nucleus is a key basal ganglia structure providing an excitatory innervation to

the globus pallidus and substantia nigra. The spontaneous activity of these neurons is sustained by an autonomous oscillation and interacts with ongoing activity in the external segment of the globus pallidus, with which it has reciprocal connections.

Detailed Description

Why Build a Model of the Subthalamic Neuron?

Interest in models of subthalamic nucleus (STN) neurons was triggered by a report that cocultures of the STN and globus pallidus external segment (GPe) generated sustained rhythmic bursting network activity (Plenz and Kitai 1999). Experimental models of Parkinson's disease in primates exhibit abnormal synchronous low-frequency (7–14 Hz) oscillations in these same nuclei (Bergman et al. 1994). This simple network's oscillations thus might contribute to the pathophysiology of Parkinson's disease. The STN consists of glutamatergic neurons that excite GABAergic neurons in the GPe. These in turn inhibit the STN.

The mean field model by Gillies et al. (2002) showed that oscillations in the STN-GPe circuit required the STN to be powerfully self-excitatory, but experimental evidence for this was lacking (Kita et al. 1983; Sato et al. 2000). The recognition that STN neurons are intrinsic oscillators (Bevan and Wilson 1999) revived the possibility of STN-GPe oscillations. An STN of independent oscillators would be self-exciting, but without lateral interactions the cells would not synchronize. STN synchronization might occur disinaptically through interactions with the GPe. These lateral interactions would be inhibitory, but might still be synchronizing, especially if they triggered rebound excitations. Simulation of these effects required a model of STN and GPe neurons.

The Terman et al. Model

Terman et al. (2002) developed conductance-based models of the STN cell and the GPe cell as components of a model of the

pallido-subthalamic network, with features added to generate the cells' firing patterns as they were known at that time. The relevant components of the subthalamic cell model were autonomous single spiking and a powerful post-hyperpolarization rebound, both of which had been emphasized in studies of cells in slices (Bevan and Wilson 1999; Beurrier et al. 1999). The model subthalamic neuron was validated by showing qualitative similarity to the slice data, including autonomous firing in the appropriate range of rates and a powerful brief depolarization and burst after termination of a hyperpolarizing current injection.

Firing Pattern

Autonomous firing was generated by a persistent sodium current. This was implemented by adjustment of the overlap of activation and inactivation curves to ensure that inactivation would be incomplete over the membrane potential range visited during most of the interspike interval (a window current). This mechanism for the persistent current was consistent with a suggestion by Bevan and Wilson (1999). Later work is inconsistent with this mechanism (Do and Bean 2003), but the model reproduces the phenomenology of the persistent current accurately. The simplification of action potential repolarization and afterhyperpolarization (AHP) currents were more sweeping, employing a single non-inactivating K^+ channel adjusted to activate and deactivate very slowly in the subthreshold range. A Ca-dependent K^+ current was present, but contributed little to the single-spike AHP. It was deemphasized because STN cells show little spike-frequency adaptation during brief episodes of high-frequency firing, rather increasing their firing over the first 100–200 ms (Hallworth et al. 2003; Wilson et al. 2004). Calcium removal was made to be slow so that Ca-dependent K^+ current was strongly accumulating and produced a long-lasting AHP after periods of high-frequency firing. Subsequent studies of the AHP currents of STN cells suggest substantially different mechanisms governing firing rate. The fast repolarizing K^+ current deactivates rapidly, and its AHP component is brief. It also depresses during

high-frequency firing (Teagarden et al. 2008). Most of the AHP is caused by SK-type Ca-dependent K⁺ current. This current does not accumulate during high-frequency firing, but produces a 10–30 ms AHP current following every action potential. Slow spike-frequency adaptation in STN neurons results from inactivation of persistent Na⁺ current (with time constant ~5 s) and the accumulation of a very slow voltage-sensitive K⁺ current (with time constant ~20 s) (Barraza et al. 2009), and the latter creates the slow AHP current seen after firing at high rates.

Rebound

Two rebound currents contribute to the low-threshold spike (LTS) that follows strong hyperpolarizations. The faster one is carried by calcium and caused by T-type Ca²⁺ channels (Hallworth et al. 2003). Longer hyperpolarizations engage HCN currents and a more prolonged depolarization. In the STN cell model, these two currents were combined into a single mechanism. Post-inhibitory rebound was thought to be critical to the oscillations in STN-GPe cocultures (Plenz and Kitai 1999). Experimental attempts to verify the presence of rebounds after brief periods of synaptic inhibition have been unimpressive. Rebounds in STN neurons require hyperpolarizations lasting much longer than typical for GABAa IPSPs (Bevan et al. 2002). On the other hand, rebound excitation in STN cells often lasts longer than in the model cell because L- and N-type Ca²⁺ channels are activated by the LTS. High-voltage-activated Ca²⁺ channels were included in the model, but did not act to prolong rebound firing.

Effective Time Constant

In the model STN cell, slope conductance is high throughout the interspike interval. When the membrane potential is not changing rapidly, it is because strong currents are balanced. Large synaptic currents are required to change the membrane potential, and it then changes rapidly. The charge deposited by synaptic currents dissipates rapidly (see Fig. 1). This enhances the response to rapid fluctuations in synaptic current, and precise timing of inhibition from the GPe. In contrast, the STN cell's I-V curve is nearly flat over most of

the voltages visited during the interspike interval (Farries et al. 2010). The rise time of synaptic potentials is slow, and charge placed on the cell by subthreshold synaptic inputs is retained and alters the membrane potential trajectory and timing of action potentials tens of milliseconds later.

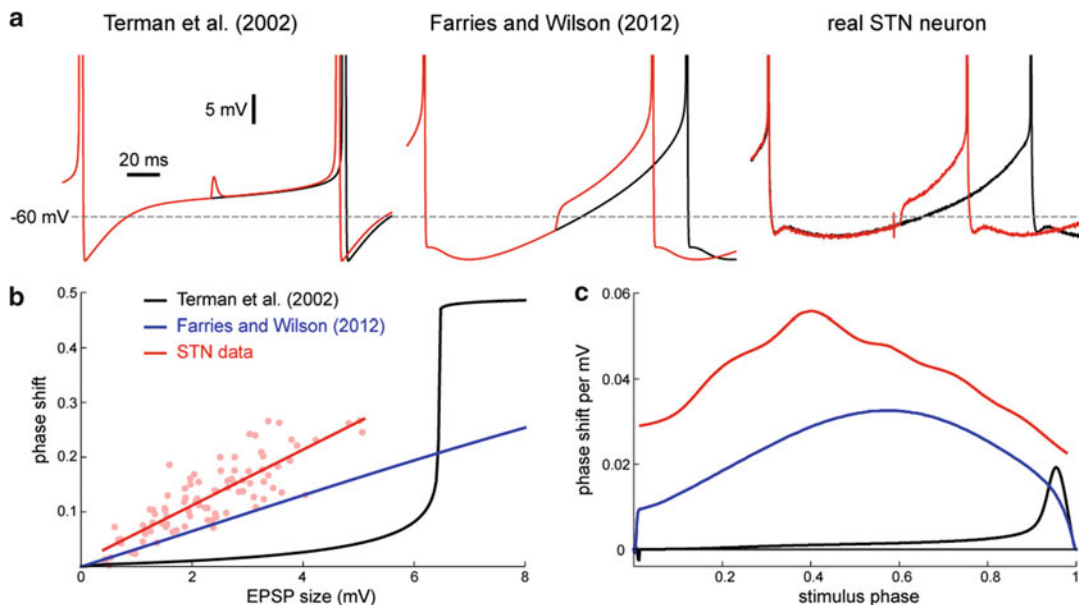
It is unknown whether any of these differences between the Terman et al. model and the real STN neuron are important in generating oscillatory activity in the STN-GPe network, or if they are, what kind of difference they would make. The model was not intended to be a complete description of every aspect of STN cell physiology, but only to include the features that were known at the time and were likely to determine activity in the STN-GPe network. Nobody ever knows in advance which features these are, however, and as always that complicates model design.

Otsuka Model and Plateau Potentials

Studies of STN neurons have described plateau potentials following applied current pulses or post-inhibitory rebound (Nakanishi et al. 1987; Beurrier et al. 1999), which depend on voltage-activated Ca²⁺ currents. A model STN cell incorporating these Ca²⁺ currents and capable of plateau potentials was presented by Otsuka et al. (2004). This was not a comprehensive model, but demonstrated that Ca²⁺ currents measured in voltage clamp possessed properties necessary for plateau potentials as in intracellular recordings. The features of the Otsuka model should be incorporated into any comprehensive model of the STN neuron. However, not all STN cells show plateau potentials, so their inclusion in STN models must be accompanied by some treatment of heterogeneity among STN neurons.

Gillies and Willshaw Model

Models of STN neurons have rarely included dendrites or an axon. One exception is the model by Gillies and Willshaw (2006). This model contains a simplified but still complex dendritic tree, separate fast and persistent Na⁺ currents, fast repolarization current, and realistic Ca²⁺- and Ca-dependent K⁺ currents. Many of its



Subthalamic Nucleus Cellular Models, Fig. 1 (a) Two STN models and an example STN neuron during autonomous oscillations (black traces) and in response to synaptic excitation (red traces). The reversal potential of the models' leak conductance was adjusted to produce autonomous ISIs of 160 ms, matching the unstimulated ISI of the recorded STN neuron. The EPSC was simulated as a product of exponentials ($\tau_{\text{rise}} = 0.8$ ms, $\tau_{\text{decay}} = 1.5$ ms), and EPSC amplitude was adjusted for each model to produce a peak depolarization of 4 mV, matching the recorded neuron's EPSP. The real STN neuron was recorded in a rat brain slice in the presence of GABA receptor antagonists. (b) Phase shift (advance in spike time caused by an EPSP divided by the duration of the autonomous ISI) as a function of EPSP size for EPSPs delivered halfway through the autonomous ISI (i.e., same time as in a, at a phase of 0.5). Because the EPSPs arrived at a phase of 0.5, the maximum possible phase shift (corresponding to a spike triggered immediately by the EPSP) was 0.5. The red circles plot average phase shift in recorded STN neurons for EPSPs arriving at phases of 0.45–0.55 against average EPSP size; each circle is from

a different neuron. The red line is a linear regression on these data ($r^2 = 0.71$, fit slope = 0.05 of phase shift per mV EPSP, $p < 0.0001$, $n = 89$). For the Terman et al. (2002) model, "EPSP size" is EPSC amplitude multiplied by 0.6 mV per unit current density, allowing the graph to include synaptic strengths that trigger spikes at short latency. This conversion factor is derived from the measured 4 mV EPSP shown in a. (c) Infinitesimal phase response curves (iPRCs) for two STN models and an example STN neuron (same cell as in a). The iPRC gives the phase shift (normalized change in spike time) caused by a stimulus per unit stimulus strength (EPSP size, in this case) in the limit of very weak stimuli. This measure of sensitivity to input (phase shift per mV EPSP) varies as a function of when during the autonomous ISI (stimulus phase) the input is delivered. For real STN neurons and the Farries and Wilson (2012) model, this sensitivity to very small inputs is a good predictor of the response to much larger inputs, as illustrated in b by the near-linear relationship between stimulus size and response magnitude

channel properties are based on measurements from other neurons, and the distribution of channels on the dendrites is largely speculative, but it reproduces a number of the neurophysiological properties of STN neurons, including long rebounds, plateau potentials, and rhythmic bursting during hyperpolarization. This model has not been extensively used in models of STN-GPe interactions.

Farries and Wilson Model

The phase-resetting curve is a simple measure of the response of a repetitively firing cell to synaptic inputs. Farries and Wilson (2012) made a simple model of the STN cell intended to reproduce its spontaneous activity and phase-resetting curve. This model did not include the response to deep hyperpolarizations, as it omitted rebound currents. It implemented more accurate

repolarizing and AHP currents, and its I-V curve was adjusted to match that of the STN cell. Slope conductance was low during most of the interspike interval, and synaptic inputs arriving during most of the interspike interval produced changes in the timing of the next spike, similar to those observed in STN neurons. The model was used to derive the phase-resetting curve from the shape of the I-V curve and the AHP conductance (see Fig. 1).

References

- Barraza D, Kita H, Wilson CJ (2009) Slow spike frequency adaptation in neurons of the rat subthalamic nucleus. *J Neurophysiol* 102:3689–3697
- Bergman H, Wichmann T, Karmon B, DeLong MR (1994) The primate subthalamic nucleus. II. Neuronal activity in the MPTP model of parkinsonism. *J Neurophysiol* 72:507–520
- Beurrier C, Congar P, Bioulac B, Hammond C (1999) Subthalamic nucleus neurons switch from single-spike activity to burst-firing mode. *J Neurosci* 19:599–609
- Bevan MD, Wilson CJ (1999) Mechanisms underlying spontaneous oscillation and rhythmic firing in rat subthalamic neurons. *J Neurosci* 19:7617–7628
- Bevan MD, Magill PJ, Hallworth NE, Bolam JP, Wilson CJ (2002) Regulation of the timing and pattern of action potential generation in rat subthalamic neurons in vitro by GABA-A IPSPs. *J Neurophysiol* 87:1348–1362
- Do MT, Bean BP (2003) Subthreshold sodium currents and pacemaking of subthalamic neurons: modulation by slow inactivation. *Neuron* 39:109–120
- Farries MA, Wilson CJ (2012) Biophysical basis of the phase response curve of subthalamic neurons with generalization to other cell types. *J Neurophysiol* 108:1838–1855
- Farries MA, Kita H, Wilson CJ (2010) Dynamic spike threshold and zero membrane slope conductance shape the response of subthalamic neurons to cortical input. *J Neurosci* 30:13180–13191
- Gillies A, Wilshaw D (2006) Membrane channel interactions underlying rat subthalamic projection neuron rhythmic and bursting activity. *J Neurophysiol* 95:2352–2365
- Gillies A, Willshaw D, Li Z (2002) Subthalamic-pallidal interactions are critical in determining normal and abnormal functioning of the basal ganglia. *Proc Biol Sci* 269:545–551
- Hallworth NE, Wilson CJ, Bevan MD (2003) Apamin-sensitive small conductance calcium-activated potassium channels, through their selective coupling to voltage-gated calcium channels, are critical determinants of the precision, pace, and pattern of action potential generation in rat subthalamic nucleus neurons in vitro. *J Neurosci* 23:7525–7542
- Kita H, Chang HT, Kitai ST (1983) The morphology of intracellularly labeled rat subthalamic neurons: a light microscopic analysis. *J Comp Neurol* 215:245–257
- Nakanishi H, Kita H, Kitai ST (1987) Electrical membrane properties of rat subthalamic neurons in an in vitro slice preparation. *Brain Res* 437:35–44
- Otsuka T, Abe T, Tsukagawa T, Song WJ (2004) Conductance-based model of the voltage-dependent generation of a plateau potential in subthalamic neurons. *J Neurophysiol* 92:255–264
- Plenz D, Kitai ST (1999) A basal ganglia pacemaker formed by the subthalamic nucleus and external globus pallidus. *Nature* 400:677–682
- Sato F, Parent M, Levesque M, Parent A (2000) Axonal branching pattern of neurons of the subthalamic nucleus in primates. *J Comp Neurol* 424:142–152
- Teagarden M, Atherton JF, Bevan MD, Wilson CJ (2008) Accumulation of cytoplasmic calcium, but not apamin-sensitive afterhyperpolarization current, during high frequency firing in rat subthalamic nucleus cells. *J Physiol* 586:817–833
- Terman D, Rubin JE, Yew AC, Wilson CJ (2002) Activity patterns in a model for the subthalamopallidal network of the basal ganglia. *J Neurosci* 22:2963–2976
- Wilson CJ, Weyrick A, Terman D, Hallworth NE, Bevan MD (2004) A model of reverse spike frequency adaptation and repetitive firing of subthalamic nucleus neurons. *J Neurophysiol* 91:1963–1980

Subthalamopallidal Loop and Oscillations

David Terman

Department of Mathematics, The Ohio State University, Columbus, OH, USA

Definition

The subthalamopallidal loop consists of reciprocally connected glutamatergic neurons of the subthalamic nucleus (STN) and GABAergic neurons of the external globus pallidus (GPe). The STN and GPe are both nuclei within the basal ganglia (BG). Oscillations correspond to regularly recurring spiking activity of a neuronal system.

Detailed Description

Activity Patterns in the Subthalamopallidal Network

During quiet wakefulness, GPe neurons maintain mean firing rates in excess of 40 Hz, while STN neurons average about 20 Hz (Wilson 2010). The neurons fire without rhythm, and there is rarely synchrony between the spontaneous discharges of different neurons in the BG of neurologically normal subjects (Rubin et al. 2012). During voluntary or passive movement, STN and GPe neurons display intricate spatiotemporal changes in activity, which relate in a complex manner to motor activity. During movement, activity is rarely correlated but it is highly structured, so that there is precise somatotopic specificity (Bevan et al. 2002).

In Parkinson's disease, rhythmic bursting activity at 4–10 Hz and 15–30 Hz is observed in the STN, GPe, and other parts of the basal ganglia (Bevan et al. 2002). This activity is often correlated within and between nuclei: Neurons that are close to each other within areas located throughout the BG and the BG-receiving areas of the thalamus and the cortex tend to fire in synchrony (Rubin et al. 2012).

Microcircuitry of the Subthalamopallidal Network

The subthalamopallidal loop forms an excitatory–inhibitory network: GPe neurons make inhibitory connections onto the STN and STN neurons make excitatory connections onto the GPe. Neurons within the GPe also make inhibitory connections with other GPe neurons and with the output neurons of the basal ganglia. The output nuclei of the basal ganglia consist of the internal segment of the globus pallidus (GPi) and the substantia nigra pars reticulata (SNr). Most inputs to the GPe arise from the striatum and are GABAergic. The GPe also receives excitatory inputs from the cerebral cortex and the intralaminar nuclei of the thalamus (Wilson 2010).

STN neurons also make excitatory connections with the output neurons. In addition to inhibitory input from GPe, the STN receives

excitatory input from the frontal cortex, from the intralaminar thalamic nuclei, and from the pedunculopontine nucleus (Wilson 2010).

The STN and GPe are made up of repeating neuronal architectures so that functionally related regions of the STN and GPe are reciprocally connected and innervate functionally related regions of the basal ganglia output nuclei. Furthermore, the majority of STN and GPe neurons in rats and monkeys have branched axons that mediate both the reciprocal connections and the innervation of the basal ganglia output nuclei (Bevan et al. 2002).

The principal source of afferent input to the basal ganglia, the cerebral cortex, influences the STN–GPe network, directly via monosynaptic projections or indirectly via GABAergic striatal or glutamatergic thalamic neurons. Neuronal projections from the striatum to the output nuclei through the STN–GPe network are often referred to collectively as the *indirect pathway*. By virtue of their extensive innervation of the GABAergic neurons of the basal ganglia output nuclei, the STN and GPe are in a position to influence powerfully the communication of the basal ganglia with the rest of the brain (Bevan et al. 2002).

Origins of Rhythmic Activity in the STN–GPe Network

There has been considerable debate on the origins of correlated, rhythmic firing in the STN–GPe network. This activity could be an emergent property of the STN–GPe network itself and/or be driven by rhythmic activity outside the STN–GPe network.

Computational Modeling of STN–GPe Network Activity

Computational modeling studies incorporating the known biophysical properties of STN and GPe neurons, using a range of network architectures within the limits of the known anatomy, have been useful in examining the principles that underlie activity patterns in the STN–GPe network. Computer simulations in (Terman et al. 2002), for example, suggest that the STN–GPe network is capable of generating patterned and persistent activity of a variety of types;

these include uncorrelated spiking activity, as arises during normal resting conditions, and synchronous bursting activity associated with pathological, Parkinsonian conditions. Rhythmic activity arises in the model through mutually coupled, excitatory-inhibitory interactions between the STN and GPe neurons: Synchronous bursting of GPe neurons generates sufficient hyperpolarization in STN neurons for rebound burst activity, which, in turn, drives bursting activity in GPe neurons and leads to continuation of the rhythm.

Recent studies have examined the role of structures, such as the striatum and cortex, outside the STN-GPe network in generating beta band and other oscillations (Bevan et al. 2002; Rubin et al. 2012). Moreover, the STN-GPe network model has been extended to include other neurons including those within the GPi, the thalamus, and the cortex. These studies have led to new hypotheses concerning mechanisms underlying the therapeutic effects of deep brain stimulation (Guo et al. 2008; Hahn and McIntyre 2010).

References

- Bevan MD, Magill PJ, Terman D, Bolam JB, Wilson CJ (2002) Move to the rhythm: oscillations in the subthalamic nucleus-external globus-pallidus network. *Trends Neurosci* 25:525–531
- Guo Y, Rubin JE, McIntyre CC, Vitek JL, Terman D (2008) Thalamocortical relay fidelity varies across subthalamic nucleus deep brain stimulation protocols in a data-driven computational model. *J Neurophysiol* 99:1477–1492
- Hahn PJ, McIntyre CC (2010) Modeling shifts in the rate and pattern of subthalamic-pallidal network activity during deep brain stimulation. *J Comput Neurosci* 28:425–441
- Rubin JE, McIntyre CC, Turner RS, Wichmann T (2012) Basal ganglia activity patterns in parkinsonism and computational modeling of their downstream effects. *Eur J Neurosci* 36:2213–2228
- Terman D, Rubin JE, Yew AC, Wilson CJ (2002) Activity patterns in a model for the subthalamic-pallidal network of the basal ganglia. *J Neurosci* 22:2963–2976
- Wilson CJ (2010) Subthalamic-Pallidal circuit. In: Shepherd G, Grinley S (eds) *Handbook of brain microcircuits*. Oxford University Press, New York, pp 127–134

Subthreshold Amplitude and Phase Resonance in Single Neurons

Horacio G. Rotstein

Department of Mathematical Sciences, New Jersey Institute of Technology, Newark, NJ, USA

Synonyms

Membrane potential resonance; Membrane potential or subthreshold preferred frequency responses to oscillatory inputs

Definition

Subthreshold (or membrane potential) resonance refers to the ability of neurons to exhibit a peak in their voltage amplitude response to oscillatory input currents at a preferred (resonant) frequency.

Subthreshold (or membrane potential) phase-resonance refers to the ability of neurons to exhibit a zero-phase (or zero-phase-shift) response to oscillatory input currents at a nonzero (phase-resonant) frequency.

Linear subthreshold resonance refers to the subthreshold resonant properties (amplitude and phase) in linear models. In this entry we focus on 2D and 3D linear and linearized conductance-based models.

Detailed Description

Introduction

Subthreshold resonance has been observed in various neuron types in the hippocampus and the entorhinal cortex (Hutcheon and Yarom 2000; Pike et al. 2000; Schreiber et al. 2004; Zemankovics et al. 2010; Hu et al. 2002, 2009; Leung and Yu 1998; Erchova et al. 2004; Heys et al. 2010; Engel et al. 2008; Wang et al. 2006) as well as in other neural systems (Hutcheon et al. 1994, 1996b; Art et al. 1986; Tohidi and Nadim 2009; Tseng and Nadim 2010; Castro-Alamancos et al. 2007; Wu et al. 2001; Gastrein et al. 2011;

Sciamanna and J 2011). The functionality of the resonant properties of neurons has not been established yet. However, since the resonant frequency of principal cells in the entorhinal cortex and the hippocampus lies in the theta frequency range, resonance has been implicated in the generation of rhythmic activity at theta and nested theta/gamma frequencies.

Theoretical studies on resonance have been performed using linear models (either caricature models or linearizations of conductance-based models) or by direct simulation conductance-based models (Richardson et al. 2003; Gutfreund et al. 1995; Schreiber et al. 2004; Haas and White 2002; Alexander et al. 1990; Izhikevich 2001, 2002; Hutcheon et al. 1994, 1996a; Reinker et al. 2004; Rotstein and Nadim 2013; Rotstein 2013).

Conductance-Based Models

In this entry we discuss the subthreshold resonant properties of neurons in the context of biophysical (conductance-based) models (Skinner 2006; Hodgkin and Huxley 1952) whose subthreshold dynamics are governed by the following equations:

$$C \frac{dV}{dt} = -I_L - \sum_k I_k + I_{app} + I_{in}(t), \quad (1)$$

$$\frac{dx_k}{dt} = \frac{x_{k,\infty}(V) - x_k}{\tau_{k,x}(V)}, \quad k = 1, 2. \quad (2)$$

In the current-balance equation (1), V is the membrane potential (mV), t is time (msec), C is the membrane capacitance ($\mu\text{F}/\text{cm}^2$), I_{app} is the applied bias (DC) current ($\mu\text{A}/\text{cm}^2$), $I_L = G_L(V - E_L)$ is the leak current, and $I_k = G_k x_k(V - E_k)$ are generic expressions for ionic currents (with k an index) with maximal conductance G_k (mS/cm^2) and reversal potentials E_k (mV), respectively. The dynamics of the gating variables x_k are governed by the kinetic equations (2) where $x_{k,\infty}(V)$ and $\tau_{k,x}(V)$ are the voltage-dependent activation/inactivation curves and time constants, respectively. The generic ionic currents I_k we consider here are restricted to

have a single gating variable x_k and to be linear in x_k . The persistent sodium, hyperpolarization-activated ($\text{h}-$) and slow potassium ($\text{M}-$) currents found to be responsible for the generation of subthreshold resonance in neurons of the hippocampus and the entorhinal cortex have this form (Schreiber et al. 2004; Hu et al. 2002, 2009; Pike et al. 2000; Rotstein et al. 2006; Izhikevich 2006). Our discussion of subthreshold resonance can be easily adapted to ionic currents having two gating variables raised to powers not necessarily equal to one such as calcium currents (Hutcheon and Yarom 2000).

The function $I_{in}(t)$ in Eq. 1 is an oscillatory input current ($\mu\text{A}/\text{cm}^2$) of the form

$$I_{in}(t) = A_{in} \sin(\Omega t) \quad \text{with} \quad \Omega = \frac{2\pi f}{1000}, \quad (3)$$

where f is the input frequency (Hz).

In this entry we focus on two- and three-dimensional models describing the dynamics of V and either one (2D) or two (3D) gating variables. Additional currents whose gating variables evolve on a very fast time scale (as compared to the other variables) can be included by using the adiabatic approximation $x_k = x_{k,\infty}(V)$. Here we include one such fast current ($I_3 = G_3 x_{3,\infty}(V)(V - E_3)$). Additional fast currents can be included without significantly changing the formalism used here.

Linearized Conductance-Based Models

Linearization of the autonomous part ($I_{in}(t) = 0$) of system (1) and (2) around the fixed-point $(\bar{V}, \bar{x}_1, \bar{x}_2)$ yields (Richardson et al. 2003)

$$C \frac{dv}{dt} = -gL v - g_1 w_1 - g_2 w_2 + I_{in}(t), \quad (4)$$

$$\bar{\tau}_1 \frac{dw_1}{dt} = v - w_1, \quad (5)$$

$$\bar{\tau}_2 \frac{dw_2}{dt} = v - w_2, \quad (6)$$

where

$$v = V - \bar{V}, \quad w_1 = \frac{x_1 - \bar{x}_1}{x'_{1,\infty}(\bar{V})}, \quad w_2 = \frac{x_2 - \bar{x}_2}{x'_{2,\infty}(\bar{V})}, \quad \frac{dw_2}{dt} = \eta(v - w_2), \quad (7)$$

$$\bar{x}_k = x_{k,\infty}(\bar{V}), \quad \bar{\tau}_k = \tau_{x,k}(\bar{V}) \quad k = 1, 2, \quad (8)$$

$$g_k = G_k x'_{k,\infty}(\bar{V})(\bar{V} - E_k), \quad k = 1, 2, 3, \quad (9)$$

and

$$g_L = G_L + G_1 x_{1,\infty}(\bar{V}) + G_2 x_{2,\infty}(\bar{V}) + G_3 x_{3,\infty}(\bar{V}) + g_3. \quad (10)$$

In Eqs. 7 and 9, $x'_{k,\infty} = dx_k/dV(k = 1, 2, 3)$. Note that the gating variables w_1 and w_2 in Eq. 7 have units of voltage ($[v] = [w_1] = V$).

The effective leak conductance g_L in Eq. 10 contains information about the biophysical leak conductance G_L , the ionic conductances, and their associated voltage-dependent activation/inactivation curves. The fast ionic current I_3 contributes to g_L with an additional term (g_3). The signs of the effective ionic conductances g_k determine whether the associated gating variables are either resonant ($g_k > 0$) or amplifying ($g_k < 0$) (Richardson et al. 2003; Hutcheon and Yarom 2000). All terms in g_L are positive except for the last one that can be either positive or negative. Specifically, g_L can become negative for negative enough values of g_3 .

System (4)–(6) can be rescaled by defining the following dimensionless time and parameters:

$$\hat{t} = \frac{t}{\bar{\tau}_1}, \quad \gamma_L = \frac{g_L \bar{\tau}_1}{C}, \quad \gamma_1 = \frac{g_1 \bar{\tau}_1}{C}, \quad (11)$$

$$\gamma_2 = \frac{g_2 \bar{\tau}_1}{C}, \quad \eta = \frac{\bar{\tau}_1}{\bar{T}_2}.$$

Substitution of Eq. 11 into Eqs. 4–6 and a further rearrangement of terms yield

$$\frac{dv}{d\hat{t}} = -\gamma_L v - \gamma_1 w_1 - \gamma_2 w_2 + \hat{I}_{in}(t), \quad (12)$$

$$\frac{dw_1}{d\hat{t}} = v - w_1, \quad (13)$$

where γ_L , γ_1 and γ_2 are the dimensionless effective conductances and

$$\hat{I}_{in}(t) = \hat{A}_{in} \sin(2\pi f \bar{\tau}_1 \hat{t}/1000) \quad (15)$$

with $\hat{A}_{in} = \frac{A_{in} \bar{\tau}_1}{C}$.

Voltage Response, Impedance, Impedance Amplitude and Phase

The voltage response of a neuron receiving an oscillatory input current is typically measured in terms of the so-called impedance function $Z(f)$ defined as the quotient between the Fourier transforms of the output voltage $V_{out}(t)$ and the input current $I_{in}(t)$

$$Z(f) = \frac{\mathcal{F}[V_{out}(t)(f)]}{\mathcal{F}[I_{in}(t)](f)}. \quad (16)$$

The impedance $Z(f)$ is a complex quantity with amplitude $|Z(f)|$ and phase $\Phi(f)$. For simplicity we refer to the impedance amplitude $|Z(f)|$ simply as the impedance $Z(f)$.

For a linear system receiving sinusoidal input currents of the form (3), the voltage response is given by

$$V_{out}(t; f) = A_{out}(f) \sin(\Omega t + \Phi(f)) \quad (17)$$

where $A_{out}(f)$ is the amplitude and the phase $\Phi(f)$ (or phase-shift) is the difference between the peaks of the input current $I_{in}(t; f)$ and the output voltage $V_{out}(t; f)$. The impedance amplitude is given by

$$|Z(f)| = \frac{A_{out}(f)}{A_{in}}. \quad (18)$$

For linear systems, Eq. 18 is equivalent to Eq. 16.

Several authors have used the so-called ZAP current (Puil et al. 1986)

$$I_{in}(t) = I_{Zap}(t) = A_{in} \sin(2\pi f(t)t), \quad f(t) = \frac{f_M t}{2T_M} \quad (19)$$

that sweeps through a given range of frequencies over time with a maximum frequency f_M and a stimulus length T_M . (Other types of time-dependent input frequencies have also been used (Tseng and Nadim 2010).) The corresponding impedance function can be computed using Eq. 16.

Impedance and Phase Profiles for 2D and 3D Linear Systems: Analytic Expressions

Analytic expressions for the impedance and phase profiles for linear systems can be computed analytically. We use the following generic system:

$$\begin{cases} X' = aX + bY + cZ + A_{in}e^{i\Omega t}, \\ Y' = \alpha X + pY, \\ Z' = \beta X + qZ, \end{cases} \quad (20)$$

where $a, b, c, \alpha, \beta, p$, and q are constant, $\Omega > 0$, and $A_{in} > 0$.

The characteristic polynomial for the corresponding homogeneous system ($A_{in} = 0$) is given by

$$\begin{aligned} r^3 - (a + p + q)r^2 + (ap + aq + pq - c\beta - b\alpha)r \\ + b\alpha q + c\beta p - apq = 0. \end{aligned} \quad (21)$$

The particular solution to system (20) has the form

$$\begin{aligned} X_p(t) &= A_{out}e^{i\Omega t}, & Y_p(t) &= B_{out}e^{i\Omega t} \\ \text{and } Z_p(t) &= C_{out}e^{i\Omega t}, \end{aligned} \quad (22)$$

Substituting Eq. 22 into system (20), rearranging terms, and solving the resulting algebraic system, one obtains

$$Z(\Omega) = \frac{A_{out}}{A_{in}} = \frac{P_r(\Omega) + iP_i(\Omega)}{Q_r(\Omega) + iQ_i(\Omega)}, \quad (23)$$

where

$$P_r(\Omega) = pq - \Omega^2, \quad (24)$$

$$P_i(\Omega) = -(p + q)\Omega, \quad (25)$$

$$Q_r(\Omega) = (a + p + q)\Omega^2 - apq + b\alpha q + c\beta p \quad (26)$$

and

$$Q_i(\Omega) = (ap + aq + pq - b\alpha - c\beta - \Omega^2)\Omega. \quad (27)$$

From Eq. 23

$$|Z|^2(\Omega) := \frac{A_{out}^2}{A_{in}^2} = \frac{P_r^2(\Omega) + P_i^2(\Omega)}{Q_r^2(\Omega) + Q_i^2(\Omega)} \quad (28)$$

and

$$\Phi = \tan^{-1} \frac{P_r(\Omega)Q_i(\Omega) - P_i(\Omega)Q_r(\Omega)}{P_r(\Omega)Q_r(\Omega) + P_i(\Omega)Q_i(\Omega)}. \quad (29)$$

For a 2D linear system ($c = q = 0$), the characteristic polynomial for the corresponding homogeneous system ($A_{in} = 0$) is given by

$$r^2 - (a + p)r + (ap - b\alpha) = 0. \quad (30)$$

The roots of the characteristic polynomial are given by

$$r_{1,2} = \frac{(a + p) \pm \sqrt{(a - p)^2 + 4b\alpha}}{2}. \quad (31)$$

From Eq. 31, the homogeneous (unforced) system displays oscillatory solutions with a natural frequency f_{nat} (Hz) given by

$$f_{nat} = \mu \frac{1000}{2\pi}, \quad \mu = \sqrt{-4b\alpha - (a - p)^2}, \quad (32)$$

provided $4b\alpha + (a - p)^2 < 0$.

The impedance amplitude and phase are given, respectively, by

$$|Z(\Omega)|^2 := \frac{A_{out}^2}{A_{in}^2} = \frac{p^2 + \Omega^2}{[ap - b\alpha - \Omega^2]^2 + (a + p)^2\Omega^2} \quad (33)$$

and

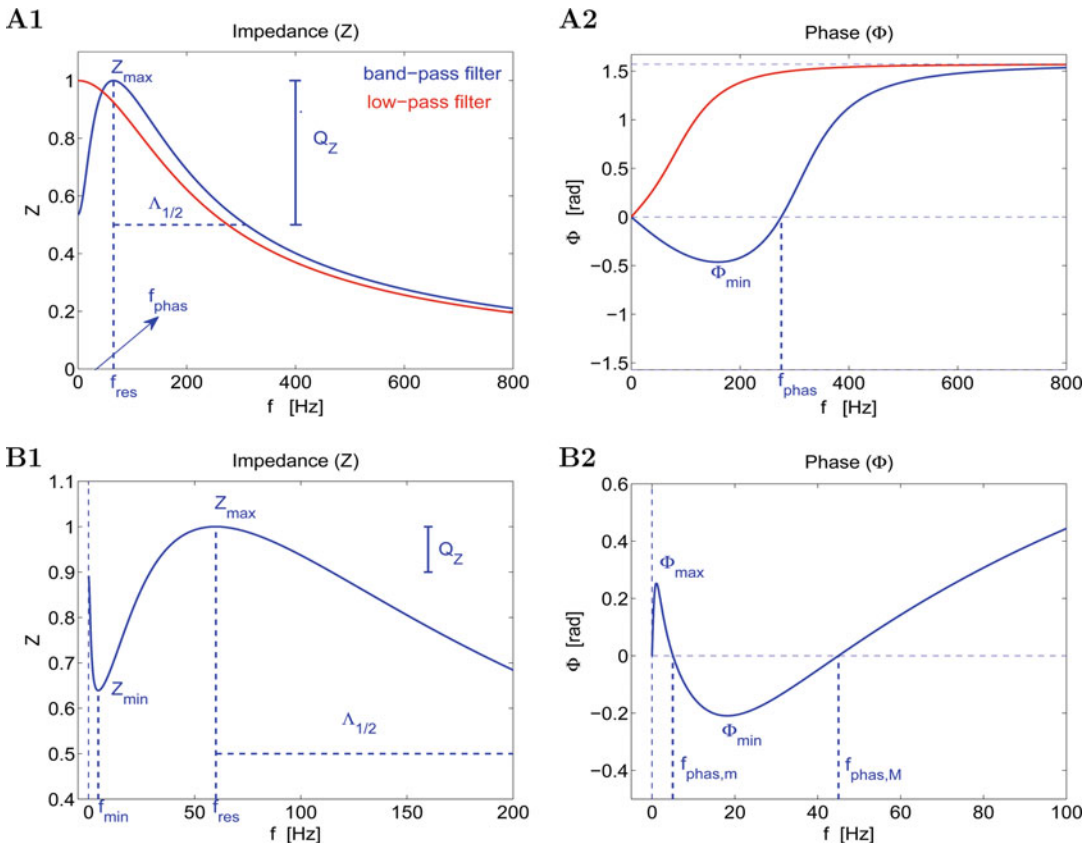
$$\Phi(\Omega) = \tan^{-1} \frac{(ap - b\alpha - \Omega^2)\Omega - (a + p)\Omega p}{(ap - b\alpha - \Omega^2)p + (a + p)\Omega^2}. \quad (34)$$

Impedance and Phase Profiles for 2D and 3D Linear Systems: Resonance and Phase-Resonance

The impedance and phase profiles are the curves of the impedance amplitude (Z) and phase (Φ) as a function of the input frequency f , respectively.

For 2D linear systems the impedance profile is either a decreasing function of f (red curve in Fig. 1-A1) representing a low-pass filter response, or it exhibits a peak at a nonzero input

frequency (blue curve in Fig. 1-A1) representing a resonant response at the resonant frequency f_{res} (impedance peak). The phase profile is either an increasing function of f converging asymptotically to $\Phi = \pi/2$ (red curve in Fig. 1-A2) representing a delayed response for all values of f , or it exhibits a zero-phase response at a nonzero input frequency (blue curve in Fig. 1-A2) called the phase-resonant frequency f_{phas} . For input frequencies $f = f_{phas}$, the input current and output



Subthreshold Amplitude and Phase Resonance in Single Neurons. **Fig. 1** Impedance (Z) and phase (Φ) profiles (curves of Z and Φ versus the input frequency f) for representative 2D (A) and 3D (B) linear systems. **(A1):** The impedance Z is characterized by four attributes: the resonant frequency f_{res} , the impedance peak Z_{max} , the resonance amplitude $Q_Z = Z_{max} - Z(0)$, and the half-bandwidth $\Lambda_{1/2}$. **(A2):** The phase Φ is characterized by two attributes: the zero-crossing frequency f_{phas} and the phase minimum Φ_{min} . For this example, $f_{phas} < f_{res}$. **(B1):** The impedance Z is characterized by two additional attributes: the antiresonant frequency f_{ares} and the impedance local minimum Z_{min} . **(B2):** The phase Φ is characterized

by two additional attributes: the phase local maximum Φ_{max} and the zero-crossing phase $f_{phas,m}$ on the descending portion of Φ . The zero-crossing phase $f_{phas,M}$ on the ascending portion of Φ is as f_{phas} in panel A1. The curves in all panels were computed using system (4)–(6) with **A1** (blue curve): $g_L = 1$, $g_1 = 0$, $g_2 = 0$, and $\tau_I = 10$. **A1** (red curve): $g_L = 0$, $g_1 = 4$, $g_2 = 0$, and $\tau_I = 1$ (red curve). **A2** (blue curve): $g_L = 1$, $g_1 = 0$, $g_2 = 0$, and $\tau_I = 10$. **A2** (red curve): $g_L = 0$, $g_1 = 0.5$, $g_2 = 0$, and $\tau_I = 1$. **B1**: $g_L = 1$, $g_1 = 0.8$, $g_2 = -0.6$, $\tau_I = 10$, and $\tau_2 = 100$. **B2**: $g_L = 1$, $g_1 = 1$, $g_2 = -0.9$, $\tau_I = 10$, and $\tau_2 = 100$. In all panels $C = 1$ and $A_{in} = 1$

voltage peak at the same time. For input frequencies $f < f_{phas}$, the voltage response is advanced, while for input frequencies $f > f_{phas}$, the voltage response is delayed.

The voltage response for 3D linear systems is more complex than for 2D linear systems. The impedance profiles may exhibit a local minimum at an input frequency f_{min} in addition to the peak at the resonant frequency (Fig. 1-B1). The phase profile may have an additional zero-frequency cross (Fig. 1-B1). For input frequencies $f = f_{phas,m}$ and $f = f_{phas,M}$, the input current and output voltage peak at the same time. The voltage response is delayed for input frequencies $f < f_{phas,m}$ and $f > f_{phas,M}$ and advanced for input frequencies f such that $f_{phas,m} < f < f_{phas,M}$.

Attributes of the Impedance and Phase Profiles for 2D and 3D Linear Systems

For mechanistic purposes one wishes to track the changes in the impedance and phase profiles as a chosen model parameter changes. To this end it is useful to characterize these graphs using a small number of attributes rather than the information corresponding to the whole curves.

For 2D linear systems the impedance profile can be characterized by four attributes (Fig. 1-A1): the resonant frequency f_{res} , the maximum impedance Z_{max} , the resonance amplitude $Q_Z = Z_{max} - Z(0)$, and the half-bandwidth $\Lambda_{1/2}$. Some authors define the resonance amplitude as $Q = Z_{max}/Z(0)$. For a low-pass filter response, $Q_Z = 0$ ($Q = 1$). Resonance requires $Q_Z > 0$ ($Q > 1$). The phase profile can be characterized by two attributes (Fig. 1-A2): the phase-resonant frequency f_{phas} and the minimum phase Φ_{min} . A phase-resonant response requires $\Phi_{min} < 0$.

For 3D linear systems the impedance profile can be characterized by f_{res} , Z_{max} , Q_Z , $\Lambda_{1/2}$, and two additional attributes (Fig. 1-B1): the minimum phase Z_{min} and the minimum frequency f_{min} . The phase profile can be characterized by f_{phas} (or $f_{phas,M}$), Φ_{min} , and two additional attributes (Fig. 1-B2): the maximum phase Φ_{max} and the minimum zero-crossing frequency $f_{phas,m}$. The maximum zero-crossing frequency $f_{phas,M}$ is equal to f_{phas} in 2D linear systems.

Resonant and Amplifying Currents and Gating Variables

Subthreshold resonance results from a combination of low- and high-pass filter mechanisms that have been described in terms of ionic currents (Hutcheon and Yarom 2000). Passive currents (in particular capacitive currents) act as low-pass filters (see Fig. 1-A1, red curve).

The so-called resonant currents create a preferred frequency band by slowly opposing voltage changes. Amplifying currents, on the other hand, have been argued to generate a positive feedback effect that amplifies voltage changes and hence make existing resonances more pronounced (Hutcheon and Yarom 2000), but they do not create resonance by themselves. Prototypical examples of resonant currents are (inward) hyperpolarization-activated h-currents (I_h) (Haas and White 2002; Schreiber et al. 2004; Hutcheon et al. 1996b) and (outward) slow potassium currents (I_{Ks} or I_M) (Gutfreund et al. 1995). Prototypical examples of amplifying currents are persistent sodium currents (I_{NaP}) (Haas and White 2002; Schreiber et al. 2004; Hutcheon et al. 1996b; Gutfreund et al. 1995) and high-threshold calcium currents ($I_{Ca,L}$) (Hutcheon and Yarom 2000). The low-threshold calcium current I_T is both resonant and amplifying (Hutcheon and Yarom 2000).

In fact, the resonant and amplifying abilities do not reside in the currents themselves but in their gating variables (Hutcheon and Yarom 2000; Richardson et al. 2003). Inward inactivating and outward activating gating variables produce resonant effects. Inward activating and outward inactivating gating variables produce amplifying effects.

The resonant or amplifying nature of a gating variable can be predicted from the definition of the effective ionic conductances g_k in Eq. 9, which are positive for resonant gating variables and negative for amplifying gating variables (Richardson et al. 2003).

In addition to generating resonance and amplifying existing resonances, changes in the resonant and amplifying conductances affect other attributes of the impedance and phase profiles (Rotstein and Nadim 2013).

Subthreshold Resonance, Phase-Resonance, and Intrinsic Oscillations

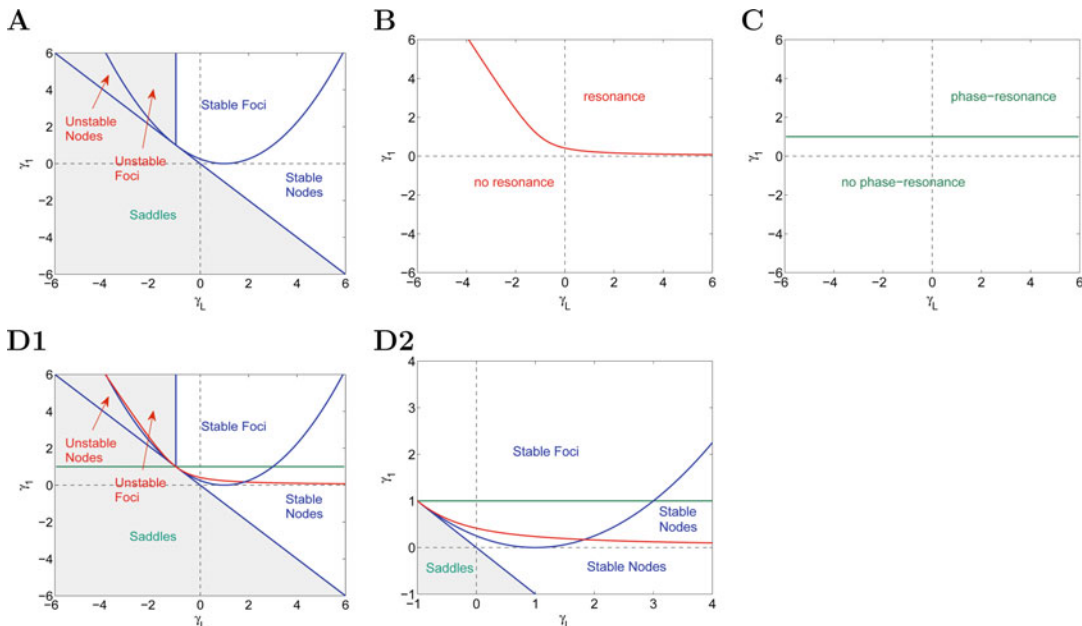
Subthreshold resonance, phase-resonance, and intrinsic (damped) oscillations are different phenomena generated by related, but different mechanisms (Richardson et al. 2003; Rotstein and Nadim 2013; Rotstein 2013). This is illustrated in Fig. 2 for the 2D linear system (12) and (13) ($\gamma_2 = 0$).

The differences between these phenomena are clearly illustrated by the so-called $\lambda - \omega$ systems (Kopell and Howard 1973)

$$\frac{dx}{dt} = -\lambda x - \omega y, \quad (35)$$

$$\frac{dy}{dt} = \omega x - \lambda y, \quad (36)$$

with $\lambda > 0$ and $\omega > 0$.



Subthreshold Amplitude and Phase Resonance in Single Neurons, Fig. 2 Stability and resonance diagrams for the reduced 2D linear system (12) and (13) ($\gamma_2 = 0$) in $\gamma_L - \gamma_1$ parameter space. (A) Stability diagram. The blue curves separate between regions with different stability properties. (B) Resonance diagram. The red curves separate between regions where the system does (above) and does not (below) exhibit resonance. (C) Phase-resonance diagram. The green line separates

The eigenvalues and natural frequency are given by

$$r_{1,2} = -\lambda \pm \sqrt{-\omega^2} \quad \text{and} \quad \Omega_{nat} = \omega. \quad (37)$$

The resonant and phase-resonant frequencies are given by

$$\begin{aligned} \Omega_{res} &= \sqrt{-\lambda^2 + \omega\sqrt{4\lambda^2 + \omega^2}} \quad \text{and} \\ \Omega_{phas} &= \sqrt{\omega^2 - \lambda^2}. \end{aligned} \quad (38)$$

For $\lambda = 0$ (no damping) $\Omega_{nat} = \Omega_{res} = \Omega_{phas}$, while for other values of λ , these three quantities are different.

System (35) and (36) can be transformed into a rescaled system of the form (12) and (13) (with $\gamma_2 = 0$) by defining

between regions where the system does (above) and does not (below) exhibit phase-resonance. (D). Superimposed stability (blue curves), resonance (red curves), and phase-resonance (green line) diagrams showing that intrinsic oscillations and resonance may occur in the absence of the other and resonance may occur in the absence of phase-resonance. The right panel is a magnification of the left one

$$v = \omega x, \quad \omega = \lambda y, \quad \hat{t} = \lambda t, \quad (39)$$

and

$$\gamma L = 1 \quad \gamma_1 = \frac{\omega^2}{\lambda^2}. \quad (40)$$

More generally, the differences among the subthreshold resonance, phase-resonance, and natural frequencies are illustrated by the 2D linear system (4) and (5) ($g_2 = 0$) where

$$\Omega_{nat} = \frac{1}{2\tau_1 C} \sqrt{4g_1\tau_1 C + (C - gL\tau_1)^2}, \quad (41)$$

$$\Omega_{res} = \frac{1}{\tau_1} \sqrt{\sqrt{\frac{g_1^2\tau_1^2 + 2g_Lg_1\tau_1^2 + 2g_1\tau_1 C}{C^2}} - 1}, \quad (42)$$

and

$$\Omega_{phas} = \frac{1}{\tau_1} \sqrt{\frac{g_1\tau_1 - C}{C}}. \quad (43)$$

Mechanisms of Generation of Subthreshold Resonance and Phase-Resonance

The investigation of the mechanisms of generation of resonance and phase-resonance consists of tracking the changes in the impedance and phase profiles that result from changes in certain model parameters of interest while keeping the remaining parameters fixed. This task is greatly simplified if one uses the attributes of the impedance and phase profiles instead of the full graphs.

This mechanistic investigation can be performed at different modeling levels by looking at (i) the dimensionless effective parameters in the rescaled system (12)–(14), (ii) the effective parameters in the linearized system (4)–(6), or (iii) the biophysical parameters in the original conductance-based model.

For the 2D rescaled system ($\gamma_2 = 0$), heat graphs of the attributes of the impedance and phase profiles can be plotted in the γ_L – γ_1 parameter space presented in Fig. 2 (Rotstein and Nadim 2013). These attribute graphs can be used to investigate the effects of changes in

parameters at the different levels of description mentioned above including (i) the effects of changes in the dimensionless effective conductances γ_L and γ_1 , by moving in either horizontal (γ_L) and vertical (γ_1) directions respectively; (ii) the effects of changes in the effective conductances g_L and g_1 , by moving in either horizontal (g_L) and vertical directions (g_1) using the rescaling Eq. 11 to account for the values of τ_1 and C ; (iii) the effects of changes in the time constant τ_1 , by moving along oblique lines (parametrized by τ_1) with slope g_1/g_L in the attribute graphs; and (iv) the effects of changes in the biophysical parameters of the original conductance-based model to the linear level of approximation, by using the formulas (9) and (10) for the effective ionic (g_k) and leak (g_L) conductances in terms of the biophysical conductances (G_L and G_k), resting potential, and other biophysical parameters. Changes in the biophysical conductances generate nonlinear curves in the γ_L – γ_1 parameter space (Rotstein and Nadim 2013). These nonlinear curves reflect the different effects caused by different types of resonant and amplifying currents (Rotstein and Nadim 2013).

This approach can be extended to 3D systems by looking at appropriate projections. Alternatively, one can investigate the linearized system (4)–(6) directly. For the rescaled system (12)–(14), one varies the dimensionless effective conductances γ_L , γ_1 , and γ_2 and the time scale parameter η .

Acknowledgments The author wishes to thank Farzan Nadim and Frances Skinner for useful comments. This work was supported by NSF grant DMS-1313861 (HGR).

References

- Alexander JC, Doedel EJ, Othmer HG (1990) On the resonance structure in a forced excitable system. SIAM J Appl Math 50:1373–1418
- Art JJ, Crawford AC, Fettiplace R (1986) Electrical resonance and membrane currents in turtle cochlear hair cells. Hear Res 22:31–36
- Castro-Alamancos MA, Rigas P, Tawara-Hirata Y (2007) Resonance (approximately 10 Hz) of excitatory networks in motor cortex: effects of voltage-dependent ion channel blockers. J Physiol 578:173–191

- Engel TA, Schimansky-Geier L, Herz AV, Schreiber S, Erchova I (2008) Subthreshold membrane-potential resonances shape spike-train patterns in the entorhinal cortex. *J Neurophysiol* 100:1576–1588
- Erchova I, Kreck G, Heinemann U, Herz AVM (2004) Dynamics of rat entorhinal cortex layer II and III cells: characteristics of membrane potential resonance at rest predict oscillation properties near threshold. *J Physiol* 560:89–110
- Gastrein P, Campanac E, Gasselin C, Cudmore RH, Bialowas A, Carlier E, Fronzaroli-Molinieres L, Ankri N, Debanne D (2011) The role of hyperpolarization-activated cationic current in spike-time precision and intrinsic resonance in cortical neurons in vitro. *J Physiol* 589:3753–3773
- Gutfreund Y, Yarom Y, Segev I (1995) Subthreshold oscillations and resonant frequency in guinea pig cortical neurons: physiology and modeling. *J Physiol* 483:621–640
- Haas JS, White JA (2002) Frequency selectivity of layer II stellate cells in the medial entorhinal cortex. *J Neurophysiol* 88:2422–2429
- Heys JG, Giacomo LM, Hasselmo ME (2010) Cholinergic modulation of the resonance properties of stellate cells in layer II of the medial entorhinal. *J Neurophysiol* 104:258–270
- Hodgkin AL, Huxley AF (1952) A quantitative description of membrane current and its application to conductance and excitation in nerve. *J Physiol* 117:500–544
- Hu H, Vervaeke K, Graham JFL, Storm J (2009) Complementary theta resonance filtering by two spatially segregated mechanisms in CA1 hippocampal pyramidal neurons. *J Neurosci* 29:14472–14483
- Hu H, Vervaeke K, Storm JF (2002) Two forms of electrical resonance at theta frequencies generated by M-current, h-current and persistent Na⁺ current in rat hippocampal pyramidal cells. *J Physiol* 545(3):783–805
- Hutcheon B, Miura RM, Puil E (1996a) Models of subthreshold membrane resonance in neocortical neurons. *J Neurophysiol* 76:698–714
- Hutcheon B, Miura RM, Puil E (1996b) Subthreshold membrane resonance in neocortical neurons. *J Neurophysiol* 76:683–697
- Hutcheon B, Miura RM, Yarom Y, Puil E (1994) Low threshold calcium current and resonance in thalamic neurons: a model of frequency preference. *J Neurophysiol* 71:583–594
- Hutcheon B, Yarom Y (2000) Resonance oscillations and the intrinsic frequency preferences in neurons. *Trends Neurosci* 23:216–222
- Izhikevich E (2006) Dynamical systems in neuroscience: the geometry of excitability and bursting. MIT Press, Cambridge, MA
- Izhikevich EM (2001) Resonate-and-fire neurons. *Neural Netw* 14:883–894
- Izhikevich EM (2002) Resonance and selective communication via bursts in neurons having subthreshold oscillations. *Biosystems* 67:95–102
- Kopell N, Howard LN (1973) Plane wave solutions to reaction diffusion systems. *Stud Appl Math* 42:291–328
- Leung LS, Yu HW (1998) Theta-frequency resonance in hippocampal CA1 neurons in vitro demonstrated by sinusoidal current injection. *J Neurophysiol* 79:1592–1596
- Pike FG, Goddard RS, Suckling JM, Ganter P, Kasthuri N, Paulsen O (2000) Distinct frequency preferences of different types of rat hippocampal neurons in response to oscillatory input currents. *J Physiol* 529:205–213
- Puil E, Gimbarzevsky B, Miura RM (1986) Quantification of membrane properties of trigeminal root ganglions in guinea pigs. *J Neurophysiol* 55:995–1016
- Reinker S, Puil E, Miura RM (2004) Membrane resonance and stochastic resonance modulate firing patterns of thalamocortical neurons. *J Comput Neurosci* 16:15–25
- Richardson MJE, Brunel N, Hakim V (2003) From subthreshold to firing-rate resonance. *J Neurophysiol* 89:2538–2554
- Rotstein HG (2013) Frequency preference response to oscillatory inputs in two-dimensional neural models: a geometric approach to subthreshold amplitude and phase resonance. *J Math Neurosci* (In press)
- Rotstein HG, Nadim F (2013) Interaction between resonant and amplifying currents in two-dimensional neural models of frequency preference response to oscillatory input currents. *J Comp Neurosci*
- Rotstein HG, Oppermann T, White JA, Kopell N (2006) A reduced model for medial entorhinal cortex stellate cells: subthreshold oscillations, spiking and synchronization. *J Comput Neurosci* 21:271–292
- Schreiber S, Erchova I, Heinemann U, Herz AV (2004) Subthreshold resonance explains the frequency-dependent integration of periodic as well as random stimuli in the entorhinal cortex. *J Neurophysiol* 92:408–415
- Sciamanna G, J WC (2011) The ionic mechanism of gamma resonance in rat striatal fast-spiking neurons. *J Neurophysiol* 106:2936–2949
- Skinner FK (2006) Conductance-based models. *Scholarpedia* 1:1408
- Tohidi V, Nadim F (2009) Membrane resonance in bursting pacemaker neurons of an oscillatory network is correlated with network frequency. *J Neurosci* 6427:6435
- Tseng H, Nadim F (2010) The membrane potential waveform on bursting pacemaker neurons is a predictor of their preferred frequency and the network cycle frequency. *J Neurosci* 30:10809–10819
- Wang WT, Wan YH, Zhu JL, Lei GS, Wang YY, Zhang P, Hu SJ (2006) Theta-frequency membrane resonance and its ionic mechanisms in rat subiculum pyramidal neurons. *Neuroscience* 140:45–55
- Wu N, Hsiao CF, Chandler SH (2001) Membrane resonance and subthreshold membrane oscillations in mesencephalic v neurons: participants in burst generation. *J Neurosci* 21:3729–3739

Zemankovics R, Kali S, Páulsen O, Freund TF, Hájos N (2010) Differences in subthreshold resonance of hippocampal pyramidal cells and interneurons: the role of h-current and passive membrane characteristics. *J Physiol* 588:2109–2132

Summary of Information-Theoretic Quantities

Robin A. A. Ince¹, Stefano Panzeri^{2,3} and Simon R. Schultz⁴

¹School of Psychology, Institute of Neuroscience and Psychology, University of Glasgow, Glasgow, UK

²Center for Neuroscience and Cognitive Systems, Istituto Italiano di Tecnologia, Rovereto (Tn), Italy

³Institute of Neuroscience and Psychology, University of Glasgow, Glasgow, UK

⁴Department of Bioengineering, Imperial College London, London, UK

Definition

Information theory is a practical and theoretic framework developed for the study of communication over noisy channels. Its probabilistic basis and capacity to relate statistical structure to function make it ideally suited for studying information flow in the nervous system. As a framework, it has a number of useful properties: it provides a general measure sensitive to any relationship, not only linear effects; its quantities have meaningful units which, in many cases, allow a direct comparison between different experiments; and it can be used to study how much information can be gained by observing neural responses in single experimental trials rather than in averages over multiple trials. A variety of information theoretic quantities are in common use in neuroscience – including the Shannon entropy, Kullback–Leibler divergence, and mutual information. In this entry, we introduce and define these quantities. Further details on how these quantities can be estimated in practice are provided in the entry “► [Estimating Information-Theoretic Quantities](#),” and examples

of application of these techniques in neuroscience can be found in the entry “► [Applications of Information Theory to Analysis of Neural Data](#).”

Detailed Description

Information Theoretic Quantities

Entropy as a Measure of Uncertainty

Information theory derives from Shannon’s theory of communication (Shannon 1948; Shannon and Weaver 1949). *Information*, as we use the word technically, is associated with the *resolution of uncertainty*. The underpinning theoretic concept in information theory is thus the measurement of uncertainty, for which Shannon derived a quantity called *entropy*, by analogy to statistical mechanics. Shannon proved that the only quantity suitable for measuring the uncertainty of a discrete random variable X is

$$H(X) = -K \sum_x P(x) \log_2 P(x). \quad (1)$$

where X can take a number of values x according to the probability distribution $P(x)$. The constant K we take to be one. When the logarithm is taken to base 2, the resulting units of the entropy $H(x)$ are called *bits* (when the natural logarithm is used, the term is *nats*).

Entropy can be thought of as a nonparametric way to measure the variability of a distribution. Spread-out distributions (with high variability) will have high entropy since all potential outcomes have similar probabilities and so the outcome of any particular draw is very uncertain. On the other hand, concentrated distributions (with low variability) will have lower entropy, since some outcomes will have high probability, allowing a reasonable guess to be made about the outcome of any particular draw. In this respect, entropy can be thought of as a generalized form of variance; unlike variance, which is a second-order statistic and only meaningful for unimodal distributions, entropy can give meaningful values for any form of distribution. For a normal distribution, the differential entropy (the continuous analogue of the discrete entropy discussed here) is

proportional to the logarithm of the variance, but for other types of distribution the two measures are not so closely related.

As an example, consider the roll of an unbiased six-sided die performed under a cup. With no external knowledge about the roll, an observer would believe any of the numbers are equally likely – a uniform distribution over the six possible faces. From Eq. 1, the entropy of this distribution is $\log_2 6$. Now a third party peeks under the cup and tells our observer that the die is showing an even number. This knowledge reduces the uncertainty about the result of the roll, but by how much? After being told that the die is showing an even number, the number of possibilities is reduced from six to three, but each of the even numbers remains equally likely. The entropy of this distribution is $\log_2 3$. So the reduction in the observers uncertainty, measured as the difference in entropy, is $\log_2 6 - \log_2 3 = \log_2 2$, or 1 bit. We can quantify the knowledge imparted by the statement “the result is even” as 1 bit of information. This corresponds to a reduction in uncertainty of a factor of 2 (from six to three possible outcomes). For this example, in both the before and after situations, all the possibilities were equally likely (uniform distributions), but the methodology can be applied to any possible distribution. Note that the uniform distribution is the maximum entropy distribution over a finite set. Any other distribution would have lower entropy since it is not possible to be less uncertain about a possible outcome than when all possibilities are equally likely – there is no structure to allow any sort of informed guess. For further applications of the concept of *maximum entropy*, see the entry on “► [Estimating Information-Theoretic Quantities](#).”

The fact that $H(X)$ should be maximized by a uniform distribution is one of three axioms Shannon started from in order to derive the form of Eq. 1. The others are that impossible events do not contribute to the uncertainty and that the uncertainty from a combination of independent events should be the sum of the uncertainty of the constituent events. These three conditions necessarily lead to Eq. 1, although it can be reached via many other routes as well (Chakrabarti and Chakrabarty 2005).

Mutual Information

The example of a die roll motivates how a difference between entropies can quantify the information conveyed about a set of possible outcomes. In the case of two discrete random variables – here we consider S , representing a set of stimuli which are presented during an experiment, and R , a set of recorded responses – this is formalized in a quantity called the *mutual information*. This is a quantity measuring the dependence between the two random variables and which can be defined in terms of entropies in the following three equivalent forms:

$$\begin{aligned} I(R; S) &= H(S) - H(S|R) \\ &= H(R) - H(R|S) \\ &= H(R) + H(S) - H(R, S) \end{aligned} \quad (2)$$

where $H(R)$ and $H(S)$ are the individual entropies of each random variable as discussed above, $H(R, S)$ is the *joint entropy* of the two variables, and $H(R/S)$ and $H(S/R)$ are *conditional entropies*. The conditional entropy is defined as

$$H(X|Y) = \sum_y P(y)H(X|Y=y) \quad (3)$$

where $H(X|Y=y)$ is defined as in Eq. 1 but with $P(x)$ replaced by the conditional probability $P(x/y)$. The conditional entropy $H(X|Y)$ represents the average entropy of X when the value of Y is known.

The three forms of Eq. 2 above each illustrates a particular interpretation of the mutual information. From the first form, we can see that it quantifies the average reduction in uncertainty about which stimulus was presented based on observation of a response R answering the question “if we observe R , by how much does that reduce our uncertainty about the value of S ?” Equivalently, the second form shows us that it similarly answers the question “if we observe S , by how much does that reduce our uncertainty about the value of R ?” As the third form shows explicitly, mutual information is symmetric in its arguments. The third form also shows that

information is the difference in entropy between a model in which the two variables are independent (given by $P(r)P(s)$ with entropy equal to $H(R) + H(S)$) and the true observed joint distribution, $P(r,s)$ (with entropy $H(R,S)$). This shows that for two independent variables, the mutual information between them is equal to zero and illustrates that information measures how far responses and stimuli are from independence.

A well known measure of difference between probability distributions is the Kullback–Leibler (KL) divergence (Kullback and Leibler 1951):

$$D_{KL}(P||Q) = \sum_x P(x)\log_2 \frac{P(x)}{Q(x)}. \quad (4)$$

Note that this is not a true “distance” metric since it is not symmetric – the KL divergence between p and q is different to that between q and p . As can be seen from the third expression of Eq. 2, the mutual information is just the KL divergence between the joint distribution and the independent model formed as the product of the marginal distributions:

$$\begin{aligned} I(R; S) &= D_{KL}(P(r,s)||P(r)P(s)) \\ &= \sum_{rs} P(r,s)\log_2 \frac{P(r,s)}{P(r)P(s)}. \end{aligned} \quad (5)$$

In the above, S and R represent discrete random variables where one is viewed as a stimulus and the other is a recorded neural response – but these could of course be any two discrete random variables (e.g. a variable representing a wild-type vs. a genetic manipulation, behavioral responses, or other intrinsic signals). We will see shortly that information and entropy can be easily generalized to continuous signals.

A natural question is “does mutual information correspond to a measure of discriminability?” If by discriminability one means the measure d-prime (Green and Swets 1966), the answer is in general “no”. However, in the specific case where we are measuring the transmission of information about one of two equiprobable stimuli (or equivalently, presence/absence of a stimulus), mutual information has

such an interpretation. This can be seen by reaching for another “distance-like measure” – this time, one that is symmetric, the Jensen–Shannon (JS) divergence, a symmetrized version of the KL divergence (Lin 1991; Fuglede and Topsøe 2004):

$$\begin{aligned} D_{JS}(P||Q) &= \frac{1}{2}D_{KL}\left(P\left\|\frac{P+Q}{2}\right.\right) \\ &\quad + \frac{1}{2}D_{KL}\left(Q\left\|\frac{P+Q}{2}\right.\right). \end{aligned} \quad (6)$$

It can be fairly easily seen that in the case where we have only two stimuli, s_1 and s_2 , the mutual information $I(R;S)$ can be written as

$$I(R; S) = D_{JS}(P(r|s_1)||P(r|s_2)). \quad (7)$$

Thus the mutual information can be considered to measure how far apart (how discriminable) the distributions of responses are, given the two stimuli. Note that while mutual information generalizes to multiple stimuli, it is not entirely clear that the concept of discriminability does, in a useful way.

In summary, the mutual information is a measure of how strongly two variables are related, similar in spirit to correlation but with some specific advantages. Firstly, it is a completely general measure; it places no assumptions or models on the variables under consideration and is sensitive to any possible relationships, including nonlinear effects and effects in high-order statistics of the distributions. Second, it has meaningful units allowing direct comparison across different experiments and even with behavioral performance. Finally, it permits several nice interpretations related to its calculation as a single trial property and involving its relationship to decoding performance.

Other Information Theoretic Quantities

Similar procedures to those used to estimate entropy and mutual information can be used to estimate a number of other information theoretic quantities. We mention several such quantities here for completeness.

Multi-information

Note that the mutual information between a pair of random variables naturally generalizes to the concept of the multivariate mutual information, or *multi-information*, the mutual information between n variables,

$$\begin{aligned} I(X_1; \dots; X_n) &= \sum_{x_1 \dots x_n} P(x_1, \dots, x_n) \log_2 \frac{P(x_1, \dots, x_n)}{\prod_i P(x_i)} \\ &= I(X_1; \dots; X_{n-1}) - I(X_1; \dots; X_{n-1}|X_n) \end{aligned} \quad (8)$$

Note that multi-information, unlike standard mutual information, can take negative values. Multi-information has found use in neuroscience in the study of patterns of activity in neural ensembles (Schneidman et al. 2006). Note that this is not the only way to generalize mutual information beyond two variables, and a related quantity, the interaction information, can also be defined (McGill 1954; Bell 2003; Jakulin and Bratko 2003).

Conditional Mutual Information

The conditional mutual information is the expected value of the mutual information between two variables given a third (Cover and Thomas 1991),

$$I(X; Y|Z) = H(X|Z) - H(X|Y, Z). \quad (9)$$

This quantifies the relationship between variables X and Y while controlling for the influence of Z . In neuroscience, this can be useful, for example, to investigate the coding of correlated stimulus features (Ince et al. 2012). Consider two correlated stimulus features S_1 and S_2 . If it is found that $I(R; S_1) > 0$, this could be because the response is modulated by feature S_1 , but it might be that the response is modulated by feature S_2 and the relationship between response and S_1 follows from the correlation between the features. Considering $I(R; S_1|S_2)$ can resolve this situation and reveal if the feature S_1 is truly represented.

Entropy and Information Rates

Most biological systems function not as discrete realizations from a static process (like the roll of a die), but rather operate continuously as

time-varying dynamic processes. This brings to mind the notion of the *rate* at which a source generates information – e.g., if we were tossing a coin once per second and the outcomes of the coin tosses were independent, then we would be generating information at a rate of 1 bit/s. In general, the *entropy rate* of a stochastic process is defined as

$$h(X) = \lim_{n \rightarrow \infty} \frac{1}{n} H(X_1, X_2, \dots, X_n). \quad (10)$$

By extension, the *mutual information rate* is

$$i(R; S) = \lim_{n \rightarrow \infty} \frac{1}{n} I(r_1, r_2, \dots, r_n; S) \quad (11)$$

with units of bits/s. Asymptotic entropy and information rates can therefore be estimated indirectly by calculating information for sufficiently long sequences of time bins. If the calculation is repeated for smaller and smaller time bins, it is possible to extrapolate the resulting discrete information value to the instantaneous limit, making the rate calculation independent of both sequence length and bin width (Strong et al. 1998). It is also possible to calculate them directly using a Bayesian probabilistic model (Kennel et al. 2005; Shlens et al. 2007).

Information Theoretic Quantities for Continuous Variables

The quantities above are all defined on random variables taking discrete values. However, entropy and other information quantities can also be defined on continuous spaces. In the case of entropy, replacing summation by integration yields the *differential entropy*:

$$h_{\text{diff}}(X) = \int_x p(x) \log_2 p(x). \quad (12)$$

Other information theoretic quantities can be defined analogously, in general, by replacing sums over the discrete spaces with integrals over the continuous spaces. Note that differential entropy does not entirely generalize the properties of the discrete Shannon entropy, and thus, this quantity has not been widely used in

neuroscience and is therefore beyond the scope of this entry. In contrast, the Kullback–Leibler divergence and mutual information both generalize in a straightforward manner to continuous spaces. For instance, the mutual information between two random variables with joint density $p(x,y)$ is

$$I(X;Y) = \int p(x,y) \log_2 \frac{p(x,y)}{p(x)p(y)} dx dy. \quad (13)$$

Acknowledgements Research supported by the SI-CODE (FET-Open, FP7-284533) project and by the ABC and NETT (People Programme Marie Curie Actions PITN-GA-2011-290011 and PITN-GA-2011-289146) projects of the European Union's Seventh Framework Programme FP7 2007–2013.

Cross-References

- ▶ [Applications of Information Theory to Analysis of Neural Data](#)
- ▶ [Estimating Information-Theoretic Quantities](#)

References

- Bell AJ (2003) The co-information lattice. In: 4th International Symposium on independent component analysis blind signal separation ICA2003, Nara, pp 921–926
- Chakrabarti CG, Chakrabarty I (2005) Shannon entropy: axiomatic characterization and application. *Int J Math Math Sci* 2005:2847–2854
- Cover TM, Thomas JA (1991) Elements of information theory. Wiley, New York
- Fuglede B, Topsøe F (2004) Jensen-Shannon divergence and Hilbert space embedding. In: Proceedings of the international symposium on information theory, 2004 (ISIT 2004), p 31, Chicago, USA
- Green DM, Swets JA (1966) Signal detection theory and psychophysics. Wiley, New York. http://andrei.gorea.free.fr/Teaching_fichiers/SDT%20and%20Psychophysics.pdf. Accessed 17 Jan 2014
- Ince RAA, Mazzoni A, Bartels A, Logothetis NK, Panzeri S (2012) A novel test to determine the significance of neural selectivity to single and multiple potentially correlated stimulus features. *J Neurosci Methods* 210:49–65
- Jakulin A, Bratko I (2003) Quantifying and visualizing attribute interactions. arXiv:cs/0308002. <http://arxiv.org/abs/cs/0308002>. Accessed 13 Feb 2012
- Kennel MB, Shlens J, Abarbanel HDI, Chichilnisky E (2005) Estimating entropy rates with Bayesian confidence intervals. *Neural Comput* 17:1531–1576
- Kullback S, Leibler RA (1951) On Information and Sufficiency. *Ann Math Stat* 22:79–86
- Lin J (1991) Divergence measures based on the Shannon entropy. *IEEE Trans Inf Theory* 37:145–151
- McGill WJ (1954) Multivariate information transmission. *Psychometrika* 19:97–116
- Schneidman E, Berry MJ II, Segev R, Bialek W (2006) Weak pairwise correlations imply strongly correlated network states in a neural population. *Nature* 440:1007–1012
- Shannon CE (1948) A mathematical theory of communication. *Bell Syst Tech J* 27:379–423
- Shannon CE, Weaver W (1949) The mathematical theory of communication. University of Illinois Press, Urbana, 19:1
- Shlens J, Kennel MB, Abarbanel HDI, Chichilnisky E (2007) Estimating information rates with confidence intervals in neural spike trains. *Neural Comput* 19:1683–1719
- Strong SP, Koberle R, de Ruyter van Steveninck RR, Bialek W (1998) Entropy and information in neural spike trains. *Phys Rev Lett* 80:197–200

Surrogate Data for Evaluation of Spike Correlation

Sonja Grün

Lab for Statistical Neuroscience, Institute of Neuroscience and Medicine (INM-6) and Institute for Advanced Simulation (IAS-6), Jülich Research Centre and JARA, Jülich, Germany
Theoretical Systems Neurobiology, RWTH Aachen University, Aachen, Germany

Definition

In the correlation analysis of experimentally recorded parallel spike trains, one has to thoroughly consider the statistical features of the data in order to prevent false-positive results. Surrogate data, i.e., modified versions of the original spike trains, are used to assess the significance of spike correlation. The objective of surrogate data generation is to leave all statistical features of the original experimental data intact except those one wants to test for: these are to be destroyed.

Detailed Description

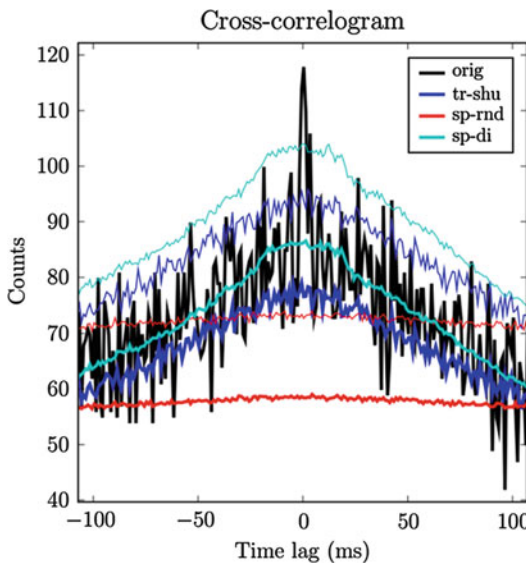
Generating artificial data from experimental data as a means for implementing a null hypothesis is becoming widely used. The reason is twofold: increasing computer power now allows for this type of approach, and it has become clear that the complexity of experimental data does not in general permit an analytical formulation of the null hypothesis. This is particularly true for the correlation analysis of parallel spike trains. Neglecting statistical features of experimental data such as non-stationarity of the firing of individual neurons in time or across trials, the spike train structure deviating from Poisson, or a co-occurrence of such features in parallel spike trains can lead to the occurrence of false-positive results. Problems can be avoided by including those features in the null hypothesis of the significance test. To this end surrogate data are used to generate the predictor by modifying the original data in such a way that the feature of interest, here as an example the temporal coordination of spikes, is destroyed but other features of the data are preserved. These data are then analyzed like the original experimental data and the outcomes are compared (See “► Significance Evaluation”; Harrison et al. 2013). Such data are used for bootstrap approaches in the significance estimation of the occurrence of features, e.g., spatiotemporal spike patterns (See “► Spatial Temporal Spike Pattern Analysis”). In the case of precise joint spike events (See “► Unitary Event Analysis”), the interest is to keep the statistical features of the spike trains of the individual neurons as similar to the original as possible but to destroy the exact relative timing of spikes from different neurons (for a comprehensive list of references, see Grün (2009) and Louis et al. (2010a, b)).

Modeling spike trains as stochastic processes is an elegant way to generate surrogate data. Often used are inhomogeneous Poisson processes that reproduce the dynamics of the firing rate according to the estimated firing rate profiles. More complicated processes which in addition reproduce the interspike interval (ISI) or higher-order interval statistics or even change their internal structure as a function of time can be modeled

(See “► Population Encoding/Decoding”; “► State-Space Models for the Analysis of Neural Spike Train and Behavioral Data”; “► Generalized Linear Models for Point Process Analyses of Neural Spiking Activity”). Although often not all parameters can be estimated from the experimental data, a formal characterization of neuronal spiking dynamics (the stochastic model) is helpful since it constitutes a precise description of the assumptions. Consequently, it enables more specific statements about the experimental data.

Other methods for generating surrogate data operate directly on the original data and modify them according to specific rules. Spike time randomization, i.e., random shuffling of the spikes of a neuron within a given time interval, assumes stationary rate within the window (Fig. 1, red). The procedure is closely related to the generation of a stationary Poisson process, but here the spike counts are additionally matched. The ISI structure of the original data, however, is destroyed. Other methods particularly focus on the conservation of the ISI distribution by shuffling the ISIs of a neuron within a trial, thereby simultaneously preserving the spike count of each trial. Furthermore, a potential covariation of spike counts across neurons is automatically preserved. In attempts to additionally account for non-stationarity in time, ISI shuffling may be performed in shorter time windows across trials, which, however, assumes cross-trial stationarity.

Trial shuffling is a way of destroying the relationship between simultaneously recorded spike trains. Trial data of one neuron are randomly assigned to trials of other neurons, thereby destroying potential spike correlation but leaving the internal structure of the spike trains and thus the spike counts intact. Potential covariation of spike counts across the neurons is thereby destroyed. Thus, non-stationarity across trials cannot be tolerated, since a recombination of these features, e.g., rate, may additionally change the chance occurrence of joint spike events (Fig. 1, dark blue). For the shift predictor, spike trains are not randomly assigned, but trial ids of the two neurons are shifted systematically against each other. The shift predictor is mainly of



Surrogate Data for Evaluation of Spike Correlation,

Fig. 1 Comparison of original and surrogate cross-correlograms (CCHs) (See “► Correlation Analysis of Parallel Spike Trains”). The CCH of an original data set (black), composed of two neurons simulated with background firing activity as non-stationary co-modulating gamma-processes, inhomogeneous across trials (40 trials), with additionally injected coincident spike events (rate: 3 Hz, coincidence width: ± 1 ms). Surrogate CCHs are generated by trial shuffling (*tr-shu*, blue), by spike time randomization (*sp-rnd*, red), or by spike dithering (*sp-di*, cyan) and are shown as the mean over 1,000 surrogates (thick lines) and the mean plus twice the standard deviation over the surrogates (thin lines). Only the surrogate CCH based on dithering reproduces well the overall shape of the original CCH reflecting chance coincidences due to the firing rates, but destroys the narrow central peak due to correlated activity. The other two surrogates underestimate the chance coincidences and thus may lead to false-positive results in independent data of the same rates but without correlated spike events (Modified from Louis et al. 2010b)

historical interest as an approximation to the full shuffle. However, e.g., in the presence of slow changes of statistical features across trials, the shift predictor may still be favorable.

Surrogate methods based on exchanging or randomizing spikes across neurons within the same trial may serve well for the evaluation of spatiotemporal spike pattern (See “► Spatial Temporal Spike Pattern Analysis”). These surrogates preserve the population histogram of each trial, but

preserve neither the PSTHs nor the ISI distributions and assume co-stationarity of the data.

Spike dithering, often also called jittering or teetering, i.e., independent randomization of the individual spike times within a small predefined time interval, destroys the exact spike timing and therefore also exact relative spike timing across the neurons. This effectively leads to some smoothing of the firing rates and also to a slight modification of the ISI distribution (Fig. 1, cyan). The latter can be minimized by weighting the dither according to the joint interspike interval distribution.

However, if firing rates change strongly on a short time scale, the smoothing effect of dithering becomes stronger, which in turn tends to lead to false-positive results. Therefore, it was suggested to first transform the data by time rescaling according to the firing rate into operational time, such that firing rates become stationary. Dithering is then applied in this representation. After transformation back into the original representation, joint spike events are detected. Even for strong rate changes, this surrogate method does not introduce false positives (Louis et al. 2010a).

Instead of modifying the individual spike times, it was suggested to shift the complete spike trains, or parts of it, against the others by random amounts (Amarasingham et al. 2012; Pipa et al. 2008; Wu et al. 2011). Thereby the structure of the spike trains or large parts of them are conserved; only the PSTHs are smoothed depending on the maximal shift. To have an effective destruction of joint spike events, the maximal shift needs to be chosen by a factor larger than the temporal precision of the joint spike events. This variant of dithering seems to be most appropriate to account for the features of the single-neuron statistics and can also be done in operational time (Louis et al. 2010a).

The creation of surrogate data is an attractive way to generate control data and is conceptually simple. However, for a proper choice of the surrogate, one has to be clear about the implicit assumptions and affected spike train features. This implies that the choice of surrogate may depend on the correlation analysis method used

and that a particular surrogate method needs to be tested in the context of the intended analysis.

Cross-References

- [Correlation Analysis of Parallel Spike Trains](#)
- [Generalized Linear Models for Point Process Analyses of Neural Spiking Activity](#)
- [Population Encoding/Decoding](#)
- [Significance Evaluation](#)
- [Spatial Temporal Spike Pattern Analysis](#)
- [State-Space Models for the Analysis of Neural Spike Train and Behavioral Data](#)
- [Unitary Event Analysis](#)

References

- Amarasingham A, Harrison MT, Hatsopoulos NG, Geman S (2012) Conditional modeling and the jitter method of spike resampling. *J Neurophysiol* 107:517–531 (review)
- Grün S (2009) Data-driven significance estimation of precise spike correlation. *J Neurophysiol* 101:1126–1140 (review)
- Harrison MT, Amarasingham A, Kass RE (2013) Statistical identification of synchronous spiking. In: Di Lorenzo P, Victor J (eds) *Spike timing: mechanisms and function*. Taylor and Francis, Boca Raton, pp 77–120
- Louis S, Gerstein GL, Grün S, Diesmann M (2010a) Surrogate spike train generation through dithering in operational time. *Front Comput Neurosci* 4:127. doi:10.3389/fncom.2010.00127
- Louis S, Borgelt C, Grün S (2010b) Generation and selection of surrogate methods for correlation analysis. In: Grün S, Rotter S (eds) *Analysis of parallel spike trains*, Springer series in computational neuroscience. Springer, New York
- Pipa G, Wheeler DW, Singer W, Nikolić D (2008) NeuroXidence: a non-parametric test on excess or deficiency of joint-spike events. *J Comput Neurosci* 25:64–88
- Wu W, Wheeler DW, Pipa G (2011) Bivariate and multivariate NeuroXidence: a robust and reliable method to detect modulations of spike–spike synchronization across experimental conditions. *Front Neuroinform* 5:14. doi:10.3389/fninf.2011.00014

Surround Modulation

- [Center-Surround Processing, Network Models of](#)

Sweeping the Parameter Space of Neuron Models

- [Neuronal Parameter Space Exploration](#)

Swimming and Walking Modes of the Salamander

- [Control of Aquatic and Terrestrial Gaits in Salamander](#)

Synaptic Connectivity in Neural Population Models

Viktor Jirsa

Institut de Neurosciences des Systèmes, Faculté de Médecine, UMR INSERM 1106, Aix-Marseille Université, Marseille, France

Synonyms

- [Synaptic footprint in neural population models](#)

Definition

Synaptic connectivity refers to the ensemble of direct chemical and electrical connections between neurons. In chemical synapses afferent presynaptic neuroelectric activity is mediated via neurotransmitters to the postsynaptic terminal, at which the postsynaptic activity can be either increased or decreased as a function of the excitatory/inhibitory character of the synapse. In electrical synapses the presynaptic and postsynaptic cell membranes are connected by special channels called gap junctions that are capable of directly passing electrical current between neurons. In neural population models the various aspects of synaptic connectivity are absorbed, typically through mean field techniques, by connectivity functions, parameters, and/or nonlinear response functions.

Detailed Description

A synapse is a connecting structure that permits a (presynaptic) neuron to pass an electrical or chemical signal to another (postsynaptic) neuron. There are hence two fundamentally different types of synapses: chemical and electrical synapses.

In a chemical synapse, electrical activity in the presynaptic neuron is converted (via the activation of voltage-gated calcium channels) into the release of a neurotransmitter that binds to receptors located in the postsynaptic cell. The binding process of the neurotransmitter initiates an electrical response on the postsynaptic neuron that may either depolarize (excitation) or hyperpolarize (inhibition) the postsynaptic neuron. The process of presynaptic neurotransmitter release, migration through the synaptic cleft, and binding on the postsynaptic side requires time, and its time course is characteristic of different neurotransmitter types giving a range of fast synapses (GABA_A , AMPA) to slower synapses (GABA_B , NMDA). Models of synaptic dynamics are typically nonlinear and expressed through ordinary differential equations involving transmitter concentration and release time, conductance strength, or reuptake time (Destexhe et al. 1994). Synaptic couplings between neurons are effectively of nonlinear and multiplicative nature. The time of synaptic transfer is sometimes referred to as synaptic transmission delay. Kinetic models of synaptic transmission are often used in the modeling of network dynamics (Destexhe 1998), as they provide a good compromise of accurate level of biological detail and computational efficiency. A simpler model of synaptic transmission is the so-called alpha function, which captures the time course of the postsynaptic response to a delta-spike (Gerstner and Kistler 2002).

In an electrical synapse, communication is electrically conductive through the cell's membrane and considered nearly instantaneous; thus, its transmission delay is negligible. Mathematically symmetric linear difference couplings

between pre- and postsynaptic neurons are based on Kirchhoff's current law and alter the respective neuronal membrane voltages. Electrical couplings between neurons are effectively of linear nature.

On the neural population level, synaptic coupling is the predominant connectivity considered. Neural population models that were derived from single neuron models (such as Brunel and Wang (2003), Wong and Wang (2006), Stefanescu and Jirsa (2008, 2011)) preserve the nonlinear nature and time scales of the synaptic couplings. Neural population models that were not derived from a microscopic level, but were rather being posed ad hoc, typically absorb the coupling's (spatial, temporal, (non)linear) effects in the nonlinear population response function and then rely on additive linear couplings between neural populations (such as Wilson and Cowan (1972, 1973), Nunez (1974), Jirsa and Haken (1996), Robinson et al (1997)). Excitatory coupling then enters as an input that increases the rate of the neural population's activity and inhibitory coupling decreases its activity. This procedure has been justified in Jirsa and Haken (1996) by the conversion properties of synaptic activities (wave) and firing rates (pulse) on the population level. Walter Freeman (1975) demonstrated that these population measures show robust dependencies; in particular wave-to-pulse conversion is highly nonlinear showing saturation, whereas the pulse-to-wave conversion is limited to the linear regime.

Other means of introducing features of synaptic connectivity into neural population models are through manipulations of the axonal propagator. A plus and minus sign may be assigned to the distribution of connection weights (see, for instance, Amari (1977)) to create coupling functions such as the Mexican hat function with central excitation and lateral inhibition. The latter has been shown to be essential for the realization of self-sustained spatial patterns thought to be involved in working memory. Local circuits of mutually coupled populations via excitatory and inhibitory connections are well known to give rise to the emergence of rhythmic firing patterns.

To characterize the time scales of synaptic processes in neural fields, linear convolutions have been introduced postsynaptically to modulate the effects of axonal propagation (see (Hutt and Atay 2005) for treatments of gamma-distributed synaptic footprints). Plasticity changes of synaptic connectivity rely on the timing of pre- and postsynaptic neuronal discharges and are established in cellular models of neurons (Abbott and Nelson 2000), but less well understood on the population level.

Cross-References

- [Amari Model](#)
- [AMPA Glutamate Receptor \(AMPA Receptor\), Conductance Models](#)
- [Axon, Modeling](#)
- [Connectome, General](#)
- [Dynamic Causal Modelling with Neural Population Models](#)
- [Gamma-Aminobutyric Acid Type-A \(GABA-A\) Receptors, Kinetic Models](#)
- [Gap Junctions, Neural Population Models and](#)
- [Mesoscopic Anatomy and Neural Population Models](#)
- [Modeling Synapses](#)
- [Multiscale Brain Connectivity](#)
- [Neural Field Model, Continuum](#)
- [Neural Population Model](#)
- [N-Methyl-D-Aspartate \(NMDA\) Receptors, Conductance Models](#)
- [Propagator, Axonal](#)
- [Synaptic Dynamics: Overview](#)
- [Wilson-Cowan Model](#)

References

- Abbott LF, Nelson SB (2000) Synaptic plasticity: taming the beast. *Nat Neurosci* 3(Suppl):1178–1183
- Amari S (1977) Dynamics of pattern formation in lateral-inhibition type neural fields. *Biol Cybern* 27:77–87
- Brunel N, Wang X-J (2003) What determines the frequency of fast network oscillations with irregular neural discharges? I. synaptic dynamics and excitation-inhibition balance. *J Neurophysiol* 90:415–430

- Destexhe A (1998) Spike-and-wave oscillations based on the properties of GABAB receptors. *J Neurosci* 18:9099–9111
- Destexhe A, Mainen ZF, Sejnowski TJ (1994) An efficient method for computing synaptic conductances based on a kinetic model of receptor binding. *Neural Comput* 6:14–18
- Freeman WJ (1975) Mass action in the nervous system. Academic, New York
- Gerstner W, Kistler WM (2002) Spiking neuron models. Single neurons, populations, plasticity. Cambridge University Press, Cambridge, UK
- Hutt A, Atay FM (2005) Analysis of nonlocal neural fields for both general and gamma-distributed connectivities. *Physica D* 203(1–2):30–54
- Jirsa VK, Haken H (1996) Field theory of electromagnetic brain activity. *Phys Rev Lett* 77:960–963
- Nunez PL (1974) The brain wave equation: a model for EEG. *Math Biosci* 21:279–297
- Robinson PA, Rennie CA, Wright JJ (1997) Propagation and stability of waves of electrical activity in the cerebral cortex. *Phys Rev E* 56:826–840
- Stefanescu R, Jirsa V (2008) A low dimensional description of globally coupled heterogeneous neural networks of excitatory and inhibitory. *PLoS Comput Biol* 4(11):26–36
- Stefanescu R, Jirsa V (2011) Reduced representations of heterogeneous mixed neural networks with synaptic coupling. *Phys Rev E Stat Nonlinear Soft Matter Phys* 83(2):026204
- Wilson HR, Cowan JD (1972) Excitatory and inhibitory interactions in localized populations of model neurons. *Biophys J* 12:1–24
- Wilson HR, Cowan JD (1973) A mathematical theory of the functional dynamics of cortical and thalamic nervous tissue. *Kybernetik* 13:55–80
- Wong KF, Wang XJ (2006) A recurrent network mechanism of time integration in perceptual decisions. *J Neurosci* 26(4):1314–1328

Synaptic Footprint in Neural Population Models

- [Synaptic Connectivity in Neural Population Models](#)

SYNOD

- [NEST: the Neural Simulation Tool](#)

Synthetic Neuronal Circuits/Networks

Padraig Gleeson

Department of Neuroscience, Physiology and Pharmacology, University College London, London, UK

Definition

Processing of information in neuronal networks involves communication between cells with complex dendritic and axonal arbors, belonging to multiple populations each having characteristic firing properties. This complex 3D structure, where synaptic connectivity between groups of cells can also be restricted to specific anatomical layers, is believed to be an important determinant of network behavior.

While many initiatives aim to reconstruct the full connectome of specific brain regions by mapping each neuron and synaptic connection in a block of tissue, other approaches take existing information on the known cell types and their overall connectivity rules and attempt to generate synthetic neuronal circuits from these. This can be useful for checking the completeness of knowledge of the circuit and to provide input to large-scale simulations of network behavior.

Detailed Description

Reconstructed and Synthetic Neurons

Recent developments in the field of connectomics are paving the way toward having access to the complete wiring diagram of specific networks in the brain. These will comprise full 3D reconstructions of all cells in the network along with all of the synaptic locations. Significant progress has been made on the complete neuronal wiring diagrams for simple species (White et al. 1986), but even a fully reconstructed cortical microcircuit from a mammalian brain is many years away. However, some regions such as the retina (Helmstaedter et al. 2013) have already been

studied in greater detail than previously possible with these methods.

For many regions however, while no complete wiring diagrams exist, plenty of statistical data is available on the overall anatomical layout of the neuronal circuitry, the types of cells present, their densities in specific layers, overall morphological features of the cell classes, connection probabilities between cell populations, as well as electrophysiological properties of the cells and synapses. This has led to various attempts to create synthetic versions of such circuits from these data, both as a means of cataloging what's known about the structure and connectivity of specific brain regions and for creating *in silico* models of the networks. These models can be used to gain a greater understanding of the networks through visualization or simulation of their electrical activity.

Simplified Synthetic Networks

Many point neuron network models (e.g., using leaky integrate and fire neuron models or two state variable extensions of this (Izhikevich 2003; Brette and Gerstner 2005)) have been created which seek to examine general operating principles of generic neural networks (Brunel 2000). Increasingly however, abstract network models are being created which incorporate data from specific brain regions on the specific cell types present, their relative densities/soma locations, and connectivity. A recent example is Potjans and Diesmann (2012), which describes a full-scale anatomically constrained model of the local cortical microcircuit using integrate and fire neurons. This can reproduce various experimentally observed features of the circuit including layer-specific cell activity patterns and propagation of transient thalamic inputs.

Conductance-based cell models aim to explain the firing patterns of cells in terms of the ion channels known to be present on the cell membrane. A number of anatomically inspired network models have been created taking this approach, often built up from detailed studies of single-cell properties. Solinas et al (2010) describe a 3D model of the granule cell layer of the cerebellum incorporating conductance-based

models of granule and Golgi cells. This network has been used to study not only temporal signal processing but also the spatial spread of activity following focused synaptic input.

Another example of an anatomically and electrophysiologically constrained network model of a distinct brain region is that of the dentate gyrus in Santhakumar et al (2005). This contains reduced (9–17 compartments) multicompartmental models of granule, basket, HIPP, and mossy cells from this region and investigates how changes in cell number and connectivity following head trauma can lead to network hyperexcitability. This model is being used as the basis for a much larger-scale model which will incorporate cell numbers in line with the actual rat dentate gyrus (Schneider et al. 2012).

The single-column thalamocortical network model of Traub et al. (2005) is one of the most detailed network models produced to date, featuring 14 cell types from the thalamus and multiple layers of the cortex, tuned to cell-type-specific firing behavior and incorporating known patterns of layer-specific synaptic connectivity. While this model too has reduced numbers of compartments in each of the cells (~80), it still requires the use of parallel computing resources to run. However, it represents a useful middle ground between more abstract cortical models and the highly detailed simulations used, for example, in the Blue Brain Project (see below), incorporating as it does sufficient detail to ask detailed questions about the contribution of specific cells, ion channels, and synaptic properties to network function, on computing resources which would be available to most researchers.

Synthetic Networks with Morphologically Detailed Cells

While abstract cells with reduced numbers of compartments are useful for generating, analyzing, and simulating large-scale networks, there is a growing need to use more morphologically realistic neurons to examine the full range of computations possible in single cells (Silver 2010) and networks. Using morphologies of reconstructed cells is an option due to the availability of databases of these (e.g.,

► [NeuroMorpho.org](#); Parekh and Ascoli 2013). For network analyses, however, there are usually not sufficient numbers of reconstructions of cells of given types to create a realistic network without using multiple, morphologically identical cells in a network. Generating a set of synthetic cells with similar morphological properties to reconstructed cells is a possible route toward more realistic large-scale models (Evans and Polavaram 2013).

TREES toolbox (Cuntz et al 2010; ► [TREES Toolbox: Code for Neuronal Branching](#); <http://www.treestoolbox.org>) is an application which has various features which can help address this. While it can be used for semiautomated reconstruction of cells from image stacks, it also allows generation of new morphologies based on extracted features of cells or groups of cells (e.g., 3D densities of branch points). This can potentially be used for generating multiple different cells of a particular class for use in network models. NETMORPH (Koene et al. 2009; <http://netmorph.org>) is an application which can also be used to generate synthetic neurons. It is based on the growth of neurons, with rules for how neurites should elongate, branch, and turn in 3D. Neural networks can be created based on the proximity of axonal and dendritic sections. NeuGen (Eberhard et al. 2006; <http://atlas.gcsc.uni-frankfurt.de/~neugen>) is a similar tool with a focus on generating 3D networks of specific cortical regions (e.g., cortex, hippocampus) using rules extracted from morphological features of the cells present in those regions. ► [Cx3D: Cortex Simulation in 3D](#) (Zubler et al. 2013; <http://www.ini.uzh.ch/~amw/seco/cx3d>) is a tool for simulating the growth of neural tissue, not only the growth of axons and dendrites in confined 3D spaces but also movement of cells. Chemical gradients can be added which influence the movement of specific entities. A recent version of this tool allows execution across multiple processors speeding up the generation of large-scale networks. More details on the different strategies and algorithms used for generation of synthetic neuronal morphologies can be found in this article.

A comparison of a number of the tools mentioned above is presented in Acimović

et al. (2011). Each of these tools has a slightly different focus and may be more or less appropriate for use depending on the research question to be addressed. None is a simulator of electrophysiological network activity; instead, they concentrate on exporting to other formats making it easier to simulate such behavior. Export to ► [NeuroML](#) (Gleeson et al. 2010) is supported by TREES toolbox and CX3D (and is also an option at ► [NeuroMorpho.org](#)) allowing generated networks to be imported into simulators like ► [NEURON](#) and visualized/analyzed by other applications, e.g., ► [neuroConstruct](#) (Gleeson et al. 2007).

Large-Scale Simulations of Synthetic Networks

A number of initiatives have started to look at the generation of simulations of morphologically detailed neural networks at the scale of macroscopic brain regions. The Neural Tissue Simulator (Kozloski and Wagner 2011) aims to make it possible to simulate a whole block of neural tissue by efficiently segmenting the region into sections, each of which is simulated on a separate processor in a parallel environment. There is initiative to reconstruct and simulate the rodent barrel cortex (Egger et al. 2012), which is developing new methods to register cell morphologies obtained from different animals against a common anatomical reference frame. The Blue Brain Project (<http://bluebrain.epfl.ch>) has been gathering data and developing methods for creating a simulation of a complete cortical column for a number of years. This work will continue as part of the 10-year EU-funded Human Brain Project (<https://www.humanbrainproject.eu>).

More details on software applications for creating detailed models of neuronal systems can be found in the entry “► [Software Tools for Modeling in Computational Neuroscience: Overview](#).”

Conclusions

While initiatives to reconstruct the complete wiring diagrams of various species or brain regions are gaining pace, there is much that can be

learned by consolidating the vast amounts of data on different brain regions into models, both describing the structure and connectivity of the networks and potentially allowing detailed simulations of the activity of the cells. This task is larger than one lab can manage on its own, and a key part of this process will be the availability of appropriate software tools and databases required to construct such models. Thankfully, more and more resources are becoming available for sharing data on neurons and their properties (e.g., ► [NeuroMorpho.org](#), ► [NeuroElectro Project](#), ► [SenseLab: Integration of Multidisciplinary Neuroscience Data](#); Bezaire and Soltesz 2013) and for sharing models (► [ModelDB](#), ► [Open Source Brain](#)) and the software required to simulate them (► [Software Tools for Modeling in Computational Neuroscience: Overview](#)).

Cross-References

- [CX3D: Cortex Simulation in 3D](#)
- [ModelDB](#)
- [neuroConstruct](#)
- [NeuroElectro Project](#)
- [NeuroML](#)
- [NeuroMorpho.org](#)
- [NEURON Simulation Environment](#)
- [Open Source Brain](#)
- [SenseLab: Integration of Multidisciplinary Neuroscience Data](#)
- [Software Tools for Modeling in Computational Neuroscience: Overview](#)
- [Synthetic Neuronal Morphology](#)
- [TREES Toolbox: Code for Neuronal Branching](#)

References

- Acimović J, Mäki-Marttunen T, Havela R, Teppola H, Linne ML (2011) Modeling of neuronal growth in vitro: comparison of simulation tools NETMORPH and CX3D. EURASIP J Bioinform Syst Biol 2011, 616382
Bezaire MJ, Soltesz I (2013) Quantitative assessment of CA1 local circuits: knowledge base for interneuron-

- pyramidal cell connectivity. *Hippocampus* 23(9):751–785
- Brette R, Gerstner W (2005) Adaptive exponential integrate-and-fire model as an effective description of neuronal activity. *J Neurophysiol* 94(5):3637–3642
- Brunel N (2000) Dynamics of sparsely connected networks of excitatory and inhibitory spiking neurons. *J Comput Neurosci* 8(3):183–208
- Cuntz H, Forstner F, Borst A, Häusser M (2010) One rule to grow them all: a general theory of neuronal branching and its practical application. *PLoS Comput Biol* 6(8):e1000877
- Eberhard J, Wanner A, Wittum G (2006) NeuGen: a tool for the generation of realistic morphology of cortical neurons and neural networks in 3D. *Neurocomputing* 70(13):327–342. doi:10.1016/j.neucom.2006.01.028
- Egger R, Narayanan RT, Helmstaedter M, de Kock CPJ, Oberlaender M (2012) 3D Reconstruction and standardization of the rat Vibrissal cortex for precise registration of single neuron morphology. *PLoS Comput Biol* 8(12):e1002837. doi:10.1371/journal.pcbi.1002837
- Evans RC, Polavaram S (2013) Growing a garden of neurons. *Front Neuroinform* 7:17
- Gleeson P, Steuber V, Silver RA (2007) neuroConstruct: a tool for modeling networks of neurons in 3D space. *Neuron* 54(2):219–235
- Gleeson P, Crook S, Cannon RC, Hines ML, Billings GO, Farinella M, Morse TM, Davison AP, Ray S, Bhalla US, Barnes SR, Dimitrova YD, Silver RA (2010) NeuroML: a language for describing data driven models of neurons and networks with a high degree of biological detail. *PLoS Comput Biol* 6(6):e1000815
- Helmstaedter MN, Briggman K, Turaga S, Jain V, Seung HS, Denk W (2013) Connectomic reconstruction of the inner plexiform layer in the mouse retina. *Nature* 500:168–174. doi:10.1038/nature12346
- Izhikevich E (2003) Simple model of spiking neurons. *IEEE Trans Neural Netw* 14(6):1569–1572
- Koene R, Tijms B, van Hees P, Postma F, de Ridder A, Ramakers G, van Pelt J, van Ooyen A (2009) NETMORPH: a framework for the stochastic generation of large scale neuronal networks with realistic neuron morphologies. *Neuroinformatics* 7(3):195–210. doi:10.1007/s12021-009-9052-3
- Kozloski J, Wagner J (2011) An ultrascalable solution to large-scale neural tissue simulation. *Front Neuroinform* 5:15
- Parekh R, Ascoli G (2013) Neuronal morphology goes digital: a research hub for cellular and system neuroscience. *Neuron* 77(6):1017–1038. doi:<http://dx.doi.org/10.1016/j.neuron.2013.03.008>
- Potjans TC, Diesmann M (2012) The cell-type specific cortical microcircuit: relating structure and activity in a full-scale spiking network model. *Cereb Cortex* 24(3):785–806.
- Santhakumar V, Aradi I, Soltesz I (2005) Role of mossy fiber sprouting and mossy cell loss in hyperexcitability: a network model of the dentate gyrus incorporating cell types and axonal topography. *J Neurophysiol* 93(1):437–453
- Schneider CJ, Bezaire M, Soltesz I (2012) Toward a full-scale computational model of the rat dentate gyrus. *Front Neural Circuits* 6:83
- Silver RA (2010) Neuronal arithmetic. *Nat Rev Neurosci* 11(7):474–489
- Solinas S, Nieuw T, D'Angelo E (2010) A realistic large-scale model of the cerebellum granular layer predicts circuit spatio-temporal filtering properties. *Front Cell Neurosci* 4:12
- Traub RD, Contreras D, Cunningham MO, Murray H, LeBeau FE, Roopun A, Bibbig A, Wilent WB, Higley MJ, Whittington MA (2005) Single-column thalamocortical network model exhibiting gamma oscillations, sleep spindles, and epileptogenic bursts. *J Neurophysiol* 93(4):2194–2232
- White JG, Southgate E, Thomson JN, Brenner S (1986) The structure of the nervous system of the nematode *Caenorhabditis elegans*. *Philos Trans R Soc Lond Ser B, Biol Sci* 314(1165):1–340
- Zubler F, Hauri A, Pfister S, Bauer R, Anderson JC et al (2013) Simulating cortical development as a self constructing process: a novel multi-scale approach combining molecular and physical aspects. *PLoS Comput Biol* 9(8):e1003173. doi:10.1371/journal.pcbi.1003173

Synthetic Neuronal Morphologies and Microcircuits

- [Synthetic Neuronal Circuits/Networks](#)
- [Synthetic Neuronal Morphology](#)

Synthetic Neuronal Morphology

Benjamin Torben-Nielsen
Computational Neuroscience Unit, Okinawa Institute of Science and Technology, Onna-son, Kunigami-gun, Okinawa, Japan

Synonyms

[Algorithms for generating neuronal morphologies](#); [Morphogenetic algorithm](#); [Virtual neuron generation](#)

Definition

A synthetic neuronal morphology is a digital representation of a neuron's morphology that is not acquired experimentally but rather generated by an algorithm. The input to such an algorithm is often a prototype, experimentally reconstructed morphology (or a set thereof). A synthesis algorithm then incorporates this prototype data in some way to generate a new digital reconstruction from scratch. Thus, synthetic neurons are *de novo*, algorithmically created digital reconstructions not originating directly from experimental data.

History of Synthesizing Neuronal Morphologies

Since the pioneering work of Golgi to visualize neurons *in vitro* and the subsequent beautiful drawings by Ramon y Cajal, neuroscientists have been fascinated by neuronal morphologies. The attempt of Hillman (Hillman 1979) to quantify neuronal morphologies kick-started the field investigating synthetic morphologies. Hillman described a set of so-called fundamental parameters that were sufficient to describe neuronal morphologies. Hence, the idea for later sampling algorithms to synthesize morphologies was born: if there exist a set of fundamental parameters that adequately capture morphologies, you can, in principle, sample from the statistical distribution of these parameters to create a new morphology that shares statistical properties with the original.

However, it took another decade before the first algorithms were presented to synthesize morphologies. One set of algorithms was based on the ideas of Hillman to sample from statistical distributions of parameters describing morphologies (Burke et al 1992; Nowakowski et al 1992). The other algorithms were based on L-systems (Pellionisz 1989; Hamilton 1993; McCormick and Mulchandani 1994). An L-system or Lindenmayer system is a mathematical formalism to generate recursively branched structures that had been successfully applied earlier to synthesize digital representations of botanical trees (Lindenmayer 1968). Quantification of

morphologies per se also generated many insights, which resulted in rigorous descriptions of morphologies (for instance, Uylings et al 1986; Van Pelt et al 1992; Tamori 1993). These combined efforts lead to a synergy between L-systems and solid quantification of fundamental parameters that accumulated in L-Neuron (Ascoli and Krichmar 2000), a sampling algorithm implicitly implementing a stochastic L-system to create a topology while relying on sampling from fundamental parameters to create a geometry. L-Neuron has become the most visible tool for the synthesis of neuronal morphologies.

Around the same time, due to advances in computational resources and recording techniques, the interest in dendritic morphologies and their role in computation grew (Traub et al 1991; De Schutter and Bower 1994). Because of the labor-intensive nature of experimentally reconstructing morphologies, many algorithms to synthesize neurons were proposed (see next section). This recent *raison d'être* contrasts with the historical reason to algorithmically generate morphologies, namely, as a testing bed to investigate hypotheses about morphological traits and their variance.

Detailed Description

Today, there are many different types of algorithms to synthesize neuronal morphologies. Most of them are specifically designed to study or mimic a particular characteristic of neurite morphology. Consequently, any classification of the algorithms is inherently artificial and post hoc. But a classification creates order and increases understanding. Therefore, the algorithms are here classified into two categories: context-independent and context-dependent ones. Clearly, neurons do not grow in a vacuum but rather take their shape from interactions with the neuronal matrix, i.e., their context (Jan and Jan 2010). But treating neurons as if they were in a vacuum makes their study more straightforward; and hence, this abstraction is widely adopted.

Context-Independent Algorithms

Sampling Algorithm

Most current algorithms are instances of the so-called sampling algorithms briefly introduced before and treat morphologies as if they were floating in a vacuum. Sampling algorithms start with a statistical description of fundamental parameters, i.e., a set of parameters that is considered sufficient to fully describe a neuronal morphology (Hillman 1979). Then, they iteratively synthesize a morphology by sampling features of the morphology under construction from the statistical model (Burke et al 1992; Tamori 1993). The majority of morphology synthesis algorithms are of the “sampling type” and one of the best known implementations is L-Neuron (Ascoli and Krichmar 2000). Differences between sampling algorithms are manifested in different characteristics of the algorithms. Firstly, the statistical descriptors can be parametric (Ascoli and Krichmar 2000; Eberhard et al 2006) or nonparametric (Lindsay et al 2007; Torben-Nielsen et al 2008). In parametric models, the researcher has to define the type of distribution that best fits the prototype data (e.g., a Gaussian distribution parametrized by its mean and standard deviation). This can be an advantage when there is little data available, and human judgment is needed to see the true distribution in the data. Nonparametric statistical models on the other hand do not make any assumptions on the type of distribution underlying the data. As such, the researcher using these models does not impose a bias on the distribution, and thus, in principle, the data is described more accurately (Torben-Nielsen et al 2008). Also, the selection and description detail of the fundamental parameters can be different: fundamental parameters can be considered independent from each other (e.g., a univariate description) or dependencies can be introduced by using multivariate descriptions (Burke et al 1992; Ascoli and Krichmar 2000; Torben-Nielsen et al 2008). For instance, the segment length can be considered to be independent of other features (=univariate) or dependent on the topological order (=bivariate) or on the topological order and the Euclidean distance to the soma (=trivariate). Generally,

these dependencies are tuned to achieve the best match between prototype and de novo data.

Growth Algorithm

One of the very first algorithms to synthesize parts of the dendritic structure is developed by van Pelt and colleagues (van Pelt et al 1986; Uylings et al 1986; van Ooyen 2001). Initially, they aimed at quantifying dendritic branching patterns. To this end, they developed an algorithm to synthesize dendritic topologies that captured experimentally observed variation. The algorithm is based on the simultaneous extension of growth cones and uses probabilities conditioned on the local branching order to decide the fate of a cone: elongate, bifurcate, or terminate. They demonstrated that plausible branching patterns of distinct morphological classes could be generated solely based on differential dependencies on branch order and the number of growing cones at any moment. Only recently, they extended their models to include a geometrical component that spatially embeds a dendrite topology into 3D, i.e., complete synthetic morphologies. The NETMORPH simulator can now be used to grow large networks of morphological model neurons (Koene et al 2009).

Context-Dependent Algorithms

Interactions Through Competition over Resources

A straightforward way to introduce interactions between synthetic neurons is by growing them simultaneously and having them compete of “resources.” A first attempt to capture competition over resources and its influence on morphology was reported in Nowakowski et al (1992). However, they extracted the hypothesized influence of competition and inserted it as a rule into generated single morphologies. The approaches listed below synthesize multiple truly interacting morphologies.

An approach based on diffusion-limited aggregation was developed by Luczak (2006) and aimed at investigating the role of competition over resources on dendritic morphology. In his approach a developing morphology starts out as a seed located in a bounded space. Inside the bounding space, “neurotrophic particles”

randomly move around and adhere to the seed (a 1-particle aggregate) and hence expand the developing morphological structure (to an $n + 1$ aggregate). The final morphology is obtained when all particles are aggregated into the synthesized morphology. By starting with several seeds in a bounded space, the growing morphologies compete over the resources (e.g., neurotrophic particles) and interactions between developing morphologies emerge. He showed that only by varying the bounding space and the initial distribution of neurotrophic particles, dendrites of distinct morphological classes could be synthesized. The resultant claim is therefore that morphologies can be interpreted as being shaped exclusively by environmental interactions through competition and without the need of detailed statistical descriptors.

A different approach is developed by Cuntz et al (2010) who first analyzed the tree structure of dendrite morphologies as well as functional implications of the dendritic diameter on voltage propagation in neurons. Based on these findings they proposed an algorithm in which “points of interest” are drawn from a distribution describing the density of the dendritic field before connecting these points by a modified minimal spanning tree (MST) algorithm. The modification consists of the introduction of a balancing factor so that not only the total wiring length (as in a pure MST algorithm) is taken into account but also the path length to the soma. Diameters are assigned during a post-processing step. The main advantage is that the algorithms have a direct biological interpretation in terms of one of the functions of dendrites, namely, its role in collecting inputs. Suppose that the sampled points of interest represent synapse (i.e., axonal boutons). Then, Cuntz’s approach is based on synthesizing a morphology that samples these inputs under the biological parsimony constraint (Cuntz 2012). By growing multiple morphologies at the same time in the same volume, competition occurs and shapes the morphologies.

Growth in the Midst of Attractors and Repellents
Other approaches are developed specifically with the goal of capturing environmental interactions

that underlie biological growth of neurons (Scott and Luo 2001; Jan and Jan 2010).

One of the first to generate dendrite morphologies based on environmental interaction were Samsonovich and Ascoli (2003). In their work they studied factors that influenced the direction of growth of neurons. They found that the strongest factor influencing the direction was the location of the soma: pyramidal cells seem to grow away from their somata. Subsequently, they constructed a synthesis algorithm based on a hidden Markov model that computed the direction of growth of dendritic branches and found that the virtual dendrites had a similar spatial embedding as their biological counterparts (Samsonovich and Ascoli 2005).

A slightly more detailed proposal involved a context-dependent L-system to model axon guidance under environmental cues (Feng et al 2005). Rather than to sample the parameters for the L-system (as in L-Neuron), the values for the parameters are computed depending on the context, i.e., the modeled neuronal substrate containing attractors and repellents exerting influence on the speed of growth and direction. In the substrate, attractors and repellents were placed by the researcher and the developing axon queried their locations.

A recently developed approach by Memelli et al. (2013) explicitly uses environmental interactions to grow dendritic morphologies. In their approach, the topology is generated according to a straightforward bifurcation process (i.e., Galton-Watson process; Uemura et al 1995). The geometry, however, is wholly based on environmental cues. Cues are then used to bias the growth direction. As a proof of principle they demonstrated how self-referential cues, that is, cues generated by the neuron itself (i.e., inertial stiffness, somatic repulsion, and self-avoidance), can readily synthesize dendrites of different neuronal classes. So far the environmental interaction is thus limited to interactions within the neuron being generated. However, a cue coming from another neuron is conceptually identical to a cue coming from the neuron itself: it is a bias on the direction of growth. Hence, this approach does not require statistical descriptors and

morphologies emerge from environmental interactions.

The most elaborate approach in this category of synthesis algorithms, CX3D, is developed by Zubler and Douglas (2009). They developed a framework in which neurons can grow in accordance to growth rules that allow interaction with the environment. Each growth cone contains the growth rules for this neuron encoded in a gene-like format (Zubler et al 2011). The growth rules may use environmental cues such as chemical gradients or other contextual information. In addition, a growing neurite can leave cues as it grows and switch on or off growth rules depending on its environment. With this setup, many of the complexities of cortical circuits can be modeled (at least at a phenomenological level).

The list of treated synthesis algorithms is not an exhaustive list of proposed synthesis algorithms. Rather the aforementioned approaches illustrate a tendency in the development of such algorithms directing away from purely statistical, context-independent approaches towards context-dependent approaches that use biophysical mechanisms (albeit phenomenological) to generate morphologies.

Outlook

Neuronal morphologies are receiving increasing attention because of improved experimental techniques to visualize and manipulate neurons at the level of dendrites and axons and because the influence of dendritic morphology on neuronal processing in normal (Silver 2010; London and Häusser 2005; Koch and Segev 2000) and pathological cases (Emoto 2011; Moolman et al 2004; Irwin et al 2000) is becoming more apparent. Consequentially, a great deal of effort is invested in identifying genetic and transcription factors that underlie the formation of neuronal morphologies. These studies already resulted in better knowledge of transcription factors involved in neuronal self-avoidance, tiling, and space filling (e.g., Scott and Luo 2001; Jan and Jan 2010). Such knowledge will harness a big leap forward

in the synthesis of neuronal morphologies and their variation, because, finally, neurons do grow in interaction with other neurons and agents in the neuronal matrix.

Cross-References

- [Algorithmic Reconstruction of Motoneuron Morphology](#)
- [Reconstruction, Electron Microscopy](#)
- [Reconstruction, Techniques and Validation](#)

References

- Ascoli GA, Krichmar JL (2000) L-neuron: a modeling tool for the efficient generation and parsimonious description of dendritic morphology. *Neurocomputing* 33:1003–1011
- Burke R, Marks W, Ulvhake B (1992) A parsimonious description of motoneuron dendritic morphology using computer simulation. *J Neurosci* 12(6):2403–2416
- Cuntz H (2012) The dendritic density field of a cortical pyramidal cell. *Front Neuroanat* 6:2. doi:10.3389/fnana.2012.00002. <http://www.frontiersin.org/Neuroanatomy/10.3389/fnana.2012.00002/full>, <http://www.frontiersin.org/Journal/DownloadFile.ashx?pdf=1&fileId=15548&articleId=16706&version=1&contentTypeId=21&fileName=fnana-06-00002.pdf>
- Cuntz H, Forstner F, Borst A, Häusser M (2010) One rule to grow them all: a general theory of neuronal branching and its practical application. *PLoS Comput Biol* 6(8), e1000877. doi:10.1371/journal.pcbi.1000877. <http://dx.doi.org/10.1371/journal.pcbi.1000877>, <http://www.ploscompbiol.org/article/fetchObjectAttachment.action?uri=info:doi/10.1371/journal.pcbi.1000877&repri>
- De Schutter E, Bower JM (1994) Simulated responses of cerebellar Purkinje cells are independent of the dendritic location of granule cell synaptic inputs. *Proc Natl Acad Sci U S A* 91(11):4736–4740. <http://www.ncbi.nlm.nih.gov/articlerender.fcgi?artid=43863&tool=pmcentrez&rendertype=abstract>
- Eberhard J, Wanner A, Wittum G (2006) NeuGen: a tool for the generation of realistic morphology of cortical neurons and neural networks in 3D. *Neurocomputing* 70(13):327–342. doi:10.1016/j.neucom.2006.01.028. <http://www.sciencedirect.com/science/article/pii/S0925231206001135>, http://www.sciencedirect.com/science?_ob=MiamiImageURL&_cid=271597&_user=626711&_pii=S0925231206001135<Dec-2006-&view=c&originContentFamily=serial&wchp=dG-LbVIV-zSkWb&md5=9da74d0e972931efe3214699d6bb6827s2.0-S0925231206001135-main.pdf

- Emoto K (2011) Dendrite remodeling in development and disease. *Dev Growth Differ* 53(3):277–286. doi:10.1111/j.1440-169X.2010.01242.x. <http://onlinelibrary.wiley.com/doi/10.1111/j.1440-169X.2010.01242.x/abstract>, <http://onlinelibrary.wiley.com/store/101111/j.1440-169X.2010.01242.x/asset/j.1440-169X.2010.01242.x.pdf?v=1&t=h4o6bw2j&s=d0acd7a2335110b46fe0e5f8f0054b76e2d8e776>
- Feng N, Ning G, Zheng X (2005) A framework for simulating axon guidance. *Neurocomputing* 68:70–84. doi:10.1016/j.neucom.2005.01.007. <http://www.sciencedirect.com/science/article/pii/S0925231205000391>, http://www.sciencedirect.com/science?_ob=MiamiImageURL&_cid=271597&_user=626711&_pii=S0925231205000391<Oct-2005&view=c&originContentFamily=serial&wchp=dGlbVlk-zSkzk&md5=799ae541d9e4614d4a88d2107b3fc06&s2.0-S0165027006001646-main.pdf
- Hamilton P (1993) A language to describe the growth of neurites. *Biol Cybern* 68(6):559–565. <http://www.ncbi.nlm.nih.gov/pubmed/8324064>
- Hillman D (1979) Neuronal shape parameters and substructures as a basis of neuronal form. In: Schmitt FO, Worden FG (eds) *The neurosciences, fourth study program*. MIT Press, Cambridge, MA, pp 477–498
- Irwin SA, Galvez R, Greenough WT (2000) Dendritic spine structural anomalies in fragile-X mental retardation syndrome. *Cereb Cortex* 10(10):1038–1044. doi:10.1093/cercor/10.10.1038. <http://cercor.oxfordjournals.org/content/10/10/1038>, <http://cercor.oxfordjournals.org/content/10/10/1038.full.pdf>
- Jan YN, Jan LY (2010) Branching out: mechanisms of dendritic arborization. *Nat Rev Neurosci* 11(5):316–328. doi:10.1038/nrn2836. <http://dx.doi.org/10.1038/nrn2836>, <http://www.nature.com/nrn/journal/v11/n5/full/nrn2836.html>, <http://www.nature.com/nrn/journal/v11/n5/pdf/nrn2836.pdf>
- Koch C, Segev I (2000) The role of single neurons in information processing. *Nat Neurosci* 3:1171–1177. doi:10.1038/81444. http://www.nature.com/neuro/journal/v3/n11s/full/nn1100_1171.html, http://www.nature.com/neuro/journal/v3/n11s/pdf/nn1100_1171.pdf
- Koene R, Tijms B, van Hees P, Postma F, de Ridder A, Ramakers G, van Pelt J, van Ooyen A (2009) NETMORPH: a framework for the stochastic generation of large scale neuronal networks with realistic neuron morphologies. *Neuroinformatics* 7(3):195–210. doi:10.1007/s12021-009-9052-3. <http://www.springerlink.com/content/b17m2162m5j78w06/abstract/>, <http://www.springerlink.com/content/b17m2162m5j78w06/fulltext.pdf>
- Lindenmayer A (1968) Mathematical models for cellular interactions in development. II. Simple and branching filaments with two-sided inputs. *J Theor Biol* 18:300–315
- Lindsay KA, Maxwell DJ, Rosenberg JR, Tucker G (2007) A new approach to reconstruction models of dendritic branching patterns. *Math Biosci* 205(2):271–296. doi:10.1016/j.mbs.2006.08.005. <http://www.ncbi.nlm.nih.gov/pubmed/17011000>
- London M, Häusser M (2005) Dendritic computation. *Annu Rev Neurosci* 28(1):503–532. doi:10.1146/annurev.neuro.28.061604.135703. <http://www.annualreviews.org/doi/abs/101146/annurev.neuro.28.061604.135703>
- Luczak A (2006) Spatial embedding of neuronal trees modeled by diffusive growth. *J Neurosci Methods* 157(1):132–141. doi:10.1016/j.jneumeth.2006.03.024. <http://www.sciencedirect.com/science/article/pii/S0165027006001646>, http://www.sciencedirect.com/science?_ob=MiamiImageURL&_cid=271055&_user=626711&_pii=S0165027006001646<Oct-2006&view=c&originContentFamily=serial&wchp=dGlbVlk-zSkzk&md5=799ae541d9e4614d4a88d2107b3fc06&s2.0-S0165027006001646-main.pdf
- McCormick B, Mulchandani K (1994) L-system modeling of neurons. *Proc SPIE* 2359:693–705
- Memelli H, Torben-Nielsen B, Kozloski J (2013) Self-referential forces are sufficient to explain different dendritic morphologies. *Front Neuroinform* 7:1–12. doi:10.3389/fninf.2013.00001. <http://www.frontiersin.org/Neuroinformatics/10.3389/fninf.2013.00001/abstract>
- Moolman DL, Vitolo OV, Vonsattel JPG, Shelanski ML (2004) Dendrite and dendritic spine alterations in Alzheimer models. *J Neurocytol* 33(3):377–387. doi:10.1023/B:NEUR.0000044197.83514.64. <http://www.ncbi.nlm.nih.gov/pubmed/15475691>
- Nowakowski RS, Hayes NL, Egger MD (1992) Competitive interactions during dendritic growth: a simple stochastic growth algorithm. *Brain Res* 576(1):152–156. doi:10.1016/0006-8993(92)90622-G. <http://www.sciencedirect.com/science/article/pii/000689939290622G>, http://www.sciencedirect.com/science?_ob=MiamiImageURL&_cid=271080&_user=626711&_pii=000689939290622G&Mar-1992&view=c&originContentFamily=serial&wchp=dGLbVIV-zSkzk&md5=b28c56d98f45a58fd67853245bc3e8a&s2.0-000689939290622G-main.pdf
- Pellionisz A (1989) Neural geometry: towards a fractal model of neurons. In: Cotterill RMJ (ed) *Models of brain function*. Cambridge University Press, Cambridge, pp 453–464
- Samsonovich AV, Ascoli GA (2003) Statistical morphological analysis of hippocampal principal neurons indicates cell-specific repulsion of dendrites from their own cell. *J Neurosci Res* 71(2):173–187. doi:10.1002/jnr.10475. <http://onlinelibrary.wiley.com/doi/101002/jnr.10475/abstract>, http://onlinelibrary.wiley.com/store/10.1002/jnr.10475/asset/10475_ftp.pdf?v=1%26t=h59wu5zz%26s=cd35b9d27%
- Samsonovich AV, Ascoli GA (2005) Statistical determinants of dendritic morphology in hippocampal pyramidal neurons: a hidden Markov model. *Hippocampus* 15(2):166–183. doi:10.1002/hipo.20041. <http://onlinelibrary.wiley.com/doi/101002/hipo.20041/abstract>, http://onlinelibrary.wiley.com/store/10.1002/hipo.20041/asset/20041_ftp.pdf?v=1%26t=h59wv506%26s=0b947fl

- Scott EK, Luo L (2001) How do dendrites take their shape? *Nat Neurosci* 4(4):359–365. doi:10.1038/86006. <http://www.ncbi.nlm.nih.gov/pubmed/11276225>
- Silver RA (2010) Neuronal arithmetic. *Nat Rev Neurosci* 11(7):474–489. doi:10.1038/nrn2864. <http://www.nature.com/nrn/journal/v11/n7/full/nrn2864.html>, <http://www.nature.com/nrn/journal/v11/n7/pdf/nrn2864.pdf>
- Tamori Y (1993) Theory of dendritic morphology. *Phys Rev E* 48(4):3124–3129. doi:10.1103/PhysRevE.48.3124
- Torben-Nielsen B, Vanderlooy S, Postma E (2008) Non-parametric algorithmic generation of neuronal morphologies. *Neuroinformatics* 6(4):257–277. doi:10.1007/s12021-008-9026-x. <http://www.springerlink.com/content/7t4wj2up5n604129/abstract/>, <http://www.springerlink.com/content/7t4wj2up5n604129/fulltext.pdf>
- Traub RD, Wong RK, Miles R, Michelson H (1991) A model of a CA3 hippocampal pyramidal neuron incorporating voltage-clamp data on intrinsic conductances. *J Neurophysiol* 66(2):635–650. <http://jn.physiology.org/content/66/2/635>, <http://jn.physiology.org/content/66/2/Z635.full.pdf>
- Uemura E, Carriquiry A, Kliemann W, Goodwin J (1995) Mathematical modeling of dendritic growth in vitro. *Brain Res* 671(2):187–194. <http://www.ncbi.nlm.nih.gov/pubmed/7743207>
- Uylings HB, Ruiz-Marcos A, van Pelt J (1986) The metric analysis of three-dimensional dendritic tree patterns: a methodological review. *J Neurosci Methods* 18(1–2): 127–151. <http://www.ncbi.nlm.nih.gov/pubmed/3540466>
- van Ooyen A (2001) Competition in the development of nerve connections: a review of models. *Network* 12(1):R1–R47. <http://www.ncbi.nlm.nih.gov/pubmed/11254084>
- van Pelt J, Verwer RW, Uylings HB (1986) Application of growth models to the topology of neuronal branching patterns. *J Neurosci Methods* 18(1–2):153–165. <http://www.ncbi.nlm.nih.gov/pubmed/3796039>
- Van Pelt J, Uylings HB, Verwer RW, Pentney RJ, Woldenberg MJ (1992) Tree asymmetry – a sensitive and practical measure for binary topological trees. *Bull Math Biol* 54(5):759–784. <http://www.ncbi.nlm.nih.gov/pubmed/1638259>
- Zubler F, Douglas R (2009) A framework for modeling the growth and development of neurons and networks. *Front Comput Neuroscience* 3:25. doi:10.3389/neuro.10.025.2009. <http://www.frontiersin.org/computationalneuroscience/10.3389/neuro.10.025.2009/abstract>, http://www.frontiersin.org/Journal/DownloadFile.ashx?pdf=1&fileId=13457&articleId=757&version=1&contentTypeId=15&fileName=025_2009.pdf
- Zubler F, Hauri A, Whatley AM, Douglas R (2011) An instruction language for self-construction in the context of neural networks. *Front Comput Neuroscience* 5:57. doi:10.3389/fncom.2011.00057. <http://www.frontiersin.org/ComputationalNeuroscience/10.3389/fncom.2011.00057/abstract>, <http://www.frontiersin.org/Journal/DownloadFile.ashx?pdf=1&fileId=35839&articleId=16467&version=1&contentTypeId=21&fileName=fncm-05-00057.pdf>

Systems Biology

► Metabotropic Receptors (G Protein Coupled Receptors)

Systems Biology Markup Language (SBML)

Michael Hucka

Computing and Mathematical Sciences,
California Institute of Technology, Pasadena,
CA, USA

Synonyms

[SBML](#)

Definition

SBML (the Systems Biology Markup Language, <http://sbml.org>) is a representation format designed to enable software systems to communicate and store computational models of biological processes. It is not intended as a universal language for quantitative models; rather, SBML's purpose is to serve as a *lingua franca* for exchanging the essential aspects of a computational model between widely different software systems and databases.

Detailed Description

A vast number of modeling and simulation software tools are available today for research in biological domains such as computational neuroscience. This wealth of resources is a boon to researchers, but it also presents interoperability problems. Different software tools for systems biology are implemented in different programming languages, run on

different operating systems, express models using different mathematical frameworks, provide different analysis methods, present different user interfaces, and support different data formats. Despite working with different tools, researchers want to disseminate their work widely, as well as reuse and extend the models of other researchers. They do not want to hardcode their models as software programs nor assume everyone uses the same computing environment; they need common exchange formats for representing their models in such a way that a variety of software systems can read and write them.

SBML (the Systems Biology Markup Language) is such an exchange format for communicating and storing computational models of biological processes (Hucka et al. 2003). It is not a universal language for representing all possible models; rather, it enables communication of the essential aspects of a model, together with annotations that permit any aspect of the model to be elaborated and linked to external data resources. An important principle in SBML is that models are decomposed into explicitly labeled constituent elements (e.g., substances involved in processes, compartments where they are located, etc.); models are *not* cast directly into a specific form such as differential equations. This abstract approach makes it possible for a software tool to translate the SBML form of a model into whatever internal form the tool actually uses – whether that be differential equations, stochastic systems, or some other framework. Although SBML has its roots in general simulations of biochemical reaction networks, it can be used more generally to express other types of models where biological entities are involved in, and modified by, processes that occur over time. It is used today in research on a number of topics, including cell signaling pathways, metabolic pathways, biochemical reactions, gene regulation, and many others.

The latest generation of SBML, which is called SBML Level 3, is modular in the sense of having a defined core set of features and optional *packages* that add features on top of the core. This modular approach means that models can declare which feature-sets they use, and likewise, software tools can declare which packages they support. It also means that the development of SBML

Level 3 can proceed in a modular fashion. SBML Level 3 package development is today an ongoing activity, with packages being created to extend SBML in many areas that its core functionality does not directly support. Examples include models whose species have structure and/or state variables, models with spatially nonhomogeneous compartments and spatially dependent processes, and models in which species and processes refer to qualitative entities and processes rather than quantitative ones.

Cross-References

- [Bimolecular Reactions, Modeling of](#)
- [CellML](#)
- [Dynamical Systems: Overview](#)
- [Enzyme Kinetics, Modeling of](#)
- [Gillespie Algorithm for Biochemical Reaction Simulation](#)
- [Model Reproducibility: Overview](#)
- [Numerical Integration Methods](#)
- [Signaling Pathways, Modeling of](#)
- [Software Tools for Modeling in Computational Neuroscience: Overview](#)

Reference

Hucka M, Finney A, Sauro HM, Bolouri H, Doyle JC, Kitano H, Arkin AP, Bornstein BJ, Bray D, Cornish-Bowden A, Cuellar AA, Dronov S, Gilles ED, Ginkel M, Gor V, Goryanin II, Hedley WJ, Hodgman TC, Hofmeyr J-HS, Hunter PJ, Juty NS, Kasberger JL, Kremling A, Kummer U, Le Novère N, Loew LM, Lucio D, Mendes P, Minch E, Mjolsness ED, Nakayama Y, Nelson MR, Nielsen PF, Sakurada T, Schaff JC, Shapiro BE, Shimizu TS, Spence HD, Stelling J, Takahashi K, Tomita M, Wagner JM, Wang J (2003) The systems biology markup language (SBML): a medium for representation and exchange of biochemical network models. *Bioinformatics* 19:524–531

Systems with Two or More Phase-Spaces

- [Multistability: Stopping Events with Single Pulses](#)